Nano Studies

14

2016

NANO STUDIES

14

2016

Nano Studies, 2016, 14

Nano Studies is a biannual scientific journal published in Georgia.

Nano Studies' topics of interest include Nanoscience and Nanotechnology, and related problems of Physics, Chemistry and Materials Science.

Nano Studies publish following categories of scientific articles: research papers, communications, reviews and discussions.

Nano Studies publish scientific articles in English and also in Georgian and in Russian.

Summaries of all the articles of **Nano Studies** are referred in **Georgian Abstracts Journal** and are accessible in **Tech Inform** (Georgia Central Institute for Scientific and Technical Information) database: **http://www.tech.caucasus.net**

Full-texts of articles published in **Nano Studies** are free-accessible at the journal's web-site: **http://www.eurchembull.com/NanoStudies/index.htm**

CONTENTS

Regular Papers

Contents.

Proceedings of the Nano – 2016: 4th International Conference "Nanotechnologies", October 24 – 27, 2016, Tbilisi, Georgia

Contents.

PERSPECTIVES OF MAGNETIC AND NANOSIZED METAL-CONTAINING AMORPHOUS CARBON COMPOSITE CHEMOSORBENTS AND CATALYSTS

T. Kocsis [1], Z. May [1], Z. Czégény [1], B. Sreedhar [2],
R. P. Pawar [3], R. Kant [4], I. E. Sajó [5], K. K. Banerji [6], L. Kótai [1]

[1] Institute of Materials & Environmental Chemistry
Research Center for Natural Sciences
Hungarian Academy of Sciences
Budapest, Hungary
kotail@eurchembull.com
[2] Indian Institute of Chemical Technology
Andra Pradesh, Hyderabad, India
[3] Department of Chemistry
Deogiri College
Aurangabad, Maharashtra, India
[4] X-ray Crystallography Laboratory
Post-Graduate Department of Physics & Electronics
University of Jammu
Jammu, Tawi, India
[5] János Szentagothai Research Center
University of Pecs
Pecs, Hungary
[6] Department of Chemistry
Jain Narain Vyas University
Jodhpur, Rajasthan, India

1. Introduction

Amorphous carbon and its composites are widely used materials in various fields of industry and environmental protection including water purification, as adsorbents in food and chemical industry, chemosorbents, catalysts and support materials [1 – 8]. The properties of these carbonaceous materials are strongly depends on the nature and size of the materials distributed within or on the surface of the carbon network [3, 9 – 11]. Therefore, controlling of these parameters opens unlimited possibilities to prepare materials with unique properties. This micro-review discusses some selected pieces of information about preparation and properties of some metal and metal-compound containing amorphous carbon composites, especially the way to prepare these materials from ion-exchangers and properties of nano-iron-containing composites with magnetic properties. Magnetic filtration is a very effective process for the fast removal of magnetic materials from waste streams, however, since most pollutants are non-magnetic, it is essential to develop efficient magnetic extractants that can absorb and magnetize organic compounds and contaminants [12].

2. Preparation and properties of metal-containing carbon composites

The most typical and known preparation method of nanosize metal or metal-compound containing-carbon adsorbents and chemosorbents consists of an impregnation step and a transformation step when a metal-containing species is adsorbed / fixed / deposited on the surface of the carbon surface then a heat or chemical treatment are performed to transform the initial metal containing species into a non-soluble and reactive materials which are bound to the surface of the carbon [6]. Typically, the active components prepared in this way are located only on the surface of the carbon [13] and theirs activity and properties strongly depends on the chemical nature and size of the surface species [14, 15]. The chemical nature of the initial metal-compounds also may play key role in the activation of the surface of the carbon via catalyzing of surface reactions which can increase the surface area [16, 17].

Another typical way to prepare the metal or metal-containing carbon materials is when a metal-compound is mixed with an organic carbon source then a controlled atmosphere carbonization process is performed when the carbon network is formed in the presence of the metal species. The chemical identity and sizes of the metal containing ones depend on many factors such as the nature of starting materials, the reaction conditions and the counter-ion of the metal salt [18].

The most promising variation of this method is, when instead of a physical mixture of metal compounds and organic polymers a chemical bound form of metals to polymer is used, e.g. the metals are fixed through functional groups onto the polymer network ensuring homogeneous distribution and mixing between the carbon and metal atoms at atomic level. This way is the most promising method prepare nanosize metal or metal compounds (oxides, sulphides) containing carbons. The precursors can be prepared easily from so called organic ion exchangers containing phenoxy, carboxylic, iminodiacetate, sulfhydryl, phosphoryl, quinolinyl or any other functional groups which can bound metals in various valence states via ionic or coordinate bonds [19].

2.1. Coating of carbon surface with metal containing species

The magnetic properties of Fe oxides and the adsorption features of activated carbon have been combined to produce magnetic adsorbents using chemical co-precipitation [20, 21]. The results indicated that maghemite is the main magnetic phase present and the presence of iron oxide did not significantly affect the surface area or pore structure of activated carbon. All composites prepared at different temperatures varying from room temperature to 70 °C had good magnetism and could be well separated from aquatic system by a magnet [20]. In situ formation of coated superparamagnetic iron nanoparticles in the pores of carbons initially impregnated with ferric salt solutions has been also described [22]. A more easy way to prepare magnetic activated carbons is to impregnate the charcoal with Fe oxalate [23] or with $Fe(CO)_5$ in absolute ether [24] and a subsequent thermal treatment in a hydrogen atmosphere.

Nickel containing metallized carbons were prepared by adsorption and thermal decomposition of nickel (II) format on activated carbon [25]. A magnetic substrate composed of nickel covered carbon could also be prepared with impregnating charcoal with $Ni(NO_3)_2 \cdot 6H_2O$ and subsequent thermal treatment [24].

2.2. Carbonization of organic materials in the presence of metal compounds

Two main kinds of organic precursors have been used in this type of syntheses, namely natural e.g. cellulose or proteins containing resources or synthetic materials such as functionalized ethylene-type polymers.

The small particles of wood were treated by aq. solutions of $Fe(NO_3)_3$, $Co(NO_3)_2$, $Ni(NO_3)_2$, and $Cu(NO_3)_2$ subsequently dried in vacuum, and then calcinated in He-flow at 293 – 1073 K by gradually increasing temperature and keeping at certain (e.g., 373 or 473 K) temperatures for 1 h. Samples calcined at > 873 K contained α-Fe and Fe_3C and α-Co and β-Co and NiO and Cu + Cu_2O, respectively. In each series surface area passed through a maximum on an increase of calcination temperature. The sorbents selectively adsorb gaseous or liquid compounds, which at normal conditions react with the metal. Cu-containing sorbents removed efficiently iodine from aq. solutions [18].

Other natural materials, for example proteins containing metal sources (e.g., 3 – 5 nm of Fe) were heat-treated under controlled oxygen atmosphere, when the produced carbon-like products could be used as oxygen reduction electrodes and humidity-controlling materials [26].

Poly(vinylidene chloride)-co-poly(vinyl chloride) was dissolved in 2-butanone and nickel powder were mixed in it, the solvent was evaporated, the dried mixture was needed to uniformly disperse the nickel, and the mass was carbonized and milled to particles of approximately 0.045 mm diameter [27].

Activated carbons as catalyst carrier materials were prepared by carbonization at 850 °C in an inert atmosphere and subsequent activation at 850 – 950 °C of polystyrene / divinylbenzene copolymers containing 4 – 18 wt. % divinylbenzene and various metal compounds such as silver and copper salts. The carbon activating agent was sulfuric acid and oleum, when the produced activated carbon is spherical having an inner BET surface of 1000 – 1750 g / cm^2 [28]. Carbonization of various divinylbenzene-derived polymers with using $ZnCl_2$ as activator produced highly mesoporous spherical activated carbons with high yield (>54%) and high mesopore fraction (around 80 %) [29].

2.3. Carbonization of ion exchange resins

The principle of the method is based on the thermal behavior of various styrene-divinylbenzene copolymers (**Figure 1**). These copolymers as alkylaromatic compounds has high carbon content and they have been used as starting materials in the preparation of carbons with high mechanical strength [30]. The properties of the products, however, strongly depend on the pyrolysis conditions and divinylbenzene content of the copolymers. The higher divinylbenzene content the harder grains of carbon are obtained [30]. Activated carbon with very high mechanical strength and sorption capacity was made from the spent sulfonated or aminated ion-exchange resins by pyrolysis at 600 °C under vacuum and activation by steam at 800 °C. The pyrolysis and activation conditions have great influence on the carbon porosity, strength, sorption capacity and other properties [31].

In various metal-containing (alkali and alkaline earth metals) sulfonated cation exchangers, both the desulfonation and the matrix degradation are mainly influenced by the initial composition (ion type, preliminary contact with organic media, degree of dehydration, etc.) of the ion exchanger [32]. Similarly, the metal complexes (Au^{3+}, Cr^{3+}, Cu^{2+}, Fe^{3+}, Mn^{2+}, and Pt^{4+}) formed from the chemically modified chloromethylated poly(styrene)–PAN (CMPS–PAN)

as a resin chelating ion exchanger was thermally degraded (in air atmosphere), and the results showed that the decomposition stages were affected by the presence of the investigated metal ions. The thermal degradation of CMPS–PAN resin in the presence of the ions showed different stability of the resin in the following decreasing order: $Au^{3+} > Pt^{4+} > Mn^{2+} > Cu^{2+} > Cr^{3+} > Fe^{3+}$ [33]. Polymeric Cu (II) complexes were prepared by using the polyampholytes PA–1, PA–22, or PA–8, or the phosphonic acid cation exchanger KFP. Redox processes occurred on heating in air. The coordination state of Cu was changed, the Cu–N bonds were broken while Cu–O bonds were formed. The conversion rates depended on temperature and type of functional groups in the ion exchanger [34]. The valence state or chemical form of the metal also had important influence on the thermal decomposition temperature of ion exchangers. For example, the decomposition temperature of the cation exchanger was higher in their Cr^{3+}-form than in the H^+-form, while the chromate-form anion exchanger showed an exothermic peak even at 200 °C owing to Hofmann degradation of quaternary ammonium groups with subsequent oxidation to ethylene [35].
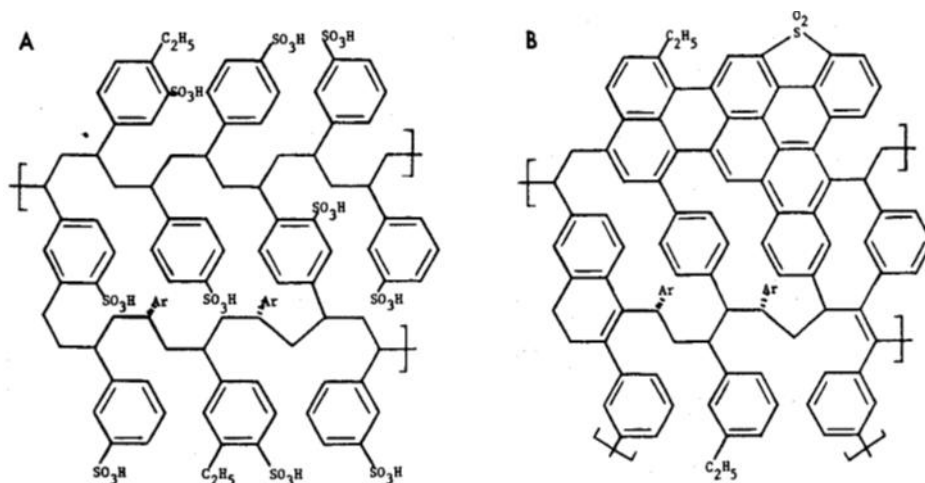
Figure 1. Schematic representation of carbon network formation.

Spherical activated carbon containing ZnO photocatalyst was prepared using strong and weak acid ion-exchange resins as starting materials. These resins were treated with an aq. solution of Zn^{2+} or $[Zn(NH_3)_4]^{2+}$ and the treated resins were carbonized and activated. When strong acid ion-exchange resins were used to prepare activated carbon containing Zn, the Zn was in ZnS form, in case of the use of weak acid ion-exchange resins in ZnO form. All the samples had spherical shape and had a good BET specific surface area [36]. If the $[Zn(NH_3)_4]^{2+}$ complex form resins were carbonized for 10 min in nitrogen gas, the activated carbons with hexagonal ZnO were prepared, and the amount of hexagonal ZnO decreases with an increase in the carbonization temperature. However, the specific surface areas of carbon samples increases with increasing the carbonization temperature of the resin [37]. The antibacterial activity on carbon samples containing ZnO prepared from $[Zn(NH_3)_4]^{2+}$ form ion exchangers increases with a decrease of the carbonization temperature and an increase of the amount of ZnO in the samples. From a comparison of the antibacterial activity against *Staphylococcus aureus* and *Escherichia coli*, it was found that the activity against *Staphylococcus aureus* was stronger than that against *Escherichia coli*. The concentration of hydrogen peroxide increased linearly with an increase in the amount of carbon in samples. The occurrence of antibacterial activity was found to be due to the generation of hydrogen peroxide from ZnO in activated carbons [38].

A sample of commercial amberlyst 200 (sulfonated divinylbenzene-styrene copolymer) ion exchange resins in Fe (III) form was pyrolyzed under 7 L / min argon stream by heating to 706 °C for 6 h and was held for 0.5 h at that temperature. The product was cooled in an oven under Ar to give 43 % yield of absorbent with surface area 222 m^2 / g, and bulk density was found to be 0.67 g / mL. The products are useful as molecular sieves and for removing impurities, such as sulfur compounds and monomers from gases, liquid streams or wastes [39]. Pyrolysis of dry amberlyst IRC–50 (DVB / methacrylic acid) resin in Fe (III) form (loaded with aq. $FeCl_3 \cdot 6H_2O$ (1 M) in a column over a period of 2 h) at 700 °C over a period of 4 h in an N_2 atmosphere get Fe–AC catalyst, acidity from ammonia gas, NH_3–TPD, analysis and was found to be 0.0130 mmol / g catalyst, specific surface areas determined by BET nitrogen isotherms was found to be 257 m^2 / g, C : H ratio was 18.4 : 1, iron was speciated as Fe_2O_3 as acylation catalysts [40].

Carbon encapsulated Fe and Ni nano particles were prepared by pyrolysis of Fe and Ni-loaded cation exchange resin (Fe–Ni / D113) at 400, 500, 600 and 700 °C. XRD and TEM results showed that the nano particle size increases with an increase in the pyrolysis temperature. Magnetic test result shows that the pyrolyzate obtained at 400 °C was superparamagnetic. The coercivities (H_c) at room temperature of the pyrolyzates obtained at 500, 600, and 700 °C were much higher than that of the corresponding bulk materials, and the H_c value was influenced by the size of the nanoparticles. The saturation magnetizations (M_s) of all the pyrolyzates were lower than that of the corresponding bulk materials and increased with the pyrolysis temperature [41]. Regarding the preparation of the catalysts, iron itself plays a promoting role in the formation or destruction of oxygen surface groups during calcinations, the latter being only observed when the activated carbon was oxidized with HNO_3. The introduction of iron enhanced the activity in phenol recovery, compared to activated carbon with the same amounts of oxygen surface groups. This can be attributed to the increase in the acidity that the iron itself provokes and the promoter role of Fe in the oxidation reaction of phenol. After the catalytic wet air oxidation process, surface area and micropore volume decreased whereas the amount of oxygen surface groups increased, as well as the total acidity, except for the activated carbon treated with HNO_3. Also the iron dispersion diminishes significantly. However, the final surface distribution did not affect the catalyst activity. The presence of Fe reduced the detrimental effect of wet oxidation on the porous structure of the activated carbons [42].

Systematical studies on various kinds of ion exchangers (styrene-divinylbenzene, acrylic acid-styrene-divinylbenzene) with various functional groups and metal forms and valences have been done in order to prepare nanosize metal or metal-compound containing carbon sorbents [43 – 46]. In this way, a simple method has been developed to prepare nanosized (10 – 100 nm) metal, metal-oxide, metal-sulphide (or nitride and carbide) containing amorphous carbon nanocomposites with ball-like (spherical) shape, better hardness, low hydrodynamic resistance, and some other advantageous physical and chemical properties which ensures wider usability in various fields of industry and environmental protection [43 – 47]. The essential step is when a metal ion (the same metal can be used in various valence or anionic or complex form, e.g. Mn (II), Mn (III), MnO_4^-, or Fe (II) or Fe (III), Cr (III) or CrO_4^{2-}, etc.) is introduced and combined with a selected functional group. The chemical nature of the metal-containing particle is primarily depends on the metal speciation fixed on the resins or on the nature of the functional group. The next important factor is the selection of the appropriate carbonization conditions. During the carbonization process of the metal-containing ion

exchangers, the conditions of functional groups loosing will be changed due to the presence of metals, and with the decomposition intermediates the metal containing species can form different kind of compounds, e.g., sulphides or oxides in case of sulphonated or carboxylated ion exchangers, respectively. Nanosized metal sulphide type chemosorbents has been prepared in the concurrent reduction of metal centers and sulphonate groups of metal forms of sulphonated ion exchangers. In the case of electronegative metals, the reduction of sulphonate groups leads to formation of lower valence metal sulphides such as MnS, FeS, ZnS or NiS, while in the case of copper, only metallic copper and sulphur dioxide are formed. Similar conditions in the case of carboxylate type ion exchangers led to metallic Cu but to ZnO, MnO, or NiO. In case of iron (II) and iron (III) forms of ion-exchangers, depending on the reaction temperature, valence state of iron salt used and the reaction time, amorphous carbons formed containing different nanosized magnetic phases (FeO, Fe_2O_3, Fe_3O_4, and Fe).

Besides the type of functional groups of ion exchanger and the type and valence of the used metals, the reaction temperature, reaction time, and cross-linking of initial polymer matrix have strong influence on the size, nature, and properties of the formed metal (metal oxide or sulphide) species located in the amorphous carbon.

Table 1. The metal-containing species formed under pyrolysis of styrene-divinylbenzene based ion-exchangers depending on the functional groups and carbonization temperature.

Cross-linker	Polymer base	Functional group	Metal-ion	Temperature / time	Product
DVB	STY	SO_3H	Mn^{II}, Ni^{II}, Zn^{II}	500 °C / 2 h	MnS, NiS, ZnS
		SO_3H	Cu^{II}	500 °C / 2 h	Cu
		$N(CH_2COO)_2$	Fe (II), Fe (III) as chloride, nitrate	400 – 800 °C / 2 – 12 h	Fe, FeO, Fe_2O_3, Fe_3O_4, Fe_3C, Fe_2N
		$N(CH_2COO)_2$	Fe (II), Fe (III) as sulphate	400 – 800 °C / 2 – 12 h	FeS, FeS_2, Fe, Fe_3C
		$N(CH_2COO)_2$	Cu(II) as sulphate	500 °C / 2h	Cu
	STY–MMA	COOH	Mn^{II}, Zn^{II}, Ni^{II}	500 °C / 2 h	MnO, ZnO, NiO
			Cu^{II}	500 °C / 2 h	Cu

The composites given in **Table 1** were prepared in a usual way with loading of hydrogen forms of sulphonated ion exchangers with using saturated aqueous metal salt solutions. The carbon composites were prepared by controlled-temperature carbonization. Depending on the ionic form and the degree of saturation of the ion exchanger the sulphur content of the ion-exchangers can partially transform into metal sulphides, SO_3 or SO_2 which could be detected by TG–MS unambiguously. The yield of metal / metal sulphide containing carbon composites strongly depends on the nature of metal, ion-exchanger and the carbonization conditions as well. Completely (100 %) and partially saturated forms (25 and 50 % of their capacity) of

variant KS and varion KSM resins were carbonized at 500 °C for 2 h. Depending on the nature of metal, sulphide (MnS, NiS and ZnS, $FeS_{0.95}$) species or elemental metal (Cu, α-Fe) were formed. In case of iron, $Fe_{0.95}S$ and α-Fe were formed together at 800 °C, the sulphide component was the major product, however the ratio of $Fe_{0.95}S$: α-Fe depended on the valence form (Fe^{II} or Fe^{III}) of the iron loaded onto the ion exchanger resin. The saturation degree had no important effect on the chemical form of the metal in the composites formed at the studied temperature range. The shape of the formed carbon particles is bead-like (**Figure 2**.) and the hardness of the formed carbon beads is proportional to the divinylbenzene content of the starting polymer. Higher is the divinylbenzene content, harder is the beads of carbon formed. All the beads have a leakage path due to evolution of gases which are emitted at the weakest part of ball-like bead causing leakage. Due to evolution of large amount of gases within the structure of beads which evolve at the time when the resistance of the resin material becomes lesser than the inner pressure, an "explosion-like" evolution of gases (SO_2, H_2O, hydrocarbon crack gases) could be observed, and the resin beads "jump" during the carbonization. The formed ball-like metal-containing activated carbon beads have low hydrodynamic resistance towards fluid streams and these materials are potential candidates for treatment of liquid flows. The SEM picture of the nickel-carbon composite with ca. 30 % nickel content can be seen in **Figure 2** [43 – 45].
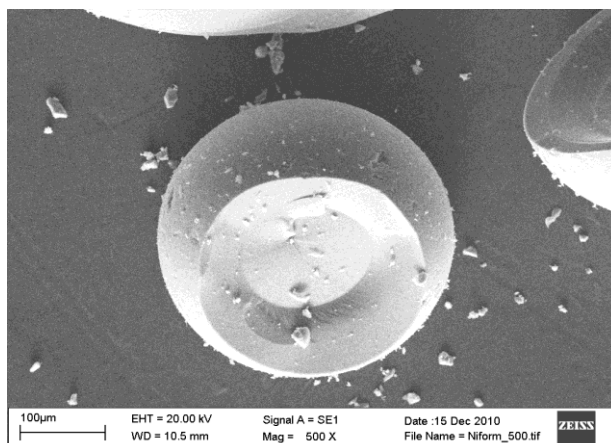
Figure 2. SEM picture of the nickel sulphide containing carbon composite bead prepared from lewatit S100 (8 % divinylbenzene content) loaded fully with Ni (II) at 500 °C for 2 h.

The bead-like resins formed in the pyrolysis of lewatit S100 resin contained 2.3 m² g⁻¹ nickel (II) result a carbon composite of NiS with 35 % nickel content. The specific surface area was found to be 371 m² g⁻¹, but the specific surface area strongly depends on the pyrolysis temperature and the divinylbenzene conten (porosity) of the starting ion exchanger. The specific surface areas of nickel sulphide containing carbons formed at 500 °C in 2 h in the case of varion KS and KS660 resins were found to be 172 and 341 m² g⁻¹, respectively [43 – 45].

Two kinds of iron form (loaded with Fe^{II} or Fe^{III}) of varion KSM resins were carbonised at 800 °C for 2 h. The same products were formed, $Fe_{0.95}S$ and metallic iron (α-Fe), however, the ratio of these products depended on the valence of the iron loaded on the ion-exchanger. The approximate ratio of iron sulphide / α-Fe were found to be 8 : 1 and 7 : 2 in the case of Fe^{III} and Fe^{II} forms of the varion KSM ion exchanger, respectively. This can be the consequence of the oxidizing nature of Fe^{III} which partially prevents the complete reduction of sulphonic acid group into sulphide. The metal or metal-compound containing activated carbons can be

activated with vapor or other methods and their metal content can also be removed by acidic treatment, e.g. with digestion in dilute HCl or HNO$_3$. The resultant metallic salt solutions can be recycled into loading new ion exchangers into metallic forms, and the residual carbons can be utilized as simple activated carbons as well [43 – 45]. The nanosized metal or metal-compound containing carbons prepared in this way are promising new materials and could effectively be used as chemosorbents or catalyst precursors, for example metal-sulphides (MnS, FeS, NiS, ZnS) containing chemosorbents for mercury removal, metal-oxide type or metal sulphide (ZnO or ZnS) carbon composites for photocatalytic reaction for COD removal from wastewaters, or metallic nanosized copper containing carbons as chemosorbents for mercury, radioactive iodine, or as catalysts for preparation of triazoles. Iron oxide containing carbons can be tested as sorbents for phosphate or arsenic removal from drinking water and as catalyst for waste free synthesis of paracetamol and nanosized iron containing carbons can be used as magnetisable carbon supports for noble metals (Pd, Au, Pt, Rh, Ir, Ru, and Ag) or Cu catalysts.
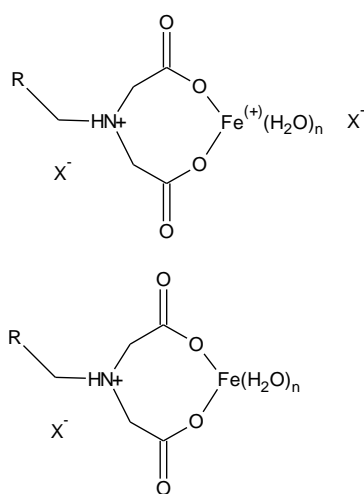
Figure 3. Valence and counter-ion relations in Fe (II)
and Fe (III) loaded iminodiacetate ion-exchangers
using FeX$_2$ and FeX$_3$ salts during the ion-exchange.

The iminodiacetate functional group containing ion-exchangers has a special interest, because the amino-group is protonated and makes an ionic group with the counter-ion of the salt used for loading the metal into the ion exchanger (**Figure 3**). Using iminodiacetate type (divalent metal ion selective) ion exchangers, the role of counter-ion of used metals salts becomes one of the key factors, especially in the case of trivalent metal salts, when not only the protonated nitrogen atom of iminodiacetate group but the third valence of the used metal (e.g. Fe (III)) are compensated with the negative charge of the original counter ion of the used metal salt). The reason for it, that in case of trivalent metals like iron (III), the chelate-forming group will compensate only two positive charges of the iron (III), but the third valence of iron will not be neutralized with the neighboring iminodiacetate group but with the original counter-ion of the salt used during the ion-exchange. It means, the amount of the counter-ion is more than in case of divalent metals, because the counter ion will neutralize the third charge of the metal and the minimum ion charge as well [45]. Due to this, for example, in case of iron (III)-loaded iminodiacetate resins, the iron (III) chloride loaded resin gives metallic iron and mainly magnetic iron oxide type carbons, but the $[-CH_2-NH^+(COO)_2{}^{2-}Fe^{3+}]SO_4{}^{2-}$ type iron (III) sulphate loaded resin gives FeS$_{0.95}$ (pyrrhotite) and FeS$_2$ containing carbon phase.

Table 2. Distribution of iron-containing species in the samples
produced during thermolysis of $Fe_2(SO_4)_3$ loaded iminodiacetate
functionalized STY–DVB ion-exchanger at 4 or 8 h heating time [45].

Carbonization temperature, ℃	Heating time, h	α-Fe	γ-Fe	Fe₃C	FeS(H)	FeS(M)	FeS₂	Fe₃O₄
400	4				5	29	51	14
500	4				7	32	44	17
600	4				3	34	47	16
700	4	16	7			39	38	
800	4	5	16	13		39	28	
900	8		20	16		41	23	

Table 3. Distribution of iron-containing species in the samples produced
during thermolysis of $Fe(NO_3)_3$ loaded iminodiacetate functionalized
STY–DVB ion-exchanger at 4 or 8 h heating time [45, 46].

Carbonization temperature, ℃	Heating time, h	α-Fe	γ-Fe	Fe₃C	Fe₃N	Fe₄N	Fe₃O₄	FeO
400	4						100	
500	4						100	
	8						100	
600	4	100						
	8	86	14					
700	4	15	8	77				
	8	17		83				
800	4	25		75				
	8	9	5	86				
900	4		9	91				
	8	8	8	84				

The especially high extent of variability of the conditions have influence on the product distribution in case of iminodiacetate resins and iron-salts, the conditions to prepare magnetisable iron species (α-Fe or Fe₃O₄) have also been found [45, 46]. Since magnetic separation of activated carbons (AC) commonly used as efficient adsorbents to remove contaminants is an important area, the conditions to prepare samples with high magnetic separatibility i.e., the effect of reaction conditions, valence of iron, counter-ion, temperature, reaction time, etc. have been studied in detail. In order to increase the amount of magnetic components, the chloride, sulphate and nitrate salts were used with iminodiacetate type (varion BIM) ion-exchanger resin. The distribution of the iron-containing species is given in **Tables 2** and **3**.

The iron particles are formed in 100 % yield at 600 °C with 10 nm size and high reactivity. The surface of the samples are covered immediately with iron (III) oxide, but it save the iron from the further oxidation and the samples keep their magnetizability. The incorporation of α-iron particles into the activated carbon could greatly enhance its manipulation through magnetic separation or mixing. High and pure Fe₃O₄ containing carbons was prepared by thermolysis of Fe(NO₃)₃ loaded on iminodiacetate functionalized STY–DVB

ion-exchanger by 4 or 8 h heating [45, 46]. Heating at 900 °C for 8 h led to carbon-nanotube covered activated carbon balls containing magnetic iron-containing particles [46].

It is a special interest to note that iron (III) nitrate loaded iminodiacetate-type resins gave mechanically strong, ball-like (due to high crosslinking with 6 % of divinylbenzene) metallic iron or magnetic iron-oxide containing carbons, which proved to be magnetic. Due to its mechanical strength this product is a promising carbon carrier with magnetic properties, which has superior importance in removing the spent valuable catalyst materials like noble metals. Although the low surface area of a balls do not allow fixing large amount of catalytically active species, by controlling the carbonization process of iron (III) nitrate loaded iminodiacetate type resins (900 °C, 2 h), a mass of carbon nanotubes covered balls are formed (**Figure 4**).
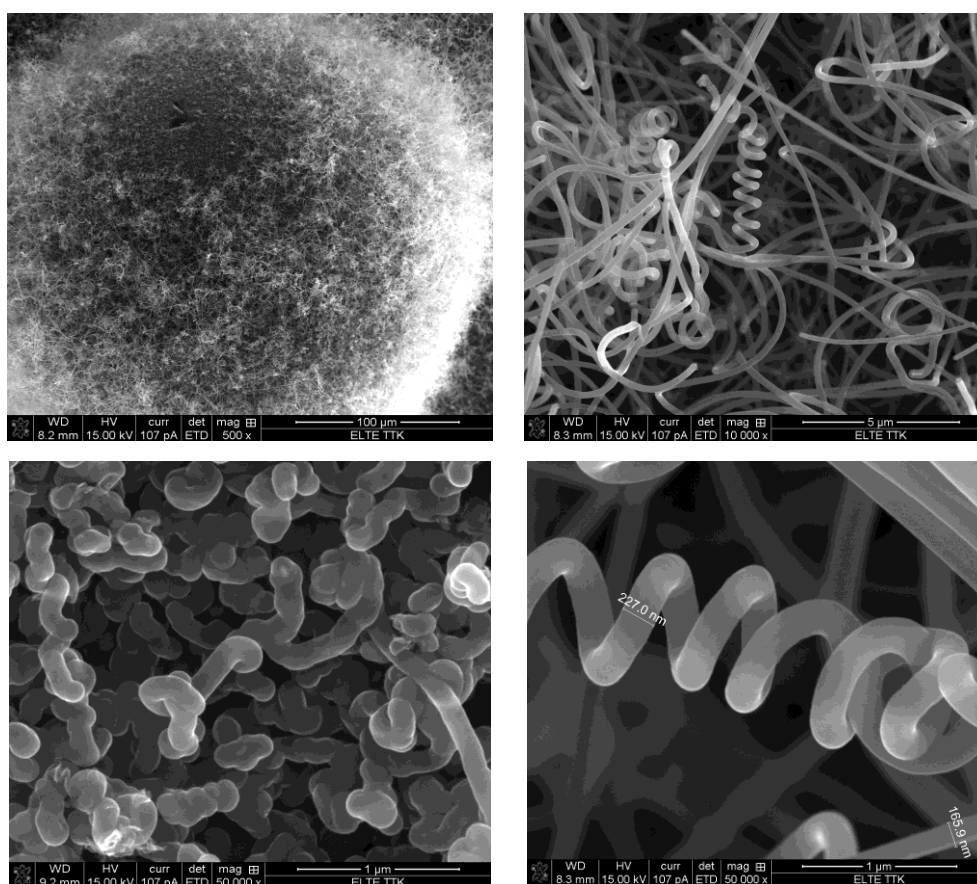
Figure 4. Scanning electron microscopic picture of carbon-nanotube covered magnetic carbon balls (iminodiacetate type resin, iron (III) nitrate loading, 900 °C , 2 h).

The magnetic particle containing Fe / C catalyst precursors can also prepared by impregnating activated C in $Fe(NO_3)_3 \cdot 9H_2O$ solution of different concentrations followed by heat treatment at 350, 500, 600, and 700 °C in Ar. Mossbauer spectra of these catalyst samples with different Fe contents indicated an interaction between Fe and activated C. The intensity of the interaction decreased with increased Fe loading. From the Mossbauer spectra of the catalysts treated at 350 °C, the amount of superparamagnetic $\alpha\text{-}Fe_2O_3$ per g of activated carbon could be counted as a function of iron loading. The dispersion of Fe on the surface of activated C is not uniform, and iron would redisperse and aggregate as iron salts decomposed. When the catalysts were treated at 600 °C, Fe_3O_4 (m) was converted to Fe_3O_4(s), giving further proof of the redispersion of the iron species. In combination with the results of treatment at 700 °C, it was

deduced that a reduced state iron with high dispersion was probably produced by the reduction of Fe_3O_4 (s). Moreover, the intensity of metal-support interaction was related to the distribution of energy on the activated carbon surface, the particle size of α-Fe_2O_3, and the degree of reduction of α-Fe_2O_3. The smaller the particle size of α-Fe_2O_3, the stronger the metal-support interaction was, and therefore, α-Fe_2O_3 was more difficult to be reduced [48]. When activated carbon/iron oxide magnetic composites were prepared with weight ratios of 2:1, 1.5:1 and 1:1 and characterized by powder XRD, TG, magnetization measurements, chemical analyses, TPR, N_2 adsorption-desorption isotherms, Mossbauer spectroscopy and SEM, the results suggested that the main magnetic phase present was maghemite (α-Fe_2O_3) with small amounts of magnetite (Fe_3O_4). Magnetization enhancement could be produced by treatment with H_2 at 600 °C to reduce maghemite to magnetite. N_2 adsorption measurements showed that the presence of iron oxides did not significantly affect on the surface area or the pore structure of the activated carbon. The adsorption isotherms of volatile organic compounds such as $CHCl_3$, phenol, chlorobenzene and drimarene red dye from aq. solution onto the composites also showed that the presence of iron oxide did not affect the adsorption capacity of the activated carbon [49].

The adsorption features of activated carbon and the magnetic properties of iron oxides may be combined in the iron-containing carbon composites to produce magnetic adsorbents. These magnetic particles can be used as adsorbent for a wide range of contaminants in water and can subsequently be removed from the medium by a simple magnetic procedure. Magnetic properties of adsorbed iron on sugar charcoal prepared by impregnating the charcoal with $Fe(CO)_5$ in absolute ether, decomposition of the carbonyl, and subsequent reduction in H_2 at 400 – 450 °C, gave a product which surface coverage was varied between 0.000052 and 1.0. Up to $q = 0.005$, the magnetic susceptibility does not depend on field strength. From $q = 0.118$ upward, a weak ferromagnetism becomes apparent; the latter becomes pronounced at $q = 0.86$. Thus dilute monolayers of Fe on C are not crystalline. Even in concentrated layers, x is much smaller than in bulk iron, the fraction of crystalline iron remaining small. Crystallization takes place during oxidation of the sample, as shown by the values of x after subsequent reduction. Furthermore, anomalously high values of x (per g Fe) are measured when q decreases. Thus for $q \sim 10^{-3}$, $x = 6 \cdot 10^{-3}$. This effect is also observed with dilute monolayers of $Ni(NO_3)_2 \cdot 6H_2O$ on charcoal [24].

However, the composite material will need to have sufficiently saturated magnetization, and as low as possible coercivity to be easily attracted by commercially permanent magnets. The sample shows superparamagnetic behavior of magnetic clusters with a wide moment (i.e. size) distribution [46]. The correlation between microstructure and magnetic behavior of Ni nanoparticles (NPs) embedded in an amorphous activated porous carbon (Ni–AC) has also been studied. The Ni-activated carbon powders have been synthesized by means of an easy and low-cost procedure. The addition of sucrose during the preparation process provides effective protection in acidic media. This Ni-activated carbon composite has a microstructure composed of crystalline nanoparticles with diameters in the range of 7 – 25 nm, and exhibits superparamagnetic behavior at room temperature with saturation magnetization values around 3 A m^2 kg^{-1} under applied magnetic field of 200 mT [15]. The coefficient of magnetism of Fe_2O_3 existing in activated charcoal is large, but less than that of the pure compound. It is a function of the particle size, becoming larger as the surface increases due to the larger quantity of air retained on the surface [50].

These nanotube covered balls have higher carbon surface as compared to the simple carbon balls, so deposition of noble metals (Pd, Pt, Ru, Rh, Ir, Au), Cu, Ag, or other metals or compounds results in a magnetically separable carbon carried catalyst with good mechanical properties, in the form of free-flowing 100 – 200 μm balls. There is an interesting and simple way for the metallization of these magnetic carbon carriers using cementation, if the deposited metal is more electropositive than the iron itself. It means that immersing the iron-containing carbon balls into the solution of noble metals, noble metals are deposited onto the surface of nanotubes and iron (II) ions go into solution. In this way, a room temperature controlled metallization can be performed. Using this method a platinum covered magnetic carbon, which can be used in hydrogenations, aminations, and some other organic reactions, and removable with a simple electromagnet from the reaction medium, has been prepared and its SEM picture is shown on **Figure 5**.
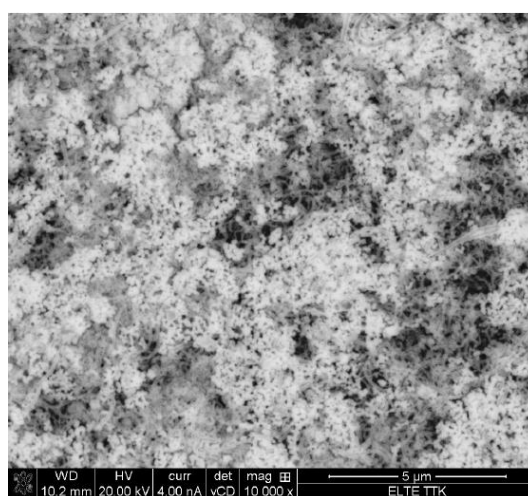
Figure 5. SEM picture of a 100 nm size over-loaded
Pt particle containing magnetic carbon ball catalyst.

The advantages of using this kind of magnetically separable and movable (within the stainless steel or glass reactors) catalyst carriers and catalysts are enormous. Further advantage is removing carbon or iron from the covered balls. For example, removing carbon (C-H_2O reaction catalyzed by iron) from the balls covered with iron on the surface gave an empty iron network in ball form, which is a prospective material to catalyze gas-gas reactions like ammonia synthesis or Fischer-Tropsch (gasoline) synthesis, because the resistance of empty ball like iron clathrate cage contains holes for gas stream and the surface area is extremely high.

3. Application fields of metal containing carbons

Other than the well known hydrogenation or hydrocarbonylation catalysts containing carbon sourced platinum metals or nickel, other metal-containing activated carbons were proved to be widely usable composites in many important chemical and environmental processes. The presence of nanosize metals results new unique properties and new application fields, and the reviewed method based on carbonization of metal-containing ion exchangers open new perspectives to prepare known materials with high metal content, low metal size or high activity, therefore in this section we summarize some selected field of application may belong to these kind of materials.

3.1. Examples on dehydrogenation reactions

Dehydrogenation of ethylbenzene into styrene with iron-containing activated carbon catalysts in the presence of CO_2 with a reverse water-gas shift reaction could be performed with high selectivity to styrene (95 – 98 %) with using alkaline earth or rare earth metal promoters at 823 K. The X-ray diffraction data indicated that carbon dioxide plays an important role in keeping the iron species at high valence and therefore, maintaining the catalytic activity in the coupling reactions. Magnetite formed during heat treatment is the active phase of the carbon-supported iron catalysts. Addition of promoters to catalysts leads to higher dispersion of the active species [5].

The activity of copper oxide supported on activated carbon catalysts, obtained by various preparative techniques, was compared in the decomposition of methanol to hydrogen and carbon monoxide. The favorable role of copper deposition from ammonia solution of copper carbonate is proved. The effect of the preparation conditions on the catalysts activity and stability as well as on the nature of the catalytic active complexes has been studied [51]. The decomposition of MeOH is studied over a large temperature range on Cu catalysts supported on activated C, prepared by active phase deposition from aq. and organic media. Cu^+ species are active sites in MeOH decomposition up to 490 K. Reduction of the active phase as well as essential changes in the chemical nature of the activated C was established during the deactivation of the catalysts. Possibilities of catalysts reactivation under mild oxidative conditions have been explored [52].

3.2. Examples on As removal from water

Metal-containing activated carbons such as iron oxide or copper containing ones can be used as effective sorbents for removal of arsenic from drinking water. Although the main factor of the chemosorption process is the chemical form of iron or copper on the surface of carbon, the size is also plays key role in the activity of the sorbent [53 – 56]. Generally, arsenate (As (V)) is the main contaminate, but some studies dealt with studying on equilibriums of the adsorption of As species from simulated groundwater containing As (III) : As (V) = 1 : 1) [53]. Almost complete removal of As could be performed with Cu^{2+} impregnated granular activated carbon (GAC–Cu) which was found to be effective sorbents for removal of total arsenic (As (III) and As (V) from drinking water [54]. Removal of arsenic (V) from aqueous solutions was evaluated with iron(II) oxide (FeO) / activated carbon. The results suggest that the main phases of the iron oxide surface are magnetite, maghemite, hematite, and goethite; fine and uniform iron oxide particles can cover activated carbon surfaces and affect the surface area or pore structures of activated carbon The optimum value of pH for arsenic (V) removal by FeO / activated carbon-H is in the pH range 3 to 7 [55]. An effective adsorbent for removal of arsenate from aq. system was synthesized by loading ferrihydrite on activated C. The effects of C types, particle size, solution pH, Fe (III) concentration and competing anions on removal rate of arsenate were studied. The results showed that coal-based activated C loaded with ferrihydrite had better arsenate removal efficiency than those of coconut- and husk-based activated C. The removal efficiency of As (V) increased significantly with decreasing the particle size of activated C. Arsenate was effectively adsorbed by activated C loaded with ferrihydrite at pH 3 – 9. The addition of F^-, Cl^- and SO_4^{2-} showed negligible effect on arsenate removal, but PO_4^{3-} and SiO_3^{2-} had large effect [56].

3.3. Examples on mercury removal

It is well known that the metal or metal sulphide containing carbons may effectively be used to remove mercury from solutions via amalgam or mercury (II) sulfide formation. The composition made from carbonized phenolic resin and metal sulphides or metal oxides after sulfurization gives a composite in the form of a flow-through structure, especially as a honeycomb monolith. The metal sulfide is a sulfide of manganese, copper, palladium, molybdenum, or tungsten. The coating further contains sulfur in addition to that present in the metal sulfide. The composite is produced by coating the substrate with a composition containing a carbon precursor, and a metal sulfide, or a combination of a metal oxide, salt or metal sulfide with an additional sulfur source, optionally curing the coating composition; carbonizing the coating composition, and activating the carbonized composition. The composite may be used, for example, for the removal of a contaminant, such as mercury, from a fluid stream [57].

An activated carbon adsorbent for removal of mercury from liquid hydrocarbons (e.g., naphtha) is impregnated with a reactant metal halide comprising a metal selected from K, Cu, Ca, Fe, and Zn, or other reducing halide. These adsorbents can remove even trace levels of Hg from liquid hydrocarbons without a leaching effect of the impregnants been used [58].

3.4. Examples on dehydroclorinations

Decomposition of chlorinated hydrocarbons with low reactivity (chlorinated phenols, biphenyls and likes) is an important task of decontamination processes and the metal containing activated carbons are widely used catalysts in these processes. Vapors of chlorobenzene (PhCl) and 1-chlorohexane (CH) diluted with octane have been (hydro)dechlorinated using Ni, Fe, W, Ni-Mo, Pt and Pd on activated carbon (AC) at temperatures from 150 °C on, void residence times ca. 1.5 s, with various H_2:N_2 ratios, usually 1 : 3, as a carrier gas. For PhCl, Pd on AC was found to be the most active catalyst, with nearly complete reaction even at 150 °C, giving HCl, benzene and cyclohexane. 10 wt. % Ni on Norit ROW 0.8 Supra is an active catalyst too, with 50 % removal at ca. 190 °C, and this reaction is ca. 5 orders of magnitude faster than on this AC alone. Products are HCl and benzene [4].

There are many concerns and challenges in existing polychlorinated biphenyl (PCB)-polluted sediment remediation strategies. Efforts were geared toward developing granular activated carbon (GAC)-impregnated with reactive Fe / Pd bimetallic nano-particles (reactive activated carbon (RAC). Mechanistic aspects of the hybrid RAC system for dechlorinating 2-chlorobiphenyl (2-ClBP) in the aq. phase have been assessed. The following reactions occurred in parallel or consecutively: 2-ClBP was promptly, completely sequestered to the RAC phase; adsorbed 2-ClBP was almost simultaneously dechlorinated by Fe / Pd particles forming a biphenyl (BP) reaction product; and the formed BP was instantly, strongly adsorbed by RAC. 2-ClBP adsorption and dechlorination rate constants were estimated using simple, first-order reaction kinetic models with an assumption for un-extractable carbon portion in RAC. The extent of 2-ClBP accumulation and BP formation in RAC phase was well explained by the kinetic model; adsorption was the rate-limiting step for the overall reaction. Based on these observations, a new strategy and concept of reactive cap/barrier composed of RAC was proposed as an environmental risk management option for PCB-polluted sites [59].

Since carbons can absorb microwave energy, a short and prompt heating of elemental copper distributed uniformly on the surface of activated carbon up to 1100 °C with microwave irradiation to decompose pentachlorophenol (PCP) can be performed. PCP-loaded GAC irradiated by microwave in a quartz reactor when most of PCP adsorbed on virgin GAC was decomposed or bound irreversibly to GAC at 850 W microwave irradiation for 10 min, and less than 2 % was transformed into intermediates. A more rapid decomposition rate of PCP was observed on copper-loaded GAC with larger amount of intermediates formed [6].

3.5. Examples of recovery of harmful chemicals

The activated carbon modified by copper has a better effect on removing cyanides from solutions than pure activated carbon. The modified activated carbon's capability to remove CN^- was improved from 22.10 to 94.07 % at pH 12 – 13. The modified activated carbon's saturation adsorption capacity was 22 mg / g. Mg^{2+}, K^+, Ca^{2+}, Cl^-, SO_4^{2-}, CO_3^{2-}, and AsO_3^- had no effects on the removal of CN^- [60]. Not only dissolved cyanides but gaseous HCN may also be removed by using Cu-containing activated carbons. Cu-containing activated carbons produced from porous sulfonated styrene / divinylbenzene resin were studied for assessing the removal efficiency of HCN vapors from air, when incorporation of Cu into starting material significantly increased HCN breakthrough times, but decreased benzene breakthrough times. The surface area and pore volume of the adsorbents also decreased with incorporation of Cu. Results of XPS analysis revealed partial or complete reduction of the starting divalent Cu on the surface of the adsorbents confirmed by the lack of formation of $(CN)_2$ during the adsorption of HCN [61].

A 10 % Zn-containing activated carbon prepared under hydrogen has modified state of Zn, and forms functional groups on the surface of activated carbon for adsorbing and degrading benzene series. This inventive purifying agent has benzene series removal rate of > 98 % [62]. The similar treatment but using ammonia instead of hydrogen resulted an adsorbent for adsorbing and degrading of formaldehyde with removal ratio > 90 % [63].

3.6. Desulfurization

The adsorption capacity of activated carbon for the natural gas contaminant dimethyl sulfide (DMS) is improved by impregnating it with $FeCl_3$, introduced in solution to affect surface modification [64]. Preparation of an activated carbon-based desulfurization adsorbent for gasoline comprises (1) oxidizing 40 – 80 mesh activated carbon with concentrated sulfuric acid (active carbon : concentrated sulfuric acid = 1 g : 20 mL) at 150 – 300 °C for 3 h for chemical modification, (2) washing with distilled water to pH of 7, and drying at 100-120 °C and (3) immersing the modified activated carbon as carrier in 0.10 – 0.30 mol / L $Mn(NO_3)_2$ solution for 6 – 42 h, drying at 100 – 120 °C for 2 h, and baking in nitrogen gas at 200 – 600 °C for 1 – 5 h. The obtained absorbent has the advantages of large adsorption capacity on sulfides in gasoline, simple preparation method, low cost, and little influence on octane number of the gasoline [65].

Thiophene-ring containing compounds may also adsorbed by metal-containing carbons. Effects of loading different metal ions on the adsorption of dibenzothiophene on the activated C were discussed by hard and soft acid and base principle. Results showed that loading of Ag^+, Cu^{2+}, Ni^{2+} or Zn^{2+} ion on the activated carbon improved its adsorption of dibenzothiophene on the activated carbon; while loading of Fe^{3+} ion on the activated carbon weakened its adsorption of dibenzothiophene (DBT) in comparison with original activated carbon. As a result, loading

Ni^{2+}, Cu^{2+} or Zn^{2+} on the activated carbon has been suggested to improve its adsorption of dibenzothiophene because of its high adsorption capacity and low costs [66]. Each TPD spectrum for DBT desorption on the activated carbons loaded separately with Ag^+, Ni^{2+}, Cu^{2+} and Zn^{2+} showed two distinct peaks, corresponding to interaction of DBT with the activated carbon surface and with the metal ions, which indicated producing new adsorption sites. In comparison with the original activated carbon, the loading of Ag^+ enhanced the interaction between DBT and Ag^+ / AC surfaces because Ag+ was a soft acid and DBT was a soft base, and the loading of Fe^{3+} weakened the interaction between DBT and Fe^{3+}/AC surfaces because Fe^{3+} was a hard acid, while DBT was a soft base. The loading of the borderline acid ion Zn^{2+}, Ni^{2+}, or Cu^{2+} on the surfaces of the activated carbon could weaken the local hard acids of the surfaces so that adsorption of DBT was enhanced to some extent [67].

When iron compounds are added to low ash activated carbons having basic surface characteristics (obtained by suitable oxidation at 800 °C with 2 % of O_2 in N_2), certain materials are obtained showing high SO_2 sorbent properties from gaseous mixtures having a composition close to that of flue gases. This behavior seems to be related to the simultaneous presence of both basic surface sites promoting the initial adsorption of SO_2 and iron promoting the transformation of the adsorbed SO_2 into other, more stable forms. The sorbent properties of these activated carbons are more stable, following consecutive cycles, in the processes of adsorption and desorption of SO_2, than those shown by similar carbons with different surface characteristics [68].

3.7. Phenol and TOC removal, photocatalysis

Wastewaters containing organic contaminants, especially less-easily-decomposable ones like phenols or substituted phenols can be treated effectively with oxidative agents like air in the presence of different kind of metal-containing activated carbon catalysts and adsorbents. For example Iron-containing carbons and magnetic carbons containing iron or Fe-compounds have also been tested on various phenol recovery processes. For example, Fe-impregnated (2.5 % Fe) activated carbon was used for the wet air oxidation of phenol in a trickle-bed reactor at 400 K and 8 atm of total pressure in a wide range of space time (20 – 320 g CAT h / g phenol) [42].

A magnetically separable photocatalyst for phenol recovery which consists of porous activated carbon, iron oxide particles, and anatase titania particles has also been studied. The photocatalytic activity of the samples was determined by degrading phenol contaminated water when enhanced photocatalytic activities were obtained comparing it with pure TiO_2. An additional advantage of these composite photocatalyst is their recyclability because it can be easily magnetically separated by an external magnetic field. The degradation rate of phenol by a titania-coated magnetic activated carbon with a Fe content of 20 % and a calcination temperature for the support of 450 °C, was still higher than 85 % after the photocatalyst has been used for 5 cycles [69].

Regeneration of activated carbons in the presence of iron oxide nanoparticles for phenol recovery raises a new possibility of utilization of iron oxide containing activated carbons. A novel approach for the recovery of spent activated carbon by an advanced oxidation process using iron oxide-based nanocatalysts has been proposed when organic contaminants, such as ethylene glycol and phenol were chosen as water pollutants for testing the regenerated carbons. It was shown that there are several advantages in using catalytic oxidation recovery of activated

carbon with iron oxide-based nanocatalysts e.g., low temperature reactivity of catalytic recovery without heating and a relatively large number of adsorption-recovery cycles, without a reduction in the adsorptive properties of the virgin activated carbon or without a performance decrease from the 1st adsorption-recovery cycle of the new modified adsorptive properties of the activated carbon. The catalytic recovery takes place without UV light or any visible radiation sources. Results show a high efficiency of catalytic recovery of spent activated carbon using iron oxide-based nanocatalysts. A 97 – 99 % efficiency of spent activated carbon catalytic regeneration was achieved under chosen conditions after 15 – 20 min of reaction. The process may be also considered as cold in situ recovery of active carbon [70].

There are dry oxidation methods as well for recovery of phenol after adsorption on metal-modified carbons. Catalytic dry oxidation of phenol adsorbed on activated carbon (AC) supported metal catalyst-sorbent (metal / AC) is promising for phenolic wastewater treatment. The process consists of adsorption of phenol on the catalyst-sorbent in a fixed-bed reactor for a long period of time and catalytic dry oxidation of phenol adsorbed upon the discharge of water from the adsorption bed in a short period of time. Both Cu / AC and Fe / AC showed high activity for catalytic oxidation of phenol, and Cu / AC was more active than Fe / AC, which showed high conversion of phenol and no production of phenol and benzene. The initial oxidation temperature of phenol was ca. 200 °C, and the ignition temperature of AC was ca. 130 °C higher than the initial phenol oxidation temperature. The difference in oxidation activity among the metal / AC catalyst-sorbents could be attributed to the differences of metal components, AC, and the interaction between the metal and support. The test of 8 adsorption-oxidation cycle of phenol on Cu / AC showed that its adsorption capacity decreased to an asymptotic level of ~ 70 mg / g with the increase of adsorption-regeneration cycle, which suggested that a steady state adsorption capacity could be reached [71].

$CuFe_2O_4$ / activated carbon magnetic adsorbents, which combined the adsorption features of activated carbon with the magnetic and the excellent catalytic properties of powdered $CuFe_2O_4$, have been developed using a simple chemical coprecipitation procedure. The prepared magnetic composites can be used to adsorb Acid orange II (AO7) in water and subsequently, easily be separated from the medium by a magnetic technique. $CuFe_2O_4$ / activated carbon magnetic adsorbents with mass ratio of 1 : 1, 1 : 1.5 and 1 : 2 were prepared. The magnetic phase present is spinel copper ferrite and the presence of $CuFe_2O_4$ did not significantly affect the surface area and pore structure of the activated carbon. The adsorption kinetics and adsorption isotherm of Acid orange II (AO7) onto the composites at pH 5.2 also showed that the presence of $CuFe_2O_4$ did not affect the adsorption capacity of the activated carbon. The thermal decomposition of AO7 adsorbed on the activated carbon and the composite was investigated by in situ FTIR [72]. A similar activated carbon / magnetite composites with nano-ceramic oxides and ferrites whose surfaces have been functionalized was used to provide binding sites for various organic pollutants. These extractants was found to be significant potential to remove alkanes and 2,4-dinitrocresol herbicide form water [12].

An original approach to the removal of phenol in synthetic wastewater is by catalytic wet peroxide oxidation with copper binding activated carbon (Cu/AC) catalysts. The characteristics and oxidation performance of Cu / AC in the wet hydrogen peroxide catalytic oxidation of phenol were studied in a batch reactor at 80 °C. Complete conversion of the oxidant, hydrogen peroxide, was observed with Cu / AC catalyst in 20 min oxidation, and a highly efficient phenol removal and COD abatement were achieved in the first 30 min. The

good oxidation performance of Cu / AC catalyst was contributed to the activity enhancement of copper oxide, which was binding in the carbon matrix. It can be concluded that the efficiency of oxidation dominated by the residual H_2O_2 in this study. An over 90 % COD removal was achieved by using the multiple-step addition in this catalytic oxidation [73]. The catalyst copper oxide/activated carbon (AC) was prepared from AC as carrier and copper nitrate as active component. After the catalyst has been used to degrade coke-plant wastewater containing phenol, the removal rate of COD was increased by more than 11 % [74].

The activated carbon-zinc oxide catalysts prepared with different portions of activated carbon (AC) have been characterized and changes in some of the physicochemical characteristics of ZnO have been observed. It is found that these changes correspond with ZnO surface acid-base property. SEM study reveals a perfect ZnO particle distribution on the AC surface in the catalyst with 9 % AC content (9AC–ZnO). Adsorption and photodegradation of 4-acetylphenol on 9AC–ZnO are much higher than bare ZnO. The higher efficiency of this photocatalyst is due to the synergistic effect between ZnO and activated carbon. The catalyst is found to be reusable [75].

3.8. Effect on microorganisms

The activated carbons with ZnO prepared from $Zn(NH_3)_4^{2+}$ treated ion-exchanger resins with carbonization show antibacterial activity in the absence of light. ZnO of hexagonal type was detected in the carbon samples, of which the amount decreased with an increase in the carbonization temperature, however, the specific surface areas of carbon samples increased with increasing the carbonization temperature of the resin. The antibacterial activity on carbon samples containing. ZnO increases with a decrease of the carbonization temperature and an increase of the amount of ZnO in the samples. From a comparison of the antibacterial activity between *Staphylococcus aureus* and *Escherichia coli*, it was found that the activity against *Staphylococcus aureus* was stronger than that against *Escherichia coli*. The concentration of hydrogen peroxide increased linearly with an increase in the amount of carbon in samples. The occurrence of antibacterial activity was found to be due to the generation of hydrogen peroxide from ZnO in activated carbons. [38, 76].

Coccidiosis is one of the sickness causes large losses in broiler chickens when the chickens breathe in the powder containing microbes. The yield of broiler chicken could be increased with decreasing the losses due to coccidiosis with using a silver-containing activated carbon composite prepared with carbonization of the silver salts of styrene-divinylbenzene copolymers [47].

3.9. Electrochemistry

High-surface-area metal-containing activated carbons were mixed with phenolic resin to prepare composite electrodes for supercapacitors. The electrochemical properties were examined for the activated carbon composites used as polarizable electrodes in an aq. electrolyte solution by constant current cycling. Activated carbons containing Mn, Cu, and Co had an improved discharge capacitance of the electrodes, with the activated carbon-Mn electrode having a capacitance as high as 265 F g^{-1} when carbonized at 700 °C [77]. An activated carbon-MnO_2 hybrid electrochemical supercapacitor cells have been assembled and characterized in K_2SO_4 aq. media. A laboratory cell achieved 195,000 cycles of stable performance. The maximal cell voltage was 2 V associated with 21 ± 2 F g^{-1} of total composite electrode materials

(including activated carbon and MnO_2, binder and conductive additive) and an equivalent series resistance (ESR) < 1.3 Ω cm^2. Long-life cycling was achieved by removing dissolved O from the electrolyte, which limits the corrosion of current collectors. Scaling up was realized by assembling several electrodes in parallel to build a prismatic cell. A stable capacity of 380 F and a cell voltage of 2 V were maintained over 600 cycles. These encouraging results show the interest of developing such devices, including nontoxic and safer components as compared to the current org.-based devices [78].

In order to enhance specific capacitance and energy density of carbon-based supercapacitor, some nanometer-scale amorphous particles of nickel oxide were loaded into activated carbon by suspending the activated-carbon in a $Ni(NO_3)_2$ solution followed by neutralization. A hybrid type electrochemical capacitor was made and tested, in which the activated-carbon loaded with nickel oxide was used as cathode material and activated-carbon was used as anode material. Although the BET surface area of the activated-carbon decreased upon nickel oxide loading compared to that of the starting material, its specific capacitance increased 10.84%, from 175.40 to 194.01 F g^{-1} and the potential of oxygen evolution on the composite material electrode was 0.076 V higher than that of the pure activated-carbon electrode, in the electrolyte of 6 mol L^{-1} KOH solution, so the hybrid capacitor had larger energy density. Similar to the pure activated-carbon electrode, no obvious change appears on the specific capacitances of the composite material electrode at various discharge currents and the composite material electrode exhibiting good power characteristics [79].

3.10. Examples on NO$_x$ removal

The efficiency of cellulose-based, microporous, metal-doped activated carbon fibers (ACF) for the NO$_x$ reduction in flue gases was investigated. The average width of the slit-shaped pores was 0.8 – 0.9 nm, which is only 2 – 3 times greater than a NO molecule and was scarcely affected by metal deposition (Ru, Pt, Cu, and Fe). The porosity decreased only slightly as a result of metal deposition, except for Fe, Ru-, Pt-, and Cu-doped fibers decomposed NO effectively (96 % after 1 h at 303 K) yielding N$_2$ (approximately 80 %) as main product besides small amounts (< 1 %) of NO$_2$ and N$_2$O. Poorer results were obtained with Fe-doped fibers [80]. The deNO$_x$ catalysts supported on chars and activation product obtained from the spent ion exchanger resin has been investigated. The research facilitated the determination of the influence of the quality of the support and the type of the active phase (copper, iron and manganese) on the activity on the catalyst used in SCR reaction. The best deNO$_x$ catalyst was CuO / A800 [81]. Active carbon promoted with Mn was studied as catalysts for selective reduction of NO with NH$_3$. The influence of the preparation method on the structure and texture of the catalysts was studied and catalytic properties such as activity, selectivity, and stability were determined [82].

3.11. Examples on other application fields

Fe-impregnated activated carbon (Fe–AC) prepared by loading of Fe (III) on activated carbon (AC) at different pH proved to be stable in acidic conditions, the dissolved iron was below the effluent standard of iron (2 ppm) suggesting a strong acid-proof property. In the batch adsorption test, removal curves of copper shifted to the higher pH region as the copper concentration increased due to the finite number of adsorption sites on Fe–AC. From the strong chemical reaction between Fe (III) on AC and Cu (II), Fe–AC showed a greater adsorption

capacity for Cu (II) than AC. Surface complexation modeling was performed by considering inner-sphere complexation reaction and using the diffuse layer model. The model predictions considering adsorption and precipitation generally well simulated the experimental removal trends of copper over the entire pH ranges. From the column test, Fe-AC was regarded as a promising filter material in the treatment of acidic wastewater contaminated with copper with proper controlling of the contact time between copper and Fe–AC [83]. The Cu (II) adsorption capacities of iron oxide-coated granular activated carbons (GACs) were significantly increased by the coating of iron oxides. Relative to adsorption onto uncoated GAC, Fe oxide coatings increased adsorption capacities for Cu (II) from about 1.4 for GAC to 5 mg / g for GAC coated with 37 mg Fe oxide / g GAC (37FeGAC, etc.). The Cu (II) adsorption capacity per g of iron oxide on FeGAC adsorbents was at least three times greater than discrete Fe oxide. Surface areas of GAC decreased slightly with increasing Fe oxide coating, from 742 for 37FeGAC, 673 for 52FeGAC and to 634 m^2 / g for 72FeGAC. Tests in a column process for Cu (II) removal demonstrated that the composite adsorbent could be reused through at least 15 adsorption and desorption cycles. Although a fraction of the adsorbed Cu (II) was retained by the solid, there was no apparent loss in adsorption capacity [84].

A kind of the magnetic adsorbent composite for water and wastewater treatment is composed of a magnetic substrate particle which is nonreactive under conditions of use and which is encapsulated with adherent activated carbon. The composite has a high adsorption rate, is easy to handle, can be easily separated from solution by a magnetic field and pumped and transferred magnetically and can be easily regenerated [27].

Using a redox process, granular activated carbon (GAC) was coated with manganese oxides to enhance its ability to absorb fluoride from aq. solutions. Compared with plain GAC, the fluoride adsorption capacity of this new adsorbent was improved and at least three times greater than that of uncoated GAC. X-ray diffraction revealed that manganese oxides are amorphous and XPS demonstrated that manganese existed primarily in the oxidation state +IV. The sorption data also indicated that the removal of fluoride by adsorption is a highly complex process, involving both boundary layer diffusion and intra-particle diffusion. The pH value of solution influences fluoride removal, and the optimum equilibrium pH value of fluoride adsorption is 3.0.

Activated carbons prepared by carbonization of polystyrene / divinylbenzene copolymers containing 4 – 18 wt. % divinylbenzene and Ag or Cu-salts after activation with sulphuric acid or oleum could be used as carbon adsorbents in adsorption filters, odor filters, for protective clothing for civil and military use against biological and chemical toxins, in air purifiers, gas mask filters, etc. [28]. A pressure-swing adsorption (PSA) process for separation of CO from a $CO-CO_2-N_2$ mixture is proposed. The adsorbent used in this process is active C-supported Cu. By cycling the pressure of a bed of this adsorbent between ambient pressure and 20 – 30 torr at room temperature, high-purity CO can be obtained from the $CO–CO_2–N_2$ gas mixture with a high recovery. The purity of CO product depends crucially on the step of CO concurrent purge after adsorption in the cycle and the regeneration of sorbent [85].

The Fe_2O_3 / carbon composite prepared form carboxylic type ion-exchanger can be used for selective acylation of amine and primary and secondary alcohol functions with acetic acid under convenient conditions. Phenolic groups cannot be acylated in this way, therefore the method can be used in preparation of paracetamol with 100 % selectivity and almost quantitative yield [40]. The catalyst advantage is that does not cause racemization, e.g. chiral

alcohols like menthol or the chiral amine, (D)-(+)-methyl benzylamine afforded corresponding O-acylated or *N*-acetylated products, respectively, in quantitative yields without any racemisation. The selectivity towards the acetylation of primary and secondary alcohols with acetic acid is found to be similar with propionic and butyric acids, but the corresponding acylated products are obtained in faster.

The preparation method led to uniform distribution of iron (III) oxide particles on activated carbon matrix, which gives an active iron oxide layer covered on the carbon surface. The generation of the acylcarbonium-ion in the presence of protic solvents can be achieved via interaction of surface crystalline sites or defects, which are located in oxide layer.
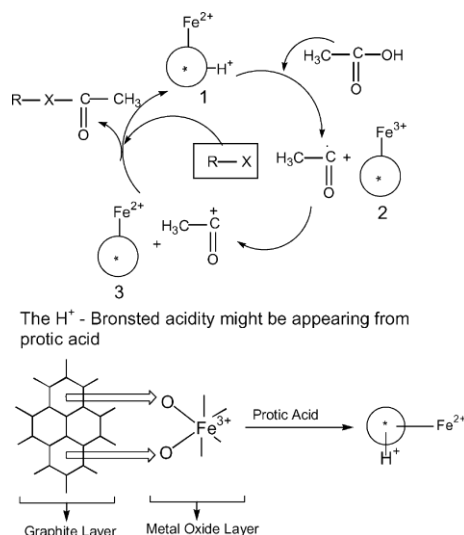
Figure 6. Mechanism of alcohols and amines
acylation in the presence of Fe_2O_3 / C catalyst [40].

The bronsted acidity of the crystalline sites of surface oxide is changed via interaction of de-localized electron density of the graphitic as well as metal oxide layers (**Figure 6**). It changes theirs reactivity. Initially, Fe^{2+}-ion containing crystalline sites are formed (1) by the reduction of Fe^{3+}-ions on surface layer of iron (III) oxide covered the activated carbon, (neither pure activated carbon nor pure iron (III) oxide catalyze these processes), therefore the interaction between graphitic and metal oxide layers in activated carbon–iron (III) oxide composite is the key-step in the formation of catalytically active species.

References

1. R. C. Bansal, M. Goyal. Activated Carbon Adsorption. 2005, Taylor & Francis.
2. Y. K. Kalpakli, I. Koyuncu. Characterization of activated carbon and application of copper removal from drinking water. Ann. Chim. (Rome), 2007, 97, 11-12, 1291-1302.
3. T.-Ch. Liu, Sh.-J.Chiu. Effect of metal loading sequence on the activity of Sn–Ni / C for methanol carbonization. Appl. Catal. A, 1994, 117, 1, 17-27.
4. V. de Jong, R. Louw. Performance of supported nickel and other metal catalysts in the hydrodechlorination of chlorobenzene and 1-chlorohexane. Appl. Catal. A, 2004, 271, 1-2, 153-163.
5. A. Sun, Zh. Qin, J. Wang. Reaction coupling of ethylbenzene dehydrogenation with water-gas shift. Appl. Catalo. A, 2002, 234, 1-2, 179-189.

6.	X. Liu, X. Quan, L. Bo, Sh. Chen, Y. Zhao, M. Chang. Temperature measurement of GAC and decomposition of PCP loaded on GAC and GAC-supported copper catalyst in microwave irradiation. Appl. Catalo. A, 2004, 264, 1, 53-58.

7.	G. Marban, R. Antuna, A. B. Fuertes. Low-temperature SCR of NO_x with NH_3 over activated carbon fiber composite-supported metal oxides. Appl. Catalo. B, 2003, 41, 3, 323-338.

8.	H.-L. Chiang, C. P. Huang, P. C. Chiang, J. H. You. Effect of metal additives on the physical-chemical characteristics of activated carbon exemplified by benzene and acetic acid adsorption. Carbon, 1999, 37, 12, 1919-1928.

9.	T. Okutani, A. Uzawa. Separation and concentration of metal ions in aqueous media using activated carbon. Bunseki Kagaku, 1995, 44, 9, 663-680.

10.	Sh Chen, G. Li, Y. Wang, B. Yu. Relation between the activity and structure of zinc acetate / activated carbon catalyst. Cuihua Xuebao, 1986, 7, 2, 155-161.

11.	J. Klinik, T. Grzybek. The influence of the addition of cobalt, nickel, manganese and vanadium to active carbons on their efficiency in sulfur dioxide removal from stack gases. Fuel, 1992, 71, 11, 1303-1308.

12.	T. M. Trad, A. W. Apblett. Ceramic-based magnetic extractants: Synthesis, characterization and environmental applications. In: Abs. 231st ACS Natl. Meeting. 2006, Atlanta, INOR-352.

13.	L. L. Murrell, N. C. Dispenziere Jr. R. T. K. Baker, J. J. Chludzinski. Evidence of a metal-surface phase oxide interaction for rhenium on tungsten oxide (WO_x) supported on activated carbon. ACS Symp. Ser., 1986, 298, 195-199.

14.	L. Dabek. The use of supercritical fluid extraction in carrier recovery from a spent active carbon-zinc acetate catalyst. Ads. Sci. Technol., 2002, 20, 2, 141-150.

15.	P. Gorria, M. P. Fernandez–Garcia, M. Sevilla, J. A. Blanco, A. B.Fuertes. Nickel nanoparticles deposited into an activated porous carbon: synthesis, microstructure and magnetic properties. Phys. Status Solidi RRL, 2009, 3, 1, 4-6.

16.	Y. A. Alhamed. Effect of preparation conditions on the characteristics of activated carbon produced by $ZnCl_2$ activation. Alexandria Eng. J., 2006, 45, 6, 739-756.

17.	O. M. Klimov, Zh. M. Kokueva, L. B. Kreinin. Preparation of metalized activated carbons from recycled materials. J. Appl. Chem. (Sankt-Petersburg), 1991, 64. 1, 135-40.

18.	T. V. Chubar, V. N. Vysotskaya, Yu. I. Khimchenko, I. Ya. Pishchai, L. G. Nadel. Formation of metal-containing carbon sorbents in pyrolysis of wood, impregnated with salts. Ukr. Chem. J. (Kyiv), 1987, 53, 3, 243-245.

19.	J. Inczedy. Ion Exchangers and Theirs Analytical Applications. 1980, Budapest, Műszaki Könyvkiadó. – in Hungarian.

20.	G. Zhang, J. Qu, H. Liu, R. Liu, R. Wu. Magnetic adsorbents: Activated carbon / iron oxide composites for AO7 removal from aqueous system. Huanjing Kexue Xuebao, 2006, 26, 11, 1763-1768.

21.	L. Guo, W. Ma, Zh. Hu, D. Shun. Removal of organic substance in drinking water by magnetic powdered activated carbon. Zhongguo Jishui Paishui, 2001, 17, 2, 71-72.

22.	T. G. Suslina, V. B. Voitovich, V. G. Shmarova. Behavior of ion-exchange resins in citric acid solutions. Proc. Voronezh State Univ., 1971, 82, 204-208.

23.	A. G. Mejlakh, V. Ya. Bulanov. Production of magnetic sorbent. USSR, CODEN: URXXAF SU 1808370 A1 19930415, 1993.

24. V. B. Evdokimov, I. N. Ozeretskovskii, N. I. Kobozev. Paramagnetism of catalytically active layers of iron. J. Phys. Chem. (Moscow), 1952, 26, 135-144.

25. X. Wang, X. Xin, A. Dai. Studies on thermal stabilities of coordination compounds by gas chromatography. XVI. Thermal decomposition of supported nickel format in helium. Cuihua Xuebao, 1986, 7, 3, 243-249.

26. J. Maruyama, I. Abe. Manufacture of activated carbon containing metals. Jpn., CODEN: JKXXAF JP 2004217507 A 20040805, 2004.

27. R. E. Brooks, G. M. J. Slusarczuk. Magnetic adsorbent composite. USA, CODEN: USXXAM US 4201831 19800506, 1980.

28. Preparation of Activated Carbon Adsorbents with Catalytic Activity. 2007, Bluecher, G.m.b.H. Ger. Gebrauchsmusterschrift.

29. B.-J. Park, S.-J. Park, S.-K. Ryu. Removal of NO over copper supported on activated carbon prepared by electroless plating. J. Colloid Interface Sci., 1999, 217, 1, 142-145.

30. Carbon product. Jpn. Kokai Tokkyo Koho, JP 57191213 A 19821125, 1982.

31. V. S. Komarov, M. I. Yatsevskaya, O. A. Sycheva. Properties of activated carbon produced from spent ion-exchange resins. Proc. Belarusian Acad. Sci., 1985, 29, 11, 1010-1013.

32. P. E. Tulupov, O. N. Karpov. Kinetics of the thermal decomposition of styrene- and divinylbenzene-based sulfonic cation exchangers according to thermogravimetric analytical data. J. Phys. Chem. (Moscow), 1973, 47, 6, 1420-1423.

33. I. M. M. Kenawy, M. A. H. Hafez, R. R. Lashein. Thermal decomposition of chloro-methylated poly(styrene)-PAN resin and its complexes with some transition metal ions. J. Ther. Anal. Calorim., 2001, 65, 3, 723-736.

34. M. V. Vinokurov, I. N. Lipunov, P. E. Tulupov, O. N. Babkin. Thermal stability of some ion exchanger complexes of copper (II). Izvestiya Vysshikh Uchebnykh Zavedenii (Chem. Chem. Technol.), 1988, 31, 6, 112-116.

35. A. Nyuzawa, T. Suzuki. Thermal degradation of various forms of ion-exchange resins. Denki Kagaku oyobi Kogyo Butsuri Kagaku, 1983, 51, 1, 205-206.

36. J.-J. Lee, J.-K. Suh, J.-S. Hong, J.-M. Lee, Y.-S. Lee, J.-W. Park. The synthesis of spherical activated carbons containing zinc and their photochemical activity. Carbon, 2008, 46, 13, 1648-1655.

37. O. Yamamoto, J. Sawai. Preparation and characterization of novel activated carbons with antibacterial function. Bull. Chem. Soc. Jpn., 2001, 74, 9, 1761-1765.

38. O. Yamamoto, J. Sawai. Preparation and characterization of novel activated carbons with antibacterial function. Bull. Chem. Soc. Jpn., 2001, 74, 9, 1761-1765.

39. Partially Pyrolyzed Particles of Macroporous Synthetic Polymers. 1976, Rohm & Haas Co.

40. B. Sreedhar, V. Bhaskar, Ch. Sridhar, T. Srinivas, L. Kótai, K. Szentmihályi. Acylation of alcohols and amines with carboxylic acids: A first report catalyzed by iron (III) oxide-containing activated carbon. J. Mol. Catalo. A, 2003, 191, 141-147.

41. J. Zhao, W.-L. Zhou, F.-M. Xu. Preparation and magnetism of carbon encapsulated Fe and Ni nanoparticles. Yingyong Huaxue, 2007, 24, 7, 823-827.

42. A. Quintanilla, J. A. Casas, J. J. Rodriguez. Catalytic wet air oxidation of phenol with modified activated carbons and Fe / activated carbon catalysts. Appl. Catalo. B, 2007, 76, 1-2, 135-145.

43. L. Kótai, T. Pasinszki, Z. Czégény, S. Bálint, I. Sajó, Z. May, P. Németh, Z. Károly, P. K Sharma, V. Sharma, K. K. Banerji. Metal and metal-sulphide containing carbons from sulphonated styrene-divinylbenzene copolymer based ion-exchangers. Eur. Chem., Bull. 2012, 1, 10, 398-400.

44. J. Szépvölgyi, L. Kótai, T. Pasinszki, E. Kuzmann, S. Bálint, Zs. Czégény, I. E. Sajó, P. Németh, K. Lázár. Preparation of uniformly distributed metal-containing bead-like carbon composites – Magnetic activated carbons and catalyst precursor. In: Eur. Mater. Res. Soc. Fall Meeting. 2012, Warsawa.

45. T. Pasinszki, Z. Homonnay, I. E. Sajó, L. Kótai. Preparation and perspectives of magnetic and nanosize metal-containing amorphous carbon composite chemosorbents and catalysts. In: Abs. 3rd Int. Conf. "Nanotechnologies". 2014, Tbilisi, Georg. Tech. Univ., 88-90.

46. T. Pasinszki, M. Krebsz, L. Kótai, I. E. Sajo, Z. Homonnay, E. Kuzmann, L. F. Kiss, T. Vaczi, I. Kovacs. Nanofurry magnetic carbon microspheres for separation processes and catalysis: synthesis, phase composition, and properties. J. Mater. Sci., 2015, 50, 7353-7363.

47. G. Papp, Z. Müller, M. Müller, I. Póczos, P. Hegyes, L. Kótai. Method to prepare a silver-containing feed additive. HU 211071, A23K1/22, 04.01.1991.

48. Y. Chen, C. Xin, X. Yang, Ch. Xu, L. Pan, D. Liang, L. Lin. Mossbauer study of iron/activated carbon catalysts. II. Metal-support interaction. Cuihua Xuebao, 1992), 13, 5, 325-331.

49. L. C. A. Oliveira, R. V. R. A. Rios, J. D. Fabris, V. Garg, K. Sapag, R. M. Lago. Activated carbon / iron oxide magnetic composites for the adsorption of contaminants in water. Carbon, 2002, 40, 12, 2177-2183.

50. C. Courty. The magnetic properties of the iron included in activated charcoals. Compt. Rend. (Paris), 1942, 215, 461-463.

51. T. Tsoncheva, S. Vankova, D. Mehandjiev. Effect of the precursor and the preparation method on copper based activated carbon catalysts for methanol decomposition to hydrogen and carbon monoxide. Fuel, 2003, 82, 7, 755-763.

52. T. St. Tsoncheva, R. N. Nickolov, Ya. G. Neinska, Ch. I. Minchev, D. R. Mehandjiev. Supported on activated carbon copper-based catalysts for methanol decomposition. Bulg. Chem. Commun., 2000, 32, 2, 218-229.

53. P. Mondal, B. Mohanty, C. B. Majumder, N. Bhandari. Removal of arsenic from simulated groundwater by GAC–Fe: A modeling approach. AIChE J., 2009, 55, 7, 1860-1871.

54. P. Mondal, B. Mohanty, C. B. Majumder. Treatment of simulated arsenic contaminated groundwater using GAC-Cu in batch reactor: optimization of process parameters. Can. J. Chem. Eng., 2009, 87, 5, 766-778.

55. Q. L. Zhang, N.-Y. Gao, Y. C. Lin, B. Xu, L.-Sh. Le. Removal of arsenic (V) from aqueous solutions using iron-oxide-coated modified activated carbon. Water Environ. Res.: A Res. Publ. WEF, 2007, 79, 8, 931-936.

56. Sh.-H. Yao, Y.-F. Jia, G.-Q. Wang, Zh.-L. Shi. Removal of As (V) from drinking water by activated carbon loaded with Fe(III) adsorbent. Guocheng Gongcheng Xuebao, 2009, 9, 2, 250-256.

57. K. P. Gadkaree, A. Liu, J. F. Mach. Composite comprising an inorganic substrate with a coating containing activated carbon and metal sulfide for mercury removal. PCT Int. Appl., 2009, 18 pp. WO 2009148501 A1 20091210, Application: WO 2009-US3085 20090519. Priority: US 2008-129907 20080530.

58. J. D. McNamara. Impregnated carbon adsorbents for removal of mercury from liquid hydrocarbon. Can. Pat. Appl., 1991, 42 pp. CA 2030369 A1 19910523.

59. H. Choi, Sh. Agarwal, S. R. Al-Abed. Adsorption and simultaneous dechlorination of PCBs on GAC / Fe / Pd: Mechanistic aspects and reactive capping barrier concept. Environ. Sci. Technol., 2009, 43, 2, 488-493.

60. M. Zhang, J. Liu, L. Qin. Preparation of Cu^{2+}-modified activated carbon and its use to removal of CN^- from wastewater. Huagong Huanbao, 2008, 28, 4, 308-311.

61. T. M. Oliver, K. Jugoslav, A. Popovic, N. Dogovic. Synthetic activated carbons for the removal of hydrogen cyanide from air. Chem. Eng. Proc., 2005, 44, 11, 1181-1187.

62. J. Peng, L. Zhou, T. Qian, Sh. Wang, L. Zhang, Zh. Zhang, W. Qu, Z. Zhang, W. Li, Sh. Guo, Sh. Zhang, R. Xie, B. Liu. Preparation of composite purifying agent for removing benzene series from air. Faming Zhuanli Shenqing Gongkai Shuomingshu, 2008, 6 pp. CN 101224383 A 20080723, Application: CN 2007-10066278 20071016.

63. J. Peng, T. Qian, L. Zhou, L. Zhang, Sh. Wang, W. Qu, Zh. Zhang, W. Li, Z. Zhang, Sh. Guo, Sh. Zhang, R. Xie, B. Liu. Preparation of composite purifying agent for removing formaldehyde from air. Faming Zhuanli Shenqing Gongkai Shuomingshu, 2008, 6 pp. CN 101224382 A 20080723 Application: CN 2007-10066277 20071016.

64. H. Cui, S. Q. Turn. Adsorption / desorption of dimethyl sulfide on activated carbon modified with iron chloride. Appl. Catalo. B, 2009, 88, 1-2, 25-31.

65. X. Tang, L. Li, X. Zeng, Zh. Yu, B. He, Y. Cui. Preparation of manganese dioxide / activated carbon used as desulfurization adsorbent for gasoline. Faming Zhuanli Shenqing Gongkai Shuomingshu, 2008, 10 pp. CN 101323795 A 20081217 Application: CN 2008-10045575 20080715.

66. M. Yu, Zh. Li, Q. Xia, Sh. Wang. Adsorption of dibenzothiophene on activated carbon loaded with different metal ions. Gongneng Cailiao, 2006, 37, 11, 1816-1818.

67. M. Yu, Zh Li,. Q. Xia, H. Xi, Sh. Wang. Desorption activation energy of dibenzothiophene on the activated carbons modified by different metal salt solutions. Chem. Eng. J. (Amsterdam), 2007, 132, 1-3, 233-239.

68. P. Davini. Influence of surface properties and iron addition on the SO_2 adsorption capacity of activated carbons. Carbon, 2002, 40, 5, 729-734.

69. Y. Ao, J. Xu, D. Fu, Ch. Yuan. A simple route for the preparation of anatase titania-coated magnetic porous carbons with enhanced photocatalytic activity. Carbon, 2008, 46, 4, 596-603.

70. A. Bach, G. Zelmanov, R. Semiat. Cold catalytic recovery of loaded activated carbon using iron oxide-based nanoparticles. Water Res., 2008, 42, 1-2, 163-168.

71. J. Zhao, Zh. Liu. Catalytic oxidation of phenol adsorbed on Cu / AC and Fe / AC catalyst-sorbents. Cuihua Xuebao, 2005, 26, 2, 143-147.

72. G. Zhang, J. Qu, H. Liu, A. Cooper, T. Wu. $CuFe_2O_4$ / activated carbon composite: A novel magnetic adsorbent for the removal of acid orange II and catalytic regeneration. Chemosphere, 2007, 68, 6, 1058-1066.

73. R.-M. Liou, Sh.-H. Chen. CuO impregnated activated carbon for catalytic wet peroxide oxidation of phenol. J. Hazardous Mater., 2009, 172, 1, 498-506.

74. L.-Y. Jin, Y.-H. Xu, M. Chen. Study on treatment of coke-plant wastewater containing phenol with copper oxides / activated carbon. Xiandai Huagong, 2006, 26 Suppl., 252-254.

75. N. Sobana, M. Muruganandam, M. Swaminathan. Characterization of AC-ZnO catalyst and its photocatalytic activity on 4-acetylphenol degradation. Catalo. Commun., 2007, 2008, 9, 2, 262-268.

76. O. Yamamoto. Antibacterial ability of activated carbon containing ZnO particles. Prep. ACS Fuel Chem. Symp., 2005, 50, 1, 66-67.

77. Q.-H. Meng, L. Liu, H.-H. Song, L.-Ch. Ling. Effect of loaded metal on electrochemical properties of the activated carbon composite electrodes Cailiao Kexue Yu Gongyi, 2005, 13, 2, 119-122.

78. Th. Brousse, P.-L. Taberna,; O. Crosnier, R. Dugas, Ph. Guillemet, Y. Scudeller, Y. Zhou, F. Favier, D. Belanger, P. Simon. Long-term cycling behavior of asymmetric activated carbon / MnO_2 aqueous electrochemical supercapacitor. J. Power Sources, 2007, 173, 1, 633-641.

79. G.-H. Yuan, Zh.-H. Jiang, A. Aramata, Y.-Zh. Gao. Electrochemical behavior of activated-carbon capacitor material loaded with nickel oxide. Carbon, 2005, 43, 14, 2913-2917.

80. Y. Nishi, T. Suzuki, K. Kaneko. NO reduction over ultrafine metal-tailored microporous carbon at ambient temperature. Carbon, 1998, 36, 12, 1870-1871.

81. M. Kulazynski, K. Bratek, W. Bratek. Removing of nitric oxide from tail gases using spherical shape catalyst based on carbon material from the waste ion exchange resins. Prace Naukowe Instytutu Chemii i Technologii Nafty i Wegla (Wroclaw), 2002, 57 427-432.

82. T. Grzybek, J. Klinik, D. Olszewska, M. Rogoz, H. Papp. Carbon supported Mn oxide catalysts for selective catalytic reduction of NO_x by NH_3. DGMK Tagungsbericht, 1997, 9704, 1827-1830.

83. J.-K. Yang, H.-J. Park, H.-D. Lee, S.-M. Lee. Removal of Cu (II) by activated carbon impregnated with iron (III). Colloids Surf. A, 2009, 337, 1-3, 154-158.

84. H.-J. Fan, T. Wang, P. R. Anderson. Removal of Cu (II) by iron oxide-coated granular activated carbon. Zhongguo Huanjing Gongcheng Xuekan, 2000, 10, 3, 193-199.

85. L. Zhu, J. Tu, Y. Shi. Separation of carbon monoxide-carbon dioxide-nitrogen gas mixture for high-purity carbon monoxide by pressure swing adsorption. Gas Separ.Purif., 1991, 5, 3, 173-176.

THEORETICAL FUNDAMENTALS OF SPECTRAL
ANALYSIS AND SPECTROSCOPIC FACILITIES IN
NANO AND MICRO BIO-OBJECTS INVESTIGATIONS

K. G. Kapanadze, T. N. Bzhalava, G. G. Chikhladze

Department of Engineering Physics
Faculty of Informatics & Control Systems
Georgian Technical University
Tbilisi, Georgia
gurchix@gmail.com

Abstract

The paper deals with selection of appropriate, acceptable and precise spectroscopic methods in investigations, related to different kinds of nano and micro biological objects, in particular, the methods of revealing and detection of viruses in surrounding environment. The article represents comparison of different spectroscopic investigation methods in line of their features, approaches, duration and expenses of experiment, needed apparatus, etc. Advantages and disadvantages of the methods are listed. The relative priorities of different methods related to revealing and detection of viruses are discussed and estimated.

The _**spectral analysis**_ is the physical method of the quantitative and qualitative analysis of the chemical composition of substances, based on investigation of their optical spectra. It is distinguished by the highest precision and accuracy, being applied in physics, chemistry, metallurgy, geological searches, medicine, etc. The spectral analysis combines investigations based on the interaction between a matter and radiation. Atomic and molecular spectral analysis provides the possibility of determination of the atomic and molecular composition of investigated elements. Its theoretical basis is the _**spectroscopy**_ [1].

The main goal of our studies consists in choosing appropriate, mostly acceptable and highly precise spectroscopic methods in investigations, concerning various nano and micro biological objects, in particular, the methods of revealing and detection of viruses, existing in the environment, surrounding humans.

The _**optical spectral analysis**_ is the easiest to be carried out, needing no complicated preanalysis preparations. Atomic spectra are received by pulling the sample into the gaseous condition appearing at its heating to 1,000 – 10,000 °C (**Figure 1**). Light rays pass through the gas, the spectral lines manifesting all elements the gas consists of. Mathematical foundations of the spectral analysis were elaborated in 19th c. by French mathematician Jean-Baptiste Joseph Fourier (**Figure 2**).

Besides the visible spectrum, the infrared – _**IR-analysis**_ in the range 800 – 40,000 nm – and the ultraviolet – _**UV-analysis**_ in the range 200 – 400 nm – areas are used in the spectral analysis. Rather frequently the nuclear-magnetic resonance – _**NMR-analysis**_ – is applied as well.

These are the most significant and widely used investigation methods providing the almost complete information concerning to the composition of organic compounds [2].

Figure 1. Spiritusfire and its spectrum.

Figure 2. Jean–Baptiste Joseph Fourier (1768 – 1830).

During our searches we have dig up a lot of scientific papers, articles and conference thesis and found out, that the leading specialists and famous laboratories carried out the wide scaled investigations on radioactive materials, semiconductors, rare metals and chemical reactive within the scopes of the analytical chemistry. Among the revealing / detection methods the most sensitive ones – radio-activating, mass-spectrometric, as well as emissive spectral analysis, luminescence, and photometric methods had been developed. All these methods are distinguished by extremely high analytical characteristics, easy access and simplicity [3 – 6].

Let us more tightly consider different spectroscopic methods in order to select further the mostly appropriate one for our purposes. First of all, notice that all of them are based on the interaction between atoms, molecules or ions of the analyzed substance and the EM-radiation. Depending on the kind of radiation two approaches should be distinguished – *emissive* and *absorptive methods*. Meanwhile, due to the particles, forming the analytical signal, specialists consider the *atomic* and the *molecular spectroscopy*.

Emissive spectral analysis is based on examination of linear spectra emitted by the colored steam of heated investigated substance. It manifests itself as the physical method of the quantitative and qualitative analysis of the composition of a substance [3]. Presence of lines of any element in the spectrum points on existence of this element in an investigated substance – this is the *qualitative analysis*, while the lines intensity in the spectrum of the element measures its concentration – the *quantitative analysis*.

Emissive spectral analysis (**Figure 3**) is simple, fast and very sensitive, needs no preliminary preparations and big number of samples. In investigations we paid the special attention to the importance of monochromatic light sources that is taken into account within the scopes of modeling study of the set problem. At the same time photoelectric registers – photometers are very important providing as fastness, exactness and simplicity of the process, as reveal of extremely small (of micro- and nano-scale) amount of investigated elements. Basic emissive methods are the atomic-emissive spectral analysis and the luminescence analysis.
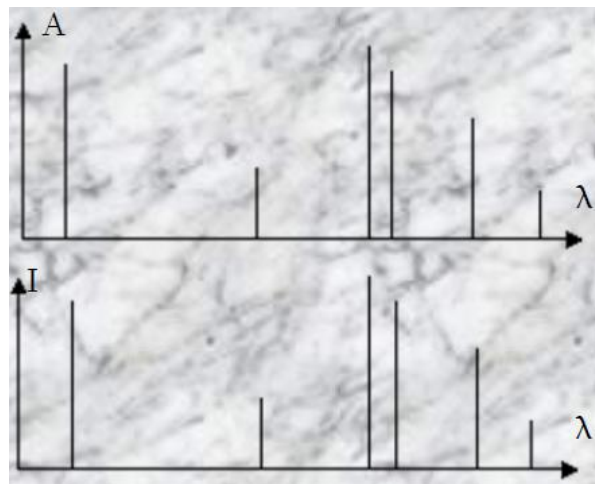
Figure 3. Absorptive (upper) and emissive (lower)
atomic spectra of the same element: A – absorptive
optical density and I – emissive intensity.

In absorptive spectral analysis (**Figure 3**) the radiation incoming from an external source passes through the sample, part of photons being absorbed by atoms and molecules. Basic methods here are **_atomic-absorptive spectral analysis_** and **_molecular-absorptive spectroscopy_**. The latter one usually is called the **_spectrophotometry_** or the **_photometric analysis_**. **_Emissive / absorptive spectra_** are registered by the **_spectrometers_**. Emissive / absorptive spectra are very similar to each other being defined by the same kind of energetic transitions of given elements.

In the schematic presentation of spectrometers we paid the special attention to significance of the monochromatic source that was taken into account in modeling study of the stated problem. In the analysis of the spectroscopic quantities we defined the meaning of the intensity, molar concentration and dependence of the optical density on light wavelength. It should be expressed as well that at change in the concentration the number and location of maxima of spectral curves relative to light wavelength axis remains unchanged. It once again proves expedience of study of single particle problems.

Let consider now emissive and absorptive spectra separately [5]:

● In emissive spectral analysis we distinguish the qualitative and the quantitative analysis. In the qualitative analysis widest spectral portfolio are used, where etalon emissive spectra for big number of elements are gathered with wavelengths and lines of the relative intensity given as well. And received experimental spectra are compared with them. In the quantitative analysis the emissive intensity is determined by the concentration of atoms. For given light wavelength the intensity I in the sample is proportional to the concentration C of an element: $I = \alpha\, C$, where α is the proportionality coefficient. Calculation of concentrations is carried out at the n-graded graphs built up beforehand.

● In absorptive spectral analysis when light passes through a substance, the light intensity decreases due to its absorption and scattering by this substance. For estimation of losses in light so called comparative solution is used, not including the investigated substance. Light passes through both basic and comparative solutions and the intensity of passed light is measured by Bouguer–Lambert–Beer law $I = I_0\, e^{-\beta C l}$, where I_0 is the incident intensity, l is thickness of the layer passed, and β is the proportionality determined by the substance absorption properties. The difference between I_0 and I is determined by nature and concentration of the investigated substance.
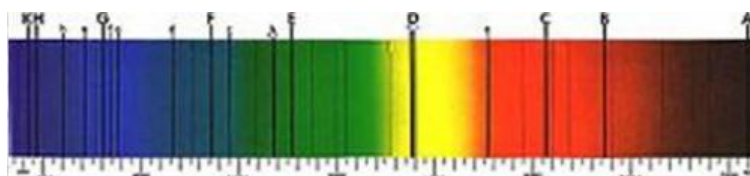
Figure 4. Absorptive spectrum.
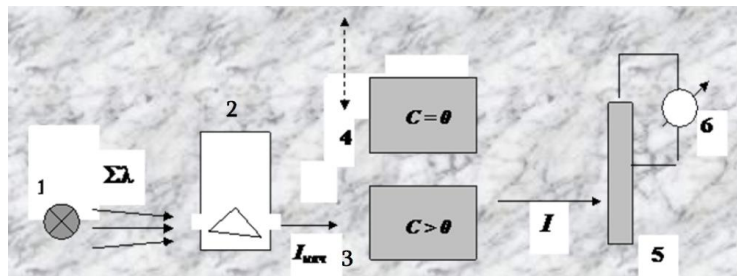
Figure 5. Spectral pyrometer. 1 – light source, 2 – prism, 3 – vessel with substance under investigation, 5 – light receiver (photocell), and 6 –microampermeter.

In molecular-absorptive spectroscopy, as an analytical signal the optical density (A) is used. It is the logarithm taken from the ratio of intensities of light passing through the basic and comparative solutions: $A = \log I_0 / I$. It is proportional to the concentration as well ($A \sim C$). For measurements of the optical density and registration of absorptive spectra (**Figure 4**) the spectral photometers (**Figure 5**) are used, consisting of mono-chrome-lens, light source, emission receiver and register.

The absorptive spectrum of the solution is given in $A - \lambda$ coordinates, at the change in the concentration the spectral curve vertically deviates, while the number and location of maxima relative to light wave scale remain unchanged and that proves the expediency of studying the single particle problems (**Figure 6**).
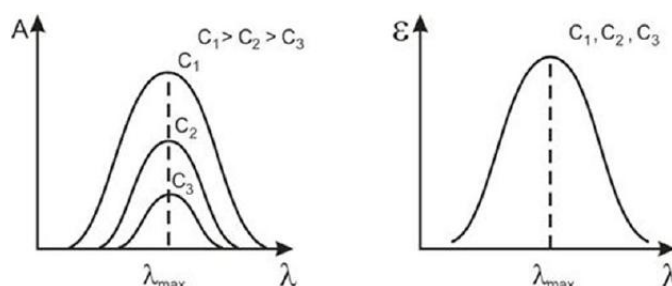
Figure 6. Absorption spectra of solutions of different concentrations.

Consider now the ***molecular electron spectroscopy*** [6] known also as the ***ultraviolet spectroscopy*** – the method of determination of composition of a substance based on the analysis of emission / absorption spectra of light (**Figure 7**). Interaction between light and the substance results in transition of excited electrons from one energetic level on another. When its energy exceeds the ionization potential electron leaves the molecule i.e. ionization occurs. When elect-ron transits from the excited level on lower energetic level – the emission of a photon occurs. It appeared that for most molecules light wavelengths corresponding to electrons transitions are located within the range of visual light – ultraviolet light (100 – 730 nm). The corresponding energy is sufficient to transit the electrons of organic molecules into excited condition. Difference in energies of signed conditions is divided into quanta, resulting in absorption of photons of strictly determined energies.
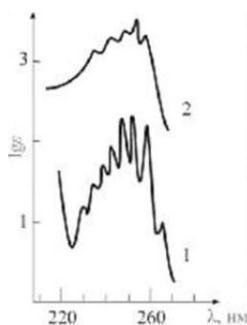
Figure 7. Electron spectra of different substances.

Figure 8. Double-ray scanner-spectrometer Lambada 35 operates in Vis. And UV regions of the spectrum (190 – 1100 nm). Its function is objects' quantitative and qualitative analysis

In ultraviolet area absorb all organic substances. The "working" region is usually composed within 190 – 730 nm range, but in most cases it varies within 200 – 380 nm. Optical materials within this range are transparent and, thus, may be used for manufacturing of lenses. While for investigations of dielectrics possessing too wide forbidden zones the wavelengths less than 190 nm (so called vacuum ultraviolet) are applied. The amount of substance for investigations is small – about 0.1 mg that greatly increases the popularity of the method [7].

And now let us overview what advantages gain *ultraviolet photoelectron spectroscopy* [6]. As it was discovered, here the ultraviolet emission excites photoelectrons and causes their release from filled electron levels in the valence and conduction zones due to photo-ionization. As the laboratory sources air-discharge bulbs are applied, mostly filled by helium (**Figure 8**). Due to application of photons with relatively low energy, during photoemission only valence levels are excited. It should be noted as well that filled orbitals of absorbed molecules strongly influence on the photoelectron spectra. This method manifests itself as the strong and effective weapon in studying the structure of valence zones in the surface of the material as well, as the various surface alternations, caused by different ongoing processes such as absorption, growth of thin films, chemical reactions, etc.

Now we arrive to the method of *dynamic scattering of light* merging such phenomena as change in the frequency (Doppler shift), intensity and direction of light are [8, 9]. The dynamic scattering of light [9] is used in the *laser correlation spectroscopy* for determination of the size of particles in suspensions. The size of particles to be considered should be of the same order that light wavelength (**Figure 9**). When light rays pass through the suspension, the elastic scattering of light (Rayleigh's) takes place. Here the laser emission is used – being coherent and monochromatic. As the quantity to be measured so called autocorrelation function is taken being considered by change in the intensity of scattered radiation in time.

The method of laser correlation spectroscopy possesses number of sufficient advantages:
● measurement time – minutes;
● analysis may be carried out within the environment of existence of bio-objects;
● reception of statistical characteristics of the strain;
● ability of reveal of even very small changes in investigated object, by comparison the light spectra, scattered by a sample before and after the change in conditions of surrounding;
● reliability of the information concerning the ongoing changes within the system, as to conditions of the sample during measurements remains unchanged despite the influence of different external factors.
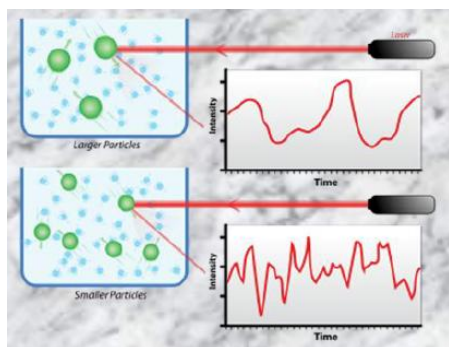
Figure 9. Dynamic scattering of light. Large and small particles are shown, respectively, in upper and lower parts.
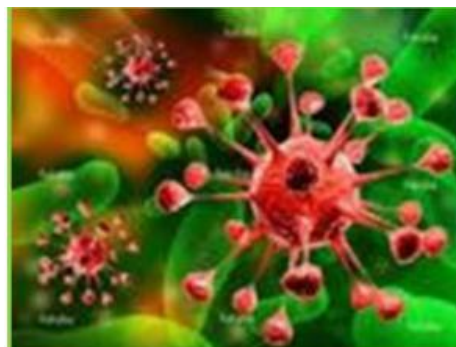
Figure 10. A virus.

The method of laser correlation spectroscopy is related to the methods of nanotechnologies, successfully used in investigations of viruses. Its main advantage consists in the ability to directly, *in vitro*, influence on live viruses by different factors, while the virus, itself, remains unchanged and still alive – whether investigations are carried out within its environment of existence.

This method is used also in stating the size of viruses. The measurements of the correlation functions of light scattered by the viruses of hepatitis A and of AIDS were carried out. The size of AIDS viruses was considered as 104 nm, while for hepatitis A – 28 nm. For control the method of electron microscopy was used, measuring the size of viruses in fixed samples. Notice though that the comparison revealed good coincidence of data.

Acknowledgement

References

1. Y. R. Shen. The Principles of Nonlinear Optics. 1984, John Wiley & Sons Inc., Chichester.
2. А. Н. Образцов. Методы исследования и диагностика нанообъектови наносистем. 2013, Москва, МГУ.
3. Е. И. Коваленко. Спектрофизические методы исследования биообъектов. 2011, Минск, БГУ.
4. И. Колесник. Спектроскопические методыдля исследования (нано)материалов. В сб.: Матер. IV Всеросс. олимпиады по нанотехнологиям. 2014, Москва, МГУ.
5. J. M. Hollas. Modern Spectroscopy (4ᵗh Ed). 2004, John Wiley & Sons Inc, Chichester.
6. J. W. Robinson. Spectroscopic Data Covering X-ray and Neutron, Photoelectron, Ultraviolet, Optical and Infrared Spectroscopy. In: Practical Handbook of Spectroscopy. 1991, Baton Rouge, CRC Press Inc., 23- 28.
7. I. Sobelman. Atomic Spectra and Radiation Transitions (2nd ed.). 1992, Springer-Verlag, Berlin–Heidelberg.
8. W. Demtröder. Laser spectroscopy. J. Mol. Spectrosc., 1981, 88,109-125.
9. S. Stenholm. Foundations of Laser Spectroscopy. 1984, Dover Publ., Inc., New York.

УСТРОЙСТВО ДЛЯ ОБЛУЧЕНИЯ ОБРАЗЦОВ ЭПИТЕРМАЛЬНЫМИ НЕЙТРОНАМИ РЕАКТОРА

Н. В. Багдавадзе, О. И. Джавахишвили

Институт физики им. Э. Андроникашвили
Тбилисский Государственный университет им. И. Джавахишвили
Тбилиси, Грузия
Nanuli.bagdavadze@yahoo.com

Аннотация

Устройство для облучения образцов эпитермальными нейтронами реактора представляет собой вертикальный канал цилиндрической формы, выполненный из радиационностойкого материала, часть которого, размещенная в активной зоне, покрыта кадмиевым экраном и имеет S-образный изгиб. Радиус кривизны изогнутой части кадмиевого экрана обеспечивает смещение верхней и нижней частей экрана на расстояние, равное трем диаметрам канала. Такая конструкция экранирующей части эффективно обеспечивает полную экранировку облучаемых образцов от тепловых нейтронов при произвольных реализуемых экспозициях, способствует увеличению производительности метода.

В практике инструментального нейтронно-активационного анализа (ИНАА) для облучения эпитермальными нейтронами экраны из нейтроннопоглощающего материала изготовляют в виде контейнеров различных форм, в которые помещают образцы в виде фольг для обертки контейнеров с образцами и экранов облучательных каналов [1]. Первые два вида приспособлений облучают в активной зоне реактора путем погружения в водозаполненные каналы реактора, изготовленные в виде труб из алюминиевого сплава.

Использование такого типа приспособлений из экранирующих тепловые нейтроны материалов связано с рядом существенных недостатков. А именно:

– исключена возможность проведения анализов по короткоживущим нуклидам из-за необходимости осуществления ряда радиационно опасных операций, связанных с разделением сильно активированных экранов и образцов; такие приспособления представляют помеху в эксплуатации аппарата (реактора) в процессе его работы вследствие влияния на нейтронное поле активной зоны сильно поглощающего материала при перемещении;

– указанные приспособления пригодны только для разового использования из-за высокой активности, требующей проведение дополнительных работ, связанных с

устранением радиоактивных отходов, ограничивающих экспрессность и массовость облучения. Систематическое облучение контейнеров в водозаполненных каналах является источником загрязнения воды бака реактора, приводит к неэкономному расходу материала экрана.

Известны конструкции горизонтальных облучательных каналов с кадмиевым экраном на конечной, расположенной в активной зоне, части, которая не пригодна для продолжительной экспозиции биологических материалов ввиду отсутствия полной экранировки и попадания на образец нейтронов со стороны их подачи и выгрузки.

Для устранения перечисленных недостатков и обеспечения массового облучения образцов эпитермальными нейтронами реактора с любой продолжительностью экспозиции активируемого материала при любых реальных мощностях, а также предотвращения прострела быстрых нейтронов на площадку, предлагается новое облучательное устройство, которое представляет собой вертикальный канал. На уровне активной зоны он имеет чехол с помещенным в него нейтроннопоглощающим экраном. В верхней части экрана канал имеет изгиб с радиусом кривизны, который обеспечивает смещение осей верхней и нижней частей экрана относительно друг друга на величину равную порядка трем диаметрам канала (см. **Рисунок 1**) [2].
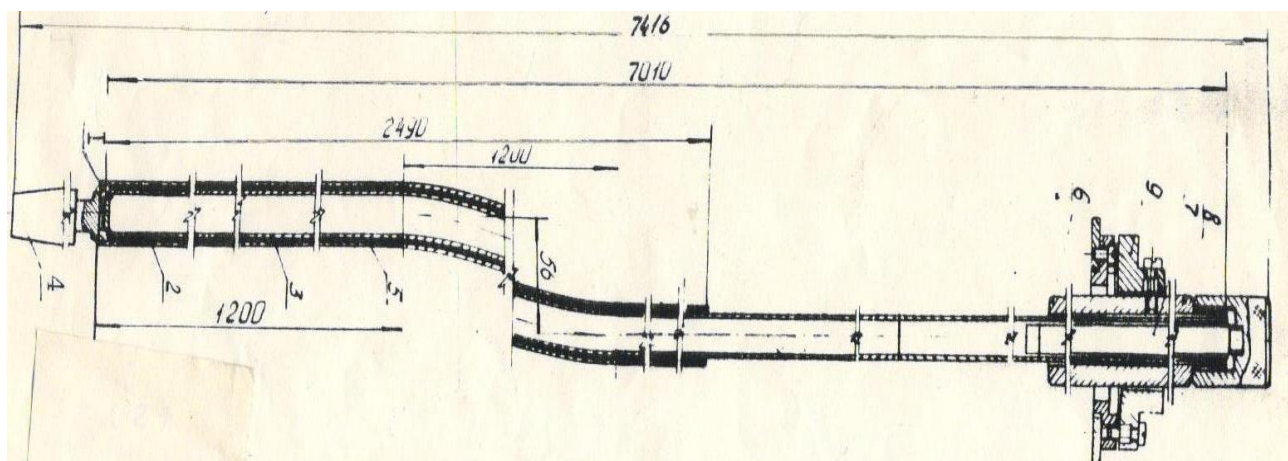
Рисунок 1. Схема канала с кадмиевым экраном: 1 – канал, 2 – чехол,
3 – экран из металлического кадмия, 4 – втулка для установления
канала в сборке, 5 – внешний чехол, 6 – крепление к крышке
бака реактора и 7 – приспособление для подвешивания образцов.

Вертикальный канал представляет собой трубу из радиационностойкого материала, например, из алюминиевого сплава А–1, в нижней части на высоте активной зоны канал имеет чехол 2 из того же материала и экран 3, помещенный между трубой 1 и чехлом 2. Экран 3 выполнен из материала, поглощающего тепловые нейтроны металлического кадмия толщиной ~ 1 мм. Для лучшей теплопередачи экран 3 с чехлом 2 плотно прилегает к трубе 1. Канал имеет изгиб в верхней части экрана для предотвращения прострела быстрых нейтронов и натечки в канал тепловых нейтронов из той его части, где нет экрана. Величина изгиба определена радиусом кривизны, обеспечивающим такое смещение верхней и нижней частей канала, которое позволяет без помех загрузить его образцами. Радиус кривизны равен 3000 мм, а величина смещения ~ 70 мм.

Нижний конец канала запаян и имеет направляющую втулку 4 для установления его в центральной плоскости тепловыделяющей сборки реактора. Верхний конец присоединен к крышке бака реактора с помощью крепления 6. В верхней части канала он имеет приспособление для подвешивания облучаемых образцов.

Устройство работает следующим образом: канал установлен в центральной плоскости тепловыделяющей сборки активной зоны реактора. На поверхность канала, расположенного в активной зоне реактора, попадают нейтроны всей энергетической области спектра деления. В кадмиевом экране поглощаются нейтроны с энергией ≥ 0.4 эВ. Благодаря наличию дна и изгиба у кадмиевого канала образцы, помещенные в полость кадмиевого чехла, облучаются только нейтронами с энергией ≥ 0.4 эВ. Высота кадмиевого экрана, равная высоте активной зоны реактора, исключает облучение образцов нейтронами полного спектра деления при загрузке и выгрузке образцов в рабочем режиме аппарата.

Предлагаемое устройство для облучения образцов эпитермальными нейтронами реактора обладает рядом положительных качеств:

– способствует облучению образцов эпитермальными нейтронами, экспозицией произвольной продолжительности при любых реализуемых на реакторах мощностях, что значительно расширяет информацию об элементном составе используемых материалов благодаря возможности проведения их анализа по короткоживущим радионуклидам;

– производительность облучения практически не ограничена благодаря наличию большего по сравнению с контейнером рабочего объема и возможности непрерывного использования канала;

– работы по удалению радиоактивных загрязнений после облучения образцов доведены до минимума и ограничиваются только переупаковкой их для спектрометрических измерений;

– эксплуатация устройства не представляет радиационной опасности ввиду наличия изгиба в верхней части кадмиевого экрана, предотвращающего пролет быстрых нейтронов на верхнюю площадку реактора, откуда производится загрузка образцов;

– возможность эксплуатации предлагаемого устройства без защитной пробки способствует естественной вентиляции образцов в процессе облучения и предотвращает перегрев облучаемых образцов, характерных для сухих облучательных каналов;

– экономится расход материала поглотителя и сокращается объем работ по изготовлению контейнеров для разового использования.

Для ИНАА на эпитермальных нейтронах важно определение кадмиевых отношений, мешающих и определяемых элементов. При отсутствии возможности проведения таких измерений в случае использования для активации кадмиевого канала необходимо иметь данные относительно энергетического распределения нейтронов в точке облучения образцов. Такие данные предоставляют возможность оценить избирательную активацию, порог обнаружения и определения отдельных элементов. Для этого было измерено распределение потока быстрых (≥ 0.5 МэВ) нейтронов по вертикали кадмиевого канала, на основании которого была найдена точка, соответствующая максимальному значению потока, в дальнейшем используемая для облучения образцов. Для указанной точки была получена картина энергетического распределения быстрых и резонансных нейтронов.

Изучение распределения потока быстрых нейтронов по вертикали кадмиевого канала проведено с помощью универсальных детекторов на основе композиции термореактивной фенолфармальдегидной смолы и продуктов ее пиролиза с элементами, имеющими пороговые сечения реакций на быстрых нейтронах [3]. В качестве детекторов для измерения потоков быстрых нейтронов были применены композиции с внедренными элементами Ni, Ti, Hg, Al и Co.

Измерения и расчеты спектров проводились согласно «Методическому указанию по восстановлению спектра быстрых нейтронов при использовании активационных методов измерения» [4]. Полученная картина распределения потоков быстрых нейтронов по вертикали кадмиевого канала приводится на **Рисунке 2** и показывает, что максимальный поток нейтронов соответствует точке, отстоящей от дна канала на расстояние 60 см, при мощности аппарата 1 МВт равен $1.56 \cdot 10^{12}$ н / см². Приведенные результаты измерений потоков быстрых нейтронов соответствуют точкам, отстоящим друг от друга на расстоянии 5 см и отличаются не более, чем на 5 %. Это указывает на необходимость учета изменения потоков для различных точек протяженных образцов. Для измерения энергетического распределения нейтронов в точке облучения был использован специальный детектор, содержащий одновременно несколько пороговых элементов, гомогенно распределенных в инертной матрице. Это позволило при помощи единичного облучения такого детектора и последующего анализа на многоканальном амплитудном анализаторе получить картину энергетического распределения нейтронов с энергией ≥ 0.5 МэВ.
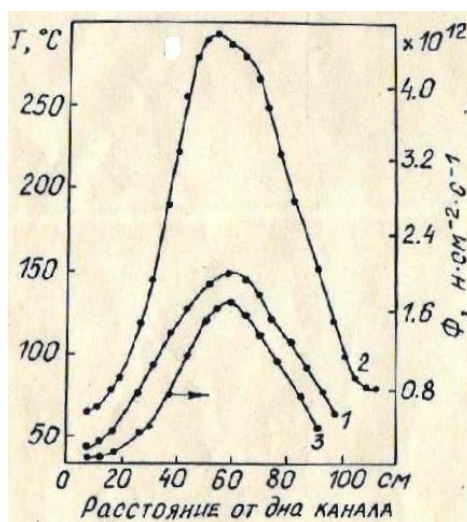
Рисунок 2. Распределение температуры и потока быстрых нейтронов в кадмиевом канале: 1 – кривая распределения температуры при мощности реактора 3 МВт, 2 – кривая распределения температуры при мощности реактора 8 МВт и 3 – кривая распределения потока быстрых нейтронов при мощности реактора 1 МВт.

Для таких измерений был использован комбинированный детектор с внедренными пороговыми элементами Ni, Ti, Hg, Al и Co. Полученная картина энергетического распределения нейтронов в точке, соответствующей максимальному интегральному потоку нейтронов, т.е. на длине подвеса равного 7200 мм, показана на **Рисунке 3**.
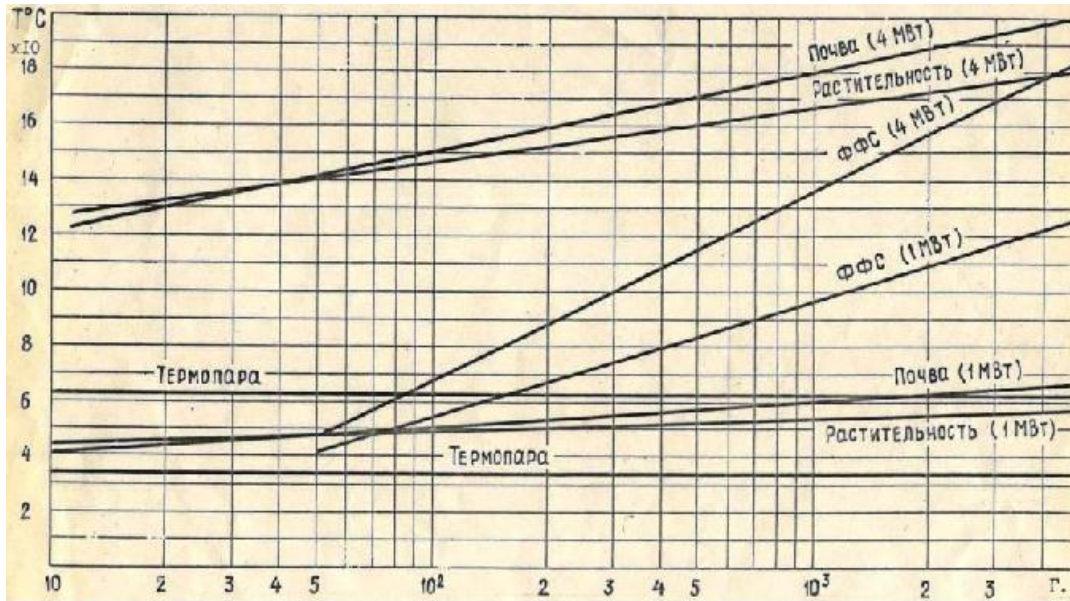
Рисунок 3. Кривые зависимости температуры радиационного
нагрева биоматериалов и ФФС от массы и потока нейтронов.

Проведенные измерения энергетического спектра эпитермальных нейтронов в точке облучения образцов в кадмиевом канале дают возможность оценить чувствительность определения элементов, имеющих большие резонансные и пороговые сечения активации. Принимая во внимание, что значение потока тепловых нейтронов в максимуме распределения по длине центральных ВЭК реактора ИРТ-М при мощности 1 МВт составляет $(1.2 - 1.5) \cdot 10^{12}$ н / см², можно предполагать, что в кадмиевом канале (также в точке максимального значения потоков нейтронов), он не будет превышать 10^{10} н / см² с [5]. Определение значения потоков нейтронов различных энергетических групп в максимуме распределения по высоте кадмиевого канала при мощности 1 Мвт показало, что оно составляет $2.2 \cdot 10^{10}$, $1.5 \cdot 10^{12}$ и $5.6 \cdot 10^{11}$ н / см² с для тепловых, быстрых и резонансных нейтронов. Приведенное соотношение интенсивностей тепловых, быстрых и резонансных нейтронов подтверждает возможность создания условий преимущественной активации элементов с большими резонансными сечениями захвата нейтронов в эпитермальной области с помощью описываемого канала. Далее будет показано, что облучение биообразцов в данном канале способствовало достижению удовлетворительной избирательной активации ряда элементов на основании чего и был разработан многоэлементный ИНАА биоматериалов.

Явление радиационного нагрева биологических образцов, наблюдаемое в процессе облучения в реакторе, является следствием взаимодействия γ-лучей и нейтронов спектра деления с веществом образца, сопровождающиеся передачей энергии и выделением тепла. Изменение температуры облучаемого образца (поглотителя) от переданной ему энергии, соответствующей 1 калории тепла, дается уравнением [3]

$$\Delta T / \Delta E = I / m\, c \qquad (\text{град / кал}), \qquad (1)$$

где T – температура, E – энергия, m – масса поглотителя, а c – удельная теплоемкость.

Приведенное уравнение показывает, что температура радиационного нагрева облученных образцов зависит от энергии падающего излучения, которая в условиях

реактора достигает значений, при которых оказывает существенное влияние на результаты элементного анализа биообразцов [6]. Отсутствие системы охлаждения в кадмиевом канале и данных относительно степени нагревания образцов в процессе облучения приводит к необходимости определения ее значения. Ввиду того, что определение температуры нагревания биообразцов по уравнению (1) связано с известными трудностями, характеризующими расчеты тепловыделения от γ-лучей и нейтронов спектра деления в поглотителях, а также отсутствием данных относительно удельной теплоемкости биоматериалов, были проведены экспериментальные измерения с помощью термопар.

Проведение внутриканального измерения температуры радиационного нагревания образцов ставило целью выбор оптимального режима облучения, обеспечивающего минимальные неконтролируемые потери при облучении образцов без охлаждения. Для этого были изучены зависимость температуры радиационного нагревания образцов от массы, зависимость температуры радиационного нагрева при разных интенсивностях потока нейтронов и распределение температуры радиационного нагрева образцов вдоль кадмиевого канала. Измерения температуры было проведено с помощью хромель-копелевой термопары, один край которого был закреплен непосредственно в центре облучаемого образца, а второй «реперный» находился при температуре таяния льда. Термопары по всей высоте канала были изолированы керамической термоизоляцией, и подключали в компенсационную мостовую измерительную цепь, обеспечивающую точность измерения ~ 0.1 % [6].

Образцы, для которых определялся радиационный нагрев, представляли собой прессованные таблетки гомогенного порошка обезвоженных биологических и упаковочного материалов, помещенные в обычно применяемые алюминевые контейнеры. Для установления зависимости нагрева образцов от их веса были взяты навески, составляющие 10, 50, 100, 500 и 5000 мг. Образцы размещались в точке, соответствующей максимальному интегральному потоку нейтронов (точно фиксируемого от дна канала), равному $n \cdot 10^{12}$ н / см^2 с при мощности аппарата 4 МВт. Измерения температуры проводились для каждого образца в отдельности при работе аппарата на стационарной мощности и после установления постоянной температуры в образце.

Таблица 1. Зависимость температуры радиационного
нагрева образцов от массы и мощности аппарата.

Материал	Мощность аппарата	Масса образца, мг				
		10	50	100	500	5000
Ткань печени	1 МВт	38	45	48	58	70
	4 МВт	90	100	110	175	230
Растительность	1 МВт	43	45	47	60	74
	4 МВт	125	127	130	180	190
ФСС	1 МВт	44	48	50	60	75
	4 МВт	105	145	148	178	185
Почва	1 МВт	40	42	60	58	65
	4 МВт	130	132	150	180	200

Приведенные в **Таблице 1** значения температуры соответствуют средним арифметическим из трех измерений, проведенных с интервалом 30 мин. Кривые зависимости температуры от массы образца показывают, что с увеличением массы навесок, а следовательно, и количества поглощаемой энергии, температура радиационного нагрева облучаемых проб значительно возрастает. Например, для образца печеночной ткани (соответствующего 10 мг) она увеличивается от 90 до 230 °C (соответствующего 5000 мг) при облучении постоянным интегральным (по энергиям) потоком эпитермальных нейтронов $5 \cdot 10^{12}$ н / см² с при мощности 4 МВт.

Распределение температуры радиационного нагрева биообразцов по вертикали канала было проведено путем измерения температуры на образце обезвоженной печеночной ткани массой 10 г, который в начале измерений находился на дне канала, а затем подтягивался вверх с интервалом в 5 см. Измерения температуры образца проводились для каждого положения после 30 мин выдержки, необходимой для установления температуры. Описываемые измерения были проведены для двух режимов работы реактора соответствующих 3 и 8 МВт мощности. Результаты измерений приводятся на **Рисунке 2**.

Сравнение кривых 1 и 2 с 3 (**Рисунок 3**) показывает, что распределение температуры радиационного нагрева строго следует закону распределения потоков нейтронов. В точке, соответствующей максимальным потокам быстрых нейтронов в 160 см от дна канала, температура радиационного нагрева соответствует также максимальным значениям – 149 и 284 °C. С другой стороны, из полученных результатов следует, что температура радиационного нагрева образцов растет с увеличением мощности аппарата. Так, от 149 °C при 3 МВт, она увеличивается до 284 °C при 8 МВт (для 10 г образцов) и от 170 °C при 4 МВт (для 50 г образцов) до 284 °C при 7 МВт (для 10 г образцов). Полученные значения температуры радиационного нагрева материалов при различных мощностях реактора (см **Таблицу** 1 и **Рисунок** 3) дают возможность выбора оптимальных навесок образцов и режима облучения в кадмиевом канале для устранения неконтролируемых потерь в процессе облучения. Вместе с тем, они подтверждают целесообразность применения в НАА биоматериалов радиационно- и термостойкой ФФС в качестве упаковочного материала биообразцов и основы для синтеза эталонов сравнения при использовании облучения в неохлажденных каналах и, кроме того, объясняют причины расхождения данных, полученных различными исследователями при использовании нестандартных эталонов НАА [7].

Ссылки

1. Е. М. Лобанов, И. А. Миранский. О возможности использования метода резонансной активации элементов для анализа образцов руд, горных пород и других объектов. 1967, Ташкент, Фан.
2. Н. В. Багдавадзе, О. И. Джавахишвили. Устройство для облучения образцов эпитермальными нейтронами реактора. Авт. свид. № 1450639.
3. Т. С. Амбарданашвили, В. Ю. Дундуа, Г. И. Кикнадзе, М. А. Коломийцев. Метрология нейтронного излучения на реакторах и ускорителях. В кн.: Тезисы докладов Всесоюзного координационного совещания по метрологии нейтронного излучения. 1971, Москва, 71-71.

4. Измерение нейтронных потоков в экспериментальных каналах ядерного реактора. Вып. 1. Препринт КМО ИФ АН ГССР 3.977. 1972, Тбилиси.

5. Н. Багдавадзе. Инструментальный нейтронно-активационный анализ биологических материалов на эпитермальных нейтронах реактора (Канд. диссер.). 1983, Тбилиси.

6. E. L. Andronikashvili, L. M. Mosulishvili, N. E. Kharabadze, N. V. Bagdavadze, N. E. Kuchava. Einice aspekt der Instrumentalian Neutron-Activierungs analyse Biologieher Materialien. J. Rad. Chem., 1980, 58, 49-59.

7. Н. В. Багдавадзе. Применение резонансной активации в элементном анализе биомаиериалов. В кн.: Ядерно-физические методы элементного анализа в биологии и медицине. 1980, Обнинск, 49-57.

იოდის სინთეზური სტანდარტული ნიმუში

ნ. ბაღდავაძე, ვ. დუნდუა, ნ. ჩიხლაძე

ე. ანდრონიკაშვილის ფიზიკის ინსტიტუტი
ი. ჯავახიშვილის სახ. თბილისის სახელმწიფო უნივერსიტეტი
თბილისი, საქართველო
Nanuli.bagdavadze@yahoo.com

ანოტაცია

იოდის სინთეზური სტანდარტული ნიმუში შეიცავს ქვეიოდმჟავის 190 – 200 °C-მდე გახურებით მიღებულ იოდის (V) ოქსიდს, ანტრაცენსა და ფენოლფორმალდეჰიდურ ფისს, კომპონენტების შემდეგი თანაფარდობით: 0.46 – 3.93, 9.62 – 9.76 და 86.37 – 89.79 მას. %, შესაბამისად. ნიმუშის გამოყენების სფეროა ანალიზის ბირთვულ-ფიზიკური მეთოდები.

იოდის სინთეზური სტანდარტული ნიმუშის მიღების ტექნოლოგია განეკუთვნება ანალიზის ბირთვულ-ფიზიკური მეთოდების სფეროს, კერძოდ, სტანდარტული ნიმუშების დამზადებას ნეიტრონულ-აქტივაციური და რენტგენო-რადიომეტრული მეთოდებით ანალიზისათვის და ის შეიძლება გამოყენებულ იქნას იოდის მასური წილის განსაზღვრისათვის სხვადასხვა ნიმუშებში, კერძოდ, მცენარეულ და ბიოლოგიურ მასალებში, გარემომცველი სამყაროს ობიექტებში და სხვა, ასევე გარემოს სამრეწველო საწარმოების ნარჩენებით დაბინძურების შესწავლის და კონტროლის მიზნით.

ამჟამად ცნობილია სტანდარტული ნიმუშების (სნ) დამზადების მეთოდები ბუნებრივი ბიოლოგიური მასალებისაგან, როგორიცაა ზღვის კომზოსტო, ხარის ღვიძლი, მცენარეების ფოთლები, ბოსტნეულის ფხვნილი, ნიადაგი, წყალი და სხვა.

ბუნებრივი მასალებისაგან სტანდარტული ნიმუშების დამზადების მეთოდები ითვალისწინებს მათ გამოშრობას ჰაერზე ან ტემპერატურის ზემოქმედებით, შემდგომში გაფხვიერებით და მექანიკური მორევით ჰომოგენიზაციის მიღწევით. მასალას ელემენტების შემცველობაზე ანალიზისათვის გადასცემენ სხვადასხვა ლაბორატორიებს. ატესტირებულ შედეგად მიიჩნევენ ლაბორატორიათაშორისო გამოკვლევების საშუალო მნიშვნელობის სიდიდეს.

ბუნებრივი მასალებისაგან დამზადებულ სნ ახასიათებს მთელი რიგი ნაკლოვანებები: არაკვლავ წარმოებადია; ატესტაციის პროცესი რთული და ძვირადღირებულია; არა აქვს გეომეტრიული ფორმა, ფხვნილისებურია და მოითხოვს სპეციფიკურ შეფუთვას; არაჰომოგენურია; ჰიგროსკოპულია; შეიცავს ელემენტების ზღვრულ რაოდენობას; შეუძლებელია რომელიმე ელემენტის კონცენტრაციის ვარირება; არასტაბილურია დროში, რადგან ხდება ბიოლოგიური ფუძის დაბერება; შესაძლებელია ადვილად პორთქლადი ელემენტების არაკონტროლირებადი კარგვა.

გამოგონების ტექნიკურ გადაწყვეტასთან ახლო მდგომ მეთოდს წარმოადგენს მცენარეული მასალების ელემენტური შედგენილობის იმიტატორის დამზადება აქტივაციური ანალიზისათვის, ფენოლფორმალდეჰიდური რეზოდური ფისის ნარევის დამზადება ელემენტების სხვადასხვა შენაერთებთან და გამხსნელთან. ნარევს გადაადენით აცილებენ გამხსნელს, მისგან იღებენ რეზიტოლს, ამზადებენ ფხვნილს, წნეხავენ აბებს, რომლებსაც შემდგომ ამყარებან ტემპერატურული ზემოქმედებით [1, 2]. მოცემული მეთოდის ნაკლს წარმოადგენს ის, რომ შეუძლებელია ნიმუშში იოდის მასური წილის ვარირება (შეიცავს იოდს 1.35 · 10⁻⁵ %), რადგანაც მასალა შეიცავს რამდენიმე ათეულ ელემენტს, რომლებიც შედის მცენარეული ნიმუშის შედგენილობაში. იოდის მასური წილის გაზრდა სტანდარტულ ნიმუშში იწვევს როგორც თვით იოდის, ისე სხვა ელემენტების ჰომოგენურობის დარღვევას და მიღებულ ნიმუშს აქვთ დაბალი მექანიკური მდგრადობა. ამ მეთოდში იოდის შენაერთად გამოიყენება ნატრიუმის იოდიდი.

ატმოსფეროს, წყლების, მცენარეული, ბიოლოგიური და ობიექტების სხვადასხვა ტექნოლოგიური ნარჩენებით დაბინძურების კონტროლისა და შესწავლისათვის საჭიროა სხვადასხვა შემადგენლობის ელემენტ-იოდის სნ, რომლებშიც იოდი ჰომოგენურად იქნება განაწილებული მთელ მოცულობაში, ექნება მაღალი მექანიკური სიმტკიცე, არ შეიცავს ხელისშემშლელ მინარევ ელემენტებს, მაგალითად, იოდს შეიცავს 3.0 მას. %-დე კონცენტრაციით.

წარმოდგენილი ტექნოლოგიის მიზანია უზრუნველვყოთ მატრიცაში იოდის განაწილების ჰომოგენურობა კონცენტრაციის ინტერვალში 0.34 – 3.00 მას. %, მასალის ადვილი წნეხვადობა, მაღალი მექანიკური სიმტკიცე, მინარევი ელემენტების შემცველობის გარეშე. დასახულ მიზანს აღწევენ იმით, რომ სტანდარტულ ნიმუშად იყენებენ თერმორეაქტიული ფენოლფორმალდეჰიდური ფისის პოლიმერულ მასალას, რომელიც შეიცავს ფენოლფორმალდეჰიდურ ფისსა და არაორგანულ გამხსნელებში უხსნადი იოდის ქიმიურ შენაერთს – იოდის (V) ოქსიდის წვრილ დისპერსიულ ფხვნილს 0.46 – 3.93 მას. % რაოდენობით.

ინტერვალის კრიტერიუმს წარმოადგენს დაყენებული კონკრეტული ამოცანა – ბირთვულ-ფიზიკური მეთოდებით ნივთიერების ანალიზისათვის საჭიროა სტანდარტული ნიმუში 3.0 მას. %-მდე იოდის შემცველობით ბუნებრივი გარემოს გაჭუჭყიანების შესწავლის და კონტროლის მიზნით.

ექსპერიმენტულად დადგენილია, რომ საუკეთესო ჰომოგენურობა მიიღწევა იოდის კონკრეტული ქიმიური ნაერთის ფორმის სახით ახლად მიღებული მისი ოქსიდის გამოყენებისას. ეს შენაერთი არ იხსნება ფენოლფორმალდეჰიდურ რეზოლურ ფისში და ორგანულ გამხსნელებში, მაგრამ იხსნება წყალში, კარგად სველდება და ადვილად ერევა ფისს, არ განშრევდება, მიღებული წნეხფხვნილი კარგად იწნეხება, ანუ ჰომოგენიზაციის ამოცანა დაიყვანება თანაზომადი რაოდენობის მექანიკურ შერევამდე.

იოდის (V) ოქსიდი მიიღება ქვეიოდის მჟავის გამოწვით 190 – 200 °C ტემპერატურაზე მუფელის ღუმელში. მიღებულ ოქსიდს აცივებენ ექსიკატორში ფოსფორის ანჰიდრიდზე, აფხვიერებენ როდინში, ცრიან 1000 – 2000 ხვრელი / სმ² საცერში, მიღებულ წვრილ დისპერსიულ იოდის (V) ოქსიდის ფრაქციას ურევენ ანტრაცენს და შეაქვთ მატრიცის სპირტხსნარში.

ანტრაცენს, ერთი მხრივ, იყენებენ როგორც დაწნეხვისათვის საჭირო დანამატს, მეორე მხრივ, ანტრაცენის შერევით იზრდება მასა, რაც უზრუნველყოფს შეყვანილი ელემენტის უკეთეს განაწილებას მასის მთელ მოცულობაში.

იოდის 0.34 მას. %-ზე ნაკლები რაოდენობით (იოდის (V) ოქსიდი 0.46 მას. % -ზე ნაკლები) შეყვანისას ჰომოგენურობა ირღვევა 5 – 7 %-ით. იოდის 0.30 მას. %-ზე მეტი რაოდენობით (იოდის (V) ოქსიდი 3.93 მას. %-ზე) შეყვანისას ჰომოგენურობა კარგია, მაგრამ მექანიკური სიმტკიცე მცირდება.

ჰომოგენური და მექანიკურად მდგრადი ხელისშემშლელი მინარევი ელემენტების შემცველობის გარეშე სტანდარტული ნიმუშების მიღებისათვის იოდის (V) ოქსიდის ოპტიმალურ კონცენტრაციას წარმოადგენს 0.46 – 3.93 მას. %.

დამუშავებული იოდის შემცველი სტანდარტული ნიმუშების მიღების მეთოდიკა შემდეგია.

46 გ ფორმალდეჰიდური რეზოლური ფისის სპირტხსნარს ათავსებენ მრგვალძირა კოლბაში, შეჰყავთ 5 გ ანტრაცენის და 0.1749 გ იოდის (ახალმიღებული წვრილდისპერსიული იოდი (V) ოქსიდის 0.23 გ) ფხვნილის ნარევი (ანტრაცენის და იოდ (V) ოქსიდის ნარევს ამზადებენ ფხვნილების გულმოდგინე შერევით). მიღებულ ნარევს აცხელებენ წყლის აბაზანაზე 70 – 75 °C-ზე და გადადენიან გამხსნელს 120 – 130 მმ ვერცხლისწყლის სვეტის წნევის ვაკუუმით (წარმოებს ნარევის ვაკუუმური შერევა). გამხსნელის გადადენის შემდეგ ნარევი გადაქვთ ფაიფურის ჯამში, ათავსებენ ვაკუუმთერმოსტატში 140 – 150 მმ ვერცხლისწყლის სვეტის სტადიამდე. რეზიტოლს აივებენ, აფხვიერებენ, წნეხავენ აბების სახით 150 – 300 კგმ / სმ² წნევაზე. მიღებული ტაბლეტები 120 – 130 °C-ზე პოლიმერიზაციით მიჰყავთ რეზიტის სტადიამდე.

მიღებულ სტანდარტულ ნიმუშებში ელემენტიოდის შემცვლელობა შეადგენს 0.34 მას. %-ს. ელემენტის კონცენტრაციის მაქსიმალური გადახრა ინდივიდუალურ სინჯში საშუალო მნიშვნელობიდან შეადგენს 2.85 მას. %-ს, ნიმუშის მექანიკური სიმტკიცეა 80 – 85 კგმ / სმ².

სტანდარტულ ნიმუშში შეყვანილი ელემენტის კონკრეტული ქიმიური ფორმის გამოყენებით მიიღწევა ჰომოგენურობა და მიღებული ნიმუშები არ შეიცავენ მინარევ ელემენტებს. შეყვანილი ელემენტის სხვა ქიმიური ფორმის გამოყენებისას არ ხერხდება ჰომოგენურობის, მექანიკური სიმტკიცის და საჭირო კონცენტრაციის ნიმუშის კვლავწარმოების განხორციელება.

შემოთავაზებული ტექნოლოგიით მიღებულ ნარეთში წარმოდგენილი ელემენტის კონკრეტული ქიმიური ფორმა ოპტიმალურია. ნარეთის ოპტიმალობა განსაზღვრულია ჰომოგენურობის უზრუნველყოფით, ფხვნილის ადვილი დაწნეხვის უნარით, მექანიკური სიმტკიცით და იმით, რომ მიღებული ნიმუშები არ შეიცავს ხელისშემშლელ მინარევ ელემენტებს.

მიღებული სტანდარტული ნიმუშები წარმოადგენენ კონგლომერატის ტიპის მყარ მასალას.

სტანდარტული ნიმუშები მიზანშეწონილია გამოყენებულ იქნენ, როგორც შედარების სტანდარტი იოდის განსაზღვრისათვის სხვადასხვა მასალებში ბირთვულ-ფიზიკური მეთოდებით.

სტანდარტული ნიმუშები ხასიათდებიან შემდეგი თვისებებით: არიან ჰომოგენური; არაჰიგროსკოპული; ზღვრული ტემპერატურა, რომლის დროსაც შეიძლება გამოყენებულ იქნას სნ არის 20 – 250 °C ნეიტრონების ინტეგრალური ფლიუენსი – 5 · 10^{18} ნ / სმ²; ნიმუშის დიამეტრია 5 – 50 მმ; სიმაღლე 1.2 – 10.0 მმ;

მექანიკური სიმტკიცეა 90 – 95 კგმ / სმ²; იოდის კონცენტრაცია მიღებულ ნიმუშებში – 0.34 – 2.99 მას. %.

ზემოაღნიშნული ტექნოლოგიის გამოყენებით შესაძლებელია დამზადდეს სტანდარტული ნიმუში, რომელიც შეიცავს იოდის შემცველ ნაერთს – ქვეიოდმჟავის 190 – 200 °C-მდე გახურებით მიღებულ იოდის (V) ოქსიდს. ნიმუში დამატებით შეიცავს ანტრაცენსა და ფენოლფორმალდეჰიდურ ფისს კომპონენტების შემდეგი თანაფარდობით, მას. %-ში:

იოდის (V) ოქსიდი   0.46 – 3.93,
ანტრაცენი   9.62 – 9.76,
ფენოლფორმალდეჰიდური ფისი   86.37 – 89.79.

დამოწმებანი

1.   სსრკ საავტორო მოწმობა # 1017076, G 01 N1/28, 1983.
2.   სსრკ საავტორო მოწმობა # 602001, G 01 N1/00, 1977.

ТЕРМОСТАБИЛЬНОСТЬ СТАНДАРТОВ СРАВНЕНИЯ НА ОСНОВЕ ФЕНОЛФОРМАЛЬДЕГИДНОЙ СМОЛЫ, ИСПОЛЬЗУЕМЫХ В НЕЙТРОННОМ АКТИВАЦИОННОМ АНАЛИЗЕ

Н. Кучава

Институт физики им. Э. Андроникашвили
Тбилисский Государственный университет им. И. Джавахишвили
Тбилиси, Грузия
e.kuchava@mail.ru

Аннотация

В работе обсуждается вопрос термостойкости стандартов сравнения, изготовленных на основе фенолформальдегидной смолы (ФФС), в зависимости от увеличения температуры при облучении исследуемого материала в канале ядерного реактора (ЯР) и отжиге в термостате. Они используются в относительном методе нейтронного активационного анализа, для определения содержания химических элементов в исследуемом материале.

Вопрос о термостабильности стандартов сравнения, используемых в относительном варианте нейтронного активационного анализа (НАА) [1, 2], рассматривают все, работающие в этой области исследователи. Неудивителен и наш интерес к этому существенному вопросу, так как он является одним из значительных факторов как природного (Bovine liver SRM–1577, Bovens kale, "Н–4" и др.), так и синтетического происхождения (синтетические растворы, таблетки из ФФС). Прежде всего были установлены пределы обнаружения одновременно определяемых четырнадцати химических элементов в стандартах сравнения на основе фенолформальдегидной смолы (ФФС), изготовленных в Институте физики АН Грузинской ССР [3]. Полученные результаты приведены в **Таблице 1**.

Стандарты сравнения на основе ФФС были облучены интегральным потоком нейтронов 10^{19} н $\cdot$ см$^{-2}$. Гамма-спектрометрические измерения были проведены с помощью детектора EGL–20VF объемом 114 см^3 в течение 1000 с, через 12 дней после прекращения облучения.

Как видно из **Таблицы 1**, самым лучшим пределом обнаружения в названных стандартах сравнения имеет Au.

Согласно ранее проведенным исследованиям [4], изменение температур облученных нейтронами исследуемых материалов в некоторых случаях является мешающим фактором правильного определения содержания в них химических элементов.

Таблица 1. Значения пределов обнаружения химических элементов в стандартах сравнения на основе фенолформальдегидной смолы (мкг).

Химический элемент	Аналитический радионуклид	Предел обнаружения элементов в стандартах сравнения
Au	Au–198	0,0000039
Sc	Sc–46	0.0000175
Sb	Sb–124	0.000111
Hg	Hg–203	0.000148
Cs	Cs–134	0.000218
Co	Co–60	0.000295
Ag	Ag–110m	0.000680
Cr	Cr–51	0.000720
Se	Se–75	0.000760
Br	Br–82	0.00154
Ba	Ba–131	0.00486
Rb	Rb–86	0.00490
Zn	Zn–65	0.00680
Fe	Fe–59	0.136

Таблица 2. Количество некоторых химических элементов (%), отожженных после облучения в холодных условиях в образцах стандартов сравнения "0".

Элемент	Температура отжига, °C					
	100	200	400	600	800	1000
Hg	98 (12)	10 (6)	0.1			
Cr	100 (13)	90 (10)	63 (10)	60 (10)	58 (14)	50 (12)
Zn	100 (10)	100 (9)	90 (9)	80 (9)	30 (9)	7 (4)
Se	100 (15)	100 (15)	94 (13)	59 (14)	52 (14)	50 (10)
Ag	100 (7)	100 (10)	95 (11)	94 (10)	80 (12)	16 (9)
Fe	100 (10)	100 (10)	95 (13)	85 (13)	85 (13)	85 (13)
Cs	100 (7)	100 7)	94 (10)	89 (10)	84 (10)	81 (10)
Tb	100 (10)	100 (10)	95 (11)	85 (10)	80 (10)	80 (10)
Sc	100 (7)	100 (7)	95 (7)	79 (7)	79 (7)	75 (7)
Co	100 (7)	100 (7)	92 (7)	80 (6)	75 (6)	75 (6)

Приведено среднее значение из 6 таблеток стандартов сравнения "0" и среднеквадратическое отклонение.

Для решения поставленной задачи по выяснению термоустойчивости, т.е. установление температурного интервала, при котором сохраняется постоянное содержание того или иного химического элемента, стандарты сравнения на основе ФФС под названием "0", ССБ–1 и ССБ–2, а также моностандарты некоторых химических элементов, были облучены в специальном низкотемпературном биологическом канале (т.н. НТБК), интегральным потоком нейтронов 10^{19} н · см$^{-2}$ при низких температурах (около − 40 °C), а затем их подвергали термическому отжигу в течение часа в термостате от

100 до 1000 °C, с увеличением температуры отжига через каждый час. Надо отметить, что матрица стандартов сравнения на основе ФФС по составу близка к биологическим материалам. Она состоит из углерода (76 %), кислорода (18 %), водорода (6 %). Результаты изменения содержания каждого радионуклида в стандартах сравнения выражались в относительных процентных единицах. Содержание каждого радионуклида в стандарте сравнения без отжига в термостате принимали за 100 %. Гамма-спектрометрические измерения проводили с использованием вышеотмеченного полупроводникового детектора. Результаты проведенных экспериментов приведены в **Таблице** 2.

Как видно из **Таблицы 2**, термические потери некоторых химических элементов, например Hg, происходящие при сравнительно низких температурах, начинаются при 100 °C и при 200 °C составляет 90 %. Безусловно, результаты HAA биологических материалов, облученных в неохлаждаемых условиях, без учета этого явления не могут быть корректными. Вторым по термочувствительности элементом, является Cr, уменьшение которого при температуре 200 °°C составляет 10 % и при 1000 °C достигает 50 %. В температурном интервале до 400 °C содержание элементов: Zn, Se, Ag, Fe, Cs, Tb, Sc и Co в стандартах сравнения "0" сохраняется почти постоянными. Процессы интенсивного улетучивания Zn и Ag наблюдаются с 600 °C и при 1000 °C в стандартах сравнения "0" они остаются в очень маленьком количестве. Остальные элементы претерпевают потери в интервале температур 400 – 1000 °C, но уровень испаренных элементов не превышает 50 %.

Мы сочли целесообразным проведение нескольких экспериментов по изучению изменения содержания химических элементов в многоэлементных стандартах сравнения ССБ-1 и СС–2, отоженных до облучения нейтронами в течение 70 часов. Результаты приведены в **Таблице 3**.

Таблица 3. Количество некоторых химических элементов (%) в стандартах сравнения ССБ–1 и ССБ–2, после отжига в термостате в течение 70 ч при разных температурах до облучения нейтронами.

Элемент	Температура отжига стандартных образцов, °C		
	100	200	300
Hg	100 (7)	7 (2)	4 (1)
Se	100 (7)	98 (8)	90 (8)
Fe	100 (6)	95 (8)	92 (9)
Cr	100 (6)	98 (7)	92 (7)
Sc	100 (4)	97 (5)	93 (5)
Cs	100 (4)	98 (4)	94 (4)
Zn	100 (5)	98 (5)	96 (5)
Au	100 (5)	98 6)	98 (6)

Приведено среднее значение из 6 таблеток стандартов сравнения и среднеквадратическое отклонение. В расчетах использована масса таблеток стандартов сравнения до отжига в термостате.

Для отжига в термостате указанных стандартов сравнения при температурах 100, 200 и 300 °C были использованы разные группы идентичных таблеток стандартов сравнения. Удельную радиоактивность нуклидов химических элементов, в

неподверженных отжигу образцах, принимали за 100 % и сравнивали с ними величины, полученные для образцов, отожженных при разных в вышеуказанных температурах. В расчетах были использованы массы стандартов сравнения до отжига в термостате. В **Таблице 3** указаны только те элементы из одновременно определяемых 14 химических элементов, содержание которых изменилось в процессе 70 часового отжига в термостате. Термостабильными оказались Ag, Co, Rb и Sb, поэтому они не внесены в **Таблицу 3**. Как видно из **Таблицы 3**, содержание Hg сохранить не удалось в указанном интервале температур, включая 200 °C, при котором испарение ртути составил около 90 %. Уменьшение содержания Se, отожженных в течение 70 ч в стандартах сравнения, около 10 %. Химические элементы: Zn, Fe, Cr после отжига в термостате при температуре 300 °C, претерпевают уменшение около 8 %. Нужно отметить, что Cs и Sc тоже оказались термостабильными в указанном интервале температур, включая 200 °C. Потери содержания вышеуказанных химических элементов в стандартах сравнения, отожженных в течение длительного времени при 300 °C, составляют около 6 – 7 %, притом форма таблеток не меняется.

В заключении можно сказать, что поставленная цель по исследованию термостабильности стандартов сравнения на основе ФФС, по нашему мнению, выполнена с определенной точностью.

Ссылки

1. Р. А. Кузнецов. Активационный анализ. 1967, Москва, Атомиздат.
2. H. J. M. Bowen. J. Radioanal. Chem., 1974, 19, 215.
3. M. A. Kolomiytsev, T. S. Ambardanashvili, V. Yu. Dundua. J. Radioanal. Chem., 1974, 20, 549.
4. Л. М. Мосулишвили, Н. Е. Кучава. Атомная энергия, 1979, 47, 392.

კორელაცია კოვალენტობის ინდექსსა და შეკავშირების
კონსტანტას შორის Ag⁺_, Cu²⁺_, Cr³⁺_ და Pb²⁺_ C-
ფიკოციანინის (*Spirulina platensis*) კომპლექსებისათვის

ე. ღელაღუტაშვილი

ე. ანდრონიკაშვილის ფიზიკის ინსტიტუტი
ი. ჯავახიშვილის სახ. თბილისის სახელმწიფო უნივერსიტეტი
თბილისი, საქართველო
eterige@gmail.com

ანოტაცია

შესწავლილ იქნა დამოკიდებულება კოვალენტობის ინდექსსა და შეკავშირების კონსტანტას შორის მძიმე და ტოქსიკურ ლითონთა იონების Ag⁺_, Cu²⁺_, Cr³⁺_ და Pb²⁺_C-ფიკოციანინის (*Spirulina platensis*) კომპლექსებისათვის. ნაჩვენებია, რომ დაიმზირება კორელაცია ფლუორესცენტული სპექტროსკოპიით მიღებულ წონასწორობის კონსტანტებსა და კოვალენტობის ინდექს შორის. რაც შეეხება წონასწორული დიალიზით მიღებულ შედეგებს, დაიმზირება წრფივი კორელაცია კოვალენტობის ინდექსსა და შეკავშირების კონსტანტას შორის მძიმე და ტოქსიკურ ლითონთა იონების Ag⁺_, Cu²⁺_, Cr³⁺_ და Pb²⁺_C-ფიკოციანინის (*Spirulina platensis*) კომპლექსებისათვის. წრფივობა ძალაშია, ერთი მხრივ, სხვადასხვა იონური ძალისათვის, ხოლო, მეორე მხრივ, შედეგების გრაფიკული დამუშავების სხვადასხვა მოდელების გამოყენებისას.

ჩვენს მიერ შესწავლილ იქნა მძიმე და ტოქსიკურ ლითონთა იონების Ag⁺_, Cu²⁺_, Cr³⁺_ და Pb²⁺_ ურთიერთქმედების ენერგეტიკა და ბუნება ციანობაქტერია *Spirulina platensis*-ის ძირითად ცილა C-ფიკოციანინთან (C-ფც) წონასწორული დიალიზისა და ფლუორესცენტული სპექტროსკოპიის მეთოდებით [1 – 3].

მოცემულ ნაშრომში წარმოდგენილია დამოკიდებულება კოვალენტობის ინდექსსა და შეკავშირების კონსტანტას შორის Ag⁺_, Cu²⁺_, Cr³⁺_ და Pb²⁺_C-ფიკოციანინის (*Spirulina platensis*) კომპლექსებისათვის.

საზოგადოდ, ლიგანდის შეკავშირების ბაზისური კონცეფცია მოითხოვს კომპლემენტარობას ლიგანდსა და შეკავშირების ადგილს შორის. ურთიერთქმედება პროტეინსა და ლითონს შორის უმთავრესად ანალოგიურია თვით პროტეინის შიგნით არსებული ურთიერთქმედებების: წყალბადური კავშირები, ვან-დერ-ვაალსის ურთიერთქმედება, ჰიდროფობური და ელექტროსტატიკური ურთიერთქმედებები. პოლარულ ჯგუფებს შორის ურთიერთქმედებისას არსებით როლს წყალბადური კავშირები ასრულებენ. ხშირად ლითონის იონები კონფორმაციულ გარდაქმნებს ახდენენ ცილებში. ეს უკანასკნელი დაიკვირვება ლითონთა იონების Cu(II), Cr(III), Hg(II), Ag(I) და Pb(II) ურთიერთქმედებისას C-ფიკოციანინთან [1 – 3], რადგან ურთიერთქმედება ატარებს კოოპერატიულ ხასიათს ანუ ერთი იონის შეკავშირება

ზრდის მეორის შეკავშირების ალბათობას. ურთიერთქმედების ასეთი ტენდენცია შეინიშნება როგორც თერმოდინამიკური (წონასწორული დიალიზი), ასევე სპექტრალური (ფლუორესცენტული ტიტრაცია) მეთოდებით შესწავლისას სხვადასხვა იონური ძალისათვის. საზოგადოდ, ლიგანდის შეკავშირება ცილასთან კოოპერატიულია, თუ ლითონის ერთი იონის შეკავშირება იწვევს ისეთ სტრუქტურულ ცვლილებებს, რომლის დროსაც შემდეგი იონის შეკავშირება გაადვილებულია. ცნობილია, რომ ფერმენტების აქტივობის რეგულაციის და მეტაბოლიზმის საფუძველია კონფორმაციის კოოპერატიული ცვლილება [4]. სავარაუდოდ, ცოცხალი ორგანიზმების ბევრი ფუნდამენტური თვისება უშუალოდაა დაკავშირებული უჯრედის სტრუქტურებში კოოპერატიულ ცვლილებებთან. თუმცა, ერთი შეხედვით, შეუძლებელია ურთიერთქმედებამ მიგვიყვანოს შეკავშირების კონსტანტის გაზრდამდე, რადგანაც ეს ნიშნავს, რომ ჭეშმარიტი კონსტანტა მეორე იონისათვის მეტია, ვიდრე პირველისათვის. თუმცა პირველი იონი უკავშირდება იმ ცენტრს, რომლის კონსტანტაც მეტია და არა – ნაკლები. პროცესის კოოპერატიულობის მიზეზს წარმოადგენს შიდამოლეკულური გადახჯუფვებები, რომლებიც ხდება პირველი და მეორე ლიგანდის შეკავშირებებს შორის შუალედში. რეალურად ცილებში არსებობს რამდენიმე სტაბილური კონფორმაცია, ხოლო მათ გარე ზედაპირზე გვაქვს მრავალი ცენტრი, რომელთაც პოტენციურად შეუძლიათ შეიკავშირონ ლითონთა იონები. თითოეული ამ ნაწილის შევსებამ შესაძლოა იქონიოს გავლენა ცილის ფუნქციონალურ თვისებებზე.

მიუხედავად იმისა, რომ ლითონდამოკიდებულ ცილებზე ბევრი რამ არის ცნობილი, ბევრი კითხვა უპასუხოდ რჩება, მაგალითად, თუ როგორ ირჩევს ცილა სპეციფიკურ ლითონის იონს უამრავ კათიონს შორის.

კრისტალურ მონაცემებზე დაყრდნობით ცილებისათვის, ლითონთა კათიონები იყოფა 3 ძირითად ჯგუფად, უპირატესად ფუნქციონალური ჯგუფების დონორული ატომების მიხედვით [5].

1. N/S ჯგუფი ანუ კლასი B: კოვალენტობის ინდექსი $X_m^2 r > 3 \rightarrow$ Ag(I), Hg(II), Pd(II), Pt(II).

2. O- ჯგუფი ანუ კლასი A: კოვალენტობის ინდექსი $X_m^2 r < 1.75 \rightarrow$ Ca(II), Al(III).

3. დემარკაციულ ლითონთა იონები, რომლებიც ამბივალენტურია O⁻, N⁻, S⁻ ტიპის დონორების მიმართ. კოვალენტურობის ინდექსი $1.75 < X_m^2 r < 3 \rightarrow$ Ni(II), Cd(II), Co(II), Mn(II), Pb(II), Zn(II), Fe(III). ერთადერთ გამონაკლისს წარმოადგენს ტყვია.

აქ X_m წარმოადგენს პოლინგის ელექტროუარყოფითობას და r – ეფექტურ იონურ რადიუსია, გამოთვლილი ბორნის მეთოდით [6].

ნიბოერისა და რიჩარდსონის მიერ [7, 8] მოძებნილ იქნა კრიტერიუმი, რომლითაც შეიძლება ერთმანეთისაგან გავმიჯნოთ კლასი A და დემარკაციულ ლითონთა იონები, მაგრამ ბოლომდე კლას B-ის და დემარკაციულ იონთა გაყოფა გაძნელდა (ტყვია(II) საერთო კონტექსტში არ ჯდება). ლითონურ კომპლექსების შექმნის თეორიაში არსებობს ზოგადი წესი: რაც უფრო ადვილად გასცემს დონორული ჯგუფი ელექტრონებს, მით უფრო ძლიერია კოვალენტური ბმა, რომელიც შეიძლება წარმოიშვას ამ ჯგუფსა და ლითონს შორის.

ცხრილში 1 მოცემულია მძიმე და ტოქსიკურ ლითონთა იონების Ag⁺-ის, Cu²⁺-ის, Cr³⁺-ისა და Pb²⁺-ის ბმის კონსტანტები, მიღებული ჩვენს მიერ: ა) წონასწორული დიალიზისა და სპექტროსკოპული მეთოდების დახმარებით; ბ) ფლუორესცენტული სპექტროსკოპიით და დამუშავებული სკეტჩარდის გრაფიკული მეთოდით [1 – 3]. როგორც ცხრილიდან ჩანს, ყველაზე მეტი ეფექტურობით გამოირჩევა Ag+, ხოლო

შემდეგ Pb^{2+}. ასე რომ, ჩვენს შემთხვევაშიც ტყვია საერთო კონტექსტიდან ამოვარდნილია. ზოგადი სურათი კი ფიკოციანინთან ლითონთა იონების ბმის ენერგიის სიდიდის ასეთია: Ag > Pb > Cu > Cr.

ცხრილი 1. მძიმე ლითონების შეკავშირების ენერგეტიკა
C-ფიკოციანინთან, მიღებული წონასწორული დიალიზით
და ფლუორესცენციული ტიტრაციის გამოყენებით.

ლითონის იონი	წონასწორული დიალიზი				ფლუორესცენციული ტიტრაცია			
	შეკავშირების კონსტანტა K, 10^5 M^{-1}	pK	გიბსის თავისუფალი ენერგია $-\Delta G°$, კკალ / მოლი	X^2	შეკავშირების კონსტანტა K, 10^5 M^{-1}	pK	გიბსის თავისუფალი ენერგია $-\Delta G°$, კკალ / მოლი	X^2
Ag$^+$	5.31	5.73	7.78	0.008	5.2	5.71	7.8	0.008
Cr^{3+}	0.22	4.34	5.90	0.007	0.7	4.85	6.59	0.007
Cu^{2+}	0.81	4.91	6.68	0.006	0.6	4.78	6.5	0.006
Pb^{2+}	3.63	5.56	7.56	0.001	2.8	5.45	7.4	0.009

სურათზე 1 წარმოდგენილია კოვალენტურობის ინდექსის $X_m^2 r$ დამოკიდებულება შეკავშირების კონსტანტაზე K: $-\text{Log} K = pK$ ლითონ–ფც კომპლექსებისათვის, მიღებული როგორც სკეტჩარდის, ასევე ჰილის გრაფიკული მეთოდების ანალიზის შედეგად ფლუორესცენციული ტიტრაციის მეთოდის გამოყენებით. როგორც სურათიდან 1 ჩანს დაიკვირვება კორელაცია $X_m^2 r$-სა და pK-ის შორის.
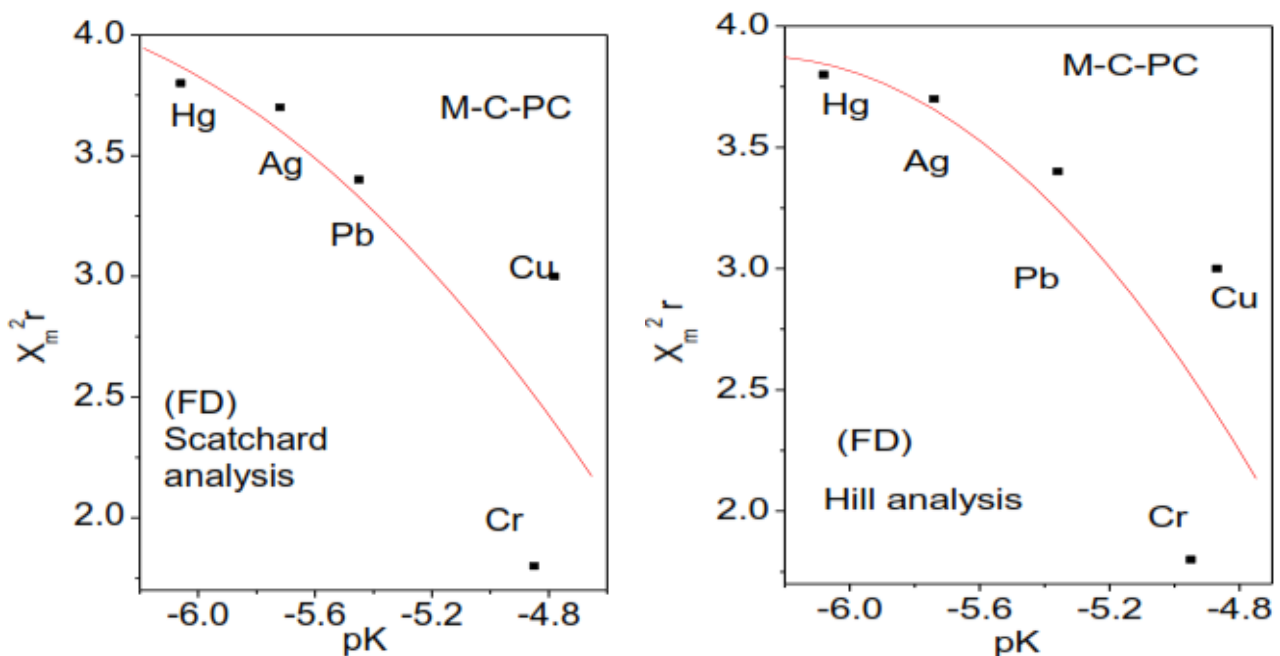
სურათი 1. კოვალენტურობის ინდექსის $X_m^2 r$ დამოკიდებულება
შეკავშირების კონსტანტაზე – $\text{Log} K = pK$ ლითონ–ფც კომპლექსებისათვის
(ფლუორესცენციული მეთოდი). სკეტჩარდის ანალიზის მონაცემები:
$R^2 = 0.66$ და ჰილის ანალიზით მიღებული შედეგები: $R^2 = 0.63$).

ვინაიდან ფლუორესცენციის ჩაქრობის მრუდების აგებისას თავისუფალ ლითონთა იონების კონცენტრაცია განსაზღვრულ იქნა არაპირდაპირი მეთოდით, ამიტომ წონასწორობის კონსტანტების განსაზღვრის ძირითად კრიტერიუმად გამოყენებულ იქნა წონასწორული დიალიზი, კლასიკური ტექნიკა, რომელიც ფლუორესცენციის მეთოდისაგან განსხვავებით იძლევა შეკავშირებულ და თავისუფალ ლითონთა იონების უშუალოდ განსაზღვრის საშუალებას და ამასთან ითვალისწინებს "დიფუზიურად დაკავშირებული იონების" წილსაც.
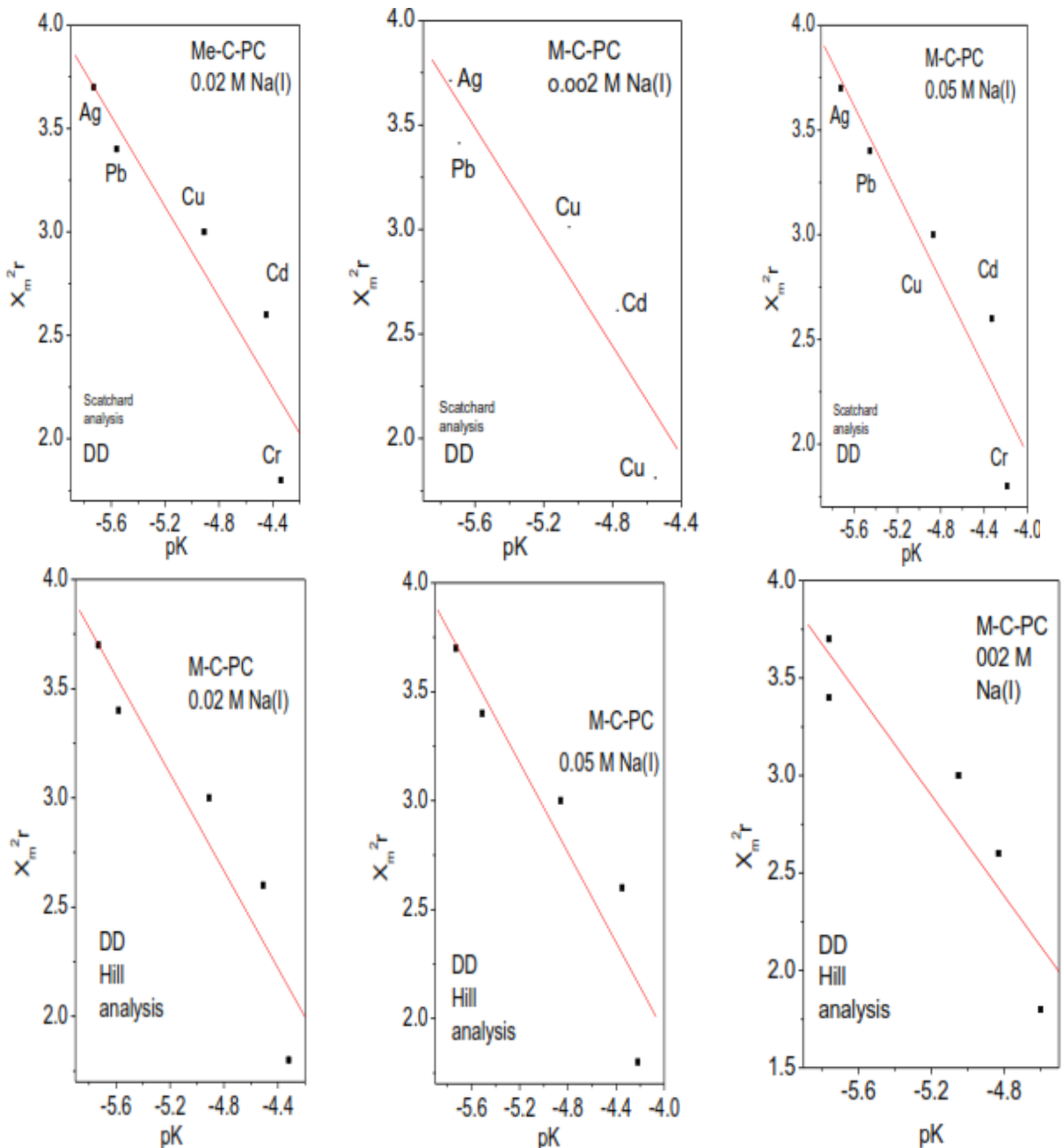
სურათი 2. დამოკიდებულება კოვალენტურობის ინდექსსა $X_m^2 r$ და შეკავშირების კონსტანტას K შორის – Log $K = p K$ ლითონ–ფც კომპლექსებისათვის, განსაზღვრული წონასწორული დიალიზისა და ატომურ-აბსორბციული ანალიზის მეთოდებით. (სკეტჩარდისა და ჰილის გრაფიკული მოდელებში 0.02, 0.002 და 0.5 მოლი იონური ძალისათვის).

ფლუორესცენციით მიღებული მონაცემების ანალიზის ანალოგიურად **სურათზე 2** წარმოდგენილია კოვალენტობის ინდექსის $X_m^2 r$ დამოკიდებულება შეკავშირების კონსტანტაზე K: $-\text{Log } K = pK$ ლითონ–ფც კომპლექსებისათვის სხვადასხვა იონური ძალისათვის (50, 20 და 2 მლმოლი), განსაზღვრული წონასწორული დიალიზისა და ატომურ-აბსორბციული ანალიზის გამოყენებით. როგორც **სურათიდან 2** ჩანს დაიმზირება კორელაცია $X_m^2 r$-სა და pK-ის შორის, როგორც მოდიფიცირებული სკეტჩარდის (R 0.91), ასევე ჰილის გრაფიკული ანალიზისას (R 0.9). ფლუორესცენტული მონაცემებისაგან განსხვავებით, თერმოდინამიკური მეთოდით მიღებული კონსტანტებისათვის ყველა იონურ ძალაზე ამგვარი დამოკიდებულება წრფივია, როგორც მოდიფიცირებული სკეტჩარდის, ასევე ჰილის ანალიზით მიღებული შედეგებისათვის.

კერძოდ, მოდიფიცირებული სკეტჩარდიის მეთოდი გვაძლევს:
1. 50 მლმოლი Na(I), $X_m^2 r = -2.21 - 1.04 \ pK$; R 0.94; SD 0.28; P 0.016.
2. 20 მლმოლი Na(I), $X_m^2 r = -2.58 - 1.09 \ pK$; R 0.93; SD 0.31; P 0.021.
3. 2 მლმოლი Na(I), $X_m^2 r = -3.82 - 1.3 \ pK$; R 0.94; SD 0.27; P 0.015.

ხოლო ჰილი: მეთოდით გვექნება:
1. 50 მლმოლი Na(I), $X_m^2 r = -2.19 - 1.03 \ pK$; R 0.94; SD 0.30; P 0.018.
2. 20 მლმოლი Na(I), $X_m^2 r = -2.69 - 1.11 \ pK$; R 0.94; SD 0.28; P 0.016.
3. 2 მლმოლი Na(I), $X_m^2 r = -3.83 - 1.29 \ pK$; R 0.93; SD 0.32; P 0.019.

წრფივი კორელაცია მიუთითებს, რომ რაც მეტია წონასწორობის კონსტანტა, მით მეტია კოვალენტური კავშირის ხარისხი მეტალ–ფც ურთიერთქმედებისას. პოლინგის განსაზღვრებით ორი ელემენტის ელექტროუარყოფითობას შორის სხვაობა დაკავშირებულია მათ რეალურ ენერგიათა და სუფთა კოვალენტური კავშირის შესაბამის ენერგიას შორის არსებულ განსხვავებასთან. $X_m^2 r$ შეფარდება, რომელიც ადარებს ვალენტური ორბიტალების ენერგიას იონურ ენერგიასთან [6] და, შესაბამისად, მიიჩნევა, როგორც ლითონის ურთიერთქმედებასთან შედარებითი უნარი (კომპეტენცია).

ზოგადად, მძიმე და ტოქსიკურ ლითონთა ბიოტიკური მოქმედება განისაზღვრება მათი უნარით, შევიდნენ რეაქციაში ბიომოლეკულის ფუნქციონალურ ჯგუფებთან, რომლებიც მონაწილეობენ მათი სივრცული სტრუქტურის ფორმირებაში და ამასთანავე ამ ჯგუფების აქტივობები სხვადასხვაა.

დამოწმებანი

1. E. S. Gelagutashvili. In: Plants and Microbes. 2014, Ch. 9, 154.
2. E. S. Gelagutashvili. Am. J. Biomed. Life Sci., 2013, 1, 12.
3. E. S. Gelagutashvili. Proc. Georg. Acad. Sci., 2011, 37, 109.
4. D. E. Metzler. Biochemistry, The Chemical Reactions of Living Cells. 1977, New York – San Francisco –,London, Acad. Press.

5.   D. R. Williams. The Metals of life. 1971, London – New York, Van Nostrand Reinhold Co.
6.   L. Pauling. General Chemistry. 1970, San Francisco, Freeman & Co.
7.   F. E. Rossetto, E. Nieboer. J. Inorg. Biochem., 1994, 54, 167.
8.   E. Nieboer, D. H. S. Richardson. Environ. Pollution B, 1980, 1, 3.

სისხლის მიმოქცევის ზოგიერთი საკითხი
ჰიდროდინამიკის თვალსაზრისით

მარიამ ჩიხლაძე [1], მანანა ჩიხლაძე [2], ომარ კეთილაძე [2]

[1] სსიპ სასწრაფო სამედიცინო დახმარების ცენტრი
თბილისი, საქართველო
[2] საინჟინრო ფიზიკის დეპარტამენტი
საქართველოს ტექნიკური უნივერსიტეტი
თბილისი, საქართველო
chixladze_manana@mail.ru

ანოტაცია

ნაშრომში გამახვილებულია ყურადღება იმ ფაქტზე, რომ ცოცხალ ორგანიზმებში სითხეთა და, კერძოდ, სისხლის მოძრაობა ზოგადად ემორჩილება კლასიკური ჰიდროდინამიკის კანონებს. ამავე დროს სისხლი, როგორც არანიუტონისეული სითხე გარკვეული თავისებურებებით ხასიათდება. კერძოდ, სხვადასხვა სისხლძარღვში, სიჩქარის გრადიენტისგან დამოკიდებულებით, მას განსხვავებული სიბლანტე გააჩნია. მოცემულია სისხლძარღვის სხვადასხვა უბნის და მათი შეერთებების ჰიდრავლიკური წინაღობის ფორმულები. განხილულია სისხლძარღვთა პათოლოგიური მდგომარეობის ყველაზე გავრცელებული ფორმის – ათეროსკლეროზის დროს ათერომატოზული ფოლაქების წარმოშობისას სისხლის მოძრაობის შეფერხება და ბერნულის კანონის გამოყენებით ფიზიკურად ახსნილია სტენოზის განვითარება და ოკლუზიის წარმოქმნის მომენტი. მკურნალობის თვალსაზრისით მოყვანილია კორონარული სტენტირების პროცედურა.

ცოცხალი ორგანიზმების გულ-სისხლძარღვთა სისტემაში სისხლის მოძრაობა ადიწერება კლასიკური ჰიდროდინამიკის ძირითადი ცნებებით და ემორჩილება მის კანონებს [1]. მაგრამ მთელი რიგი თავისებურებებიდან გამომდინარე, იგი ფიზიოლოგიის, კერძოდ, ჰემოდინამიკის ცალკე შესწავლის საგანია.

სისხლი არანიუტონისეულ სითხეებს მიეკუთვნება, რაც იმას ნიშნავს, რომ სხვადასხვა სისხლძარღვში, სიჩქარის გრადიენტისაგან დამოკიდებულებით, სისხლს განსხვავებული სიბლანტე გააჩნია. სისხლის უწყვეტი მოძრაობა სისხლძარღვებში ანუ სისხლის მიმოქცევა ჰემოდინამიკაში ასეთნაირად ჩამოყალიბდება: სისხლძარღვთა კვეთაში (**სურათი 1**) სისხლის დინების მოცულობითი გასავალი $Q = \Delta V / \Delta t$ მუდმივია:

$$S_1 v_1 = S_2 v_2 = S_3 v_3 = \cdots = const.$$ (1)

გამოსახულება (1) ნაკადის უწყვეტობის განტოლებას წარმოადგენს.

სისხლძარღვთა კვეთის ფართობში იგულისხმება ერთი განტოტების ჯამური ფართობი. მაგალითად, სისხლის მიმოქცევის დიდ წრეში აორტის კვეთაში სისხლის დინების მოცულობითი გასავალი ტოლია აორტის ყველა განშტოების (არტერიების)

ჯამურ ფართობში სისხლის დინების მოცულობითი გასავალის. ყველაზე დიდი ფართობი გააჩნია კაპილარულ ქსელს. იგი ~ 800-ჯერ აღემატება აორტის კვეთის ფართობს. ადამიანის მოსვენებითი მდგომარეობისას, სისხლის დინების საშუალო წრფივი სიჩქარე აორტაში დაახლოებით 0.4 – 0.5 მ / წმ-ია, ხოლო კაპილარებში – 0.5 მმ / წმ, რაც შესაბამისობაშია ნაკადის უწყვეტობის პირობასთან.
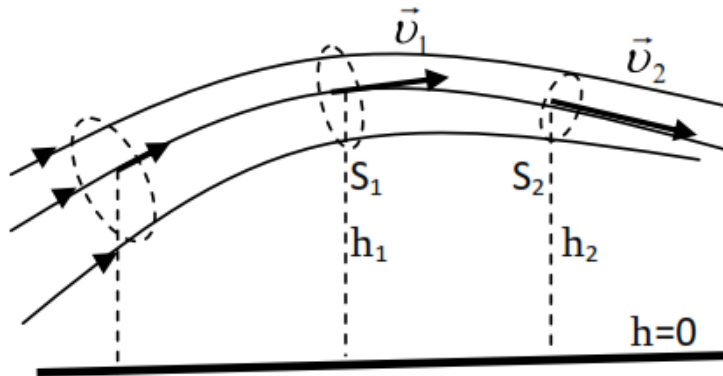
სურათი 1.

ჰემოდინამიკაში არსებითი როლი ენიჭება ბერნულის კანონს. იგი სამართლიანია იდეალური სითხის სტაციონარული ლამინარული დინებისას, მაგრამ საკმაოდ ზუსტია ბლანტი ნაკადის დროსაც, თუ ნაკადის რაიმე ელემენტის კინეტიკური ენერგია საგრძნობლად აღემატება ამ ელემენტის სიბლანტის ძალთა დაძლევაზე შესრულებულ მუშაობას:

$$p_1 + \rho g h_1 + \frac{\rho v_1^2}{2} = p_2 + \rho g h_2 + \frac{\rho v_2^2}{2}.$$

თუ ნაკადი ჰორიზონტალურია $(h_1 = h_2)$:

$$p_1 - p_2 = \frac{\rho\left(v_2^2 - v_1^2\right)}{2}. \tag{2}$$

მოცემულ შემთხვევაში წნევის ცვლილება გამოწვეულია მხოლოდ ნაკადის სიჩქარის ცვლილებით. კერძოდ იქ, სადაც სიჩქარე დიდია (დენის მილი ვიწროა) წნევა მცირდება და პირიქით, სადაც სიჩქარე ნაკლებია (დენის მილიგანიერია) წნევა იზრდება.

ფრანგი ექიმის პუაზეილის და გერმანელი მეცნიერის ჰაგენის მიერ ერთმანეთისგან დამოუკიდებლად დადგენილ იქნა, რომ სტაციონარული ლამინარული დინებისას უკუმშვადი ნაკადის მოცულობითი გასავალი პირდაპირპროპორციულია დინების გასწვრივ სიგრძის ერთეულზე წნევის ცვლილებისა და მილის რადიუსის მეოთხე ხარისხის ნამრავლის, და უკუპროპორციულია სიბლანტის კოეფიციენტის:

$$Q = \frac{\Delta p \pi R^4}{8\eta L} = \frac{\Delta p}{Z} \tag{3}$$

(η სიბლანტის კოეფიციენტია). მედიცინაში (3) გამოსახულებას ჰაგენ–პუაზეილის განტოლებას უწოდებენ. აქ შემავალი სიდიდე

$$Z = \frac{8\eta L}{\pi R^4} \tag{4}$$

სისხლძარღვის მოცემული უბნის ჰიდრავლიკური წინაღობაა. იგი ისევე გამოითვლება, როგორც ელექტრული წინაღობა ელექტრულ წრედებში.

კერძოდ, მიმდევრობითი შეერთებისას ჯამური წინაღობა ცალკეულ წინაღობათა ჯამის ტოლია:

$$Z = \sum_{i=1}^{n} Z_i \, ,$$

ხოლო პარალელური შეერთებისას – ჯამური წინაღობის შებრუნებული სიდიდე ცალკეულ წინაღობათა შებრუნებული სიდიდეების ჯამის:

$$\frac{1}{Z} = \sum_{i=1}^{n} \frac{1}{Z_i} \, .$$

ადამიანთა ჯანმრთელობასთან დაკავშირებულ სერიოზულ რისკთა ჯგუფს მიეკუთვნება არტერიოსკლეროზი –პათოლოგიური მდგომარეობა, რომლის დროსაც არტერიების კედლები სქელდება, კარგავს ელასტიურობას, თანდათან იზღუდება ისხლის მიმოქცევა ქსოვილებში [2]. მისი ყველაზე გავრცელებული ფორმაა ათეროსკლეროზი. ესე ხება ძირითადად მსხვილ სისხლძარღვებს – არტერიებს, რომელთა მეშვეობითაც სისხლით მარაგდება გული, ტვინი, თირკმელები, ქვედა კიდურები და სხვ.

ავადმყოფობის დასაწყისში ხდება სისხლძარღვთა გარეთა გარსის (გლიკოკალიქსის) დაზიანება, რასაც შემდეგში მოსდევს ცხიმოვანი ზოლის და ლაქების, და ათერომატოზული ფოლაქების განვითარების სტადიები. ათერომატოზული ფოლაქი ამობურციულია – ოვალურია ან ასიმეტრული. ის სხვადასხვა სიდიდით იჭრება სისხლძარღვის სანათურში. სანამ იგი მთლიანია, იწვევს რეგიონული სისხლის მიმიქცევის მოშლას, მაგრამ როგორც კი დაირღვევა მისი მთლიანობა წარმოიშობა თრომბი და სისხლძარღვი სწრაფად ვიწროვდება. ვითარდება სტენოკარდია, სრული დახშობისას კი – ინფარქტი. ათერომატოზული ფოლაქის ბოლო სტადიაა კალციფიცირება. ამ დროს ფოლაქი მყიფე – მსხვრევადი ხდება, სკდება და ვითარდება მწვავე თრომბოზი [3]. ათეროსკლეროზით ყველაზე ხშირად ზიანდება მუცლის აორტა, ხოლო შედარებით ნაკლებად კორონარული, ტვინის, ქვედა და ზედა კიდურების სისხლძარღვები და ფილტვის არტერია. ათეროსკლეროზის განვითარებისას ფერხდება ორგანოებისათვის სისხლის მიწოდება და ვითარდება იშემია.
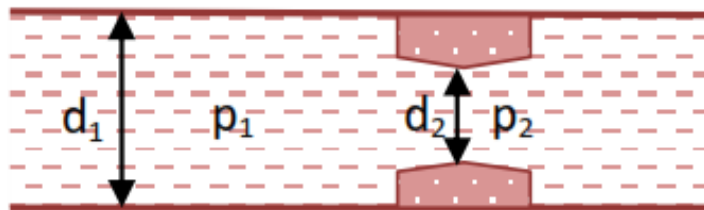
სურათი 2.

განვიხილოთ ეს საკითხი ჰიდროდინამიკის თვალსაზრისით: როდესაც არტერიის კედელზე წარმოიქმნა ათერომატოზული ფოლაქი, მაშინ ამ უბანზე მოხდება არტერიის სტენოზი – შევიწროება (სურათი 2). ნაკადის უწყვეტობის (1) პირობიდან გამომდინარე

$$\frac{\upsilon_2}{\upsilon_1} = \frac{d_1^2}{d_2^2} \, , \tag{5}$$

დინების სიჩქარე შევიწროვებულ არეში გაიზრდება, ხოლო სტატიკური წნევა p_2 პროპორციულად შემცირდება (2). თუმცა სისხლის დინება არტერიაში გაგრძელდება

მანამ, სანამ p_2 მეტი დარჩება არტერიის კედელზე გარედან წარმოებულ წნევაზე, რომელიც ჩვეულებრივ პირობებში ატმოსფერული წნევის p_0-ის ტოლია. ანუ სისხლის ნორმალური დინების პირობა სისხლძარღვში ასე ჩაიწერება:

$$p_2 - p_0 \geq 0. \tag{6}$$

ეს პირობა სრულდება სანამ d_2 არაა ნაკლები კრიტიკულ მნიშვნელობაზე ($d_2 \geq d_{kr}$). თუ $d_2 < d_{kr}$, გარედან წარმოებული წნევა p_0 და ახშობს – ჩაკეტავს ათეromატოზულ ფოლაქთან არსებულ გასავალს. ესაა არტერიის ოკლუზია. არტერიის თავისუფალ ნაწილში წნევა რომ p_1-ის ტოლი რჩებოდეს, სისხლის დინება შეწყდებოდა. მაგრამ გული იწყებს მუშაობას დატვირთულ რეჟიმში, რის შედეგად წნევა იწყებს ზრდას და სისხლი მაინც წყვეტილად – ბიძგებით გადის შევიწროებულ არეს. ეს ბიძგები მოისმინება, როგორც წყვეტილი შუილი, რაც ადასტურებს სისხლის ნორმალური მიმოქცევის დარღვევას. d_{kr} კრიტიკული მნიშვნელობა სხვადასხვა სისხლძარღვისათვის სხვადასხვაა და მისი გამოთვლა შესაძლებელია ნაკადის უწყვეტობის და ბერნულის განტოლების გამოყენებით. რადგან ოკლუზიის დასაწყისისათვის $d_2 = d_{kr}$ და $p_2 = p_0$, თანაფარდობის (5)თანახმად

$$d_{kr} = d\sqrt{\frac{v}{v_{kr}}}, \tag{7}$$

ხოლო გამოსახულებიდან (2)

$$v_{kr} = \sqrt{\frac{2 \cdot (p - p_0) + \rho v^2}{\rho}}. \tag{8}$$

ვღებულობთ

$$d_{kr} = d \cdot \sqrt[4]{\frac{\rho v^2}{2 \cdot (p - p_0) + \rho v^2}}. \tag{9}$$

გულის სისხლძარღვების დაზიანების გამოვლენის საუკეთესო მეთოდად **კორონაროგრაფია** ითვლება [4]. ამ დროს რენტგენის სხივების დახმარებით ირკვევა გულის მკვებავი კორონარული არტერიების შევიწროების ადგილი და ხარისხი.

ა ბ გ
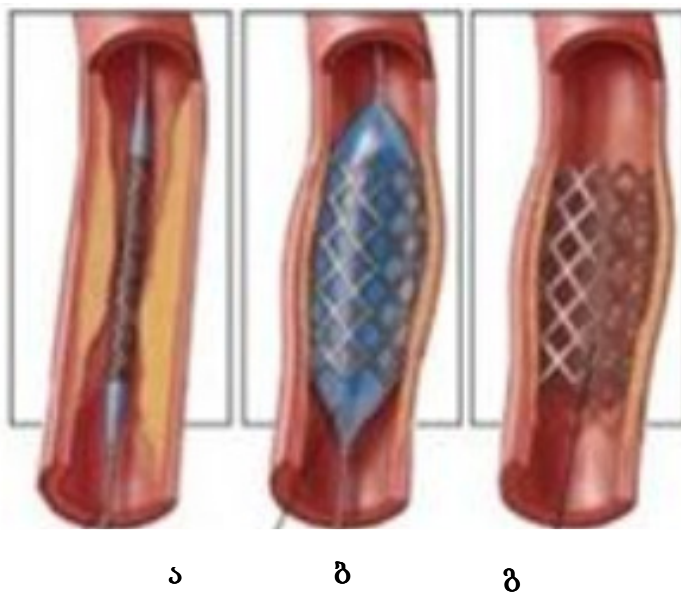
სურათი 3. ა – სტენტი ბალონ-კათეტერით, ბ – გაშლილი სტენტი ბალონის გაბერვისას და გ – არტერიაში ჩადგმული სტენტი.

კორონაროგრაფია განსაკუთრებით საჭიროა მაშინ, როცა პაციენტს დასმული აქვს გულის იშემიური დაავადების დიაგნოზი. ამ დროს საჭიროა ინვაზიური ჩარევა. თუ დაზიანება დიფუზიურია, ტარდება შუნტირება, სეგმენტური დაზიანებისას კი – კორონარული სტენტირების პროცედურა. კორონარული სტენტირებისათვის გამოიყენება სპეციალური კათეტერი (**სურათი** 3), რომლის ბოლოზეც განლაგებულია პატარა ბალონი. აღნიშნული კათეტერი ექიმს ფეხში ბარძაყის (ზოგ შემთხვევაში წინამხრის) არტერიიდან მიჰყავს არტერიის სტენოზის ან ოკლუზიის ადგილამდე. ბალონის გაბერვის შედეგად მოხდება სისხლძარღვის აღნიშნული მონაკვეთის გაფართოება. იმისათვის, რომ ისევ არ მოხდეს სტენოზის განვითარება დაზიანებულ ადგილას ათავსებენ სტენტს. სტენტი ლითონის სპირალური ბადეა, რომელიც წამოცმულია ბალონ-კათეტერზე. ბალონის გაბერვისას სტენტი გაიშლება და არტერიაში აღდგება სისხლის ნორმალური დინება. შევიწროვებულ სისხლძარღვში დაზიანების ხარისხისა და რაოდენობის შესაბამისად შეიძლება მოთავსდესერთი ან მეტი სტენტი.

სისხლძარღვთა დაავადების ერთ-ერთი ფორმაა აორტისანევრიზმა. აორტის კედელი ძალზე ელასტიურია და უნარი შესწევს სისხლის ნაკადის სიძლიერის მიხედვით გაიწელოს და დაიბრუნოსპ ირვანდელი ფორმა. ზოგიერთი დაავადება ასუსტებს აორტის კედელს. თუ ამას დაერთო ასაკობრივი ცვლილებები, შესაძლოა სისხლძარღვის კედელმა დაკარგოს ელასტიურობა, გაიწელოს და გამოიბეროს. ანევრიზმა სისხლძარღვის გამობერილი ადგილია, რომელიც სწრაფად იზრდება და ივსება სისხლით. ცხადია, რომ აორტის კედლები გათხელებულია, რამაც შეიძლება გამოიწვიოს აშრევების და შემდგომი გასკდომის საფრთხე, რაც სიცოცხლესთან შეუთავსებელ ძლიერ სისხლდენას იწვევს.
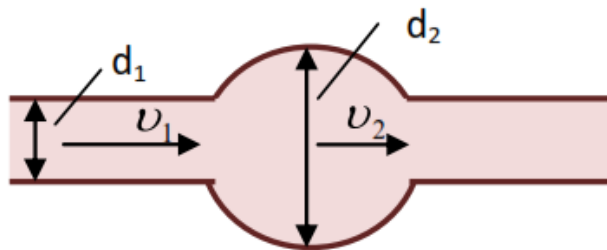
სურათი 4.

განვიხილოთ ეს საკითხი ჰემოდინამიკის თვალსაზრისით: **სურათზე** 4 სქემატურად მოცემულია ამგვარი სისხლძარღვი. ნაკადის უწყვეტობის პირობიდან გამომდინარე, სისხლის v_2 სიჩქარე ანევრიზმის განვითარების d_2 დიამეტრის არეში ნაკლებია, ვიდრე სისხლის სიჩქარე v_1 სისხლძარღვის სავ ნაწილში. ამიტომ ბერნულის განტოლების თანახმად, ანევრიზმის ადგილას სტატიკური წნევა p_2 მეტია სისხლძარღვის დაუზიანებელ კვეთაში არსებულ p_1 წნევაზე. შესაბამისად, სისხლძარღვის გაგანიერებულ უბანზე დატვირთვა იზრდება და წარმოქმნილი ანევრიზმა მომატებული წნევის გამო თანდათან ფართოვდება. პროცესს შეუქცევადი ხასიათი გააჩნია. წნევათა $p_1 - p_2$ სხვაობა კონკრეტული სისხლძარღვისათვის შეიძლება გამოითვალოს ბერნულის განტოლებით. მართალია, წნევათა ეს სხვაობამცირეა, მაგრამ ამ სიდიდის ჭარბი წნევაც კი ზიდგს აძლევს ანევრიზმის გაფართოებას, რაც იწვევს სისხლდენი სსიჩქარის კიდევ მეტად შემცირებას დეფორმირებულ უბანში და სტატიკური წნევის შემდგომ ზრდას, შედეგად მოსალოდნელია ანევრიზმის გასკდომა.

დამოწმებანი

1. მ. ჩიხლაძე, ო. კეთილაძე. ზოგადი ფიზიკის კურსი. 2013, თბილისი, გრიფონი.
2. А. С. Галявич, А. Шайдуллина. Р. Ш. Миннетдинов, И. Ф. Якупов. Ретроспективная оценка методов раннего лечения больных инфарктом миокарда. Каз. мед. журн., 2010, 4, 476-479.
3. Г. П. Ишмурзин,А. А. Подольская, А. В.Бондарев. Тромболитическая терапия при инфаркте миокарда. Рос.Кардиолог. журн., 2009, 6 (79), 547-551.
4. ა. ციბაძე, ი. კვაჭაძე. სამედიცინო ფიზიკა და ბიოფიზიკა. 2006, თბილისი.

ოპტიკურ ლინზებზე გასხივოსნების
შრეების გამოყენების მიმოხილვა

ზ. ვ. ბერიშვილი, ი. ი. კორძახია, დ. გ. ზარდიაშვილი,
ი. მ. ავალიანი, გ. გ. დეკანოზიშვილი

სსიპ ინსტიტუტი "ოპტიკა"
თბილისი, საქართველო
zaurberi7@yahoo.com

ანოტაცია

დღეს ოპტიკური ლინზები გასხივოსნების შრეებით ფართოდაა წარმოდგენილი
ყველა ოპტიკური სალონის ასორტიმენტში. აღნიშნული დანაფარები საგრძნობლად
აუმჯობესებს ოპტიკური ხელსაწყოების ხარისხს და, შესაბამისად, ზრდის
მომხმარებლის კომფორტულობას. წარმოდგენილ სამუშაოში აღწერილია ოპტიკურ
ლინზებზე გასხივოსნების შრეების მოქმედების საფუძვლები. ის ეძღვნება ოპტიკურ
ლინზებზე გასხივოსნების შრეების გამოყენების მიმოხილვას და   მისი რეალიზების
პერსპექტივებს.   კონკრეტულად,   წარმოდგენილია ოპტიკურ ხელსაწყოებზე
გასხივოსნების შრეების გამოყენების განსხვავებული ტიპების აღწერა და
მრავალშრიანი გასხივოსნების დანაფარების სტრუქტურა. აგრეთვე, მოყვანილია
ლინზაზე დამაკავშირებელი და განმამტკიცებელი (ზრდიან ცვეთაგამძლეობას),
მრავალშრიანი გასხივოსნების (იხსნება ხელშემშლელი ანარეკლები) და ჰიდროფობური
(იცავს გასხივოსნების შრეებს და აადვილებს მის მოვლას) დანაფარების მიღების
ტექნოლოგიების ზოგადი განხილვა.

ოპტიკურ ლინზაში სინათლის სხივის ნაკადის გავლისას ხდება მისი
ნაწილობრივ შთანთქმა და არეკვლა. სინათლის ნაკადის არეკვლა ხდება სხვადსხვა
გარდატეხის მაჩვენებლის მქონე ორ ოპტიკურად გამჭვირვალე გარემოს (ლინზის
მასალა და ატმოსფერო) გამყოფ ზედაპირზე. სინათლის სხივი ირეკლება ლინზის
როგორც წინა, ისე უკანა ზედაპირებიდან, რაც იწვევს თვალში მოხვედრილი საგნის
გამოსახულების ხარისხის გაუარესებას. ამ პრობლემის გადასაჭრელად თანამედროვე
ოპტიკაში იყენებენ ე.წ. გასხივოსნების დანაფარებს.

ოპტიკურ ლინზებზე გასხივოსნების შრეების მოქმედების საფუძველს
წარმოადგენს სინათლის ტალღის ინტერფერენცია. დანაფარების სტრუქტურა, ანუ მისი
ცალკეული ფენების სისქეები და გარდატეხის მაჩვენებლები შერჩეულია ისე, რომ,
ჰაერი–დანაფარი და დანაფარი–ლინზა ზედაპირებიდან არეკლილ სინათლის
ტალღების სვლათა სხვაობა იყოს ტალღის სიგრძის ნახევარი. გარდა ამისა, ამ ტალღების
ამპლიტუდა და ტალღის სიგრძეები უნდა იყოს იდენტური. ამ შემთხვევაში, ხდება
ანარეკლი ტალღების ინტერფერენცია და ისინი აქრობენ ერთმანეთს (**სურათი 1**), რაც
ზრდის ლინზის შუქგამტარობას. ჩვენს მიერ გასხივოსნების შრეების მასალად არჩეული

იქნა სილიციუმის ორჟანგი (SiO₂, *n* = 1.45) და ცირკონიუმის ორჟანგი (ZrO₂, *n* = 1.98). შემუშავებულია გასხივოსნების შრეების მიღების ტექნოლოგიები და დამზადებულია, პოლიმერული მასალის ლინზების ლაბორატორიული ნიმუშები ორივე მხარეზე დაფენილი გასხივოსნების (ანტირეფლექტური) შრეებით.
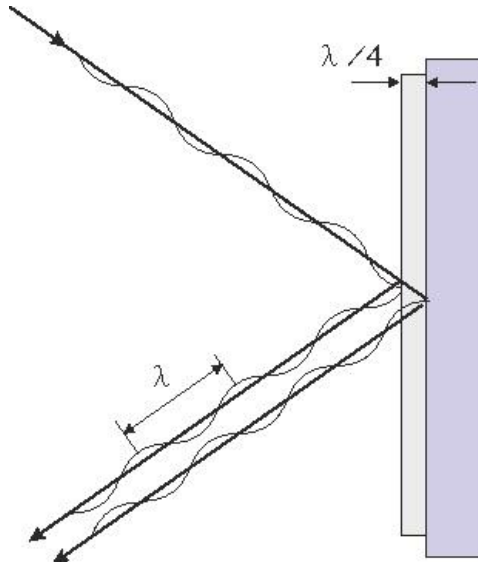
სურათი 1. ერთშრიანი გასხივოსნების მქონელინზის ზედაპირიდან არეკლილი ორი სინათლის სხივის ტალღის ინტერფერენცია, ურთიერთჩაქრობა.

ლინზის ზედაპირიდან ანარეკლის შესამცირებლად გამოიყენება ერთ- და მრავალშრიანი გასხივოსნება. ერთშრიანი გასხივოსნების დროს სინათლის სხივის ანარეკლს ამცირებენ მხოლოდ სხივის ხილული დიაპაზონის ერთ შეზღუდულ ნაწილში. როდესაც ლინზაზე დაფენილი გასხივოსნება შედგება ორი, დაბალი და მაღალი გარდატეხის მაჩვენებლების მქონე შრეებისაგან, ანარეკლის შემცირება ხდება სპექტრის საკმაოდ ვიწრო დიაპაზონში. სინათლის სხივის ხილულ არემი გასხივოსნების მაღალი ეფექტის მისაღებად გამოიყენება მრავალშრიანი (3, 5, 7 და მეტი ფენა) გასხივოსნება, რაც საშუალებას იძლევა არეკვლა 10 – 15 %-დან შემცირდეს 1 %-მდე ან უფრო მეტად.

მრავალშრიანი ანტირეფლექტიური გასხივოსნება სხვადასხვა ოპტიკურ ხელსაწყოების ლინზებზე საგრძნობლად ზრდის მათ შუქგამტარებლობას. იმისათვის, რომ შევამციროთ გაბნეული და არეკლილი სინათლის სხივის რაოდენობა ოპტიკური ელემენტების ზედაპირიდან დურბინდების, ჭოგრიტების ტელესკოპების, მიკროსკოპების, სამიზნეების და სხვა კონსტრუქციის ოპტიკურ ხელსაწყოებში, ლინზების და პრიზმების ზედაპირზე აფენენ სპეციალურ შრეებს, კერძოდ, გასხივოსნების (ანტირეფლექტურ) შრეებს. აღნიშნული მაღალი ხარისხის ხელსაწყოების ოპტიკურ ელემენტებზე აუცილებლად უნდა იყოს მრავალშრიანი ანტირეფლექტიური შრეები და არამარტო გარე ელემენტებზე, არამედ – ყველა ოპტიკურ ლინზაზე და პრიზმაზე. მაღალი ხარისხის ანტირეფლექსურ შრეებს შესწევთ შუქგამტარობის კორექტირების უნარი, იზრდება გამოსახულების სიკაშკაშე და კონტრასტულობა, რაც განსაკუთრებით მნიშვნელოვანია ობიექტზე დაკვირვებისას სუსტი განათების პირობებში.

ოპტიკურ ხელსაწყოებზე განასხვავებენ შემდეგი ტიპის გასხივოსნების შრეებს [1]:

- ერთშრიანი გასხივოსნება. გასხივოსნების შრე დაფენილია მხოლოდ გარე ლინზების გარე ზედაპირზე (Coated, C);
- მთლიანი ერთშრიანი გასხივოსნება. გასხივოსნების ერთი შრე დაფენილია ყველა ოპტიკურ ზედაპირზე (Fully Coated, FC);
- მრავალშრიანი გასხივოსნება. მრავალშრიანი გასხივოსნება დაფენილია მხოლოდ ცალკეულ ზედაპირებზე, დანარჩენებზე დაფენილია გასხივოსნების ერთ შრე (Multi-Coated, MC);
- მთლიანი მრავალშრიანი გასხივოსნება. ყველა ოპტიკურ ზედაპირზე დაფენილია მრავალშრიანი გასხივოსნება (Fully Multi-Coated, FMC).

დღეს ოპტიკური ხელსაწყოების მწარმოებელი ფირმები ოპტიკურ ელემენტებზე გასხივოსნების ფენების მისაღებად იყენებენ სხვადასხვა ტექნოლოგიურ მეთოდს. ზევრი მათგანი დაპატენტებულია. მიუხედავად ამისა, არ არსებობს საერთო კრიტერიუმები გასხივოსნების დანაფარების ხარისხის შედარებისთვის, გარდა სინათლის სხივის გატარების კოეფიციენტის დადგენისა.

ხშირ შემთხვევაში მინის და ორგანული მინის ლინზებზე გასხივოსნების (ანტირეფლექტიურ) შრეებს დებულობენ ვაკუუმური დაფენის სპეციალურ დანადგარებში რთული ტექნოლოგიური პროცესებისა და მაღალი სისუფთავის მასალების გამოყენებით. ბოლო წლებში სულ უფრო მეტ გავრცელებას პოულობს მრავალშრიანი (განმამტკიცებელი, განმსხივოსნებელი და ჰიდროფობური) დანაფარები სათვალეების ორგანული მინის ლინზებზე (სურათი 2).
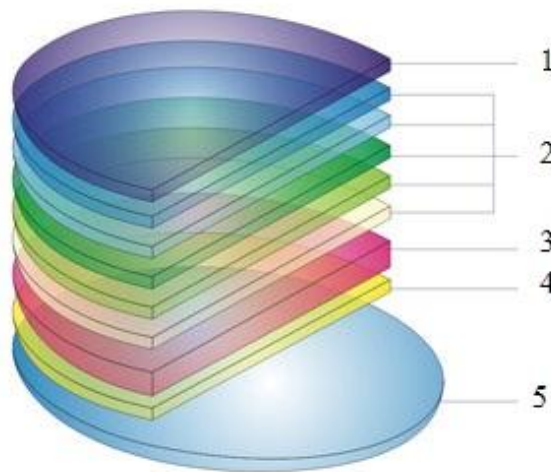
სურათი 2. მრავალშრიანი გასხივოსნების დანაფარების სტრუქტურა:
1 – ჰიდროფობური დანაფარი; 2 – მრავალშრიანიგასხივოსნების დანაფარი;
3 –განმამტკიცებელი დანაფარი; 4 – დამაკავშირებელი ფენა; და 5 – ლინზა.

ასეთი მრავალშრიანი გასხივოსნების დანაფარების მქონე სათვალეების ლინზებს არ აქვთ ანარეკლი, იზრდება გამოსახულების სიმკვეთრე, მცირდება თვალის დაძაბულობა.

ორგანული მინისაგან დამზადებული ლინზის ზედაპირზე განმამტკიცებელი შრეების მისაღებად დღეისათვის ფართოდ გამოიყენება პოლისილოქსანის ლაქი (სილიციუმორგანული შენაერთი), რომელსაც გააჩნია მთელი რიგი უნივალური

თვისებები, კერძოდ მაღალი მდგრადობა ღრმა ნაკაწრების წარმოშობისადმი, მაღალი ლღუნვადობა და საგრძნობლად დაბალი ხახუნის კოეფიციენტი.

ორგანული ლინზის ზედაპირის განმამტკიცებელი შრეების მიღება ხდება სუფთა გარემოში, ხოლო ლინზების ზედაპირების მაღალი ხარისხის სისუფთავის მისაღწევად იყენებენ მათ ქიმიურ და ულტრაბგერით დამუშავებას. ამის შემდეგ ლინზები მაგრდება სპეციალურ მოწყობილობაში, რომლის მეშვეობით ხდება განმამტკიცებელი შრის მიღება ლინზის თხევადი პოლისილოქსანის ლაქის აბაზანაში ჩაირვით (სურათი 3). განმამტკიცებელი შრის სისქე რეგულირდება პოლისილოქსანის ლაქის სიბლანტის და ლინზის აბაზანაში ამოწევის სიჩქარეების შერჩევით. აბაზანიდან ამოღების შემდეგ ლინზები თერმულად მუშავდება, რის შედეგადაც ხდება პოლისილოქსანის ლაქის პოლიმერიზაცია და იზრდება ლინზის ზედაპირთან მისი შეერთების სიმტკიცე. პოლისილოქსანის ლაქს გააჩნია მაღალი ელასტიურობა, რის შედეგადაც წარმოიქმნება ზედაპირი, რომელიც არ ზიანდება გარემოსთან კონტაქტის დროს. პოლისილოქსანის ლაქის მთლიანი პოლიმერიზაციის შემდეგ ლინზის ზედაპირი მდგრადი ხდება კაწვრისადმი.

ჩაირვა   ამოწევა და შრის ფორმირება   გამხსნელის აორთქლება
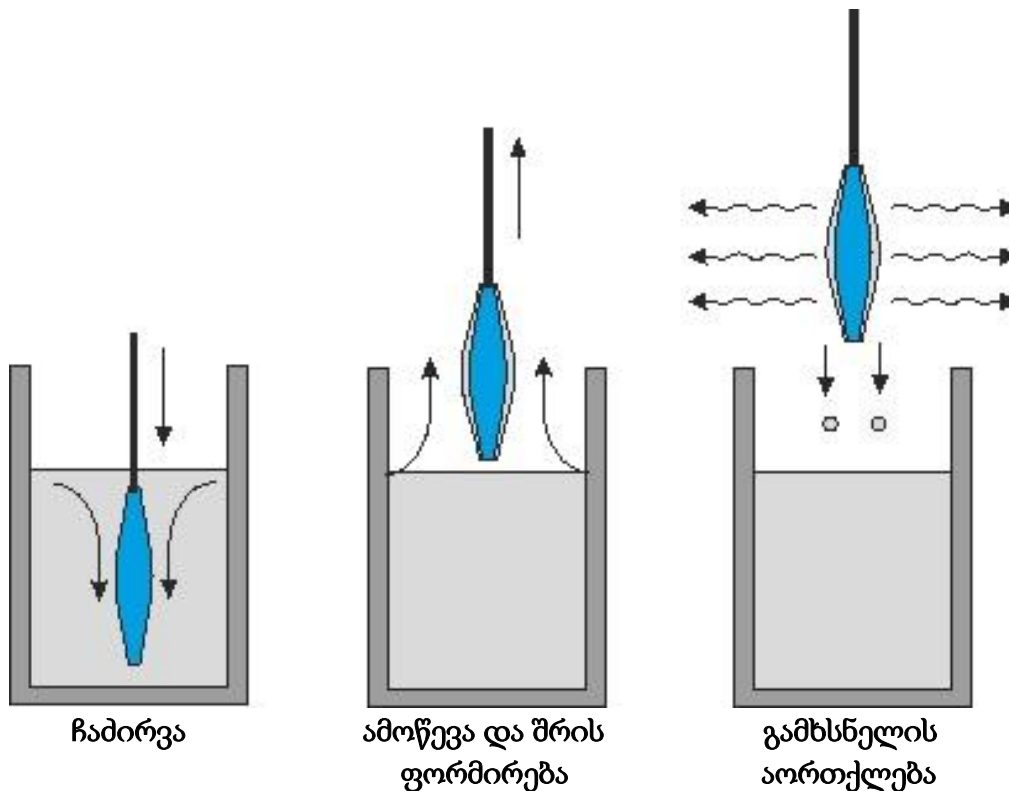
სურათი 3. ჩაირვის მეთოდით დანაფარების მიღების სქემა.

ლინზები გასხივოსნების დანაფარებით ხასიათდებიან სინათლის მაღალი გამტარებლობით და მინიმალური ანარეკლით. ასეთი ლინზები განსაკუთრებით მგრძნობიარენი არიან სისველისა და ჭუჭყისადმი, რადგან ამ დროს იცვლება გარემოს გარდატეხის მაჩვენებელი. ამ უსიამოვნო ეფექტის თავიდან აცილების მიზნით იყენებენ ჰიდროფობიურ შრეს, რომელიც ხელს უშლის ლინზის ზედაპირზე წყლის წვეთების და ჭუჭყის ნაწილაკების გაჩერებას. ჰიდროფობიური შრეების მისაღებად გამოიყენება ალკილსილანების ჯგუფის ნივთიერებები. ალკილსილანის ყოველი მოლეკულის შემადგენლობაში არის თუნდაც ერთი SiO ჯგუფი, რომელიც ქმნის ჰიდროფობიურ

შრის მტკიცე შენაერთს, აგრეთვე ნახშირწყალბადის ჯაჭვი, რომელიც ანიჭებს ნივთიერებას ჰიდროფობიურ თვისებებს. ჰიდროფობიური შრეების სისქე ძალიან მცირეა. ის, ჩვეულებრივ გასხივოსნების ერთი შრის 1 / 10-ს არ აღემატება.

სსიპ ინსტიტუტში "ოპტიკა" შექმნილია პოლიმერული ოპტიკური ლინზების დამზადების და გასხივოსნების დანაფარების მიღების ტექნოლოგიური უბნები. ეს უბნები შედგება ლინზების ზედაპირის გაწმენდის, განმამტკიცებელი დანაფარების მიღების, გასხივოსნების შრეების დაფენის და წყალგანზიდვის დანაფარების მიღების სამუშაო ადგილებისაგან.

თავიდან, პოლიმერული მასალისაგან დამზადებული ლინზის ზედაპირი გულმოდგინედ იწმინდება. აბაზანაში სხვადასხვა სარეცხი საშუალებების გამოყენებით გასუფთავებულ ლინზის ზედაპირზე განმამტკიცებელი დანაფარების და გასხივოსნების ბოლო შრეებზე ჰიდროფობური (წყალგანზიდვის) დანაფარების მისაღებად გამოიყენება ჩაძირვის მეთოდი, ჩვენს მიერ კონსტრუირებული და დამზადებულ იქნა ექსპერიმენტული მოწყობილობა, რომელიც იძლევა ლინზის სითხეში ჩაძირვის შემდეგ მისი ამოღების სიჩქარეების კონტროლის საშუალებას. ქიმიურად დამუშავებული პოლიმერული ლინზა იღება აბაზანაში, რომელშიც წინასწარ ჩასხმულია პოლისილოქსანის ლაქი ან ფტოროპლასტის Ф–32ЛН ფხვნილისაგან დამზადებული ხსნარი. აბაზანის ტემპერატურა, ლინზის აბაზანიდან ამოღების სიჩქარეები, და სხვა გარეშე პირობები მკაცრად კონტროლდება. ხსნარის სიბლანტისა და ლინზების ამოღების სიჩქარეების რეგულირებით მიიღწევა 20 ნმ-დან 50 მკმ-მდე სისქის შრეების ფორმირება.

აბაზანიდან ამოღების შემდეგ თერმოსტატში 60 – 70 °C ტემპერატურაზე ხდება ლინზების თერმული დამუშავება 3 – 4 სთ განმავლობაში და ლაქის პოლიმერიზაცია.

ლინზას, რომელზეც დაფენილია განმამტკიცებელი შრე, ამაგრებენ სპეციალურ დამჭერებზე და ათავსებენ ჰერმეტულ ვაკუუმურ კამერაში, სადაც მიიღება მაღალი ვაკუუმი. ვაკუუმურ კამერაში დამონტაჟებულია ორი იდენტური მაგნეტრონული გაფრქვევის მოწყობილობა. აღნიშნული დანადგარი დეტალურადაა აღწერილი სტატიაში [2]. ლინზაზე ეფინება თხელფენოვანი პირველი შრე (SiO$_2$, n = 1.45). შრეების სისქეები კონტროლდება მაგნეტრონული გაფრქვევის სიჩქარეების მართვით. პირველ შრეზე ზემოდან ეფინება მეორე შრე (ZrO$_2$, n = 1.98). ეს შრეები მეორდებიან რიგრიგობით და აყალიბებენ გასხივოსნების დანაფარებს.

ლინზებზე განმამტკიცებელი და გასხივოსნების შრეების დაფენის შემდეგ საჭიროა გასხივოსნების გარე შრეზე ჰიდროფობური შრის, ჩვენს შემთხვევაში ფტოროპლასტის თხელი შრის დაფენა. რომელიც უზრუნველყოფს ლინზის ზედაპირის დაცვას წყლის და წყლის ორთქლის ზემოქმედებისაგან და წყლის წვეთების წარმოქმნისაგან. ფტოროპლასტის თხელი შრისაგან დამზადებულ ჰიდროფობიურ შრეს გააჩნია ძალიან დაბალი ხახუნის კოეფიციენტი, ზრდის დასველებადობის კუთხეს და ამით ამცირებს ლინზების დაორთქლვას.

ისევე, როგორც განმამტკიცებელი შრის შემთხვევაში, ლინზებზე ჰიდროფობური შრეების დასაფენად გამოიყენება ჩაძირვის მეთოდი. ლინზას ამაგრებენ დამჭერზე და ჩაძირავენ აბაზანაში, სადაც არის წინასწარ მომზადებული გარკვეული სიბლანტის ფტოროპლასტის Ф–32ЛН ფხვნილისაგან დამზადებული ხსნარი. ამასთან, ლინზის ხსნარიდან ამოღების სიჩქარეები მუდმივია. შემდეგ ლინზა თავსდება თერმოსტატში და 60 – 70 °C ტემპერატურაზე ხდება ჰიდროფობური შრის გაშრობა.

აღწერილი ტექნოლოგიის საფუძველზე ჩვენ მიერ დამზადებულია პოლიმერული, გასხივოსნების მრავალშრიანი დანაფარების მქონე ლინზების ლაბორატორიული ნიმუშები.

დამოწმებანი

1. А. И. Игнатьев, С. С. Киселев, Н. В. Никоноров, А. И. Сидоров, А. С. Рохми. Материалы и технологии интегральной и волоконной оптики. 2009, Санкт-Петербург, 58-61.
2. ზ. ვ. ბერიშვილი, ი. ი. კორძახია, დ. გ. ზარდიაშვილი, გ. გ. აბრამიშვილი, ი. მ. ავალიანი, დ. მ. შალამბერიძე, ი. დ. ივანიძე. ვაკუუმში ВУ–1А ტიპის დანადგარის მოდერნიზაცია მრავალშრიანი პერიოდული სტრუქტურის მქონე ოპტიკური დანაფარების მისაღებად. Nano Studies, 2014, 9, 169-176.

ВЛИЯНИЕ РАЗМЕРА ЧАСТИЦ НА ТЕМПЕРАТУРУ ПЛАВЛЕНИЯ

А. А. Капанадзе, И. Ш. Сиранашвили, Г. Д. Табатадзе, М. С. Тактакишвили

Департамент инженерной физики
Грузинский технический университет
Тбилиси, Грузия

Аннотация

В статье рассмотрено влияние размера частиц на температуру плавления твердых тел. Рассмотрению подверглись в основном 10 – 20 атомные частицы. В частности, определена зависимость предельного размера частицы от температуры плавления, в жидком состоянии вещества. Указаны значения вышеуказанной величины для различных металлов – Hg, Ga и Sn. Также показано, что понижение температуры плавления с уменьшением размера частиц связано с тем, что плавление частицы и переход от геометрии твердого тела к геометрии капли, т.е. сферы, приводит к уменьшению поверхности частицы и выигрышу в поверхностной энергии, что облегчает переход в жидкое состояние.

Давайте зададимся вопросом, который необычайно актуален при рассмотрении связанных с плавлением твердых тел фазовых переходов – можно ли считать рассмотренные в [1] фазовые переходы как плавление 10 – 20 атомных частиц, размытие которых снято за счет взаимодействия и кристаллического упорядочения цеолитом? Ниже будет показано, что параметры этого явления примерно такие же, как и для частиц 30 – 100 Å диаметра, когда термин «плавление» еще вполне применим.

Остановимся вкратце на существующих теориях объяснения снижения температуры плавления при уменьшении размера частиц. Первые расчеты понижения температуры плавления в зависимости от размера частиц провел Павлов еще в 1909 г. [2]. Он определил точку плавления твердой сферы как температуру, при которой давление паров над твердой сферой такое же, как и над жидкой, образующейся при плавлении твердой сферы. По расчетам Павлова, относительное понижение температуры плавления составляет:

$$T_0 - T_r = \frac{2T_0}{L\rho_S r}\left\{\sigma_S - \left(\frac{\rho_S}{\rho_\ell}\right)^{2/3}\sigma_\ell\right\}, \tag{1}$$

где σ_S – радиус частицы, T_0 – температура плавления массивного металла, T_r – температура плавления дисперсной частицы, L – теплота плавления массивного металла, ρ_S – плотность в твердом состоянии, ρ_ℓ – плотность в жидком состоянии, σ_S – поверхностное натяжение твердого металла, σ_ℓ – поверхностное натяжение металла в жидком состоянии.

В 1929 году Рай [3] показал, что это определение соответствует тройной точке для массивных тел и необязательно определяет точку плавления твердой сферы, т.к. когда

происходит плавление, твердое тело находится в контакте не с газообразной фазой, а с жидкой. Рай вывел выражение для температуры плавления твердой сферы, окруженной большим количеством плавящей жидкости. По Раю, относительное понижение температуры плавления может быть выражено следующим образом:

$$T_0 - T_r = \frac{2T_0}{L\rho_S r}\sigma_{S\ell}, \qquad (2)$$

где $\sigma_{S\ell}$ – поверхность натяжения между твердой фазой и жидкостью.

Рейс и Вильсон [4] предположили, что при плавлении сферической частицы наружные слои кристалла плавятся в первую очередь, в результате чего получается система частиц, которая состоит из сферических твердых сердцевин и окружена сферической жидкой оболочкой. Авторы [4] использовали стандартную теорию термодинамического равновесия между твердой сердцевиной и жидкой оболочкой, когда оболочка бесконечно тонка. При этих обстоятельствах равновесная температура та же, что и точка плавления твердой сферы, существовавшей до образования жидкой оболочки.

Отсюда следует, что понижение температуры плавления малой частицы сферической формы по сравнению с массивным металлом:

$$T_0 - T_r = \frac{2T_0}{L\rho_S r}\left\{\sigma_{S\ell} + \left(1 - \frac{\rho_S}{\rho_\ell}\right)\sigma_S\right\}. \qquad (3)$$

Накоплен богатый экспериментальный материал, свидетельствующий о зависимости понижения температуры плавления от размера частиц. Экспериментально установлен факт плавления очень малых частиц металла диаметром 30 Å (например, частицы In, $\varnothing \sim 30$ Å, температура плавления понижена по сравнению с массивным In: $\sim 100\,°C$ [5]; частицы Bi, $\varnothing \sim 20$ Å, температура плавления понижена по сравнению с массивным Bi, $\sim 150\,°C$ [6]. С этой точки зрения весьма интересен вопрос, каков же предельный размер отдельной частицы, в которой можно наблюдать плавление?

Существующие теории позволяют описать снижение температуры плавления при уменьшении размера частиц следующей общей приведенной формулой:

$$\frac{T_{\text{пл}}}{T_0} = 1 - \frac{D_{\text{пред}}}{D}, \qquad (4)$$

где T_0 – температура плавления массива, $T_{\text{пл}}$ – температура плавления частицы с диаметром D, $D_{\text{пред}}$ – параметр, физический смысл которого состоит в том, что это есть предельный размер частицы, жидкой уже при абсолютном нуле. Во всех теориях $D_{\text{пред}}$ считается непрерывной функцией, но для кластеров малого размера это явно не так. Что принимать за диаметр двух-, трех- и четырехатомных частиц? Поскольку диаметр атомоа составляет около 3 Å, значение $D_{\text{пред}}$, меньшее, чем 3 Å, представляется бессмысленным. По-видимому, теория для очень маленьких частиц должна учитывать их реальную геометрию.

В разных конкретных континуальных моделях плавления величина $D_{\text{пред}}$ имеет различные значения (см. **Таблицу 1**). Для Hg, Ga и Sn ее можно оценить, основываясь на полученных нами значениях температуры плавления кластеров. В экспериментах с большими частицами значение $D_{\text{пред}}$ не может быть точно определено из-за сравнительно малого изменения температуры плавления.

Уменьшение размера частиц резко понижает температуру плавления, но при этом существенное значение приобретает точное определение их размера. В нашем случае кластеры прокалиброваны матрицей цеолита. Они весьма малы (9 Å), вследствие чего значение $D_{\text{пред}}$ определялось с большой точностью.

Таблица 1. Экспериментальные и расчетные
значения $D_{\text{пред}}$ при различных моделях плавления.

Метал	Экспери-ментальные значения $D_{\text{пред}}$	Плавление поверхностного слоя [4] $\frac{4}{L\rho_S}\left\{\sigma_{S\ell} + \left(1 - \frac{\rho_S}{\rho_\ell}\right)\sigma_S\right\}$	Теория Рая [3] $\frac{4}{L\rho_S}\sigma_{S\ell}$	Теория Павлова [2] $\frac{\sigma}{L\rho_S}\left[\sigma_S - \left(\frac{\rho_S}{\rho_\ell}\right)^{2/3}\sigma_\ell\right]$	Термодинамическая теория плавления [6] $\frac{\sigma}{L\rho_S}\left[\sigma_S - \left(\frac{\rho_S}{\rho_\ell}\right)^{2/3}\sigma_\ell\right]$
Hg	HgX = 2.4 Å	4.2 Å	8.3 Å	14.3 Å	21.4 Å
Ga	GaX = 2.9 Å GaA = 2.0 Å 1.7 Å 1.4 Å	6.5 Å	4.6 Å	10.5 Å	15.8 Å
Sn	SnX = 2.7 Å SnA = 2.5 Å	2.4 Å	3,6 Å	11.2 Å	16.9 Å
Pb	–	4.0 Å	6.8 Å	10.7 Å	16.1 Å
In	–	5.5 Å	8.3 Å	10.6 Å	15.9 Å
Cd	–	1.3 Å	3.6 Å	5.8 Å	8.7 Å

Как видно из таблицы, экспериментальные значения наиболее близки к расчетным, полученным на базе предположения, что плавлению частицы предшествует возникновение тонкого поверхностного жидкого слоя [4]. Следует еще раз обратить внимание на то, что в случае частицы трехатомного диаметра обычные континуальные представления большей частью неприменимы. Говорить о жидком поверхностном слое в такой частице, по-видимому, бессмысленно, хотя поверхностное натяжение еще сохраняет смысл [7, 8]. Наилучшее соответствие получается для Sn. Для Hg и Ga экспериментальные значения остаются ниже наиболее близких к ним расчетных в 1.5 – 2-раза. При сопоставлении теоретических и экспериментальных значений $D_{\text{пред}}$ следует принимать во внимание, кроме сказанного выше, что исследованные кластеры взаимодействуют с диэлектрическими стенками полости, образующими своеобразную подложку. Во всех моделях плавления такое взаимодействие не учитывается, хотя реально оно всегда имеет место. В случае плоской подложки взаимо-действие должно увеличивать температуру плавления (при этом $D_{\text{пред}}$ уменьшается). В случае кластеров, находящихся в сферической полости, может иметь место как увеличение, так и уменьшение температуры плавления (увеличение $D_{\text{пред}}$). Последнее связано с навязыванием кластеру формы сферической полости. Этим обстоятельством можно объяснить отсутствие пиков плавления для кластеров In, Pb и Cd, но для окончательного вывода необходимы дополнительные эксперименты.

Предположения, лежащие в основе упомянутых теорий, чисто континуальные. Они теряют смысл при переходе к частицам трехатомного диаметра (например, «жидкий» поверхностный слой для частицы, у которой один атом в центре, а остальные располагаются на поверхности одноатомным слоем). Поэтому грубое совпадение $D_{\text{пред}}$, экспериментально полученного и теоретически вычисленного, может рассматриваться не как случайность, а скорее как результат некоторой верной идеи, которую та или иная теория выражает более или менее точно.

В упомянутых теориях причина снижения температуры плавления малых частиц заключается в конкуренции теплоты плавления и выигрыша в поверхностной энергии

при переходе от геометрии твердого состояния к сферической геометрии жидкого. В случае кластеров атомного диаметра очевидна необходимость более строгого учета геометрии кластера в «твердых» и «жидких» фазах.

Мы полагаем, что только при точном учете именно этого фактора можно составить теоретическое описание, наиболее близкое к экспериментам с частицами малых диаметров. Однако, задача эта представляется в настоящее время достаточно сложной. Изложенные ниже рассуждения приводят к формуле типа (3).

Если использовать соотношение типа *правила Трутора* − теплота испарения пропорциональна температуре кипения ($Q_{\text{исп}} = AT_{\text{кип}}$) − для случая плавления массивных тел, то можно предположить, что $Q_{\text{пл}} = BT_{\text{пл}}$

$$T_{\text{пл}} = \frac{Q_{\text{пл}}}{B}. \tag{5}$$

Плавление частицы и переход от геометрии твердого тела к геометрии капли, т.е. сферы, приводит к уменьшению поверхности частицы и выигрышу в поверхностной энергии $\Delta S \Delta E$, что облегчает переход в жидкое состояние, т.е. плавление:

$$T_{\text{пл.малых част.}} = \frac{Q_{\text{пл}} - \Delta S \Delta E}{B} = T_{\text{пл}} - \frac{\Delta S \Delta E}{B}. \tag{6}$$

Таким образом,

$$\frac{T_{\text{пл.малых част.}}}{T_{\text{пл}}} = 1 - \frac{\Delta S \Delta E}{B}, \tag{7}$$

где

$$\frac{D_{\text{пред}}}{D} = \frac{\Delta S \Delta E}{B}. \tag{8}$$

В этой формуле ΔE является разницей поверхностной энергии твердого и жидкого состояния, а ΔS − разница поверхностей частиц в твердом и жидком состоянии. ΔS есть функция диаметра частицы и может вести себя сложным образом, если принимать во внимание реальную геометрию частицы из $10 - 20$ атомов. Различие всех рассмотренных теорий − в точности учета ΔS и ΔE.

Таким образом, показано, что трехмернопроводящая система кластеров металла Hg, Ga и In в цеолите сохраняется только при давлениях выше критического. При снятии внешнего давления происходит скачкообразный переход из металлического состояния кластеров Hg, Ga и In в неметаллическое.

Ссылки

1. В. Н. Богомолов, А. И. Задорожный, А. А. Капанадзе, Э. Л. Луценко, В. П. Петрановский, ФТТ, 1976, 18, 3050.
2. P. E. Pawlow. Phys. Chem., 1909, 65, 545.
3. E. Rie. Phys. Chem., 1923, 104, 354.
4. H. Reiss, I. B. Wilson, G. Golbied. Science, 1948, 3, 551.
5. B. P. Berman, A. E. Curzon. Can. J. Phys., 1974, 52, 923.
6. S. I. Peppiatt, F. R. Sambler. Proc. Roy. Soc. A1, 1975, 345, 487.
7. С. Н. Задумкин, Х. Р. Хоконов. Поверхностные явления в расплавахи возникающих из них твердых фазах. Нальчик, 1965.
8. В. Н. Богомолов, А. И. Задорожный. ФТТ, 1975, 17, 1652.

ВОССТАНОВЛЕНИЕ ПОЧВЕННЫХ ЭКОСИСТЕМ ПРИРОДНЫМИ ЦЕОЛИТАМИ

**Л. Эприкашвили, Т. Кордзахия, М. Дзагания,
М. Зауташвили, Н. Пирцхалава**

Институт физической и органической химии им. П. Меликишвили
Тбилисский государственный университет им. И. Джавахишвили
Тбилиси, Грузия
leprikashvili@hotmail.com

Аннотация

Загрязнение нефтью и нефтепродуктами приводит к значительным изменениям физико-химических свойств почв и загрязняет подземные воды. В результате этого плодородный слой земли в течение длительного времени не восстанавливается. Все больше сельхозпроизводителей обращается к использованию нетрадиционных минерально-сырьевых ресурсов. Большой научный и практический интерес для получения дешевой и доброкачественной продукции при сохранении агроресурсов, прежде всего почвы, представляет использование в качестве мелиорантов местных ресурсов, в том числе таких нанопористых материалов как природные цеолиты, месторождения которых имеются в Грузии. В работе изучено влияние нанопористых цеолитсодержащих туфов, внесенных в загрязненную нефтью почву, на некоторые биометрические показатели сельскохозяйственных растений. Изучено влияние природного цеолита (клиноптилолита), внесенного в почву, загрязненную нефтью, на рост и развитие озимой пшеницы. В работе показано, что природные цеолиты, ввиду их специфических свойств можно считать перспективным сорбирующим материалом, предотвращающим миграцию углеводородов загрязнения в низлежащие слои почвы, а также способствующим увеличению биодеградации загрязнителя, в процессах очистки и восстановления почвогрунтов, загрязненных нефтепродуктами.

1. Введение

С каждым годом все больше внимания уделяется проблемам, связанным с загрязнением окружающей среды. Почвенный покров Земли представляет собой важнейший компонент биосферы Земли. Именно почвенная оболочка определяет многие процессы, происходящие в биосфере. Почвенный покров выполняет функции биологического поглотителя, разрушителя и нейтрализатора различных загрязнений. При нарушении этого звена биосферы, необратимо разрушается и сложившееся функционирование биосферы.

Почвенный покров является важнейшим природным образованием. Его роль в жизни общества определяется тем, что почва представляет собой основной источник продовольствия, обеспечивающий 95 – 97 % продовольственных ресурсов для населения планеты. Почва – это медленно возобновляемый ресурс, являющийся сложной экосистемой, обеспечивающей рост растений. Чтобы растения (продуцены) могли нормально расти и развиваться, почва, как среда обитания, должна удовлетворять их

потребности в элементах питания, воде и кислороде, а также обладать рядом других свойств. Взаимосвязь между почвой и растительностью – динамическое равновесие, а не стационарное состояние и является наиболее чувствительной к антропогенному воздействию [1 – 3].

Углеводороды являются одним из приоритетных загрязнителей окружающей среды. В почву эти соединения поступают в результате аварий и утечек на предприятиях химической и нефтехимической промышленности, как продукты и отходы деятельности нефтедобывающих и нефтеперерабатывающих предприятий, а также из атмосферы – при сжигании нефтепродуктов. Общая токсичность нефти, как правило, невысока. В то же время, отдельные компоненты нефти и продукты ее биоразложения, преимущественно, полиароматические и полициклические соединения, отличаются мутагенностью, канцерогенными свойствами и тератогенностью. Последствия их воздействия на живые организмы, в том числе и на человека, могут проявляться через многие годы и в последующих поколениях. Проявления этого воздействия весьма многообразны, но наибольшую опасность при этом составляют генетические нарушения. Определяющим фактором воздействия нефти и нефтепродуктов на почву является соотношение лёгких и тяжёлых фракций. Летучие фракции обладают повышенной токсичностью для обитателей почвы, но действие их кратковременно. Тяжелые фракции нефти малоподвижны и могут создавать в почве устойчивый очаг загрязнения [4, 5]. Зеленые растения, грибы и микроорганизмы, развивающиеся в грунтах и донных отложениях водоемов, содержащих даже следы нефти, накапливают и концентрируют в своих тканях тяжелые металлы, радионуклиды, канцерогенные вещества и генетические яды и передают их по пищевой цепи высшим организмам с соответствующими последствиями. Таким образом, нефтяное загрязнение природных сред надолго создает угрозу здоровью населения региона [6, 7].

В почвах, загрязненных нефтью, происходят такие процессы как: 1. нарушение экологического равновесия почвенной системы; 2. изменение морфологических, физических, физико-химических и химических характеристик почвенных горизонтов и строения почвенного профиля; 3. нарушение природного соотношения между отдельными группами и фракциями органического вещества почв; 4. проникновение нефти и нефтепродуктов в грунтовые воды; 5. снижение почвенного плодородия и возникновение токсикологически опасных ситуаций. Загрязнение почв нефтью нарушает водно-воздушный режим и структуру почвы, взаимосвязи почва–растение–вода, функционирование почвенных микробных сообществ и снижает почвенное плодородие. Для рекультивации загрязненных почв необходимо создание оптимальных условий для развития естественного углеводородокисляющего микробиоценоза посредством внесения органического или минерального удобрения – для оптимизации пищевого режима и мелиорантов – для улучшения водно-физических свойств почвы [8]. Рекультивация земель, загрязненных нефтью и тяжелыми нефтепродуктами, предполагает снижение их содержания в почве и воде до биологически безопасных концентраций. Однако, величина этих концентраций до настоящего времени не установлена из-за сложного и непостоянного химического состава нефти и вряд ли будет установлена однозначно [9 – 11]. В реальных производственных условиях фактической целью проведения рекультивационных работ является лишь снижение содержания в почве нефти и нефтепродуктов до условного предела, при котором возможно развитие, рост и

размножение зеленых растений, и достижение близкого к первоначальному общепроективного покрытия растениями «рекультивированной» земли [12, 13].

Мировая практика проведения рекультивационных работ располагает различными методами восстановления почвенных и водных экосистем. На нефтезагрязненных почвах используются различные рекультивационные мероприятия такие как: сжигание нефти, засыпка загрязненных участков грунтом, вывоз загрязненной почвы в отвалы, но эти мероприятия могут привести к необратимому уничтожению плодородного слоя почвы. Такие способы рекультивации совершенно неприемлемы, они достаточно энерго- и ресурсоемки и зачастую экологически не оправдываются. Механические и физические методы не могут обеспечить полного удаления нефти и нефтепродуктов с почвы, а процесс естественного разложения их в почвах чрезвычайно длителен, поэтому в настоящее время предпочтение отдается механическим и биологическим способам очистки, наиболее приемлемым с экологической точки зрения. Они направлены в первую очередь на создание оптимальных условий жизнедеятельности почвенных микроорганизмов, на стимуляцию их деятельности и повышение метаболической активности [14].
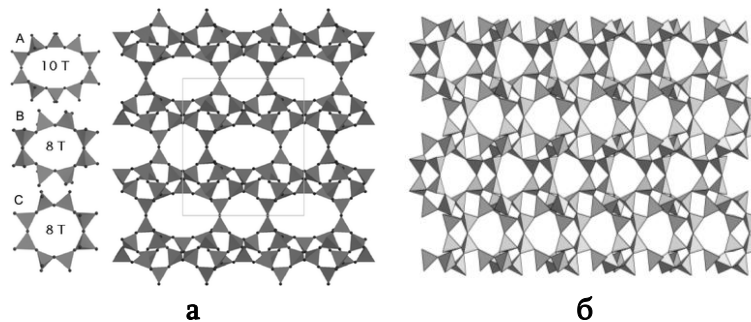

Рисунок 1. Структуры природных цеолитов:
а) клиноптилолита и б) филлипсита.

Большой научный и практический интерес для получения дешевой и доброкачественной продукции при сохранении агроресурсов, прежде всего почвы, представляет использование в качестве мелиорантов местных ресурсов, в том числе природных цеолитов, месторождения которых имеются в Грузии. Все больше сельхозпроизводителей обращается к использованию нетрадиционных минерально-сырьевых ресурсов. Это, прежде всего, породы с высоким содержанием кремния: диатомиты, трепелы, опоки, природные цеолиты. Природные цеолиты – перспективный вид полезных ископаемых, масштабы применения которых во всем мире растут, и далеко не последнюю роль в этом играет их все увеличивающееся применение в сельском хозяйстве. Научными исследованиями подтверждено положительное влияние цеолитовых туфов на урожайность сельскохозяйственных культур [15 – 18]. С каждым годом ассортимент их расширяется и все чаще для обеспечения экологической безопасности сельскохозяйственной продукции используются эти нанопористые материалы- природные цеолиты, в частности, клиноптилолит и филлипсит (**Рисунок 1**) [19 – 22].

Внесение цеолитсодержащей породы в почву является перспективным подходом для предотвращения миграции углеводородов загрязнения в низлежащие слои почвы, а также для увеличения биодеградации загрязнителя.

Наиболее важными характеристиками цеолитов, имеющими первостепенное значение в оценке их агромелиоративных качеств, являются: каркасная структура, высокая ёмкость катионного обмена, наличие в составе элементов зольного питания растений, высокая способность к поглощению воды. В результате целенаправленных исследований было установлено, что внесение цеолитов положительно влияет на свойства почвы, улучшает ее физические и сорбционные свойства, являясь источником и регулятором питания растений некоторыми элементами [23].

2. Эксперимент

Целью настоящей работы было изучение влияния природного цеолита (клиноптилолита), внесенного в почву, загрязненную нефтью, на рост и развитие озимой пшеницы. Токсикологическое действие нефтезагрязненной почвы проявляется в первую очередь на высших растениях, которые по разному устойчивы к различным концентрациям загрязнителя.

Таблица 1. Физико-химические характеристики нефти.

№	Показатели	Нефть месторождения Самгори
1	Плотность, кг / м^3	822.5
2	Молекулярная масса	178
3	Вязкость. сСт 20 °C 50 °C	 4.87 2.60
4	Температура, °C Застывания Вспышки в закрытом тигле	 3 ниже 35
5	Коксуемость, мас. %	1.0
6	Кислотное число, мг KOH / г	0.06
7	Содержание мас.% Сера Азот Асфальтены Силикагелевые смолы Парафины	 0.12 0.07 0.90 4.10 6.9 (52 °C)
8	Выход фракции, мас. % до 200 °C до 350 °C до 500 °C	 31.50 60.3 86.9

1

В эксперименте использовалась садовая серо-коричневая почва. Почву загрязняли нефтью месторождения Самгори (Грузия). Физико-химические характеристики нефти приведены в **Таблице 1** [24].

Природный цеолит – клиноптилолитовый туф месторождения Тедзами, участок Хандаки (Грузия). Содержание основного минерала, в этой горной породе колеблется в пределах 70 – 80 %, в катионном составе превалирует кальций [19]. Природные цеолиты являются довольно уникальным нанопористым материалом с весьма сложной структурой.

Клиноптилолит (HEU) относится к группе гейландитовых цеолитов [19]. Минералы этой группы являются наиболее распространенными в природе цеолитами. Кристаллическая структура клиноптилолита характеризуется наличием достаточно открытых каналов, образованных десятью- и восьмичленными тетраэдрическими кольцами, расположенными в трех направлениях: каналы параллельные оси С имеют относительные размеры 0.705 × 0.425 нм и 0.460 × 0.395 нм, соответственно. Восьмичленные каналы, расположенные параллельно оси А и под углом 50° к этой оси имеют диаметры 0.540 × 0.390 и 0.520 × 0.390 нм [25].

В качестве тестового растения использовалась пшеница. Зерна высеивались в кюветы (1 кг), в шести вариантах, каждый в трех повторностях. Первый вариант – чистая почва (объект сравнения). Второй вариант – субстрат: почва + 50 % цеолита. Третий вариант – почва, со степенью загрязнения нефтью 5 %. Четвертый вариант – почва, со степенью загрязнения нефтью 10 %. Пятый и шестой варианты – субстраты с соответственной степенью загрязнения нефтью (5 и 10 %). Эксперимент проводился в лабораторных условиях на лугово-коричневом типе почвы, со слабощелочной, почти нейтральной, реакцией водного раствора (pH = 7.1 – 7.5). Почва характеризуется низким содержанием гумуса от 1.93 до 2.90 %, по гранулометрическому составу относится к тяжелым суглинкам.

Перед началом эксперимента были определены посевные качества семян пшеницы (сорта «Иасаули»): всхожесть и энергия прорастания. Всхожесть – количеством семян, которое проросло в установленный для этой культуры срок (в данном случае – 10 дней). Оно выражается в процентах от общего количества семян, взятого для проращивания, и характеризует способность образовывать нормально развитые проростки при оптимальных условиях проращивания. Энергия прорастания характеризует дружность и скорость прорастания семян. Определяется она в одном анализе со всхожестью, но подсчет нормально проросших семян проводится ранее. В качестве ложа для проращивания семян использовался увлажненный кварцевый песок. Эксперименты подтвердили хорошие посевные качества семян пшеницы (98.5 %), которые были использованы в дальнейшем в отмеченных выше вариантах эксперимента [26]. Было проведено два последовательных посева с перерывом между ними в один месяц. Наблюдения за продуценами каждого посева проводились в течение 30 дней.

3. Результаты исследований и их обсуждения

Были определены следующие биометрические показатели: энергия прорастания (ЭП), всхожесть (В), а также такие показатели как: высота ростков (ВР), относительная величина высоты ростков. Энергию прорастания определяли через три дня после посева, а всхожесть на десятый день. В **Таблице 2** приведены среднеарифметические данные. Анализ табличных данных первого и второго посевов показывает, что внесение цеолита в почву, безусловно, оказывает положительное влияние на энергию прорастания и всхожесть растений.

Так, энергия прорастания на субстрате повышается на 12.5 и 15.5 %, а всхожесть – на 5.9 и 6.7 % соответственно (варианты I и II). При загрязнении почвы нефтью (5 и 10 %), как видим из данных таблицы, при первом посеве зерна не взошли в контрольные сроки (варианты III и IV), а на субстрате, загрязненном 5 % нефтью (вариант V) проросло 10 % семян по сравнению с чистым субстратом (вариант II). На субстрате, загрязнённом 10 %

нефти, при первом посеве семена не взошли (вариант VI). Следует отметить, что данные, приведённые в **Таблице 2**, рассчитывались на 3 день после посева (энергия прорастания) и на 10 день (всхожесть).

Таблица 2. Энергия прорастания и всхожесть семян пшеницы на вариантах эксперимента.

Биометрические показатели	Посевы	Варианты эксперимента					
		Почва (контроль)	Почва + цеолит (субстрат)	Почва + 5 % нефти от массы почвы	Почва + 10 % нефти от массы почвы	Почва + цеолит + 5 % нефти от массы субстрата	Почва + цеолит + 10 % нефти от массы субстрата
		I	II	III	IV	V	VI
Энергия прорастания	1 посев	70	81	–	–	10	–
	2 посев	80	90	30	5	60	40
Всхожесть	1 посев	85	90	–	–	55	30
	2 посев	90	96	50	35	75	55

На **Рисунке 2** показана картина прорастания семян на 22 день после первого посева, а диаграмма (**Рисунок 3**) отражает динамику роста семян на 3-й и на 22-й день после посева. Во всех экспериментальных вариантах семена прорастают с различной степенью интенсивности и скоростью. Несколько иная картина наблюдается при втором посеве. Представленные данные значительно превосходят биометрические показатели растений первого посева.

Рисунок 2. Картина прорастания семян на 22 день после первого посева:
а) вариант I – почва (контроль); б) вариант II – субстрат; в) вариант III –
почва + 5 % нефти от массы почвы; г) вариант IV – почва + 10 % нефти от
массы почвы; д) вариант V – почва + цеолит + 5 % нефти, от массы
субстрата и е) вариант VI – почва + цеолит + 10 % нефти от массы субстрата.

Известно, что поддержание почвы во влажном состоянии является одним из агротехнических приемов управления биологической активностью и оказывает эффективное воздействие на темпы разложения нефти и нефтепродуктов. Благоприятный водный режим почвы достигается путем полива. Улучшение водного режима путем полива обусловливает улучшение агрохимических свойств почв, в частности влияет на подвижность питательных веществ, микробиологическую деятельность и активность биологических процессов [8-9].
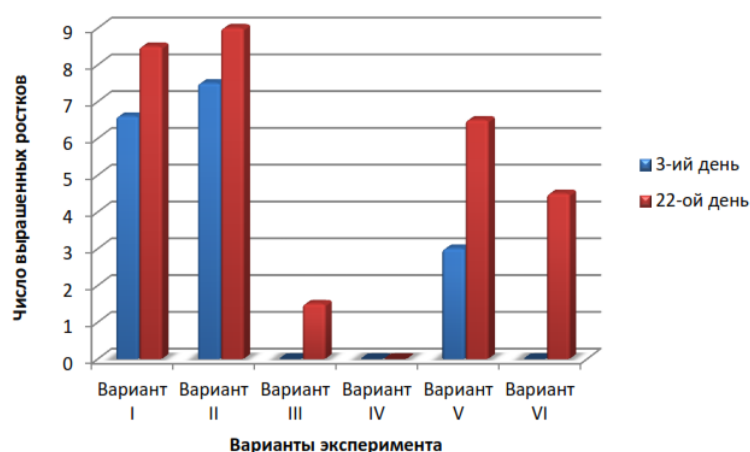
Рисунок 3. Диаграмма динамики роста
семян на 3-й и на 22-й день после посева.

Можно предположить, что систематическое увлажнение почвы, присутствие цеолита в субстратах, своеобразного «депо» влаги и питательных элементов, а также активатора биоты почвы, оказало положительное влияние на динамику процессов, происходящих в экспериментальных вариантах, что также отразилось и на биометрических показателях продуцена.

4. Заключение

Таким образом, исходя из вышеизложенного, следует перспективность использования природных цеолитсодержащих туфов в сельском хозяйстве как в целях защиты и реабилитации почвенного покрова от загрязнителей, так и как средств, повышающих урожайность и устойчивость различных растений, выращенных, главным образом, на бедных почвах.

Ссылки

1. Ю. В. Евтефеев, Г. М. Казанцев. Основы агрономии. 2013, Москва, Форум.
2. В. Д. Валова. Основы экологии. 2001, Москва, Изд. дом «Дашков и К».
3. Ред. М. А. Глазковский. Восстановление нефтезагрязненных почвенных экосистем. 1988, Москва, Наука.
4. С. Л. Давыдова, В. И. Тагасов. Нефть как топливный ресурс и загрязнитель окружающей среды. 2004, Москва, Изд. РУДН.
5. C. D. Franci, M. Guillemette, E. Pelletier, O. Chostel, S. Bonnfoi, J. Verreault. Endocrine status of bird potentially exposed to the Deepwater Horizont oil spill: A case study of northern ganmets breeding on Bonaventure Island, Estern Canada. Sci. Total Environ., 2014, 473-474, 110-116.
6. C. B. Vidal, G. S. C. Raulino, A. L. Barros, A. C. A. Lima, J. P. Ribeiro, M. J. R. Pires, R. F. Nascimento. BTEX removal from ugueous solutious by HDTMA-modified Y-zeolite. J. Environ. Manag., 2012, 112, 178-185.
7. C. P. Moura, C. B. Vidal, A. L. Barros, L. S. Costa, L. C. G. Vasconcellos, F. S. Dias, R. F. Nascimento. Adsorption of BTX (benzene, toluene, o-xylene, p-xylene) from aqueous solutions by modified periodic mesoporous organosilica. J. Colloid Interf. Sci., 2011, 363, 626-634.

8. Н. И. Исмаилов, Ю. И. Пиковский. Восстановление нефтезагрязнённых почвенных экосистем. 1988, Москва, Наука.

9. О. Н. Логинов, Н. Н. Силищев, Т. Ф. Бойко, Н. Ф. Галимзянова. Биотехнологические методы очистки окружающей среды от техногенных загрязнений. 2000, Уфа, ГИНТЛ «Реактив».

10. С. Я. Трофимов, Я. М. Аммоева, Д. С. Орлов. Влияние нефти на почвенный покров и проблема создания нормативной базы по влиянию нефтезагрязнения на почвы. Вест. МГУ, 2000, 17, 2, 30-34.

11. Т. В. Коронелли. Принципы и методы интенсификации биологического разрушения углеводородов в окружающей среде. Прикл. биохим. микробиол., 1996, 32, 6, 579-585.

12. Р. А. Афанасьев, Г. Е. Мерзлая, Н. В. Русаков. Пригодность почв загрязненных нефтью, для сельскохозяйственного использования. Плодородие, 2006, 3, с32-34.

13. M. Wdowin, W. Franus. Fly ash derived zeolites in the removal of toxic compounds. In: Materials Science, "Metals and Nonmetals", "Zeolites-Useful Minerals" (Ed. C. Belviso). 2016, 67-79.

14. Ф. М. Кузнецов, А. П. Козлов, В. В. Середин, Е. В. Пименова. Рекультивация нефтезагрязнённых почв. 2003, Пермь.

15. С. Д. Мирошникова. Природно-сырьевые ресурсы: Классификация видов, уровень мировых запасов, вовлечение в хозяйственный оборот. Анал. журн. РИСК, 1997, 3-4, 116-119.

16. Н. Н. Терещенко, С. В. Лушников, А. Б. Бубина. Применение природных цеолитов для ускорения очистки нефтезагрязнённой почвы. Энергя, 2007, 1, 23-30.

17. N. N. Tereshchenko, S. V. Lushnicov, A. B. Bubina. Using of zeolites for biological remediation of oil contaminated soil. Geominas, 2008, 36, 45, 23-26.

18. К. Е. Колодезникова. Актуальные проблемы освоения цеолитвого сырья месторождения Хонгуру. 2005, Якутск, Изд. ЯНЦ СО РАН.

19. Ch. Baerlocher, L. B. McCucker, D. H. Olson. Atlas of Zeolite Structure Types. 2007.

20. Г. В. Цицишвили, Т. Г. Андроникашвили, М. А. Кардава. Природные цеолиты в земледелии. 1993, Тбилиси, Мецниереба.

21. Г. В. Цицишвили, Т. Г. Андроникашвили, Н. Несторов, В. Г. Лабутин. Применение природных цеолитов в сельском хозяйстве. 1997, Тбилиси, Мецниереба.

22. T. Andronikashvili, T. Urushadze. Use of zeolite containing rocks in plant-growing. Agrokhimia, 2008, 12, 63-79.

23. G. V. Tsitsishvili, T. G. Andronikashvili, G. N. Kirov, L. D. Filizova. Natural Zeolites. 1992, Ellis Horwood Ltd.

24. Г. Ш. Хитири, Л. Ф. Топуридзе, Н. Т. Хецуриани, Э. А. Ушараули, И. Г. Эдилашвили. Основные направления переработки нефтей Грузии. Журн. хим. проблемы, 2005, 4, 46-48.

25. L. Eprikashvili, T. Kordzakhia, T. Andronikashvili. Zeolites – The unique desiccation agent for organic liquids. 2015, LAP Lambert Acadю Publ.

26. L. Eprikashvili, M. Zautashvili, T. Kordzakhia, N. Pirtshkalava, M. Dzagania, I. Rubashvili, V. Tsitsishvili. Intensification of bioproductivity of agricultural cultures by adding natural zeolites and brown coals into the soil. Ann. Agrarian Sci., 2016, 14, 67-71.

რადიონუკლიდების სამარხის სიღრმისეული დიაგნოსტიკა მცენარე-ინდიკატორების საშუალებით

ა. ლონდაძე, პ. იმნაძე, ვ. ცანავა, ც. გაბუნია, გ. გოგოლაძე,
ი. მამულაიშვილი, მ. გოგებაშვილი, ნ. ივანიშვილი, ს. ოსიძე

[1] ე. ანდრონიკაშვილის სახ. ფიზიკის ინსტიტუტი
ი. ჯავახიშვილის სახ. თბილისის სახელმწიფო უნივერსიტეტი
platon.imnadze@gmail.com
[2] ჩაის, სუბტროპიკული კულტურებისა და ჩაის მრეწველობის ინსტიტუტი
(ა)იპ საქართველოს აგრარული უნივერსიტეტი

ანოტაცია

ნაშრომში ნაჩვენებია რადიონუკლიდების შემცველობის სიღრმული დიაგნოსტიკის შესაძლებლობა მცენარე-ინდიკატორების გამოყენებით. კვლევის ობიექტს წარმოადგენს ანასეულის რადიონუკლიდების სამარხის შემოსაზღვრული ტერიტორია. ჩატარებულია ზედაპირული რადიაციული დაბინძურების სკანირება მობილური გამა-სპექტრომეტრით და დაფიქსირებულია ტერიტორიის განსაკუთრებულად დაბინძურებული მონაკვეთები. ვერტიკალური მიგრაციის მარკერად გამოყენებულია [137]Cs. კვლევას საფუძვლად უდევს მცენარე-ინდიკატორების ფესვთა სისტემის სხვადასხვა სიღრმეზე განვითარების პარამეტრები, აგრეთვე, ფესვების მიერ რადიოიზოტოპების შთანთქმისა და მცენარის მიწისზედა ნაწილებში მათი ტრანსპორტირების უნარის ამსახველი მახასიათებლები. ჩვენ მიერ შემოთავაზებული მეთოდოლოგია, ზედაპირული მონიტორინგისგან განსხვავებით, გამიზნულია იმ შემთხვევებისთვის, როდესაც რადიაციული დაბინძურება საწყისს იღებს არა ნიადაგის ზედა ფენებიდან, არამედ სიღრმისეული ჰორიზონტებიდან.

შესავალი

ბირთვული ენერგეტიკის სწრაფმა განვითარებამ, ადამიანის საქმიანობის სხვადასხვა სფეროში რადიონუკლიდებისა და მაიონიზებელი რადიაციის ფართო გამოყენებამ განაპირობა ის ფაქტი, რომ რადიოაქტიური ნივთიერებები იქცნენ დაბინძურებული ბიოსფეროს ერთ-ერთ მუდმივ შემადგენელ კომპონენტად. მაიონიზებელი რადიაცია კი განიხილება, როგორც გარემოს ეკოლოგიური ფაქტორი. აღნიშნულიდან გამომდინარე, ბიოლოგიური მოქმედების შესწავლის კვალდაკვალ, დიდი მნიშვნელობა ენიჭება რადიონუკლიდების ბიოგეოქიმიურ "ზედის" კვლევას. დედამიწის ზედაპირზე სხვადასხვა გზით მოხვედრილი რადიონუკლიდები ერთვებიან რა მიგრაციის ბიოგეოქიმიურ პროცესებში, ნაწილდებიან ნიადაგის საფარველის ისეთ სისტემებში, როგორიცაა: ნიადაგი–ზედაპირული და გრუნტის წყლები, ნიადაგი–მცენარე და შემდგომ, კვებით და ბიოლოგიურ ჯაჭვებში. რადიონუკლიდების

მიგრაციის პროცესების სიჩქარე და მიმართულება განისაზღვრება სხვადასხვა ფაქტორთა ერთობლიობით, პირველ რიგში, თვით რადიონუკლიდების ფიზიკურ-ქიმიური თვისებებითა და ბუნებრივი პირობებით, უმთავრესად, კონკრეტული ეკოსისტემის ტიპითა და მდგომარეობით.

დედამიწის ზედაპირზე რადიონუკლიდების მოხვედრის ერთ-ერთ გზას გლობალური რადიოაქტიური გაფრქვევა წარმოადგენს. ჩერნობილისა და შემდგომში, ფუკუსიმას ატომურ სადგურებზე მომხდარი ავარიების შედეგების შესწავლის საფუძველზე, დაგროვდა უდიდესი ფაქტობრივი მასალა ატმოსფეროდან ნიადაგში, მცენარეში, კვების პროდუქტებში, ადამიანის და ცხოველის ორგანიზმში რადიოაქტიური პროდუქტების გლობალური მოხვედრის ინტენსივობის შესახებ [1 – 5].

გამოქვეყნებულია მთელი რიგი ნაშრომებისა, რომლებშიც ნაჩვენებია ბუნებრივი პირობების, სახელდობრ, ბიოგეოცენოზური, ჰიდროლოგიური და ნიადაგობრივ-გეოქიმიური მდგომარეობის უპირატესი როლი გაფრქვეული რადიონუკლიდების მიგრაციაში, მოყვანილია მონაცემები ნიადაგის საფარში მათი განაწილების კანონზომიერებათა შესახებ [6]. საქართველოში ჩატარებული კვლევებით დადგენილია, რომ ჩერნობილის ატომურ სადგურზე მომხდარი ავარიის დროს, დასავლეთ საქართველოს ტერიტორიის რადიონუკლიდებით დაბინძურების თავისებურებები განაპირობა, როგორც კლიმატურმა პირობებმა, ისე კონკრეტული ეკოსისტემების ნიადაგობრივ-მცენარეული საფარის თავისებურებების სპეციფიკამ [7].

რადიოიზოტოპების მიგრაციის პროცესი, გარდა ეკოსისტემის ტიპისა და მდგომარეობისა, მნიშვნელოვნად არის დამოკიდებული დაბინძურების წყაროს იზოტოპურ შემადგენლობაზე, რადიოიზოტოპების კონცენტრაციაზე და დაბინძურების წყაროს მდებარეობაზე. რაც შეეხება დაბინძურების წყაროს მდებარეობას, როგორც წესი, განიხილება გარემოს ზედაპირული დაბინძურების შემთხვევა და არ იხილავენ ტექნოგენური დაბინძურების იმ შემთხვევებს, როდესაც ნიადაგის დაბინძურების წყარო იმყოფება არა ნიადაგის ზედაპირზე, არამედ – განსაზღვრულ სიღრმეში. ასეთი შემთხვევები შეიძლება წარმოიშვას ყოფილი ან მოქმედი საცავების ტერიტორიაზე, მათ შორის, საქართველოშიც. ასეთი ტიპის დაბინძურების სპეციფიკის კვლევის მიზნით, ჩვენ მიერ შერჩეულ იქნა რადიოაქტიური ნარჩენებით დაბინძურებული ეკოსისტემა, რომელიც განლაგებულია ყოფილი რადიოლოგიის ლაბორატორიის ტერიტორიაზე დასავლეთ საქართველოში.

კვლევის ობიექტი და მეთოდები

კვლევის ობიექტს წარმოადგენს დაბა ანასეულის მიმდებარე ტერიტორია, რომელიც გამოირჩევა რადიონუკლიდების ლოკალიზაციის ლაქობრივი ხასიათით. ამასთანავე, აღნიშნულ ზონაში არსებობს ამჟამად გაუქმებული რადიოლოგიის ლაბორატორიის კომპლექსის რადიაციული მასალების სამარხი, რომელშიც მოთავსებულია სხვადასხვა სახის იზოტოპების ნარჩენები. ამჟამად აღნიშნულ ტერიტორიაზე შეინიშნება რადიოიზოტოპებით დაბინძურების მრავალფეროვანი ხასიათი. აქედან გამომდინარე, კვლევის პირველ სტადიაზე, განხორციელდა საკვლევი ზონის ზედაპირული რადიაციული დაბინძურების სკანირება მობილური გამა-სპექტრომეტრით InSpector–1000, modelIPRON–N (Canberra) და დაფიქსირდა, რადიაციული თვალსაზრისით, ტერიტორიის განსაკუთრებულად დაბინძურებული მონაკვეთები. საკვლევი ზონის ნიადაგსა და მცენარეებში რადიონუკლიდების

შემცველობის განსაზღვრისთვის, გამოყენებულ იქნა გამა-სპექტრომეტრული ანალიზის მეთოდი. გაზომვები ჩატარდა მაღალი სისუფთავის გერმანიუმის ნახევარგამტარული (HpGe) დეტექტორისა და მრავალარხიანი ანალიზატორის InSpector–2000-ის გამოყენებით. ჩატარებული გაზომვების დამუშავებისათვის გამოყენებულ იქნა სპექტრომეტრული გაზომვების პროგრამული უზრუნველყოფა Genie–2000 და გაზომვების შედეგების რაოდენობრივი დამუშავების პროგრამული უზრუნველყოფა ISOCS/LabSOCS. ნიადაგის ნიმუშების აღება განხორციელდა როგორც ზედაპირული ფენებიდან, ისე სიღრმისეული ჭრილებიდან. საკვლევი ზონის დაბინძურების დონის დადგენისთვის მიგრაციის მარკერს წარმოადგენდა ^{137}Cs.

შედეგები და მათი განხილვა

საქართველოში ბოლო წლებში განსაკუთრებული ყურადღება ეთმობა სხვადასხვა სახის რადიოაქტიური წყაროების აღმოჩენისა და მათი უტილიზაციის საკითხებს. უპირველეს ყოვლისა, ეს ეხება ყოფილი სამხედრო ბაზების, სამრეწველო და სამედიცინო დაწესებულებების მიერ მიტოვებულ ტერიტორიებს. აღნიშნულთან მიმართებაში ნაკლებად არის შესწავლილი იმ სამეცნიერო ცენტრების რადიოეკოლოგიური მდგომარეობა, რომელთა საქმიანობა რადიოიზოტოპური მეთოდოლოგიის გამოყენებასთან იყო დაკავშირებული. ამ თვალსაზრისით საყურადღებოა სამარხები, სადაც თავსდებოდა რადიოიზოტოპური ნარჩენები და რადიაციით დაბინძურებული ობიექტები. ანასეულის ერთ-ერთი ასეთი სამარხის შემოსაზღვრული ტერიტორიის რადიოეკოლოგიური კვლევისას ჩვენ მიერ აღმოჩენილი იქნა რადიონუკლიდების არა მარტო ზედაპირული, არამედ სიღრმისეული ლოკალიზაციის კერებიც (სურათი 1).

როგორც **სურათიდან 1** ჩანს, რადიოაქტიურობის მაქსიმალური მაჩვენებელი ფიქსირდება 10 – 30 სმ სიღრმიდან აღებულ ნიადაგის ნიმუშებში, სიღრმის მატებასთან ერთად შეინიშნება რადიოაქტიურობის ინტენსივობის შემცირება. საყურადღებოა საკვლევი ზონის ზედაპირიდან (0 – 10 სმ) აღებული ნიადაგის ნიმუშის შედარებით მაღალი რადიოაქტიურობა (30.5 კბკ / კგ). თუ გავითვალისწინებთ იმ გარემოებას, რომ სამარხის დახურვის შემდეგ მის ზედაპირზე დაყრილ იქნა რადიოაქტიურად სუფთა ნიადაგის ფენა, მაშინ, სამარხის ზედაპირიდან აღებულ ნიადაგის ნიმუშებში რადიონუკლიდის კონცენტრაციის მაღალი მნიშვნელობები მიგვითითებს დაბინძურებული ზონების ქვედა ფენებიდან ზედაპირისკენ გადააადგილებაზე. აღსანიშნავია ისეთი სამეცნიერო კვლევების სიმრავლე, რომელთა მიხედვით სწორედ ნიადაგის ზედაპირზეა კონცენტრირებული ანთროპოგენური წარმოშობის რადიონუკლიდთა ძირითადი რაოდენობა. ეს დებულება ასახავს ზედაპირზე გაფრქვეული რადიონუკლიდების მიგრაციის შეზღუდვას მათი ბიოტებში ინტეგრირების გზით. საყურადღებოა ნიადაგის ზედა ფენებში რადიონუკლიდების მოხვედრის შესაძლო მექანიზმების კვლევა. მცენარეული საფარის არ არსებობის შემთხვევაში, ეს შესაძლებელია ქარით გამოწვეული ნიადაგის ეროზიის შედეგად. ჩვენ შემთხვევაში, ნიადაგის ეროზია პრაქტიკულად გამორიცხულია, ვინაიდან აღნიშნული სამარხის ზედაპირი ხასიათდება რამდენიმე იარუსიანი ფიტოცენოზის არსებობით. აქედან გამომდინარე, ვვარაუდობთ, რომ ნიადაგის ქვედა ფენებიდან ზედა ფენებისკენ რადიონუკლიდების მიგრაცია და მათი ზედაპირზე დაფიქსირება ფიტობიოტების მეშვეობით არის შესაძლებელი. ჩვენი ვარაუდის დადასტურების მიზნით ჩავატარეთ

87

ექსპერიმენტები, რათა დაგვედგინა ანთროპოგენური რადიონუკლიდების სამარხის სიღრმული დიაგნოსტიკის შესაძლებლობა მცენარე-ინდიკატორების საშუალებით.
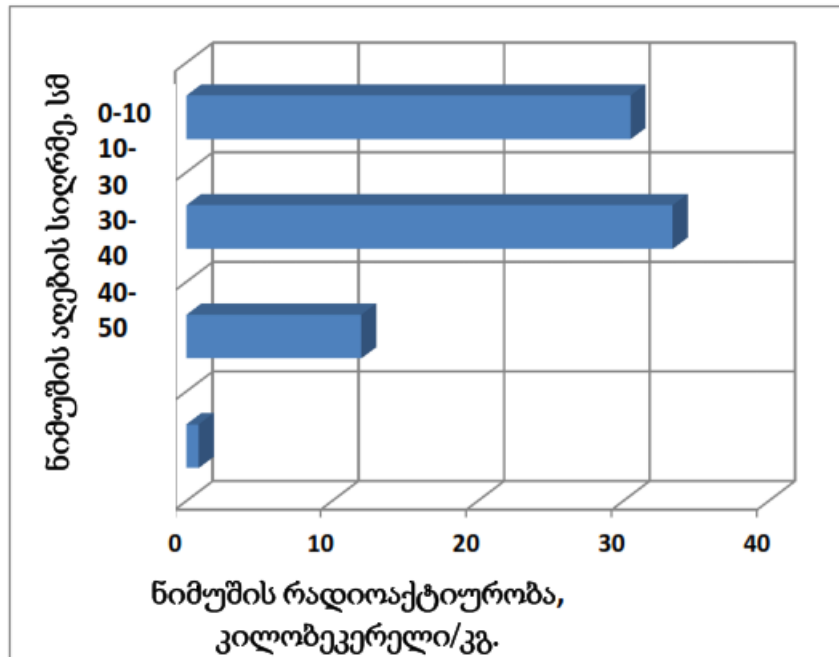
სურათი 1. რადიონუკლიდების (^{137}Cs) ვერტიკალური
განაწილება სამარხის შემოსაზღვრულ ტერიტორიის ნიადაგში.

სახელდობრ, კონკრეტული ფიტოცენოზიდან, რომელთა უმრავლესობა ადგილობრივ ნაირსახეობებს მიეკუთვნება, შევარჩიეთ მცენარეთა სამი სახეობა: ეწრის გვიმრა (*Pteridium tauricum*), იაპონური გრაკლა (*Spiraea japonica*) და ჩაი (*Thea sinensissinensis*). აღნიშნული მცენარეები ხასიათდებიან ნიადაგში ფესვთა სისტემის სხვადასხვა სიღრმეზე განვითარებით (გვიმრა – 30, გრაკლა – 30 – 40 და ჩაი – 50 სმ-დან). საკვლევ მცენარეთა მიწისზედა ვეგეტატიური ნაწილების ნიმუშებში განისაზღვრა ^{137}Cs-ის შემცველობა. ეს მახასიათებელი დაფიქსირდა: გვიმრაში – 260, იაპონურ გრაკლაში – 12 და ჩაიში – 45 ბკ / კგ. თუ გავაანალიზებთ საკვლევ მცენარეთა ფესვთა სისტემის სხვადასხვა სიღრმეზე განვითარების მონაცემებსა და რადიონუკლიდების ვერტიკალური განაწილების მაჩვენებლებს სამარხის შემოსაზღვრული ტერიტორიის ნიადაგში (**სურათი** 1), აღმოჩნდება, რომ ეს ორი მახასიათებელი ერთმანეთთან გარკვეულ კავშირში იმყოფება. სურათიდან ჩანს, რომ სიღრმის მატებასთან ერთად მცირდება ნიადაგის ნიმუშებში რადიოაქტიურობის მაჩვენებელი, შესაბამისად, მცენარეში (ჩაი), რომელსაც შედარებით ღრმად აქვს ფესვთა სისტემა განვითარებული, ასევე დაბალია ^{137}Cs-ის შემცველობა. აღნიშნულის საპირისპიროდ, გვიმრას ვეგეტატიურ ნაწილებში ^{137}Cs-ის შემცველობის შედარებით მაღალი მაჩვენებლები ფიქსირდება.

გასაგებია, რომ მოცემული პარამეტრები ნიადაგში ^{137}Cs-ის ვერტიკალური განაწილების მხოლოდ ზოგადი დახასიათების საშუალებას იძლევა. ამასთანავე, ცალკეული მცენარეები რადიონუკლიდების აკუმულაციის უნარით განსხვავებიან ერთმანეთისგან. მიუხედავად ამისა, მიგვაჩნია, რომ მცენარე-ინდიკატორების გამოყენებით შესაძლებელია ანთროპოგენური წარმოშობის რადიონუკლიდებით (^{137}Cs)

დაბინძურების სიღრმული დიაგნოსტიკა, ვინაიდან ეს რადიოიზოტოპი ბუნებაში არ არსებობს. რადიოაქტიური მასალების სამარხის საიმედოდ დაცვისა და გარემოსაგან რადიონუკლიდების იზოლაციის საკითხები მოითხოვენ ინდივიდუალურ მიდგომას. აქ გასათვალისწინებელია რადიონუკლიდების გავრცელების კონკრეტული ლანდშაფტის თავისებურებანი. ნიადაგში მოხვედრილი რადიონუკლიდების შემდგომი მიგრაცია და მათი ბიოლოგიურ ციკლში ჩართვა ორგვარ ხასიათს ატარებს: ერთი მხრივ, ნიადაგით სორბცია, როგორც წესი, ამცირებს მცენარეში რადიონუკლიდების შეღწევის დონეს და, მეორე მხრივ, სორბირებული რადიონუკლიდების აკუმულაცია ნიადაგის ზედა ჰორიზონტებში ზრდის მცენარისათვის მათ მისაწვდომობას, რაც იწვევს ფიტოცენოზებში რადიონუკლიდების დიდი რაოდენობით დაგროვებას. რადიონუკლიდების ნიადაგის სიღრმეში მიგრაციის დროს მნიშვნელოვნად შესუსტებულია სორბციის პროცესები და უფრო აქტიურად მიმდინარეობს მათი გავრცელება. ამგვარად, სიღრმისეული დიაგნოსტიკა მიგრაციის ინტენსივობისა და სამარხის მიმდებარე ვერტიკალურ ზონაში რადიონუკლიდებით დაბინძურების გავრცელების დინამიკის კვლევის შესაძლებლობას ქმნის. ჩვენ მიერ მოწოდებული მეთოდის მიხედვით, მცენარე-ინდიკატორების სწორად შერჩევა, საორიენტაციო მონაცემების მიღების საშუალებას იძლევა, როგორც საკვლევი ზონის იზოტოპური შემადგენლობის, ისე მათი სიღრმისეული განლაგების შესახებ და სხვა სახის კვლევებთან ერთად ქმნის სრულ სურათს რადიოაქტიური ნივთიერებების სამარხის მდგომარეობის შესახებ [8].

დამოწმებანი

1. G. Steinhauser, A. Brandl, T. E. Johnson. Comparison of the Chernobyl and Fukushima nuclear accidents: A review of the environmental impacts. Sci. Total Environ., 2014, 470–471, 1800-817.
2. Y. Onishi. Fukushima and Chernobyl nuclear accidents'environmental assessments and U.S. Hanford Site's waste management. Procedia IUTAM, 2014, 10, 372-381.
3. O. Masson, J. Bieringer, E. Brattich, A. Dalheimer, S. Estier, I. Penev, W. Ringer, C. Schlosser, T. Steinkopff, P. Steinmann, L. Tositti, P. Van Beek, A. de Vismes–Ott. Variation in airborne ^{134}Cs, ^{137}Cs, particulate ^{131}I and ^{7}Be maximum activities at high-altitude European locations after the arrival of Fukushima-labeled air masses. J. Environ. Radioact., 2016, 162-163, 14-22.
4. C. Bernhardsson, C. L. Rääf, S. Mattsson. Spatial variability of the dose rate from ^{137}Cs fallout in settlements in Russia and Belarus more than two decades after the Chernobyl accident. J. Environ. Radioact., 2015, 149, 144-149.
5. I. Yordanova, D. Staneva, L. Misheva, T. Bineva, M. Banov. Technogenic radionuclides in undisturbed Bulgarian soil. J. Geochem. Exploration, 2014, 142, 69-74.
6. J.-M. Bonzom, S. Hättenschwiler, C. Lecomte–Pradines, E. Chauvet, S. Gaschak, K. Beaugelin–Seiller, C. Dellavedova, N. Dubourg, A. Maksimenko, J. Garnier–Laplace, C. Adam–Guillermin Effects of radionuclide contamination on leaf litter decomposition in the Chernobyl exclusion zone. Sci. Total Environ., 2016, 562, 15, 596-603.

7.   Л. М. Мосулишвили, Н. И. Шония, Н. М. Катамадзе, Э. И. Гинтури. Радионуклиды чернобыльской этиологии на территории Грузии. Кинетика их аккумуляции и миграции. Радиац. иссл., 1990, 7, 252-261.

8.   S. A. Geras'kin, J. K. Kim, A. A. Oudalova, D. V. Vasiliyev, N, S. Dikareva, V. L. Zimin, V. G. Dikarev. Bio-monitoring the genotoxicity of populations of Scots pine in the vicinity of a radioactive waste storage facility. Mutation Res. / Genetic Toxicol. Environ. Mutagenesis, 2005, 583, 1, 55-66.

HEXAGONAL BORON NITRIDE AS A SOLID
LUBRICANT ADDITIVE (AN OVERVIEW)

**L. Chkhartishvili, G. Tabatadze, D. Nackebia,
T. Bzhalava, I. Kalandadze**

Department of Engineering Physics
Georgian Technical University
Tbilisi, Georgia
chkharti2003@yahoo.com

Abstract

An overview is given on utilizing of hexagonal boron nitride nanopowders as a solid additive to liquidlubricant materials.

Lubricants are extensively used by industry to control friction and wear in a large variety of mechanical and tribological applications, because without lubricants most moving parts of machines and engines fail or wear out and become useless. Most lubricants come in a liquid- or grease-consistency. But, liquid lubricants alone cannot meet the increasingly more stringent application conditions under very high and low temperatures, ultra-high vacuum, radiation, extreme contact pressure, very low and high sliding speeds, etc. It is a reason, why the idea of combined uses of solid and liquid lubricants is becoming more popular.

Solid additives in current liquid lubricants containing heavy metals, carbon (graphite), sulfur and phosphorus bearing substances, etc. are environmentally harmful and cause pollutions. They can be displaced by light boron-based nano-scale powders in oils and greases providing much better tribological performance.

The most part of boron compounds are the superhard materials. But, some of them stand out as very effective solid lubricants. In particular, boron compounds with layered structures possess high potential to provide various surfaces with low friction and wear under both dry and lubricated sliding conditions [1]. Among them powdered hexagonal boron nitride, h-BN, has a capacity to significantly reduce friction and wear when mixed at low concentrations (as little as ~ 1 wt. %) with liquid lubricants – oils, greasers, and fuels. Previously tribological interest in h-BN was limited to lubrication for metalworking processes where lubrication at high temperatures and / or cleanliness of working environments is of critical concern. However, later it was reevaluated as a "clean" lubricant, which can be an alternative to above mentioned "dirty" ones (e.g., carbon C in graphite-structure or molybdenum disulfide MoS_2) in more general applications as a solid lubricant.

Hexagonal BN has a lamellar crystalline structure, in which the bonding between molecules within each layer is strong covalent, while the binding between layers is almost entirely by means of weak van der Waals forces. This structure is similar to that of graphite and MoS_2, which are highly successful solid lubricants too, and the mechanism behind their

effective lubricating performance is understood to be owing to easy shearing along the basal plane of the hexagonal crystalline structures. BN captured attention as a potential solid lubricant for general use because of this similarity. However, a number of results showed that, as a solid lubricant, BN was inferior to graphite and MoS_2.

From the fundamental investigations of h-BN lubricant properties performed in [2], h-BN in general was found less effective than other solid lubricantsexcept for high-temperature applications. However, a series of sliding experiments showed somewhat curiousbehavior of BN when added into lubricating oil, e.g., in the case of sliding of bearing steel versus itself. BN slightly increased the coefficient of friction, but drastically decreased wear. In sliding of steel bearing, boron is present in small cavities on wear scars (**Figure 1**). Not all boron is present there as h-BN, but in other forms too. Although boron nitride is known to have high thermal stability, the observation of the wear scars had shown coexistence of boron and oxygen at the same locations, evidence which suggests oxidation during sliding. BN introduced to the actually rubbing parts strongly adhered to steel surfaces, and works to decrease wear.
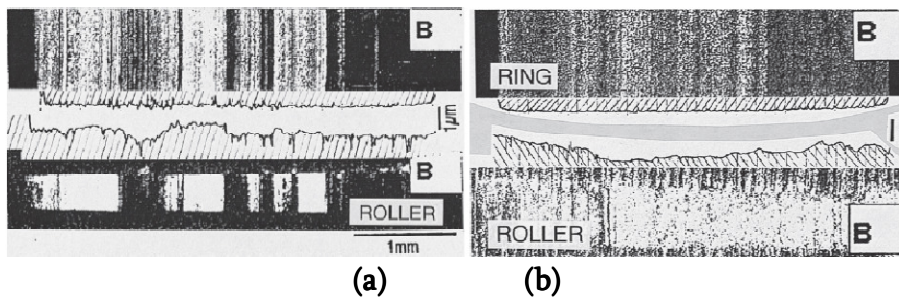

(a)   (b)

Figure 1. Distribution of B on wear scars (a) steel ring / steel roller and (b) steel ring / cast iron roller [2].
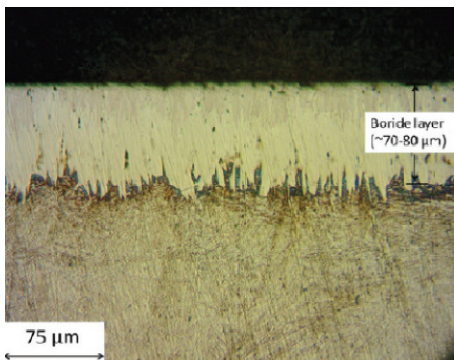

Figure 2. Cross section micrograph of surface-treated (electrochemically borided) steel sample [3].
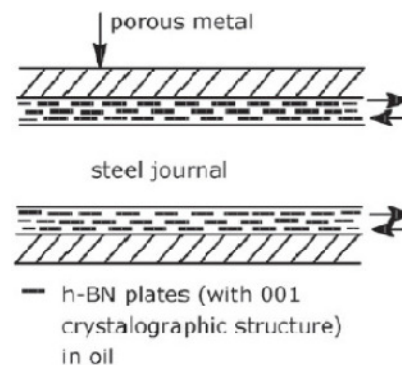

Figure 3. Schematic representation of the lamellar lubrication in journal bearing [5].

Different approach to modification of sliding surface by h-BN lubricant has been suggested for gears. Gears and other mechanical assemblies are some of the key components for conversion of wind energy to electrical energy in wind turbines, but their durability and efficiency are severely impaired by some tribological issues like micropitting, wear, scuffing, and spalling. To address these issues, in [3] a combinational approach was proposed to incorporate surface treatment in coordination with the use of nanocolloidal lubricant additives. In particular, boron nitride based solid lubricants were manufactured and flat gear steel samples were borided using an electrochemical boriding process. The borided surfaces (**Figure 2**) enhanced the mechanical properties of the surface layer, leading to improved wear resistance.

As for the boron nitride itself, it was observed to be stayed well dispersed within the oil and formed a stable tribofilm, which was important to achieve improved tribological performance.

It looks that h-BN particles interact with sliding surfaces and form low-friction boundary films protecting these surfaces against wear and providing low friction due to their low shear. Correspondingly, there was found a preferential orientation of h-BN nanocrystalline sheets of hexagonal boron nitride (formed from the tribochemical reaction between a borated additive and a nitrogenous compound using mineral oil containing a little amount of synthetic base as the base-oil) parallel to the sliding direction [4]. It was evidenced the formation of a lamellar solid from the tribochemical reaction of a borated additive and a succinimide additive. The result is the formation of h-BN in the tribofilm. The tribofilm was mainly composed of an amorphous borate matrix containing highly-dispersed h-BN nanoparticles in the form of sheets 10 nm wide and 5 nm thick. Thus, when present at sliding interface the atomic layers of hexagonal BN, the self-lubricated solid, align themselves parallel to the direction of sliding motion and then shear with relative ease to provide the levels of low friction.

Such orientation of nanosheets (**Figure 3**) has a favorable effect on friction – this statement was proved by the combination phospholipid molecules with h-BN. Phospholipid in vivo and hexagonal boron nitride in vitro are good examples of frictionless lubricants. Phospholipid molecules and BN have the ability to form multibilayer or layered structures similar to lamellate solid. It has been confirmed experimentally that phospholipid molecules as lamellar lubricants protect the surface of joints against wear while acting as frictionless lubricant. The experiment strongly suggested [5] that h-BN has the ability to lubricate under load with very low friction coefficient comparable to phospholipids. Relatively low surface energy and low adhesion between the crystallites are giving the additives low friction coefficient. The results of the experimental studies showed that h-BN as an additive in vaseline possesses friction reducing properties, and excellent antiwear properties.

It should be noted that hexagonal BN is a versatile ceramic material with unique properties and a wide application area in industry. Because of complex of important properties – resistance to oxidation up to high temperatures, lubricity, high corrosion resistance, high thermal conductivity and high electrical resistivity – it is used mostly as a high temperature lubricant material. However, powdered h-BN when added into plastics not only reduces friction coefficient, but also increases their thermal conductivity, decreases thermal expansion and increases use temperatures. There are number of suggestions on practical utilizing BN-based lubricants useful for metallic, ceramic, polymer, etc. interfaces.

Although, aluminum is one of the most prominent metals in the fabrication of metal matrix composites, frequently the oxidation of aluminum prevents the precisely measuring the wetting of ceramics. In [6], an improved sessile drop method was devised to prevent the oxidation of the aluminum. Using this method, the contact angle between h-BN and molten Al was measured in a purified He + H_2 atmosphere and in a very high vacuum at high-temperature. It was confirmed that AlN was produced at the solid / liquid interface and caused the contact angle to decrease to 0°. AlN had good structural properties, whereas h-BN did not. Accordingly, it was suggested that h-BN particles, which have good wetting, be inserted into the Al-melt. This causes the surface of the h-BN to be converted into AlN which has good structural properties. Using this process, a metal matrix composite, which has good structural properties, should be produced. In particular, since h-BN is lubricous, a material should be produced which has high wear resistance.

Results of friction force in small-size bearings lubricated with the amount of oil contained boron nitride additives were presented in [7]. The investigated bearings were porous journal bearing and thrust bearing of the type sphere-on-plane operating with low velocity under spinning friction regime. The comparison of the results obtained for oil with boron nitride additives with one without such additives, magnetically active lubricant and oil with other than BN additives showed a significant reduction of the friction coefficient and contact temperature.

The antiwear capacity of a borate containing nitrogen was evaluated in [8]. Rubbing surface analyses revealed that there were borate and boron nitride under high load in comparison to only borate found under low load. Therefore, it can be considered that, under mild conditions, the borate ester is absorbed physically and chemically on the rubbing surface providing antiwear function at low load, and under severe conditions some of absorbed borate films degrade and form boron nitride tribochemically developing antiwear performance at high load.

In [9], the modified borate powder also was synthesized as an oil additive. The results of studying its tribological properties showed that it had good extreme pressure, antiwear and friction reduction properties. The viscosity of base-oil and the water content in the modified borate had great effect on the wear resistance with extreme pressure. It can form a tribological mixed reaction-film on friction surface. Boron mainly existed in the form of BN on friction surface, while nitrogen content was higher than sodium content.

Thus, borate esters possess friction-reducing, antiwear, and antioxidant characteristics when blended in lubricating oils. However, they are susceptible to hydrolysis. The formation of a stable five-member ring structure in the ester molecules, involving coordination of nitrogen with boron, contributes substantially to the resistance to hydrolysis of borate esters. The susceptibility of borates to hydrolysis can be reduced by introducing N,N-dialkylaminoethyl groups with alkyl radicals containing more than three carbon atoms [10]. It was revealed that the borate ester can be adsorbed on the rubbing surface, and some of the adsorbed borate film degrades and forms boron nitride. Wear tests indicated that the combination of oil-soluble metals (copper, tin, and cadmium) compounds with organoborates gives better antiwear properties than the components separately. An antiwear synergistic mechanism can be postulated, in which borates with electron-deficient boron p-orbitals catalyze the triboreduction of the metal compounds on the rubbing surfaces, producing elemental metals.

AISI–1045 steel was duplex surface modified by deposition of a Si–B–N composite film and a MoS_2-based film [11]. It was found that composite film was composed of h-BN and c-BN, which had much larger hardness than the steel substrate and were able to form interfacial transition layer with the steel substrate and, hence, the tribological behavior of the steel was greatly improved. Moreover, the friction and wear behavior of the Si–B–N film was further significantly improved by the introduction of the Mo.

The tribological performance of grease lubricant plus h-BN micro-particles additive was studied on steel / steel tribopair under vibrating fretting and sliding fretting conditions [12]. The grease compounded with boron nitride was found to be the best for industrial applications.

In [13], it was performed a comparative study on the tribological behavior of hexagonal boron nitride as lubricating microparticles – an additive in porous sliding bearings for a car clutch. The main effect of h-BN microparticles lamellar lubricant plus oil in comparison to a standard Mobil-lubricant appears to be that the impregnation of h-BN microparticles in Cu – Fe

porous bearings persists for a long period of time and the microparticles are gradually released, being supplied to the contact surfaces. In the bench test, porous bearings have demonstrated that such impregnation will satisfy up to ~ 10^5 h of clutch operation in a real engine.

Ni-based alloy / nano-hexagonal boron nitride (nano-h-BN) self-lubricating composite coatings were successfully produced on medium carbon steel substrate by means of Nd:YAG laser cladding [14]. A novel high energy ball milling method was adopted to clad nano-Ni onto nano-h-BN with an aim to enhance the compatibility between the h-BN and the metal matrix during laser cladding process. It was found that nano-h-BN was hardly to be composed into Ni 45 matrix coating even if increasing the weight percentage of h-BN from 5 to 10 wt. % with a conventional mechanical mixing. The high energy ball milling of nano-Ni onto nano-h-BN significantly improved the interfacial compatibility between h-BN and Ni 60 matrix. The friction coefficient of the laser clad Ni 60 / nano-Ni-clad h-BN coating was reduced obviously.

The results of the recent experimental studies have demonstrated [15] the high potential of h-BN as an additive forpreventing fretting sliding, and can be very useful for application in grease-based compound lubrication of a steel surface in industrial equipment.

Cubic, amorphous and hexagonal boron nitride films were deposited onto a silicon substrate and a reciprocating tribometer was used to examine friction and wear properties for these three BN films [16]. The c-BN film showed the highest wear and peeling resistance of the tested films. The lubricating performance of the c-BN film proved significant following a long lubricating life and low friction. In contrast, the a-BN and h-BN films showed short lubricating endurance lives and large friction changes inspite of the fact that they are good, in general, as solid lubricants. These unexpected results were speculated to reflect the premature debonding of the h-BN and a-BN films during sliding and the subsequent discharge of their flakes out of the nip between the substrate and the ball indenter, owing to their lower adhesion to the substrate.

The high-temperature friction and wear characteristics of ceramic matrix composites incorporated with various solid lubricants including hexagonal BN have been investigated from room temperature up to ~ 1000 °C [17]. On the basis of general design considerations relevant to solid lubrication proposed for friction and wear data of self-lubricating composites, such optimized composites appear to be promising candidates for long-duration, extreme environment applications with low friction and small wear rate.

The results of investigation of the tribological behavior of Si_3N_4–h-BN composites with different hexagonal boron nitride volume fractions under distilled water lubrication showed [18] that the addition of h-BN into Si_3N_4 matrix significantly decreased the friction coefficient for Si_3N_4 against Si_3N_4 pair under titrimetric water lubrication. The morphological analysis and chemical characterization of the worn surfaces via scanning reveal that under titrimetric water lubrication, the h-BN in Si_3N_4–h-BN spalled off during the wearing tests and the spalled pits formed on the wearing surface of Si_3N_4–h-BN, and then the debris dropped into the pits to react with water, thus a tribochemical film formed on the wearing surface. It facilitated smoothing the surfaces of Si_3N_4–h-BN and Si_3N_4 to create a fine lubrication environment.

The ring compression tests of the interfacial friction and flow behavior of an Al_2O_3-based ceramic composite have indicated [19] that boron nitride lubricant can be used effectively at elevated temperature range of 1400 – 1600 °C.

It is known that the processability of polymers by extrusion is related to the interface between the polymer melt and the die wall, because the wall surface energy affects the flow of

polymer melts in extrusion die. On the other hand, BN powders act as a solid lubricant lower the surface energy. It is the reason why the effects of BN powders on the rheological properties and the extrusion processability of metallocene-catalyzed low-density polyethylene were investigated [20]. Small crystal size and uniform size distribution were found to be more effective. Also, the influence of a hot-pressed BN die on the instability of capillary flow was found to be quite effective in delaying surface and sharkskin defects and postponing gross melt fracture. A synergistic effect of processability improvement could be obtained when both BN powder and die are used together.

During the die flow of metallocene polyethylenes, flow instabilities may occur. Namely, wall slip, "sharkskin", and stick-slip (pressure oscillations) and gross fracture may be obtained depending on the volume flow rate and die geometry. Fluoroelastomers and boron nitride powders with hexagonal crystal structure can be used as suitable processing aids in melt extrusion processes. Fluoroelastomers at low concentrations act as die lubricants and may eliminate flow instabilities such as surface and stick-slip melt fracture. On the other hand, specific BN powders may not only eliminate surface and stick-slip melt fracture, but also postpone gross melt fracture to higher volume flow rates. In [21], it was shown a way for quantitative differentiation of the influence of polymer processing additives on rheological behavior.

Boron nitride as a solid lubricant wastested [22] as an additive to the lubricants used in the polytetrafluoroethylene paste extrusion in order to identify enhancedprocessing aids. It was found that the addition of boron nitride not only increases the extrusionpressure but at the same time improves the final mechanical properties of the final extrudates. This offers possibilities for controlling these properties by controlling the degree of fibrillation, i.e., by adding a small amount of solid BN lubricant to adjust pressure,fibrillation, and thus the final mechanical properties.

Calcined petroleum coke and hexagonal boron nitride were used as the friction modifiers to improve the friction and wear properties of phenolic resin-based friction composites too [23]. It was found that the hybrid of the two friction modifiers was effective to significantly decrease the wear rate and stabilize the friction coefficient of the friction composites at various temperatures by forming a uniform lubricating and / or transferred film on the rubbing surfaces. The uniform and durable transfer films were also able to effectively diminish the direct contact between the friction composite and the cast iron counterpart and hence prevent severe wear of the latter as well. The effectiveness of the hybrid of calcined petroleum coke and h-BN in improving the friction and wear behavior of the phenolic resin-based friction modifiers could be attributed to the complementary action of the "low temperature" lubricity of calcined petroleum coke and the "high temperature" lubricity of h-BN. The optimum ratio of these two friction modifiers in the friction composites was suggested to be 1:1, and the corresponding friction composite showed the best friction-reducing and antiwear abilities.

Some of our recent works [24 – 29] are devoted to obtaining by a chemical method of nanopowdered h-BN (with disc-shaped particles; mean diameter and mean thickness, respectively, 240 and 25 nm) and utilizing.

Summarizing above brief overview on powdered h-BN lubricity, one should emphasize that in general the larger grain size and higher crystallinity lead to better lubricating properties and high temperature-stability of h-BN. However, there is a problem of sedimentation: micro-scale powders added into lubricating oil and other liquid materials may settle out unless very

effective surfactants or dispersing agents are added too. In case of nano-scale particles, mainly because of their very large surface-to-volume ratio, as well as light weight (due to BN low specific gravity), these powders may stay in dispersion for a long time without the use of additional surfactants. Fortunately, boron nitride can be produced in nano-powders and, therefore, is easy to incorporate within liquid lubricants.

References

1. A.Erdemir. Advances in boron-based lubricants and lubricant additives. In: Proc. 4th Int. Boron Symp. (Eds. A. Konuk, H. Kurama, H. Ak, M. İphar). 2009, Eskişehir, Osmangazi Univ. Press, 3-9.
2. Y.Kimura, T.Wakabayashi, K.Okada, T.Wada, H.Nishikawa. Boron nitride as a lubricant additive. Wear, 1999, 232, 2, 199-206.
3. A.Greco, K.Mistry, V.Sista, O.Eryilmaz, A.Erdemir. Friction and wear behavior of boron based surface treatment and nanoparticles lubricant additives for wind turbine gearbox applications. Wear, 2011, 271, 9-10, 1754-1760.
4. R.Ladavière, J.M.Martin, T.leMogne, B.Vacher, B.Constans, S.Iovine. Tribochemistry: Friction-induced lamellar solids from lubricant additives. Trib. Ser., 2003, 41, 15-22.
5. Z.Pawlak, R.Pai, E.Bayraktar, T.Kaldonski, A.Oloyede. Lamellar lubrication in vivo and vitro: Friction testing of hexagonal boron nitride. Bio Syst., 2008, 94, 3, 202-208.
6. H.Fujii, H.Nakae, K.Okada. Application of wetting to fabrication of boron nitride / aluminum composites. In: Proc. Int. Conf. Adv. Composite Mater., 1993, 1001-1007.
7. J.Burcan, K.Krzeminski. Effect of lubricant additives on operation of machine friction pairs. Sci. Bull. Lodz Tech. Univ. Mech. Eng., 1996, 85, 31-36.
8. J.Yao. Antiwear function and mechanism of borate containing nitrogen. Trib. Int., 1997, 30, 6, 387-389.
9. Y.Qiao, B.Xu, Sh.Ma, Sh.Liu, W.Liu, Q.Xue. Investigation on tribological properties of modified borate as oil additive. Trib. (Mocaxue Xuebao), 1998, 18, 1, 25-31.
10. J.B.Yao, Q. L.Wang, S.Q.Chen, J.Z.Sun, J.X. Dong. Borate esters used as lubricant additives. Lubr. Sci., 2002, 14, 4, 415-423.
11. X.Yu, C.-B.Wang, G.-W.Jiang. Structure and tribological behavior of Si–B–N composite film. Trib. (Mocaxue Xuebao), 2004, 24, 2, 119-122.
12. Z.Pawlak, T.Kaldonski, M.Lisewski, A.Oloyede. Fretting of a steel surface in the presence of grease compounded with boron nitride (h-BN). In: Proc. World Trib. Cong., 2009, 814-814.
13. Z.Pawlak, T.Kaldonski, R.Pai, E.Bayraktar, A.Oloyede. A comparative study on the tribological behavior of hexagonal boron nitride (hBN) as lubricating microparticles – An additive in porous sliding bearings for a car clutch. Wear, 2009, 267, 5-8, 1198-1202.
14. H.Yan, A.H.Wang, X.L.Zhang, Z.W.Huang, W.Y.Wang, J.P. Xie. Nd:YAG laser cladding Ni base alloy / nano-h-BN self-lubricating composite coatings. Mater. Sci. Technol., 2010, 26, 4, 461-468.
15. Z.Pawlak, T.Kałdoński, M.Lisewski, W.Urbaniak, A.Oloyede. The effect of hexagonal boron nitride additive on the effectiveness of grease-based lubrication of a steel surface. Ind. Lubr. Trib., 2012, 64, 2, 84-89.

16. S.Watanabe, S.Miyake, M.Murakawa. Tribological properties of cubic, amorphous and hexagonal boron nitride films. Surf. Coat. Technol., 1991, 49, 1-3, 406-410.

17. J.-H.Ouyang, T.Murakami, S.Sasaki, Y.-F.Li, Y.-M.Wang, K.Umeda, Y.Zhou. High temperature tribology and solid lubrication of advanced ceramics. Key Eng. Mater., 2008, 368-372, 2, 1088-1091.

18. W.Chen, Y.Gao, F.Ju, Y.Wang. Tribochemical behavior of Si_3N_4–h-BN ceramic materials with water lubrication. J. Xi'an Jiaotong Univ., 2009, 43, 9, 75-80.

19. H.G.Wang, F.Wang, Y.P.Song, K.F.Zhang. Friction and flow behavior of ceramics in ring compression test. Adv. Mater. Res., 2011, 154-155, 1752-1756.

20. S.M.Lee, G.Nam, J.W.Lee. The effect of boron nitride particles and hot-pressed boron nitride die on the capillary melt flow processing of polyethylene. Adv. Polymer Technol., 2003, 22, 4, 343-354.

21. R.Vogel, S.G.Hatzikiriakos. Rheological evaluation of metallocene polyethylenes with processing aids by multi-wave oscillations. Polymer Eng. Sci., 2004, 44, 11, 2047-2051.

22. I.Ochoa, S.G. Hatzikiriakos, E.Mitsoulis. Paste extrusion of polytetrafluoroethylene: Temperature, blending and processing aid effects. Int. Polymer Proc., 2006, 21, 5, 497-503.

23. G.Yi, F.Yan. Effect of hexagonal boron nitride and calcined petroleum coke on friction and wear behavior of phenolic resin-based friction composites. Mater. Sci. Eng. A, 2006, 425, 1-2, 330-338.

24. L. Chkhartishvili, T. Matcharashvili, R. Esiava, O. Tsagareishvili, D. Gabunia, B. Margiev, A. Gachechiladze. Powdered hexagonal boron nitride reducing nano-scale wear. In: Physics, Chemistry and Application of Nanostructures (Eds. V.E.Borisenko, S. V. Gaponenko, V. S. Gurin, C. H. Kam), 2013, Singapore, World Scientific, 438-440.

25. L. Chkhartishvili, M. Darchiashvili, A. Gachechiladze, B. Margiev, L. Rukhadze, O. Tsagareishvili. Effect of nanocrystalline boron nitride on wear processes in brass. In: Proc. ICANM 2013: Int. Conf. Exh. Adv. Nano Mater., 2013, Quebec-City, IAEMM, 245-252.

26. L. Chkhartishvili, M. Darchiashvili, A. Gachechiladze, B. Margiev, L. Rukhadze, O. Tsagareishvili. Influence of hexagonal boron nitride nanocrystals on wear processes in brass. Nano Studies, 2013, 7, 169-176.

27. O. Tsagareishvili, A. Gachechiladze, M. Darchiashvili, B. Margiev, L. Rukhadze, L. Chkhartishvili.Friction processes in metallic composite materials modified with hexagonal boron nitride. In: Abs. 18th Int. Symp. Boron, Borides & Rel. Mater., 2014, Honolulu, UH, 135-135.

28. O. Tsagareishvili, A. Gachechiladze, M. Darchiashvili, B. Margiev, L. Rukhadze, L. Chkhartishvili. Wear processes in metallic composites modified with boron nitride. In: Abs. 3rd Int. Conf. "Nanotechnologies" (Eds. A. Gerasomov, L. Chkhartishvili, G. Chikhladze), 2014, Tbilisi, Publ. House Tech. Univ., 111-112.

29. A. Gachechiladze, O. Tsagareishvili, M. Darchiashvili, B. Margiev, L. Rukhadze, L. Chkhartishvili. Antifrictional metallic materials modified with hexagonal boron nitride. In: Proc. 2nd Int. Conf. "Modern Technologies and Methods of Inorganic Materials Science" (Eds. J. Khantadze, L. Chkhartishvili, D. Ramazashvili,L. Tavadze), 2015, Tbilisi, Sachino, 121-131.

CARBON COATED (Fe–Fe₃C) AND Ag-DOPED LANTHANUM MANGANITE (Ag$_x$La$_{1-x}$MnO₃) NANOCOMPOSITES FOR MAGNETIC HYPERTERMIA OF CANCER CELLS

T. Berberashvili [1], Z. Buachidze [1], A. Chirakadze [1], L. Chakhvashvili [1],
D. Jishiashvili [1], G. Kacharava [1], P. Kervalishvili [1], I. Khomeriki, S. Aleqsanyan [2],
H. Gyulasaryan [2], A. Manukyan [2], A. Papoyan [2], E. Sharoyan [2], L. Sajti [3]

[1] Department of Engineering Physics
Georgian Technical University
Tbilisi, Georgia
t.berber@mail.com
[2] Laboratory of Solid State Physics
Institute for Physical Research
National Academy of Scinces of Armenia
Ashtarak – 2, Armenia
[3] Department of Nanotechnology
Laser Zentrum Hannover e.V.
Hannover, Germany

Abstract

The presented research deals with two promising materials for cancer hyperthermia: ferromagnetic (Fe–Fe₃C)&C nanocomposites and carbon black–Ag$_x$La$_{1-x}$MnO₃ hybrid nanocomposites. Carbon-coated (Fe–Fe₃C)&C nanocomposites were synthesized using the solid-phase pyrolysis (SPP) of metal-organic compounds in a wide range of experimental conditions (temperature, time and pressure in the reaction ampoule) resulting in various concentrations of Fe–Fe₃C core–shell. The ultrasound processing and size separation of nanoparticles have been made after synthesis of nanocomposites. The structure, morphology and magnetic characteristics of these nanocomposites were investigated by electron microscopy, X-ray diffraction, Raman spectroscopy and magneto-metric experiments. Ag-doped LaMnO₃ nanoparticles and modified carbon black were used to produce a hybrid nanocomposite. AgLaMnO₃ nanoparticles were synthesized using both the microwave enhances paper method and microwave combustion method. The morphology and magnetic characteristics of the modified carbon black–LaMnO₃ hybrid nanocomposites was characterized by electron microscopy, X-ray diffraction and magneto-metric experiments. Ag$_x$La$_{1-x}$MnO₃ nanoparticles (after sintering at 300 °C) were uniformly dispersed in the carbon matrix, which had a hollow quasi-spherical structure. All synthesized and studied materials proved to be very promising materials, while carbon black AgLaMnO₃ hybrid nanocomposites represented unique properties as materials for cancer hyperthermia with "self-controlled" working temperature in the range about 41 – 43 °C.

1. Introduction

Different unique properties of magnetic nanomaterials cause continuously increasing interest to synthesis and investigation of a wide variety of conducting and semiconducting composites aimed to their commercial use in high-capacity dry batteries [1], highly sensitive devices and sensing systems [2], spintronic devices [3], data storage [4], magnetic separation [5], bio-engineering [6], therapeutic drug delivery [7], hyperthermia for cancer therapy [8], contrast enhancement agents for magnetic resonance imaging applications [9, 10], water purification [11], and catalysis [12]. Microwave absorbing materials (MAMs) have been in the focus of scientific interest for more than 60 years, especially in microwave technology and radar detection [13], high-capacity and ultra-fast electro-optic communication and sensing systems [14], etc. Nanoparticles of magnetic metals are characterized with high Snoek limit and relatively low Foucault currents current losses [15]. At the same time, metal based nanoparticles are easily agglomerated and oxidized and both these factors strongly limit their practical application. Oxide coating of magnetic metal nanoparticles by forming a SiO_2 shell is widely used to stabilize the metal nano-core and prevent it from agglomeration and oxidizing [16].

However, it increases the weight of nanocomposites and prevents the proper wideband matching of magnetic core with the applied microwave field, especially in the high-frequency range. To solve the problem of producing of magnetic nanomaterials having low-density, small thickness, strong stability and proper matching in the wideband frequency range graphene [15] and carbon [16] coated metal cores have been extensively synthesized and investigated during last ten years. Magnetic nanoparticles in an alternating magnetic field show remarkable heating effects due to hysteresis losses during the magnetization reversal process. Magnetic nanoparticle-based (MNP) hyperthermia uses a similar principle, because magnetic nanoparticles are introduced into the tumor tissue producing local heat when subjected to an alternating magnetic field (AMF).

In a number of recent appropriate scientific papers different types of MNPs with various shape anisotropy, morphology and magnetic properties have been examined and proposed for magnetic hyperthermia applications. Their performance depends on a wide range of parameters, such as concentration, average size and size distribution (dispersion), type of magnetic hysteresis, saturation magnetization, as well as on amplitude and frequency of the applied AMF [17 – 32]. The magnetic moment of iron oxide nanoparticles may be increased due to doping of magnetite with metal ions, such as manganese, cobalt and nickel. In addition, $r2$ relaxivity increases proportionally to the diameter of the magnetic core. These factors have recently been used to create magnetic nanoparticles with significantly higher relaxivity for applications of MR diagnostics. It is generally accepted that the temperature of exposure to the agent should be within 42 – 44 °C (in some papers, 41 – 43 °C), as lower temperatures do not provide the desired therapeutic effect, whereas higher temperature causes irreparable damage to healthy tissues.

Obviously, maintaining of temperature in this range is a nontrivial task and requires precise control of the field parameters, accurate measurement of the temperature of exposure and tissue at the point of impact, as well as other parameters of the whole process (mass transfer, heat supply, etc.). That is why the search and exploration of new magnetic materials, methods of control of the applied AMF and temperature of heating agents and exposed areas, as well as

precise setting of the basic parameters of the process and their visualization, becomes so important.

Thus, magnetic nanoparticles with temperature of ferromagnetic–paramagnetic phase transition (Curie temperature T_C) in the range of about 42 – 44 °C are of particular interest, because they can be used as media for self-regulated ("negative feedback") magnetic hyperthermia. Such particles can provide a local self-regulated heating of cancer cells by AMF, without damaging the healthy (not diseased) tissues, since at temperature above T_C magnetic nanoparticles become paramagnetic and are not heated by the external electromagnetic field. At temperature below T_C as a result of paramagnetic-ferromagnetic transition nanoparticles are again heated by AMF and thereby, the affecting temperature is kept in the relatively narrow range, contributing to the aimed therapeutic effect and avoiding any significant damaging of the healthy tissues. Obviously, for in-vivo biomedical applications, these nanoparticles should be non-toxic (or as low-toxic as possible) materials and / or they must be sufficiently coated with any inert substances harmless to healthy cells. All this should ensure biocompatibility and prevent side-effects involving the surrounding tissues. As mentioned, the ability to change of T_C in more or less broad limits is important for improvement of the efficiency of magnetic hyperthermia due to more precise control and variability of temperature. Thus, new materials with controlled and variable T_C should be investigated and new, more simple and low-cost methods of their synthesis should be examined.

2. Experimental part

2.1. Synthesis of carbon-coated ferromagnetic (Fe–Fe₃C)&C nanocomposites using solid-phase pyrolysis.

Carbon-coated ferromagnetic (Fe–Fe₃C) nanocomposites have been synthesized using solid-phase pyrolysis (SPP) of metal-organic compounds [19, 31, 32]. Depending on the pyrolysis conditions (temperature, time and pressure in a reaction ampoule) it is possible to regulate concentration of Fe–Fe₃C core-shell. The ultrasound processing and size separation of nanoparticles have been made after synthesis of nanocomposites.The structure, morphology and magnetic characteristics of these nanocomposites were investigated by electron microscopy, X-ray diffraction, Raman spectroscopy and magneto-metric experiments.

2.2. Microwave enhanced synthesis of carbon black–Ag$_x$La$_{1-x}$MnO₃ hybrid nanocomposite

Ag-doped LaMnO3 and modified carbon black were used to produce a hybrid nanocomposite. Physical mixing of modified carbon and Ag doped lanthanum manganite nanoparticles, followed by sintering at different temperatures. The method was analogue to the one utilized in [33]. Ag$_{0.05}$La$_{0.95}$MnO₃, Ag$_{0.1}$La$_{0.9}$MnO₃, Ag$_{0.15}$La$_{0.85}$MnO₃, Ag$_{0.2}$La$_{0.8}$MnO₃, and Ag$_{0.25}$La$_{0.75}$MnO₃ nanoparticles were first synthesized via paper synthesis [34]. The carbon component, yielded from microwave processing of scrap tires using circulating catalyst method [35] was modified using graphitization and, HNO₃ and ammonia treatments [33]. All heating, annealing, and combustion and sintering procedures were carried in the microwave oven in the range of 0.1 – 1 kW of continuous operation. The morphology and magnetic characteristics of

the modified carbon black–LaMnO$_3$ hybrid nanocomposites was characterized by electron microscopy, X-ray diffraction and magneto-metric experiments. Ag$_x$La$_{1-x}$MnO$_3$ nanoparticles (after sintering at 300 °C) were uniformly dispersed in the carbon matrix, which had a hollow quasi-spherical structure.

2.3. Synthesis of nanocomposites on the base of Ag-doped lanthanum manganite nanoparticles using microwave combustion method

Preliminary study of black carbon–Ag-doped lanthanum manganite hybrid nanocomposites with Ag$_x$La$_{1-x}$MnO$_3$ nanoparticles synthesized using microwave combustion method [36] was started. All precursors (lanthanum, manganese and silver nitrates, and glycine as a fuel) were AR grade. Precursor salts were mixed together in stoichiometric amounts i.e. 1 : 1 equimolar ratio followed by addition of glycine as fuel and double distilled water. The stoichiometric composition of the mixture was calculated based on oxidizing valence of metal nitrates and reducing valence of glycine [37]. Materials were synthesized by partial substitution of La (Ag$_x$La$_{1-x}$MnO$_3$) or Mn (LaMn$_{1-x}$Ag$_x$O$_3$) atoms. The resulting mixtures were stirred for few minutes and evaporated in a microwave oven at the relatively low power (about $0.1 - 0.2$ kW) to obtain a gel. The gels were heated in a microwave reactor at a relatively high power ($0.4 - 0.8$ kW). After auto-combustion the samples were cooled at room temperature. During the synthesis fuel to oxidizer ratio (r), irradiation time (t) and irradiation power (p) were varied to optimize synthesis conditions and obtain pure phase products: $r = 1.2$, $t = 12$ min and $p = 4.8$ kW were considered as the optimum parameters. The powders were characterized using various analytical techniques.

3. Results

3.1. Characteristics of synthesized nanocomposites (Fe–Fe$_3$C)&C

The TEM images and heating saturation for (Fe-Fe$_3$C)&C nanocomposites are shown in **Figures 1** and **2**.
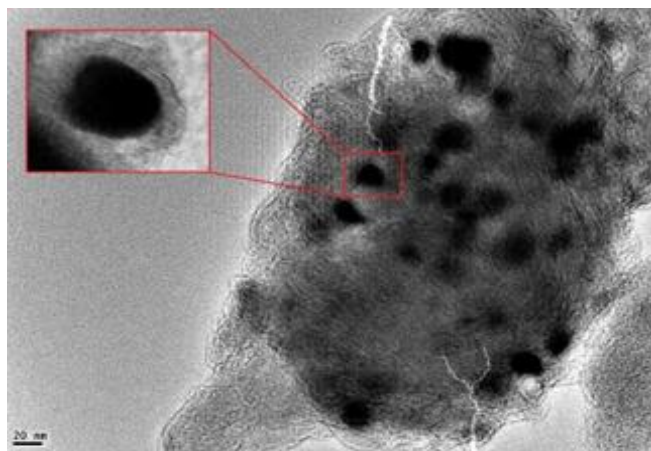

Figure 1. TEM image of the (Fe-Fe$_3$C)&C nanocomposite.

The magnetic characteristics, such as saturation, magnetization and coercivity as well, as the specific absorption rate (SAR), make these materials attractive for magnetic hyperthermia

applications. Hysteresis loop of the (Fe-Fe$_3$C)&C nanocomposites is of special interest, as it shows almost square behavior, where Mr / M (200 Oe) = 0.75. The limitation of the magnetic field amplitude and frequency (H × f) ≤ 10.625 · 10^6 Oe / s makes this factor important that provides a high energy absorption even in case of low magnetic fields. The Curie temperature of the obtained composites is substantially higher than 132 °C (the Curie temperature of Fe$_3$C). Thus, special attention has to be paid to the control of the electromagnetic wave power and provide the tissue treatment temperature in the range of 41 – 43 °C.

3.2. Characteristics of synthesized nanocomposites Ag$_{0.2}$La$_{0.8}$MnO$_3$

The TEM images of Ag$_{0.2}$La$_{0.8}$MnO$_3$ nanoparticles and carbon black–Ag$_{0.2}$La$_{0.8}$MnO$_3$ hybrid nanocomposites, the dependence of the specific magnetic moment on the applied magnetic field and the dependence of the Curie temperature T_C on the Ag content in Ag$_x$La$_{1-x}$MnO$_3$ nanoparticles are represented in **Figures 2 – 4** and **Table 1**.
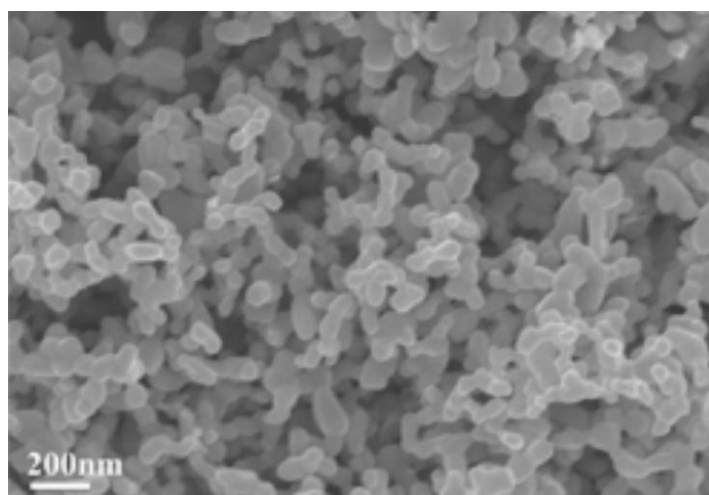
Figure 2. TEM image of Ag$_{0.2}$La$_{0.8}$MnO$_3$ nanoparticles.
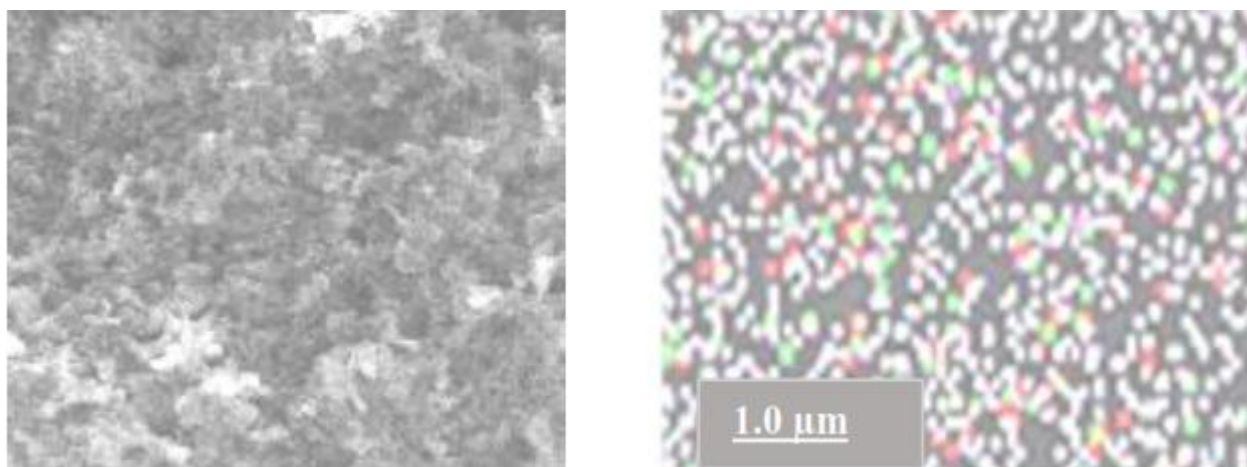
Figure 3. TEM image of carbon black–Ag-doped lanthanum
manganite hybrids and corresponding mapping of Ag, La, Mn and C.
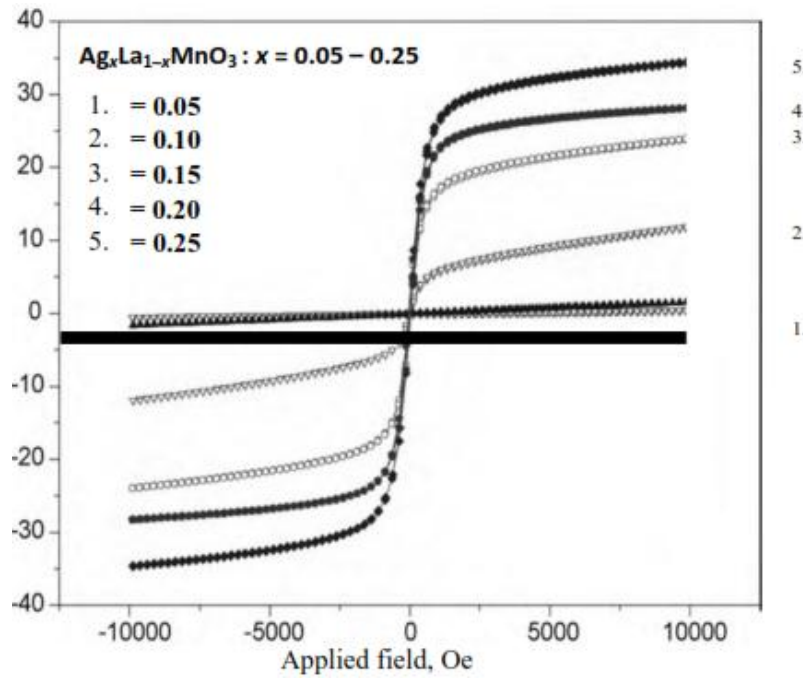
Figure 4. Dependence of the specific magnetic moment on the applied magnetic field.

Table 1. Dependence of Curie temperature T_C on the Ag content in $Ag_xLa_{1-x}MnO_3$ nanoparticles.

#	Composition (x)	T_C (°C)
1	0.05	31 ± 1
2	0.10	40 ± 1
3	0.15	42 ± 1
4	0.20	44 ± 1
5	0.25	45 ± 1

The demonstrated uniformity of $Ag_xLa_{1-x}MnO_3$ nanoparticles in the carbon matrix, relatively high specific magnetic moment and dependence of Curie temperatures on Ag content indicate the possibility of application of synthesized nanocomposites with silver content in the range of $x = 0.05 - 0.22$ for magnetic hyperthermia of cells. The achieved uniformity and decrease of nanoparticle size and shape show that the demonstrated method (which utilizes the microwave enhanced processing) can be used for obtaining suitable nanocomposites for magnetic hyperthermia of cells. The obtained material combines the imaging contrast enhancement capability with targeted "self-controlled" (in the range of 41 - 43 °C) hyperthermia treatment.

3.3. Nanocomposites on the base of Ag-doped lanthanum manganite nanoparticles synthesized using microwave combustion method

The $Ag_xLa_{1-x}MnO_3$ nanoparticles were characterized with substantially improved uniformity and smaller size than the $LaMn_{1-x}Ag_xO_3$ and both of them were of substantially

smaller size than the nanoparticles synthesized by paper synthesis or spray synthesis methods. The TEM images of $Ag_xLa_{1-x}MnO_3$ and $LaMn_{1-x}Ag_xO_3$ nanoparticles are given in **Figure 5**.
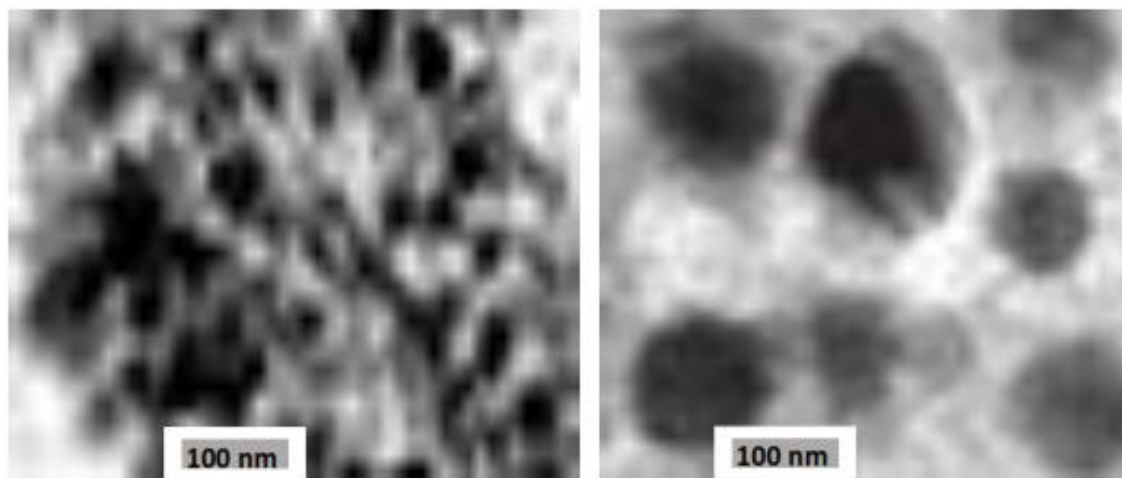
Figure 5. TEM images of $Ag_xLa_{1-x}MnO_3$ and $LaMn_{1-x}Ag_xO_3$ nanoparticles.

The hybrid nanocomposites obtained using the $Ag_xLa_{1-x}MnO_3$ magnetic nanoparticles showed also a better H × f limitation, which makes more prospective the application of carbon black–silver-doped lanthanum manganite nanocomposites in magnetic hyperthermia of cancer cells.

Acknowledgement

References

1. Z. Yang, S. Wang. High cycling performance cathode material: Interconnected $LiFePO_4$ / carbon nanoparticles fabricated by sol–gel method. J. Nanomater., 2014, Article ID 801562, 1-7.
2. L.-G. Zamfir, I. Geana, S. Bourigua, L. Rotariu, C. Bala, A. Errachid, N. Jaffrezic–Renault. Highly sensitive label-free immunosensor for ochratoxin A based on functionalized magnetic nanoparticles and EIS / SPR detection. Sensors & Actuators B, 2011, 159, 1, 178-184.
3. P. Kervalishvilia, A. Lagutin. Nanostructures, magnetic semiconductors and spintronics. Microelectronics J., 2008, 39, 1060-1065.
4. G. Reiss, A. Hütten. Magnetic nanoparticles: applications beyond data storage. Nat' Mater., 2005, 4, 10, 725-726.
5. M. Colombo, S. Carregal–Romero, M. F. Casula, L. Gutiérrez, M. P. Morales, I. B. Böhm, J. T. Heverhagen, D. Prosperi, W. J. Parak. Biological applications of magnetic nanoparticles. Chem. Soc. Rev., 2012, 41, 11, pp. 4306-4334.

6. M. Ishii, R. Shibata, Y. Numaguchi, T. Kito, H. Suzuki, K. Shimizu, A. Ito, H. Honda, T. Murohara. Enhanced angiogenesis by transplantation of mesenchymal stem cell sheet created by a novel magnetic tissue engineering method. Arteriosclerosis, Thrombosis &Vascular Biology, 2011, 31, 10, 2210-2215.

7. O. Veiseh, J. W. Gunn, M. Zhang. Design and fabrication of magnetic nanoparticles for targeted drug delivery and imaging. Adv. Drug Delivery Rev., 2010, 62, 3, 284-304.

8. S. Yanase, J. Nomura, Y. Matsumura, H. Kato, T. Tagawa. Hyperthermia enhances the antitumor effect of photodynamic therapy with ALA hexyl ester in a squamous cell carcinoma tumor model. Photodiagnosis & Photodynamic Therapy, 2012, 9, 4, 369-375.

9. H. B. Na, I. C. Song, T. Hyeon. Inorganic nanoparticles for MRI contrast agents. Adv. Mater., 2009, 21, 21, 2133-2148.

10. A. Ruiz, G. Salas, M. Calero, Y. Hernández, A. Villanueva, F. Herranz, S. Veintemillas–Verdaguer, E. Martínez, D. F. Barber, M. P. Morales. Short-chain PEG molecules strongly bound to magnetic nanoparticle for MRI long circulating agents. Acta Biomaterialia, 2013, 9, 5, 6421-6430.

11. R. D. Ambashta, M. Sillanpää. Water purification using magnetic assistance: A review. J. Hazardous Mater., 2010, 180, 1-3, 38-49.

12. X. Zuo, C. Peng, Q. Huang Sh. Song, L. Wang, D. Li, Ch. Fan. Design of a carbon nanotube / magnetic nanoparticle-based peroxidase-like nanocomplex and its application for highly efficient catalytic oxidation of phenols. Nano Res., 2009, 2, , 617-623.

13. F. Qin, H. Peng. Ferromagnetic micro-wires enabled multifunctional composite materials. Prog. Mater. Sci., 2013, 58, 183-259.

14. Z. Buachidze, G. Kochlashvili, A. Semionov, A. Chirakadze. An electrooptic waveguide travelling-wave waveguide light modulator with low control Power. Sov. J. Quantum Electrnics, 1989, 16, 11, 2317-2318.

15. X. Zhao, Z. Zhang, L. Wang, K. Xi, Q. Cao, D. Wang, Y. Yang, Y. Du. Excellent microwave absorption property of graphene-coated Fe nanocomposites. Sci. Rep., 2013. 3, 03421.

16. M. Sanaee, E. Bertran. Synthesis of carbon encapsulated mono- and multi-iron nanoparticles. J. Nanomater., 2015, 2015, Article: ID 450183, 1-10.

17. L. A. Avakyan, A. S. Manukyan, A. A. Mirzakhanyan, E. G. Sharoyan, Y. V. Zubavichus, A. L. Trigub, N. A. Kolpacheva, L. A. Bugaev. Atomic structure of nickel phthalocyanine probed by X-Ray absorption spectroscopy and density functional simulations. Optics & Spectroscopy, 2013, 114, 347-352.

18. N. A. Kolpacheva, L. A. Avakyan, A. S. Manukyan, A. A. Mirzakhanyan, E. G. Sharoyan, V. V. Pryadchenko Y. V. Zubavichus, A. L. Trigub, A. G. Fedorenko, L. A. Bugaev. Synthesis and investigation of the structure of nanocomposites based on nickel nanoparticles dispersed in a phthalocyanine matrix. Phys. Solid State, 2016, 58, 5, 1004-1010.

19. A. Manukyan, A. Mirzakhanyan, L. Sajti, R. Khachaturyan, E. Kaniukov, L. Lobanovsky, E. Sharoyan. Magnetic properties of carbon-coated Ni nanoparticles prepared by solid-phase pyrolysis of nickel-phthalocyanine. Nano, 2015, 10, 1550089-1.

20. A. S. Manukyan, A. A. Mirzakhanyan, R. D. Khachaturyan, A. T. Gyulasaryan, A. N. Kocharian, Yu. I. Yuzyuk, E. G. Sharoyan. Structure and magnetic properties of

carbon microspheres prepared by solid-phase pyrolysis of organic compounds. J. Contemporary Phys. (Arm. Acad. Sci.), 2015, 50, 195-199.

21. A. S. Manukyan, A. A. Mirzakhanyan, T. I. Butaeva, A. A. Guda, A. V. Soldatov, L. A. Bugaev, H. R. Asatryan, P. G. Baranov, E. G. Sharoyan. Room-temperature molecular ferromagnetism based on nickel phthalocyanine. magnetic resonance, optical and XANES spectra. Arm. J. Phys., 2010, 3, 272-275.

22. A. S. Manukyan, A. A. Mirzakhanyan, G. R. Badalyan, G. H. Shirinyan, E. G. Sharoyan. Preparation and characterization of nickel nanoparticles in different carbon matrices. J. Contemporary Phys. (Arm. Acad. Sci.), 2010, 45, 132-136.

23. E. Sharoyan, A. S. Manukyan. High temperature molecular magnetism caused by π-electrons: Copper phthalocyanine doped with alkaline metals. J. Porphyrins & Phthalocyanines, 2005, 9, 12, 846-851.

24. M. Movsisyan, S. Shmavonyan, A. Papoyan. Amplification of radiation in atomic vapor induced by a linearly polarized laser radiation. Cent. Eur. J. Phys., 2011, 9, 4, 948-955.

25. S. Shmavonyan, A. Papoyan. Intensity-dependent features in hydrogen-buffered cesium spectra. Int. J. Mod. Phys. Conf. Ser., 2012, 15, 140-146.

26. M. Movsisyan, S. Shmavonyan, A. Papoyan. Amplification of radiation in atomic vapor induced by a linearly polarized laser radiation. Cent. Eur. J. Phy., 2011, 9, 4, 948-955.

27. S. Shmavonyan, A. Khanbekyan, A. Gogyan, M. Movsisyan, A. Papoyan. Selective reflection of light from Rb_2 molecular vapor. J. Mol. Spectroscopy, 2015, 313, 14-18.

28. N. Aghamalyan, R. Hovsepyan, Y. Kafadaryan, R. Kostanyan, S. Petrosyan, A. Eganyan, M. Mezdrogina, R. Kuz'min. Annealing effect on the structural, electrical and optical properties of Er, Li-codoped ZnO films. J. Mater. Sci. & Eng. B, 2013, 3, 2, 119-123.

29. N. R. Aghamalyan, G. G. Demirkhanyan, R. K. Hovsepyan, R. B. Kostanyan, D. G. Zargaryan. Spatial distribution of green UC emission in $PbMoO_4 : Er^{3+}$ crystals: Effect of relative movements of PL excitation and detection positions. Opt. Mater., 2013, 35, 9, 1714-1718.

30. N. R. Aghamalyan, R. K. Hovsepyan, E. A. Kafadaryan, R. B. Kostanyan, S. I. Petrosyan, G. H. Shirinyan, A. Kh. Abduev, A. Sh. Asvaro. Features of phase formation of Er_2O_3 films during electron beam evaporation. J. Contemp. Phys. (Arm. Acad. Sc.), 2012, 47, 5, 236-240.

31. A. Manukyan, A. Mirzakhanyan, T. Khachatryan, G. Badalyan, K. Abdulvakhidov, L. Bugaev, E. Sharoyan. Copper-carbon Nanocomposites prepared by sold-phase pyrolysis of copper phthalocyanine. J. Contemp. Phys. (Arm. Acad. Sci.). 2012, 47, 16, 292–295.

32. A. Manukyan, A. Mirzakhanyan, H. Gyulasaryan, R. Khachaturyan, E. Sharoyan. Characterization of ferromagnetic metal–carbon nanocomposites prepared by solid-phase pyrolysis of metal-phthalocyanines. In: Conf. Booklet "Nanotech France 2015", 2015, Part 2, 51-51.

33. J. Liu, X. Jin, W. Song, F. Wang, N. Wang, Y. Song. Facile preparation ofmodified carbon black–$LaMnO_3$ hybrids and the effect of covalent coupling on the catalyticactivity for oxygen reduction reaction. Chinese J. Catalysis, 2014, 35, 1173-1188.

34. O. Melnikov, O. Gorbenko , M. Markelova, A. Kaul, V. Atsarkin, V. Demidov, C. Soto, E. Roy, B. Odintsov. Ag-doped manganite nanoparticles: New materials for temperature-controlled medical hyperthermia. J. Biomed. Mater. Res. A, 2009, 12, 1-9.

35.   P. Kervalishvili, A. Chirakadze, Z. Buachidze, D. Jishiashvili1, T. Bjalava, G. Kervalishvili, W. Toscano, V. Gvakharia, G. Sergeenko. Microwave in environmental technologies and synthesis of nano-materials: Georgian experience. In: Nuclear Radiation Sensors and Nanosensory Systems (Eds. P. J. Kervalishvili, P. H. Yannakopoulos). 2016, Springer, 22-86.

36.   P. Desai, A. Athawale. Microwave combustion synthesis of silver doped lanthanum Ferrite magnetic nanoparticles. Defence Sci. J., 2013, 63, 3, 285-291.

37.   S. R. Jain, K. C. Adiga. A new approach to thermo-chemical calculations of condensed fuel-oxidizer mixtures. Combustion & Flame, 1981, 40, 71-79.

ABOUT THE BEHAVIOR OF WAVE FUNCTION AT INTERACTION

T. T. Barnaveli

E. Andronikashvili Institute of Physics
I. Javakhishvili Tbilisi State University
Tbilisi, Georgia
tengiz.barnaveli@gmail.com

Abstract

The processes accompanying the interaction (localization) of the particle's Ψ-function cause debates and discussions for a very long time. Let us cite the extract from de Broglie's book [1]. "As soon as the particle is discovered in the point "A", the probability to discover it at any other point "B" gets equal to zero, since only one particle is connected with the wave psi". And further: "... any of mechanisms, based on the classical or even on relativistic forecasts about the space or time, evidently is not able to explain such an instantaneous squeezing, which is tightly connected with the indivisible character of a particle". However, it seems to be possible, remaining within the frames of quantum mechanics to build a sufficient logical picture, where these difficulties will be avoided. This consideration is based on the collation of the particle and the wave packet motions and on the possibility of dual description of wave packet, coming from two uncertainties $\Delta x\,\Delta P_x \sim \hbar$ and $\Delta t\,\Delta E \sim \hbar$, and was partly stimulated by the mentionedinde Broglie's book. Within the frames of this model, the infinity is removed from the description of collapse process, while the interaction of two elementary particles turns out to be thetwo stages process. At the first, preliminary stage the object to interact with will be discovered. As a result the symmetry of the system changes, so the second, final stage necessarily proceeds within the frames of Feynman's mechanism of path integrals.

Grounds and substantiation of the model

Let the motion of the particle of the energy E and momentum Pbe described by almost monochromatic wave (group of waves, wave packet). One can represent this group from two points of view.

The first one:

$$\Psi(x,t) =\int_{k_0-\Delta k}^{k_0+\Delta k} c(k)e^{-i(\omega t-kx)}\, dk, \tag{1}$$

where$\omega$is the frequency of the waves composing the group, k is the wave vector, k_0 is the wave number, in the vicinity of which the lengths of the waves composing the group are distributed, x is the coordinateof the some arbitrary axis of space; Δk is meant to be small.

The second one:

$$\Psi(x, t)=\int_{\omega_0-\Delta\omega}^{\omega_0+\Delta\omega} c^*(\omega)e^{-i(\omega t-kx)}\, d\omega, \tag{2}$$

where ω is the frequency of the wave, in the vicinity of which the frequencies of the waves composing the group are distributed; $\Delta\omega$ is meant to be small. So in version (1) integration is performed by the variable k, in version (2) integration is performed by the variable ω.

The frequency ω and the wave vector k are related to the energy and momentum of the particlevia de Broglie's equations $E = \hbar\omega$ and $P = \hbar k$. It is easily seen that k and ω are in mutually one-to-one functional dependence, are smooth functions and, thus, ω may be expanded into the power series with respect to k and vice versa.

Smallness of Δk and $\Delta\omega$ in (1) and (2) is necessary to provide the possibility to confine with couple of terms of expansion into seriesthat in both cases leads to the simple and obvious picture and interpretation of the wave packet.Such a possibility to confine just with couple of terms of expansion exists only in the region being farfrom the relativism. However, the relativistic corrections obviouslywill not upset the smoothness of the mutual dependence $\omega(k)$ as well, as the possibility of expansion of ω and k into the infinite series.In both cases these series are convergent that in both cases allowsone tochoose the arbitrary size of integration area by increasing the number of expansion terms. It means that the whole following logic and all conclusions will be valid in the whole region $v < c$.

As a rule, the wave group is represented as (1). Taking into account that ω is a function of k and confining with two terms in the expansion of ω in powers of $(k - k_0)$one can represent the group as:

$$\Psi(x,\ t)= 2c(k_0)\frac{sin\ \{[\left(\frac{d\omega}{dk}\right)_0 t-x]\cdot\Delta k\}}{[\left(\frac{d\omega}{dk}\right)_0 t-x]}e^{-i(\omega_0 t-k_0 x)}. \tag{3}$$

The derivative $\left(\frac{d\omega}{dk}\right)_0$ here is taken in the point k_0.

Firstly, for the clarity, let usconsider this traditional representation. According to it, the distribution of the intensity $|\Psi(x)|^2$ as a function of space coordinate in such group for some fixed moment of time t is shown in the **Figure 1**.
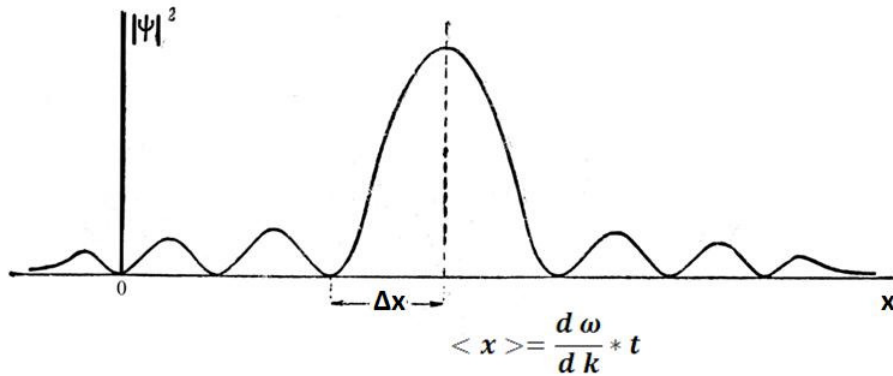

Figure 1.

It is obvious from (3) that the spatial coordinate of the group center (of the amplitude maximum) $<x> = \left(\frac{d\omega}{dk}\right)_0 t$. Besides that, $<x>$ itself and the whole picture, depending on time going on, will move along the axis x with the velocity (group velocity)

$$V = \frac{dx}{dt} = \left(\frac{d\omega}{dk}\right)_0.$$

The doubled distance Δx from the maximum point of $|\Psi(x)|^2$ to the first minimum is usually taken as a group linear dimension $2\Delta x$. From (3) it follows, that $\Delta x = \pi / \Delta k$.From here

$$\Delta x \, \Delta k = \pi. \tag{4}$$

Hence, decreasing the size of integration region Δk in (1), we can receive the arbitrary size of the group linear dimension $2\Delta x$.

Multiplying (4) by $\hbar$, and taking into account the de Broglie's equation $P_x = \hbar k$, we get

$$\Delta x \, \Delta P_x = \pi \hbar. \tag{5}$$

In identical experiments, in the time moment t, the median result of the measurements of the group center (maximum of intensity) spatial coordinates will be $<x> = \left(\frac{d\omega}{dk}\right)_0 t$. The separate measurements will be resulting within the frames $<x> \pm \Delta x$. Besides that, $<P> = P_0 = \hbar k_0$, while the separate measurements will be resulting within the frames $<P> \pm \hbar\Delta k$.

Thus, we have considered the Ψ-function of wave group for some given arbitrary moment of time, where Ψ-function (its (k,x)-component) occupies some linear region of space. Itmeans,that at some given arbitrary moment of time Ψ-function could initiate the interaction by means of any of its spatial parts and become real at any place in the frames $<x> \pm \Delta x$.

However, there is a possibility as well to consider $\Psi(x,t)$ not for a given moment of time t, but for some point x of spatial coordinates, formally completely analogously to the above mentioned(such possibilitywas considered for example in [2]).

Actually, the almost monochromatic wave (group of waves) may be considered not only in a way (1), but in a way (2) as well. Considering k as a function of ω and confining with two terms in theexpansion of k inpowers of $(\omega - \omega_0)$ one can now represent the group $\Psi(x, t)$ as:

$$\Psi(x,t) = 2\dot{c}(\omega_0) \frac{\sin\left\{\left[t - \left(\frac{dk}{d\omega}\right)_0 x\right]\Delta\omega\right\}}{\left[t - \left(\frac{dk}{d\omega}\right)_0 x\right]} \cdot e^{-i(\omega_0 t - k_0 x)}. \tag{6}$$

Here the derivative $\left(\frac{dk}{d\omega}\right)_0$ is taken in the point ω_0.

The distribution of intensity $|\Psi(x)|^2$ as a function of timecoordinate in such group of waves for some given coordinate point$x$ is shown in the **Figure 2**.
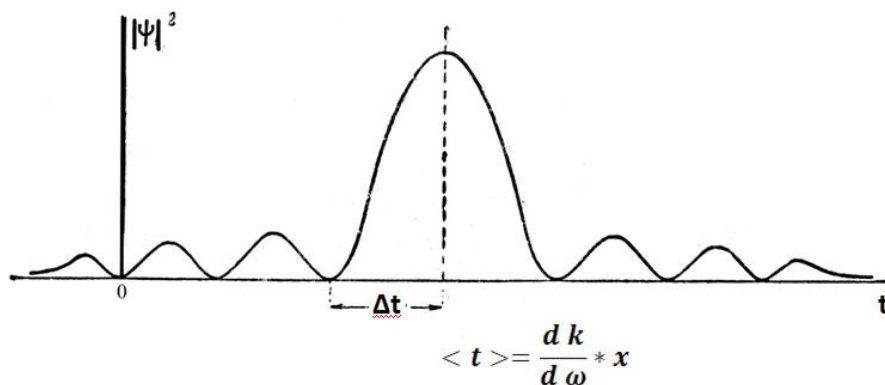

$$<t> = \frac{dk}{d\omega} * x$$

Figure 2.

It is obvious from (6),that the time coordinate of the group center (maximum of intensity) $<t> = \left(\frac{dk}{d\omega}\right)_0 x$. Now, let us imagine the "flow" of spatial coordinate x, as it took place for time coordinate in the first version. Here $<t>$ itself and the whole picture with it will move along the time axis with the "velocity" $\frac{dt}{dx} = \left(\frac{dk}{d\omega}\right)_0$.The physical sense of this "velocity" may be expressed as follows: "this value will shift the time in the expression for the state of packet (i.e. the whole picture) shifting the coordinate x by the length unit".In other words, if observers with the mutually synchronized clocks arearranged along the space axis (as if one

imitates the flow of the spatial coordinate x), then at the same moment of their (external) time the observers will see the different pictures of **Figure 2** with the different internal time shifted by the value $t_{shift} = \frac{dt}{dx}\Delta x$. Here Δx is the spatial distance between the observers; we take $\frac{dt}{dx}$ as a function changing slowly with the change of x.

So, this time we have considered Ψ- function of wave group for some given arbitrary coordinate of space, where the Ψ- function (its (ω,t) component) occupies some gap of time, the same in duration for any of these spatial points, but displaced by the value t_{shift}.

Absolutely analogously to the first version of consideration, the doubled distance Δt from the maximum of $|\Psi(x)|^2$ to the first minimum one can take for the group linear size in time $2\Delta t$. From (6) it follows that $\Delta t = \pi/\Delta\omega$, i.e.,

$$\Delta t\,\Delta\omega = \pi. \tag{7}$$

Thus, decreasing the size of integration region $\Delta\omega$ in (2), we can receive the arbitrary size of the group linear dimension in $2\Delta t$ time.

Multiplying (7) by $\hbar$, and taking into account de Broglie equation $E = \hbar\omega$, we have:

$$\Delta t\,\Delta E = \pi\hbar. \tag{8}$$

Similarly to the first representation (3) of this packet, for the second case (6) one can say that in identical experiments at the coordinate point x the median value of the measurements of the temporal packet center will be $<t> = \left(\frac{dk}{d\omega}\right)_0 x$, while the separate measurements will be resulted within the frames $<t> \pm \Delta t$. Besides that, $<E> = E_0 = \hbar\omega_0$, while the separate measurements will be resulted within the frames $<E> \pm \hbar\Delta\omega$.

This means that, at some given arbitrary coordinate x of space Ψ-function could initiate the interaction by means of any of its temporal parts and become real at any time within the frames $<t> \pm \Delta t$. Thus, the time in expression of Ψ-function may be considered completely analogously to the space coordinate.

Let us consider all this in details.

The mutual synchronization of this internal time with our external time is possible only at the instant of interaction. The mutual reference by the spatial coordinates takes place in the point of interaction.

What can we see in the quoted graphs? There are the distributions by internal coordinates (i.e. the coordinates of different spatial points of the spatial packet) for the given instant of time (**Figure 1**), and by the internal time (i.e. the time in the different temporal points of the temporal packet) for the given spatial coordinate (**Figure 2**). Each of these curves corresponds to some single point on the other curve. These curves represent one unified state distributed as in space and as in time.

It is obvious that the state of Ψ-function in each small area depends on the state in all areas located within the limits of the finite region of Ψ-function definition.

Therefore, in the both versions (1) *and* (2) *the wave packet is extended, as along x, as along t correspondingly, and it is unclear, which of its parts had initiated the interaction with the target.*

In the further consideration we'll concentrate mainly on the (ω,t)-component of the wave packet due to its special and very important role in the picture under consideration.

We will use three basic statements:

1. The state of the particle may be described by Ψ-function (2), where E and t can take the values $E\pm\Delta E$ and $t \pm \Delta t$ correspondingly.

2.   The time t in exponent is the evolution parameter of Ψ-function and is counted from the moment of the previous interaction, which was resulted in "preparation" of the state under consideration. Let us note that the time in this consideration is not the duration of observation – it is the internal time of evolution of Ψ-function. The observation can't be included in description of interaction, because the observation itself requires the measurement, i.e. an interaction.

3.   Let t^* be the moment of time t in Ψ-function expression, which corresponds to the maximum of $|\Psi(x)|^2$, and let us write t as $t = t^* \pm \Delta t$. Then, during the process of development of the packet in time the quantity Δt may accept the values from 0 to t^*, otherwise the time t in the exponent will change the sign at negative Δt.

Now let us collate the motion of particles and the wave packet. Within the frames of this statement, it becomes natural that from the instant of generation of Ψ-function of the particle the range of acceptable values of Δt starts to increase and, thereby, the range of uncertainties ΔE of the energy E decreases. As a result, the shape of the spectrum of allowed values of E changes and, therefore, changes the spectrum of frequencies of the oscillation components of Ψ-function.

Let us underline once more that one can take doubled Δt for the time region occupied by packet (which specifies the diapason of possible results of time measurements). The same is valid for doubled Δx.

Now it is possible to consider more detailed what is happening inside the interval between the "preparation" of Ψ-function and its interaction with some object.

As we have noticed above, the time passed after the creation of Ψ-function of the particle to some moment t^* defines the diapason of principally possible values of Δt: $0 < \Delta t \le t^*$. In other words, the duration t^* of evolution of Ψ-function automatically provides the possibility to substitute the different values of quantity t into the exponent: from $t = t - (\Delta t = t^*) = 0$ to $t = t^* + (\Delta t = t^*) = 2t^*$. Composing the packet as in (2), it will be natural to make the integration region $\Delta\omega = \pi / 2t^*$, where t^* is the time of the Ψ-function evolution. Exactly, such $\Delta\omega$ as a variable depending on t^* may be inserted into the both limits of integral (2). In this case for any t^* there will be provided the optimal (reasonable) diapason of the possible target discovery distances in time.

Due to this fact the Ψ-function principally is able to "discover" virtually (for the external observer) the object of possible interaction from the distance in time of the order of already passed by the center of the packet from the moment of its generation and, at presence of other conditions, to interact virtually (for the external observer) with this object. Let us note that some contribution to this process may come as well from the known phenomenon of the natural spread of the packet in time.

Note, that the external observer so far can't see this interaction. His clock so far shows $t = t^*$, but no $(t^* + \Delta t)$. This interaction for (ω, t)-component of Ψ-function gets possible due to the linear dimension of the wave packet in time and takes place in some area of its internal time.

Thus, the spectrum of the internal time of the wave packet (its (ω, t)-component) turns out to be prolonged up to the some moment $(t^* + \Delta t)$ of the future, when the interaction with some other object will take place. This is represented from observer's point of view. From the "internal point of view" this time is real. It is the part of the time interval occupied by the packet. The so prolonged (ω, t)-component of Ψ-function, interacting with the found object, marks it as a potential target. From this moment t^* of Ψ-function evolution the situation inside

the system changes radically. Now in the system is "known" not only the generation point of Ψ-function but the coordinates of the target are "known" as well.

As we have noticed above, the temporal coordinate here plays the peculiar role. The point is that, as it is clear from expressions (1) and (2), for some given instant t the (ω,t)-componentis the same,common in the whole volume of Ψ-function in any of its representation and for any of spatial coordinates. So, here it is not necessary to overcome the spatial interval to access the each point of Ψ-function. Here, we evidently are dealing with some kind of non-locality.As a result, the interaction of (ω,t)-component leads to the interruption of Shrodingerian development in time of whole Ψ-function for the internal time $t = t^*$, i.e. for the moment of achieved stage of evolution.

Emerge of distinctly marked two points (1 for start and 1 for finish) leads to the change of the symmetry of the system. Thereby, the spontaneous change of Ψ-function takes place. One can say conventionally that Ψ-functionhereundergoes the structural (configuration) phase transition.

At arising of the symmetry "start–finish" the whole process starts to develop in different way. Inevitably (and seemingly it is the only possibility) it goes within the frames of Feynman's path integrals.

The Ψ-function, which was formed after the fulfillment of Feynmanian process, one can call the "final Ψ-function" (F Ψ-function). It is represented by the sufficient compact bunches of the possible trajectories. They are rather close to the classical trajectories of the minimal classical action, deflecting from these trajectories just within the frames ofthe uncertainty relations.The final part of Ψ-function gradually unwraps in the observer's real time and leads to the real result.

Within the frames of the described picture of "collapse" everything is natural. The whole problem turns out to be into the limits of the virtual process, into the time virtual for the observer. The quoted picture does not require the infinite velocity of propagation of the signal about the happened interaction to the places outside the localization point. The described picture does not affect at all the probability interpretation – the Ψ-function really "visited" the future (for the external observer) time, where the event under consideration was realized by means of the probability way. Besides that, no physical parameters of the interaction (the spatial coordinates, the time, and the cross-section) change. Really, the target turns out to be discovered still in the process of the Shrodingerian development of the system due to prolongation of the packet representing the Ψ-function as in version (1),as in version (2). Discovery of the target leads to the instantaneous change of the symmetry of system, and the whole following evolution of the system proceeds within the frames of Feynman's path integrals process, which,in its results, does not differ from the Shrodingerian description as well.

Thereby, the interaction of two elementary particles turns out to be two stages process. At the first, preliminary stage, the object, to interact with, will be found. As a result, the symmetry of the system changes, so the second, final stage with necessity proceeds within the frames of Feynman's mechanism of path integrals.

It seems that within the frames of the quoted approach the symmetry between the spatial coordinates x, y, z on the one hand and t – on the other, is restored at least partly. All above mentioned allows us to hope that the quoted model in any case contains the grain of truth and, as it seems to us, includes some additional possibilitiesthat may turn out to be useful.

Appendix

Let us consider the second object with which our packet had interacted. For the second object everything is the same, but now from its own "point of view" and in its internal time. Here, only the moment of interaction is mutually synchronized – it is the common reference point for the both interacting objects. The situation is schematically shown in **Figure 3**. Really, the interaction takes place at the moment $T_1 = (t_1 + \Delta t_1)$ for the object 1 and at the moment $T_2 = (t_2 + \Delta t_2)$ for the object 2. Here t_1 and t_2 are the halves (see above) of internal times correspondingly of the 1 and the 2 objects, remained till their meeting in the point of interaction.
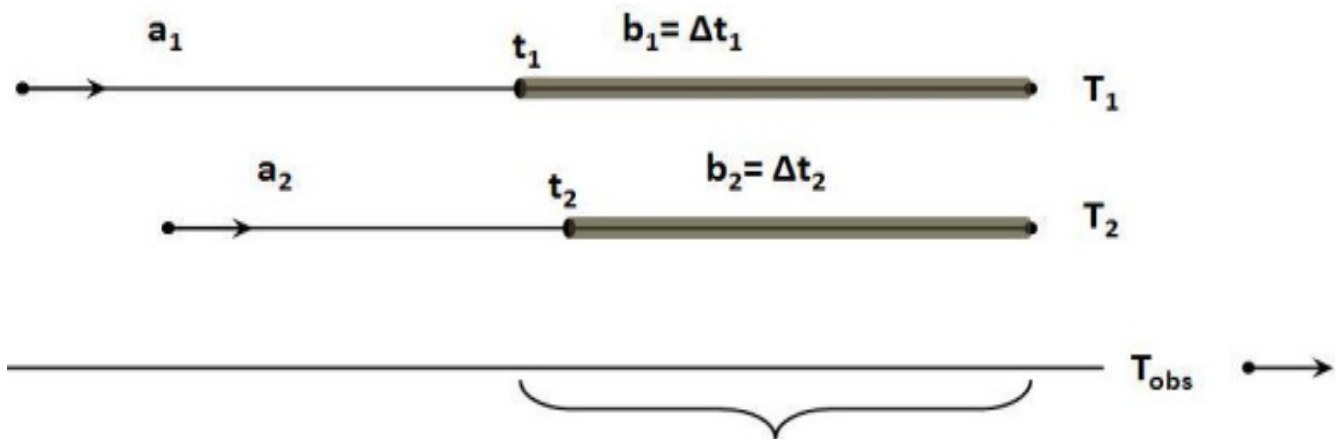
Figure 3.

If the location of the source is far enough we definitely have time to place the additional detector (the target) in any region of the observation time axis T_{obs}.

In particular, even after the creation of part "b" the conditions may be changed occasionally or deliberately, say the new object will emerge, which was not there before the creation of "final Ψ-function" (see above) in the region "b". Now this F Ψ-function has the chance to interact with this object with some probability. So, the first interaction, which has formed this F Ψ-function, may not proceed farther. The symmetry of the kind "start–finish" inside the system will be maintained, however the final point may be changed. The Feynmanian process now may proceed via new trajectories.

In case if the new object will emerge in the region "a", here again will work the described mechanism and the problem of collapse will not arise.

Therefore, with some probability we are able to change the future. However, in each separate case we completely loose the information of "what could take place". Everything depends on what version of the target will "feel" the final Ψ-function – placed farther in time or the closer one – that one will be realized. So in "identical experiments" we can expect the alternation of different results in accordance with the probability of their realization. At the interference into experiment our "free will" was acting, evidently in its "restricted" version [3]. Actually it happens in any of our activities. Just in macro mechanics we usually can say "what exactly would happen if we acted other way" (even here, not always). But, in the case being under discussion it is practically excluded, though this problem deserves the separate consideration.

Thus, in the first stage of Ψ-function propagation the traditional Schrodingerian representation is transparent and effective. However, as we have seen, after the discovery of the point, where future interaction will take place, the symmetry "start–finish" emerges. And here the mechanism of the path integrals becomes inevitable and effective, as we have tried to show.

Acknowledgements

References

1. L. de Broglie. Les Incertitudes d'Heisenberg et l'interpretacion probabiliste de la mecanicue ondulatoire. 1986. – *in Russian*.
2. L. I. Schiff. Quantum Mechanics. 1957. – *in Russian*.
3. G. Hooft. On the free will postulate in quantum mechanics. 2007, arXiv: quant-ph/0701097v1.

თუთიის გავლენა Na-ისა და K-ის შეთვისების როცესზე რძემჟავა ბაქტერიებში

ნ. რჩეულიშვილი[1], ე. კაკაბაძე[1],
ა. რჩეულიშვილი[2], ო. რჩეულიშვილი[2]

[1] გ.ელიავას ბაქტერიოფაგიის, მიკრობიოლოგიისა და ვირუსოლოგიის ინსტიტუტი
თბილისი, საქართველო
[2] ე. ანდრონიკაშვილის ფიზიკის ინსტიტუტი
ი. ჯავახიშვილის სახ. თბილისის სახელმწიფო უნივერსიტეტი
თბილისი, საქართველო
archeuli@gmail.com

ანოტაცია

შესწავლილია თუთიის იონების გავლენა *Lactobacillus spp.* და *Streptococcus thermofiles* ბაქტერიების მიერ K-ისა და Na-ის შეთვისების პროცესზე. ბაქტერიები საკვებ გარემოში იზრდებოდნენ 12, 20, 36, 44 და 68 სთ-ის განმავლობაში. ბაქტერიებს გამოვყოფდით საკვები გარემოდან, მიღებულ მასებს ვრეცხავდით, ვაშრობდით, ვწონიდით და ვუტარებდით ანალიზს Na-ისა და K-ის შემცველობაზე. როგორც მიღებული შედეგებიდან ჩანს, კალიუმის ინტენსიური შეთვისება ბაქტერიების მიერ ხდება პირველი 20 სთ-ის განმავლობაში. შემდეგ ბაქტერიები იწყებენ კალიუმის გამოდევნას თავისი ორგანიზმიდან. 68 სთ-ის შემდეგ იწყება ბაქტერიებში კალიუმის შემცველობის შემცირება ~ 5-ჯერ მის მაქსიმალურ რაოდენობასთან შედარებით. Zn-ის იონების არსებობა საკვებ გარემოში ხელს უწყობს Na-ის შეთვისებას *Streptococcus thermofiles*-ის ტიპის ბაქტერიების მიერ. როდესაც ბაქტერიების გამოზრდის დრო შეადგენს 12 სთ-ს, მაშინ Na-ის შემცველობა იმ ბაქტერიებში, რომლებიც იზრდებოდნენ Zn-ით გამდიდრებულ გარემოში ~ 3-ჯერ მეტია, ვიდრე იმ ბაქტერიებში, რომლებიც იზრდებოდნენ გარემოში Zn-ის გარეშე და 68 სთ-იანი კულტურებისთვის შეადგენს მხოლოდ ~ 1.3. *Lactobacillus spp.*-ის ტიპის ბაქტერიებისთვის Na-ის შემცველობის ასეთი სხვაობა არ დაიკვირვება. Zn-ის იონების არსებობა ხელს უწყობს, აგრეთვე, K-ის შეთვისებას, როგორც *Streptococcus thermofiles*-ის ტიპის, ასევე *Lactobacillus Spp.* -ის ტიპის ბაქტერიების მიერ. ფარდობა K-ის შემცველობებს შორის Zn-იან და მის გარეშე გარემოში გაზრდილ ბაქტერიებში იზრდება საკვებ გარემოში ბაქტერიების ზრდის დროის მატებით.

რძემჟავა დუღილის სასურსათო პროდუქტები ფართოდ გამოიყენება მოსახლეობის კვებაში. აღნიშნული პროდუქტები მდიდარია ცილებით, ნახშირწყლებით, ცხიმებით, სასარგებლო ელემენტებით და ვიტამინებით. აქედან გამომდინარე, ძალზე აქტუალურია მაღალი ხარისხის რძემჟავა დუღილის სასურსათო

პროდუქტების წარმოება. რძემჟავა დუღილის ბაქტერიები წარმოადგენს ძირითად რგოლს რძემჟავა პროდუქტების მიღების პროცესში.

რძემჟავა ბაქტერიები (Lactic Acid Bacteria – LAB) წარმოადგენენ გრამ-დადებითი ბაქტერიების ჯგუფს, რომლებიც არ წარმოქმნიან სპორებს, წარმოადგენენ ანაერობულ ან მიკროაეროფილურ კოკებსა და ჩხირებს, რომლებიც ნახშირწყლების ფერმენტაციის ტოლერანტული მირკოორგანიზმები. რძემჟავა ბაქტერიები ნახშირწყლების რძემჟავად გარდაქმნას ახორციელებენ ჟანგბადის მცირე რაოდენობის თანაობისას. ყველა რძემჟავა დუღილის ბაქტერია ენერგიის წყაროდ საჭიროებს ნახშირწყლოვანი სუბსტრატის კომპლექსს. მათ მიერ წარმოებული რძემჟავა ეფექტურად აინჰიბირებს სხვა ბაქტერიების ზრდას, რომლებიც სასურსათო პროდუქტის გაფუჭებას იწვევენ ფერმენტირებულ პროდუქტებში არასასურველი მიკროფლორის ინჰიბირებას იწვევს გარემოს pH-ის მკვეთრი დაცემა.

ცნობილია, რომ **კალიუმი** აქტიურებს მთელ რიგ ფერმენტებს და მონაწილეობს უმნიშვნელოვანეს მეტაბოლიზურ პროცესებში (ენერგიის წარმოქმნა, გლიკოგენის, ცილების დაგლიკოპროტეინების სინთეზი). K არეგულირებს უჯრედული მემბრანებიდან საკვები ნივთიერებების შეღწევის პროცესს უჯრედებში. არეგულირებს შიდაუჯრედულ ცვლას, წყლისა და მარილების სვლას [1]. **ნატრიუმი** კი მნიშვნელოვან როლს თამაშობს წყლისა და მარილების მიმოცვლაში [1, 2]. აღნიშნული ელემენტები გარკვეულ ზეგავლენას ახდენენ რძემჟავა დუღილის ბაქტერიებში მიმდინარე ბიოქიმიურ პროცესებზე. კერძოდ, შესაძლებელია ამ ლითონების გავლენა დუღილის ბაქტერიებზე რძემჟავა პროდუქტების მიღების პროცესში.

დღემდე ძალზე მცირე რაოდენობის შრომებია მიძღვნილი ბაქტერიასთან ლითონის ურთიერთქმედებაზე სხვა ლითონების იონების თანაარსებობისას [3 – 5].

აქედან გამომდინარე, დიდ ინტერესს იწვევს დუღილის ბაქტერიების მიერ Na-ისა და K-ის შთანთქმის პროცესის შესწავლა და ამ პროცესებზე თუთიის გავლენის შესწავლა. საინტერესოა, აგრეთვე, ამ ლითონების ზეგავლენის შესწავლა ბაქტერიების აქტივობაზე რძემჟავა პროდუქტების მიღების პროცესში.

სამუშაოს მიზანი

სამუშაოს მიზანია რძემჟავა დუღილის ბაქტერიების მიერ, მათი ზრდა-განვითარებისას, Na-ისა და K-ის შთანთქმის პროცესებისა და ამ პროცესებზე Zn-ის გავლენის შესწავლა. ამ მიზნით გამოყოფილ იქნა ლაქტოზის ფერმენტაციის უნარის მქონე ბაქტერიული შტამები. ჩატარდა მათი სახეობრივი იდენტიფიკაცია და დახასიათება. ბაქტერიების მიერ ლითონების აბსორბციის შესასწავლად შერჩეულ იქნა *Lactobacillus spp.* E11 K3 და *Streptococcus thermofiles* 2N K2 ბაქტერიული შტამები. ბაქტერიების გამოზრდა ხდებოდა საკვებ გარემოებში MRS [6] და M17 [7], სადაც დამატებული იყო საკვლევი ლითონები, Na და K.

ჩვენი გაზომვების თანახმად Na-ის კონცენტრაციები საკვებ გარემოებში MRS და M17 იყო: MRS – 3.6 მგ / მლ და M17 – 1.4 მგ / მლ. K-ის კონცენტრაციები კი ამ საკვებ გარემოებში შეადგენდა: MRS – 1.3 მგ / მლ და M17 – 1.1 მგ / მლ.

რძე შეიცავს უამრავ საკვებ ნივთიერებას, რომლებიც აკმაყოფილებს ორგანიზმის მოთხოვნას (კალციუმი, მაგნიუმი, სელენი, რიბოფლავინი, ვიტამინი B12, ვიტამინი B5) [8]. მაწონი – რძემჟავა პროდუქტია, რომელიც გავრცელებულია კავკასიაში [9].

ზოგიერთი ბაქტერია, მაგალითად, *Leuconostoc citrovorum L. Dextranicum, Streptococcus lactis, S. Cremis* & *liquefaciens* და *Brevibacterium*-ის სახეობები მნიშვნელოვან როლს ასრულებს რძის პროდუქტების ფერმენტაციის პროცესში [10].

ანალიზები

ანალიზებისათვის აღებული იყო Na-ისა და K-ის საწყისი (დედა) ხსნარები 1 მგ / მლ კონცენტრაციებით. მათგან ვამზადებდით სხვადასხვა კონცენტრაციების ეტალონურ ხსნარებს.

ბულიონები MRS და M17 ჩავასხით მაკარტნის 40 მლ-იან სინჯარებში. საკვლევი *Lactobacillus spp.* E11 K3 ბაქტერიული შტამები შევიტანეთ – MRS, ხოლო *Streptococcus thermophiles* 2N K2 შტამები – M17 ბულიონიან სინჯარებში. ანალოგიურად შევიტანეთ ბაქტერიული შტამები სინჯარებში, იმ განსხვავებით, რომ სინჯარებში წინასწარ ჩასხმული იყო თუთიით გამდიდრებული საკვები ბულიონები MRS და M17. შეტანილი თუთიის (საბოლოო) კონცენტრაცია შეადგენდა 20 მკგ / მლ. სინჯარები მოთავსდა თერმოსტატში 37 °C-ზე, სადაც ხდებოდა ბაქტერიების გამოზრდა. ბაქტერიების გამოზრდის შემდეგ სინჯარებიდან გამოვყოფდით ბაქტერიულ მასებს. ამისათვის ხდებოდა ნიმუშების ცენტრიფუგირება 40 წთ-ის განმავლობაში წთ-ში 10000 ბრუნით (Thermo IEC MIcromax RF). მიღებულ ნალექს ვრეცხავდით გამოხდილი წყლით და ისევ ვახდენდით ცენტრიფუგირებას (იმავე პირობებში). შემდეგ ნალექები გადაგვქონდა ერთჯერად პეტრის ფინჯნებზე. ბიოუსაფრთხოების კაბინაში (Labconco, Model # 3601024) ხდებოდა მათი გაშრობა. შემდეგ გამომშრალი უჯრედოვანი მასები ავწონეთ და გადავიტანეთ სინჯარებში.

მიღებული ბაქტერიული მასების სველი დანაცრების (თხევად მდგომარეობაში გადაყვანის) მიზნით ნიმუშებიან სინჯარებში დავამატეთ 1 მლ კონცენტრირებული (70 %) აზოტმჟავა (HNO₃). ამგვარ მდგომარეობაში ნიმუშები დაყოვნდა 3 დღე, რის შემდეგაც მოხდა ნიმუშების გაცხელება დუღილის ტემპერატურამდე. ნიმუშების თხევად მდგომარეობაში გადაყვანის შემდეგ თითოეულ სინჯარას დაემატა 10 მლ ბიდისტილირებული წყალი. შემდეგ ვახდენდით ბაქტერიების ნიმუშების ანალიზს Na-ისა და K-ის შემცველობაზე ატომურ-აბსორბციული სპექტრომეტრის Analyst 800 (Perkin Elmer) დახმარებით (ემისიური რეჟიმი) [11]. გამოყენებული იყო აცეტილენ–ჰაერისალი. ექსპერიმენტით მიღებული შედეგები მოცემულია **ცხრილებში 1 – 4**.

ცხრილი 1. Na-ის შემცველობა რძემჟავა ბაქტერიებში
Streptococcus thermophiles 2N K2 (მკგ / გ), გარემო – M17.

T-ბაქტერიების გამოზრდის დრო, სთ	12	20	36	44	68
Na-ის კონცენტრაცია	307	532	617	504	501
Na-ის კონცენტრაცია. საკვებ გარემოში დამატებულია Zn	949	981	985	469	645

ცხრილი **2.** Na-ის შემცველობა რძემჟავა ბაქტერიებში
Lactobacillus spp. E11 K3 (მკგ / გ), გარემო – MRS.

T-ბაქტერიების გამოზრდის დრო, სთ	12	20	36	44	68
Na-ის კონცენტრაცია	200	629	1110	1227	998
Na-ის კონცენტრაცია. საკვებ გარემოში დამატებულია Zn	333	640	974	1067	548

ცხრილი **3.** K-ის შემცველობა რძემჟავა ბაქტერიებში
Streptococcus thermophiles 2N K2 (მკგ / გ). გარემო – M17.

T-ბაქტერიების გამოზრდის დრო, სთ	12	20	36	44	68
K-ის კონცენტრაცია	9406	13500	6670	4550	2810
K-ის კონცენტრაცია. საკვებ გარემოში დამატებულია Zn	12600	17535	11746	9927	7292

ცხრილი **4.** K-ის შემცველობა რძემჟავა ბაქტერიებში
Lactobacillus spp. E11 K3 (მკგ / გ). გარემო – MRS.

T-ბაქტერიების გამოზრდის დრო, სთ	12	20	36	44	68
K-ის კონცენტრაცია	14080	23830	9514	9333	4555
K-ის კონცენტრაცია. საკვებ გარემოში დამატებულია Zn	20448	24296	12917	12453	8072

შედეგებმა აჩვენა, რომ *Lactobacillus spp.* E11 K3 ტიპის ბაქტერიებს გააჩნიათ K-ის ათვისების უკეთესი უნარი Na-თან შედარებით. ლითონის იონების შეთვისება ინტენსიურია ბაქტერიების ზრდის პირველ საათებში. ბაქტერიების ზრდის გარკვეული

პერიოდის შემდეგ ხდება ბაქტერიების მიერ ლითონის იონების გამოდევნა ორგანიზმიდან.

როგორც მიღებული შედეგებიდან ჩანს (**ცხრილი 1**), Na-ის შემცვლელობა ბაქტერიებში *Streptococcus thermophiles* 2N K2 იზრდება ბაქტერიებისა და Na-ის იონების ურთიერთქმედების (ბაქტერიების გამოზრდის) დროის გაზრდით. ნატრიუმის შემცვლელობა აღწევს მაქსიმუმს, როდესაც ბაქტერიების გამოზრდის დრო შეადგენს 36 სთ-ს, შემდეგ განიცდის ოდნავ შემცირებას და ინარჩუნებს ამ მნიშვნელობას 6 სთ-მდე.

Na-ის შემცვლელობა რძემჟავა ბაქტერიებში *Lactobacillus spp.* E11 K3 (**ცხრილი 2**) იზრდება ბაქტერიების გამოზრდის დროის გაზრდით 44 სთ-მდე, ხოლო შემდეგ ოდნავ მცირდება.

Lactobacillus spp. E11 K3 ტიპის ბაქტერიები ახდენენ გაცილებით მეტი Na-ის დაგროვებას (~ 2-ჯერ), ვიდრე *Streptococcus thermophiles* 2N K2 ტიპის ბაქტერიები. აღნიშნულს ადგილი აქვს, როდესაც ბაქტერიების ზრდის პერიოდი Na-იან გარემოში შეადგენს $T \geq 36$ სთ. ეს შესაძლოა აიხსნას იმით, რომ გარემო, რომელშიც იზრდებოდნენ *Lactobacillus spp.* E11 K3 ტიპის ბაქტერიები, შეიცავდა 2-ჯერ მეტ Na-ს, ვიდრე – გარემო, რომელშიც იზრდებოდნენ *Streptococcus thermophiles* 2N K2 ტიპის ბაქტერიები.

როგორც მიღებული შედეგებიდან ჩანს (**ცხრილები 3** და **4**), კალიუმის ინტენსიური შეთვისება აღნიშნული ბაქტერიების მიერ ხდება კალიუმიან საკვებ გარემოში ზრდის 20 სთ-ის განმავლობაში. ზრდა-განვითარების შემდეგ პერიოდში ბაქტერიები იწყებენ კალიუმის გამოდევნას თავისი ორგანიზმიდან. K-იან გარემოსთან ურთიერთქმედების 68 სთ-ის შემდეგ ხდება ბაქტერიებში კალიუმის შემცვლელობის შემცირება ~ 5-ჯერ მის მაქსიმალურ რაოდენობასთან შედარებით. ანალოგიური მოვლენა დაფიქსირებული იყო ქრომრეზისტენტულ ბაქტერიებზე [12]. ქრომრეზისტენტული ბაქტერიების მიერ ხდება ზრდა-განვითარების დასაწყისში კალიუმის ინტენსიური შეთვისება და შემდეგ მისი გამოდევნა.

Zn-ის იონების არსებობა საკვებ გარემოში ხელს უწყობს Na-ის შეთვისებას *Streptococcus thermofiles* ტიპი სბაქტერიების მიერ. როდესაც ბაქტერიების გამოზრდის დრო შეადგენს 12 სთ-ს, Na-ის შემცვლელობა ~ 3-ჯერ მეტია იმ ბაქტერიებში, რომლებიც იზრდებოდნენ Zn-ით გამდიდრებულ გარემოში, ვიდრე იმ ბაქტერიებში, რომლებიც იზრდებოდნენ გარემოში Zn-ის დამატების გარეშე. ბაქტერიების გამოზრდის დროის მატებით ეს თანაფარდობა მცირდებადა 68 სთ-იანი კულტურებისათვის შეადგენს მხოლოდ ~ 1.3. *Lactobacillus spp.* ტიპის ბაქტერიებისთვის Na-ის შემცვლელობის ასეთი სხვაობა არ დაიკვირვება. Zn-ის იონების არსებობა ხელს უწყობს, აგრეთვე, K-ის შეთვისებას, როგორც *Streptococcus thermofiles* ტიპის, აგრეთვე, *Lactobacillus spp.* ტიპის ბაქტერიების მიერ. ფარდობა K-ის შემცვლელობებს შორის Zn-იან და მის გარეშე გარემოებში გაზრდილ ბაქტერიებში, მატულობს ბაქტერიების ზრდის დროის მატებით.

დამოწმებანი

1. http://www.studfiles.ru/preview/5810627/
2. http://www.rudana.in.ua/showanalit_8_lang.htm
3. K. J. Hardoyo, H. Ohtake. Effect of heavy metal cations on chromate reduction by Enterobacter cloacae strain H01. J. Gen.Appl.Microbiol., 1991, 37, 519.

4. Y. Ishibashi, C. Cervantes, S. Silver. Chromium reduction in Pseudomonas putida. Appl. Environ. Microbiol., 1990, 56, 2268-2270.

5. J. McLean, T. J. Berveridge. Chromate reduction by a pseudomonad isolated from a site contaminated with chromate copper arsenate. Appl. Environ. Microb., 2001, 67, 1076-1089.

6. http://himedialabs.com/TD/M1164.pdf

7. http://www.himedialabs.com/TD/M1029.pdf

8. V. Capozzi, P. Russo, M. T. Dueñas, P. López, G. Spano. Lactic acid bacteria producing B-group vitamins: A great potential for functional cereals products. Appl. Microbiol. & Biotechnol., 2012, 96, 6,1383-1394.

9. ი. მალხაზოვა. მაწვნის დედოებიდან გამოყოფილი ენდემური რძემჟავა ბაქტერიების გენოტიპური და ფენოტიპური დახასიათება. გეოლოგიის მეცნ. კანდ. სამეცნ. ხარისხის მოსაპ. წარმ. დისერტაცია. 2006, თბილისი, ბაქტერიოფაგიის, მიკრობიოლოგიისა და ვირუსოლოგიის ინსტიტუტი, 39-40.

10. Food and Agriculture Organization: http://www.fao.org/docrep/x0560e/x0560e10.htm

11. http://www.perkinelmer.com/Catalog/Product/ID/N3050417

12. O. A. Rcheulishvili, N. O. Metreveli, A.N. Rcheulishvili, T. L. Kalabegishvili, H. Y. Holman. Uptake of Cr, Fe, Mg and K by Bacteria Arthrobacteroxydans. In: Abs. 12th Int. Conf. Biogeochem. Chem. Trace Elem. 2013, Athens, 1-1.

МЕХАНИЧЕСКАЯ ПРОЧНОСТЬ ТОНКИХ ПЛЕНОК ТВЕРДЫХ РАСТВОРОВ GeTe–SnTe

М. Тетелошвили, И. Табатадзе,
З. Джабуа, А. Гигинейшвили, В. Саратова

Департамент инженерной физики
Грузинский технический университет
Тбилиси, Грузия
mziateteloshvili@yahoo.com

Аннотация

Методом прямого ампульного синтеза приготовлены объемные кристаллы твердых растворов состава $(Ge_{0.9}Sn_{0.1})_{0.5}Te_{0.5}$ и $(Ge_{0.5}Sn_{0.5})_{0.5}Te_{0.5}$ и после гомогенизирующего отжига измерены их коэффициенты теплового расширения. Методом дискретного вакуумно-термического испарения получены тонкие пленки объемных кристаллов указанных сплавов на различных подложках (кварц, монокристаллический кремний, ситалл, сапфир). Методом полного исстирания измерены относительные механические прочности приготовленных пленок. Показано, что, чем больше разница между коэффициентами теплового расширения подложки и пленки, тем меньше механическая прочность пленок.

В последнее время большое внимание уделяется пленочным термоэлектрическим элементам, которые имеют малые размеры в сочетании с высокими параметрами. Часто применение пленочных термоэлементов ограничено низкими механическими свойствами, что, в свою очередь, связано с влиянием подложки [1 – 3]. Поэтому, актуальной является изучение механических свойств термоэлектрических материалов в пленочном виде. Как известно, твердые растворы GeTe–SnTe авляются перспективными термоэлектрическими материалами в средней области температур [4], но в научной литературе нет данных о механических свойствах этих материалов в пленочном виде.

В представленной работе проведен синтез объемных кристаллов твердых растворов GeTe–SnTe состава $(Ge_{0.9}Sn_{0.1})_{0.5}Te_{0.5}$и$(Ge_{0.5}Sn_{0.5})_{0.5}Te_{0.5}$, измерен коэффициент теплового расширения пленок, приготовленных методом дискретного вакуумного испарения, на различных подложках и исследована их относительная механическая прочность.

Объемные кристаллы приготовлены методом прямого ампульного синтеза, проведен гомогенизирующий отжиг сплавов в течении 5 месяцев при температуре 700 K Рентгенодиффракционный и электронографический анализы показали, что, в пределах ошибки измерения, состав приготовленных сплавов совпадает с составом исходной шихты.

На дилатометре конструкции Стрелкова измерен коэффициент теплового расширения в области температур 300 – 410 K. Схема дилатометра приведена на **Рисунке 1**. Дилатометр состоит из двух основных частей: передающее и измерительное устройства. В передающем устройстве образец 1 устанавливается на кварцевый полированный столик 2,

который приварен к держателю 3, изготовленному из кварцевой трубки. На образец, с помощью имеющейся на верхнем конце серьги, надевается толкатель 4, передающий разностьудлинения образца и плавленного кварца измерителю удлинения, который состоит из магнитного столика 5, полированного инварного ярма 6, закрепленного с помощью стального зажима на нижнем конце кварцевого толкателя и цилиндрической иглы 7, на которой закреплено зеркальце. Ярмо втягивается в поле, создаваемое магнитным столиком, и прижимает иглу к полированной поверхности полюсов, толкатель, следуя изменению длины образца, перемещает ярмо, что, в свою очередь, вызывает поворот иглы вместе с зеркальцем. Поворот зеркальца вызывает перемещение изображения светового указателя в фокальной плоскости автоколимационной трубы 8. Это перемещение измеряется окулярным микрометром. На передающее устройство надевается кварцевый стакан 9, а на стакан – печка 10. Пространство между образцом и стаканом откачивается и, для улучшения теплообмена между печкой и образцом,заполняется гелием до давления ~ 10 мм. рт. ст. Температура образца измерялась платина–платинародиевой термопарой. Королек термопары находился вблизи образца на расстоянии 0.5 мм. При определении абсолютного значения температуры образца такое расположение термопары вносило ~ 1 град.
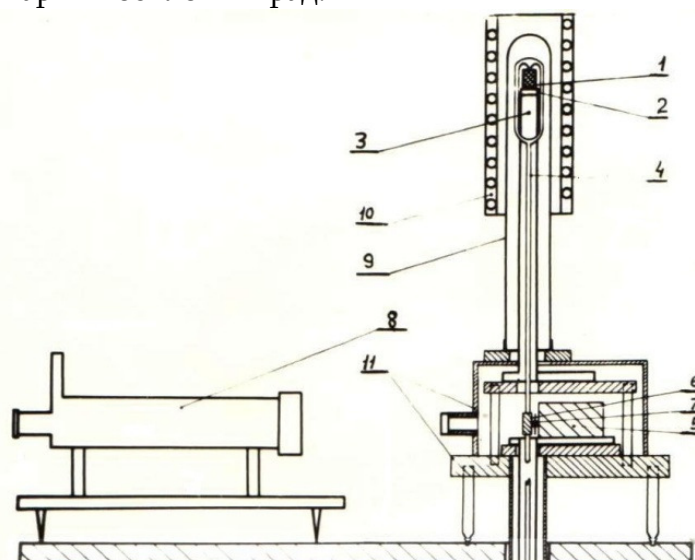
Рисунок 1. Схема дилатометра конструкции Стрелкова.
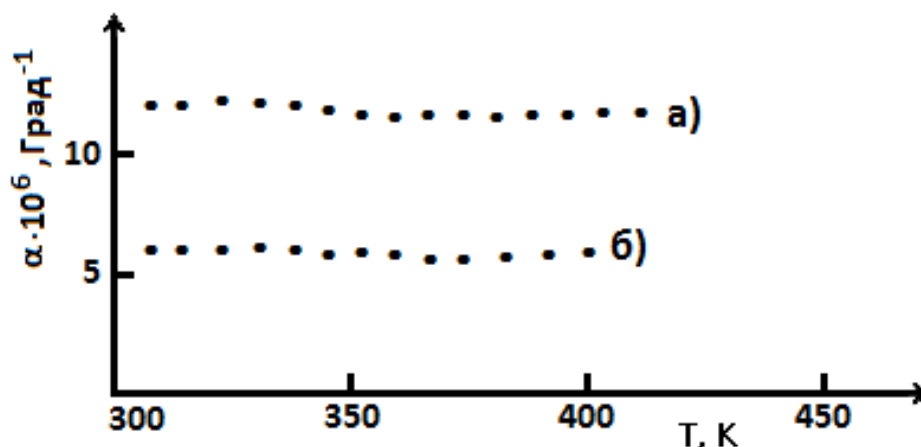
Рисунок 2. Зависимость коэффициента теплового расширения от температуры для а) $(Ge_{0.9}Sn_{0.1})_{0.5}Te_{0.5}$и б) $(Ge_{0.5}Sn_{0.5})_{0.5}Te_{0.5}$.

На **Рисунке 2** приведены результаты измерения температурной зависимости коэффициентов теплового расширения образцов. Как видно из рисунка, с изменением температуры коэффициент теплового расширения не изменяется и имеет значения $11.1 \cdot 10^6$ град$^{-1}$ для сплава $(Ge_{0.9}Sn_{0.1})_{0.5}Te_{0.5}$ и $6.1 \cdot 10^6$ град$^{-1}$ для сплава $(Ge_{0.5}Sn_{0.5})_{0.5}Te_{0.5}$, соответственно. Точность измерения составляла ~ 1.5 %, температура стабилизировалась с точностю ± 0.1 град.

Из образцов, на которых были измерены коэффициенты теплового расширения, были приготовлены пленки методом дискретного вакуумно-термического испарения (**Рисунок 3**). Сутьметодазаключается в следующем: предварительно синтезированный материал размельчается впорошок, который помещается в вибропитатель 4. С вибропитателя порошок с определительной скоростью подается на испаритель 2, откуда испаренный материал попадает на предварительно нагретую подложку 1 и конденсируется на ней. Использование этого метода особенно эффективно для получения тонких пленок таких материалов, которые при нагревании распадаются на фракции.
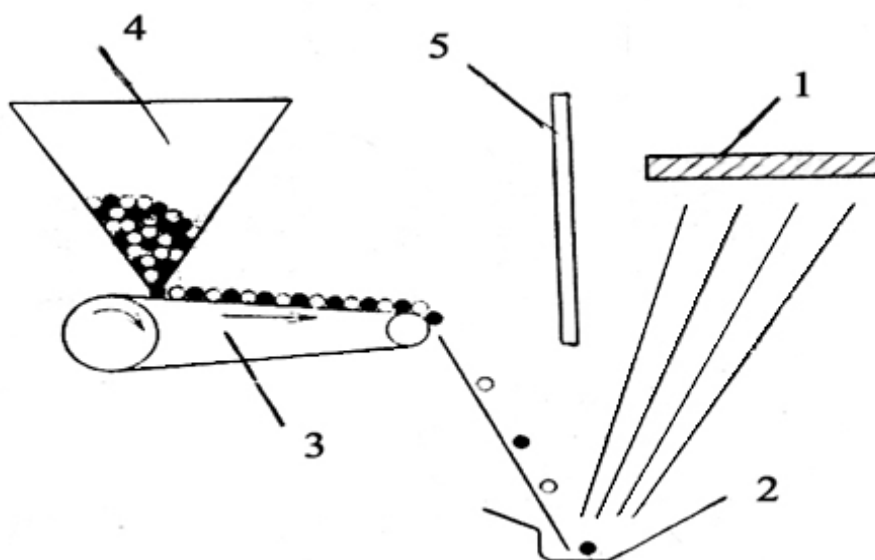
Рисунок 3. Схема для получения тонких пленок методом Дискретного вакуумно-термического испарения предварительно синтезированного материала: 1 – подложка, 2 – испаритель, 3 – транспортер и 4 – вибропитатель.

В качестве подложек ипользовались кварц, монокристаллический кремний, ситалл и лейкосапфир. Подложки сначала помещали в раствор 20 % NaOH на несколько мин, а затем промывали дистиллированной водой и переносили в раствор состава 30 % HCl + 60 % HNO_3 + 10 % H_2O, а затем опять промывали дистиллированной водой. После очистки подложкизакрепляли на подложкодержатель в вакуумной камере, и выдерживали при температуре 1100 К в течение 1 ч в вакууме ~ 10^{-6} мм. рт. ст. Непосредственно перед процессом осаждения пленки поверхность подложек бомбардировали электронным пучком. Многочисленные эксперименты показали, что адгезия пленок на подложке,очищенной указанным методом, довольно высокая.

Важным фактором успешного осуществления указанного метода является размер испаряемых частиц, температура испарителя и температура подложки. Многочисленные

эксперименты показали также, что оптимальными являются размеры частиц ~ 32 – 45 нм, температура испарителя и подложки – 2550 и 950 K ,соответственно.

В данной работе исследование механической прочности пленок было проведено методом полного исстирания. Схема соответствующей установки приведена на **Рисунке 4**.
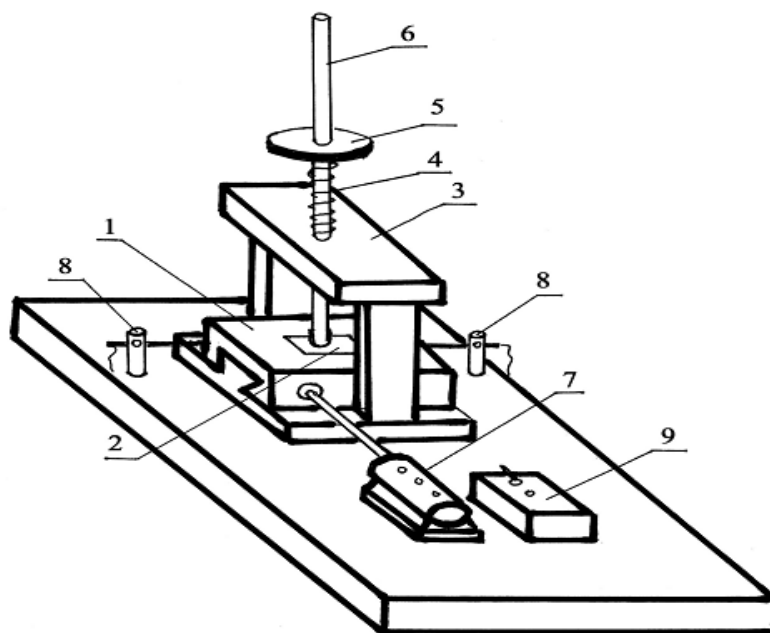

Рисунок 4. Схема установки для исследования относительной
Механической прочности пленок: 1 – массивная плитка,
2 – образец, 3 – опора, 4 – пружина, 5 – пластина, 6 – стержень,
7 – электродвигатель, 8 – электрические щупальцы и 9 – блок питания.

Исследуемая пленка 2 помещается намассивную плитку 1. На пленке сверху ставится стержень 6, на нижний конец которого надет замшевый слой, который покрыт алмазной пастой. Стержень нагружается различным весом. Спомощью специального механизма (двигатель 7 и щупальца 8) массивная плитка совершает поступательное движение вперед и назад. При этом считают число проходов, необходимое для полного исстирания пленки. Для сравнения механической прочности исследуемых пленок эксперименты проводили при одинаковой толщине пленок при одинаковых нагрузках. При наших экспериментах толщина пленок составляла 0.7 мкм, а нагрузка равнялась 150 г.

Результаты исследования относительной механической прочности приведены в **Таблице 1**.

Как видно из **Таблицы 1**, число проходов для полного исстиранияпленок как для первого,так и второго состава, напыленных на кварцевую подложку, меньше, чем для пленок, напыленных на остальные подложки.Соответственно, пленки, конденсированные на кварцевую подложку, харатеризуются низкой относительной механической прочностью. Для пленок обоих составов, осажденных на различных подложках, относительная механическая прочность в зависимости от материала подложки возрастает в следующей последовательности: кварц, монокристаллический кремний, ситалл, лейкосапфир. Возможной причиной такой закономерности является тот факт,что, чем меньше разность между коэффициентами теплового расширения подложек и пленок

(**Табица 2**), тем меньше дефектов появляется в пленках при охлаждении от температуры напыления до комнатной, что влияет на относительную механическую прочность пленок.

Таблица 1. Данные относительной механической прочности исследованных пленок.

Состав пленки	Толщина пленки, мкм	Нагрузка, г	Число проходов для полного исстирания			
			Материал подложки			
			Кварц	Моно-кристаллически кремний	Ситалл	Лейко-сапфир
$(Ge_{0.9}Sn_{0.1})_{0.5}Te_{0.5}$	0.7	150	12 – 15	28 – 32	41 – 45	72 – 79
$(Ge_{0.5}Sn_{0.5})_{0.5}Te_{0.5}$	0.7	150	27 – 30	39 – 44	59 – 72	85 – 93

Таблица 2. Значения коэффициентов теплового расширения.

Сплав	Коэффициент теплового расширения, α^6 град$^{-1}$	Среднее значение для температурны интервалов, К	Ссылки
$(Ge_{0.9}Sn_{0.1})_{0.5}Te_{0.5}$	11.9	300 – 530	[5]
$(Ge_{0.5}Sn_{0.5})_{0.5}Te_{0.5}$	7.5	300 – 530	[5]
Кварц	1.4	300 – 850	[6]
Моно-кристаллический кремний	2.5	300 – 1050	[6]
Ситалл	4.1	298 – 573	[6]
Лейкосапфир	8.1	298 – 573	[6]

Таким образом, можно отметить, что разница между коэффициентами теплового расширения подложки и напыленного на ней материала играет существенную роль в значении относительной механической прочности, что хорошо согласуется с данными работы[7].

Ссылки

1. Б. М. Гольцман, З. М. Дашевский, В. И. Кайданов, Н. В. Коломоец. Пленочные термоэлементы: Физика и применение. 1985, Москва, Наука.
2. K. A. Cambell, Ch. M. Anderson. Phase-change memory devices with stacked Ge-chalcogenide / Sn-chalcogenide layers. Microelectr. J., 2007, 38, 1, 52-59.
3. M. Sondergaard, M. Christensen, S. Johsen, C. Stiewe, T. Dasgupta, E. Mueller, B. B. Versen. Thermoelectric and microstructural properties of $Pb_{0.9-x}Sn_{0.1}Ge_xTe$ compounds prepared by spinodal decomposition. J. Solid State Chem., 2011, 184, 5, 1172-1175.
4. Д. И. Чернобровкин, С. А. Кутолин. Материалы для тонкопленочных микросхем. 2016, Куйбышев, Изд. КАИ.

5. З. Джабуа. Исследование теплового расширения и электрических свойств SnTe и сплавов системы GeTe–SnTe в облати фазового превращения. 2007, Тбилиси, ГТУ.
6. С. И. Новикова.Тепловое расширение твердых тел. 1974, Москва, Наука.
7. Z. Jabua, A. Gigineishvili., T. Dadiani, K. Davitadze, M. Stamateli. Mechanical strength of some rare-earth sulfide and antimonide thin films. In: Novel Materials – Suppl. Ed. Georg. Eng. News, 2006, 26-30.

PHOTOCHROMIC HYBRID COMPOUNDS OBTAINED
BY COUPLING SPIROPYRANS AND AZOBENZENE

J. Maisuradze, L. Devadze, Sh. Akhobadze,
Ts. Zurabishvili, N. Sepashvili, Zh. Urchukhishvili

V. Chavchanidze Institute of Cybernetics
Georgian Technical University
Tbilisi, Georgia
devadze2005@yahoo.com

Abstract

Considerable efforts of investigators have been devoted to improving the properties of the photochromic compounds to fulfill the requirements of the different applications. The most remarkable properties of these compounds are their absorption spectra, particularly the position of the absorption maxima, the intensity of color obtained upon irradiation with UV light. As the theory of conjugated chromophores suggests, introduction of a second photochromic center to a photochromic molecules improves the spectral properties of such hybrid molecules (e.g. extinction coefficient increases), and conjugated system π is elongated resulting in a bathochromic shift of the absorption band.Photochromic organic hybrid materials have attracted considerable attention owing to their potential application in photoactive devices, such as optical memories, optical switches, filters, drug delivery vehicles, non-linear optics materials and etc. The growing interest in this field has largely expanded the use of photochromic materials for the purpose of improving existing materials and exploring new photochromic hybrid systems. We have synthesized new hybrid photochromic compounds, calling them I, II, and III, based on azobenzene and different spiropyrans, synthesized by us. Compounds II and III were first synthesized and investigated by us. According to the spectral data, in the compound III, unlikecompounds I and II, the union of the electron cloud does not occur apparentldue to steric hindrance. Physico-chemical studies of the synthesized new hybrid compounds will be continued.

Introduction

Photochromic materials are a type of photoresponsive compounds, which undergo reversible transformations between two (or more) well-defined states possessing different physical, chemical and optical properties. In recent years they have attracted much attention for their fundamental properties and for their emerging applications in high level technologies, photo-switchable molecular devices, optical memory storage systems, nonlinear optical materials, optical shutters, biological applications, nanoparticle-based drug delivery vehicles, which can be engineered to release cargo molecules upon activation with a variety of external stimuli, and etc.Therefore,photochromic compounds suitable for photonic applications must meet the following requirements: high efficiency of photochromic transformations, thermal stability, high cross section for two-photon absorption, the fatigue resistance and nondestructive readout by any suitable method.

Photochromic spiropyrans and azobenzene

One of the most unique examples of molecular switches is spiropyran (SP) (**Figure 1**), whose closed-ring, relatively lowpolar (3D), hydrophobic isomer transforms into a highly polar (18D), open-ring merocyanine (MC) form upon exposure to ultraviolet light (UV), whereas the reverse reaction can be induced by visible light, or heating. This reversible isomerization can be triggered by a variety of other external stimuli, such as acids and bases, metal ions, temperature, redox potential and mechanical force. Among these different stimuli, light is the most attractive: it is a stimulus that can be delivered instantly, into a precise location, and in the form of different wavelengths, to which different photoresponsive molecules selectively respond.
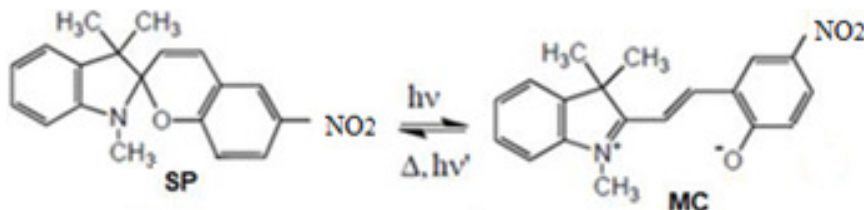
Figure 1. Spiropyran isomerization.

Considering the structure of the spiropyran molecule we see that it consists of two noninteractingπ-electron systems causing the presence of bands in the absorption spectrum of the spiropyran in the ultraviolet region of the spectrum. On the other hand, the merocyanine molecule has a single π-electron system providing the molecule absorption in the visible spectrum.

Spiropyransattract the attention as a result of a number of interesting features that include reversible ring closure have owing to the well-separated absorption bands of the two isomers, facile synthesis, distinct chromic transition, and fluorogenic nature of one isomeric form (usually the ring opened form) in certain environments.

The main parameters that are normally used for describing photochromic properties of spiropyrans are: the high photosensitivity, thermal stability (sometimes this can be achieved by incorporating the molecules in a rigid matrix), possess the highest among all known photochromic systems of two-photon absorption coefficients of both isomeric forms (which are an important parameters for three-dimensional recording devices) and fatigue resistance.

Many scientific centers and companies worldwide carry out studies and are working to optimize the parameters of the spiropyrans which is evidenced by a large number of published works and patents in the field [1 – 11].

Our research teamwithin a long time synthesizes and investigates photochromic compounds including spiropyransin order to optimize of spectrokinetic properties by substitution of functional groups in the photochromic molecules, since the stability and photosensitivity of a spiropyran are strongly dependent on the substituent, with the effects of structural changes of the parent spiropyran.It is possible to increase the photosensitivity by modification of a molecule: 1) by varying the substitutes of different electronic natures (electrodonor and electroacceptor) in the indoline and chromen parts and their position in the molecule and 2) by changing the molecule skeleton. By using this kind of approach, we have synthesized and studied several hundreds of spiropyrans. For instance, changing the indoline ring by azaindoline allowed us to obtain spiropyrans with increased photosensitivity to the UV light as compared with the known analogues [12] and introduction of an additional fragment in

the indoline part of the molecule (tetrahydroquinoline products) increased photosensitivity to visible light [13, 14]. By modifying the molecules of spiropyran in amphiphilic, under certain conditions, the system becomes self-organized. The effectiveness ofphotosensitivity increases by the internal energy [15]. The MC structure usually shows poor stability. The stability of the MC should be improved essentially for it to be used in practical applications. Some isolated MCs are readily converted to the closed spiropyran. But the electrostatic attraction between the zwitterionic MCs, packed intermolecularly, often induces aggregation such as the formation of micelles structure, and the conversion to the closed spiropyran can be interrupted and will stabilize the colored form [16]. The novel spiropyrans obtained on the basis of pyridoxal have demonstrated photochromic properties [17].

At the present time, when the limit to the improvement of multi-functional materials is almost reached the attention of researchers are drawn to the creation of hybrid multifunctional materials promising for practical applications in molecular electronics and photonics. Theazobenzene (AZ) (**Figure 2**) and spiropyran derivatives have been chosen by us among wide range of photochromic systems due to their particular properties. Azobenzene, which has been thoroughly studied as photoswitche, undergoes a reversible transto cisa particular isomerization upon exposure to UV light, corresponding to the $\pi - \pi^*$ transition. The reverse reaction, a cisto transisomerization, occurs upon exposure to visible light or by thermal relaxation corresponding to the $\pi - \pi^*$ transition.
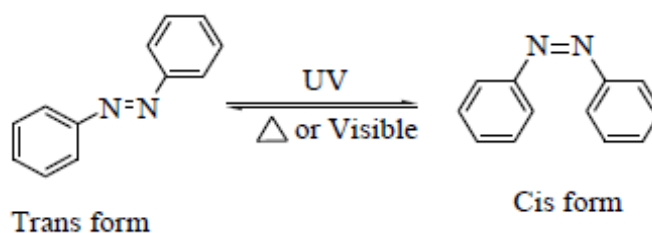
Figure 2. Azobenzene isomerization.

From the **Figures 1** and **2,** it is seen that azobenzene and spiropyran molecules undergo different types of isomerization reactions, such as trans-cisisomerization (AZ), ring opening (SP) upon UV irradiation.

Above describedspiropyrans can undergo reversible photoisomerization between the stable and the metastable states using UV and / or visible light, whereinspiropyran isomer can be reversibly converted to zwitterionicmerocyanine isomer. The thermal conversion from the merocyanine isomer back to the closed spiropyran occurs with a half-life at room temperature of tens of minutes in non-polar media, while the photochemical isomerization with visible light occurs on a much faster timescale. Since the two isomers of spiropyrans have dramatically different dipole moment, which causes the different physical and chemical properties they have been exploited in the development of photosensitive "smart" devices. In addition to the above-listed parameters of spiropyrans, the position of maximum absorption is also very important. For practical use, it is desirable to be located in the area of an inexpensive diode laser radiation (λ = 780 nm) which can be achieved by increasing the length of the molecule conjugation. Recently, studies have demonstrated that low power irradiation using light emitting diodes (LEDs, with an irradiance of approximately 1 mW · cm^{-2}) can be used to effective trigger the SP to MC isomerization [18].

As the theory of conjugated chromophores suggests, introduction of a second photochromic center to a photochromic molecule improves the spectral properties, the conjugated system π is elongated resulting in increase in a bathochromic shift of the absorption band and extinction coefficient.The latter was confirmed in the work [19], where the molar absorption coefficient increases from $0.31 \cdot 10^4$ to $1.35 \cdot 10^4$ $M^{-1} \cdot cm^{-1}$ for simple spiropyran (**Figure 1**) and the spiropyranin the presence of an azo moiety in the mero form (**Figure 3**), respectively. It is well-known that the higher molar absorption coefficient leads to higher sensitivity and resolution, and distinguishes the spiro form from the mero ones in photochromic applications.
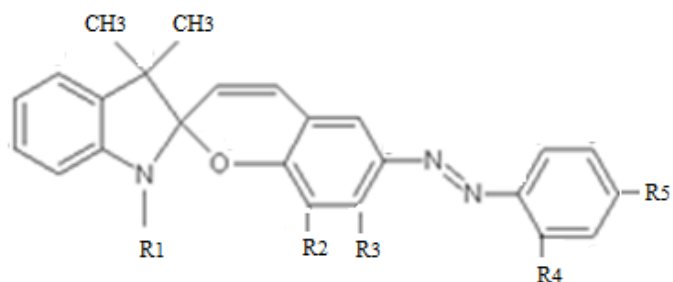
Figure 3. 1. $R_1 = C_4H_9$; $R_2 = R_5 = NO_2$; $R_3 = R_4 = H$.
2. $R_1 = CH_3$; $R_2 = OCH_3$; $R_3 = H$; $R_4 = R_5 = NO_2$.
3. $R_1 = CH_3$; $R_2 = H$; $R_3 = OH$; $R_4 = R_5 = NO_2$.

Based on the above mentioned, the introduction of a photochromic azobenzene molecule to a photochromic spiropyran molecule as the second absorption center was considered expedient by us (**Figure 3**). Thus, on the base of two photochromic compounds: SP and AZ, we synthesized three types ofphotochromic hybrid compounds by coupling azobenzene: with indolinespiropyran (compound I); with azaindoline spiropyran with increased photosensitivity to the UV light (compound II**)** and tetrahydroquinoline spiropyran with increased sensitivity to visible light (compound III).

Hybrid compound I obtained by coupling indolinespiropyran and azobenzene

Toimprove the properties of photochromic spiropyrans, we considered the synthesis of new hybrid photosensitive compounds on the spiropyran basis expedient. The hybrid compounds obtained by couplingspiropyran and different photochromic compounds had been synthesized and studied by a number of authors [19 – 24]. Half-life times of the ring-closure reaction of the hybrid molecules obtained by the pairingspiropyran and azobenzene in ethanol are about 0.3 – 14 s [19]. The introduction of the NO_2 group in position 8 of such hybrid molecule we were able to increase the lifetime of the photoinducedformby two orders. For improving the stability of photoinduced form we introduced 2-hydroxy-8-nitro-5[(4'-phenyl) diazenyl] benzaldehyde at Fisher's base analogs and gained hybrid compound **1** (**Figure 3**). The lifetime of photoinducedform of compound I is by two orders higher than mantioned in [19], hencethe photochromic transformations can be observed at room temperature. This was the result of inserting the electroacceptor group NO_2 in the position – 8. Such compounds as compared to those known in literature will be of a wider practical use, in our opinion. Combining two photochromes SPand AZ in one molecule increases the length of the conjugation chain of a photoinduced form resulting in the long-wave shift of the relevant absorption band.

Under the influence of the UV light, C–O bond is disturbed and the molecule transforms into a coplanar state and a long conjugated chain is formed. So, it is expected that a hybrid molecule, under the influence of active light, may serve two functions: disturbance of intramolecular bond C–O in the spiropyran fragment and geometrical changes – trans-cis isomerization in the azobenzene fragment. As it is known, the photochromic transformations can be observed at a room temperature by weakening C–O bond. This can be done by varying the electrical properties of the substitute and their positions in a hybrid molecule. It turned out that among the gained compounds the desirable properties were demonstrated by compound I. As the **Figure 3** shows, groups NO_2 were substituted in the chromene part position – 8 of spiropyran and position 4' of azobenzene. Such positioning of electroacceptor groups weakens bond C–O and the thermal equilibrium of a compound I in polar solvents shows a certain equilibrium shift to a colored form (**Figure 4**). The samples kept in the dark are colored. Under the influence of UV light ($\lambda = 365$ nm), the color deepens gradually to reach photoequilibrium. Under the influence of the visible light, the sample gets totally colorless. In the dark, the thermodynamic equilibrium is restored. The process is observed at a room temperature.

Figure 4. The image generated by a photomasked UV irradiation
($\lambda = 365$ nm) of thePMMA film doped with hybrid compound I.

For practical use, hybrid compound I was integrated with a polar polymer-polymethylmethacrylate (PMMA). We studied the spectral properties of the sample as shown in **Figure 5**. A short-wave absorption band belongs to azobenzene, while a long-wave absorption band is typical to the photoinduced form of a spiropyran.
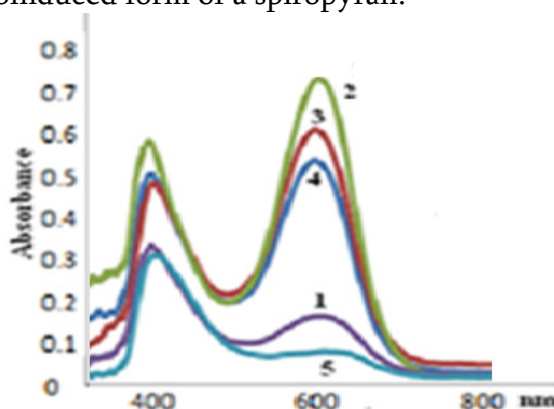
Figure 5. Absorption spectra of film of compound I integrated
in the polymer PMMA.1 – thermodynamic equilibrium; **2** – after
irradiationwith UV light; 3 and 4 – relaxation process taking
place in the dark; and **5** – after irradiation with visible light.

The absorption bands of a photoinduced form of a hybrid compound **I** as compared to the absorption bands of model compounds (SP and AZ) are shifted bathochromically what must be caused by the origination of a long conjugated chain of an open molecule form. The absorption spectrum corresponding to the thermodynamic equilibrium established in the dark shows that the sample is colored. The photoequilibrium established by the UV light radiation is shown in spectrum 2. The relaxation processes taking place in the dark are presented by 3 and 4. The relaxation process continues up to the establishment of thermodynamic equilibrium spectrum 1. Complete decoloration of a sample tooks place under the influence of the visible light which is active for a spiropyran fragment only.It was expected that the light would effects only on long-wave part of absorption spectra. As the figure shows, the visible light influenced a short-wave absorption band as well, what is a proof of a unity of the electronic cloud of the molecule. The UV / Vis absorption spectrum of PMMA film doped with compound **I** after stay at dark showed two peaks at around $\lambda = 400$ and 600 nm. When film is irradiated by UV light with the wavelength $\lambda < 365$ nm, weak long length absorption peak around at $\lambda = 600$ nm is increased, the shortlength absorption peak around at $\lambda = 400$ nm is increased too. It is noteworthy, that it should not have happened the photoisomerization of azobenzene moietyunder wavelength $\lambda < 365$ nm irradiation condition. This indicates that photoisomerization in the azobenzene moietyis induced by photoisomerization in the spiropyran moiety. After $\lambda = 365$ nm irradiation, the spectral changeis quite similar to $\lambda < 365$ nm irradiation. All this prove. The emergence of a common electron cloud of the two fragments of the hybrid molecule.

Hybrid compound II obtained by coupling SP$_{azaind}$ and AZ

The hybrid compound based on azaindoline was obtained by condensation of 1,2,3,3-tetramethyl-4-azaindolenin iodidewith the corresponding azoconjugatedhydroxyaromatic aldehydes (**Figure 6**). Thismethod was developed by us [12].

As it was noted above, replacement of indoline to azaindolineincreases the photosensitivity of spiropyran to UV light. The thermodynamic equilibrium is shifted toward the closed form thereby reducing the spontaneous degradation.The constant of relaxation rate of photoinduced form is increased.
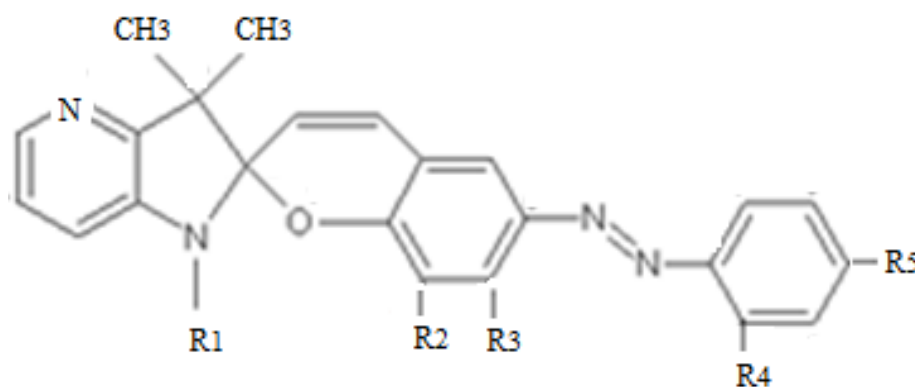

Figure 6. 1. R$_1$ = C$_4$H$_9$; R$_2$ = R$_5$ = NO$_2$; R$_3$ = R$_4$ = H.
2. R$_1$ = CH$_3$; R$_2$ = OCH$_3$; R$_3$ = H; R$_4$ = R$_5$ = NO$_2$.
3. R$_1$ = CH$_3$; R$_2$ = H; R$_3$ = OH; R$_4$ = R$_5$ = NO$_2$.

The properties of hybrid molecules consisting of azobenzene and azaindole are different from parentmolecule of azaindole. The thermodynamic equilibrium is shifted towards the colored form. The thermodynamic equilibrium constant is greater than photochemicalone $K_T > K_{PH}$, decoloration of system occurs not only by visible butby UV light too.

The spectral dataindicate that the visible light influenced a short-wave absorption band as well, what is a proof of a unity of the electronic cloud of the molecule like compound I. In polar solvents compound Iexhibits "positive"photochromism, because the thermodynamically less stable state is thecoloured form, on the contrary for compound II the thermodynamically less stable state is the colourless form and so it exhibits "negative" photochromism.

Hybrid compound III obtained by coupling SP$_{THQ}$ and AZ

The marriage of two photochromic molecule on the base of tetrahydroquinolinespiropyran, which is twice more photosensitive to visible light than its indoline analog, and azobenzene can lead to the birth of novel hybrid compound SP$_{THQ}$AZ (**Figure 7**).
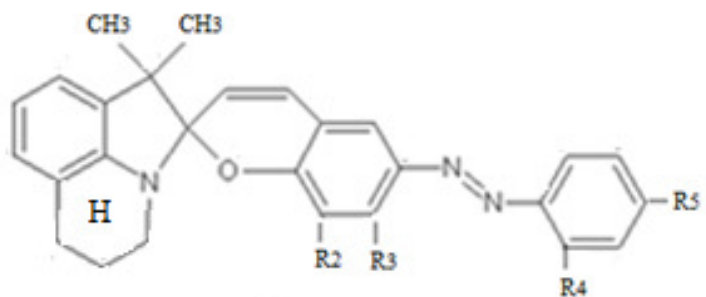
Figure 7. 1. $R_2 = R_5 = NO_2$; $R_3 = R_4 = H$.
2. $R_2 = OCH_3$; $R_3 = H$; $R_4 = R_5 = NO_2$.
3. $R_2 = H$; $R_3 = OH$; $R_4 = R_5 = NO_2$.

The hybrid compound based on tetrahydroquinoline (III) was obtained by condensation of 1,7-propano-2-methylene-3,3-dimethylindoline with the corresponding azoconjugated hydroxyaromatic aldehydes in alcoholic medium [14]. The left fragment of hybrid molecule is indolinespiropyran modified by us with additional cyclic moiety which makes it rigid. Such compound exhibits in polar solvents negative photochromism, because the coloured MC form is more stable than the colourless SP form. The irradiation by visible light causes decoloration of MC to generate SP form. When SP form is placed in the dark, it returns to the colored MC form. Therefore, this thermally reversible photochromic system for its photochromic transformation does not need the irradiation by UV light, which may cause degradation of the compound. Due to the fact that thermodynamic equilibrium of the compounds with additional cyclic moiety in polar solvents is more than photochemical one – $K_T > K_{PH}$ decoloration of system occurs with UV light too. The right side of the molecule – azobenzeneextends π-conjugation system and causes bathochromic shift of the absorption band of the colored-zwitterionic form of SP$_{THQ}$AZ. The UV / Vis absorption spectrum of compound III in ethanol after stay at dark showed two peaks at around $\lambda = 400$ nm and $\lambda = 600$ nm (**Figure 8**). When compound is irradiated by UV light with the wavelength $\lambda < 365$ nm, or by visible lightlongwave absorption peak around at $\lambda = 600$ nm is decreased, butthe shortwave absorption peak around at $\lambda = 400$ nm is not decreased. Its intensity does not depend on the range of the inducing radiation light.
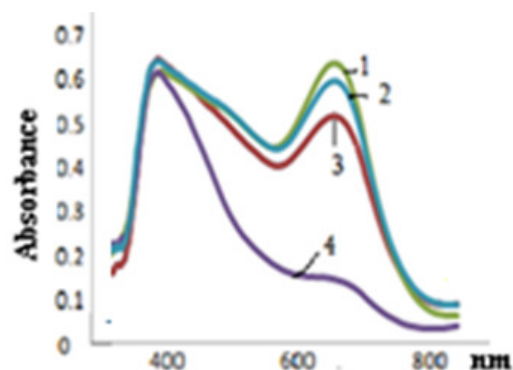
Figure 8.Absorption bands of compound III in ethanol.
1 – thermodynamic equilibrium, 2 – photo chemical
equilibrium after irradiation with UV light;
3 – expozition light 400 nm; 4 – after stay at daylight.

Evidently in the molecule conjugation carried out, but due to steric factors, unlike compounds **I** and **II** the electron cloud does not become common.
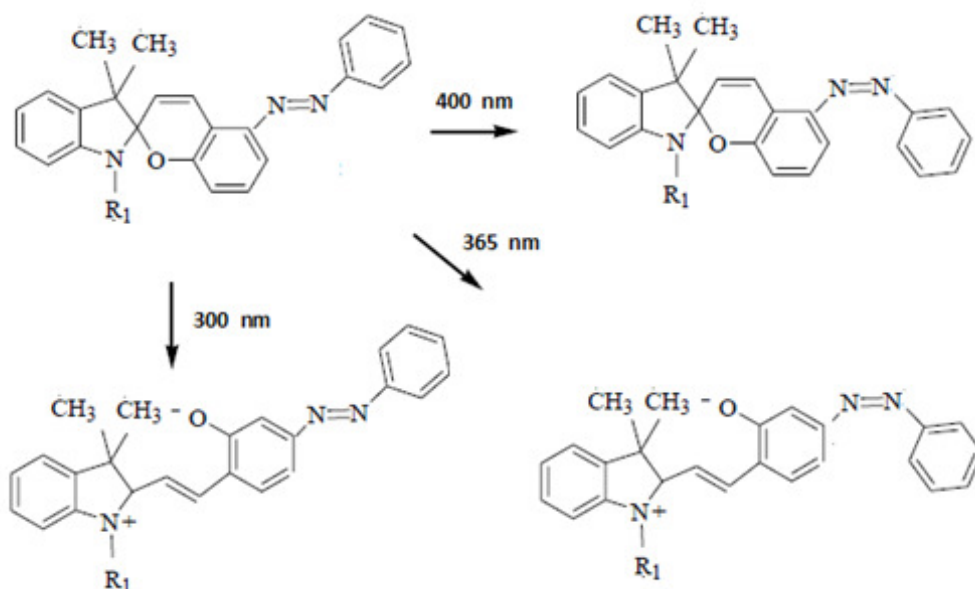

Figure 9. Fragments of hybrid molecule.

The independence of the fragments of hybrid molecule is particularly evident in low-polar solutionoftoluene.When toluene solution is irradiated by UV light with the wavelength of $\lambda = 400$ nm, AZ fragment in SPAZ is photoisomerized from trans-form to cis-form independly. Upon $\lambda = 300$ nm light irradiation SP moiety is photoisomerized from SP-form to MC-form independly. Upon $\lambda = 365$ nm light irradiation SP fragment is photoisomerrized to MC-form in addition to trans-cisphotoisomerization of AZ since this wavelength reacts both fragments of hybrid molecule (see **Figure 9**). The molecule SP${}_{THQ}$AZ combines the beneficial characteristics and properties of both components. Consequently photochromic properties can be controlled by lasers with different frequencies.

Set of spectral methods, and using method of photo kinetics analysis data were obtained on the photochromic propertiesof compounds I, II, III and their derivatives. These data represent the electronic absorption spectra of the original and photo-induced forms of kinetic

and thermodynamic parameters of the dark processes, efficiency phototransformations. These parameters, along with theestablishment of structure-property correlations, allow us to characterize them as effective photochroms for practical use.

Stationary electronic UV / Vis absorption spectra were measured on a optical-fiber spectometre Avantes 2048.

The spectral studies were performed in solutions of organic solvents (polar ethanol and weakly polar toluene) and in PMMA-polymethylmethacrylate polymer films doped byspiropyran, at room temperature. The solutions were preparedat daylight or under dark conditions as needed.

The compounds were irradiated with UV light and the decrease in absorbance was recorded against time.Photoisomerization of the hybrid molecule was induced by a illumination with 365 nm (filter UVG–1) and visible (filter YG–17) light from a 250 W high pressure Hg lamp.

Purity of the compounds was controlled by thin-layer chromatography and by melting points.

Conclusion

New hybrid photochromic compounds based on azobenzene and different spiropyrans synthesized by us (see **Figures 3**, **6** and **7)** were synthesized and investigated. Compounds II and III were firstly synthesized and investigated by us. The photochromic transformation of the compounds I, modified by us of compound described in the literature, we observed at room temperature. In all compounds theconjugation and bathochromic shift of the absorption band of coloured moleculewere realized (see **Figures** 4, **5** and **8**). According to the spectral data, in the compound III, unlikecompounds I and II, the union of the electron cloud does not occur apparentlydue to steric hindrance (see **Figure 8**). Physical-chemical studiesof the synthesized new hybrid compounds will be continued. This type of photochromic compounds will find applicationin future development of high-performance photochromic materials.

References:

1. R. Guglielmetti. Photochromism. Molecules and Systems (Eds. H. Dürr, H. Boua–Laurent), 1990, Elsevier.
2. R. C. Bertelson. Organic Photochromic and Thermochromic Compounds (Eds. J. C. Crano, R. Guglielmetti).1999, L. 1 – 11.
3. K. G. Japaridze. Spirokhromeny. 1979, Tbilisi.
4. G. Berkovic, V. Krongauz, V. Weiss. Chem. Rev., 2000, 100, 1741.
5. V. I. Minkin. Chem. Rev., 2004, 104, 2751.
6. V. I. Minkin. In: Molecular Switches, 1 (Eds. B. L. Feringa, W. R. Browne). 2011, Weinheim, Wiley–VCH, 37.
7. V. A. Barachevsky. Org. Photonics Photovolt., 2015, 8, 41.
8. V. I. Minkin. Chem. Rev., 2004, 104, 2751.
9. R. Klajn. Chem. Soc. Rev., 2014, 43, 148.

10. N. A. Voloshin, A. V. Chernyshev, S. O. Bezuglyi, A. V. Metelitsa, E. N. Voloshina, V. I. Minkin. Rus. Chem. Bull., 2008, 57, 151.
11. B. S. Lukyanov, M. B. Lukyanova. Chem. Heterocyclic Comp., 2005, 41, 281.
12. J. P. Maisuradze, Sh. A. Akhobadze, L. V. Devadze, K. G. Japaridze. KhGS, 1982, 10, 1367.
13. J. P. Maisuradze, N. I. Makhashvili, L. V. Devadze, N. O. Sepashvili, L. P. Shishkin, K. G. Japaridze. Herald Acad. Sci. Georg SSR (Ser. Chem.), 1989, 15, 1, 44.
14. N. I. Makhashvili, J. P. Maisuradze, K. G. Japaridze, L. V. Devadze. Herald Acad. Sci. Georg. SSR (Ser. Chem. & Chem. Technol.), 1988, 1, 99.
15. K. Japaridze, L. Devadze, J. Maisuradze, I. Mzhavanadze, N. Sepashvili. Bull. Georg. Natl. Acad. Sci., 2010, 4, 67.
16. K. Japaridze, L. Devadze, J. Maisuradze, N. Sepashvili. High Energy Chem., 2009, 43, 527.
17. K. Japaridze, L. Devadze, J. Maisuradze, G. Petriashvili, Ts. Zurabishvili, I. Mzhavanadze, N. Sepashvili. Bull. Georg. Natl. Acad. Sci., 2013, 7, 57.
18. S. Stitzel, R. Byrne, D. Diamond. J. Mater. Sci., 2006, 41, 5841.
19. F. Nourmohammadian, A. A. Abdi. Bull. Korean Chem. Soc., 2013, 34, 6.
20. K. Kinashi, K. Furuta, Y. Ueda. Chem. Letters, 2006, 35, 298.
21. K. Kinashi, Y. Ueda. Mol. Cryst.& Liquid Cryst., 2006, 445, 1.
22. R. Mardaleishvili, L. S. Koltsova, N. L. Zaichenko, A. I. Shienok, P. P. Levin, A. S. Tatikolov. High Energy Chem., 2013, 47, 5, 205.
23. R. Mardaleishvili, L. S. Koltsova, N. L. Zaichenko, A. I. Shienok, P. P. Levin, A. S. Tatikolov. High Energy Chem., 2015, 49, 30.
24. S.-R. Keum, M.-J. Lee. Bull. Korean Chem. Soc., 1999, 20, 12.

ULTRASONICWAVESAND WATER
PURIFICATIONFROM NANOPARTICLES

A. Bakhtiari, T. Berberashvili, P. Kervalishvili, L. Klimiashvili

Department of Engineering Physics
Georgian Technical University
Tbilisi, Georgia
t.berber@mail.com

Abstract

Ultrasonic wave as a high frequency longitudinal wave passes through liquid, makes acoustic cavitation and forms fine bubbles in low-pressure region of fluid. Because of pressure decrease thermodynamic phase changes the liquid to gas. Liquid atomizing effect, which produces the fine nanoparticles of liquid, is the basis of the water purification. Ultrasonic atomizing process in practice is a little far from bubbles mathematical models, because of different actual parameters effect in real conditions, but in the range of particles size below 1 μm it is relevant. There are some conditional considerations that make thermal processes as the best choice for nanoparticles treatment especially, when there is a source of heat energy, because the most important factor of thermal processes is thermodynamic water phase change. According to the data and analysis, acoustic cavitation by ultrasonic waves is effective method to purification of water from nanosize particles of different origin as well, as from their clusters and molecular assemblies.

1. Introduction

Ultrasonic wave as a high frequency sound wave affects on substances that refer to quantity and quality, and this property can be used in different fields. One of the most interesting applications is thermodynamical property change of fluids by ultrasonic waves, which is possible to use for water purification of different unpleasant nanoscale particles [1]. Generally, water purification considered and compared with routine water treatment methods. For instance ultrasonic wave can be used to produce pure water and some technical advantages of water treatment by ultrasonic waves comprised with the most common membrane method [2]. As sound waves travel, particles of medium vibrate more than common vibration then some

physical properties of medium like density, temperature and pressure will change [3]. These pressure changes are divided into two parts – as low-pressure and high-pressure regions. On the other hand, wave rhythm in fluid depends on longitudinal wave rhythm. Generally, there are three parts for water purification: Microbial purification is based on organism pollutants removal, Suspended solids purification is based on undissolved solids removal like sand, and Dissolved solids purification is based on ions and particles dissolved in water that is totally called the salinity and it should be considered as a the most important and complicated part of water purification.

Generally, a water treatment factory works as a huge treatment plant and is based on screening, coagulation, flocculation, sedimentation, filtration and disinfection processes, which are organized for purification of water. The process of coagulation, flocculation and sedimentation might be improved by flash mixing ultra sonication. At the same time dispersion and deagglomeration of clusters of impurities by ultra sonication are also highly depending on ultrasonic cavitation. The sound waves that propagate into the liquid result in alternating high-pressure and low-pressure cycle that applies mechanical stress on the attracting forces between the individual particles. Ultrasonic cavitation in liquids causes high speed liquid jets of up to 1000 km / h (approx. 600 mph). Such jets press liquid at high pressure between the particles and separate them from each other. Smaller particles are accelerated with the liquid jets and collide at high speeds. This makes ultrasound an effective means not only for the dispersing but for the milling of micron-size and submicron-size particles as well. Refer to last investigations this method does not decrease coagulant consumption that should be important in sludge management.

Physical properties of nanoparticles make high potentials for materials with extraordinary strengths but the extra small size of nanoparticles treatment and process is more difficult than routine processes then special method usage is inevitable. High power ultrasound is often the only method to affect nanoparticles effectively. As an illustration, mostly, high power ultrasonicators are the only efficient tool to achieve the desired milling and dispersing results of nanoparticles [4, 5].

One way of utilization of nanotechnology refers to the liquidus environment that is very common in different fields like water treatment, pharmacy, medical diagnosis and so on. Ultrasonic waves can help to improve and make nanopurification feasible then it can be so effective in different industries.

There is a routine method for surface water treatment that based on screening, coagulation, flocculation, filtration and disinfection. On the other hand, the speed and efficiency of the method is the basic feasible parameter for treatment. Ultrasound can improve coagulation, flocculation and then sedimentation that as the most important water treatment process step is efficiency and fixed price determinant.

2. Ultrasonic waves

Ultrasonic investigation and application started in 1912 after Titanic ship sinking by collision with an iceberg. Nature gave a solution to scientists then they used old communication method of sea creatures like dolphins for iceberg detection in the seawater. The method was

based on high frequency acoustic waves that created ultrasonic wave as a solution. Ultrasound was indebted to Langevin activities, and he is generally credited as the father of field of ultrasonic [2].

Despite of primer ultrasound application for obstacle detection, there are many other applications according to medium properties physical changes. Whenever ultrasonic wave as a high frequency longitudinal wave passes through liquid making the acoustic cavitation. Indeed, it forms fine bubbles in low-pressure region of fluid; because of pressure decrease then thermodynamic phase change of liquid to gas; growth of bubbles and after reach a critical size they collapse. The event of collapsing is microscopic implosion that generates high local turbulence, intense shear forces, microscopic stream and release of heat energy [6].

Dispersion and deagglomeration by ultra sonication are a result of ultrasonic cavitation. The sound waves that propagate into the liquid result in alternating high-pressure and low-pressure cycles apply mechanical stress on the attracting forces between the individual particles. Ultrasonic cavitation in liquids causes high speed liquid jets of up to 1000 km / h (approx. 600 mph). Such jets press liquid at high pressure between the particles and separate them from each other. Smaller particles are accelerated with the liquid jets and collide at high speeds. This makes ultrasound an effective means for the dispersing but also for the milling of micron-size and submicron-size particles [1].

Effective means of deagglomerating and dispersing are needed to overcome the bonding forces after wettening the powder. The ultrasonic breakup of the agglomerate structures in aqueous and non-aqueous suspensions allows utilizing the full potential of nanosize materials (**Figure 1**). Investigations at various dispersions of nanoparticulate agglomerates with a variable solid content have demonstrated the considerable advantage of ultrasound when compared with other technologies, such as rotor stator mixers piston homogenizers or wet milling methods [7].
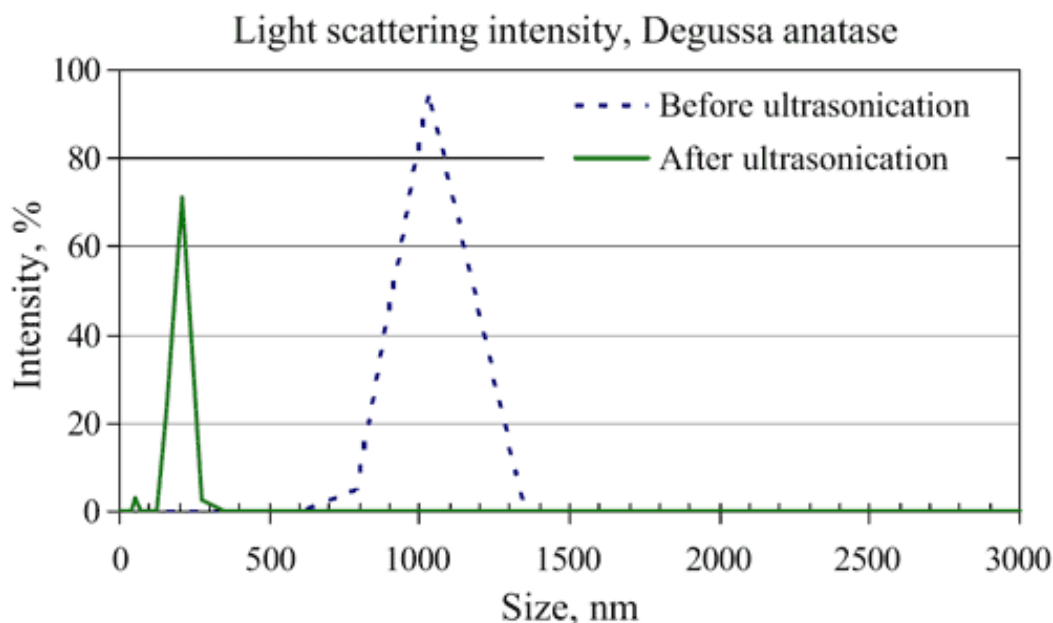
Figure 1. Ultrasonication improvement [9].

Meanwhile, because of dependence of rhythm of longitudinal wave and fluid vibration rhythm, cavitation speed (bubbles generation and collapse) is controlled by longitudinal wave

frequency. Therefore, higher frequency makes faster cavitation that clarifies the role of ultrasonic in this process but stable cavitation is commonly observed at frequencies more than 200 kHz.

3. Coagulation and flocculation in water treatment

The scheme of water treatment factory (**Figure 2**) consists of many important parts representing the different stages of water treatment process from screening, coagulation, flocculation, filtration and disinfection to storage and distribution [8].

Totally, there are three water pollution types: (1) *Colloid*, (2) *Gas* and (3) *Ion*. Colloid pollutants are tiny and suspended in water that is base of turbidity. There are different sources of turbidity but all of them are known as pollutions. Colloid routine removal are coagulation and flocculation that coagulate suspended particles and flocculate them then settle out of the water with time what called sedimentation. Adding chemical coagulate by making a homogenous solution will increase rate of suspended sedimentation by small particles combination into larger flocculates [9].
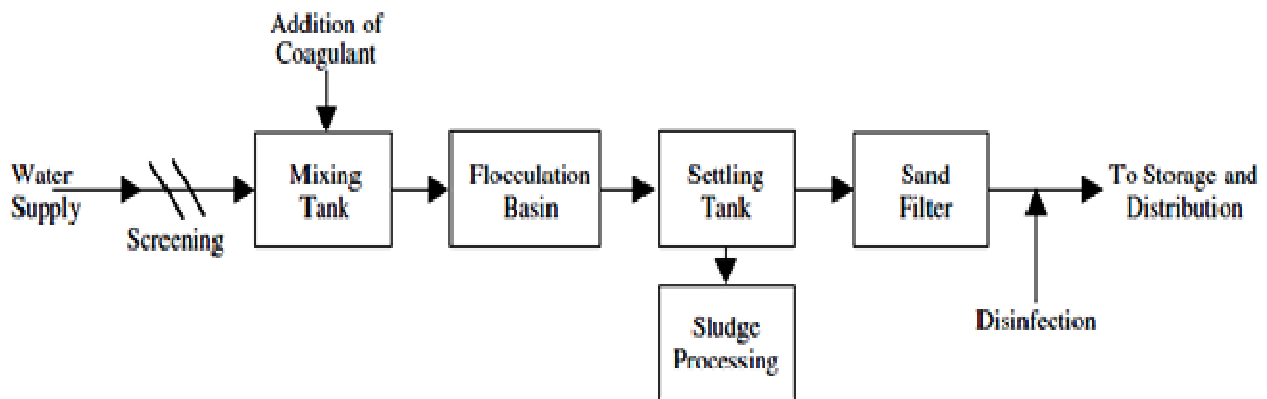
Figure 2. Basic water treatment scheme.

4. Flash mixing by ultrasound

Basically, by coagulation and flocculation turbidity, color, pathogens, algae, phosphates, bad smelland bad taste factors and some others are removed, and this is considered as an important step of water treatment. According to **Figure 2**, the treatment process mostly involves coagulation and flocculation. On the other hand, most of the parts of municipal routine method are civil constructions and their size, strengthen and isolation are total price determinative. Meanwhile, coagulants should be added to water in flash mixer for flocculation in flocculation basin. Flocculation improvement depends on different factors like PH, temperature, coagulant efficiency and so on.

Refer to coagulation efficiency as an important factor for flocculation and sedimentation, more efficient process makes some advantages as:

- Lower coagulant consumption;
- Smaller construction.

As in **Figure 2**, in the same conditions, ultrsonication improves the size of particles in solution up to 1/4 that means better mixing and 20 % lower scattering intensity,which means more homogenous solution. Totally, both of them conduct coagulation improvement, and the more efficient are flocculation and sedimentation, the more feasible is the construction.

Consequently, these important factors, not only make shorter flocculation and sedimentation time but lower coagulant consumption produce lower sludge as well,and its management after the treatment would be easier.

5. Conclusion

Using the ultrasound waves the water purification process from nanosize particles became more effective as well, as the possibility of preparation of high purity water.The nature of this process lies in ultrasound wave properties, which through the influence on oscillation characteristics of nanoparticles increase their surface energy and make them more active for participation in different physical and chemical interactions.

Ultrasound waves usage for water treatment because of lower coagulant consumption decreases the price of cleaning water: improvement of coagulation by ultrasound flash mixing not only causes the technical improvement but the financial one as well.

References

1. T. Leong, M. Ashokkumar, S. Kentish. The fundamentals of power ultrasound – A review. Acoustics Australia, 2011, 39, 2, 54-63.
2. J. Cheeke, N. David. Fundamentals and Applications of Ultrasonic Waves. 2002, Montreal, CRC Press LLC.
3. H. A. Bakhtiari, T. M. Berberashvili, P. J. Kervalishvili. Study of ultrasonic heating process for water purification. Nanotechnology Perceptions, 2016, 12, 3, 165-172
4. J. J. Ramsden. The impact of nanotechnology. Nanotechnology Perceptions, 2011, 7, 1, 28-66.
5. T. Häkkinen. Ultrasonic atomizer. US Patent # 5,063,922, Nov. 12, 1991.
6. J. H. Lienhard V, J. H. Lienhard IV. A Heat Transfer Textbook (3rd Ed.). 2006, Cambridge (MA), Phlogiston Press, 19-21 & 457-470.
7. M. Ashokkumar, R. Bhaskaracharya, S. Kentish, J. Lee, M. Palmer, B. Zisu. The ultrasonic processing of dairy products – An overview. Dairy Sci. & Technol., 2010, 90, 2, 147-168.

8. N. K. Akafuah. Visualization and Characterization of Ultrasonic Cavitating Atomizer and Other Automotive Paint Sprayers Using Infrared Thermography. 2009, Kentucky, Univ. Kentucky.

9. L. Ebensperger. Review of the CurrentS of Desalination.Water Policy Working Paper 2005-008.2005, New York, Andrew Young School of Policy Studies.www.issuelab.org/permalink/resources/4717

ANOMALIES OF MECHANICAL PROPERTIES OF LiF CRYSTALS CONTAINING HIGH CONCENTRATION OF LEAD IMPURITY

M. Galustashvili, M.Abramishvili, D. Driaev,V. Kvatchadze, S. Tsakadze

E. Andronikashvili Institute of Physics
I. Javakhishvili Tbilisi State University
Tbilisi, Georgia
maxsvet@yahoo.com

Abstract

In alkali halide crystals (AHC), the atoms of bivalent metals are basic hardening impurities. The role of impurities such as Ca and Mg is well known: they increase the yield strength and microhardness, decrease the degree of plastic deformation, etc. As for the Pb impurity, its presence in AHC causes anomalies in many parameters of the crystal. We conducted a detailed study of the peculiarities of the mechanical properties of LiF crystals containing high concentration ($1.2 \cdot 10^{-1}$ mol. %) impurity Pb. Deformable crystals (uniaxial compression, microindentation) were subjected to high-temperature (800 °C) annealing, quenching (from 500 °C) and gamma-irradiation (10 MRad). This revealed anomalous dependence of yield strength on the annealing time with a maximumat 2 h on the curve yield strength–time. Radiation processing has shown the indistinctive phenomenon for irradiated AHC plasticizing – the ultimate strain (degree of plastic deformation) is increased from 15 to 30 %. The observed effects are explained by changes in the atomic configurations of impurity Pb and their concentration at all stages and in all types of processing.

1. Introduction

Thermal, mechanical and radiation effects create various structural defects leading to hardening of the crystal and reduction of its plasticity [1, 2]. The mechanical characteristics of the crystal can be preserved or even improved by a simultaneous effect of the above-mentioned fields in different combinations, which we demonstrated by the example of alkali halide crystals [3]. The mechanical parameters of the crystal can be controlled the most efficiently by its doping [2], varying the impurity type and concentration, heat treatment conditions (annealing and quenching), and the ratio of masses and radii of matrix and impurity ions [2, 4].

In alkali halide crystals (AHC), the atoms of bivalent metals are basic hardening impurities. The role of impurities such as Ca and Mg is well known: they increase the yield strength τ_y and microhardness H, decrease the degree of plastic deformation ε_m, etc.

As for the Pb impurity, its presence in AHC causes anomalies in many parameters of the crystal, such as, in particular, heat conductivity and heat capacity [5]. The Pb impurity significantly hardens the NaCl crystal, exerts an adverse impact on the magnetoplastic effect in

a weak field instead of plasticization which is observed in the case of Ca and Mg; hardening of the sample occurs [6].

Taking into consideration a wide application of doped LiF crystals (quantum electronics, radiation dosimetry, etc.), the investigation in detail of the specific features manifested by LiF : Pb crystals during their deformation is quite topical. It represents the objective of this work.

2. Experiment

The experiments were carried out with the crystals (BJP Company) possessing a high concentration of the Pb impurity ($1.2 \cdot 10^{-1}$ mol. %) – LiF–1.For comparative experiments, we used crystals (of the same company) with the Mg impurity ($3 \cdot 10^{-2}$ mol. %) – LiF–2 and "pure" crystals LiF–3 with total concentration of bivalent impurities $\sim 10^{-4}$ mol. %.

From blocks, along cleavage planes {100}, the samples $2 \times 3 \times 6$ mm in dimensions were cut out. Part of them were annealed at 800 °C (the annealing time varied from 1 to 20 h) and cooled slowly to room temperature, another part of samples was quenched from 500 °C. The annealing temperature was maintained with accuracy of ± 5 °C. The stress-strain ratios $\tau(\varepsilon)$ of initial and annealed samples were determined. The samples were tested in rigid deformation machine DY–22 by uniaxial compression at constant rate of 10^{-3} s^{-1}. Besides, microindentation of the samples with the Vickers pyramid was carried out. The dislocation pattern on the chemically etched surface of the sample was registered with the help of an optical microscope with transmission of images to the computer monitor. Series of tests were carried out on gamma irradiated LiF–1 (10 MRad, ^{137}Cs-based source). The initial mechanical data on the samples of all three types are listed in the **Table 1** below.

Table 1. Initial mechanical data on LiF crystals.

	Yield strength, MPa	Maximal plastic deformation, %	Indentation diagonal, µm	Microhardness, GPa
LiF–1	23.0	15.0	53	1.2
LiF–2	36.0	13.0	50	1.5
LiF–3	4.4	23.0	58	1.1

3. Results and discussion

In ANC the bivalent metallic impurity with concentrations lower than the solubility limit enters the lattice in the form of substitution ion Me^{2+}; for electroneutrality, it is accompanied by cation vacancy V forming the dipole Me^{2+}V with the impurity ion. These dipoles can unite forming the dimers, trimers and more complex systems. With slow cooling from high temperature, the main portion of the impurity exists in the form of clusters of such complexes. If the concentration of Me exceeds the solubility limit or the metal is poorly soluble, with slow cooling the formation of the second phase occurs: the impurity is deposited as a precipitate having the spatial lattice differing from that of the matrix (for instance, MgF$_2$ in the LiF : Mg^{2+} crystal).

In our case, crystals LiF–1 are characterized by a high concentration of the Pb impurity ($1.2 \cdot 10^{-1}$ mol. %). It is obvious that, because of the difference between the radii of impurity and basic cations of the lattice ($R_{Pb} = 0.175$ nm; $R_{Li} = 0.155$ nm) and considerable difference of their masses ($M_{Pb} / M_{Li} \approx 30$), the solubility of Pb is low, and considerable part of the Pb impurity exists in the crystal as large second-phase particles. After chemical etching, they are manifested as recesses with flat bottoms, so-called background (ripple). In LiF-1 the density of such recesses 100 nm in size makes up 10^6 cm^{-2}.

As a rule, the process of precipitation is accompanied by a considerable increase in the yield stress, and the component of τ_y due to the formation of the second-phase particles turns out to be considerably larger than the one determined by the impurity being in the solid solution. Very large precipitates, sometimes visible to the naked eye, do not contribute to the hardening value – as if the matrix is cleared of the impurity [2, 7]. This is clearly evidenced by the initial values of τ_y given in the **Table 1**; inspite of a lower concentration of the readily soluble Mg impurity, the hardness of LiF–2 is higher than that of LiF–1.

In **Figure 1** (Curve 1) the diagram of compression $\tau(\varepsilon)$ of the initial LiF–1 sampleis shown, illustrating the behavior, being typical for rigid samples [1]: an extended yield line and high yield stress; the strain hardening is actually linear within the measurement accuracy, which is the characteristic of single slip in AHC.
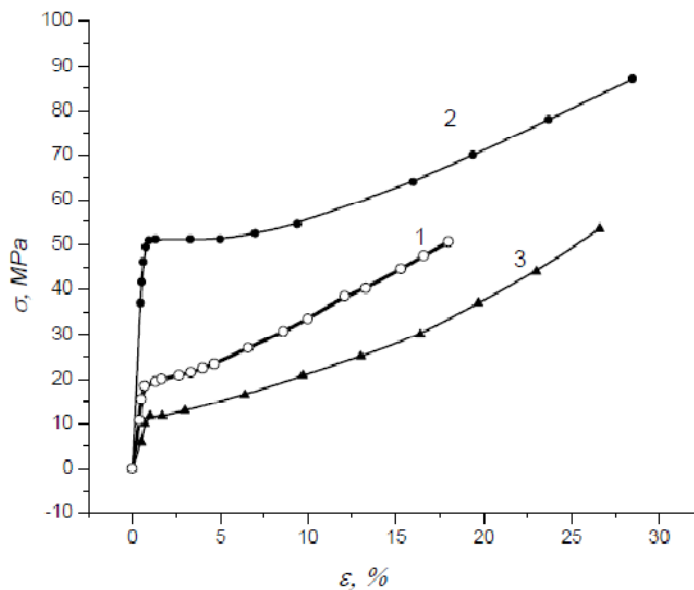
Figure 1. Stress–strain diagrams of crystals LiF–1: 1 – initial; 2 – gamma-irradiated; 3 – quenched from 500 °C.
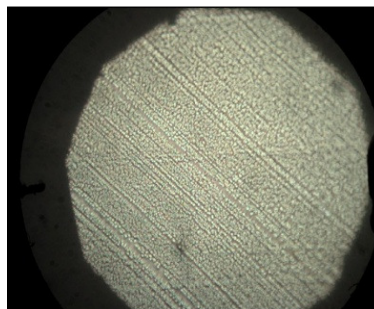
Figure 2. Dislocation pattern of the deformed initial sample LiF–1 ($\varepsilon \approx 2\%$).

With the uniaxial compression along the <100>, usually two slip systems along which the deformation occurs are distinguished [1]. However, in crystals LiF–1 doped to high concentrations, asymmetry of the slip systems (the average starting stress of the formation of slip strips in one of the systems is lower than in another one) intensifying during the deformation is observed. That is, we observe the spontaneous release of the main slip system (**Figure 2**), which considerably reduces the hardening coefficient and extends the yield area contributing to the plasticization of the crystal.

In addition to the high concentration of the impurity, the rigidity of LiF–1 is provided by a unique dislocation-free structure of the crystals (which is evidenced by the chemically etched surface), rarely occurred in AHC, which can be explained by the absence of thermal stress during crystal growth.

Isothermal high-temperature annealing (800 °C) is characterized by a nonmonotonic time dependence of the yield stress (**Figure 3**, solid curve).
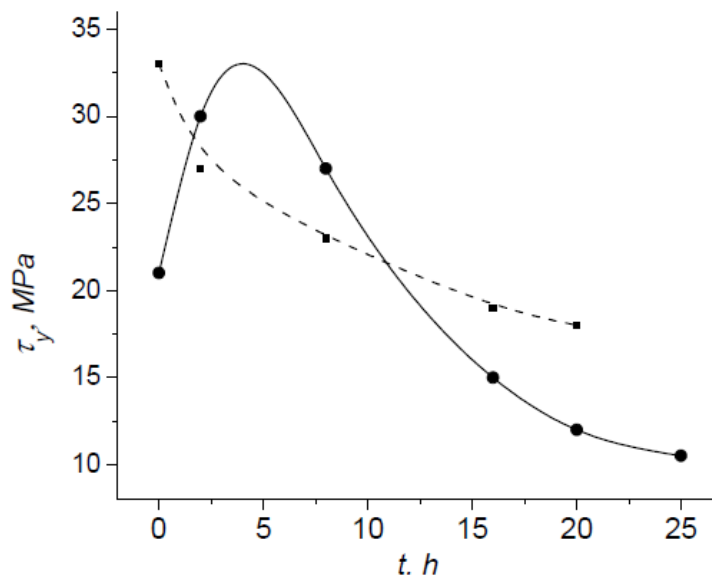
Figure 3. Time dependence of the yield stress τ_y of crystals LiF–1 (solid curve) and LiF–2 (dotted curve) during annealing at 800 °C.

The observed increase in the yield stress τ_y at the initialstages of annealing (1 – 2 h) is accompanied by downsizing of the second-phase particles (characteristic ripple on the surface of the etched sample disappears). As this process, i.e. transition of the impurity into a dispersed state with formation of dipole clusters, develops, $\tau_y$increases due to the interaction of dislocations with these clusters. With the increasing time of annealing (up to 20 h), the size of clusters decreases, while their number increases; a typical situation for annealing of LiF is observed: increasing τ_y and decreasing ε_m. Really, in the case of LiF–2 with high concentration of the readily soluble Mg impurity (dotted curve in **Figure 3**) and "pure" crystals LiF–3, τ_y decreases with acquiring the constant value, and plasticity $\varepsilon_m$increasesfrom the first hours of annealing.

Quenching of LiF–1 at 500 °C gives a significant effect. As it is seen in **Figure 1** (Curve 3), softening of the quenched sample takes place: the yield strength decreases by a factor of three and the plasticity increases significantly (30 %). Besides, within the elastic limit, a deviation of the stress–strain dependence from the y-axis, which indicates that, in the "softened" sample, a

microflow is initiated. It is well known that quenching transfers the impurity into the dispersed state, reducing the number of both large and small clusters. If, in the annealed crystals, τ_y is generally determined by the interaction of dislocations with relatively large complexes, in the quenched samples it is determined by the elastic interaction between dislocations and impurity-vacancy dipoles. It should be noted that, in the case of "soft" crystals LiF–3, the quenching from 500 °C does not result in considerable changes in mechanical parameters, moreover, embrittlement of the sample takes place.

The γ-irradiated sample LiF–1 behaves unusually (**Figure 1**, Curve 2). The character of strain curves hardly changed after irradiation, while the irradiation resulted in the extension of the yield area (up to $\varepsilon_m \approx 5$ %) and somewhat reduction of the strain hardening coefficient (**k**). Both these factors facilitate the preservation of the irradiated sample plasticity ($\varepsilon_m \approx 30$ %) (**Figure 1**, Curve 2) (Earlier we observed a similar effect with the LiF crystals irradiated with neutrons [8]). It is well known that the yield stress of the crystal increases with the increasing fluence and approaches the strength limit of the sample. Inspite of intensification of the initial asymmetry and a low value of k, eventually, after anomalously high plasticity, its sharp decrease should be observed.

The results of microindentation of LiF–1 supplement the data on the uniaxial compression. Along with the yield strength measurements, this method is widely used for determination of the hardening effect of the impurity. We can judge both about quantitative and qualitative changes in the crystal rigidity caused by the impurity by the changes in the dislocation rosette, because the link between the quantities τ_y and ε_m, and the parameters characterizing the local strain – the indentation diagonal d (or microhardness $H = 1854\, P/d^2$) and the length l of the rays of the dislocation rosette was traced. The investigation of impurity hardening showed that the increase in microhardness H was accompanied by reduction of dislocation mobility (l became shorter), the latter parameter being especially sensitive to the changes in the crystal state whether it is irradiation, doping or thermal treatment [9]. Besides, impurity complexes, which are rigid athermal stoppers, stimulate the process of double transversal slipping (DTS) of screw dislocations [1, 9] and determine the frequency of these actions.

Figure 4 illustrates the above-given statement. It shows the indentations and the dislocation structure on plane (001) of crystals LiF–1 and LiF–2: bypassing of the second-phase particles by dislocations promotes the shear in the slip strip and the observed transverse slipping (**Figure 4a**). In a more rigid sample LiF–2, the Mg impurity inhibits the dislocations more strongly (the dislocation rosette ray in **Figure 4b** is shorter), but, due to high solubility of the impurity and absence of its clusters, there are no sources of transverse slipping which cause the distortion of the rosette rays.
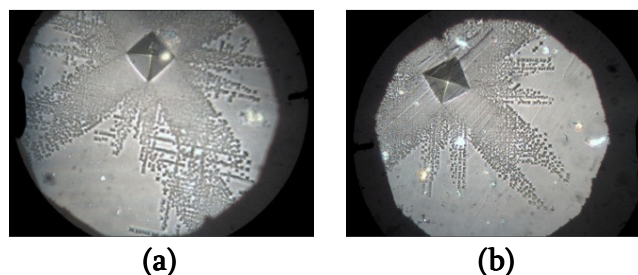

(a)　　　　　　　　　　(b)

Figure 4. Fragments of the dislocation rosette on
plane (001) of crystals LiF–1 (a) and LiF–2 (b).

Thus, crystal LiF with the high concentration of lead showed a strong dependence of mechanical properties on thermal treatment and irradiation: hardness changed from 8 to 27 MPa, and maximum strain ε_m – from 10 to 30 %. It is likely that, extending the types of effects and using the procedure of their combining, we developed, in combination with the data on atomic configurations of the Pb impurity and their concentrations at all stages of treatment, we will obtain a spectrum of targeted effects.

Acknowledgement

References

1. B. I. Smirnov. Dislocation Structure and Crystal Hardening.1981, Leningrad, Nauka.
2. L. M. Soifer. Hardening of alkali halide crystals with bivalent impurities. In: Physics of Condensed State, XXIV. 1973, Kharkiv, 45.
3. E. L. Andronikashvili, M. V. Galustashvili, R. D. Dokhner. Defects in alkali halide crystals irradiated under applied stress. In: Defects in Insulating Crystals. 1981, Riga, 439.
4. R. B. Morgunov. Generation modes of nonequilibriumEu^{2+}dimers and influence of a magnetic field on their reconstruction in NaCl : Eu crystals. Phys. Solid State, 2011, 53, 4, 786.
5. V. I. Altukhov, V. G. Kvatchadze. Phonon scattering on small-radius colloids in KCl crystals. Physica Status Solidi B, 1978, 85, 2, 769.
6. E. V. Darinskaya, M. V. Koldaev. Magnet-stimulated hardening of the NaCl(Pb) crystals. JETP Lett.,1999, 70, 3, 226.
7. R. P. Zhitaru, N. A. Palistrant. The influence of thermal processing on the specific mobility of edge and screw dislocations in NaCl crystals.Phys. Solid State, 1999, 41, 6, 947.
8. M. V. Galustashvili, D. G. Driyaev, Z. K. Saralidze. Spontaneous separation of the main slip systemin alkali halide crystals under uniaxial compression. Phys. Solid State, 1985, 27, 1, 8.
9. Y. S. Boyarskaya, D.Z. Grabko, M. S. Katz. The Physics of Microindentetion Processes. 1986, Chisinau, Shtinitsa.

INFLUENCE OF GOLD NANOPARTICLES ON MORPHOLOGICAL AND FUNCTIONAL CHARACTERISTICS OF BONE MARROW MESENCHYMAL STEM CELLS: MTT ASSAYS AND SPECTROSCOPIC DATA

N. Volkova [1], O. Pavlovich [1], O. Fesenko [2], O. Budnyk [2], A.Goltsev [1]

[1] Institute for Problems of Cryobiology & Cryomedicine
National Academy of Sciences of Ukraine
Kharkiv, Ukraine
[2] Institute of Physics
National Academy of Sciences of Ukraine
Kyiv, Ukraine
fesenko@iop.kiev.ua

Abstract

The rapid emergence of gold nanoparticles (AuNPs) technology holds great promise for future applications in medicine, including stem cell therapy. But for wide biomedical applications of AuNPs it is needed to define the optimum quantity of nanoparticles by the balance between pronounced direct effect and low side effects like unwanted cytotoxicity. This study reports about impact the different concentrations of uncovered AuNPs have on both morphological and functional properties of bone marrow mesenchymal stem cells (MSCs). It was found that AuNPs at the concentration of 1.5 µg / ml are safe of MSCs, while increase it up to 6 – 9 µg / ml has a toxic effect, manifested by the reduction of colony formation, proliferative activity and apparent apoptosis in MSCs observed by MTT method and FTIR spectroscopy of single cells.

1. Introduction

Au NPs are very attractive for usage in biomedical products due to their unique physical and chemical properties and conventional methods of synthesis [1, 2]. Many approaches to development of medical nanotechnology are based on involvement of metal nanoparticles [3, 4]. These nanoscale metals can have different impact on both physical and chemical properties of cells, depending on their quantity or therapeutic dose [5, 6]. AuNPs are used for cancer targeted therapy and as a contrast agent for biomedical imaging [7], hence, identification of their possible cytotoxic effects is an important direction of nanobiotechnological research [8].

Despite the fact that cytotoxycity of NPs is a hot topic nowadays, there is a serious lack of complete information describing interaction of AuNPs with mammalian tissues. More precisely, intracellular localization of NPs still remains an issue to be addressed [9]. The mammalian tissues consist of many specialized cells, such as epidermal skin ones, bone marrow mesenchymal stem cells, neuronal or immune system cells. Such variety is possible to the differentiation process. This process includes an activation of some genes and deactivation of others, resulting in production of specific cells. Generally, only stem cells and progenitor cells have the ability to differentiate into specialized cell types. Stem cells derived from embryos or adult tissues of organisms can reproduce themselves for a limited period of time [10].

The impact of metal NPs on stem cells has been scarcely studied so far [11]. Possible interaction could lead to unpredictable consequences in the functioning of organs and tissues as long as all the cells encountered in the primary division of stem cells do not cease to exist. There is a growing interest to employ MSCs as vehicles for targeting drug delivery therapy due to their inherent tumor-trophic migratory properties [12]. MSCs are normally taken from various tissues, such as bone marrow, fat and muscles involved in tissue homeostasis and regeneration [13]. Apart from some preliminary studies [14, 15] there is no data that describes the impact of uncovered AuNPs on the proliferative characteristics of MSCs. For studying the effect of influence of uncovered AuNPs on stem cells the bone marrow MSCs of rats we selected as a model object. As it has been reported [16], AuNPs have a size-dependent cytotoxicity and NPs less than 15 nm are only considered to be toxic.

Determination of the metal NPs' influence on different types of cultured cells requires evaluation of morphological and functional parameters, namely, viability (membrane integrity), capacity to adhesion and proliferation. To determine the biosafety and compatibility of metal NPs with cells, most researchers used cytological, biochemical and biophysical methods. Infrared and Raman spectroscopies are complimentary informative and non-invasive techniques, capable to provide the essential information for the diagnosis and evaluation of the cell's functionality without damaging it and use of additional markers [17]. Generic from them is the Single Cell Spectroscopy (SCS), a label-free method for the analysis of individual parameters of living cells both in vivo and in vitro [18], because obtained spectrum contains the marker bands (associated with characteristic functional groups) of nucleic acids, proteins, carbohydrates and lipids, thus, reflecting cellular genotypes, phenotypes and physiological states.Here we present the study of what effect will have different concentrations of 15 nm Au NPs on the morphologycal and functional characteristics of bone marrow MSCs.

2. Experimental

2.1. Samples

MSCs were isolated from resected femur of mice ($n = 7$, weighing $20 - 25$ g) by washing out with Hanks' solution (PAA, Pasching, Austria), followed by flushing through a needle with gradually decreased diameter. The next step was centrifugation at $834 \times g$ for 5 min. The cells were resuspended in culture medium and plated on culture flasks (PAA) with 10^3 cells per cm^2 density. Cultural medium contained: Iskove's Modified Dulbecco's Medium (PAA), 10% fetal bovine serum (FBS) (HyClone, Logan, UT, USA), gentamicin (150 mg/mL) (Farmak, Kyiv, Ukraine), and amphotericin B (10 mg/mL) (PAA). Cultural medium was changed every three days. We used standard culture conditions (37 °C, 5 % CO_2, 95 % humidity) in a CO_2 incubator (Sanyo, Osaka, Japan). MSCs were detached with 0.25% trypsin-EDTA (Hyclone), which was replanted in other flasks with 1 : 2 ratios at 80 % confluence. Third passage MSCs were used in all experiments [19]. All manipulations were carried out in a strict accordance with the requirements of the "European Convention for the Protection of Vertebrate Animals used for Experimental and other Scientific Purposes". The protocol was approved by the Committee in the Ethics of Animal Experiments of the Institute for Problems of Cryobiology and Cryomedicine of the National Academy of Sciences of Ukraine (Permit No 2014 – 02).

AuNPs were obtained by citrate synthesis [20] with an initial metal concentration of 45 mkg / ml. The average size of AuNPs was 15 nm. The range of investigated concentrations was 1.5, 3, 6 and 9 mkg/ml. AuNPs were entered into the MSCs by a passive diffusion.

2.2. Methods

*Morphological characteristics of MSCs and localization of AuNPs.*Morphological characteristics of cells at culturing conditions were evaluated on the inverted microscope. The preparations of MSCs were fixed with 4 % paraformaldehyde solution (PanEco, Moscow, Russia) and stained with crystal violet (Sigma–Aldrich, USA) for 10 min at room temperature. Localization of AuNPs was evaluated by confocal scanning microscopy (Carl Zeiss LSM 510 Meta, Germany) with excitation λ = 405 nm. Processing of the data was carried out using LSM Image Examiner and AxioVision Rel. 4.7.

*Fibroblast colony forming unit assay.*Cloning efficiency was determined on $1 \cdot 10^6$ seeded cells by counting the colonies which contained at least 30 cells that defined as colony forming unit of fibroblasts (CFU–F). Cells were seeded in 6-well plates at low density limiting dilution (initial concentration 100 cells / cm², final concentration 15 cells / cm²) and cultured in IMDM with 20 % FBS for 14 days. The cells were fixed with 4 % paraformaldehyde solution and stained with crystal violet. Number and size of colonies and cells in them were determined.

MTT (3-(4,5-dimethylthiazol-2-yl)-2,5-diphenyl tetra-zolium bromide) assay. On the 1, 3, 5, 7, 10 and 14 days of cultivation the number of viable cells was determined by MTT test, which is based on the ability of living cells to reduce a dehydrogenase 3-(4.5 dimetiltiazolil-2) – 2.5-difeniltetrazolium bromide (MTT, Sigma–Aldrich, USA) to insoluble in water blue formazan crystals [21]. Culture medium without cells was used as a control.

*IR measurements.*The FTIR (Fourier transform infrared) spectra of single cells were acquired in reflection mode on a FTIR Spectrometer VERTEX–70 equipped with Hyperion 1000 Microscope (Bruker). For the data processing the following protocol has been adopted: (1) collecting of IR spectrum, (2) baseline correction, (3) spectrum normalization in OH–NH range, (4) spectrum normalization in amide I range, and (5) spectrum normalization in amide II region.

*Statistical analysis.*The results were processed with a non-parametric Mann–Whitney U-test using "Statistica 8" program. The results were presented as mean±standard deviation. $p < 0.05$ was considered statistically significant.

3. Results and discussion

In our previous studies [22, 23], it was found that AuNPs added to the culture medium accumulated on the cell membranes and at high concentrations (> 9 μg / ml) adsorbed on the nucleus membrane. At a temperature of 37 °C endocytosis occurs in cells, i.e. process of capturing substances by retracting cell plasma membrane portion, followed by formation of vesicles inside the cells with extracellular content. All types of cells in the body use the process of endocytosis to communicate with the biological environments. This process is energy-dependent through which cells assimilate ions and biomolecules. Particularly, the cells assimilate nutrients and signaling molecules to obtain energy and interact with other cells, respectively [24, 25].

The experimental data point to the fact that the nanoparticles enter the cell passively along with other substances. AuNPs at concentrations ≥ 12 μg / ml reduce the rate of SPEV cells proliferation if compared with the control [22]. Early we studied the viability, proliferative capacity and apoptosis / necrosis in human fibroblast culture prior to and after cryopreservation in the presence of gold nanoparticles. The use of AuNPs under low concentrations resulted in an increased proliferative activity of human fibroblast culture with no activation of apoptosis and necrosis [23].

Using a scanning microscopy of MSCs culture preparations it was found that AuNPs (6 µg / ml) partially localized in the cytoplasm and nucleus (**Figure 1**). The images shown on the **Figure 1** clearly reveal the outline of the cells and the red regions indicating the presence of gold, especially around the nucleus. Background glow of the environment was absent. Thus, it was found that AuNPs added to the culture medium penetrated through cell cytoplasm by passive diffusion and localized on the nucleus (luminescence in 540 – 583 nm and emission 593 – 647 nm).
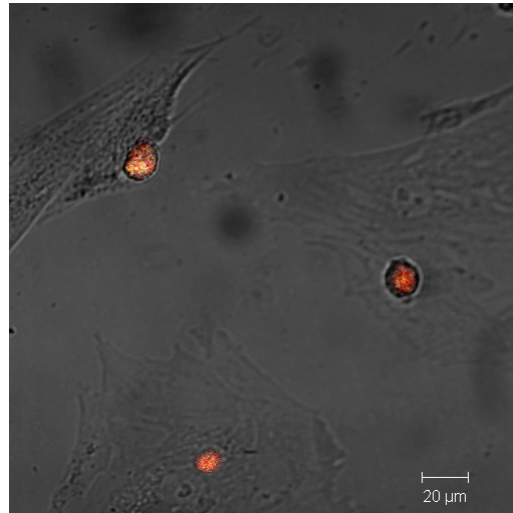
Figure 1. Bone marrow MSCs with AuNPs 6 µg / ml, 7th day culturing. Confocal laser microscopy. Pointers is a localization of AuNPs on the nucleus of cells.
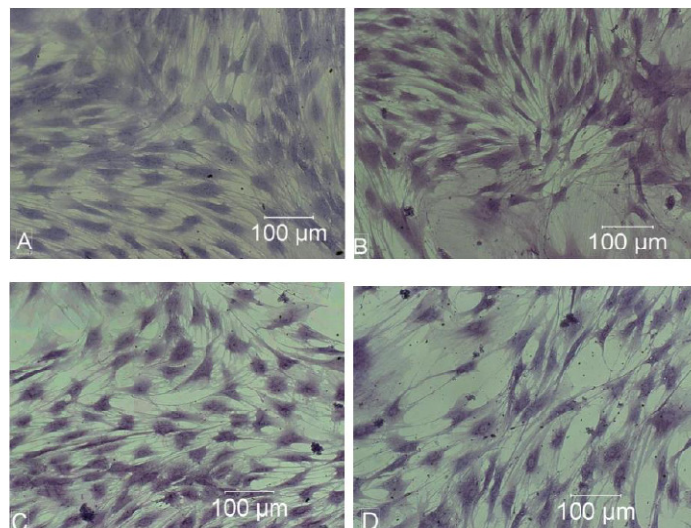
Figure 2. The culture of bone marrow MSCs: Control (A), AuNPs_1.5 (B), AuNPs_6 (C), and AuNPs_9 µg / ml (D), 7th day culturing.

During the bone marrow cells subculture the heterogenity of adhesive cells decreased and on the 3th passage most of the cells had fibroblast-like morphology. Their morphological characteristics after addition of different doses of AuNPs to the culture medium were examined under light microscopy (**Figure 2**).The cells which adhered to plastic had fibroblast-like morphology and formed the monolayer sites with 10 – 15 cells on the 5 – 7th observation dayThe organization of the cell cytoplasm, shape and size of cells in all groups did not change.In

the culture of MSCs with addition of AuNPs in concentrations of 1.5, 6, 9 µg / ml the small fibroblast-like cells were observed. On the 14th day of MSCs culturing a 90 % confluent was found in the control samples. In the cell cultures with add of 9 µg / ml AuNPs the monolayer density reached a 75 %.

Single-cell bone marrow suspensions can be cultured in vitro under conditions that facilitate the formation of stromal fibroblast colonies. Circumstantial evidence supports the conclusion that each colony is derived from a single initiating cell termed a colony-forming unit-fibroblast (CFU–f). A proportion of CFU–f demonstrates extensive proliferative potential both in vitro and in vivo [26]. Usage of low cell concentration ($10 - 15$ cells / cm^2) promotes the formation of individual colonies of fibroblasts with a frequency of $3 - 4$ per 100000 of planted cells.
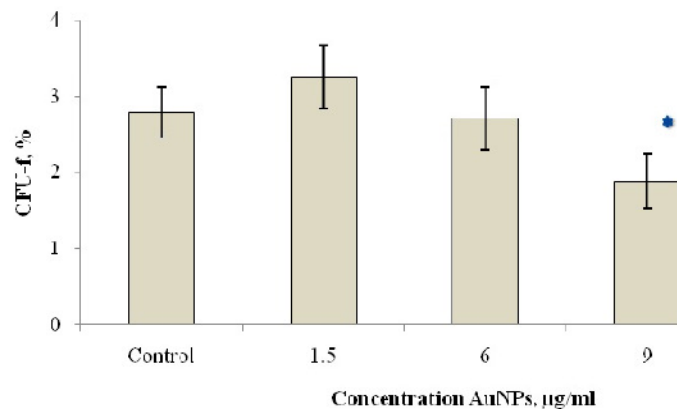
Figure 3. Clonogenic ability of MSCs cultured with addition of AuNPs.
Note: *The result significantly differs with the control ($p \leq 0.05$).

After addition of AuNPs to the culture medium large (> 300 cells), average (50 to 300 cells) and small (30 to 100 cells) colonies were formed. It is known that differences in colony morphology indicate their different qualities of CFU–f within one population of stromal cells. For the analysis the wells that contain all types of fibroblast cell colonies with more than 30 cells were selected [27]. The results are shown in **Figure 3**.

After isolation of individual colonies of MSCs cultured with the addition of AuNPs at a concentration of 1.5 µg / ml and further passaging the formation of new colonies was observed. Descendants of MSC colonies cultured with the addition of low concentrations of AuNPs actively proliferated and formed a monolayer. In this application AuNPs at concentrations of 9 µg/ml decreased the colony-formation activity in the further subculture.

The results of influence of AuNPs in different concentrations in the composition of growth medium on the expansion of bone marrow MSCs in vitro are shown in **Figure 4**.

After a day of culturing with AuNPs in concentration of 1.5 and 9 µg / ml a cell number did not significantly differ from the control. It was found that the use of AuNPs in a concentration of 6 and 9 µg / ml in the culture medium led to a significant reduction in population growth since the 3rd day of culture, namely in 1.6 and 1.7 times compared to control respectively. On the 7th day this difference was 1.3 and 1.4 times, on the 14th day it was 1.5 and 1.7 times respectively for the concentration of 6 and 9 µg / ml in the culture medium. Adding of AuNPs at concentration of 1.5 µg / ml did not lead to significant changes in the studied index during the entire period of observation. The dynamics of culture growth in the control and groups with AuNPs at concentrations of 1.5, 6 and 9 µg / ml was similar, but it differed in a rate.
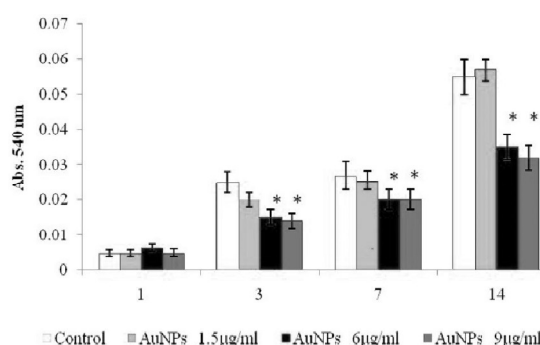
Figure 4. Proliferative ability of MSCs cultured with addition of AuNPs.
Note: *The result significantly differs with the control ($p \le 0.05$).

With the aim of having more detailed information about how AuNPs influence the cell, the following issues should be addressed: (i) a possible impact of AuNPs on cellular metabolism; (ii) applicability of AuNPs as cellular markers; (iii) an identification of cellular components, which might got affected by AuNPs, e.g. lipid membrane or macromolecular nucleic acids (DNA, RNA); and finally, (iv) which cellular components give maximum contribution to the IR signal from a single cell with AuNPs. Working on solving this puzzle we analyzed the profiles of so-called marker bands of a cell's main components, which are presented in **Table 1**.

Table 1. The regions of marker bands for a cell.

Amide I, cm⁻¹	Amide II, cm⁻¹	Nucleic acids, cm⁻¹	vCH₂, cm⁻¹	vCH₃, cm⁻¹
1600 – 1710	1483 – 1595	1000 – 1140	2900 – 2944	2945 – 2980

Table 2. IR band positions for Amide I and Amide II and their ratio.

Sample	IR band for Amide I		IR band for Amide II		Amide I / Amide II IR bands ratio
	Position, cm⁻¹	Intensity, a.u.	Position, cm⁻¹	Intensity, a.u.	
Control (MSCs no Au NPs)	1646	0.0573	1535	0.0388	1.314 ± 0.070
1.5 µg / ml of Au NPs	1647	0.1126	1549	0.0801	1.231 ± 0.020
6 µg / ml of Au NPs	1639	0.0224	1536	0.0182	1.406 ± 0.140
9 µg / ml of Au NPs	1643	0.0670	1543	0.0510	1.477 ± 0.160

We proceeded by performing FTIR spectroscopy of bone marrow MSCs as such (control set) and those cultivated with AuNPs in concentrations of 1.5, 6 and 9 µg / ml for 10 days. The measured curves are presented in **Figure 5**. The spectra were analyzed by starting with comparison of absolute intensities of the marker bands and followed with normalization on vN–H intensity at ~3285 cm⁻¹ for the NH ligand, on Amide I band at ~ 1640 cm⁻¹ and on Amide II band at ~ 1540 cm⁻¹ (marked with dotted lines in **Figure 5**). The exact values of IR marker bands intensities for Amide I and II are reported in **Table 2** together with their ratio for different concentrations of AuNPs. The Amide I / Amide II ratio is believed to reflect some processes occurring in the cell and it increases when apoptosis is taking place [28]. From **Table 2** it comes out that Amide I / Amide II ratio raises with increasing concentration of AuNPs, hence, evidencing the occurrence of apoptosis in the cells under study.
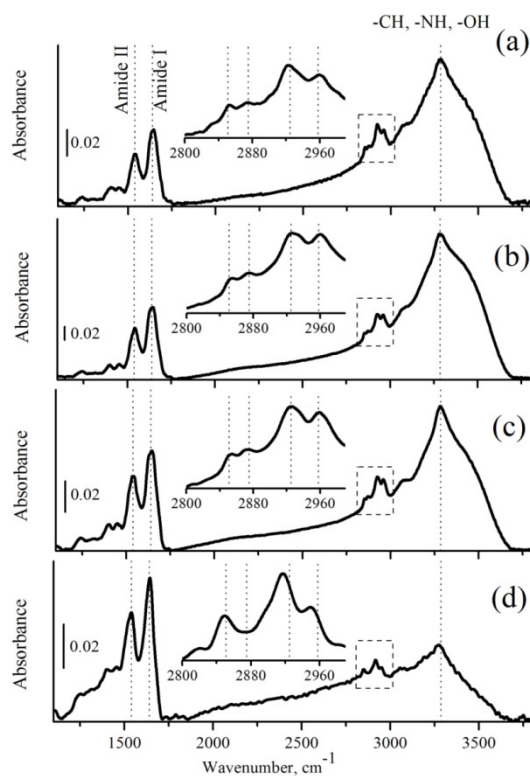
Figure 5. FTIR spectra of bone marrow MSCs after
10 days of culturing: control set (a), and sets with AuNPs
of different concentrations: 1.5 (b), 6 (c), and 9 μg / ml (d).
Enlarged the C–H stretching region is shown in the inset.

The insets in **Figure 5** show a zoom of CH stretching region for each sample. The reference dotted lines mark the positions for asymmetric and symmetric stretching modes of methyl ($v_{as}(CH_3)$ = 2958 cm^{-1} and $v_s(CH_3)$ = 2875 cm^{-1}) and methylene ($v_{as}(CH_2)$ = 2925 cm^{-1} and $v_s(CH_2)$ = 2851 cm^{-1}) groups [29]. Similarly to amide bands, we processed the IR intensities in the regions of asymmetrical stretching of CH_2 groups (2900 – 2944 cm^{-1}) and of CH_3 ones (2945 – 2980 cm^{-1}) defining precisely positions of the respective bands for each sample and taking the CH_2 / CH_3 ratio, which might be considered as a marker for the cell growth. We found that there is an increase of CH_2 / CH_3 ratio over the time of cell culturing, which stands for the cell growth. The calculated CH_2 / CH_3 ratios for all the samples are visualized in figure 6a as a histogram. Excluding the control sample, there is a trend for almost exponential growth of CH_2 / CH_3 ratio with increase of AuNPs concentration. The molecular mechanism defining the increase of CH_2 / CH_3 ratio is still unclear, but it could be attributed to the increasing number of lipid second messengers that regulate the cell's growth or to a slight decrease in the volume of the cells after the cells were grown. Indeed, the reduction of cell volume corresponds to increase in their surface-to-volume ratio.

In order to evaluate the relations between CH_2 and CH_3 groups the integral area of respective vCH bands were calculated and their ratios versus concentration of Au NPs are shown in **Figure 6b**. Apart of the control sample, there is clear linear decline of CH_2 / CH_3 ratio with increasing AuNPs concentration. This is an opposite tendency to what was observed for IR band intensities CH_2 / CH_3 ratio (**Figure 6b**). This means that with addition of AuNPs in quantities more than 1.5 μg / ml the $v_{as}CH_2$ bands become more intense and narrower. Relative increase of CH_2 groups is indicative for inhibition of cell growth and may suggest occurrence of

apoptosis. It has to be mentioned that in case of MSCs cells the region $2800 - 3000$ cm^{-1} is dominated by the absorption bands of aliphatic chains (mainly phospholipids and fatty acids), hence, observed changes in IR bands are due to the expanding proportion of phospholipids in biomass. On the other side thin-layer chromatography confirmed [30] that a dynamic and / or compositional change of the plasma membrane, rather than increases in lipase activity or fatty acid production, appears to account for the increase in the CH$_2$ / CH$_3$ signal intensity ratio during apoptosis.
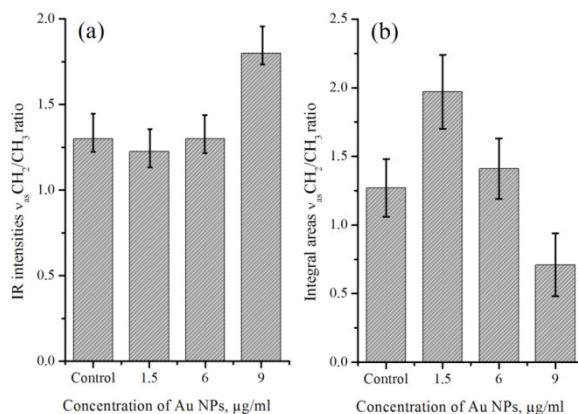
Figure 6. Ratio of IR intensities of asymmetrical CH$_2$ / CH$_3$ stretching modes (a) and ratio of their integral summations (b) measured on bone marrow MSCs after having been cultivated with AuNPs of different concentrations.

Above mentioned observations of FTIR data allowto conclude that addition of AuNPs in concentrations of $6 - 9$ μg /ml to bone marrow MSCs results in inhibition of cells growth due to some degradation processes, while 1.5 μg / ml of AuNPs does not affect appreciably the vibrational profile of cells. It should be noted that the effect of AuNPs on MSCs is dose-dependent, increasing of concentrations up to 9 μg / ml leads to dramatic changes in the range of spectra which assigns to cell membranes and decreasing of signal from RNA / DNA because AuNPs can cause to structural chromosome rearrangement, having a prolonged nature, namely their decondensation. This process may be accompanied be the dissociation or redistribution of minor components of chromatin.

Thus, our study indicates that toxic effect of AuNPs on bone marrow MSCs can be avoided if the concentrations of about1.5 μg / ml are used; higher concentrations cause the reduction of cell colonies, proliferative activity and increase in Amide I / Amide II ratio, which might indicate the presence of apoptotic processes.

Thus, the development of nanobiotechnologies is based on the study of the interaction of nanoparticles with biological systems, biosafety in usage of nanostructured inert materials which can be used in the design of the new biosensor systems. Also, the obtained results are related to the field of applied nanotechnology, which extends to clinical medicine, especially in development of addressed drug delivery to target cells or organs.

4. Conclusions

It was concluded that the use of AuNPs concentrations of 1.5 μg / ml in the culture medium does not cause changes in morphology, colony formation and proliferation of bone marrow MSCs. The applying of AuNPs concentrations 6 and 9 μg/ml to bone marrow MSCs has a cytotoxic effect, manifested in the reduction of colony formation, proliferative activity and

apparent apoptotic processes. The results obtained by FTIR spectroscopy of single cells show the presence of changes in spectra of MSCs with AuNPs concentration 9 µg / ml which are characteristic markers for apoptosis too. So, FTIR spectroscopy can be used jointly with MTT assays as non-invasive experimental tool for cell studies and for additional data providing.

Acknowledgements

References

1. X. Zhang. Gold nanoparticles: Recent advances in the biomedical applications. Cell Biochem. Biophys., 2015, 72, 771-775.
2. L. Dykman, N. Khlebtsov. Gold nanoparticles in biomedical applications: Recent advances and perspectives. Chem. Soc. Rev., 2012, 41, 2256-2282.
3. N. S. Abadeer, C. J. Murphy. Recent progress in cancer thermal therapy using gold nanoparticles. J. Phys. Chem. C, 2016, 120, 4691-4716.
4. W. Zhou, X. Gao, D. Liu, X. Chen.Gold nanoparticles for in vitro diagnostics. Chem. Rev., 2015, 115, 10575-10636.
5. A. M. Alkilany, C. J. Murphy. Toxicity and cellular uptake of gold nanoparticles: what we have learned so far? J. Nanopart. Res., 2010, 12, 2313-2333.
6. A. Gerber, M. Bundschuh, D. Klingelhofer, D. A. Groneberg. Gold nanoparticles: recent aspects for human toxicology. JOMT, 2013, 8, 32-38.
7. K. Y. Choi, G. Liu, S. Lee, X.Chen.Theranosticnanoplatforms for simultaneous cancer imaging and therapy: Current approaches and future perspectives.Nanoscale, 2012, 4, 330-342.
8. E. Boisselier, D. Astruc. Gold nanoparticles in nanomedicine: Preparations, imaging, diagnostics, therapies and toxicity. Chem. Soc. Rev., 2009, 38, 1759-1782.
9. R. Levy, U. Shaheen, Y. Cesbron, V. See. Gold nanoparticles delivery in mammalian live cells: A critical review. Nano Rev., 2010, 1,doi: 10.3402/nano.v1i0.4889.
10. M. F. Pittenger, A. M. Mackay, S. C. Beck, R. K. Jaiswal, R. Douglas, J. D. Mosca, M. A. Moorman, D. W. Simonetti, S. Craig, D. R. Marshak. Multilineage potential of adult human mesenchymal stem cells. Science, 1999, 284, 143-147.
11. Y. Kohl, E. Gorjup, A. Katsen–Globa, C. Büchel, H. von Briesen. H. Thielecke.Effect of gold nanoparticles on adipogenic differentiation of human mesenchymal stem cells. J. Nanopart. Res., 2011, 13, 6789-6803.
12. K. Shah. Mesenchymal stem cells engineered for cancer therapy. Adv. Drug Deliv. Rev., 2012, 64, 739-748.
13. C. Greulich, S. Kittler, M. Epple, G. Muhr, M. Köller.Studies on the biocompatibility and the interaction of silver nanoparticles with human mesenchymal stem cells. Langenbecks Arch. Surg., 2009, 394, 495-502.
14. J. H. Fan, W. I. Hung, W. T. Li, J. M. Yeh. Biocompatibility study of gold nanoparticles to human cells. In: 13th Int. Conf. Biomed. Eng. (Eds. C. Lim, J. H. Goh) – IFMBE Proc., 23. 2009, Springer, Berlin, 870-873.

15. C. Yi, D. Liu, C. Fong, M. Yang. Gold nanoparticles promote osteogenic differentiation of mesenchymal stem cells through p38 MAPK pathway. ACS Nano, 2010, 4, 6439-6448.
16. Y. Pan, S. Neuss, A. Leifert, M. Fischler, F. Wen, U. Simon, G. Schmid, W. Brandau, W. Jahnen–Dechent. Size-dependent cytotoxicity of gold nanoparticles. Small, 2007, 3, 1941-1949.
17. K. Ataka, J. J. Heberle. Functional vibrational spectroscopy of a cytochrome C monolayer: SEIDAS probes the interaction with different surface-modified electrodes. J. Am. Chem. Soc., 2004, 126, 9445-9457.
18. M. Li, J. Xu, M. Romero–Gonzalez, S. A. Banwart, W. E. Huang. Single cell Raman spectroscopy for cell sorting and imaging. Curr. Opin. Biotechnol., 2012, 23, 56-63.
19. N. Volkova. Study of morphological characteristics of cryopreserved cell cultures of stromal origin. Probl. Cryobiol., 2012, 22, 118-125.
20. L. A. Dykman, V. A. Bogatyrev, S. Yu.Shchegolev, N. G. Khlebtsov. Gold Nanoparticles: Synthesis, Properties, and Biomedical Applications. 2008, Moscow, Nauka.
21. T. Mossman. Rapid colorimetric assay for cellular growth and survival: Application to proliferation and cytotoxicity assays. J. Immunol. Meth., 1983, 65, 55-63.
22. E. V. Pavlovich, N. A. Volkova. Effect of gold nanoparticles on proliferative properties of SPEV cells. In: Nanocomposites, Nanophotonics, Nanobiotechnology, and Applications (Eds. O. Fesenko, L. Yatsenko) – Springer Proc. Phys., 156. 2013, New York, Springer, 207-214.
23. E. V. Pavlovich, N. A. Volkova. Influence of gold nanoparticles of human fibroblast before and after cryopreservation. In: Nanoplasmonics, Nano-Optics, Nanocomposites, and Surface Studies (Eds. O. Fesenko, L. Yatsenko) – Springer Proc. Phys., 167. 2014, New York, Springer, 413-420.
24. N. Oh, J.-H. Park. Endocytosis and exocytosis of nanoparticles in mammalian cells. Int. J. Nanomed., 2014, 1, 51-63.
25. Y. S. Chen, Y. C. Hung, I. Liau, G. S. Huang. Assessment of the in vivo toxicity of gold nanoparticles.Nanoscale Res. Lett., 2009, 4, 858-864.
26. S. Sethe, A. Scutt, A. Stolzing. Aging of mesenchymal stem cells. Ageing Res. Rev., 2006, 5, 91-116.
27. O. Y. Rogulska, O. B. Revenko, Y. A. Petrenko, A. Y. Petrenko. Proliferative and differentiation potential of adipose tissue-derived mesenchymal stromal cells in the presence of platelet lysate. Cell.Transplant. Tissue Eng., 2014, 9, 63-65.
28. F. Gasparri, M. Mnzio. Monitoring of apoptosis of HL60 cells by Fourier-transform infrared spectroscopy. Biochem. J., 2003, 369, 239-248.
29. L. K. Tamm, S. A. Tatulian. Infrared spectroscopy of proteins and peptides in lipid bilayers. Quar. Rev. Biophys., 1997, 30, 365-429.
30. A. Filchenkov, V. Mikhaĭlenko, M. Zavelevich. Detection of early apoptotic changes in cells in vitro using nuclear magnetic resonance spectroscopy. Ukr. Biochem. J., 2007, 79, 76-81.

FEATURES OF MICROWAVE MAGNETIC DYNAMICS IN NANOSTRUCTURES WITH STRONG SPIN–ORBIT INTERACTION

A. M. Korostil, M. M. Krupa

Institute of Magnetism
National Academy of Sciences of Ukraine
Ministry of Education & Science of Ukraine
amand@rambler.ru

Abstract

Features of the current spin–orbit induced magnetic dynamics in multilayer nanostructures with nonmagnetic heavy metal layers possessing a strong spin-orbit interaction are studied. The spin Hall's effect of the conversion of an incoming charge current into a transverse (with respect to the charge current) spin current impacting on the magnetic dynamics through a spin-transfer torque provides the excitation of the magnetic dynamics including magnetic precession and switching. The magneto-dynamic effect of a spin current pumping generation together with the inverse spin Hall's effect of conversion of the spin current into the incoming charge current provide the influence of the magnetic dynamics on the incoming charge current. These feed forward and feedback between the incoming charge current and the magnetic dynamics can be the basis for the spin–orbit driven self-sustained and auto-oscillations of a magnetic order in ferro- and antiferromagnetics layers of the nanostructures. It is shown that the considered magnetic nanostructures possess the properties of controlled microwave radiation attaining tens THz in the antiferromagnetic case. Magnetic-induced changes of the electric resistance in the mentioned nanostructure are considered.

1. Introduction

There appears the sufficient current interest in dynamical processes in magnetically ordered systems both from scientific and technological viewpoints. The special interest is related to the problem of the intercoupling between a spin-polarized electron current and the magnetic dynamics in multilayer magnetic nanostructures that can be exhibited in such phenomena, as magnetic switching and a sustained precession of magnetic order vectors.

The interrelation between the spin-polarized current and magnetic order vectors in magnetic multilayer nanostructures, permitting their mutual control, constitutes the basis of the operation of novel nano-devices with properties of a magnetic random-access memory (MRAM), magnetic logic and coherent microwave radiation sources that presents considerable fundamental and application interest [1 – 8]. The operation of these devices relies on the spin-polarized current-induced magnetization switching together with tunnel magnetoresistance effect and the like induced magnetization precession. Such phenomena have real potential for application in systems of high-speed magnetic processing information and high frequency fine-tuned GHz and THz electromagnetic radiation.

The intercoupling between a spin current and magnetic state in magnetic nanostructures constitutes the basis of the current-induced manipulation by magnetic dynamics and vice-versa, i.e. the magnetic state-induced manipulation by the spin current [9, 10]. The spin current can be converted from an incoming charge current under internal effective magnetic fields of interactions of a different origin (including s–d exchange and spin–orbit interactions) with corresponding features of the action of a spin torque on the magnetic states and their dynamics. Inducing magnetic dynamics such as the spin torque can cause switching and precession of the magnetic order vectors (including ferro- and antiferromagnetic orders) in magnetic nanolayers with ferromagnetic (FM) and antiferromagnetic (AF) interactions. The frequency of the magnetic dynamics is determined by the magnitude of magnetic exchange interaction, which is the largest for antiferromagnetic materials. The prospect of obtaining the technological magnetic nanostructures with low threshold incoming currents, low power consumption and controlled high frequency operation is related to utilization of the spin-orbit effects of the spin polarization and magnetic nanostructures with AF exchange interactions.

Generally, the spin–orbit interaction includes the bulk spin Hall effect (SHE) [7, 8] of the transverse (relatively to an incoming current) deflection of electrons with opposites spins in opposite sides and the interface (two-dimensional) Rashba spin–orbit (RSO) effect [9, 10] of the spin splitting of an electron disperse along an electron wave vector. The impact of the spin current on the magnetic states realizes via the spin torque F consisting of so-called a field-like and dumping-like part $F_\parallel$ and $F_\perp$, respectively, which are related to the effects of magnetic order switching and precession dumping or antidumping. The field-like torque $F_\parallel$ originates predominantly by the spin–orbit coupling at the interface in combination with the perturbation of the electron distribution function. The torque $F_\perp$ originates predominantly by the perturbation of electronic states by the applied electric field.

The current spin–orbit controlled microwave magnetic dynamics is realized for nanostructures composed of a heavy metal nanolayer (for instance, Pt, Ta) possessing the strong enough spin–orbit interaction and the adjacent active magnetic nanolayer with a strong exchange interaction attaining maximum values of the order of tens THz in the AF cases. For multisublattice magnetic structures (for instance, for AFs) a general magnetic dynamics is a combined effect of dynamics of each of magnetic sublattices coupled by the strong exchange interaction. The interconnection between the incoming charge current and magnetic dynamics occurs in the mentioned case via the spin current and the spin transfer effect for the each sublattice singly. The mentioned magnetic systems with feedback, realizing via of the direct and inverse SH effects of the spin pumping with spin backflow, possess the properties of sustained

steady-state microwave spin torque oscillations, convertible via a magnetoresistance effect into an AC voltage and high frequency radiation.

This paper is organized as follows: In Section 2, the conversion of an incoming current into the spin current under internal effective bias fields of the exchange interactions of a different origin in magnetic nanostructures is studied. In Section 3, the spin and charge density diffusions in the bilayer magnetic structures with the strong spin–orbit interaction are considered in the framework of nonlinear kinetic leading to renormalization of parameters of a magnetic precession. Section 4 is devoted to dynamic feedback in F/SH nanostructures. It is shown that spin pumping and transfer torques as two reciprocal processes result in a dynamical feedback effect interconnecting energy dissipation channels of both magnetization and current. In Section 5, features of spin pumping and spin-transfer torques as two reciprocal phenomena are considered in AF based nanostructures. In Section 6, the current-induced magnetic dynamics is considered in the bilayer nanostructures composed of an insulating AF and adjusted heavy normal metal with the spin Hall's effect. It is shown that the combined effect of current-induced torque and spin pumping introduces a dynamical feedback that sustains steady-state oscillations with amplitudes controllable via the applied current.

2. Spin polarization and spin current

The electric control of the magnetic dynamics in the mentioned magnetic nanostructures occurs through the exchange interaction between the spin current and a localized magnetic order. The spin current induces the spin torque causing magnetic dynamics in the form of the precession or switching of the magnetization in Fs and AF order in AFs [11 – 13]. The magnitude of the spin torque is determined by the mechanism of the conversion of incoming charge current into the spin current interacting with the magnetic order via an exchange interaction.
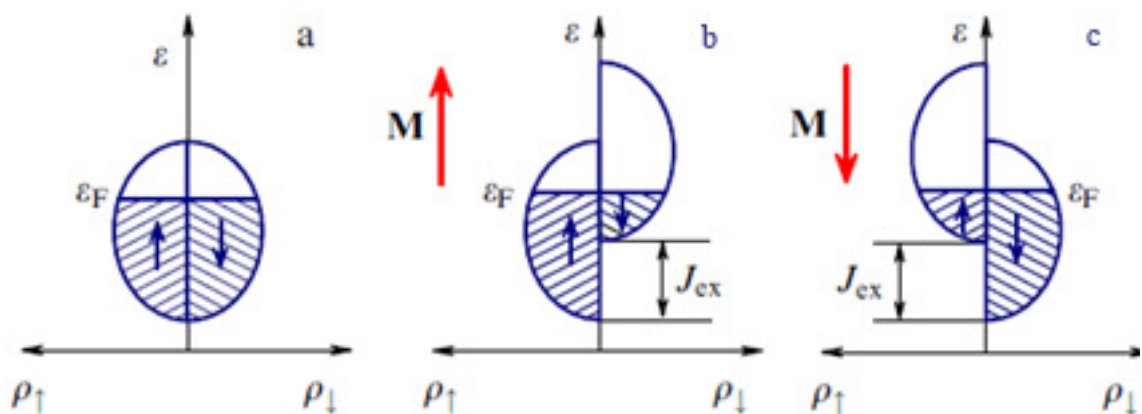

Figure 1. Scheme of the spin-splitting of the band spectrum caused by the exchange interaction J_{ex}, where $\rho_\uparrow$ and $\rho_\downarrow$ are the densities of electron states with different spin projections $(\uparrow,\downarrow)$, $\mathbf{M}$ is the magnetization vector: (b) – ferromagnetic metal, (c) – magnetic semimetals

The conversion of the incoming electric current into spin polarization state in the ferromagnetic nanostructures can be produced by the effective bias field of the *s-d* exchange interaction in the magnetic layer acting as a spin polarizer. The spin polarization occurs as the results of the spin splitting of the electron band spectrum on the two branches with and without their intersection by the Fermi level (**Figure1**) (see [6]) that correspond to two (**Figure 1b**) and single (**Figure 1c**) channel conductions of the electrons with different spin projections relatively to the magnetization. .

In the usual two-channel case, the majority electrons with the spin projection parallel to the magnetization, occupy the one conduction channel, while the minority electrons with the antiparallel spin projection occupy the another conduction channel. This results in the incomplete spin polarization of the electric current. In the single-channel case, which is realized for magnetic semimetals [6], the conduction electrons with the fixed spin projection occupy only one conduction band and the incoming current converts into the pure spin current.

The impact of the polarized electric current on the magnetization occurs through the exchange interaction between the corresponding spin polarized current and the controlled localized spins. The passage of the spin-polarized current into the controlled magnetic nanolayer causes the spin torque exerting the magnetization switching or precession.

In the mentioned case, the transfer of electrons into the controlled magnetic layer results in thermal losses and increase of a power consumption. This imposes restrictions on contact sizes, which have to provide the threshold density of the spin current subject to the condition that the electric current does not exceed the value of an electrical breakdown. These problems can be avoided by the utilizing the spin-orbit interaction for the spin polarization. In this case, the exchange interaction of the spin current with the localized spins is provided without passage of the charge current in the magnetic nanolayer [1 − 7].
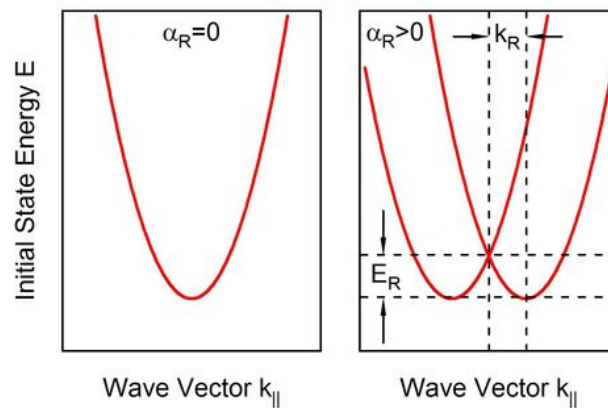

Figure 2. The dispersions of the two-dimensional electron gas previous to (on the left) and after (on the right) action of the Rashba spin-orbit interaction causing the spin-splitting along of planar momentum vector $k_{\parallel}$; a_R is the Rashba parameter, k_R is the offset away from $k_{\parallel} = 0$ of the spectral curves relative to the initial position.

The spin–orbit interaction in the two-dimensional systems with of the broken structure inversion symmetry, known as the Rashba spin–orbit interaction [1, 2, 10, 11], is realized in the interfaces of the magnetic nanostructures with two-dimensional electron properties and an interfacial potential drop. In a single-electron approximation, this interaction is described by the two-dimensional expression for a quasi-relativistic correction [2]. Taking into account the

electric field $E = E_z \cdot z$ along growth direction z, the corresponding Rashba Hamiltonian can be represented as

$$H_R = B_R \sigma, \quad B_R = \left(\frac{\alpha_R}{\hbar}[z \times p] \right), \tag{1}$$

where $\alpha_R \sim E_z$ is the Rashba parameter, B_R is the effective Rashba magnetic field which is dependent on the electron momentum p and σ is the vector of the Pauli spin matrices. Eq. (1) describes the characteristic properties of the Rashba spin–orbit interaction, although in realistic systems, the broken inversion symmetry causes distorts of the free electron wave functions near to atomic nuclei and consequently, it changes a spin-orbit interaction [2]. Due to Eq. (1), the effective Rashba field B_R exerts the spin precession of the conduction electrons. In addition, one leads to the symmetric spin splitting of the single-electron dispersion along the conduction electron momentum that experimentally observed in interfaces of magnetic nanostructures (**Figure 2**).

The spin-polarized electric current lies in the plane of the magnetic layer and one does not pass in the normal direction. Its interaction with the localized magnetization occurs through s–d-exchange interaction of $H_{sd} = J_{sd} S \cdot \sigma$ type, where $J_{sd} \sim J_c$ and J_c is the input electric current, and S is the localized spin. Thereby, the change of the incoming electric current results in the corresponding change of the magnetization. The application of an electric field along the vector z results in changes of the Rashba parameter and magnetization dynamics, which is restricted by the magnetization switching.
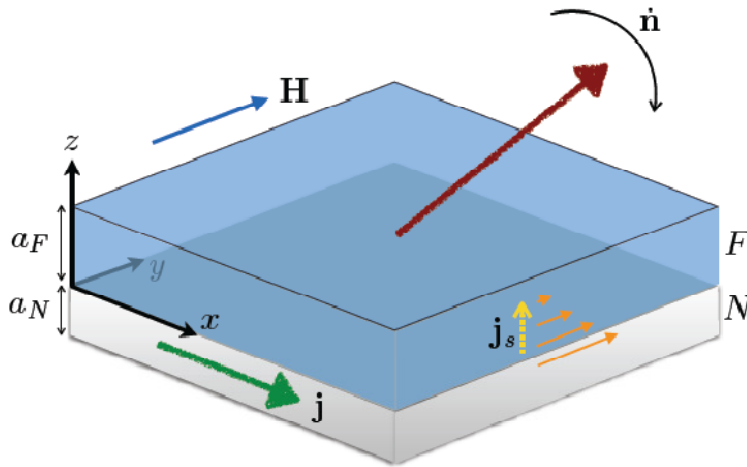
Figure 3. The spin Hall effect of the spin–orbit-conversion of the input electric current j in the transverse spin current j_s with the spin polarization denoted by arrows along the y axis in the two-layered magnetic nanostructure. The latter is composed of the bottom layer made of heavy normal metal (*N*) and the strong spin–orbit interaction and the upper ferromagnetic layer (FM). The spin current exerts on the dynamics of magnetization **n** of the magnetic layer, **H** is external magnetic field.

The spin polarization of the electric current can be caused by the spin Hall's effect (SHE) [7, 8], in which the passage of the electric current through heavy metal (for instance, Pt, Ta) with the strong spin–orbit interaction exerts the spin dependent transverse deviation of the electric current and the transverse pure spin current. The spin orientation of the latter is perpendicular to the electric current and the interface normal (**Figure 3**). The electric current

lies in the plane of the adjacent heavy metal nanolayer and do not pass into the magnetic nanolayer. This avoids the mentioned constraints on contact sizes in the magnetic nanostructure and leads to reduction of the threshold current densities and the energy consumption.

The reciprocal of the SHE is the inverse spin Hall's effect (ISHE), i.e. the conversion of an injected spin current into a traverse electric current or voltage. The SHE generates spin currents and spin accumulations. Together with the spin pumping effect originated from magnetic dynamics, SHE and ISHE provide the interconnection between the magnetic dynamics and the electric current. While the SHE generates spin currents and spin accumulations, the ISHE detects spin currents and can generate the spin-based electric power (see [7]).

The additional transverse momentum component $p_{\sigma\perp}$ in the spin Hall's effect is proportional to the derivative of the spin-orbit interaction $H_{so} = \beta \left[\nabla V \times p \right] \sigma$ with respect to the momentum p, i.e. $p_{\sigma\perp} \sim \beta$ (see [8]). The solution of the corresponding Schrödinger Hamiltonian with the spin–orbit interaction gives that the action of the latter on the conduction electrons is equivalent to the action of the effective spin-dependent Lorentz force $F_\sigma \sim [v \times B_\sigma]$, where v is the electron velocity, and $B_\sigma = \left[\nabla \times A_\sigma \right]$ is the spin-dependent effective magnetic field. Here, A_σ $\left[\nabla \times E_{tot} \right]$ is the effective magnetic potential with E_{tot} being the total electric field [8]. The effective field B_σ causes the transverse deviation of the electric current with generation of the transverse spin current. The charge current passes along the heavy metal nanolayer and the generated spin current passes into the controlled magnetic layer where owing the exchange interaction through the torque changes the magnetization dynamics. This can lead to the magnetization precession or switching.

Features of the electron transport in the mentioned magnetic nanostructures are related to the spin dependent scattering on interfaces. The electron scattering on the normal metal (N)/magnetic metal (M) interface represents the special interest for magnetic heterostructures with the strong spin–orbital interaction and the spin Hall's effect (SHE). In the ferromagnetic case, by scattering theory [14], the spin current $j_s^{(N/F)}$ through an N|F interface (on the N side, flowing into F) can be expressed in terms of the F magnetization M and the (vector) spin accumulation μ_{sN} in N:

$$j_{sN}(m) = (j_\uparrow - j_\downarrow)m - \frac{G_r}{e} m \times (m \times \mu_{sN}) - \frac{G_i}{e}(m \times \mu_{sN}),\tag{2}$$

where $e = -|e|$ is the charge of an electron, $m = M/|M|$ is the and

$$e j_{\uparrow\downarrow} = G_{\uparrow\downarrow}\left[(\mu_{cN} - \mu_{cF}) \pm (m \cdot \mu_{sN} - \mu_{cF}) \right]\tag{3}$$

are the flows of electrons with spin-up and down electrons along m driven by the difference between effective charge chemical potentials in N and F $(\mu_{cN} - \mu_{cF})$ and the difference between spin accumulations at both sides of the interface $(m \cdot \mu_{sN} - \mu_{cF})$. Here, $G_{\uparrow\downarrow}$ and G_i are the spin-dependent conductances at the interface which are related to reflection coefficients $r_{nm}^{\uparrow(\downarrow)}$ of electron at the N|F interface (n and m are transport channels in N) by the relations

$$\frac{G_{\uparrow(\downarrow)}}{G_0} = \sum_{nm}\left[\delta_{nm} - |r_{nm}^{\uparrow\downarrow}|^2 \right],\ G_i = \text{Im}[G_{\uparrow\downarrow}],\ G_r = \text{Re}[G_{\uparrow\downarrow}],\tag{4}$$

$G_i = \text{Im}[G_{\uparrow\downarrow}]$. Here, $G_{\uparrow\downarrow}$ is the spin-mixing conductance at the interface defined by the elements of the spin-dependent scattering matrix

$$G_{\uparrow\downarrow} = G_0 \sum_{nm} \left[\delta_{nm} - r_{nm}^{\uparrow} (r_{nm}^{\downarrow})^* \right], \tag{5}$$

The conductances G_i G_r parameterize spin currents transverse to the magnetization, which are described by the last two terms in Eq. (3). The part of the spin current with spin polarization along the magnetization orientation m , can flow in a metallic F, while the transverse components described by two last terms in Eq. (3) are absorbed at the interface on an atomic length scale and, therefore, acts as a torque on the magnetization. The spin-transfer torque at the interface is obtained from Eq. (3) by the projection

$$T_{STT} = \frac{\hbar}{2e} m \times (m \times j_s^{(N|F)}). \tag{6}$$

Electron and spin transport in N|F bilayers in the current-in-plane (CIP) configuration attracted attention recently because of the observed large current-induced spin-transfer torques generated by the SOC [15]. Signed spin–orbit torques can result from the spin currents generated by the SHE in the N layer [16], and converted to a magnetization torque by the conventional exchange interaction at the interface. This contributes a so-called "damping-like "torque proportional to Gr with symmetry identical to the exchange-mediated term. The magnetic (Gilbert) damping in N|F bilayers subject to an in-plane electric current is modulated by the spin-transfer torque in (16) generated by the direct SHE [17]. While the SHE generates spin currents, the ISHE in a normal metal is an efficient detector of spin currents.

3. Spin–orbit-induced torque

The current-driven magnetization by spin-orbit torques related to the nonequilibrium spin density of different origin subject to contributions of the interface spin–orbit Rashba effect the bulk spin Hall's effect in the layered magnetic nanostructure. Dependences of the corresponding Rashba (T_R) and spin Hall (T_{SH}) torques on the spin polarization and localized magnetization are similar, though the ratio of longitudinal and transverse components of each are different. The latter is related to features of their spin and charge density diffusion.

Two different mechanisms have been suggested that give rise to spin-orbit torque in bilayers consisting of a heavy metal substrate and a thin ferromagnetic layer deposited on top of it. The first mechanism is attributed to the spin Hall's effect [2],which generates a spin current from the substrate towards the ferromagnet. The second mechanism is due to the generation of a current-induced spin accumulation at the interface between the two materials, where magnetism, spin–orbit coupling and broken inversion symmetry coexist.

The characteristic features of the spin-orbit torque in magnetic nanolayers can be described in the framework of the *s-d* model Hamiltonian [10, 11]

$$H = \left(\frac{p^2}{2m} + V(r) \right) - J_{sd} (s \cdot S_d) + \frac{1}{mc^2} \left[\nabla V \times p \right] s \ , \tag{7}$$

where the first bracket separated expression is the sum of kinetic and potential energy, the second term is the *s–d* exchange interaction between itinerant electron spin *s* and the localized

spin S_d. Introduction of the spin or wave function $\Psi(r,t) = \left(\Psi^{\uparrow}(r,t), \Psi^{\downarrow}(r,t) \right)$, spin current density magnetization $m = \Psi^*(r,t) s \Psi(r,t)$ and current density $J_s = -(\hbar/m) \left[\Psi^*(r,t) s \nabla_r \Psi^*(r,t) \right]$ give equations, which after a quantum-mechanical averaging gives

$$\frac{dm}{dt} = \nabla J_s - \frac{J_{ex}}{\hbar} M \times m + \frac{1}{mc^2} < \left[\nabla V \times p \right] \times s >,$$

$$\frac{dM}{dt} = -\gamma M \times H + \alpha M \times \frac{dM}{dt} + \frac{J_{ex}}{\hbar} M \times m,$$
(8)

where M is the unite vector of the localized magnetization, H is the effective field, γ is the gyromagnetic ratio, α is the Gilbert damping. Here the latter term in the first equation describes the spin-orbit torque T, which at a uniform magnetization ($\nabla J_S = 0$) takes the form

$$T = \frac{J_{ex}}{\hbar} M \times m = \frac{1}{mc^2} < \left[\nabla V \times p \right] \times s >.$$
(9)

The spin-orbit torque can be represented in the general form

$$T = T_{\parallel} + T_{\perp},$$
(10)

where $T_{\parallel}$ is the field-like torque dominating in interfaces with the spin-orbit Rashba effect leading to magnetization switching. The damping-like torque $T_{\perp}$ is small in interfaces but large in the bulk of magnetic layer where the spin Hall's effect operates.

For ferromagnetic nanolayers

$$T_{\parallel} \sim [\quad \times \quad], \quad T_{\parallel} \sim \quad \times [\quad \times \quad],$$
(11)

where $\quad$ is the spin polarization direction. Omitted coefficients in Eq.(11) are determined by features of spin and charge density diffusion, which in the two-dimensional interfaces have the form of the coupled system [11]

$$\frac{\partial n}{\partial t} = D\nabla^2 n + B\nabla_z \cdot s + \Gamma \nabla_z \cdot Mn + R \cdot M (\quad) + R \cdot M (\quad)$$
(12)

$$\frac{\partial s}{\partial t} = D\nabla^2 s - \frac{1}{\tau_{\parallel}} s_{\parallel} - \frac{1}{\tau_{\perp}} s_{\perp} + B\nabla_z \cdot s - J_{sd} s \times M - \frac{1}{T_{sd}} M \times (s \times M) + B\nabla_z n$$

$$+ 2C\nabla_z \times s + 2R(M \cdot \nabla_z n)M + \Gamma \left[M \times (\nabla_z \times s) + \nabla_z \cdot (M \times s) \right].$$
(13)

Here n and s are the charge and spin densities $\nabla_z = z \times \nabla$. The spin density $s_{\parallel} = s_x x + s_y y$ relaxes at a rate $1/\tau_{sd} + 1/\tau_{sf}$ while $s_{\perp} = s_z z$ has a rate $1/\tau_{\perp} = 2/\tau_{sd} + 1/\tau_{sf}$.

For a broad range of the relative strength between the spin-orbit coupling and the exchange splitting, the Eqs. (12) and (13) describe the spin dynamics in ferromagnetic layer. The B-term provides a source that generates spin density electrically. The C-term describes the coherent precession of the spin density around the effective Rashba field. The precession of the spin density (induced by the Rashba field) around the exchange field is described by the Γ-term. The R-term contributes to the magnetization renormalization.

4. Conditions of a robustness of magnetic dynamics

In ferromagnet / normal metal heterostructures, spin pumping and spin-transfer torques are two reciprocal processes that occur concomitantly. Their interplay introduces a dynamic feedback effect interconnecting energy dissipation channels of both magnetization and current.

The solution of the spin diffusion process in the presence of the spin Hall's effect in the normal metal represents that the dynamic feedback gives rise to a nonlinear magnetic damping that is crucial to sustain uniform steady-state oscillations of a spin Hall's oscillator [18 – 21].

In ferromagnet (FM)/normal metal (NM) heterostructures, nonlocal effects arise because conduction electrons and magnetization reside in different materials and couple only at the interface. In this regime, spin pumping plays the role of spin electromotive force (SMF), which refers to the generation of spin current from a precession FM into the NM [20]. The pumped spin current is accompanied by a backflow of spin current [19, 20], which reacts on the FM through the spin transfer torque (STT). The combined effect of spin pumping and backflow-induced STT renormalizes the spin-mixing conductance at the interface [12, 18]. However, in the presence of the spin Hall's effect (SHE), spin pumping and spin backflow are also connected by the combined effect of the spin Hall's effect (SHE) and its inverse process, which forms a feedback loop as illustrated in **Figure 4**.
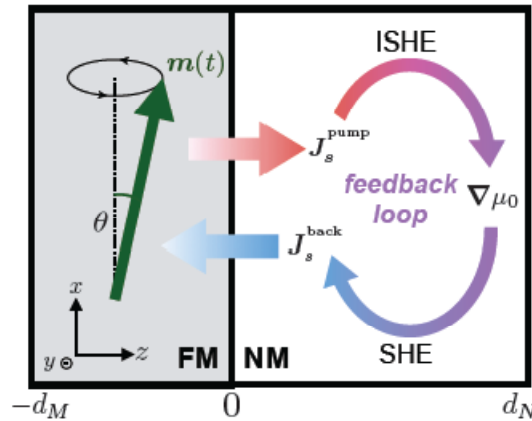
Figure 4. In a FM/NM bilayer, spin pumping and spin backflow
are connected by the SHE and it inverse process (ISHE).

This additional feedback mechanism, proportional to θ_s^2, where θ_s is the spin Hall's angle, that is essential to the electron transport in FM/NM heterostructures. Consequently, this feedback effect is important to the magnetization dynamics. In a reciprocal sense, if we apply an ac current density to the NM, the SHE will drive the magnetization precession via the STT, which in turn can pump spin current back into the NM and renormalize the resistivity by means of the inverse SHE.

The feedback effect qualitatively modifies the dynamical behavior of an FM/NM heterostructure. The feedback manifests as a novel nonlinear damping effect in the magnetization dynamics. It enables uniform auto-oscillations of a spin Hall's oscillator and prevents magnetic switching. The feedback effect gives rise to a spin Hall's magnetoimpedance in the electron transport, which reduces to the observed SMR in the DC limit.

Consider a FM/NM bilayer structure as shown in **Figure 4**, where the layer thicknesses are d_M and d_N, respectively. The coordinate system is chosen such that the magnetization direction at rest is along x, and the interface normal is along z. It is assumed that the FM is insulating (e.g., YIG), but the essential physics remains valid for a conducting FM since the feedback process takes place only on the NM side. Let $\mu_0 / 2$ be the electrochemical potential and μ the vector of spin accumulation in the NM. The charge current density is

$$J_c = -\frac{\sigma}{2c}\left[\partial_i\mu_0 + \theta_s\varepsilon_{ijk}\partial_k\mu_0\right]$$

with i the transport direction and j the direction of spin polarization. In given device geometry, only the spin current flowing along z-direction is relevant, thus we assume $\boldsymbol{\mu} = \boldsymbol{\mu}(z,t)$. Correspondingly, the spin current density reduces to a vector $\boldsymbol{J}_s$; we scale it in the same unit as the charge current density $\boldsymbol{J}_c$. The electron and spin dynamics in the NM are described by three equations

$$\frac{\partial\mu}{\partial t} = D\frac{\partial^2\mu}{\partial z^2} - \frac{1}{\tau_{sf}}\mu \ , \tag{14}$$

$$\boldsymbol{J}_c = -\frac{\sigma}{2e}\left[\nabla\mu_0 + \theta_s z \times \frac{\partial\mu}{\partial z}\right] \ , \tag{15}$$

$$\boldsymbol{J}_s = -\frac{\sigma}{2e}\left[\frac{\partial\mu}{\partial z} + \nabla\mu_0 + \theta_s z \times \frac{\partial\mu_0}{\partial z}\right] \ , \tag{16}$$

where D is the diffusion constant, τ_{sf} is the spin-flip relaxation time, σ is the conductivity, e is the electron charge, and θ_s is the spin Hal's angle.

To solve the spin accumulation $\boldsymbol{\mu}$, we assume that the charge current density $\boldsymbol{J}_c$ is fixed by external circuit and is uniform in space. Besides that, we have two boundary conditions

$$\boldsymbol{J}_s(d_N) \equiv \boldsymbol{J}_{s0} = 0$$

and

$$\boldsymbol{J}_{s0} = \frac{G_r}{e}\left[\boldsymbol{M}\times(\boldsymbol{M}\times\boldsymbol{\mu}_{s0}) + \hbar\boldsymbol{M}\times\dot{\boldsymbol{M}}\right] \ , \tag{17}$$

where $\boldsymbol{\mu}_{s0} = \boldsymbol{\mu}(0)$ and G_r is the real part of the areal density of the spin-mixing conductance (the imaginary part is the real part of the areal density of the spin-mixing conductance (the imaginary part G_i is neglected since $G_r \quad G_i$). On the right hand side of Eq. (17), the first term is the STT and the second term is the spin pumping. They are two fundamental ingredients bridging the electron (spin) transport in the NM with the magnetization dynamics of the FM. Due to the conservation of spin angular momentum, the spin current density $\boldsymbol{J}_{s0}$ is absorbed by the FM, which is reflected by the Landau–Lifshitz–Gilbert's (LLG) equation

$$\frac{d\boldsymbol{M}}{dt} = \gamma\boldsymbol{H}_{eff}\times\boldsymbol{M} + \alpha_0\boldsymbol{M}\times\frac{d\boldsymbol{M}}{dt} + \frac{\hbar\gamma_{ex}}{2eM_s d_M}\boldsymbol{J}_{s0}, \tag{18}$$

where γ is the gyromagnetic ratio, $\hbar$ is the reduced Planck's constant, M_s is the saturation magnetization, α_0 is the Gilbert's damping constant, and $\boldsymbol{H}_{eff}$ is the effective magnetic field. For typical FMs, the magnetization dynamics is much slower than the spin relaxation rate in the NM so that $\omega r_{sf} \quad 1$. In this limit, the spin accumulation $\boldsymbol{\mu}(z,t)$ adapts to the instantaneous magnetization orientation and is kept quasi-equilibrium. As a result, the spin dynamics described by Eq. (14) reduces to a stationary spin diffusion process at any specified time. Retaining to second order in θ_s^2, Eq. (14) is solved as

$$\boldsymbol{\mu}(z) = \theta_s\frac{2e\lambda}{\sigma}z\times\boldsymbol{J}_c\frac{\sinh\frac{2z-d_N}{2\lambda}}{\cosh\frac{d_N}{2\lambda}} + \frac{2e\lambda}{\sigma}\left[\boldsymbol{J}_{s0} + \theta_s^2 z\times(z\times\boldsymbol{J}_{s0})\right]\frac{\cosh\frac{z-d_N}{\lambda}}{\sinh\frac{d_N}{\lambda}} \ , \tag{19}$$

where $\lambda = \sqrt{D\tau_{sf}}$ is the spin diffusion length. Here, it is suppressed the t variable in $\mu(z)$ since its time dependence simply originates from J_c and J_{s0}. Combining Eqs. (14) and (19), we can either eliminate the electron degrees of freedom (J_c and J_{s0}) to derive an effective dynamics of the magnetization, or eliminate the time derivative of the magnetization ($\dot{M}$) in order to get an effective magneto-transport of the electrons. These operations amount to invoking the dynamic feedback mechanism.

Assume that J_c is an applied dc charge current density. Our goal is to express the total spin current density J_{s0} flowing into the FM in terms of the magnetization $M(t)$, by which the LLG Eq. (18) will no longer involve any electron degrees of freedom, and the feedback effect is thus implemented mathematically. To this end, we combine Eqs. (17) and (18) which gives two convoluted relations of J_{s0} and μ_{s0}. By means of iterations truncating at θ_s^2 order, we can solve J_{s0} as a function of J_c, m(t) and its time derivative. Then we insert this J_c into Eq. (18), which yields the effective magnetization dynamics

$$\frac{dM}{dt} = \gamma H_{eff} \times M + \omega_s M \times \left[(z \times j_c) \times M\right] + (\alpha_0 + \alpha_{sp}) M \times \frac{dM}{dt} + \alpha_{rb}\left(M_z^2 M \times \frac{\partial M}{\partial t} + \frac{\partial M_z}{\partial t} M \times z\right), \quad (20)$$

where j_c is the unite vector of J_c and

$$\omega_s = \theta_s J_c \frac{\hbar\gamma}{eM_s d_M} \frac{\lambda G_r \tanh\frac{d_s}{2\lambda}}{\sigma + 2\lambda G_r \coth\frac{d_s}{\lambda}} \quad (21)$$

is the strength of the STT (driven by J_c) scaled in the frequency dimension. The two damping coefficients are

$$a_{sp} = \frac{\hbar^2\gamma}{2e^2 M_s d_M} \frac{\sigma G_r}{\sigma + 2\lambda G_r \coth\frac{d_N}{\lambda}} \, , \quad (22)$$

$$a_{fb} = \theta_s^2 \frac{\hbar^2\gamma}{e^2 M_s d_M} \frac{\sigma_r \lambda G_r^2 \coth\frac{d_N}{\lambda}}{(\sigma + 2\lambda G_r \coth\frac{d_N}{\lambda})^2} \, , \quad (23)$$

Here, a_{sp} describes the conventional enhanced damping from spin pumping with the spin backflow effects taken into account [20]; it is independent of the SHE. By contrast, the a_{sp} term is completely new. It reflects the dynamic feedback realized by virtue of the combined effect of the SHE and its inverse process as schematically shown in **Figure 4**. From Eq. (20), we see that this novel damping term is nonlinear in $M_{\perp}:|$ the component of M transverse to the effective field H_{eff}, whereas the Gilbert's damping term is linear in $M_{\perp}$.

The feedback-induced nonlinear damping effect can be understood in an intuitive way. If the magnetization precession is getting larger, it will trigger a chain reaction: first the pumped spin current J_{s0} increases, then the spin diffusion becomes stronger (i.e., $|\partial_z \mu_s|$ gets larger). This will necessarily lead to a larger $\nabla\mu_0$ in the NM according to Eq. (15), as we have fixed the current density J_s. Finally, the change of the emf will feed back into J_{s0} according to Eq. (16), preventing its further increase. Therefore, the growing magnetization precession is inhibited. The entire process realizes a negative feedback and respects Lenz's law.

5. Interconnection of spin currents and magnetic dynamics in AF based nanostructures

The spin pumping and spin-transfer torque in AF based nanostructures represent the combined effect of their action in each of magnetic sublattices of the AF coupled by a strong exchange interaction. Magnetization dynamics of these coupled sublattices leads to an AF order (l) dynamics manifesting as precession and switching. Similarly, to the magnetization in the ferromagnetic case, the AF order precession generates the spin pumping current which via the inverse spin Hall's effect in adjacent nonmagnetic nanolayers can converts into the transverse charge current. Thereby, the influence of the AF dynamics on the charge current in AF nanostructures is realized [22]. The inverse impact of the charge current on the AF precession is realized via the spin Hall's effect of the conversation of the charge current into the transverse spin current which owing to the exchange interaction exerts the spin transfer torque on the AF order precession.

Characteristic features of the AF dynamics and its interconnection with the spin currents in the form of the precession-induced spin pump and spin transfer torque is manifested in the AF two-sublattice model with an easy axis is directed along the axis z with magnetization unite vectors m_1 and m_2. These vectors are driven by the exchange interaction, the anisotropy, and a magnetic field in the z direction. In units of frequency, they are represented by ω_E, ω_A, and $\omega_H = \gamma H_0$, respectively. The equations of motion in a free precession approximation are

$$\dot{m}_1 = m_1 \times \left[\omega_E m_2 - (\omega_E + \omega_H) z \right] + T_1,$$
$$\dot{m}_2 = m_2 \times \left[\omega_E m_1 - (\omega_E - \omega_H) z \right] + T_2,$$

(24)

where the effective field causing the magnetization precession in a magnetic sublattice contains the contribution from the exchange interaction with an adjacent magnetic sublattice. In line response when $m_{1(2)} = z + m_{1(2)\perp} \exp(i\omega t)$ at $|m_\perp|$ 1 the resonance frequencies are then

$$\omega = \omega_H \pm \omega_R = \omega_H \pm \sqrt{\omega_A (\omega_A \pm 2\omega_E)},$$

(25)

where the two corresponding eigenmodes are characterized by different chiralities. The left-handed (right-handed) mode, both m_1 and m_2 undergo a circular clockwise (counterclockwise) precession with π phase difference. In the absence of magnetic field, viz. $\omega_H = 0$, the two modes are degenerate.

Due to grasp the essential feature of spin pumping by AF is to consider m_1 and m_2 as two independent F subsystems. Then, spin currents pumped from them will be proportional to $m_1 \times \dot{m}_1$ and $m_2 \times \dot{m}_2$, respectively. Since from $m_1 \approx -m_2$ and $\dot{m}_1 \approx -\dot{m}_2$, the total spin current is roughly proportional to $l \times \dot{l}$, where $l = (m_1 - m_2)/2$ is the staggered field. However, a more careful analysis reveals that the cone angles of m_1 and m_2 are different: in the left-handed (right-handed) mode, $\theta_2 / \theta_1 = \eta$ ($\theta_1 / \theta_2 = \eta$), where $\eta \approx \left(1 + \sqrt{\omega_A / \omega_E} \right)^2$, so that a small magnetization $m = (m_1 + m_2)/2$ will be induced in the AF dynamics state.

The spin currents in AF nanostructure determined by mixed scattering channels associated with different sublattices on a N/AF. Typical AF materials are insulators and incident electrons from the normal metal cannot penetrate far. Only a single atomic layer of AF directly connected to N suffices to describe the dominant contribution to interface scattering. Therefore, the essential physics is captured by modeling the N/AF interface as being semi-infinite in the transport direction and infinite in the transverse direction.

In the nearest-neighbor tight-binding model on a cubic lattice, in terms of the hopping energy in N and AF t and t_m, respectively, and the exchange coupling J between conduction electron spins and magnetic moments, in the linear approximation in the small the small $\boldsymbol{m}$, the scattering matrix S is

$$S = S_0 + S_\omega \tau_1 \sigma_0 + \Delta S[\tau_3 (\boldsymbol{l} \cdot \boldsymbol{\sigma}) + \tau_0 (\boldsymbol{m} \cdot \boldsymbol{\sigma})], \qquad (26)$$

where $\tau_{1,2,3}$ are pseudospin Pauli's matrices for sublattice degree of freedom, σ are the vector of spin Pauli's matrices, and τ_0 and σ_0 are identity matrices. The last two terms of Eq. (26) with a common coefficient ΔS are spin dependent and represent umklapp and normal scatterings, respectively. Pumping currents are related to the coefficients in Eq. (26) through the spin-mixing conductance $G_{mix} = G_r + iG_i$, where

$$G_r = (e^2 A / \hbar \pi^2) \iint |\Delta S|^2 dk_y dk_z$$

And

$$G_i = (e^2 A / \hbar \pi^2) \iint \mathrm{Im} |S_0^* \Delta S| dk_y dk_z,$$

where dk_y and dk_z are the transverse momenta and A the interface cross section. The conductance is determined by the scattering matrices with spin flip on a N/AF interface. By integrating over the Fermi's surface, it can be shown that spin transfer on a compensated N/AF interface is similar in magnitude to the case of an uncompensated N/F interface. This implies the similarity between the nature of the spin pumping and the spin transfer torque effects in AF and F nanosystems.

Although the AF resonance frequency reaches the THz region (1 10 meV), the motion of the staggered field remains adiabatic, as evidenced by comparing the resonance frequency with two characteristic energy scales: (i) the Fermi's energy in N is a few eV; (ii) the exchange coupling between conduction electron spins and magnetic moments can be as large as eV. As a result, the spin eigenstates and the scattering matrix Eq. (26) adiabatically adapt to the instantaneous configuration of AFs. Regarding the staggered field $\boldsymbol{l}$ and the magnetization $\boldsymbol{m}$ as two independent adiabatic parameters [23], we obtain the pumped spin current $\boldsymbol{I}_s$ with the scattering matrix S in Eq. (26)

$$\frac{e}{\hbar} \boldsymbol{I}_s = G_r (\boldsymbol{l} \times \dot{\boldsymbol{l}} + \boldsymbol{m} \times \dot{\boldsymbol{m}}) - G_i \dot{\boldsymbol{m}}. \qquad (27)$$

Eq. (27) can indeed be interpreted as arising from a coherent sum of two independent F spin pumping contributions by $\boldsymbol{m}_1$ and $\boldsymbol{m}_2$. However, the spin-mixing conductance G_r and G_i are different from those of F due to the mixing of scattering channels from different magnetic sublattices. Moreover, AF dynamics is much faster than F that corresponds to a stronger spin pumping.

By taking a time average of Eq. (27) over one period of oscillation, only the first two terms survive and contribute to the dc component of spin current I_s^{dc}. Despite that $|\boldsymbol{m}|$ $|\boldsymbol{l}|$,

the contribution of $\boldsymbol{m} \times \dot{\boldsymbol{m}}$ to I_s^{dc} can be comparable to that of $\boldsymbol{l} \times \dot{\boldsymbol{l}}$. This is because I_s^{dc} is proportional to the cone angle θ^2 of precession and the cone angle associated with the staggered field is much smaller than the one associated with the magnetization, $\theta_l \approx 0$ but $\theta_m \approx \pi / 2$.

From the sublattice degree of freedom involved in the AF dynamics it is follows a staggered spin pumping. A staggered spin current represents the imbalance between the spin current carried by the two sublattices. It has three components $I_{ss}^{(i)}$ ($i = (1, 2, 3)$ associated with three pseudospin Pauli's matrices. In a similar manner as spin pumping, we find that

$$\frac{e}{\hbar} I_{ss}^{(3)} = G_r (\boldsymbol{l} \times \dot{\boldsymbol{m}} + \boldsymbol{m} \times \dot{\boldsymbol{l}}) - G_i \dot{\boldsymbol{l}}, \quad \frac{e}{\hbar} I_{ss}^{(2)} = -\mathrm{Re}[G_\omega] \dot{\boldsymbol{l}}, \quad \frac{e}{\hbar} I_{ss}^{(1)} = -\mathrm{Im}[G_\omega] \dot{\boldsymbol{m}}, \tag{28}$$

where

$$G_\omega = (e^2 A / \hbar \pi^2) \iint \mathrm{Im} \,|\, S_\omega^* \Delta S \,|\, dk_y dk_z$$

results from intersublattice scattering that is unique to AFs. After the time average, $I_{ss}^{(1)}$ and $I_{ss}^{(2)}$ drop out, only $I_{ss}^{(3)}$ survives. This time, the dc component I_{ss}^{dc} is an even function of ω in the absence of static magnetic field. Elastic scattering in the normal metal will destroy any staggered spin accumulation, which decays on the time scale of $\hbar / t$. Therefore, the staggered spin current can only be well defined within a distance of the mean free path away from the interface.

The reciprocal effect of spin pumping is STT, which describes the back action that a spin current exerts on the AF. In linear response, an AF is driven by two thermodynamic forces c and $f_l = -\delta F / \delta l$ and $f_m = -\delta F / \delta m$ (energy dimension), where

$$F = (\hbar / 2) \int dv [\omega_0 \boldsymbol{m}^2 / a^2 + \omega_l \sum_{i=x,y,z} (\partial_i \boldsymbol{l})^2 / a \omega_H - \omega_H \boldsymbol{H} \cdot \boldsymbol{m} \,/\, (Ha)^3]$$

is the free energy. Here ω_0 and ω_n are the homogeneous and inhomogeneous exchange frequencies, respectively. It can be easily shown that $\omega_0 = \omega_A + 2\omega_E$. Enforced by $\boldsymbol{m} \cdot \boldsymbol{l} = 0$ and $(\boldsymbol{l})^2 \approx 1$, the symmetry allowed dynamics are $\hbar \dot{\boldsymbol{l}} = (a^3 / v) f_m \times \boldsymbol{l}$ and $\hbar \dot{\boldsymbol{m}} = (a^3 / v) f_l \times \boldsymbol{l} + f_m \times \boldsymbol{m}$ [24], where v is the system volume. Inserting them into Eq. (27) gives the response of the spin current to f_m and f_l. Invoking the Onsager's reciprocity relation, we derive the response of $\boldsymbol{l}$ and $\boldsymbol{m}$ to a given spin voltage V_s in the normal metal, which are identified as two STT terms τ_l and τ_m. To linear order in $\boldsymbol{m}$

$$\tau_l = -\frac{a^3}{ev} [G_r \boldsymbol{l} \times (\boldsymbol{m} \times V_s) - G_i \boldsymbol{l} \times V_s], \quad \tau_l = -\frac{a^3}{ev} G_r \boldsymbol{n} \times (\boldsymbol{m} \times V_s), \tag{29}$$

that treats STTs on the two sublattices as completely independent.

In solving the AF dynamics, it is instructive to eliminate $\boldsymbol{m}$ and derive a closed equation of motion in terms of $\boldsymbol{l}$ alone [25]. Truncating to linear order in V_s, $\boldsymbol{m}$, and $\dot{\boldsymbol{l}}$, we obtain the effective dynamics

$$\boldsymbol{l} \times (\ddot{\boldsymbol{l}} + \alpha \omega_0 \dot{\boldsymbol{l}} + \omega_R^2 \boldsymbol{l}_\perp) = \frac{\omega_0 a^3 G_r}{ev} \boldsymbol{l} \times (\boldsymbol{l} \times V_s), \tag{30}$$

where α is the Gilbert's damping constant, and $\boldsymbol{l}_\perp$ are perpendicular components of $\boldsymbol{l}$ with respect to the easy axis. Since the STT only acts on the interface and we consider a thin AF film,

we have disregarded a possible nonuniform motion of l. Solution of Eq. (30) for the spectrum in the case V_s which is collinear with the easy axis has the form

$$\omega / \omega_0 = (1/2)[-i\alpha \pm \sqrt{-\alpha^2 + 4\omega_A / \omega_0 + 4i\alpha^3 G_r V_s / (ev\omega_0)}] .$$

For small V_s, ω has a negative imaginary part so that any perturbed motion will decay exponentially in time and the system is stable. However, a sufficiently large V_s will flip the sign of $\text{Im}[\omega]$, which makes the system unstable and marks the onset of uniform AF excitation. The condition $\text{Im}[\omega] = 0$ determines the threshold spin voltage $V_s^{th} = \pm \dfrac{ev\alpha\omega_l}{a^3 G_r}$, where $+(-)$ corresponds to the excitation of the right-handed (left-handed) mode. The chirality selection by the sign of the spin voltage is just consistent with the direction control of spin pumping by the microwave polarization. Since G_r scales linearly with the interface area, V_s^{th} scales linearly with the thickness of the AF layer.

In real experiments, a challenge arises from the large ω_R, but we can still get reasonable V_s^{th} by reducing the layer thickness. For MnF2 of few nm thick, the threshold spin voltage is estimated to be 10–100 µV. The STT-driven AF dynamics suggests the feasibility of building a spin-torque nano-oscillator using AFs, which generates a THz signal from a dc input without the need of static magnetic field.

6. Current-induced dynamics of AFs in spin Hall geometry

In the framework the current-induced dynamics of insulating antiferromagnets in a spin Hall geometry, sufficiently large in-plane currents perpendicular to the Néel AF order can trigger spontaneous oscillations at frequencies between the acoustic and the optical eigenmodes [12, 18, 21]. The direction of the driving current determines the chirality of the excitation. When the current exceeds a threshold, the combined effect of current-induced torques and spin pumping introduces a dynamic feedback that sustains steady-state oscillations with amplitudes controllable via the applied current. This permits to obtain the spin Hall's (SH) nano-oscillator with operating frequencies in THz range.

When an applied STT compensates the magnetic damping, the magnetization becomes unstable: it either switches to another direction or evolves into a steady-state oscillation. While the former improves writing operations in magnetic memory devices, the latter enables sustainable ac signal generation from dc inputs, giving rise to spin-torque oscillators (STOs) [26, 27]. In ferromagnets, currents or magnetic fields can tune the STO output frequency from the MHz to the GHz regime.

STOs can potentially be operated at much higher THz frequencies, when antiferromagnets (AFs) replace ferromagnets. Two features make this possible: 1) the eigenfrequencies of typical AFs fall into the THz range. 2) an anti-damping STTs can trigger spontaneous excitations of an AF. While most AFs are insulators where STTs cannot be operated by passing through a current, the spin Hall's effect (SHE) can produce STTs even when electrons do not flow through the magnet [20]. Therefore, integrating STOs with the SHE paves the way towards low-dissipation spin Hall's nanooscillators (SHNOs).

However, to realize AF-based SHNOs, current-induced excitations should not grow indefinitely, but instead should evolve into steady-state oscillations and generate a substantial ac output. Although an AF under the action of an anti-damping STT does not suffer magnetic switching, its Néel's AF vector experiences either no dynamics or a right-angle precession around the direction of the spin accumulation [5]. Since the oscillation amplitude is not continuously tunable via the applied current, the device does not meet the requirements of an SHNO.

Steady-state oscillations are realizable in ferromagnetic STOs for the following reasons. In a spin-valve device, the angle dependence of the Gilbert's damping and that of the anti-damping STT differ. As a result, when the driving current is above the threshold, there exists a unique angle where the two competing effects compensate. In addition, steady-state oscillation is stabilized at that angle.

However, this feature is no longer active where the SHE creates the anti-damping STT. Therefore, one needs to introduce alternative mechanisms to prevent a spontaneous excitation from growing into magnetic switching. For instance, the bullet mode localized in space exhibits a strong non-collinearity that can sustain auto-oscillations. On the other hand, to enable uniform excitations, the dipolar interaction is required. However, the dipolar interaction is negligible in AFs where the magnetization is vanishingly small.

We will exploit an above-mentioned feedback mechanism to justify that a THz SHNO is realizable in an AF/heavy-metal heterostructure. The feedback effect originates from the combined effect of the SHE and its reverse process that connects the spin pumping with the spin backflow [28, 29], which is independent of the dipolar interaction. First, we determine the threshold of spontaneous excitations by solving the AF order dynamics in the linear response regime and relate the threshold to a current density by studying the SHE in the heavy metal. Then, we numerically explore the nonlinear Néel's AF order dynamics beyond the threshold by considering the feedback effect, and show that the feedback is indispensable to sustain uniform auto-oscillations. In the considerate case, THz SHNO generates a substantial ac voltage output with its amplitude continuously tunable via the applied dc current.

For description of magnetic dynamics we assume that the AF has the two-sublattice crystal structure with the sublattice magnetizations characterized by two unit vectors M_A and M_B. We introduce the AF vector $l = (M_A - M_B) / 2$ and the small magnetization $M = (M_A + M_b) / 2$; they satisfy $M \cdot l = 0$ and $M_A^2 + M_B^2 = 1$. In the exchange limit, $M \ll 1$, thus $l \approx 1$ and $l \cdot \dot{l} = 0$. The Cartesian coordinates are chosen such that the hard axis is along z, and the in-plane easy-axis along x. We scale everything in (positive) angular frequency, where the hard axis anisotropy is described by $\omega_\perp$, the easy in-plane anisotropy $\omega_\parallel$, and the Heisenberg exchange interaction ω_E. In the macrospin description, the free energy

$$F = -\hbar\omega_E l^2 - \hbar\omega_\parallel \left[(x \cdot l)^2 + (x \cdot M)^2 \right] / 2 - \hbar\omega_\perp l^2 - \hbar\omega_\parallel \left[(z \cdot l)^2 + (z \cdot M)^2 \right] / 2 \, , \tag{31}$$

which defines two thermodynamic forces $\hbar f_l = -\partial F / \partial l$ and $\hbar f_M = -\partial F / \partial M$. The coupled equations of motion are

$$\dot{M} = f_l \times l + f_M \times M + \alpha (M \times \dot{M} + l \times \dot{l}) + T_M \, ,$$

$$\dot{l} = f_M \times l + f_l \times M + \alpha (M \times \dot{l} + l \times \dot{M}) + T_l \, , \tag{32}$$

where α is the Gilbert's damping constant, and T_M and T_l are the STTs given by [29]

$$T_M = l \times (\boldsymbol{\omega}_s \times l) + M \times (\boldsymbol{\omega}_s \times M),$$
$$T_l = l \times (\boldsymbol{\omega}_s \times M) + M \times (\boldsymbol{\omega}_s \times l).$$

(33)

Here, $\boldsymbol{\omega}_S$ is the vector of spin accumulation; its magnitude (in frequency unit) represents the STT strength. To derive the current-induced excitations, we decompose the AF vector as $l = l_\perp e^{i\omega t}$, assuming $|l_\perp| \ll 1$. Restricting to linear order in $l_\perp$, we eliminate M in Eq. (31), and obtain the eigenfrequencies as $\omega_\pm / \omega_E = i\alpha + [(\omega_\perp + 2\omega_\parallel \pm \sqrt{(\omega_\pm^2 - 4\omega_S^2)})] / \omega_E - \alpha^2]^{1/2}$, where the $+$ ($-$) sign corresponds to the optical (acoustic) mode. Due to the latter equation, dependences of real and imaginary parts $\text{Re}[\omega_\pm]$ and $\text{Im}[\omega_\pm]$ are characterized by the degenerate lower of which $\text{Im}[\omega_\pm]$ remain degenerate and unaffected. However, at $\omega_S > \omega_\perp / 2$ $\text{Im}[\omega_\pm]$ reduces (grows) rapidly, indicating that the damping is diminished (enhanced) by the STT. At the threshold [29]

$$\omega_S^{th} = \sqrt{\frac{\omega_\perp^2}{4} + \alpha^2 (2\omega_\perp + \omega_\perp)\omega_E}$$

$\text{Im}[\omega_\pm]$ vanishes, which marks the onset of spontaneous excitation of the optical mode and the breakdown of the linear response approximation. The uniaxial symmetry enforces that $\text{Im}[\omega_\pm]$ also vanishes for ω_S^{th} so that the auto-oscillation can be triggered by a reversed current as well. In the absence of the hard-axis anisotropy ($\omega_\perp = 0$), the threshold Eq. (32) is linear in α, so the anti-damping effect occurs when the STT is turned on. However, in the general case where $\omega_\perp > 0$, the anti-damping effect appears only when $\omega_S > \omega_\perp / 2$. Vectors M_A and M_B always exhibit opposite chiralities, i.e., they rotates counterclockwise (clock-wise). However, at the degenerate point $\omega_S = \omega_\perp / 2$, the chirality of M_A (M_B) in the optical (acoustic) mode reverses. Consequently, when $\omega_S > \omega_\perp / 2$, both M_A and M_B, hence the Néel vector l, all acquire the same chirality. At the threshold ω_S^{th}, the excited optical mode is right-handed. If ω_S changes sign, the optical mode is still excited, but its chirality becomes left-handed. These suggest that the direction of the current determines the chirality of the excitation.

Consider the critical current the two-layered nanostructure insulating AF/heavy normal metal (HM) with strong spin-orbit coupling (**Figure 5**)
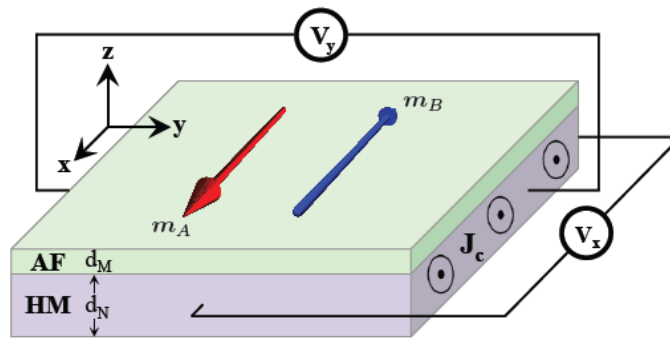

Figure 5. An insulating AF/HM heterostructure. The applied dc
current density J_c drives the AF via the SHE. The dynamics of
the AF pumps spin current back into N, and converts into electric
field via the inverse SHE, which is monitored by two voltmeters.

A current density J_C is applied along the y-direction; it is perpendicular to the Néel vector of the AF. The SHE in the HM generates anti-damping STTs to drive the Néel vector dynamics, which in turn pumps spin current back into the HM. The pumped spin current converts into a charge voltage due to the inverse SHE. By solving the spin diffusion equation in the presence of the SHE under boundary conditions involving both spin-pumping and STT, we relate the threshold STT Eq. (32) to a critical current density

$$J_C^{th} = \omega_c^{th} \frac{d_M(h\sigma + 2\lambda e^2 g_r \coth\frac{d_N}{\lambda})}{2\theta_s \alpha^3 \lambda e g_r \tanh\frac{d_N}{\lambda}}, \tag{34}$$

where θ_s is the spin Hall angle, g_r is the areal density of the transverse mixing conductance [29]. From Eq. (6.3) it is follows that the critical current density J_c^{th} can be lowered by reducing (increasing) the thickness of the AF d_M (HM d_M).

The sustained steady-state oscillation of the Néel vector in the mentioned nanostructure can be realized via the dynamic feedback effect. The pumped spin current from a precessing AF vector into the HM experiences a backflow [29]. In HMs, however, the spin pumping and the spin backflow are also connected via the combined effect of the SHE and its inverse process, which feeds the Néel vector dynamics back into itself. In ferromagnets, such a feedback mechanism manifests as a nonlinear damping effect in the magnetization dynamics. Similar feedback-induced damping effect can occurs for AFs. In this case, the pumped spin current into the HM converts into an electric field E due to the inverse SHE.

According to Ohm's law, $J_C = \sigma E - \theta_s(\sigma/2e)z \times \partial_z \mu_s$, where μ_s is the spin accumulation in the HM. At the fixed current density J_C through external circuits, a change of the electric field E necessarily leads to a change of the spin accumulation μ_s. Subsequently, the change of μ_s diffuses and generates an additional spin current, which will finally deliver the influence of spin pumping back into the Néel vector through STTs. By closing such a feedback loop, we obtain a feedback torque that should be added to Eq. (32) as

$$T_{FB} = \alpha_{NL}\left[l_z^2 l \times \dot{l} - \dot{l}_z(z \times l)\right], \tag{35}$$

where the feedback coefficient is

$$a_{NL} = \theta_s^2 \frac{\alpha^3}{d_M} \frac{2\hbar\lambda e^2 g_r^2 \coth\frac{d_N}{\lambda}}{(\hbar\sigma + 2\lambda e^2 g_r \coth\frac{d_N}{\lambda})}. \tag{36}$$

While the feedback effect seems to be a higher order effect as a_{NL} is proportional to θ_s^2, it can be significantly enhanced by searching for materials with large θ_s. The feedback-induced nonlinear damping is a critical ingredient because it dramatically modifies the dynamical behavior of an SHNO using AF.

A salient feature of the considered stable oscillation phase is that the applied DC current density J_c controls the output power and that the output power is substantial that is indispensable for an SHNO. In the stable oscillation phase, the actual frequency output lies between the acoustic and the optical modes. The AC voltage output is determined by the inverse SHE and the spin pumping. For a fixed J_c the total electric field $E = J_c/\sigma + \Delta E$ includes a time varying part

$$\Delta \boldsymbol{E} = \theta_s \frac{\hbar}{d_n} \frac{\lambda e g_r \tanh \dfrac{d_N}{2\lambda}}{h\sigma + 2\lambda e^2 g_r \coth \dfrac{d_N}{2\lambda}} (\boldsymbol{l} \times \dot{\boldsymbol{l}}) \times z, \tag{37}$$

whence it results that the effective value $\boldsymbol{E}_x = \lim\limits_{t \to \infty} \int\limits_{t}^{t+T} dt' |\Delta \boldsymbol{E}_x(t')|$ is appreciably large in the stable oscillation phase reaching the maximum values 10 V/a.

7. Magnetic dynamic impacts on a charge transport in hybrid nanostructures

Interconnection between the magnetic dynamics in magnetic layers and the charge current in the adjacent nonmagnetic heavy metal (HM) nanolayers with the strong spin-orbit interaction can exhibit via the so-called the spin Hall magnetoresistance effect (SME) [30 – 33] of the magnetic-induced change of the charge current. The impact of the magnetic dynamics on the charge current in nonmagnetic layers is related to the conversion of the spin current magnetic induced in HM into the transverse charge current by the ISHE. The impact of the charge current on the magnetic states occurs via its SHE conversion into the transverse spin accumulation and the spin torque force.

Especially clearly SME is exhibited in the case of insulating magnetic (IM) nanolayer (specifically, yttrium iron garnet (YIG)), adjusting to the HM nanolayer (specifically, Pt) possessing the strong enough spin-orbit interaction. In such the nanostructure the change in resistance due to SMR is related to a combination of the SHE and ISHE, acting simultaneously. When a charge-current $\boldsymbol{J}_e$ is sent through a Pt nanolayer, a transverse spin-current $\boldsymbol{J}_s$ is generated by the SHE following $\boldsymbol{J}_e \propto \sigma \times \boldsymbol{J}_s$, where σ is the polarization direction of the spin-current. Part of this created spin-current is directed towards the interface as it is shown in **Figure 6**.
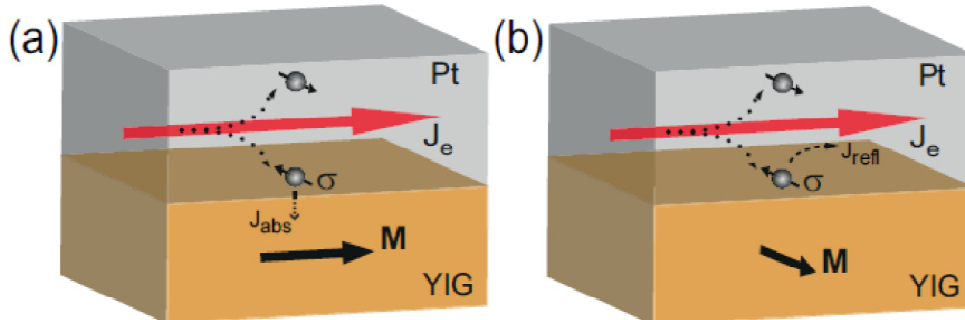
Figure 6. Schematic of the passage of spin and charge currents at the SMR in a YIG/Pt nanostructure. (a) When the magnetization $\boldsymbol{M}$ YIG is perpendicular to the spin polarization σ of the spin accumulation created in the Pt by the SHE, the spin accumulation will be absorbed ($\boldsymbol{J}_{abs}$) by the localized moments in the YIG. (b) For $\boldsymbol{M}$ parallel to σ, the spin accumulation cannot be absorbed, which results in a reflected spin-current back into the Pt, where an additional charge-current $\boldsymbol{J}_{refl}$ will be created by the ISHE.

At the interface, the electrons in the Pt will interact with the localized moments in the YIG. Depending on the magnetization (M) direction of the YIG, electron spins will be absorbed ($M \perp \sigma$) or reflected ($M \parallel \sigma$). By changing the direction of the magnetization of the YIG, the polarization direction of the reflected spins, and thus the direction of the additional created charge-current, can be controlled. A charge-current with a component in the direction perpendicular to J_e can be created as well, generating a transverse voltage.

In a diffusion approximation for both magnetic and HM nanolayers the spin and charge currents are expressed in terms of gradients of charge and spin accumulations (or spin-dependent electrochemical potentials and densities). The charge current density is the expectation value of the current operator $j = e(nv + vn)/2$, where e is the electron charge, n is the electron density, and v is the velocity operator. For a normal metal with constant density n_N and rift velocity v_N, $j_{eN} = en_N v_N$. The spin current in the non-relativistic limit is the second-order tensor

$$\overset{\leftrightarrow}{j}_{sN} = e\langle j \otimes \sigma + \sigma \otimes j \rangle / 2 = \left(j_{sx}, j_{sy}, j_{sz}\right)^T,$$ (38)

where σ is the vector of Pauli spin matrices, and $< \cdots >$ denotes an expectation value. The row vectors $j_{si} = en(v\sigma_i + \sigma_i v)/2$ are the spin current densities polarized in the i-direction. In metallic ferromagnets with homogenous texture, the average spin current is projected along the unit vector of the magnetization direction m, so the charge current and spin current tensor have the form

$$j_{cF} = e(n_{\uparrow F} v_{\uparrow F} + n_{\downarrow F} v_{\downarrow F}), \quad \overset{\leftrightarrow}{j}_{sF} = j_{sF} \otimes m = (j_{\uparrow F} - j_{\downarrow F}) \otimes m,$$ (39)

where j_{cF} is the spin current density direction vector, "$\otimes$" denotes that the polarization is locked along m. In contrast to the charge current, the spin current is not conserved in the presence of the spin-orbit interaction and non-collinear magnetizations, leading to spin-transfer to the lattice or magnetization, respectively.

In the diffusion approach for the two-current model currents close to the interface of the heterostructure are determined via gradients of the spin-depedent chemical potentials $\mu_{\varsigma F}$, $j_{\varsigma F} = -(\sigma_{\varsigma F} / e)\nabla \mu_{\varsigma F}$, where $\varsigma = (\uparrow, \downarrow)$ represents the spin direction along of the magnetization and $\sigma_{\varsigma F}$ is the spin-dependent conductivity. The charge and spin currents $j_{cF} = j_{\uparrow F} + j_{\downarrow F}$ and $j_{cF} = j_{\uparrow F} - j_{\downarrow F}$, respectively, are expressed via charge and spin chemical potentials $\mu_{cF} = (\mu_{\uparrow F} + \mu_{\downarrow F})/2$ and $\mu_{cF} = (\mu_{\uparrow F} - \mu_{\downarrow F})/2$, respectively, in the form of Ohm's law

$$\begin{pmatrix} j_{cF} \\ j_{sF} \end{pmatrix} = \sigma_F \begin{pmatrix} 1 & P \\ P & 1 \end{pmatrix} \begin{pmatrix} -\dfrac{1}{e}\nabla \mu_{cF} \\ -\dfrac{1}{e}\nabla \mu_{sF} \end{pmatrix},$$ (40)

where $P = (\sigma_{\uparrow F} - \sigma_{\uparrow F})/(\sigma_{\uparrow F} + \sigma_{\uparrow F})$ is the conductance spin polarization, $\sigma_F = \sigma_{\uparrow F} + \sigma_{\downarrow F}$ is the total conductivity. The mentioned potentials are determined by the diffusion equations

$$\nabla^2 \mu_{sF} = \frac{\mu_{sF}}{\lambda_F^2}, \quad \nabla^2(\mu_{cF} + P\mu_{sF}/2) = 0,$$ (41)

where the spin-flip diffusion length $\lambda_F = 1/\sqrt{\lambda_{\uparrow F}^{-2} + \lambda_{\downarrow F}^{-2}}$ is expressed in terms of the spin-diffusion length for each spin $\lambda_{\varsigma F} = \sqrt{D_{\varsigma F}\tau_{sf,sF}}$. The spin-dependent charge diffusion constant

$D_{\varsigma F} = \tau_{\varsigma F} v_{\varsigma F}^2 / 3$ depends on the spin-dependent relaxation time and Fermi velocity, and $\tau_{\varsigma F}$ is the spin-dependent spin-flip time. With boundary conditions, solutions of Eq. (7.4) determine the charge and spin currents of Eq. (40).

In normal metals, the induced spin accumulations is represented by the (position dependent) vector $\boldsymbol{\mu}_{sN} = (\mu_{sx}, \mu_{sy}, \mu_{sz})^T - \mu_{cN} \mathbf{1}$, components of which together with the charge chemical potential obey the diffusion equation system

$$\nabla^2 \mu_{si} = \frac{\mu_{si}}{\lambda^2}, \quad \nabla^2 \mu_{cN} = 0 \tag{42}$$

with the boundary condition is determined at the interface by Eq. (2.1). Without the SHE, charge and spin currents are governed by the equations

$$\boldsymbol{j}_{cN} = -\frac{\sigma_{cN}}{e} \nabla \mu_{cN}, \quad \boldsymbol{j}_{si} = -\frac{\sigma_{si}}{e} \nabla \mu_{si}. \tag{43}$$

The spin polarization in the case of the NM layers has arbitrary direction in contrast to the case of the magnetic layers.
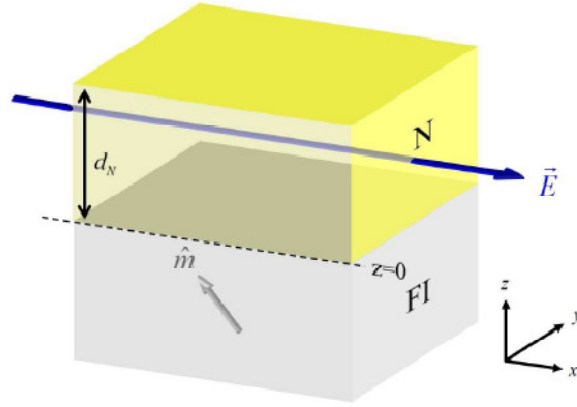
Figure 7. The N|FI bilayer nanostructure with charge flow along of an applied electric field.

In the considered case of the bilayer nanostructure HM/FI (FI denotes insulating magnetic) represented in **Figure 7**, in which the charge current flow in the metal parallel to the applied electric field $\boldsymbol{E}$ and the SHE generate a spin accumulation, generalization of the Ohm's law (Eq. (40)) can be represented by the system [14]

$$\boldsymbol{j}_{cN} = -\frac{\sigma_N}{e} \left(\nabla \mu_{cN} - \frac{\theta_{SH}}{2} \sum_i \boldsymbol{x}_i \times \nabla \mu_{sN} \right), \tag{44}$$

$$\boldsymbol{j}_{si} = -\frac{\sigma_N}{e} \left(\theta_{SH} \nabla \mu_{cN} + \frac{1}{2} \boldsymbol{x}_i \times \nabla \mu_{si} \right), \tag{45}$$

where $\boldsymbol{\mu}_{sN} = (\mu_{sx}, \mu_{sy}, \mu_{sz})^T - \mu_{cN} \mathbf{1}$ is the spin accumulation, i.e. the spin-dependent chemical potential relative to the charge chemical potential $\mu_{cN} = e\varphi$, σ_N is the electric conductivity, θ_{SH} is the spin Hall angle, and "×" denotes the vector cross product operating on the gradients of the spin-dependent chemical potentials. The SHE is represented by the first term in Eq. (45) that generates the spin currents parallel to the applied electric field $\boldsymbol{E} = E_x \boldsymbol{x}$ (**Figure 7**). The

ISHE is governed by the second term in Eq. (44) that connects the gradients of the spin accumulations to the charge current density.

According to Eqs. (44) and (45), the spin current in N consists of conventional diffusion and spin Hall drift contributions. The spin current density flowing in the z-direction is described by the expression

$$\boldsymbol{j}_{sz} = -\frac{\sigma_N}{2e}\nabla_z\boldsymbol{\mu}_{sN} - j_{s0}^{SH}\boldsymbol{y},\tag{46}$$

where $j_{s0}^{SH} = \theta_{SH}\sigma_N E_x$ is the bare spin Hall's current, i.e., the spin current generated directly by the SHE. Due to the boundary conditions $\boldsymbol{j}_{sz}(z)$ is continuous at the interfaces ($z = d_N, 0$). The spin current density at a vacuum interface ($z = d_N$) vanishes, while at the magnetic interface ($z = 0$), it is governed by the spin accumulation and spin-mixing conductance according to Eq. (1), $\boldsymbol{j}_{sz}(0) = -\boldsymbol{j}_s^{(N|F)}$. With these boundary conditions, the solution of Eq. (42) for the spin accumulation can be represent as

$$\boldsymbol{\mu}_{sN}(z) = -\boldsymbol{y}\mu_s^0\frac{\sinh A(z)}{\sinh A(d_N)} + \frac{\cosh B(z)}{\sinh B(2d_N)}\boldsymbol{C}_{\boxminus\succ}\left[\frac{2\lambda G_{\uparrow\downarrow}}{\sigma_N + \lambda G_{\uparrow\downarrow}\coth B(2d_N)}\right],\tag{47}$$

where

$$A(z) = \frac{2z - d_N}{2\lambda},\quad B(z) = \frac{z - d_N}{\lambda},\quad \boldsymbol{C}_{\boxminus\succ} = \left[\boldsymbol{m}\times(\boldsymbol{m}\times\boldsymbol{y})\,\text{Re} + (\boldsymbol{m}\times\boldsymbol{y})\,\text{Im}\right],$$

μ_s^0 is the spin accumulation at the interface in the absence of spin-transfer. The distribution spin current in N is described by the expression

$$\frac{\boldsymbol{j}_s^z(z)}{j_{s0}^{SH}} = \boldsymbol{y}\left(\frac{\cosh A(z)}{\cosh A(d_N)} - 1\right) - \frac{\tanh A(d_N)\sinh B(z)}{\sinh B(2d_N)}\boldsymbol{C}_{\boxminus\succ}\left[\frac{2\lambda G_{\uparrow\downarrow}}{\sigma_N + \lambda G_{\uparrow\downarrow}\coth B(2d_N)}\right],\tag{48}$$

from which it follows that when the magnetization is along $\boldsymbol{y}$, the spin current at the N|FI interface vanishes. When the magnetization is along $\boldsymbol{x}$, the spin current at the NF interface and the spin torque on the magnetization is activated, while the spin accumulation is dissipated correspondingly. The x-components of both spin accumulation and spin current vanish when the magnetization is along $\boldsymbol{x}$ and $\boldsymbol{y}$, and are largest at $(\boldsymbol{x} + \boldsymbol{y})/2$.

The SMR effect is exhibited via the ISHE which drives a charge current in the $x - y$ plane by the diffusion spin current component flowing along the z-direction. The total longitudinal (along $\boldsymbol{x}$) and transverse or Hall's (along $\boldsymbol{x}$) charge currents become

$$\frac{j_{c\parallel}(z)}{j_c^0} = 1 + \theta_{SH}^2\left(\frac{\cosh A(z)}{\cosh A(d_N)} + (1 - m_y^2)\frac{\tanh A(d_N)\sinh B(z)}{\sinh B(2d_N)}\varphi_R(G_{\uparrow\downarrow})\right),\tag{49}$$

$$\frac{j_{c\perp}(z)}{j_c^0} = \theta_{SH}^2\frac{\tanh A(d_N)\sinh B(z)}{\sinh B(2d_N)}(m_x m_y\varphi_R(G_{\uparrow\downarrow}) - m_z\varphi_I(G_{\uparrow\downarrow})),\tag{50}$$

where $j_c^0 = \sigma_N E_x$ is the charge current driven by the external electric field, and

$$\varphi_{R(I)} = \text{Re(Im)}\frac{2\lambda G_{\uparrow\downarrow}}{\sigma_N + \lambda G_{\uparrow\downarrow}\coth B(2d_N)}.$$

The charge current vector is usually expressed in terms of the longitudinal and transverse (Hall) resistivities. Averaging the electric currents over the film thickness z and expanding the longitudinal resistivity or current in the $\boldsymbol{x}$-direction of the applied field to leading order in θ_{SH}^2 SH, we obtain

$$\rho_{\parallel} = \left(\overline{\frac{j_{c\parallel}}{E_x}} \right)^{-1} = \sigma_N^{-1} - \theta_{SH}^2 \frac{\tanh A(d_N)}{\sigma_N A(d_N)} + \theta_{SH}^2 (1 - m_y^2) \frac{\tanh^2 A(d_N)}{\sigma_N A(d_N)} \varphi_R(G_{\uparrow\downarrow}), \tag{51}$$

$$\rho_{\perp} = \frac{\overline{j_{c\perp}}}{\sigma_N^2 E_x} = -\theta_{SH}^2 m_x m_y \frac{\tanh^2 A(d_N)}{\sigma_N A(d_N)} \varphi_R(G_{\uparrow\downarrow}) - \theta_{SH}^2 m_y^2 \frac{\tanh^2 A(d_N)}{\sigma_N A(d_N)} \varphi_I(G_{\uparrow\downarrow}) . \tag{52}$$

Hence it is evidently decreasing $A^{-1}(d_N) \to 0$ when the N layer thickness increases relatively the spin-flip diffusion length ($\lambda / d_N \to 0$) SMR effect vanishes. The SMR magnitude is proportional to the second power of the spin Hall angle (θ_{SH}^2) and it is related to the spin-mixing conductance ($G_{\uparrow\downarrow}$) at the interface which is determined by the spin-dependent scattering matrix.

References

1. L. Zutic, J. Fabian, S. Sarma. Rev. Mod. Phys., 2004, 76, 323.
2. A. Manchon, H. C. Koo, J. Nitta, S. M. Frolov, R. A. Duine. Nat. Mater., 2015, 36, 871.
3. J. Sinova, S. Valenzuela, J. Wunderlich, C. H. Back, T. Jungwirth. Rev. Mod. Phys., 2015, 87, 1213.
4. L. Liu, C.-F. Pai, Y. Li, H. W. Tseng, D. C. Ralph, R. A. Buhrman. Science, 2012, 336, 555.
5. R. H. Liu, W.L. Lim, S. Urazhdin. Phys. Rev. Lett., 2013, 110, 147601.
6. N. V. Volkov. Physics – Uspekhy, 2012, 55, 263.
7. J. E. Hirsch. Phys. Rev. Lett., 1999, 83, 1834.
8. E. M. Chudnovsky. Phys. Rev. Lett., 2007, 99, 206601.
9. I. M. Miron, G. Gaudin, S. Auffer, B. Rodmacq, A. Schuhl, S. Pizzini, J. Vogel, P. Gambardalla. Nat. Matter., 2010, 9, 230.
10. A. Manchon, S. Zhang. Phys. Rev. B., 2009, 79, 094422-1.
11. X. Wang, A. Manchon. Phys. Rev. Lett., 2012, 108, 117201.
12. R. Cheng, J.-G. Zhu, D. Xiao. arXiv: 01618v1 (2016).
13. H. V. Gomonay, V. M. Loktev. Phys. Rev. B., 2010, 81, 144427.
14. A. Brataas, G. E. W. Bauer, P. J. Kelly. Phys. Rep., 2006, 427, 157.
15. P. Gambardella, I. M. Miron. Phil. Trans. R. Soc. A, 2011, 369, 3175R.
16. J. SinovaJ, S. O. Valenzuela, J. Wunderlich, C. H. Back, T. Jungwirth. Rev. Mod. Phys., 2015, 87, 1213.
17. K. Ando, S. Takahashi, K. Harii, K. Sasage, J. Ieda, S. Maekawa, E. Saitoh. Phys. Rev. Lett., 2008, 101, 036601.
18. Ch. D. Xiao. arXiv: 1509.09229v2 (2016).
19. Ya. Tserkovnyak, S. A. Bender. Phys. Rev B, 2014, 90, 014428.
20. Ya. Tserkovnyak, A. Brataas, E.W. Bauer. Phys. Rev. B, 2002, 66, 224403.
21. R. Cheng, J. Xiao, Q. Niu, A. Brataas. Phys. Rev. Lett., 2014, 113, 057601-1.
22. M. Hagiwara, K. Katsumata, I. Yamada. J. Phys. Condens. Matter, 1996, 8, 7349.
23. P. W. Brouwer. Phys. Rev. B, 1998, 58, R10135.
24. O. A. Tretiakov, A. Brataas. Phys. Rev. Lett. 2013, 110, 127208.

25.   R. Cheng, Q. Niu. Phys. Rev. B, 2012, 86, 245118.

26.   K.-W. Kim, J.-H. Moon, K.-J. Lee, H.-W. Lee. Phys. Rev. Lett., 2012, 108 217202.

27.   C. H. Wong, Ya.Tserkovnyak. Phys. Rev. B, 2009, 80, 184411.

28.   L. Berger. Phys Rev. B., 1996, 54, 9353.

29.   A. Brataas, Ya. Tserkovnyak, E.W. Bauer. Phys. Rev. B., 2002, 66, 060404.

30.   N. Vlietstra, J. Shan, V. Castel, B. J. van Wees, J. Ben Youssef. Phys. Rev. B, 2013, 87, 184421.

31.   H. Nakayama, M. Althammer, Y.-T. Chen, K. Uchida, Y. Kajiwara, D. Kikuchi, T. Ohtani, S. Geprägs, M. Opel, S. Takahashi., R. Gross, G. E. W. Bauer, S. T. B. Goennenwein,   E. Saitoh. Phys. Rev. Lett., 2013, 110, 206601.

32.   M. B. Jungfleisch, V. Lauer, R. Neb, A. V. Chumak, B. Hillebrands. Appl. Phys.Lett., 2013, 103, 022411.

33.   Y.T. Chen, S. Takahashi, H. Nakayama, M. Althammer, S. T. B Goennenwein, E. Saitoh, G. E. W. Bauer. J. Phys.: Condens.Matter, 2016, 28, 1.

PREPARATIONAND CHARACTERIZATION OF ANOVEL GELATIN / NANODIOPSIDE / NANOHYDROXYAPATITE COMPOSITE SCAFFOLDSFOR TISSUE ENGINEERING APPLICATIONS

M. Azadi [1], Z. Shams Ghahfarokhi [2], A. Teimouri [1]

[1] Chemistry Department
Payame Noor University
Tehran, Iran
mohammad_azadi60@yahoo.com
[2] University of Birjand
Birjand, Iran

Abstract

Gelatin/nanodiopside/nanohydroxyapatite (GE/nDP/nHAp) composite scaffolds were prepared from the mixture of GE, nDP and nHAp in different inorganic/organic weight ratios by using the freeze-drying method. The prepared nHAp and composite scaffolds were investigated using BET, TG, FT–IR, SEM and XRD techniques. The composite scaffolds had 50 – 85 % porosities with interlinked porous networks. Moreover, investigation of the cell proliferation, adhesion and viability using MTT test, and mouse preosteoblast cell proved the cytocompatibility nature of the composite scaffolds with improved cell attachment and proliferation. All these results essentially illustrated that this composite could be a potential for tissue engineering application.

1. Introduction

The aim of tissue engineering is to repair or regenerate damaged tissue using the substitution of engineered tissue. It will help to restore the functions through regeneration and merging with the host tissue. Thus, meaningful attention is being given to three-dimensional (3-D) polymer scaffolds for tissue engineering applications [1].

A full understanding of the structures, compositions and biochemical and biomechanical properties of natural bone is needed to design the ideal biomimetic artificial scaffold. These parameters may provide adequate insights in the engineering. A scaffold must be synthesized into a 3-D structure with a high porosity and a proper pore size for cell implantation. A scaffold should play the role of natural extracellular environment of the tissue, the time-space matching charter of the degradation disappearance of materials, new tissues structure, and good mechanical strength [2 – 4].

Generally, the living bone in the human system is composed of 10 – 20 % collagen, 60 – 70 % inorganic phase, and 9 – 20% water, by weight. Also, other organic materials, such as proteins, polysaccharides and lipids, are included in small quantities. The important composition of the inorganic phase is hydroxyapatite with the chemical formula $Ca_{10}(PO_4)_6(OH)_2$ [5]. It is a non-toxic, osteoconductive and non-inflammatory biomaterial

[6 – 8]. The incorporation of bioactive polymers, such as gelatin, can improve the nHAp poor formability, intrinsic brittleness and out-migration of nHAp particles from the transplanted tissue [8]. Hence, single component system cannot assist and mimic all the properties of bone. Therefore,development of multicomponent system for bone repair becomes necessary.

Gelatin is a partially degraded product of collagen. Gelatin has been incorporated into scaffolds to promote cell migration, adhesion, differentiation and proliferation [1]. Studies have shown that composite scaffolds of gelatin and hydroxyapatite improve the osteoblast cell viability and proliferation, osteoconductivity, and fibroblast cell attachment [9 – 14]. In addition, to increase the fracture toughness of HAp, the composite of diopside (CaO–MgO– $2SiO_2$) and HAp can be prepared [15]. The bending strength and fracture toughness of the diopside-HAp composite were two or three times higher, than those of nHAp, and it was proved that the composite had no general toxicity in cell culture test [16].

Diopside ceramics possess excellent degradability, in vitro apatite-formation ability and in vivo bioactivity [17, 18].

Hydroxyapatite/Al_2O_3/diopside scaffold and other multi component scaffolds and their properties have been investigated by comparing them with bi-component scaffolds [19, 20]. However, the influence of nHAp on nDP/GE composite scaffolds is not well understood. In continuation of our recent study on the construction of composite scaffolds [21 – 25], in this work, we focus on the preparation, characterization, bioactivity, biodegradation, mechanical and in vitro properties of nano-composite scaffolds GE/nDP/nHAp in detail.

2. Experimental

2.1. Materials

For the in vitro study of cytotoxicity, a mouse preosteoblast cell line ($MC_3T_3–E_1$) was purveyed by Riken Cell Bank (Ibaraki, Japan). The$MC_3T_3–E_1$cells were cultured with low glucose-Dulbecco's modified Eagle's medium (DMEM), which contained 10% fetal bovine serumand 1% penicillin–streptomycin (GIBCO, Gaithersburg, MD, USA) in a humidified 37 °C incubator with 95% air and 5% CO_2. Ascorbic acid and 3-(4,5-dimethylthiazol-2-yl)-2,5-diphenyltetrazoliumbromide (MTT) were supplied from Amersco Co. (Solon, OH, USA). Fetal bovine serum (FBS) was purchased from Wisent (Montreal, Canada). Magnesium chloride, gelatin, tetraethyl orthosilicate (TEOS), calcium nitrate, diammoniumhydrogenphosphate, n-Hexane, ammonium hydroxide, ethanol, glutaraldehyde, dimethyl sulfoxide (DMSO), and all other solvents and chemicals were bought fromSigma Chemical (St. Louis, MO, USA).

2.2. Preparation of gelatin hydrogel

Gelatin hydrogel was synthesized according to the literature [4]. 1 gram of gelatin was added to 25 ml distilled water and stirred powerfully to get a perfectly transparent solution.

2.3.Diopside synthesis

The diopsidenanopowder was prepared by a modified sol–gel method [18]. In short, we dissolved 0.125 mol of $Ca(NO_3)_2 \cdot 4H_2O$ and $MgCl_2 \cdot 6H_2O$ in ethanol and stirred powerfully for 30 min at 80 °C to dissolve in the solvent. $Si(OC_2H_5)_4$ (TEOS) was added to the homogenous solution and was slowly stirred to acquire a wet gel. After drying in an oven at 100 °C for 24 h, a

dried powder was resulted which was grounded in a hand-mortar and calcinated at 700 °C for 2 h and at 1100 °C for further 24 h. At last, it was ball-milled in a zirconia Mechanical Ball Mill (Daehan Science, Seoul, Korea) for 8 h to obtain diopside nanopowder with 35 – 65 nm particle sizes.

2.4. Preparation of nHAp powder

nHAp was prepared based on the available literature [26] by adding a solution of 30 mmol $(NH_4)_2HPO_4$ in 250 ml double distilled water to a solution of 50 mmol $Ca(NO_3)_2 \cdot 4H_2O$ in 600 ml water. After that, 30 ml of ammonium hydroxide (30 % in water) and an additional quantity of 5 mmol $Ca(NO_3)_2 \cdot 4H_2O$ were added. The mixture was stirred powerfully and 10 ml of ammonium hydroxide was added after 5 h. The resulted mixture was stirred moderately for 12 h. Afterwardsthe solution was filtered and washed in distilled water. The final product was dried at 80 °C for 15 h. The sample was pulverized and suspended in an ultrasonic sonicator bath filled with 300 ml of distilled water for 15 min. Subsequently, this powder was filtered and dried. After calcination at 1000 °C for 1 h the particles showed high crystallinity.

2.5. Preparation of composite scaffold

nDP was added into gelatin hydrogel and stirred for 12 h at 4 °C.ThennHAp was added to the mixture and stirred for 24 h to dispersenHAp in the GE/nDP blend. The resultant combination was transferred intoanultrasonication bath to further disperse the particles and reduce particle size. Then, 0.25 % (v/v) glutaraldehyde was added in 1:32 ratio (2 h) for crosslinking. The resultant mixture was transferred to the 24-well culture plates and pre-freezed at –20 °Cfor 12 h. This was followed by freeze-drying (Dena vacuum industry) at –80 °C for 48 h. The nHAp content of each specimen was scaled according to the GE/nDP/nHAp weight ratios of 30/15/55, 50/11/39, and 70/6.5/23.5, which were listed in **Table 1**.

Table 1. Characteristics of GE/nDP/nHApcomposites.

GE/nDP/nHAp Composition (wt/wt)	Characteristics of the composite scaffolds			
	Porosity (%)	Water-uptake capacity	Scaffold surface / volume ratio (mm^{-1})	Pore Size (μm)
30/15/55	50±2.2	640±35	709.66±21	82±4
50/11/39	75±1	7401±26	772.05±18	93±5
70/6.5/23.5	85±3	13176±36	855.93±25	100±3

2.6. Characterization

The samples were characterized by X-ray diffraction (BrukerD8ADVANCE, Cu Kα radiation), FT–IR spectroscopy (Nicolet 400D in KBr matrix, with the range of 4000–400 cm^{-1}), BET specific surface areas and BJH pore size distribution (Series BELSORP 18, at 77 K) and SEM (Philips, XL30, SE detector). To investigate the weight loss of the GE/nDP/nHAp composite scaffolds during thermogravimetric (TG) analysis, a test was carried out using a DuPont TGA 951 at temperatures ranging from room temperature to 900 °C in the air and at a heating rate of 10 °C/min.

2.7. Porosity studies

The porosity of the scaffolds was computed by using a liquid displacement technique [27]. Hexane was employed as the displacement liquid, because it was a nonsolvent agent for gelatin and could be easily penetrated through the scaffold without any swelling or shrinkage of the scaffold. Scaffolds were cut into 1×1×1 cm pieces and immersed in a cylinder containing a preselected volume of hexane (V_1). The volume of hexane and the hexane-impregnated scaffold was recorded as V_2 and obtained after the scaffold was placed in hexane for 1h. The volume difference ($V_2–V_1$) was the volume of the composite scaffold. V_3 wass elected as the residual hexane volume in the graduated cylinder after the removal of the scaffold. The quantity ($V_1–V_3$), volume of hexane within the scaffold was assayed as the void volume of the scaffold. The total volume of the scaffold was $V = (V_2–V_1) + (V_1–V_3) = V_2–V_3$. The porosity of the scaffold (ε) was measured as follows: ε (%) = $(V_1–V_3)/(V_2–V_3) \times 100$.

2.8. Water-uptake capacity

The scaffolds were immersed in water at room temperature for 48 h. The water uptake of the porous scaffolds was calculated as Water-uptake (%) = $(W_w–W_d)/W_d \times 100$, where W_w and W_d display the wet weight of the scaffolds and initial dry weight sponges, respectively.

2.9. Mechanical properties

Mechanical properties including compressive strength and modulus of the samples were measured in thedry state at a crosshead speed of 2 mm / min in a materialprufung 1446–60 machine (Zwick). The samples of 1×1×1 cm size were used in compressive property test.

2.10. In vitro degradation

The degradation of the GE and(GE/nDP/nHAp)composite scaffolds was investigated in a PBS medium at 37 °C. All samples were placed in PBS medium and incubated at 37 °C for different time intervals (1, 4, 7, 14, 21 and 28 days). $W_o$showstheinitial weightof thescaffolds. After each period, the scaffolds were washed in deionized water for the removal of the surface adsorbed ions and freeze dried. W_t denotes the dry weight of scaffolds. The degradation of the scaffolds was computed by the following formula: Degradation % = $(W_o–W_t)/W_o \times 100$. Degradation rate was recorded as mean ± S.D. ($n = 5$).

2.11. In vitro biomineralization

The composite scaffolds of equal weight and same shape were placed in 1× simulated body fluid (SBF) solution and then incubated at 37 °C in closed Falcon tubes for different time intervals (1, 4, 7 and 14 days). The SBF solution was prepared according to a reported procedure in the literature [28]. After the specified period, the scaffolds were washed three times in deionized water for the removal of the adsorbed minerals. After 14 days, the scaffolds were lyophilized and characterized using SEM, XRD and FT-IR for mineralization.

2.12. In vitro evaluation of cytotoxicity

The MTT test was used as a symptom of relative cell viability [29]. Mouse preosteoblast cell line MC_3T_3-$E_1$was used to obtain the in vitro cytotoxicity ofthe extractions. The isolated and passaged cells (cells less than passage 7) were trypsinised, pelleted and resuspended in a known

amount of DMEM media. The cell concentration of $1 \cdot 10^5$ cells/mlwas seeded onto 24-well culture plates for 24 h. The scaffolds were sterilizedbyplacinginethanol, and irradiated by UV for 30 min.The scaffolds (1 cm × 1 cm × 1 cm) were immersed in separate steriletubes with 5 ml DMEM solution and incubated at 37 °C for 24 h. For investigation the in vitro cytotoxicity of the extractions, a 4ml extraction of each sample was collected. The culture media were changed with the extraction every 48 h. MTT assay was conducted in 1, 3 and 7 days by changing the media with MTT solution in the wells for 4 h.MTT solution was removed and formazan crystals were dissolved in DMSO.Amicroplate reader (Bio–RAD 680, USA) recorded the optical density in a spectrophotometer at a stimulus wavelength of 540 nm. DMSO was used as a blank. The same numbers of cells in contact with culture media were presumed as the control groups.

2.13. Statistical analysis

Statistical analyses were carried out by SPSS v.16.0 software. Data were denoted as the mean ± significant if ρ values obtained from the test were less than 0.05 (ρ< 0.05).

3. Results and discussion

3.1. Scaffold characterization

3.1.1. SEM analysis

Scanning electron microscopy was used for investigation of the morphology of the samples. In pure gelatin (**Figure 1a**), the number of oval and interconnected pores was high. **Figure 1b** showed the external morphology of the nHAp nanoparticles that consisted of approximately spherical agglomerates with a size ranging from 98 to 108 nm.
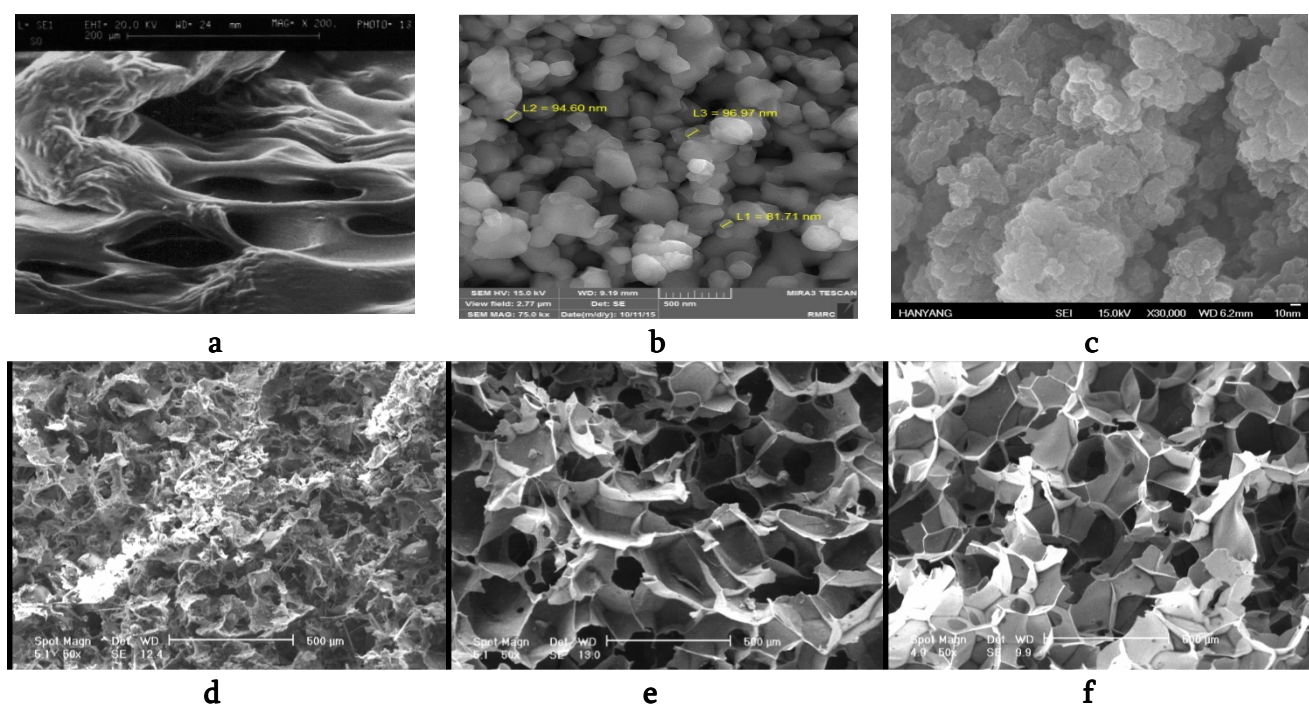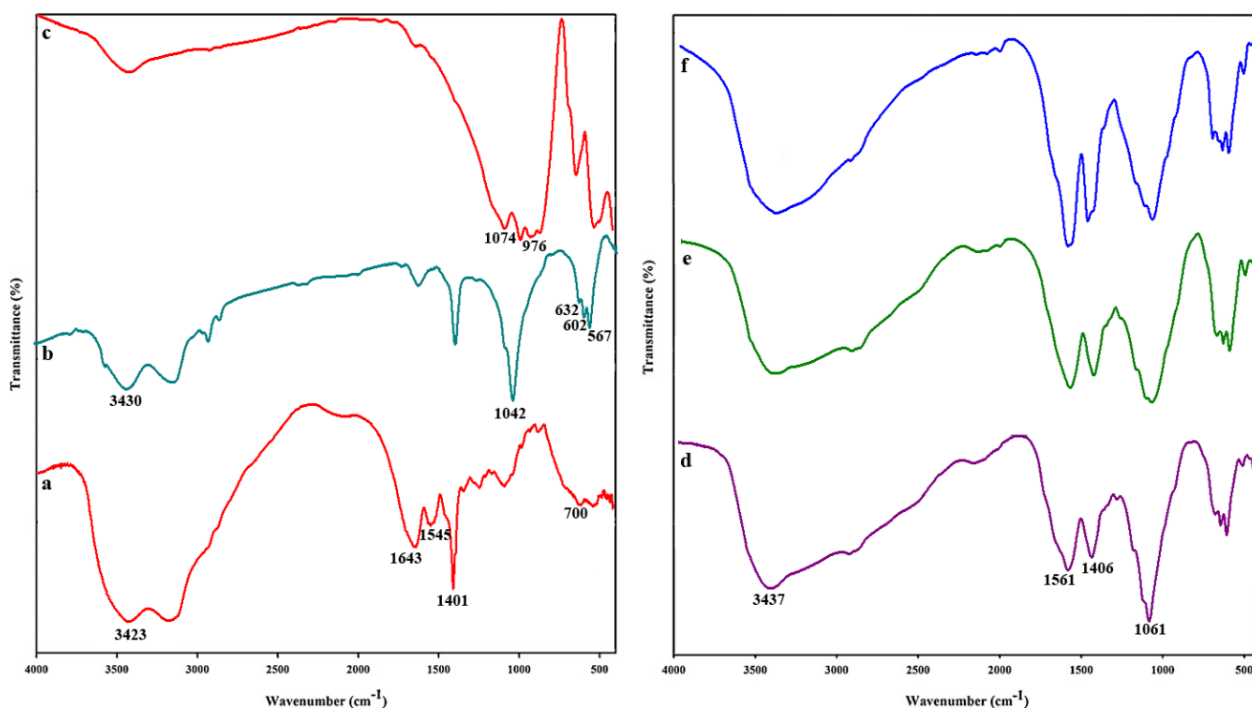

Figure 1. SEM images of (a) pure GE, (b) pure nHAp, (c) pure nDP,
(d) composite 30 %, (e) composite 50 %, and (f) composite 70 %.

The diopside grain size and surface morphology of the particles are shown in **Figure1c**, displaying that,particles agglomerated because of high surface energy. It is evident that the dimensions of agglomerated grains are in nano range (35 – 65 nm). In the scaffolds, fluid exchange and native tissue ingrowth were promoted by forming networks of interconnected and open pores (**Figures 1d, e,** and **f**). In the presence of hydroxyapatite nanoparticles, rough pore walls were seen. They could be, therefore, advantageous for cell adhesion. In the composite scaffolds, the average porosity and the degree of interconnectivity were mainly affected by the nHAp content. As it is obvious from **Figures 1d**, **e**, and **f**, the increase in the amount of nHAp led to a decrease in the number of pores. This was due to the interaction between the polymer chains. However, the transfer of nutrients, oxygen and cells was still continued through it.

3.1.2. FT–IR studies

Figure 2 shows the characteristic FT–IR peaks of nHAp, nDP, GE and their composite scaffolds. The FT-IR spectra of gelatin indicated peaks at 3423 cm^{-1} and 3174 cm^{-1} due to –NH stretching of the secondary amide, C–H stretching at 2922 cm^{-1} and 2850 cm^{-1}, C=O stretching at 1643 cm^{-1}, –NH bending at 1545 cm^{-1}, and –NH out-of-plane wagging at 700 cm^{-1}(**Figure 2a**) [30]. FT–IR spectrum of nHAp showed peaks at 632 and 3430 cm^{-1}, which were corresponded to –OH bending and stretching vibration mode. The bands at 602 and 567 cm^{-1}were related to γ4 of phosphate, the one at 963 cm^{-1}reffered to γ1 of phosphate and the other at 1042 cm^{-1}ascribed to γ3 of the phosphate mode (**Figure 2b**) [31]. In the FT–IR spectra of the diopside bands in the 400 – 2000 cm^{-1} spectral range in the region 700 cm^{-1} can be ascribed to the bending vibrations, and bands in the region 850 – 1100 cm^{-1} which are assigned to the stretching vibrations of the silicate structure. They attributed to the Si–O symmetric stretching of bridging & non-bridging oxygen atoms, Si–O–Si symmetric stretching, and Si–O–Si asymmetric stretching (**Figure 2c**) [32]

Figure 2. FT–IR spectra of (a) pure GE, (b) pure nHAp, (c) pure nDP,
(d) composite 30 %, (e) composite 50 %, and (f) composite 70 %.
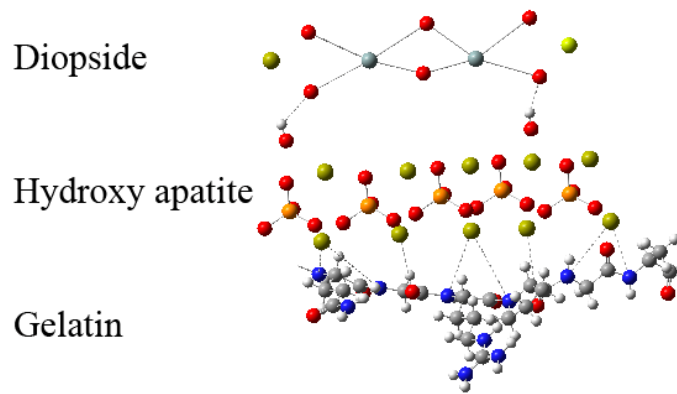
Figure3.The interactions between the nDP and GE network
and nHAp in (GE/nDP/nHAp) composite scaffolds.

The FT–IR spectra of all composite scaffolds showed the typical peaks of phosphate vibration at 1042 cm^{-1}, which implied the existence of nHAp on the surface of composite scaffolds (**Figures 2d – f**). The intensity of peaks at 567 and 602 cm^{-1} was less in (f) scaffold; because the concentration of nHAp is less. But in (d) scaffold, the peaks have resolved and intensity was also increased [33]. For GE/nDP/nHAp composite scaffolds, the absorption at 1659 cm^{-1} can be attributed to COOH groups of gelatin in GE/nDP/nHAp composite scaffolds. It shifted to the direction of higher wave number compared with COOH groups (1643 cm^{-1}) of gelatin itself. These differences were indicator for a noticeably chemical interaction between the nHAp crystal, nDP and GE (**Figures 2d, e,** and **f**). COOH of gelatin in GE/nDP/nHAp exists in the form of COO[-] and the ionic or polar interaction between COO[-] and Ca^{2+} could be formed. So,the characteristic absorptions of COOH and OH in GE/nDP/nHAp composite scaffolds suggested the formation of hydrogen bond between –NH groups of gelatin and –OH groups of nHAp also between –NH groups of gelatin and oxygen of Si-O-Si groups of nDP (**Figure 3**) [29, 34].
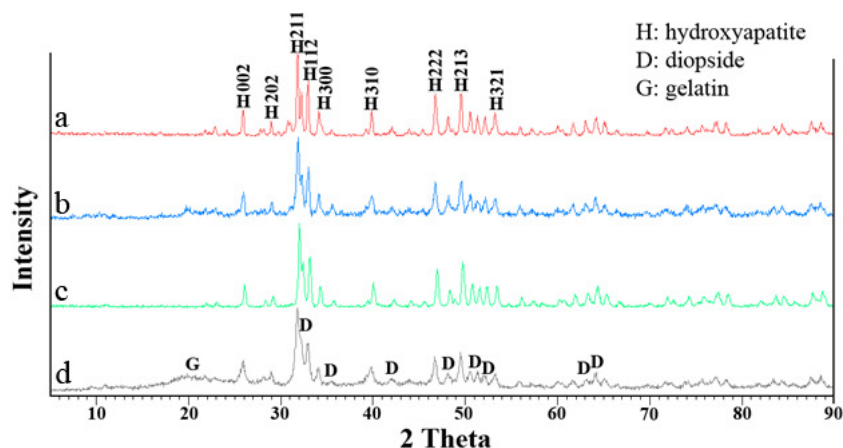
Figure 4. XRD patterns of (a) pure nHAp, (b) composite
30 %, (c) composite 50 %, and (d) composite 70 %.

3.1.3. XRD analysis

X-ray diffraction patterns for the pure nHAp and composite scaffolds with the weight ratios of nHAp are shown in **Figures 4a–f**. The peaks of the synthesized nHAp particles corresponded to the characteristic XRD spectrum of HAp (JCPDS File No. 09–0432). Many sharp diffractions attributed to (211), (112), (300), (002), (213), (222), (202), (310), and (321)

reflections of nHAp crystal, respectively. These were of a typical apatite crystal structure. The sharp diffraction demonstrated that nHAp was composed of well-developed crystals. The XRD patterns of the composites simultaneously presented the characteristic peaks of nHAp, and gelatin [6]. In 23.5% nHAp incorporated scaffolds the peaks had intensities less than the higher concentration of nHAp. The intensity of GE peaks was decreased in the case of nHAp incorporated composite scaffolds.

3.1.4. BET analysis

Figure 5 represented the N_2 adsorption-desorption isotherms of GE/nDP/nHAp sample. The isotherms were similar to the Type III isotherm with H3-type hysteresis loops at high relative pressure according to the IUPAC classification. This is known as a characteristic of porous materials with highly uniform size distributions. The Type III isotherm shows unrestricted multilayer adsorption [35, 36]. The two branches of adsorption-desorption isotherms showed that the materials processed a well-defined and regular array of porous materials. The specific surface area and the pore volume were computed using Brunauer-Emmett-Teller (BET) and Barrett-Joyner-Halenda (BJH) methods, respectively. The structure data of all these materials BET showed that GE/nDP/nHAp had a high BET surface area (11.024 m^2/ g) and a large pore volume (0.012 cc / g) expressive of its potential application as the proper cell growth by adhesion to the scaffold surfaces.
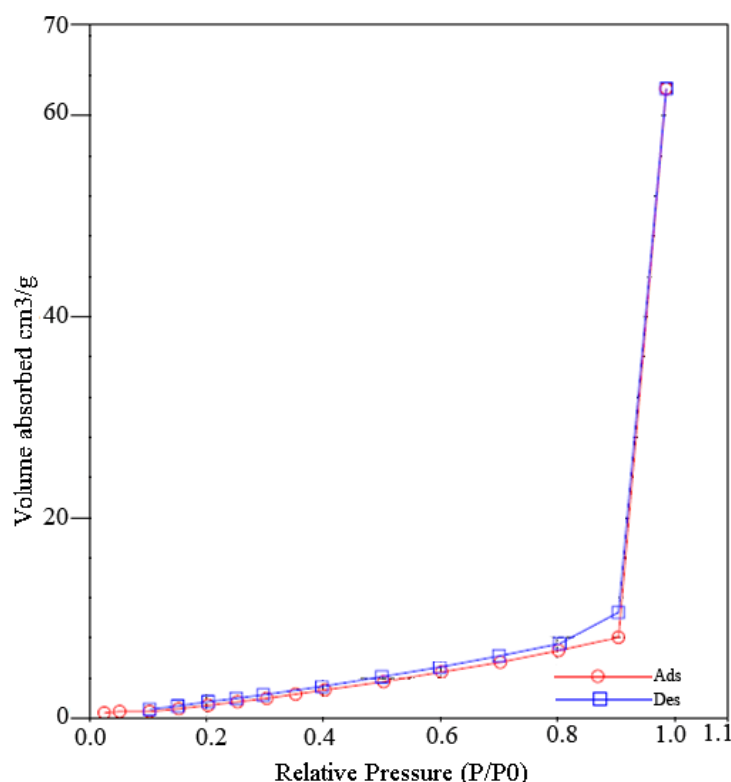
Figure 5.N_2 adsorption–desorption isotherm and
The pore size distribution (inset) of composite 30 %.

3.1.5. Thermogravimetric analysis (TGA)

TG curves of pure nHAp and GE/nDP/nHAp composite scaffolds are displayed in **Figure 6**. TG curve of pure HA particles shows a continuous weight loss of 7.6 %, which can be attributed to loss of moisture. There is no weight loss, showed above 400 °C, suggesting that

pure nHAp is thermally stable at high temperature. The weight of three composite scaffolds decreases quickly with increasing temperature. The initial weight loss performed around 100 °C is assigned to water evaporation. The thermal decomposition of the organic component in GE/nDP/nHAp composite scaffolds occurred mostly in the range of 200 – 350 °C.
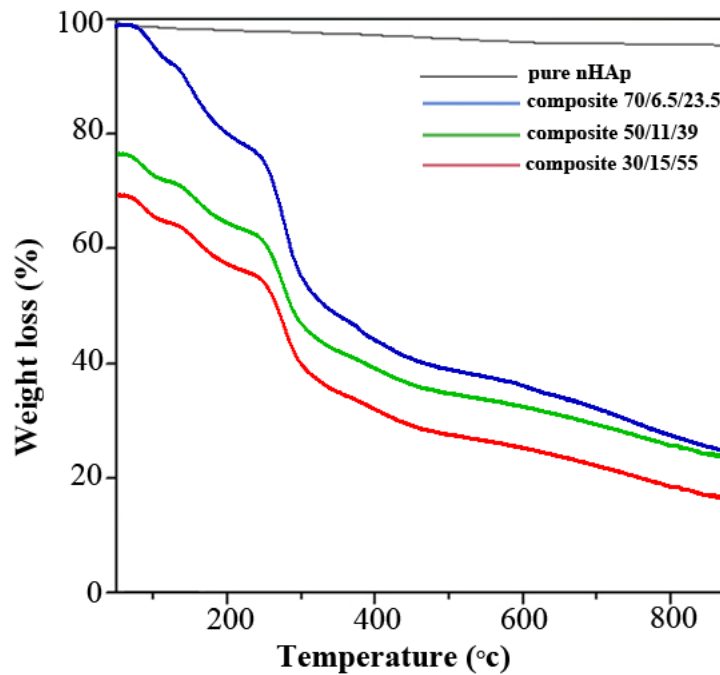
Figure 6. TG curves of samples.

The organic components are decomposed completely at 400 °C. Since inorganic phase of composite scaffold 70 % is less than that of others, its thermal stability is less than the others. The organic/inorganic weight ratios in GE/nDP/nHAp composite scaffolds except from water content calculated to be 28.6/71.4. It is according to the theoretical weight ratio (30/70). Thermal analysis represented that GE molecules have been well interacted with nHAp [2, 6, 30].
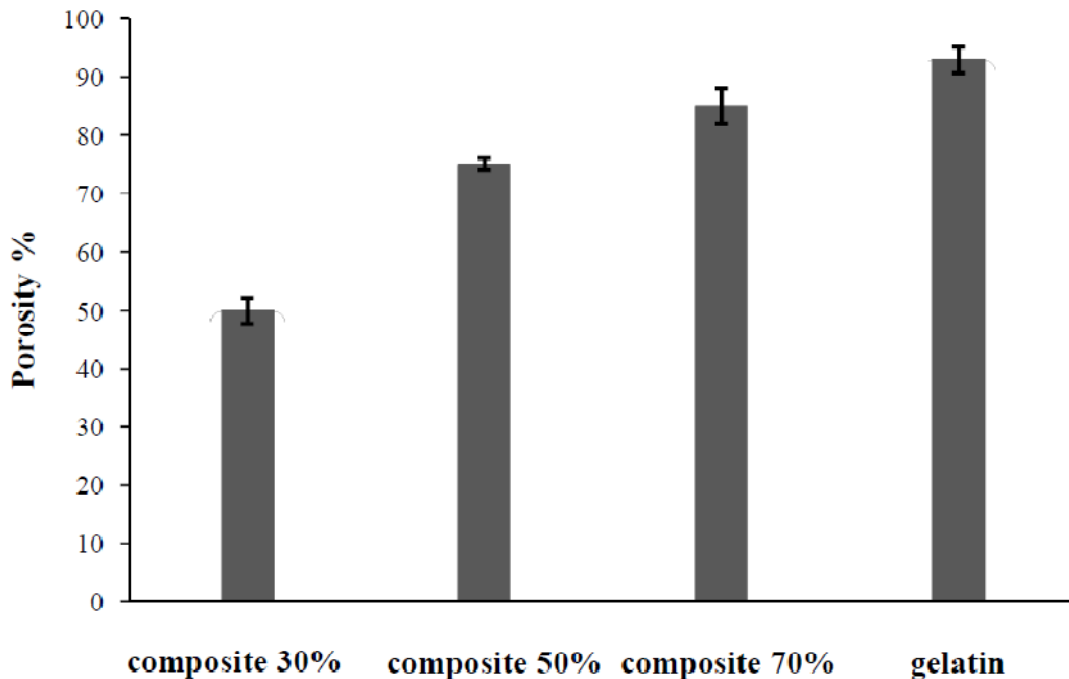
Figure 7. Porosity values of GE and composite scaffolds.

3.2. Porosity measurements

The porosities of the prepared scaffolds are shown in **Figure 7**. When the content of GE was increased from 30 to 70 wt. %, the porosities were increased from about 50 to 85 %. The reason is evident as with the decrease of gelatin amount, the actual volume fraction held by the materials itself decreases [37]. Cells could move through the pores and get attached at proper positions in the scaffold for further proliferation. Porosity improved the transport of oxygen and nutrients to the inner portions of the composite scaffolds. The reduction in porosities along with the increase in nHAp content (the decrease in GE content) was due to the presence of nHAp in the scaffold which kept the polymer chains of GE [30]. Pore sizes were affected by the time for the growth of ice crystals. Therefore, controlling the key freeze-drying process parameters such as rate of cooling and pre-freezing temperature could result in larger pore sizes.

3.3. Water-uptake capacity

Water-uptake studies of GE and GE/nDP/nHAp composite scaffolds showed the ability to maintain water more than their original weight and very good water-uptake capacity (**Figure 8**). It was seen that as the content of GE was increased, the water-uptake ratio was also enhanced. The addition of GE (with the decrease in the amount of nHAp) increased the water-uptake of GE/nDP/nHAp composite scaffolds. This could be because nHAp formed cross-linking chains that decreased the hydrophilicity of gelatin by grafting phosphate and calcium to the hydrophilic NH_2or OH groups. The increase in water-uptake allowed the samples to acquire nutrients from culture media more efficiently. Water-uptake promoted the cells permeation into the scaffolds in a 3-D design, during cell culture. Water-uptake also enhanced the internal surface area of the scaffolds owing to increasing the pore size and total porosity. Samples expressing a higher degree of water-uptake could have the maximum probability of cell infiltration into the 3-D scaffold as well as the maximum cell growth by attachment to the scaffold surfaces.
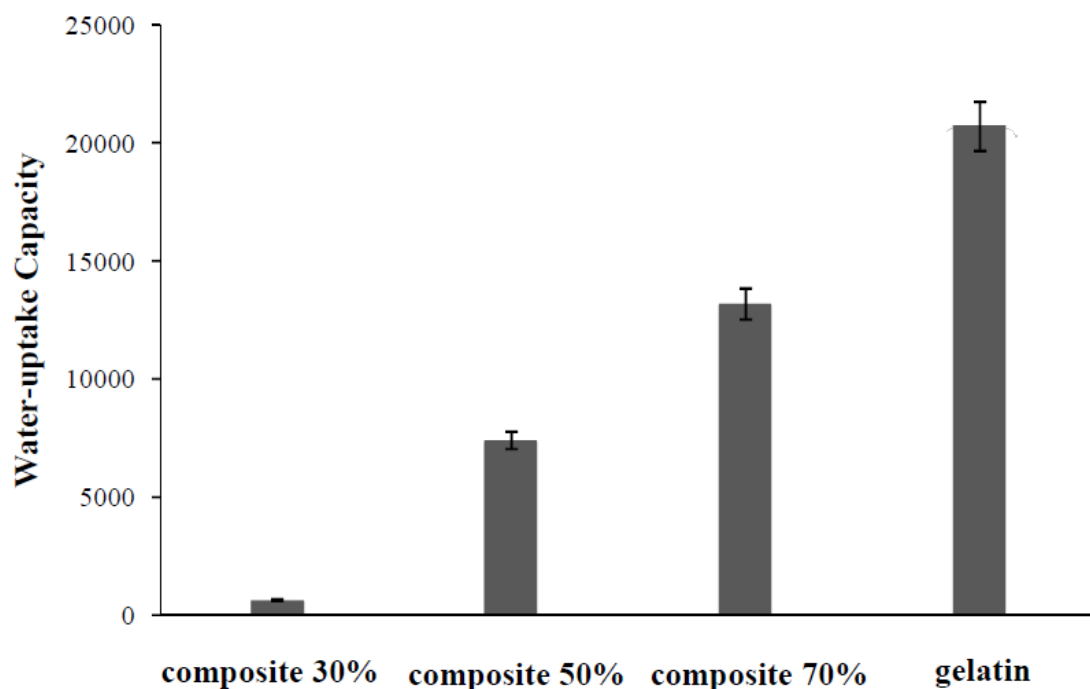
Figure 8. Water-uptake values of GE and composite scaffolds.

3.4. Mechanical properties

The composite scaffolds must have sufficient porosity for cell proliferation, but they must also provide good mechanical strength to support the frame during tissue regeneration. The tenacity of the composite scaffolds was compared according to amount of nHAp. In this work, the effect of the nHAp incorporation on the compressive strength (**Figure 9a**) and compressive modulus (**Figure 9b**) of the composite scaffolds was studied. The increase in pore wall thickness and the reduction in pore sizes by the addition of nHAp could be a reason for the suitable mechanical properties in composite scaffolds, in comparison to the GE scaffolds. However, while the water uptake of scaffolds would enhance cell adhesion, it could lower its mechanical properties.
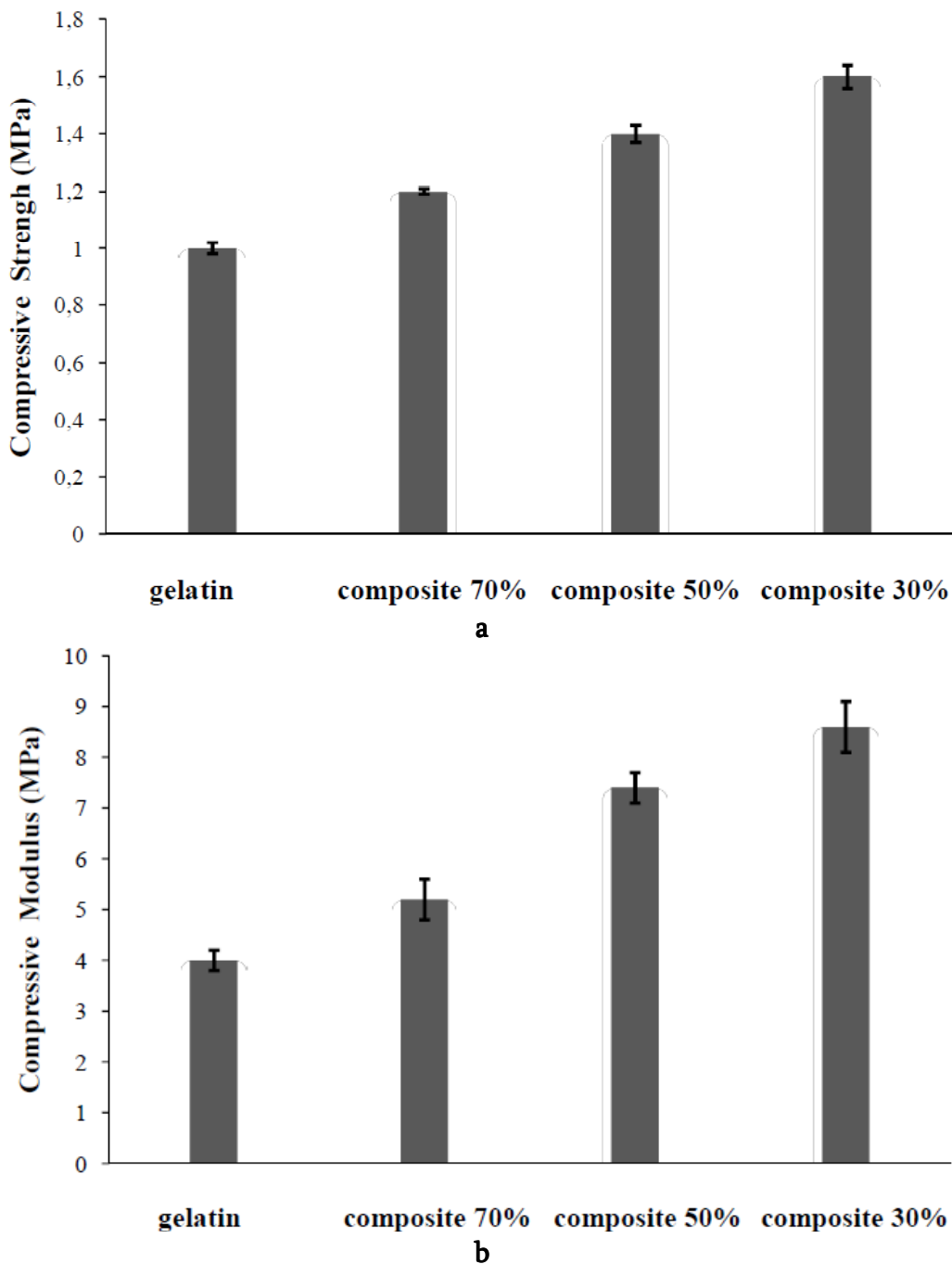
Figure 9. Mechanical properties of GE and composite scaffolds: (a) compressive strength; and (b) compressive modulus. Values are mean ± SD ($n = 5$).

3.5. In vitro degradation studies

Figure 10 shows the degradation profiles of composite scaffolds after incubation in PBS solution at 37 °C and pH = 7.4 conditions for 4 weeks. It was presumed that the macromolecules of the scaffolds surface underwent preferential hydrolytic scission into small molecules (oligomeric units), which could be dissolved in PBS [38]. All composites were slowly degraded during the degradation period. The percentages of weight loss of composites were 15 – 20 % after 4 weeks. The degradation rate of composite scaffolds was lower than the pure GE and it was decreased with the addition of nHAp into the matrix. These shows that changing the amount of nHAp or gelatin could be modify the degradation of the composite scaffolds.
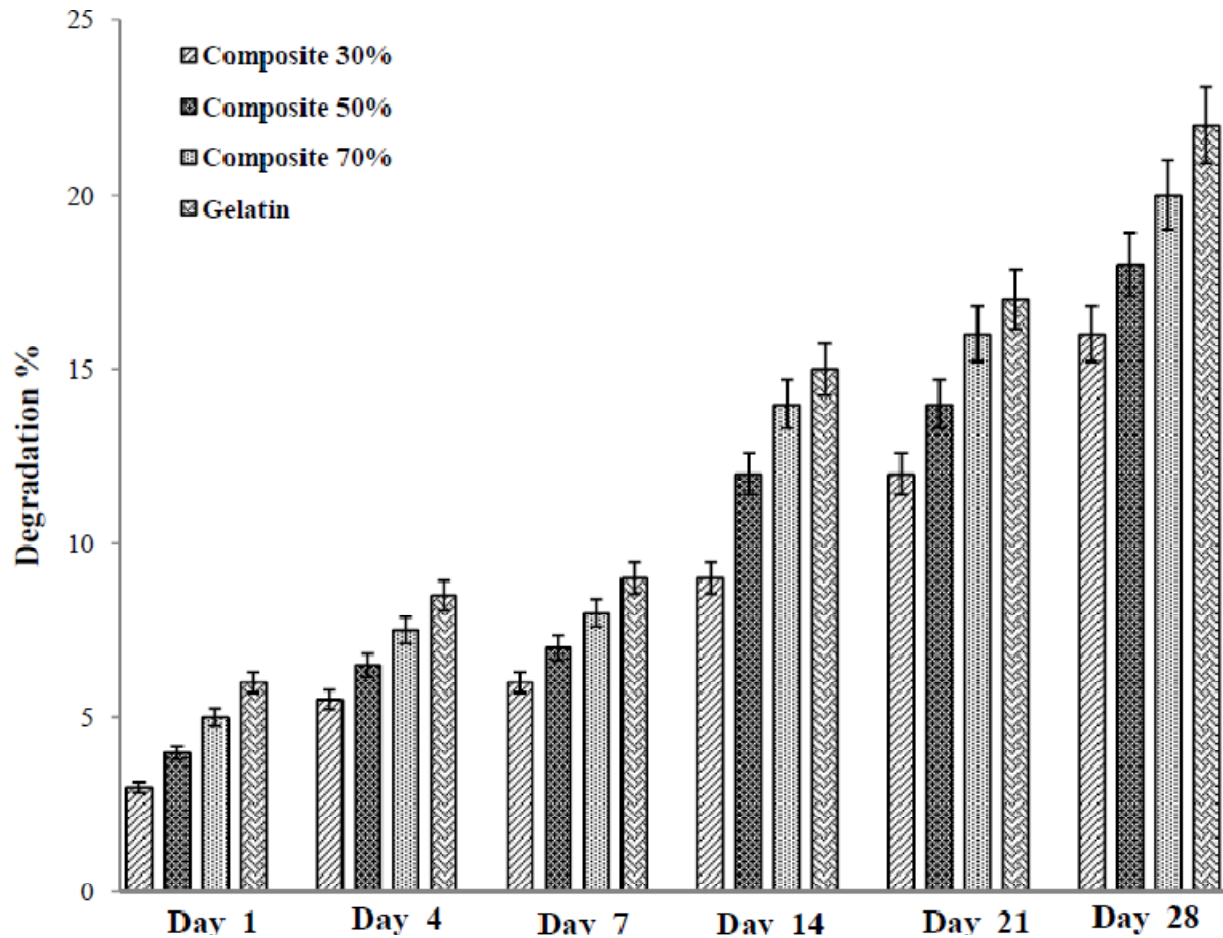
Figure 10. Degradation behavior vs time curve of scaffolds in PBS at 37 °C.

3.6. In vitro biomineralization studies

The scaffolds showed a good potential to endure mineralization at physiological temperature and pH in SBF solution. The apatite deposition morphology was changed after 14 days of incubation. After 14 days of incubation in 1× SBF, minerals were seen to deposit on the surface of pores (**Figure 11**). FT–IR studies (**Figure 12**) illustrated that the phosphate peaks intensity at 603 and 633 cm^{-1} was increased [39]. This showed that the mineral deposition was enhanced. There were many nHAp particles on the composite scaffolds, which played as nucleation sites role that decreased the surface energy minerals. So, apatite could be formed more effectively on the composite containing 55 % nHAp than 23.5 % nHAp (30 % GE than 70% GE). It has been implied that the formation of apatite on scaffolds is caused by negative

charge functional groups which can further induce apatite by the formation of amorphous calcium phosphate [40]. Once the apatite nuclei are formed, they grow naturally by serving the phosphate and calcium ions present in the medium. X-ray diffraction patterns for the composite scaffolds are presented in **Figure 13**. The peaks of calcium phosphate particles that related to the characteristic XRD spectrum of $Ca_2P_2O_7$ (JCPDS File No. 03–0605) were increased with the addition of nHAp content. These results showed that the addition of nHAp increased the bioactivity of the composite scaffolds.

a   b   c
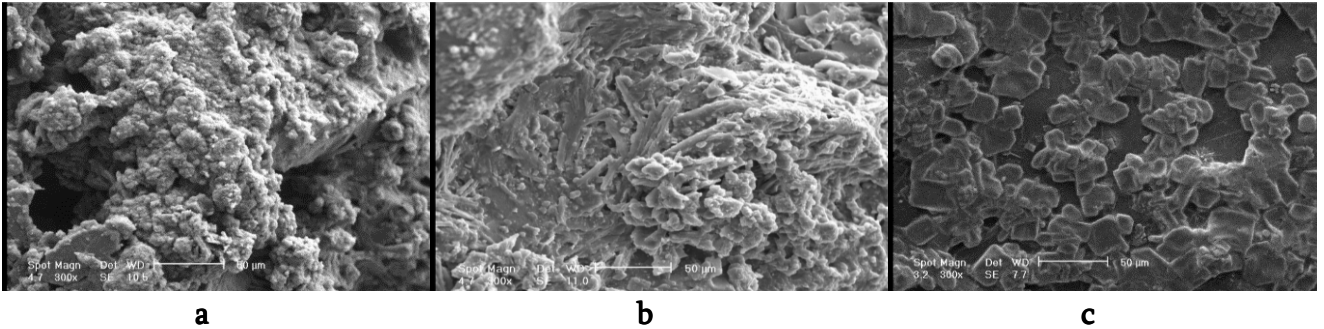
Figure 11. SEM of (a) composite 30 % gelatin (55 % nHAp), (b) composite 50 % gelatin (39 % nHAp), and (c) composite 70 % gelatin (23.5 % nHAp), allshowing the mineralization of composite scaffolds immersed in SBF after 14 days.
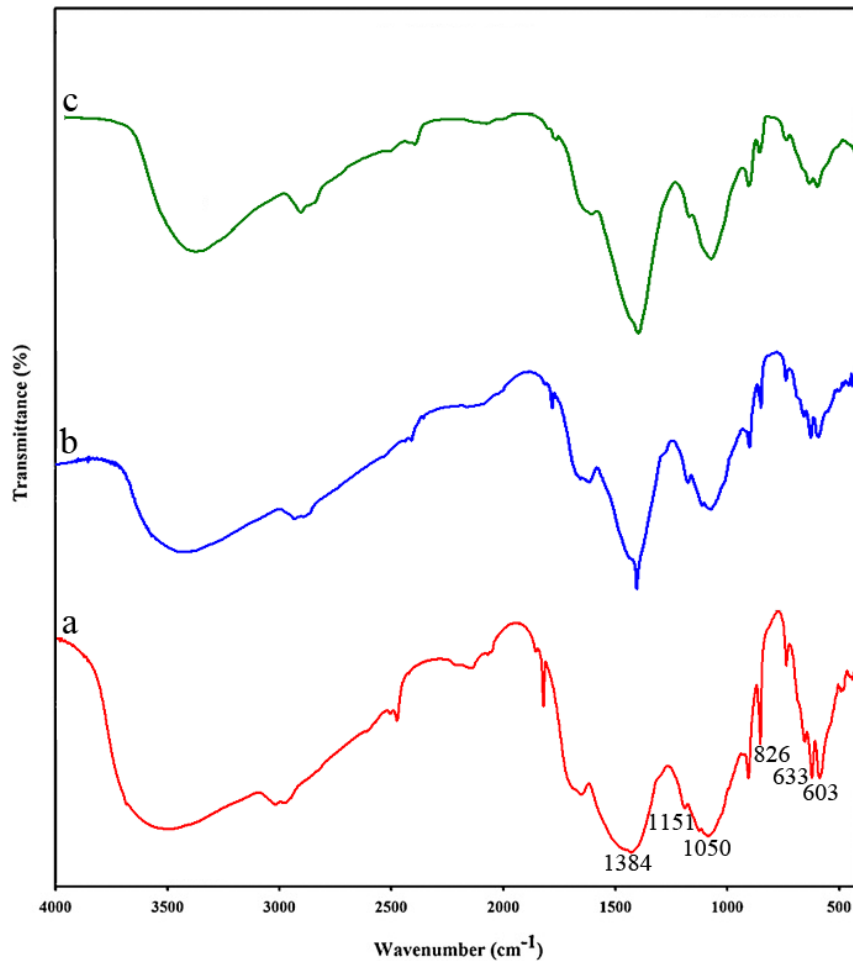
Figure 12. FT–IR spectrum of (a) composite 30% gelatin (55 % nHAp), (b) composite 50 % gelatin (39 % nHAp), and (c) composite 70 % Gelatin (23.5 % nHAp) when immersed in SBF solution after 14 days.
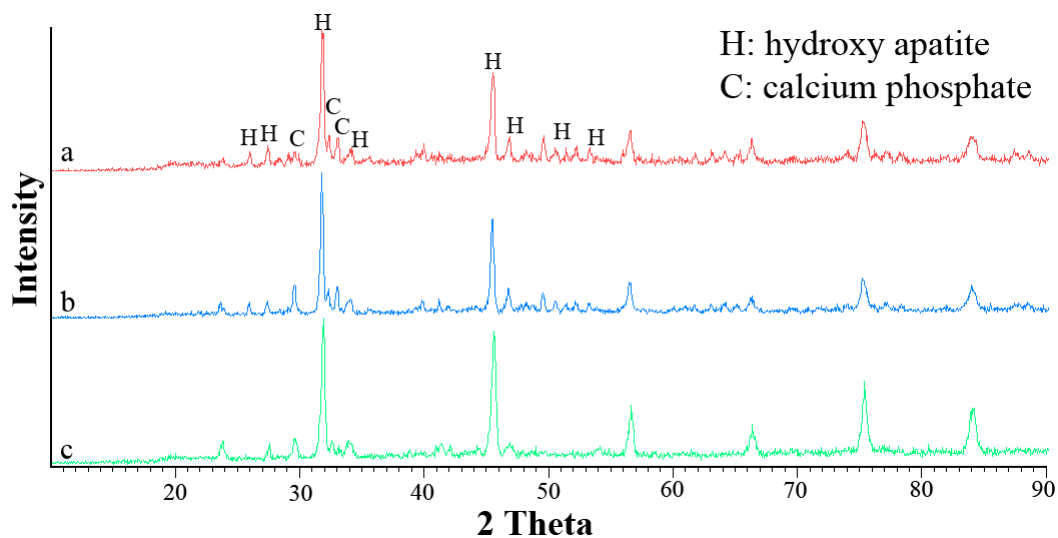
Figure 13. XRD patterns of (a) composite 30% gelatin (55 % nHAp), (b) composite 50 % gelatin (39 % nHAp), and (c) composite 70 % gelatin (23.5 % nHAp) when immersed in SBF solution after 14 days.

3.7. In vitro evaluation of cytotoxicity

For the scaffolds to be employed in the tissue engineering, they should be biocompatible. The scaffolds should not be toxic to the bone cells. Therefore, the scaffold materials were investigated by subjecting the cytotoxic to mouse preosteoblast cells. The ingrowth of MC_3T_3-E_1cells in contact with the extraction of the scaffolds was assayed after 1, 3 and 7 days of culture period by use of MTT test (**Figure 14**).
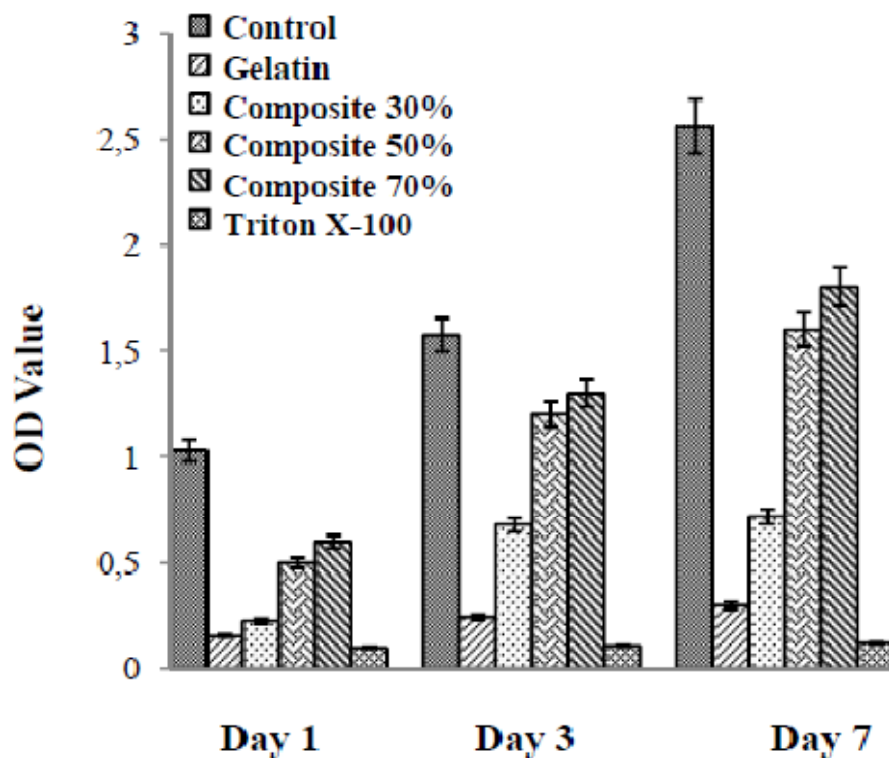
Figure 14. In vitro cytotoxicity evaluation of MC3T3 cells in contact with scaffolds for different periods of time. Dataare presented as the mean ±SD. Significant difference (p ≤ 0.05).

The addition of GE (with the decrease in the nHAp content) enhanced the cell proliferation of GE/nDP/nHAp composite scaffolds. This could be owing to the low crystallinity of nHAp, resulting in the dissolution of phosphate and calcium into the media. This leaded to the increase in intracellular phosphate and calcium concentration and further induction of the cell death. There were obvious differences between days 1, 3 and 7 for all groups. As a positive control, cell incubated with Triton X-100 presented a meaningful loss of cell viability. The results showed an obvious increase in cell numbers over time. It was indicated that the GE/nDP/nHAp composite scaffolds were cytocompatible, suggesting that these scaffolds were non-toxic to osteoblastic cells.

4. Conclusions

GE/nDP/nHAp composite scaffolds were fabricated by using the freeze-drying method. The resulted scaffolds were characterized and compared with each other. The composite scaffold was found to have good pore size and porosity. The mechanical and biological characters of the scaffolds were influenced by adding nHAp and changing the ratio of GE and nDP in the scaffold. The addition of GE (with the decrease in the amount of nHAp) enhanced the cell proliferation of GE/nDP/nHAp composite scaffolds. The increase in density was referred to a decrease in water-uptake and total porosity. It was implied that nHAp substantially improved cell adhesion on the internal scaffold surfaces. It could be, therefore, concluded that nHAp played the role of improving the biological and mechanical properties of the scaffolds.

References

1.   M. Peter, N. Ganesh, N. Selvamurugan, S. V. Nair, T. Furuike, H. Tamura, R. Jayakumar. Preparation and characterization of chitosan–gelatin/nanohydroxyapatite composite scaffolds for tissue engineering applications. Carbohydr. Polym., 2010, 80, 687-694.

2.   J. He, D. Wang, S. Cui. Novel hydroxiapatite/tussah silk fibroin/chitosan bone-like nanocomposites. Polym. Bull., 2012, 68, 1765-1776.

3.   G. Wen, J. Wang, M. Li, X. Meng. Study on tissue engineering scaffolds of silk fibroin chitosan/nano-hydroxyapatite composite. Key Eng. Mater., 2007, 330, 971-975.

4.   K. R. Mohamed, H. H. Beherei, Z. M. EL-Rashidy. In vitro study of nanohydroxiapatite/chitosan–gelatin composites for bio-applications. J. Adv. Res., 2014, 5, 201-208.

5.   S. Wu, X. Liu, K. W. K. Yeung, C. Liu, X. Yang. Biomimetic porous scaffolds for bone tissue engineering. Mater. Sci. Eng. R, 2014, 80, 1-36.

6.   J. Venkatesan, Z. J. Qian, B. Ryu, N. A. Kumar, S. K. Kim. Preparation and characterization of carbon nanotube-grafted-chitosan–natural hydroxyapatite composite for bone tissue engineering. Carbohydr. Polym., 2011, 83, 569-577.

7.   M. C. Chang. Modification of Hydroxyapatite/gelatin nanocomposite with the addition of chondroitin sulfate. J. Kor. Ceram. Soc., 2008, 45, 573-578.

8. M. Kazemzadeh Narbat, F. Orang, M. Solati Hashtjin, A. Goudarzi. Fabrication of porous hydroxyapatite-gelatin composite scaffolds for bone tissue engineering. Iran. Biomed. J., 2006, 10, 215-223.

9. D. S. Hwang, U. K. Kim, M. C. Chang, Y. D. Kim, S. H. Shin, I. K. Chung.Osteogenic differentiation ofstem cells in a gelatin-hydroxyapatite nanocomposite. Tissue Eng. Regen. Med., 2009, 6, 1107-1113.

10. M. Azami, M. Rabiee, F. Moztarzadeh. Gelatin/hydroxyapatite nanocomposite scaffolds forbone repair. Soc. Plast. Eng., 2010, 10, 1-2.

11. H. W. Kim, H. E. Kim, V. Salih. Stimulation of osteoblast responses to biomimetic nanocompositesof gelatin-hydroxyapatite for tissue engineering scaffolds.Biomater., 2005, 26, 5221-5230.

12. H. W. Kim, J. C. Knowles, H. E. Kim. Hydroxyapatite and gelatin composite foams processed vianovel freeze-drying and crosslinking for use as temporary hard tissue scaffolds. J. Biomed. Mater.Res. A, 2005, 72, 136-145.

13. M. Azami, M. Rabiee, F. Moztarzadeh. Glutaraldehyde crosslinked gelatin / hydroxiapatite nanocomposite scaffold, engineered via compound techniques. Polym. Compos., 2010, 31, 2112-2120.

14. K. Askarzadeh, F. Orang, F. Moztarzadeh. Fabrication and characterization of a porous composite scaffold based on gelatin and hydroxyapatite for bone tissue engineering.Iran. Polym. J., 2005, 14, 511-520.

15. M. Zhang, C. Liu, J. Sun, X. Zhang. Hydroxyapatite/diopside ceramic composites and their behaviour in simulated body fluid.Ceram. Int., 2011, 37, 2025-2029.

16. J. M. Le Parc, P. Plantin, G. Jondeau, M. Goldschild, M. Albert, C. Boileau. Bone Mineral Density in Sixty Adult Patients with Marfan Syndrome. OsteoporosInt., 1999, 10, 475-479.

17. C. Wu, H. Zreiqat. Porous bioactive diopside ($CaMgSi_2O_6$) ceramic microspheres for drug delivery.Acta Biomaterialia, 2010, 6, 820-829.

18. L. Ghorbanian, R. Emadi, S. M. Razavi, H. Shin, A. Teimouri. Fabrication and characterization ofnoveldiopside/silk fibroin nanocomposite scaffolds for potential application in maxillofacial boneregeneration.Int. J. Biol. Macromol., 2013, 58, 275-280.

19. Z. Xihua, L. Changxia, L. Musen, B. Yunqiang, S. Junlong. Fabrication of hydroxiapatite / diopside / alumina composites by hot-press sintering process.Ceram. Int., 2009, 35, 1969-1973.

20. M. F. Zhang, X. H. Zhang, C. X. Liu, J. L. Sun. Treatment of postoperative keratoplasty astigmatism using femtosecond laser-assisted intrastromal relaxing incisions. Mater. Sci. Technol., 2013, 29, 378-382.

21. A. Teimouri, L. Ghorbanian, A. NajafiChermahini, R. Emadi. Fabrication and characterizationof silk/forsterite composites for tissue engineering applications. Ceram. Int., 2014, 40, 6405-6411.

22. A. Teimouri, R. Ebrahimi, R. Emadi, B. Hashemi Beni, A. Najafi Chermahini. Nano-composite ofsilk fibroin-chitosan/nanoZrO_2 for tissue engineering applications: fabrication and morphology. Int. J. Biol. Macromol., 2015, 76, 292-302.

23. A. Teimouri, R. Ebrahimi, A. Najafi Chermahini,R. Emadi. Fabrication and characterization of silk fibroin/chitosan/nano c-alumina composite scaffolds for tissue engineering applications. RSC Adv., 2015, 5, 27558-27570.

24. A. Teimouri, M. Azadi, R. Emadi, J. Lari, A. NajafiChermahini. Preparation, characterization, degradation and biocompatibility of different silk fibroin based composite scaffolds prepared byfreeze-drying method for tissue engineering application. Polym. Degrad. Stab., 2015, 121, 18-29.

25. M. Azadi, A. Teimouri, G. Mehranzadeh. Preparation, characterization and biocompatibleproperties of b-chitin/silk fibroin/nanohydroxyapatite composite scaffolds prepared by freeze-dryingmethod. RSCAdv., 2016, 6, 7048-7060.

26. C. Stotzel, F. A. Muller, F. Reinert, F. Niederdraenk, J. E. Barralet, U. Gbureck. Ion adsorptionbehaviour of hydroxyapatite with different crystallinities.Coll. Surf. B Biointer., 2009, 74, 91-95.

27. R. Nazarov, H. J. Jin, D. L. Kaplan. Porous 3-D scaffolds from regenerated silk fibroin. Biomacromolecules, 2004, 5, 718-726.

28. T. Kokubo, H. Takadama. How useful is SBF in predicting in vivo bone.Bioactivity. Biomaterials, 2006, 27, 2907-2915.

29. J. Li, Y. Dou, J. Yang, Y. Yin, H. Zhang, F. Yao, H. Wang, K. Yao. Surface characterization and biocompatibilityof micro- and nano-hydroxyapatite/chitosan-gelatin network films.Mater. Sci. Eng. C, 2009, 29, 1207-1215.

30. M. Meskinfam, M. S. Sadjadi, H. Jazdarreh. Biomimetic preparation of nanohydroxyapatite in gelatin–starch matrix. Eng. Technol., 2011, 52, 395-398.

31. J. K. Han, H. Y. Song, F. Saito, B. T. Lee. Synthesis of high purity nano-sized hydroxiapatite powder by microwave-hydrothermal method.Mater. Chem. Phys., 2006, 99, 235-239.

32. L. Ghorbanian, R. Emadi, M. Razavi, H. Shin, A. Teimouri. Synthesis and characterization of novel nanodiopsidebioceramic powder. J. Nano Struc., 2012, 2, 357-361.

33. P. T. Sudheesh Kumar, S. Srinivasan, V. K. Lakshmanan, H. Tamura, S. V. Nair, R. Jayakumar. β-Chitin hydrogel/nano hydroxyapatite composite scaffolds for tissue engineering applications.Carbohydr.Polym., 2011, 85, 584-591.

34. K. S. Katti, D. R.Katti, R. Dash. Synthesis and characterization of a novel chitosan/montmorillonite/hydroxiapatite nanocomposite for bone tissue engineering. Biomed.Mater., 2008, 3, 034122.

35. B. D. Zdravkov, J. J. Cermak, M. Sefara, J. Janku. Pore classification in the characterization ofporous materials: A perspective. Cent.Europ. J. Chem., 2007, 5, 385-395.

36. K. S. W. Sing, D. H. Everett, R. A. W. Haul, L. Moscou, R. A. Pierotti, J. Rouquero, T. Siemieniewska. Reporting physicsoption data for gas/solid systems with special reference to the determination of surface area and porosity. Pure & Appl. Chem., 1985, 57, 603-619.

37. N. Bhardwaj, S. C. Kundu. Silk fibroin protein and chitosan polyelectrolyte complex porous scaffolds for tissue engineering applications. Carbohydr. Polym., 2011, 85, 325-333.

38. W. W. Thein–Han, R. D. Misra. Biomimetic chitosan-nanohydroxyapatite composite scaffolds forbone tissue engineering.ActaBiomaterialia, 2009, 5, 1182-1197.

39.   Y. Maeda, R. Jayakumar, H. Nagahama, T. Furuike, H. Tamura. Synthesis,characterization and bioactivity studies of novel b-chitin scaffolds for tissueengineering applications. Int. J. Biolog. Macromol., 2008, 42, 463-467.

40.   A. P. Marques, R. L. Reis. Hydroxyapatite reinforcement of different starch-based polymers affects osteoblast-like cells adhesion/spreading and proliferation. Mater. Sci. Eng. C, 2005, 25, 215-229.

THERMOELECTRIC X-RAY DETECTOR

A. A. Kuzanyan, V. R. Nikoghosyan, A. S. Kuzanyan

Laboratory of Materials Science
Institute for Physical Research
Ashtarak, Armenia
astghik.kuzanyan@gmail.com

Abstract

The increased interest in recent years to sources and detectors of single photons is due to remarkable progress in different areas of science and technology. The thermoelectric single-photon detector is one of the real competitors to conventional and superconducting detectors for single photon detection. The results of computer simulation of heat distribution processes taking place after absorption of single photons of 1 – 9 keV energies in the sensor of the thermoelectric detector are presented. Different geometries of the detection pixel with tungsten absorber, lanthanum or lanthanum-cerium hexaboride sensing element and tungsten heat sink are considered. According to the results of computer simulation it can be stated that detection of single photons from "soft" X-ray to "hard" X-ray with energy accuracy no less than 1% is realistic. The count rate exceeding 200 GHz can be achieved.

1. Introduction

There are a number of natural sources of obtaining X-ray radiation, such as from the Sun, neutron stars, from galaxy clusters, through black holes in active galactic nuclei (AGN) to galactic objects such as supernova remnants, stars, and binary stars containing a white dwarf (cataclysmic variable stars and super soft X-ray sources). While artificial sources of X-ray radiation are X-ray machines, nuclear power plants, etc. X-ray radiation detection and investigation can serve to the development of science and technology, especially it can be a valuable addition for the advancement of space astronomy, high-energy physics, medicine, analysis of defects in microchips, X-ray synchrotrons and free-electron lasers, etc.[1 – 10].

To develop the aforementioned areas of science and technology, it is very important to have relevant devices (single-photon detectors), that can determine the quantity and energy of the X-ray photons with pinpoint accuracy. The single-photon detectors can also serve as a basis for the development of a new generation of measuring systems.

An ideal single-photon detector generates an electrical signal only upon absorption of a photon [3]. Next to superconducting single photon detectors [11, 12] and semiconductor detectors [13], thermoelectric single photon detectors (TSPD) can also be considered for the X-ray applications. TSPD was firstly proposed by the Armenian-American research group in 2000 [14, 15]. The current article is the continuation of the researches published previously on the computer modeling for the processes of heat propagation in the single-layer [16 – 18] and multi-layer [19] sensor of thermoelectric detector for X-ray photons. The results of the detailed studies of heat distribution processes' features in lanthanum-cerium hexaboride sensor after absorbing photons with 1 keV energy and comparison of the characteristics of single-layer and three-layer sensors in the case of absorption of photons with 1 – 9 keV energies are presented.

2. Computer simulation

The design of the single- and three-layer detection pixel of TSPD with tungsten absorber, cerium (CeB_6) or lanthanum-cerium hexaboride ($La_{0.99}Ce_{0.01}B_6$) sensor and tungsten (W) heat sink, as well as the parameters of used materials at 9 and 0.5 K are presented in [20].

The computer simulation was based on the equation for heat propagation from the limited volume with the use of three-dimensional matrix method. The details of the approaches and approximations are given in [16, 21].

The thickness of an absorber is the most important parameter of the TSPD sensor. Taking the Bouguer–Lambert's law and using the values for the coefficient of linear attenuation in W for 1, 3, 6 and 9 keV energy photons equal to respectively 5.775, 3.273, 0.614 and 0.327 μm^{-fl} [22], it is easy to calculate the probability of absorption in 1.5 μm thick W of a photon of 1 keV energy that will be 0.9998, 3 keV – 0.9926, 6 keV – 0.602, and 9 keV – 0.388. So we can use 1.5 μm thick W for the registration of 1keV and 3 keV photons, but not for the registration of 6 and 9 keV photons due to the fact of small probability of absorption. **Figure 1** shows the curves of the probability of 1– 9 keV energy photons' reaching definite depths in W absorber. The probability of reaching 5 μm depth in W of a photon of 1, 3, 6 and 9 keV energy is equal to $2.88 \cdot 10^{-13}$, $7.83 \cdot 10^{-8}$, 0.046 and 0.19, respectively. It can be noted that the absorber thickness of 5 mm is sufficient to ensure high probability of absorption of photons of 1 – 9 keV energies.
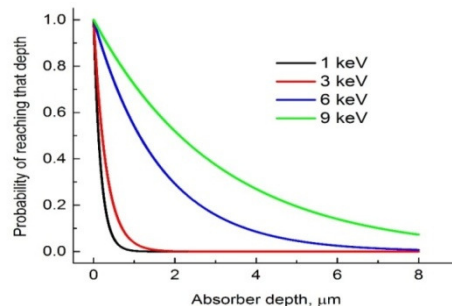
Figure 1. The probability of 1 – 9keV energy photons reaching a certain depth in tungsten.

3. Results

3.1. The results for 1 keV photon absorption

The results of computer simulation for 1 keV photon absorption in $W/La_{0.99}Ce_{0.01}B_6/W$ three-layer sensors are presented in this paragraph. The geometrical dimensions of sensors and results of calculations of heat propagation in the three-layer sensor are presented in **Table 1**.

The columns in the table give the calculation number, the geometric dimensions of absorber (X, Y, Z_1), the distance from surface of absorber in which photon is absorbed (h), the thickness of thermoelectric layer (Z_2), the thickness of heat sink (Z_3), the photon energy (E), the maximum temperature difference on the thermoelectric layer after photon absorption – (ΔT_m), the time duration to achieve ΔT_m – (t_m), the maximum of voltage on the sensor (U_m), the time of recession ΔT to the background 0.1mK – (t_b), its inverse (count rate) – (R). The geometric dimensions X and Y of the thermoelectric layer and of the heat sink are similar to those of absorber. In the calculations it is assumed that the photon is thermalized in the center of the absorber surface.

Table 1. Sensor geometry, E, ΔT_m, t_m, U_m, t_b and count rate (R).

#	X,Y,Z, μm	h, μm	Z_1, μm	Z_2, μm	E, keV	ΔT_m, m K	t_m, ps	U_m, μV	t_b, ps	R, GHz
tL1	10,10,1.5	0.4	1	1	1	204.5	0.0204	17.38	350	2.8
tL2	10,10,1.5	0.4	0.5	1	1	204.5	0.0204	17.38	95.7	10.4
tL3	10,10,1.5	0.4	0.1	1	1	204.5	0.0204	17.38	7.39	135
tL4	10,10,1.5	0.4	0.05	1	1	204.5	0.0204	17.38	2.66	376
tL5	10,10,1.5	0.4	0.01	1	1	191.1	0.0172	16.24	0.41	2439
tL6	10,10,1.5	0.4	0.01	2	1	191.1	0.0166	16.24	0.85	1177
tL7	10,10,1.5	0.4	0.01	5	1	191.1	0.0168	16.24	1.61	621
tL8	10,10,1.5	0.4	0.01	1	1.1	210.3	0.0172	17.86	0.41	2439
tL9	10,10,1.5	0.4	0.01	1	0.9	172.0	0.0168	14.62	0.41	2439
tL10	10,10,1.5	0.4	0.01	1	1.01	193.0	0.0167	16.41	0.41	2439
tL11	5,5,1.5	0.4	0.01	1	1	191.1	0.0172	16.24	0.73	1370
tL12	15,15,,1.5	0.4	0.01	1	1	191.1	0.0172	16.24	0.39	2500
tL13	20,20,1.5	0.4	0.01	1	1	191.1	0.0172	16.24	0.40	2500
tL14	25,25,1.5	0.4	0.01	1	1	191.1	0.0172	16.24	0.40	2500
tL15	30,30,1.5	0.4	0.01	1	1	191.1	0.0172	16.24	0.40	2500
tL16	35,35,1.5	0.4	0.01	1	1	191.1	0.0172	16.24	0.40	2500
tL17	40,40,1.5	0.4	0.01	1	1	191.1	0.0172	16.24	0.40	2500
tL18[a]	10,10,1.5	0.4	0.01	1	1	251.1	0.0250	21.34	0.48	2083
tL19[a]	10,10, 1.5	0.1	0.01	1	1	199.2	0.0193	16.93	0.49	2041
tL20[b]	10,10,1.5	0.1	0.01	1	1	191.7	0.0171	16.30	0.50	2000
tL21[c]	10,10,1.5	0.1	0.01	1	1	191.2	0.0171	16.25	0.50	2000
tL22	10,10,1.5	0.7	0.01	1	1	352.3	0.0094	29.95	0.39	2564
tL23	10,10,1.5	0.9	0.01	1	1	571.9	0.0059	48.61	0.37	2703
tL24	10,10,1.5	1.1	0.01	1	1	732.5	0.0036	62.26	0.35	2857
tL25	10,10,3	0.4	0.01	1	1	18.9	0.07	1.61	0.77	1299
tL26	10,10,3	0.7	0.01	1	1	23.4	0.06	1.99	0.75	1333
tL27	10,10,3	0.9	0.01	1	1	29.5	0.05	2.51	0.73	1370
tL28	10,10,3	1.1	0.01	1	1	39.8	0.04	3.38	0.69	1449

Photon absorbed in the corner. The center of termalization area is located at a distance from the corner: [a] 0.5; [b] 0.9, and [c] 1.3 μm.

It follows from the table data that for the calculations tL1 and tL2 decay time to the background level is above 300 ps. Its reason is the low value of the coefficient of thermal conductivity for $La_{0.99}Ce_{0.01}B_6$. Acceleration of the heat transfer from absorber to the heat sink can be achieved by decreasing the thickness of the thermoelectric layer. In tL1 – tC5 calculations, the thermoelectric latter was gradually decreased from 1 μm to 0.01 μm. The graphs of $\Delta T(Z_1)$ and $R(Z_1)$ dependencies of these calculations are presented in **Figure 2**. We can see that t_b parameter decreases upon the decrease of the thickness of thermoelectric layer, while the values of the parameter ΔT_m remain practically unchanged up to 0.05 μm thicknesses. ΔT_m parameter is somewhat smaller for the 0.01 μm thick thermoelectric layer but at the same time the signal is going down to the background value much faster, thus providing for counting rate of the order of 2439 GHz. In further calculations we shall use this value for the thickness of the thermoelectric layer.
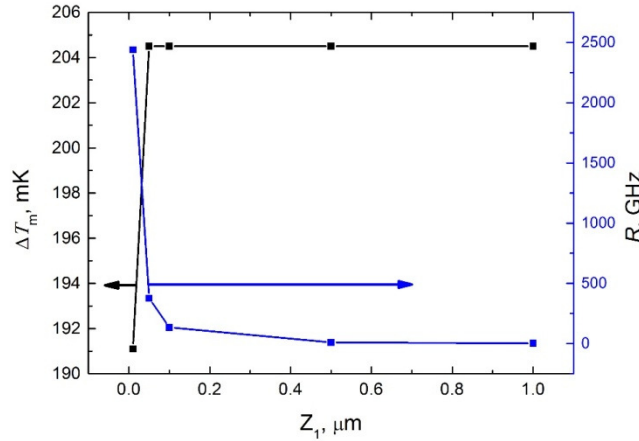
Figure 2. Dependence of the ΔT_m and R parameters of calculations tL1 – tL5 on the thickness of the thermoelectric layer Z_1.

Let's compare the results of calculations tL5 – tL7 for sensors with 1, 2 and 5 μm thicknesses of the tungsten heat sink. It is seen from **Table 1** that variation of the heat sink thickness does not influence the value of ΔT_m and the count rate R. It can be concluded that the thickness of the heat sink does not have influence on the ΔT_m parameter, but the increase of the thickness of the heat sink leads to significant count rate decreases.

Figure 3 shows $\Delta T(t)$ graphs for the cases of photon absorption with different energies. It can be seen that the change of photon energy leads to the change in ΔT_m value, while t_m changes slightly. It follows from **Table 2** that U_m values differ by 1.62 μV, if the photon energies differ by 10%, and by 0.17 μV, if they differ by 1%. It should also be mentioned that the change in photon energy does not lead to the change of the count rate. In the insert of **Figure 3** can be seen that dependence $\Delta T(E)$ is linear.
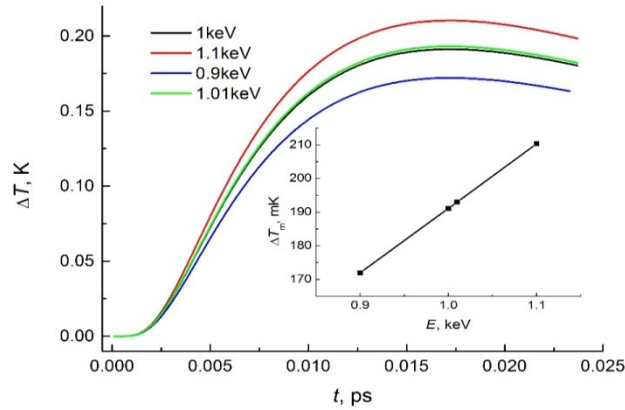
Figure 3. $\Delta T(t)$ dependencies of tL5, tL8, tL9 and tL10 calculation numbers for the cases of absorption of photons with 1 keV, 1.1, 0.9, and 1.01 keV energies.

The next tL11 – tL17 calculations in Table 1 are performed for sensors having different X, Y dimensions of the three-layer sensor. Comparison of their characteristics with those of tL5 calculation number shows that, when X and Y increase from 5 to 15 μm, the count rate increases from 1370 to 2500 GHz. Further increase in sensor sizes up to 40 mm does not change the value of the count rate (**Figure 4**). For all these calculations, the parameters ΔT_m and t_m are the same. The data for CeB_6 thermoelectric layer are also presented for comparison. You can see the same behavior, but the values of count rate are significantly low for this thermoelectric with higher working temperature.
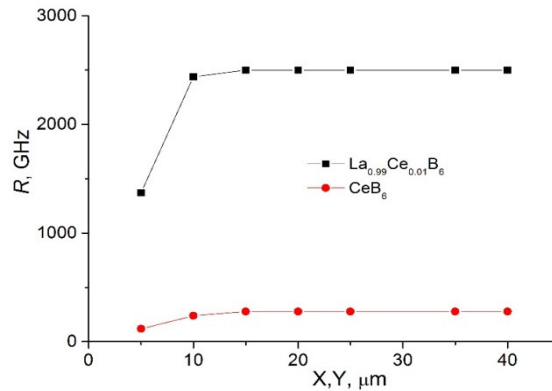
Figure 4. Count rate vs. X, Y dimension of the three-layer sensor.

Let's consider how the location of surface area, in which the photon is thermalized, influences over the recorded signal. All previous calculations were performed in an assumption that the photon is thermalized in the geometrical center of the absorber surface in the uppermost layer. tL18 – tL21 calculations have been carried out for cases, when a photon incidents on the absorber angle. If we exclude the possibility of incidence of the photon in the areas along the perimeter of the sensor surface of small width that can be easily done using a simple screen, we will have a sensor that allows one to identify the energy of a photon uniquely by the maximum value of the detected signal.

In the conclusion of this paragraph, the differences of temporal dependencies ΔT, when the photon thermalizes at different depths in the central region of the absorber, are considered. Most of the calculations shown in **Table 1** are carried out with an assumption that the photon thermalizes in the upper layer of the absorber. From the absorption of a photon at a greater depth (calculations tL22 – tL24), we get a signal with a higher value of ΔT_m (compared with tL5). Moreover, the closer the thermalization area of the photon to the thermoelectric layer is, the greater is the ΔT_m value. At the same time, the signal falls to the background value slightly faster, and we have a higher count rate.

No doubt that these regularities will be observed for the calculations with other parameters as well, if the depth of bedding of thermalization zone there is changed. It is possible to get the decrease of dependence of signal characteristics on the depth of the photon thermalization zone by the increase of the absorber thickness (tL25 – tL28 calculations, the thickness of the absorber is 3 μm). By increasing the thickness of the absorber, the values of ΔT_m parameter become smaller, but at the same time the difference of this parameter's decreases for the cases of absorption of the photon at different depths.

Analysis of data of **Table** 1 allows conclude that, at the same architecture of the sensor, t_m parameter depends on the distance from absorber surface at which photon is absorbed (h), while t_m and ΔT_m parameters uniquely define the energy of the absorbed photon.

3.2. The results for 1 – 9 keV photon absorption

Let's consider the results of the calculations carried out for the thermoelectric single- or three-layer sensor made of $La_{0.99}Ce_{0.01}B_6$ or CeB_6 for 1 – 9 keV energy photons absorption in the center of surface of W absorber (**Table 2**). The length of the thermoelectric bridge (in the case of single-layer sensor) and the thickness of the thermoelectric layer (in the case of three-layer sensor) are equal to 10 nm. In the columns of **Table 2** are given the same parameters as in **Table 1**. In calculations for single-layer sensor we consider absorbers of $5 \times 5 \times 5$ μm³ and bridge

of $0.01 \times 5 \times 5 \ \mu m^3$ sizes. For three-layer sensor absorber is $5 \times 5 \times 5 \ \mu m^3$ sizes and thickness of heat sink is $1 \ \mu m$.

Table 2. Calculations of parameters for $1 - 9$ keV photon absorption.

#	$E,$ keV	$\Delta T_m,$ m K	$t_m,$ ps	$U_m,$ μV	$t_b,$ ps	$R,$ GHz
Single-layer sensor with CeB_6 *thermoelectric bridge*						
C23M-5-1	1	0.69	0.9	0.104	16.8	59.5
C23M-5-3	3	2.07	0.9	0.311	33.9	29.5
C23M-5-6	6	4.1	0.9	0.615	44.4	22.5
C23M-5-9	9	6.21	0.9	0.315	50.7	19.7
Single-layer sensor with $La_{0.99}Ce_{0.01}B_6$ *thermoelectric bridge*						
12M1-5-8	1	2.08	0.48	0.18	6.84	146.2
12M-5-3	3	6.25	0.48	0.531	8.82	113.4
12M-5-6	6	12.5	0.48	1.063	9.9	101
12M-5-9	9	18.74	0.48	1.593	10.4	96.2
Three-layer sensor with CeB_6 *thermoelectric layer*						
kC24M	1	0.095	1.5	0.014	-	-
kC25M	3	0.284	1.5	0.043	6.3	158.7
kC26M	6	0.567	1.5	0.085	9.9	101
kC27M	9	0.851	1.5	0.128	12	83.3
Three-layer sensor with $La_{0.99}Ce_{0.01}B_6$ *thermoelectric layer*						
kL24M	1	3	0.19	2.55	1.25	800
kL25M	3	9	0.19	7.65	1.65	606
kL26M	6	18	0.19	15.3	2	500
kL27M	9	27	0.19	22.95	2.1	476
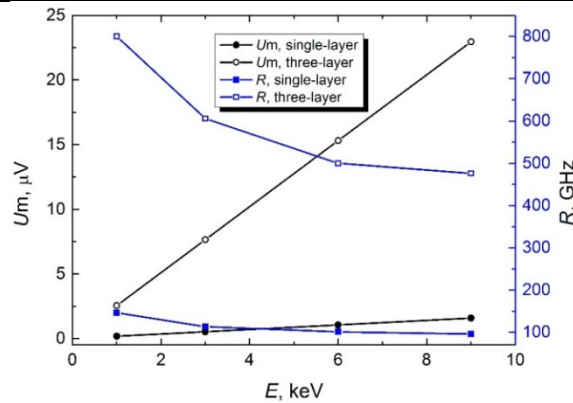
Figure 5. Maximal signal (U_m) and count rate (R) vs. photon energy (E) for single- and three-layer sensors of $La_{0.99}Ce_{0.01}B_6$ thermoelectric.

Firstly, let's consider the characteristics received for the single-layer sensor. As expected, ΔT_m and U_m parameters increase while increasing the photon energy. When the geometric sizes of the absorber are unchanged, the time of heat distribution from the center of the surface of the absorber (the thermalization area of the photon) to the boundary with the thermoelectric bridge for the photons with different energies is equal. Thus, we have the same values of t_m parameter for the sensors with a bridge of the same thermoelectric. The time to achieve the

background value increases and the count rate decreases while increasing the photon energy, which is not surprising, as the photon with higher energy during absorption generates larger amount of heat, that needs more time to pass to the heat sink and substrate.

The similar regularities are also observed for the three-layer sensor. It should be mentioned that for the both constructions of the sensor the main parameters (U_m and R) are higher for $La_{0.99}Ce_{0.01}B_6$ thermoelectric. The dependence of these parameters on the photon energy represents **Figure 5**. A very important result is that U_m parameter increases linearly while increasing the photon energy.

4. Conclusions

The results of computer simulation of heat distribution processes taking place after absorption of single photons of 1 – 9 keV energies in the sensor of the thermoelectric detector show that using 5 μm thick W absorbers, we can record the X-ray photons with energies ranging from 1 to 9 keV with high energy resolution and high count rate.

Obviously, the results of computer simulation of the heat propagation processes in such a complex system, as the sensor of the single-photon detector is, may not be qualified as accurate, comparable with the data of experimental verification of the sensor parameters. Nevertheless, the revealed peculiarities show the advantages of multilayer sensor in comparison with the single layer thermoelectric sensors, avalanche photodiodes and superconducting detectors. Particularly, it follows from the literature data that for the X-ray photons the count rate of the superconducting detectors ($R \approx 1$ kHz, [11]) and semiconductor detectors ($R \approx 2$ MHz, [13]) is much lower from the values received in the present work.

In combination with the high energy resolution, which for both sensor designs is not less than one percent, the existence of these benefits enables to foresee the further development and creation of the thermoelectric photon detector with a multilayer sensor, to be used in various fields of modern science and high technology.

The authors hope that the present publication will attract attention to thermoelectric detectors, and that the experimental results on TSPD research will appear soon, since following the results of computer simulation it can be stated as a quite perspective direction.

Acknowledgements

References

1. P. Feautrier, E. le Coarer, R. Espiau de Lamaestre, P. Cavalier, L. Maingault, J. C. Villégier, L. Frey, J. Claudon, N. Bergeard, M. Tarkhov, J.-P. Poizat. High-speed superconducting single photon detectors for innovative astronomical applications, J. Phys.: Conf. Ser., 2008, 97, 012087.
2. T. Hatsui, H. Graafsmab. X-ray imaging detectors for synchrotron and XFEL sources..IUCrJ, 2015, 2, 371.
3. Ch. M. Natarajan, M. G. Tanner, R. H. Hadfield. Superconducting nanowire single-photon detectors: physics and applications. Supercond. Sci. Technol., 2012, 25, 063001.

4. R. H. Hadfield. Single-photon detectors for optical quantum information applications, Nat. Photonics, 2009, 3, 696.

5. Y. Liang, H. P. Zeng, Single-photon detection and its applications. Sci. China – Phys Mech. Astron., 2014, 57, 1218.

6. A. Bergamaschi, R. Dinapoli, B. Henrich, I. Johnson, A. Mozzanica, X. Shi, B. Schmitt, Beyond single photon counting X-ray detectors. Nucl. Instr. Meth. Phys., 2011, 628-1, 238.

7. R. Dinapoli, A. Bergamaschi, B. Henrich, R. Horisberger, I. Johnson, A. Mozzanica, E. Schmid, B. Schmitt, A. Schreiber, X. Shi, G. Theidel. EIGER: Next generation single photon counting detector for X-ray applications. Nucl. Instr. Meth. Phys., 2011, 650-1, 79.

8. I. Johnson, A. Bergamaschi, H. Billich, S. Cartier, R. Dinapoli, D. Greiffenberg, M. Guizar–Sicairos, B. Henrich, J. Jungmann, D. Mezza, A. Mozzanica, B. Schmitt, X. Shi, G. Tinti. Eiger: A single-photon counting X-ray detector. J. Instr., 2014, 9, C05032.

9. R. Ballabriga, J. Alozy, M. Campbell, E. Frojdh, E. H. M. Heijne, T. Koenig, X. Llopart, J. Marchal, D. Pennicard, T. Poikela, L. Tlustos, P. Valerio, W. Wong, M. Zuber. Review of hybrid pixel detector readout ASICs for spectroscopic X-ray imaging. J. Instr., 2016, 11, P01007.

10. C. Frojdh, B. Norlin, E. Frojdh, Spectral X-ray imaging with single photon processing detectors. J. Instr., 2013, 8, C02010.

11. X. Zhang, Q. Wang, A. Schilling. Superconducting single X-ray photon detector based on W0.8Si0.2. AIP Adv., 2016, 6, 115104.

12. Y. F. Song, C. H. Chang, C. Y. Liu, S. H. Chang, U. Jeng, Y. H. Lai, D. G. Liu, G. C. Yin, J. F. Lee, H. S. Sheu, S. C. Chung, K. L. Tsang, Y. Hwu, K. S. Liang. Performance of X-ray Beam lines at Superconducting Wavelength Shifter. AIP Conf. Proc., 2007, 879, 808.

13. K. Kowase, K. Ogawa. Photon counting X-ray CT system with a semiconductor detector. IEEE Nucl. Sci. Symp. Conf. Record, 2006, M14-177.

14. G.G. Fritz, K.S. Wood, D. van Vechten, A. L. Gyulamiryan, A. S. Kuzanyan, N. Giordano, T. M. Jacobs, H.-D. Wu, J. S. Horwitz, A. M. Gulian. Thermoelectric single-photon detectors for X-ray / uv radiation. Proc. SPIE, 2000, 4140, 459.

15. A. Gulian, K. Wood, D. van Vechten, G. Fritz. Cryogenic thermoelectric (QVD) detectors: Emerging technique for fast single-photon counting and non-dispersive energy characterization. J. Mod. Opt., 2004, 51, 1467.

16. A. Kuzanyan, V. Nikoghosyan, A. Kuzanyan. Modeling of kinetic processes in thermoelectric single photon detectors. Proc. SPIE, 2015, 9504, 95040O.

17. A. Kuzanyan, V. Nikoghosyan, A. Kuzanyan. CeB6 Sensor for thermoelectric single-photon detector. Sensors & Transducers, 2015, 191, 57.

18. A. A. Kuzanyan, A. S. Kuzanyan, V. R. Nikoghosyan. Ultrafast TSPD on the basis of CeB6 sensor. J. Phys.: Conf. Ser., 2016, 673, 012007.

19. A. A. Kuzanyan, A. S. Kuzanyan, V. R. Nikoghosyan, V. N. Gurin, M. P. Volkov. Investigation of processes of heat propagation in multilayer sensor of thermoelectric single-photon detector. J. Contem. Phys. (Arm. Acad. Sci.), 2016, 51, 181.

20. A. S. Kuzanyan, A. A. Kuzanyan, V. R. Nikoghosyan. Thermoelectric sensor for single-photon detection from infrared to hard ultraviolet. Nano Studies, 2016, 13, 175.

21. A. A. Kuzanyan. Nanosensor for thermoelectric single-photon detector. Nano Studies, 2014, 9, 93.

22. C. T. Chantler. Theoretical form factor. Attenuation, and scattering tabulation for $Z = 1 – 92$ from $E = 1 – 10$ eV to $E = 0.4 – 1.0$ MeV. J. Phys. Chem. Ref. Data, 1995, 24, 71.

SYNTHESIS OF ORGANICALLY MODIFIED SILICA NANOPARTICLE–EPOXY ACRYLATE HYBRID RESIN

M. Karahasanoglu [1], E. Serhatlı [2]

[1] Department of Polymer Science & Technology
Institute of Science & Technolog
Istanbul Technical University
Istanbul, Turkey
karahasan5@itu.edu.tr
[2] Department of Chemistry
Istanbul Technical University
Istanbul, Turkey
serhatli@itu.edu.tr

Abstract

Well defined, spherical silica nanoparticles (SNPs) within desired size range were synthesized according to Stöber method. Physical and chemical structure of the SNPs such as particle size, specific surface area were characterized clarifying their surface properties for the modification of silica nanoparticles.Surface modification of the SNPs was achieved with the reaction over isocyanate groups of toluene di-isocyanate (TDI) in order to gain both improved dispersion in organic phase and further reaction possibility of spherical SNPs over unreacted o-isocyanate groups of SNPs. TDI grafted SNPs (Si–TDI) were incorporated into preformed epoxy acrylateresin (EA) by covalent bonding between hydroxyl groups of epoxy resin and free isocyanate groups of Si–TDI forming urethane linkage. Si–TDI incorporated EA hybrid resin (EA–Si) was cured under UV treatment in the form of film. The effect of uniform, well-dispersed, covalently incorporated Si–TDI nanoparticles on the thermal, morphological and mechanical behavior of UV-cured EA–Si hybrid films was investigated.

1. Introduction

Organic–inorganic hybrids exhibit multifunctional characteristics and show superior properties compared to their pure components [1 – 3]. Inorganic nanoparticles have already had an impact in fields such as surface coatings, mechanics, optics, electricity, magnetism, medicine, aerospace, thermodynamics and bionics. One of the main interests to nanocomposite materials is the fact that nanostructure containing materials have higher surface areas than normal materials, with a decrease in the size, the surface area per unit volume increases enhancing the properties due to the available surface area [4, 5].

Silica nanoparticles (SNPs) have attracted much interest due to their low toxicity, extreme increase in interfacial area, chemical inertness, ease of formation in a wide range of sizes and morphologies, high stability, and the flexible and robust surface that can be further functionalized [6–8].The most common method for silica preparation is the sol-gel method and

usually soluable silicates or alkoxysilanes are used as starting materials and their hydrolysis and condensation steps occur simultaneously during the siloxane (Si–O–Si) formation over acid or base catalyst [9 – 12].Base catalysed preparation of SNPs by Stöber method is based on the hydrolysis and polycondensation of tetraethylorthosilicates (TEOS) as silica precursor [13, 14].

The efficiency of SNPs in organic polymeric matrices requires uniform dispersion and strong interfacial bonding between two components of the composites [15, 16]. The strong hydrophilic character and the tendency of SNPsto agglomeration, which is mainly due to their high silanol content and, specific surface area cause the difficulty for the SNPs to become monodispersed in organic and polymeric phases. Efficient functionalization / modification of silica nanoparticles has the great importance for enabling both the well dispersion of such nanoparticles into organic phase of the hybrid materials and also possible strong and chemical interactions of the nanoparticles with the organic precursor or polymer components of the hybrid.Common strategies have been developed to improve the poor dispersion of SNPs in polymer matrices and also organic solvents for advanced interfacial bonding of nanoparticles and matrices. By this manner chemical compounds with active groups are employed to substitute silanol groups of silica nanoparticles forming various functionalites on silica nanoparticle surfaces [17 – 20]. The most popular method is the surface functionalization of SNPs by silane coupling agents (organo-silanes), which contain both organic moieties and silane moeities in one precursor[21 – 25]. Rarely, some organic moieties with functional groups are also employed to substitute the hydroxyl groups of silica particle in order to bring organic properties on the surface of silicaparticles [26 – 28].

In case of the use of organo-silanes as silica coupling agents some ambiguities may occur reducing the modification efficiency of the nanoparticles [29 – 31]. In order to overcome such diffuculties, contrary to common coupling methods of SNPs with organo-silanes, toluene diisocynate (TDI) was considered to be an ideal activator having two isocyanate groups for the surface modification of silica nanoparticles [32]. Grafting of TDI onto surface of SNPs improved the dispersibility of SNPs in organic phase of the hybrids and brought possibility for further reactions over the isocyane groups of TDI as studied in our previous study [33].

In the presented study, spherical and uniform SNPs with the diameter below 100 nm were synthesized by following Stöber method, which is a type of so–gel process. Well-defined spherical SNPs succesfully grafted with TDI (Si–TDI)gaining reactive isocyanate functionality. Synthesized Si–TDI nanoparticles with improved dispertion and reactivity were further incorporated into preformed epoxy-acrylate resin over the covalent bonding between hydroxyl groups of epoxy acrylate resin and free isocyanate groups of Si–TDI by the formation of urethane linkage. Epoxy-acrylate–SNPs hybrid resin (EA–Si hybrid resin) was cured under UV treatment in the form of film. The effect of uniform, well-dispersed, covalently incorporated silica nanoparticles on the thermal, morphological and mechanical behavior of cured EA–Si hybrid film was investigated.

UV-curing technology for coating applications surpass more conventional processing techniques by their distinct advantages such as very rapid and selective curing even at ambient temperatures, low energy consumption, high production efficiency, less environmental pollution and lower process cost [34, 35]. Epoxy acrylate oligomers are widely used for UV-curable coatings due to the potential to combine a wide range of excellent application properties of epoxy resin such as high impact and tensile strength, abrasion resistance, thermal durability, resistance to chemicals and solvents with the application performances of polyacrylates[36, 37].

2. Experimental

Spherical, monodispersed silica nanoparticles(SNPs)were prepared by the sol–gel process based on the Stöber method using tetraethoxysilane (TEOS) as a starting material and ammonia (NH_3) as the base catalyst. The procedure of formation of 87 nm of SNPs was as follows: 1.5 mL of TEOS was added directly into the solution of 4 mL of NH_3 in 50 mL of absolute ethanol and the mixture was stirred for 24 h at a constant temperature of 60 °C and stirring speed of 300 rpm. The overall reaction takes place as seen in **Figure 1**.
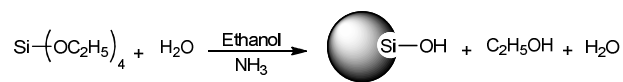
Figure 1. General process for the synthesis of silica nanoparticles.

SNPswere dispersed by ultrasonication in dry toluene and added into a three-necked round bottom flask, equipped with nitrogen inlet. Toluene diisocyanate (TDI) and catalytic amount of dibutyltin dilaurate (DBTL) were also added into the flask and isocyanate functionalization of SNPs was carried out at 65 °C for 12 h resulting in Si-TDI nanoparticles as represented in **Figure 2**.

Figure 2. Toluene diisocyanate functionalization of SNPs.
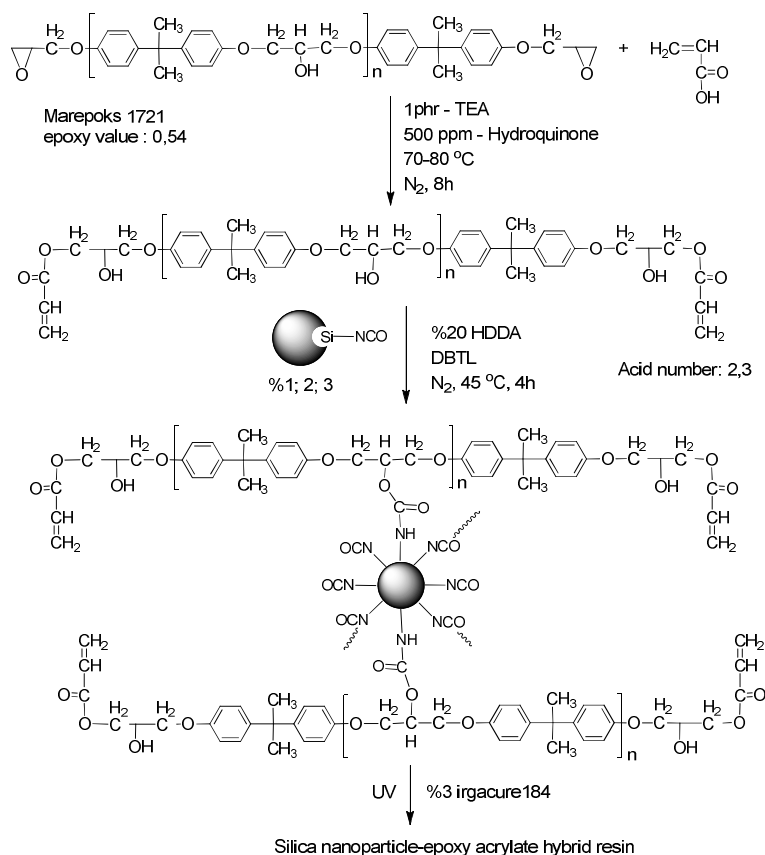
Figure 3. The synthetic route for silica nanoparticle / epoxyacrylate hybrid resin.

213

Isocyanate functionalized Si-TDI nanoparticles were incorparated into preformed epoxy acrylate resin formulations following UV curing process. The synthetic route for the whole process is shown in **Figure 3**. Bisphenol A type, solvent free epoxy resin with low viscosity (Marepoks 1721) was reacted with acrylic acid for the synthesis of epoxy acrylate resin (EA). Then, EA resins stirred with 20% of hexanediol diacrylate (HDDA) in order to dilute the resin and increase the acrylate functionality following the incorporaion of Si–TDI nanoparticles in a variety of ratio and catalytic amount of DBTL. Si–TDI incorporated EA resins were stirred at 40 °C for 4 hunder nitrogen obtaining SNP / epoxyacrylate hybrid resin formulations (EA–Si). Viscous hybrid resin formulations were poured on to a Teflon™ mold and before irradiation, covered by a transparent Teflon™ film in order to prevent oxygen inhibition. A quartz glass plate was also placed over the Teflon™ films to obtain a smooth surface of cured film. As last, the formulations were irradiated 240 s under a high pressure UV lamp (OSRAM, 300 W).

Particle size and distribution analysis were carried out with Scanning Electron Microscopy (SEM), Philips XL30 ESEM–FEG. Specific surface area of nanoparticles (SSA) was determined by BET model with the data provided by Nova 2200e model (Quantachrome) instrument, samples preheated at 160 °C for 2 h and degassed.

The reaction between organic compounds and silica nanoparticles was followed by Fourier Transform Infrared (FTIR) Spectroscopy, Nicolet 850 FT–IR operating in the 4000 – 400 cm^{-1} range. ^{13}C CP/MAS NMR measurement was carried out on a Bruker Avance 300 solid-state NMR spectrometer. The ^{13}C CP/MAS spectra was recorded at the resonance frequency of approximately 75.4 MHz with a 4 mm rotor spinning at 8.5 kHz using $\pi/2$ pulsewidth of 4.5 μs and averaging over 15000 scans. The contact time was 2 ms and relaxation delay was 4 s.

Grafting amounts of organic groups on the surface of SNPs were determined by thermogravimetric analysis (TGA) using Q50 TGA analyzer from TA instruments under nitrogen with a ramp rate of 20 °C / min. Thermal behaviour of UV-cured EA-Si hybrid resins was also evaluated by differantial scanning calorimetry (DSC) analysis performed on a Q10 TA instrument with a heating rate of 10 °C / min under nitrogen flow.

Stress–strain tests for mechanical properties of UV-curedEA–Si hybrid resins were carried out by Zwick Z010 Universal Tensile Tester under a 50 N load cell with a crosshead speed of 2 mm / min at room temperature.

3. Results and discussion

Adjusting the sol–gel process by the amounts of base catalyse NH$_3$ and precursor TEOS resulted in the formation of SNPs with the particle size below 100 nm.Spherical structure and particle size of SNPs were determined by SEM analysis (**Figure 4**). Specific surface area (SSA) of SNPs with the average diameter of 87 nm was characterized by BET method and determined as 46.5 m^2 g^{-1} which may be considered slightly higher for Stöber type non-porous SNPs comparing to calculated geometric SSA (36.3 m^2 g^{-1}). This might be attributed to possible micro-porous structure of smaller particles (less than 100 nm) resulting in higher number of hydroxyl groups of SNPs.

The high number of hydroxyl (–OH) groups of SNPs was aimed to modify with reactive isocyanate functionality for this purpose, spherical and uniform bare SNPs with an average diameter of 87 nm, were modified with TDI moeity forming Si–TDI. The high reactivity of TDI

molecule increase the ability of grafting so the concentration of functional isocyanate groups on the surface of SNPs. Grafting of TDI on the surface of silica nanoparticles was achieved by the reaction of silanol (–OH) groups of SNPs and isocyanate groups of TDI molecules forming urethane linkage. It was assumed that most of the urethane linkages formed by p-isocyanate group of TDI molecule considering para located isocyanate group of TDI to be much more reactive than its o-isocyanate group. Furthermore, excess TDI was used to ensure that more reactive p-isocyanate group react preferentially with the silanol groups of SNPs enabling o-isocyanate group to remain free for further reactions.
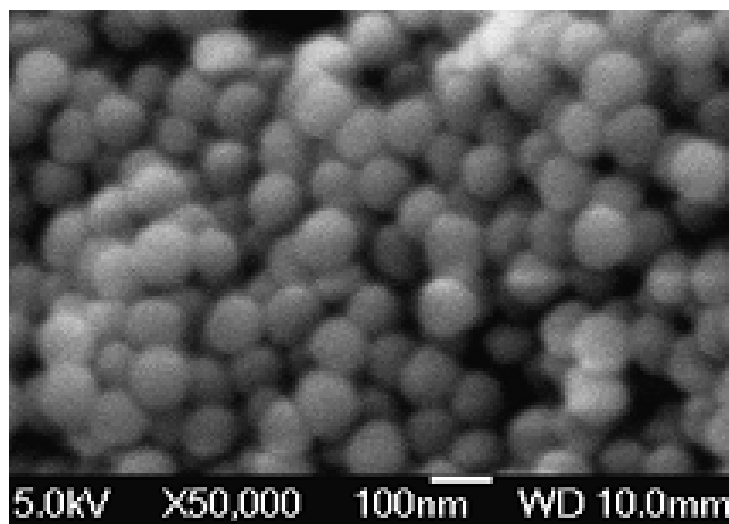
Figure 4.SEM image of SNPs of 87nm.

The FTIR spectrums of the bare and TDI grafted silica nanoparticles are shown in **Figure 5**. In the FTIR spectrum of bare SNPs (**Figure 5A**), characteristic peaks of Si–O–Si at 1050 cm^{-1}, Si–O at 800 cm^{-1} and broad peak of SiO–H group at 3200 – 3700 cm^{-1} can be seen. The appearance of new bands at 3302 and 1670 cm^{-1} which are characteristic for –NH and –NCOO urethane groups, respectively, confirms the urethane bond formation between the SNPs and isocyanate groups of TDI (**Figure 5B**). The strong absorption of –N=C=O group at 2274cm^{-1} shows the existence of free o-isocyanate groups of Si–TDI.
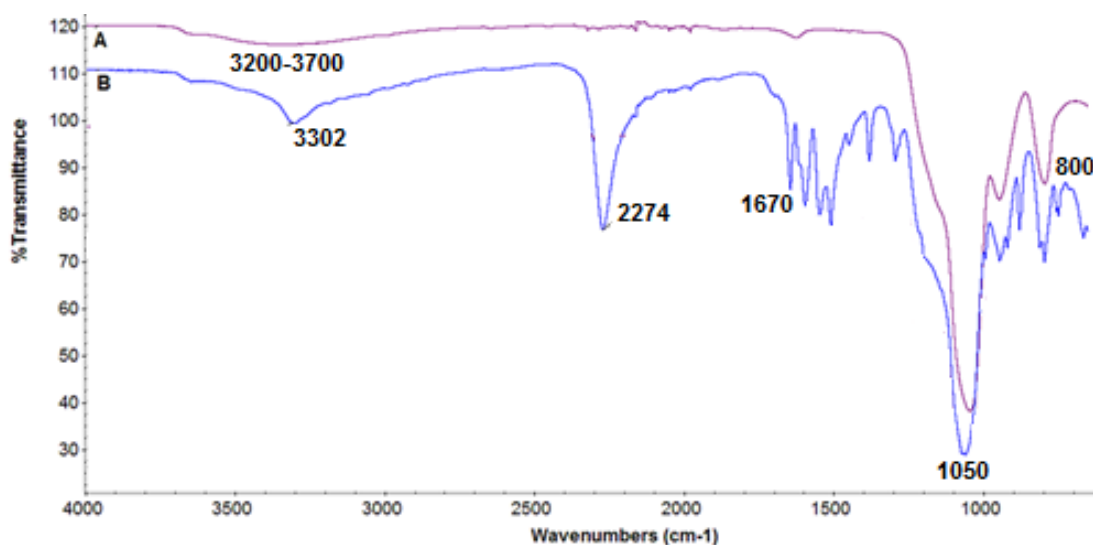
Figure 5.FTIR spectra of bare SNPs (A), and Si-TDI (B).

^{13}C CP/MAS NMR spectrum of Si–TDI (**Figure 6**) shows the characteristic peaks of grafted TDI moiety. The carbonyl peak at 151 ppm is indicative of urethane formation confirming TDI bonding on silica nanoparticles. The other carbonyl peak at 116 ppm is assigned to isocyanate group of TDI confirming the remaining free isocyanate functionality of TDI. The three peaks at 110, 112, 128 ppm correspond to unsubstituted aromatic carbons of TDI and the peaks at 125, 130, 131 ppm correspond to substituted aromatic carbons of TDI. The characteristic methyl peak of TDI appears at 13 ppm.
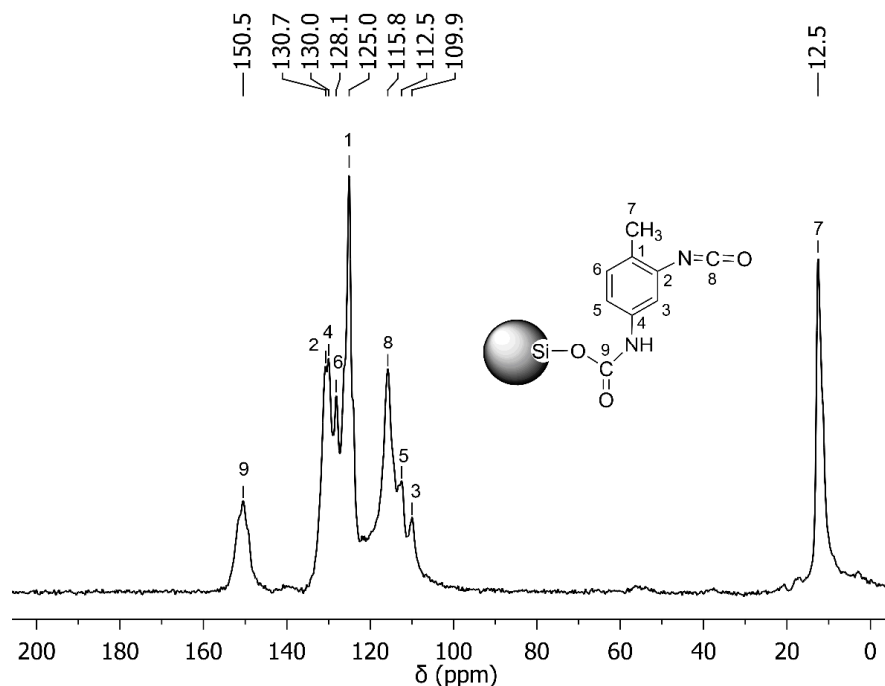
Figure 6.^{13}C CP/MAS NMR spectra of Si–TDI.

Bisphenol A type epoxy resin (Marepoks 1721) was succesfully reacted with acrylic acid over epoxy functionalities of the resin obtaining epoxy acrylate (EA) resin.Si–TDI nanoparticles with 1, 2 and 3 % weight ratios of total acrylates (EA and HDDA) were well dispersed in HDDA by ultrasonication and reacted with preformed EA. HDDA was used with the ratio of 20 % of EA in order to dilute EA resin and increase the acrylate functionality. Prepared hybrid resin formulations with the addition of irgacure-184 photoinitiator were successfully cured under UV radiation. EA-control resin (EA–Si 0 %) also prepared without the addition of Si–TDI and cured under UV. The ratios for the formulations of EA–Si hybrid resin are given in **Table 1**.

Table 1. Ratios of the components of EA-Si hybrid resin formulations.

Sample	EA resin (% w)	HDDA (% w)	Si-TDI (% w)	Irgacure-184 (% w)
EA–Si 0%	80.8	16.2	0	3
EA–Si 1%	80	16.0	1	3
EA–Si 2%	79	15.8	2	3
EA–Si 3%	78.3	15.7	3	3

Figure 7 shows the FTIR spectrum for Si–TDI and UV-cured control and EA–Si hybrid resins. FTIR spectrum of UV-cured acrylated epoxy resin (control resin) on **Figure 7A** showed characteristic ester absorption band (–COO) at 1724 cm^{-1} and no band appearance around 1640

and 920 cm⁻¹ which belong to –C=C and epoxy ring absorptions, respectively. The appearance of ester band and disappearance of–C=C and epoxy bands indicated that almost all of the epoxy groups of bisphenol A type epoxy resin acrylated by acrylic acid and EA resin was cured by acrylate groups under UV treatment. In addition to all of the characteristic absorption bands of cured EA-control resin (**Figure 7A**), the broaden apperance of the band at 3425 cm⁻¹ is observed in **Figure 7C** and attributed to –NH absorption of urethane bond between Si–TDI and EA resins. The appearance of the new bands at 1182 and 1071 cm⁻¹, which are characteristic for Si–O groups, also indicated Si–TDI incorporation into EA resin. And the complete disapperance of the band at 2264 cm⁻¹(**Figure 7B**) that belongs to free – NCO groups of Si–TDI nanoparticles indicated that there is no any unreacted isocyanate group remaining.
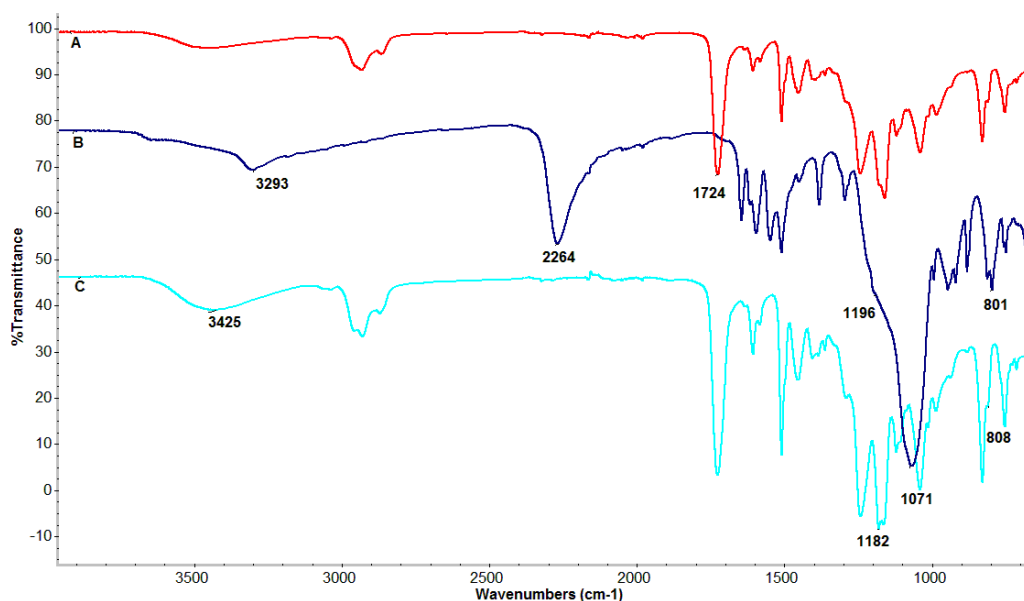
Figure 7.FTIR spectra of UV cured EA-control resin
(A), Si–TDI (B), UV-cured EA–Si 2 % hybrid resin (C).
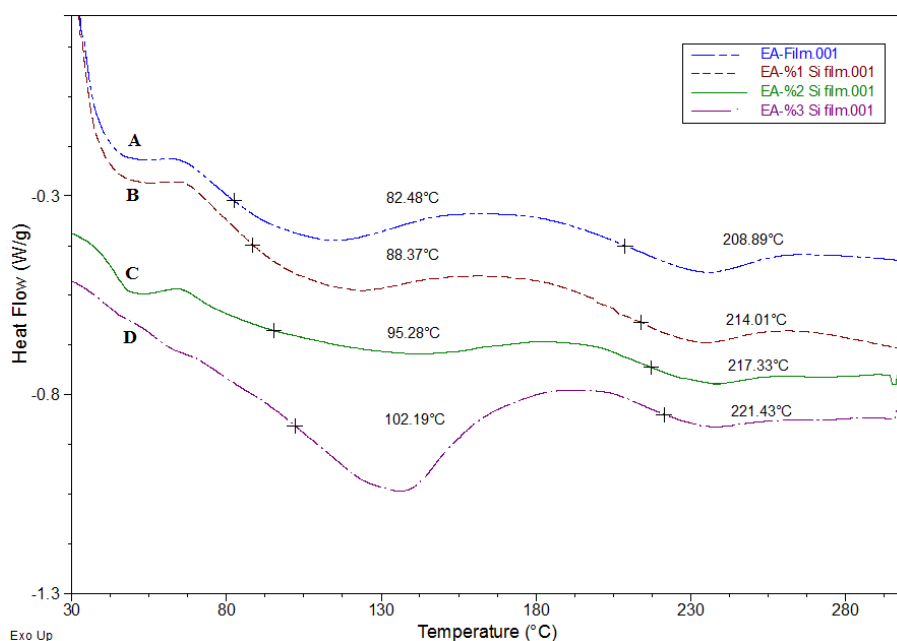
Figure 8. DSC thermogram of UV-cured EA-control film
(A), 1 (B), 2 (C), 3 % (D) UV-cured EA–Si nano hybridfilms.

The glass transition temperature (T_g) of the cured control EA resin film and SNP–EA hybrid resin films were analyzed by DSC and thermograms are seen in **Figure 8**. It was found from the DSC thermograms that control EA resin and EA–Si hybrid resin films showed $T_g$and exothermic post curing transitions. As it is seen in **Figure 8**, T_g value of acrylate region and postcuring transition value were 82.5 and 209 °C, respectively for control EA resin. T_g value of EA–Si hybrid films increased with the increasing content of Si–TDI nanoparticle reaching to approximately 102.2 °C for 3% Si–TDI content (**Figure 8**). The intensity of exothermic post curing transition was decreased with the increasing content of Si–TDI indicating almost disappearance of the exothermic curing behavior of Si–EA resin for 3% Si–TDI incorporation. The significant and consistent increase in T_g valuesand the decrease in the intensity of exothermic transitions of the Si–EA hybrid films were both atributed to monodispersed incorporation of inorganic Si–TDI nanoparticles and the effect of the increased crosslinking density. Diisocyanate functionality of Si–TDI nanoparticles acts as cross-linking points of EA–Si hybrid resin because of the reaction between isocyanate groups of Si–TDI and hydroxy groups of EA resin.
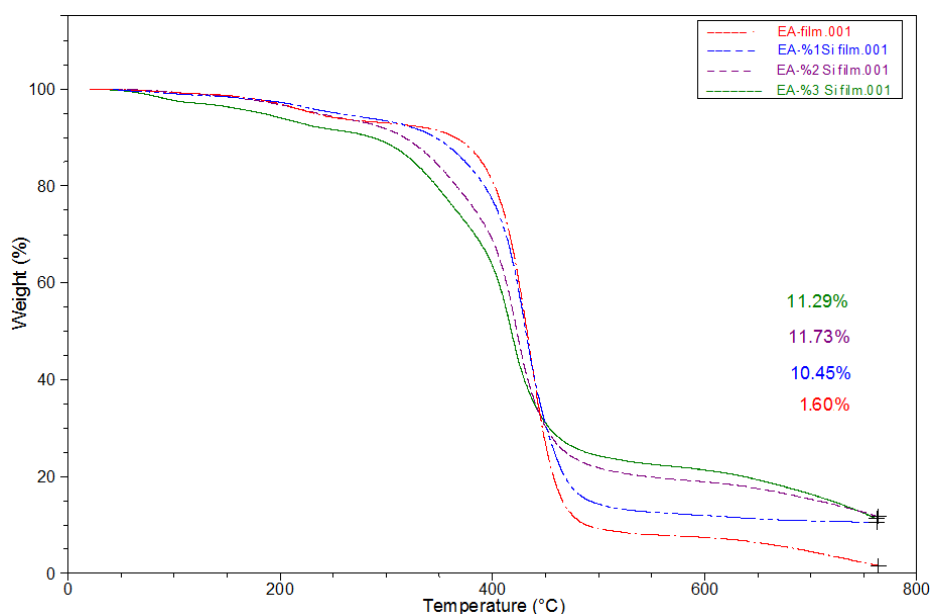
Figure 9.TGA thermogram of cured EA-control film and
1, 2, 3 % Si–TDI containing UV-cured EA–Si hybrid films.

The TGA thermograms of cured EA-control film and EA–Si hybrid films are shown in **Figure 9**. The samples were heated up to 800°C by the rate of 20 °C /min. The weight loss at the temperature less than 280 °C can be attributed to trapped volatile content of the cured resins, which is less than 5 %. Then the thermal decomposition of the cured EA film continued up to 450 °C due to aromatic and aliphatic structure of the resin. The temperatures above 450 °C indicated the complete thermal degradation of the cured films. The residue of cured EA-control film at 800 °C was 1.6 %, and such residue for totally organic structure might be attributed to inert nitrogen atmosphere of thermal analysis. The increased content of Si–TDI nanoparticles in cured EA–Si hybrid films resulted in the increase of residues at 800 °C as 10.5, 11.7 and 11.3 % for 1 % Si–TDI, 2 % Si–TDI and 3 % Si–TDI, respectively. It was obviously seen that incorporation of Si–TDI nanoparticles into EA–Si hybrid film had a significant effect on the residue content of the hybrid films resulting in much higher char content than own proportions

of Si–TDI nanoparticles. The results evaluated from TGA (**Figure 9**) confirmed the synergistic effect of Si–TDI nanoparticles on cured EA–Si hybrid films that SNPs promote char formation by forming the protective coat over the organic content of the hybrid film. The small decrease in the residue of EA–Si 3 % film (11.3 %) compared to the residue of EA–Si 2 % film might indicate the optimum proportion of Si–TDI nanoparticles in EA–Si hybrid resin to be 3 % above which the residues will not increase.

Table 2. Mechanical properties of
UV-cured EA–Si hybrid resins.

Sample	*E*-modulus (MPa)	Tensile strengt (MPa)	Elongation at break (%)
EA–Si 0 %	2437	23	1.4
EA–Si 1 %	2748	28	1.2
EA–Si 2 %	3342	34	0.8
EA–Si 3 %	3527	36	0.7

The application of nano hybrid materials is highly dependent on tensile properties, particularly modulus, tensile strength and elongation. These properties are also related to the crosslinking density of the resins as well as to the chemical structures. The mechanical specification of UV-cured EA–Si nano hybrid resin films of $50 \times 10 \times 1$mm dimensions made with the measurement of stress-strain values. In **Table 2**, evaluated stress-strain data of UV-curedSi–TDI modified epoxy acrylate resins are given as ultimate tensile strength, elongation at break and modulus. As it can be seen in **Table 2**, both *E*-modulus and tensile strength of EA–Si resins increase with the increasing silica nanoparticle content because of increased photocrosslinking ability of the cured system. Thus, resins become more rigid and elongation values decrease with the increasing Si–TDI content.
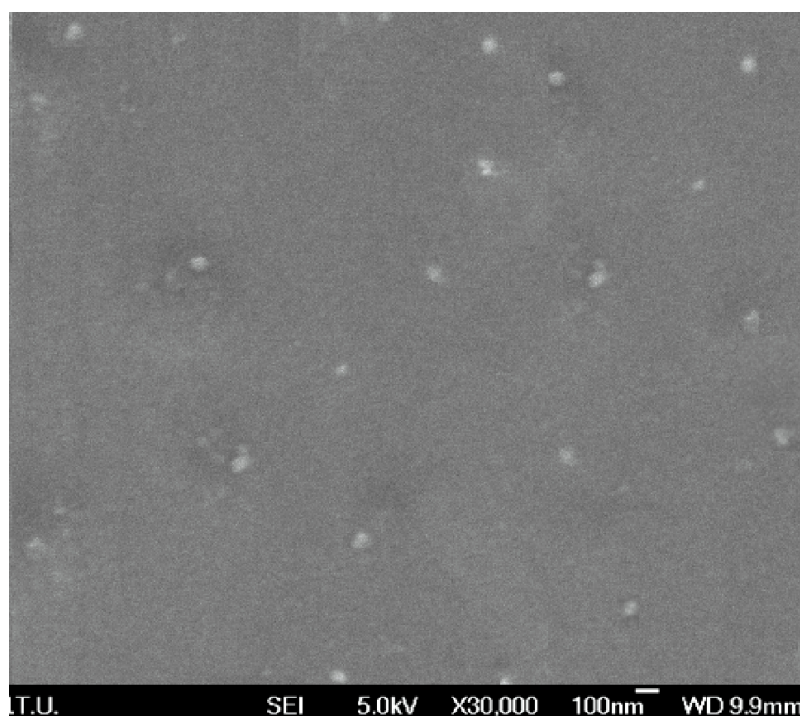
Figure 10.SEM image of UV-cured EA–Si 3 % hybrid resin.

The SEM image of UV-cured EA–Si 3 % nano hybrid resin is shown in **Figure 10**. The observation of the SEM image clearly showed that aggregation of SNPs was prevented despite the relatively high surface area of SNPs. Morover, mainly homogenous dispersion of SNPs in EA resin was achieved. Obviously, the reason to that is attributed to TDI functionalization of SNPs, which is further incorporated into EA resins.The isocyanate functionality together with the aromatic nature ofSi-TDI particles was chosen as the appropriate structure for an optimum compatibility with bisphenol-A based epoxy acrylate resin. Also, isocyanate functionality of Si–TDI nanoparticles was aimed to react with the hydroxyl groups of EA resin by covalent bonding, regardless of the complete achivement of the aim, the SEM image in **Figure 10** clearly indicated that Si–TDI nanoparticles in EA resin dispersed mainly homogenous without aggregation.

4. Conclusions

The structures and the properties of all synthesized compounds and materials were characterized and evaluated by the instruments based on the spectral (^{13}C–CP/MAS, IR),thermal (DSC, TGA), microscopic (SEM) and stress-strain calculating methods.

Spherical, uniformsilica nanoparticles (SNPs) were synthesized by Stöber process. The size of particles of SNP below 100 nm was achieved adjusting the reaction conditions such as temperature, concentration of TEOS and ammonia. Physical and chemical structure of the synthesized nanoparticles such as the size of particles, specific surface area were characterized clarifying their surface properties for the modification of silica nanoparticles.

After the definition of SNPs, surface modification of the silica nanoparticles was achieved with the reaction of p-isocyanate groups of toluen di-isocyanate (TDI) obtaining Si–TDI nanoparticles in order to gain both improved dispersion of SNPs in organic phase and ability for further possible reactions over the free m- isocyanate group of TDI.

Well defined Si-TDI nanoparticles were incorporated into preformed epoxy-acrylate resin over the urethane bond formed between hydroxyl groups of EA resin and free isocyanate groups of Si-TDI creating inorganic crosslinking points. The curing process of EA hybrid resin films was performed under UV irradiation. Chemical structure of the UV-cured hybrid filmswas evaluated by FTIR and confirmed the expected structures. Thermal properties of the cured films were investigated by DSC and TGA. The increase in Si–TDI content of EA hybrid resins resulted in the consistent increase in T_g values and decrease in the intensity of exothermic post curing transition of hybrid films indicating both monodispersed incorporation and crosslinker effect of Si–TDI nanoparticles into EA hybrid resin. The results evaluated from TGA confirmed the synergistic effect of Si-TDI nanoparticles on cured EA–Si hybrid film significantly promoting the char formation most likely due to the protective coat occured by SNPs over the organic content.The observation of the SEM image clearly confirmed that aggregation of SNPs was prevented despite the relatively high surface area of SNPs. Moreover, mainly homogenous dispersion of SNPs in EA resin was achieved. Evaluating stress-strain data of UV-cured Si–TDI modified epoxy acrylateresins, it could be seen that both *E*-modulus and tensile strength of EA–Si resins increase with the increasing silica nanoparticle content because of increased photocrosslinking ability of the cured system. Thus, resins become more rigid and elongation values decrease with the increasing Si–TDI content.

References

1. J. Patrick, S. Clement. J. Mater. Chem., 1996, 6, 511-525.
2. M. F. Ashby, Y. J. M. Brechet. Acta Mater., 2003, 51, 5801-5821.
3. G. Kickelbick. Hybrid Materials. Synthesis, Characterization, and Applications. 2007, Weinheim, Wiley–VCH.
4. C. Sanchez, G. Soler–Illia, F. Ribot, D. Grosso. Comp. Ren. Chim., 2003, 6, 1131-1135.
5. C. Sanchez, B. Julian, P. Belleville, M. Popall. J. Mater. Chem.,2005, 15, 3559-3592.
6. I. A. Rahman, V. Padavettan. J. Nanomater., 2012, 2012, 1-15.
7. Q. Wang, R. Hou, Y. Cheng, J. Fu. Soft Mater., 2012, 8, 6048-6056.
8. S. Quignard, S. Masse, G. Laurent, T. Coradin. Chem. Commun., 2013, 49, 3410-3412.
9. R. K. Iler. The Chemistry of Silica: Solubility, Polymerization, Colloid and Surface Properties, and Biochemistry. 1979, Chichester, John Wiley & Sons.
10. J. J. Guo, X. H. Liu, Y. C. Cheng, Y. Li, G. J. Xu, P. Cui. J. Colloid Interface Sci., 2008, 326, 138-142.
11. J. H. Balthis, P. Mendenhall. US Patent,1989, # 2614994 (1952).
12. S. K. Park, K. D. Kim, H. T. Kim. Colloids Surf. A, 2002, 197, 7-17.
13. W. Stöber, A. Fink, E. Bohn. J. Colloid Interface Sci.,1968, 26, 62-69.
14. D. L. Green, J. S. Lin, Y. F. Lam, M. Z. Hu, D. W. Schaefer, M. T. Harris. J. Colloid Interface Sci., 2003, 266, 346-358.
15. F. Caruso. Adv. Mater., 2001, 13, 11-22.
16. P. Mansky, Y. Liu, E. Huang, T. P. Russell, C. Hawker. Science, 1997, 275, 1458-1460.
17. N. Nishizawa, J. Nishimura, H. Saitoh, K. Fujiki, N. Tsubokawa. Prog. Org. Coat.,2005, 53, 306-311.
18. J. N. Kizhakkedathu, D.E. Brooks. Macromolecules, 2003, 36, 591-598.
19. E. F. Vansant, P. van der Voort, K. C. Vrancken. Characterization and Chemical Modification of the Silica Surface. 1995, Amsterdam,Elsevier.
20. R. Badley, W. Ford, F. McEnroe, R. Assink. Langmuir, 1990, 6, 792-801.
21. S. A. Torry, A. Campbell, A. V. Cunliffe, D. A. Tod. Int. J. Adhes., 2006, 26, 40-49.
22. E. T. N. Bisanda, M. P. Ansell. Composites Sci. &Technol., 1991, 41, 165-178.
23. M. Bengtsson, K. Oksman. Composites Sci. &Technol, 2006, 66, 2177-2186.
24. S. M. B. Nachtigall, G. S. Cerveira, S. M. L. Rosa. Polym. Test., 2007, 26, 619-628.
25. M. Abdelmouleh, S. Boufi, M. N. Belgacem, A. Dufresne. Composites Sci. & Technol., 2007, 67, 1627-1639.
26. G. Kickelbick, D. Holzinger, S. Ivanovici. Organically Functionalized Silica Nanoparticles, Materials Syntheses. 2008, Vienna, Springer.
27. S. Bachmann, H.Wang, K. Albert, R. Partch. J. Colloid Interface Sci., 2007, 309, 169-175.
28. Y. Huang, Q. Liu, X. Zhou, S. Perrier, Y. Zhao. Macromolecules, 2009, 42, 5509-5517.
29. A. P. Wight, M. E. Davis. Chem. Rev., 2002, 102, 3589-3614.
30. Y. Wang, X. Pei, K. Yuan. Mater. Lett.,2005, 59, 520-523.
31. S. K. Parida, S. Dash, S. Patel, B. K. Mishra. Adv. Colloid Interface Sci., 2006, 121, 77-110.
32. J. Che, Y. Xiao, X. Wang, A. Pan, W. Yuan, X. Wu. Surf. Coat. Technol., 2007, 201, 4578-4584.

33. M. Karahasanoglu, A. Onen, I. E. Serhatlı. Prog. Org. Coat.,2014, 77, 1079-1084.
34. R. Schwalm. UV Coatings Basics, Recent Developments and New Applications. 2007, Amsterdam, Elsevier.
35. A. Tiwari, A. Polykarpov. Photocured Materials.2015, Cambridge., Royal Soc. Chem.
36. D. Hull, T. W. Clyne. In: An Introduction to Composite Materials. 1996, Cambridge, Cambridge Univ. Press, 30-34.
37. T. Ueki, S. Nishijima, Y. Izumi. Cryogenics, 2005, 45, 141-148.

INFLUENCE OF SYNTHESIS CONDITIONS ON THE PHASE FORMATION, PHOTOELECROCHEMICAL AND PHOTOCATALYTIC PROPERTIES OF NANOSIZED IRON TITANATE FILMS

N. Smirnova [1], N. Chorna [1], O. Linnik [1], V. Vorobets [2], G. Kolbasov [2]

[1] Laboratory of Photonics of Oxide Nanosystems
O. O. Chuiko Institute of Surface Chemistry
National Academy of Sciences of Ukraine
Kyiv, Ukraine
smirnat@i.ua
[2] Department of Electrochemistry
Institute of General & Inorganic Chemistry
National Academy of Sciences of Ukraine
Kyiv, Ukraine

Abstract

TiO_2 and TiO_2/Fe^{3+} films were synthesized by sol–gel method and characterized by XRD, EDS and UV–Vis spectroscopy. The multicomponent TiO_2/Fe^{3+} films treated at temperatures 450 – 600 °C have the pseudobrookite (Fe_2TiO_5) structure with landaunite ($Fe_2Ti_2O_7$) impurities. Raise in the treatment temperatures leads to the accumulation of iron ions onto the material surface and formation of the $Fe_2Ti_2O_7$ phase. Higher crystallinity of TiO_2/Fe^{3+} calcined at 500 °C films was obtained compared with TiO_2/Fe^{3+} 450 °C systems. Band gap energy and the position of the flat band potentials of TiO_2 and TiO_2/Fe^{3+} electrodes produced by precursor coating on the titanium plates were estimated by photoelectrochemical measurements showing the cathodic shift of the flat-band potential position in comparison with unmodified TiO_2 electrodes. High photocatalytic activity of the films under visible as well as UV irradiation correlates with their high adsorption capacity.

1. Introduction

Widespread use of a semiconductor photocatalysts for environmentally important processes of neutralization of toxic organic compounds and heavy metals in the waste water, drinking water and air caused by the need to create the new nanomaterials with high surface area, define structure with enhanced activities under both UV and visible light irradiation, improving the efficiency of solar energy utilization. Among the semiconductor materials titanium dioxide attracts the great attention of the researchers because of its chemical stability, biological inertness, low toxicity, and relatively low cost [1, 2]. Doping with nonmetals, such as B, C, N, S and F [3, 4] or metal elements, such as Fe, Cr, Co, Mn and V [5 – 7] have been employed to tune the electronic structure and enhance the photocatalytic activity of titanium dioxide under visible light. The light absorption properties of $M^{n+}–TiO_2$ systems have been traditionally considered as a hint to determine whether they are photoactive with visible light. Iron ions are the most studied because their radius is identical to Ti^{4+} one, the half-filled d electronic configuration and ability to trap holes or electrons. The presence of iron extended the light absorption band [9]. Optical bandgaps of titanium nanoparticles were found to

decrease with the increase in iron content in host lattice [10]. Authors [11] reported the results of the comparison of the absorption properties of the M^{n+}–TiO_2 thin films with their photoelectrochemical behavior. As a general result it has been found that no improvement of the photoactivity of the system takes place, but it decreases with respect to pure TiO_2. This behavior shows that a shift toward the visible in the light absorption of M^{n+}–TiO_2 materials does not ensure that they have enhanced photocatalytic efficiency at longer wavelengths. According to [12]Fe^{3+} doping effectively improve the photocatalytic activity under both UV light irradiation and visible light irradiation with an optimal doping concentration of 0.1 and 0.2%, respectively. Some authors [10] demonstrated the Fe–TiO_2 photoactivity under the visible light using as the model Rhodamine or aso-dyes degradation. Obviously, there is no increase of semiconductor photoresponse in visible spectral region but rather self sensibilisation pathway of dye destruction took place in that case. The theoretical computation based on the density functional theory [13] shows that the Fe ions in TiO_2 bulk are localized, and mainly act as the recombination centers of photoinduced electrons and holes. The photocatalytic activity first increases and then decreases as the Fe concentration increases, which is co affected by the bulk-doped and surface-doped Fe ions. The predicted mechanisms for the enhancement of the photochemical response for doped or surface deposited M^{n+}/TiO_2 or M_2O_n/TiO_2 systems are quite different. Only in few papers [11, 14 – 16], the formation of new active oxide phases and the photoelectrochemical properties of new materials were reported, although, they are of basic importance for estimation of semiconductor efficiency and perspectives of its application in ecological photocatalysis.

Herein, we report on a simple preparation of iron-titanate films, their structure, photoelectrochemical characterization, and their photocatalytic properties by UV and visible light degradation of biogenic (anthropogenic) pollutant – tetracycline hydrochloride as a representative of the broad class of antibiotics.

2. Experimental

Iron titanate films were synthesized according to [17] with slight modification. An appropriate amount of anhydrous iron chloride (Aldrich) was dissolved in 25 ml of absolute ethanol (Riedel-de Haen) previously heated to 40 °C and stirred for 20 min till the complete dissolution. After that, the calculated amount of titanium isopropoxide (99.999%, Aldrich) was added slowly to the solution. The sol was ready for dip-coating after stirring for 15 min. The glass plates were previously cleaned by soap with subsequent washing with distilled water and dried in the oven at 80 °C. Hot glass slides were immediately used for dip-coating. An optimum withdrawal speed of 1.5 mm/s was used. The obtained films were left for 24 h at room temperature for hydrolysis and then calcined (heating rate was 10 °C/min) at 450, 500 or 600 °C for 20 min.

The iron-free titanium film was prepared as follows: a mixture of TTIP (5 ml), HCl (some drops) and $EtOH_{abs}$ (25 ml) was kept on the ice-bath for 15 min. After dip-coating the films were left for 20 min at room temperature for hydrolysis and heated at a rate of 10 °C / min to 450, 500 or 600 °C and left for 20 min at this temperature.

The photoelectrochemical properties of the TiO_2 and Fe/TiO_2 electrodes were estimated using the spectral dependence of the photoelectrochemical current ($i_{ph.}$), measured with a commercial spectrometer KSVU–1 (LOMO, Russia) with spectral resolution 1 nm. The experiments were carried out at 22°C under pure argon bubbling in the temperature-controlled

quartz cell. The $i_{ph.}$ spectra were measured using the mechanical light chopper of 20 Hz frequencies and standard circuit synchronous detection. A high-pressure xenon lamp with stabilized discharge current was used as the light source. The $i_{ph.}$ spectra were expressed in units of quantum efficiency (electron / photon).

Tetracycline hydrochloride (TC) degradation was used to assess the photocatalytic efficiency of the films through the oxidative pathway. The film was immersed in 40 ml of an aqueous solution of $2 \cdot 10^{-5}$ mol / L TC. The reaction temperature was kept constant (20 °C) during the experimental procedure. The change of TC concentration was monitored with a Lambda 35 UV–Vis spectrophotometer (PerkinElmer) every 20 min at $\lambda = 357$ nm. The film was immersed in the solution until the complete adsorption in the dark occurred and then irradiated by a 1000 W middle-pressure mercury lamp for 90 min. The conversion percentage was calculated from the change in absorption intensity

3. Results

The heat treatment temperature is a critical step in the TiO$_2$ based photocatalysts manufacturing, because it has implication on their phase composition and specific surface area as the key factor of photocatalytic activity. For the iron titanate materials, the calcination can lead to the formation of following compounds: anatase, rutile, hematite, pseudobrookite and various solid compounds of $Fe_xTiO_{1-x}O_y$ type. The iron titanate films covered onto the glass substrates were characterized by XRD (**Figure 1**).
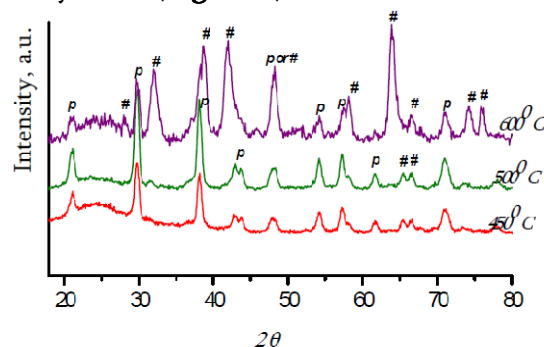
Figure 1. XRD patterns of Fe/TiO$_2$ films (Fe:Ti=1: 1)
heatedat 450, 500 and 600 °C. p means the pseudobrookite
and # – landaunite structures of iron titanate phases.

Figure 2 shows XRD diagrams for Fe/TiO$_2$ films (Fe : Ti = 1 : 1) heated at different temperatures. Only pseudobrookite was detected after 450 °C treatment. An increase in the heat treatment temperature from 450 to 500 °C leads to higher step of crystallinity reflected in the considerably sharper and well-defined diffraction peaks, when particle size of pseudobrookite calculated by Scherrer equation was similar for all samples (16 nm). Peaks located at the diffraction angle $2\theta = 65.5$ and 66.5 ° corresponded to landaunite phase identified for TiO$_2$/Fe^{3+}– 500 °C films. The decrease in crystallinity degree in the case of TiO$_2$/Fe^{3+} (600 °C) films coincides with the acceleration of landaunite phase formation. However, it cannot be excluded the formation of minor content of rutile, which cannot be identified because its peaks are overlapped with landaunite reflexes. No other phases, such as anatase and α-Fe$_2$O$_3$ phase (hematite) were detected for these films.

EDS data (**Table 1)** show 10 % decrease of iron content on the surface of the film, when calcination temperature increased to 500 °C.

Table 1. Influence of film preparation condition
on the elemental composition of the surface.

Element / Film treatment condition	Fe	Ti	O	Fe : Ti : O
	Ar, %			
TiO₂/Fe³⁺, 450 °C	18.99	19.43	39.30	1 : 1 : 2
TiO₂/Fe³⁺, 500 °C	19.64	20.91	40.86	0.9 : 1 : 2

Optical absorption spectra of air sintered iron titanate films showed high optical absorption in visible part of the spectrum (**Figure 2**). It is clear that the spectra of all the Fe doped samples have wide absorbance in the visible range that increase with the annealing increase from 450 to 600 °C. Fe-doped TiO_2 showed a shoulder at wavelengths of around 590–470 nm, corresponding to the absorption energy of 2.1 – 2.6 eV.
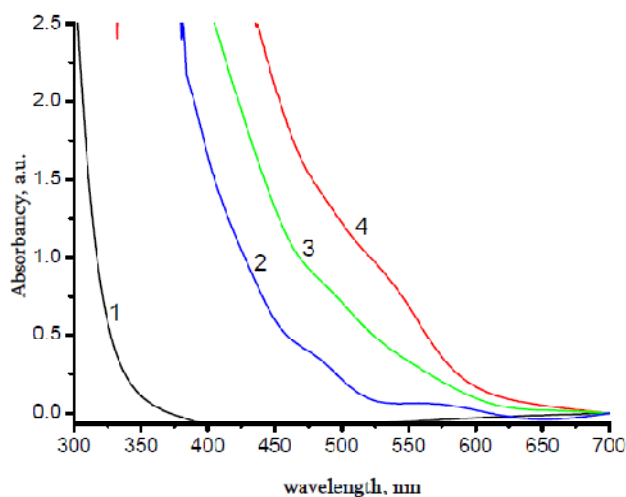
Figure 2. UV–Vis absorption spectra of TiO_2 and Fe/TiO_2 films after annealing at 450 – 1 and 2, 500 – 3 and 600 °C – 4.

As established by F. Gracia [11] and observed in our previous work [15], the shift of the absorption threshold of metal doped TiO_2 toward visible light is not always the sufficient condition for the photocatalyticefficiency under visible light.

Photoelectrochemical investigations were performed to evaluate photoactivity of the Fe/TiO_2 films under both UV and visible light. Spectral dependences of photocurrent were measured for the undopedTiO_2 and Fe/TiO_2 electrodes produced via coating of films on Ti substrate (**Figure 3**) to obtain the value of the band gap energy. Photocurrent quantum yield for all doped films is much lower than that for undoped TiO_2. Maximum of photocurrent spectral dependences for iron doped films shifted significantly (up to 100 nm) to visible spectral region. The effect of the annealing temperature on photocurrent was investigated. The incident photon conversion efficiency was the largest for films treated at 500 °C. It is important to note that in spite of the significant decrease of photocurrent under UV light compared to bare TiO_2, photoresponce in this spectral region is not totally suppressed. So it can be predicted the photocatalytic activity of iron titanate film under both visible and UV irradiation.

226
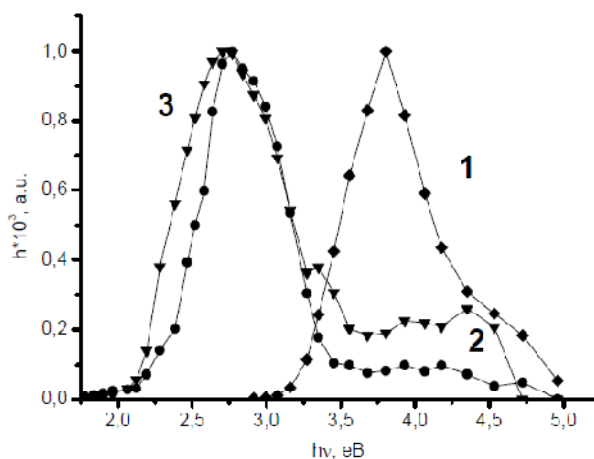
Figure 3. Quantum yield of photocurrent of TiO₂ and Fe/TiO₂
electrodes: TiO₂(1), Fe/TiO₂ (2, 3) annealed at 450 (1, 2) and 500 °C (3).

For the tested TiO₂ and Fe/TiO₂ compositions, photocurrent spectra were presented as $(\eta h\nu)^{1/2} = f(\text{hv})$ dependence, which was linear in the wide range of wavelength.

Experimental data fit better to an indirect transition. Band gap (E_g) values were calculated from these dependences by the extrapolation of straight line to the abscissa [18, 19]. Obtained by this method, E_g values are located in the range of 2.0 – 3.1 eV (**Table 2**). For Fe/TiO₂ films, the E_g values decrease with the increase of annealing temperature. That is probably associated with the formation of new phases. Flat band potentials that corresponded to E_{cb} position were estimated from $i_{ph.}$ changes measured at the photocurrency maximum for TiO₂ and Fe/TiO₂ films. The values of photovoltage were plotted against applied potential and the straight line extrapolation of these dependences to the abscissa determines the flat band potential (**Table 1**). The flat band potential values for the TiO₂ insignificantly differ and are comparable with the value $E_{fb} = -0.58$ V vs. NHE, obtained at pH ≈ 7 for anatase single crystal [20, 21]. For the iron titanate samples E_{fb} is shifted to positive values in the range of $-0.02 - +0.02$ V.

Table 2: Photoelectrochemical characteristics
for the TiO₂ and Fe/TiO₂ electrodes.

Sample	Temperature,°C	E_{fb} , V (±0.01)	E_g, eV
TiO₂	450	−0.46	3.1
Fe/TiO₂	450	−0.02	3.2; 2.3
Fe/TiO₂	500	+0.02	3.1; 2.1

Photocatalytic activity of bare TiO₂ and Fe-doped TiO₂films under UV as well as under visible light irradiation was examined by studying the photodegradation of tetracycline hydrochloride that represents frequently used antibiotics and, nowadays, established as dangerous pollutant of wastewater from medicine and food production. The adsorption ability of TC onto the surface of the films after calcinations at 450, 500 and 600°C carried out in the dark was also studied (**Figure 4**). As shown previously [22], the formation of new adsorption sites takes place and the percentage of the adsorbed TC molecules strongly depends on the iron ions content and film composition. It is obvious that the higher iron ions content, the higher adsorption of TC onto the film surface. For tested iron titanate (Fe : Ti = 1 : 1) films, the highest adsorption was observed for films treated at relatively low temperature, as namely 450 °C,

allowing the keeping of the developed surface area leading to the high adsorption of the pollutant molecules (**Figure 4**). When the annealing temperature is increased to 500 and 600 °C, the dramatical decrease of TC adsorption onto Fe/TiO$_2$-films is noted. Our previous results clearly showed that the adsorbed TC molecules are firstly involved into the photocatalytic reaction rather than the molecules from liquid-solid interface. Therefore, the high adsorption ability of the films treated at the 450 °C is one of the key points for photocatalytic efficiency.
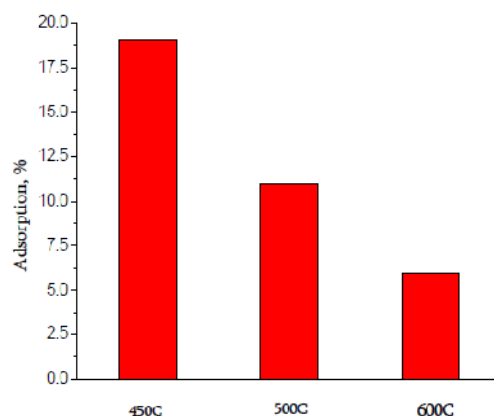
Figure 4. Percentages of TC molecules adsorption ontothe Fe/Ti films treated at different temperatures (the average values of two experiments were taken).

The photocatalytic activity of the films was tested in the process of TC destruction under both UV and visible light. The light action on the aqueous TC solution without film did not lead to the significant change in TC absorption spectra, i.e. the TC concentration was decreased on 6 and 2 % after 90 min irradiation under UV and visible light, respectively.
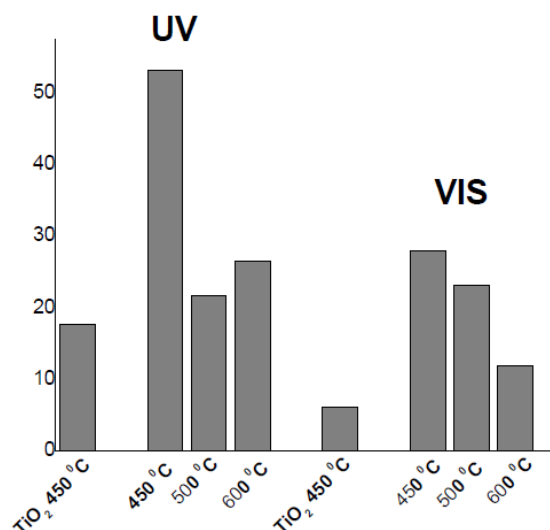
Figure 5. Photocatalytic activity of TiO$_2$ treated at 450 °C and Fe^{3+}/TiO$_2$ films treated at 450, 500 and 600 °C in TC degradation process under both UV and visible light.

The increase of TC conversion degree (**Figure 5**) compared with undoped TiO$_2$ film is observed for all synthesized iron titanate films under UV as well as visible light. It can be caused by the formation of iron titanate phase possessing by the lower band gap values (**Table 2**).

Many research groups have prepared TiO_2 doped with iron ions in low concentration (up to 5 %), and all the Fe-doped TiO_2 materials show expanded light absorption band and improved photocatalytic activity due to the lower recombination rate [23]. However, independent on the origin of visible light absorption in discrete energy states of semiconductor E_g, the low photocatalytic efficiency is mainly attributed to the limited photo-excitation of electrons in such narrow states, the very low mobility of the corresponding photo-generated holes and the concomitant increase of the recombination rate due to the creation of oxygen vacancies by doping [24].

4. Conclusions

Multicomponent TiO_2/Fe^{3+} films synthesized by sol–gel method and heat treated at a relatively low temperature (450 °C) have the pseudobrookite structure (Fe_2TiO_5) with landaunite ($Fe_2Ti_2O_7$) traces.The films doped with iron ions showed the lower photocurrent quantum yield than for undoped samples, while the highest photocurrent was observed at the wavelength within the visible region. Doping with iron ions leads to the cathodic shift of the bottom of conduction band with the E_g decrease. The significant changes of the flat band potential values were observed for annealed Ti : Fe samples treated at 500 °C. It is suggested that the formation of $Fe_2Ti_2O_7$phase stimulates the efficiency of visible light absorption. High photocatalytic activity of the iron titanate film calcined at 450 °C correlates with its high adsorption capacity to pollutant molecules.

References

1. A. Fijushima, T. N. Rao, D. A. Tryk. Titanium dioxide photocatalysis. J. Photochem. Photobiol. C, 2000; 1, 1-21.
2. X. Fujishima, C. R. Zhang. Titanium dioxide photocatalysis: Present situation and future approaches. Chimie, 2006, 9, 750-760.
3. A. Zaleska. Doped TiO_2: A review. Recent Patents on Engineering, 2008, 2, 157-164.
4. S. Sakthivel, M. Janczarek, H. Kisch. Visible light activity and photoelectrochemical properties of nitrogen-doped TiO_2. J. Phys. Chem. B, 2004, 108, 19384-19387.
5. J. O. Carneiro, V. Teixeira, A. Portinha, L. Dupak, A. Magalhaes, P. Coutinho. Study of the deposition parameters and Fe-dopant effect in the photocatalytic activity of TiO_2 films prepared by dc reactive magnetron sputtering. Vacuum, 2005, 78, 37-46.
6. D. L. Gomathi, K. Nagaraju, M. B. Narasimha, K. S. Girish. Enhanced photocatalytic activity of transition metal ions Mn^{2+}, Ni^{2+} and Zn^{2+} doped polycrystalline titania for the degradation of Aniline Blue under UV/solar light. J. Mol. Catalysis A, 2010, 328, 44-52.
7. J. Yu, Q. Xiang, M. Zhou. Preparation, characterization and visible-light-driven photocatalytic activity of Fe-doped titania nanorods and first-principles study for electronic structures. Appl. Catalysis B, 2009, 90, 595-602.
8. W. Choi, A. Termin, M. R. Hoffmann. The role of metal ion dopants in quantum-sized TiO_2: Correlation between photoreactivity and charge carrier recombination dynamics. J. Phys. Chem., 1994, 98, 13669-13679.

9.   Y. Zhang, Y. Shen, F. Gu, M. Wu, Y. Xie, J. Zhang. Influence of Fe ions in characteristics and optical properties of mesoporous titanium oxide thin films. Appl. Surf. Sci., 2009, 256, 85-89.

10. S. D. Delekar, H. M. Yadav, S. N. Achary, S. S. Meena, S. H. Pawar. Structural refinement and photocatalytic activity of Fe-doped anataseTiO$_2$ nanoparticles. Appl. Surf. Sci., 2012, 263, 536-545.

11. F. Gracia, J. P. Holgado, A. Caballero, A. R. Gonzalez–Elipe. Structural, optical, and photoelectrochemical properties of M^{n+}–TiO$_2$ model thin film photocatalysts. J. Phys. Chem. B, 2004, 108, 17466-17476.

12. J. Tong, J. Zhang, B. Tian, F. Chen, D. He. Preparation of Fe^{3+}-doped TiO$_2$ catalysts by controlled hydrolysis of titanium alkoxide and study on their photocatalytic activity for methyl orange degradation. Hazard. Mater., 2008, 155, 572-579.

13. L. Wen, B. Liu, X. Zhao, K. Nakata, T. Murakami, A. Fujishima. Synthesis, characterization, and photocatalysis of Fe-doped TiO$_2$: A combined experimental and theoretical study. Int. J. Photoenergy, 2012, 368750, 1-10.

14. O. Linnik, H. Kisch. On the mechanism of nitrogen fixation at nanostructured iron titanate films. Photochem. Photobiol. Sci., 2006, 5, 938-948.

15. I. S. Petrik, O. P. Linnik, N. P. Smirnova, A. M. Eremenko, G. Ya. Kolbasov, V. S. Vorobets. Photoelectrical and photocatalytical properties of nanosizedTiO$_2$ and Fe^{3+}/TiO$_2$ films. Phys. &Chem. Solid State, 2007, 8, 336-341.

16. N. P. Smirnova, Yu. Gnatyuk, A. Eremenko, G. Kolbasov, V. Vorobetz, I. Kolbasova, O. Linyucheva. Photoelectrochemical characterization and photocatalytic properties of mesoporous TiO$_2$/ZrO$_2$ films. Int. J. Photoenergy, 2006, 8, 1-6.

17. O. Rusina, O. Linnik, A. Eremenko, H. Kisch. Nitrogen photofixation on nanostructured iron titanate films. Chem. Eur. J., 2003, 9, 561-565.

18. Yu. Gurevich, Yu. Pleskon. Photoelectrochemistry of Semiconductors. 1983, Moscow, Nauka.

19. G. Kolbasov, A. Gorodyskyi. Photoinduced Charge-Transfer Processes in Semiconductor –Electrolyte Systems. 1993, Kyiv, Naukova Dumka.

20. S. Sakthivel, H. Kish. Photocatalytic and hotoelectrochemical properties of nitrogen-doped titanium dioxide. Chem. Phys., 2003, 4, 487-490.

21. M. Gratzel, S. E. Gilbert, C. Klemenz, H. J. Scheel. Electrochemical and photoelectrochemical investigation of single-crystal anatase. J. Am. Chem. Soc., 1996, 118, 6716-6723.

22. N. Chorna, O. Linnik, N. Smirnova. Synthesis, optical and photocatalytic properties of mesoporous iron doped titania films. Chem. Phys. &Technol. Surf., 2016 – *in press*.

23. K. Hashimoto, H. Irie, A. Fujishima. TiO$_2$ photocatalysis: A historical overview and future prospects. Jpn. J. Appl. Phys., 2005, 44, 8269-8285.

24. R. Katoh, A. Furube, K. Yamanaka, T. Morikawa. Charge separation and trapping in N-doped TiO$_2$ photocatalysts: A time-resolved microwave conductivity study. J. Phys. Chem. Lett., 2010, 29, 3261-3265.

NEW COMPOSITE COATINGS, THEIR STRUCTURE AND PROPERTIES

L. Markashova, G. Grigorenko, Yu. Tyurin, O. Kolisnichenko, O. Berdnikova, O. Kushnarova, E. Titkov

E. O. Paton Electric Welding Institute
National Academy of Sciences of Ukraine
Kyiv, Ukraine
omberdnikova@bigmir.net

Abstract

The effect of structure and phase composition of composite coatings on their service properties under extreme working conditions (high temperatures and pressure, intensive wear by friction, external loads and corrosion environments) was considered. Here, the coatings of Al_2O_3–Ti; and Al_2O_3–Al systems and others, produced by applying the installation of a multi-chamber detonation of spraying, developed at the E.O. Paton Electric Welding Institute of the NAS of Ukraine, were investigated. In order to evaluate the efficiency of the coatings being investigated under different service conditions, the analytical estimations of structure ↔ properties relations were used. It was shown that the greatest contribution to the properties of strength, ductility and crack resistance of the investigated coatings were made by: dispersion of grain and sub-grain structures, uniform distribution of forming strengthening phases of dispersed sizes in absence of lengthy and dense dislocation clusters, being the concentrators of local internal stresses (potential zones of incipience and propagation of cracks).

1. Introduction

One of the most widespread and at the same time perspective way to improve operation properties and durability of products is deposition of different functional coatings on their surfaces using different spraying technologies [1, 2]. It is thought that among the most advanced and dynamically developing technologies for spraying coatings are the methods of high-velocity gas flame spraying GFS (high-velocity oxygen fuel (HVOF) and high-velocity air fuel (HVAF)). In many cases they replaced other widespread technologies for deposition of coatings due to a very high quality of produced coatings and efficiency of the process. However, one of the most significant disadvantages of above-mentioned technologies for high-velocity deposition of coatings is a very big expense of the gas mixture. An alternative to high-velocity GFS methods is the method of detonation-gas spraying (DGS), which allows obtaining coatings with a quality comparable to the methods of HVO(A)F. Thus, they are characterized with a lower materials utilization factor (MUF) and the process discreteness [3, 4].

At the E. O. Paton Electric Welding Institute of the NAS of Ukraine the technology and equipment for cumulative-detonation spraying (CDS) were developed by which high-quality coatings are formed with high MUF and productivity. They thus differ from the

aforementioned most advanced methods GFS methods by simplicity of equipment, significantly lower specific expenses and pressure of gases, as well as energy intensity [5]. The features of this technology are several specially profiled detonation chambers and heightened frequency of the fuel mixture detonation (20 Hz). They practically nullify negative effects of detonation spraying associated with increments of classical methods [6].

The demanded direction for application of cumulative-detonation method is spraying of powders of different systems: Ni–Cr–Si; WC–Co–Cr; Cr_3C_2–NiCr; Cr_3C_2–TaC–NiCr; Al_2O_3–Ti,Al_2O_3–Al,$ZrSiO_4$, etc. for producing functional coatings, operating under extreme conditions (high temperature and pressure, intensive friction, external loads and corrosive environments). Such coatings possess high strength and corrosion resistance and provide the formation of phase components with a high level of hardness and high indicators of wear resistance [7, 8].

However, now there is not enough true and unambiguous information about the effect of different technological parameters of CDS on structural and phase state of the coatings sprayed by such a way and on their operational properties respectively.

Therefore, the *aim of the work* is the evaluation of the influence of technological mode parameters of cumulative-detonation spraying on structural-phase composition of coatings of aluminum oxide powder (Al_2O_3) with additives of pure powders of Al and Ti, and the role of structural factors on the properties of strength and crack resistance of the investigated coatings.

2. Materials and methods

For spraying coatings the mechanical mixtures of the initial powder Amperit 740.0 (99.5 % Al_2O_3; 0.05 % Fe_2O_3; 0.3 % Na_2O; 0.1 % SiO_2) were applied containing fraction composition $d_{fr} = 5 \ldots 22$ μm with additives (3 ... 5 %) of pure Ti and Al powder, $d_{fr} < 60$ μm (**Figure 1**, **Table 1**). The mode of detonation spraying was the following: detonation frequency 20 Hz; distance to specimen 55 mm; travel velocity 1500 mm / min with the same number of passes; ratio of length (l) / diameter (d) of gun barrel $l/d = 500$ mm /16 mm and ratio of a fuel gas to O_2 (β) 5.38 … 5.40.

| a | b | c |
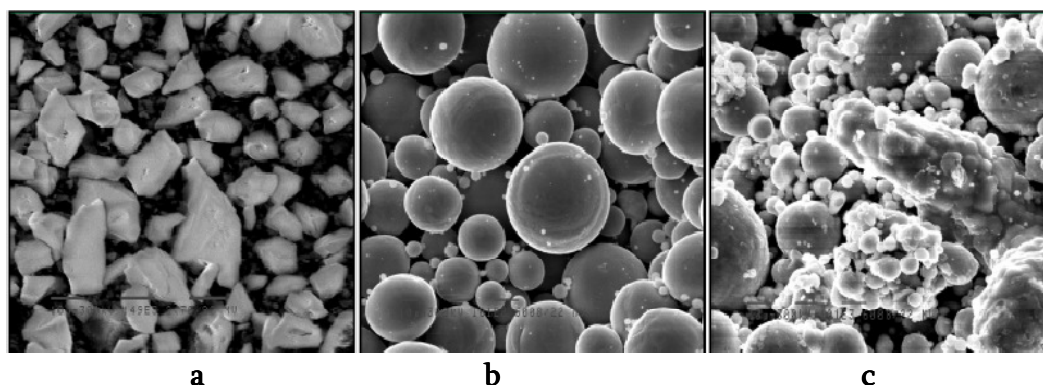
Figure1. Appearance of sprayed powders: a – the initial powder Amperit740.0; additives of powders of: b – Ti and c – Al.
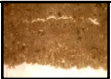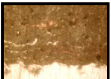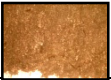
The investigations of structural-phase state of coatings (micro-hardness, volume fraction of pores, phase composition, distribution of dispersed phases, character of grain, sub-grain and dislocation structures, etc.) were carried out at all the structural levels using comprehensive methodological approach including optical metallography (Versamet–2, Japan; Leco–M400,

USA), analytical scanning electron microscopy (Philips SEM–515, Holland and JEOLJAMP9500F with energy dispersion spectrometer Oxford EDS INCA Energy 350, Japan), X-ray structural phase analysis (DRON–UM1), as well as transmission micro diffraction electron microscopy (JEM–200CX, company JEOL with accelerating voltage of 200kV, Japan). As a result of executed works, the experimental data on the full complex of structural and phase parameters of coatings, sprayed at different modes of cumulative-detonation spraying, were obtained.

3. Results and discussion

Four groups of coatings were produced with the thickness (δ) of up to 250 μm (**Table 1**). The investigations using the *method of optical metallography* showed, that the porosity of such coatings is at the level of 0.7 … 2.5 %, the volume fraction of lamellae ($V_{F/L}$, %) in them amounts to 1.5 … 5.0 %. The minimum porosity (P, %) and the maximum integrated microhardness ($HV_{0.3}$) are characteristic for coatings No. 1 – 2 produced using the powders Amperit 740.0 with the additives of 3 … 5 % Ti.

Table 1. Results of investigations of coating structure.

No.	Powder (substrate)	δ, μm	P, %	$V_{F/L}$, %	$HV_{0.3}$, MPa	Appearance
1	Amperit 740.0 + 3 % Ti	135 … 200	1.5 … 2.0	2.5 … 3.0	8900 … 10990	
2	Amperit 740.0 + 5 % Ti	100 … 230	0.7 … 1.5	4.5 … 5.0	9660 … 13770	
3	Amperit 740.0 + 3 % Al	115 … 250	1.7 … 2.4	1.5 ... 2.5	8900 … 10520	
4	Amperit 740.0 + 5 % Al	90 … 225	1.9 … 2.5	1.9 ... 2.5	7900 … 10250	

Using *X-ray diffraction phase analysis* of the produced coatings, it was revealed that the use of powders Amperit 740.0 + 3 % Ti (mode No. 1) and Amperit 740.0 + 5 % Ti (mode No. 2) promotes the formation of coatings of identical phase composition (γ-Al_2O_3, α-Al_2O_3, $AlTi_3$) at approximately equivalent content of the forming phase components. However, in the coatings Amperit 740.0 + 5 % Ti (mode No. 2) integrated microhardness ($HV_{0.3}$) is by 17 % increased (from 8900 … 10990 to 9660 … 13770 MPa as compared to coating Amperit 740.0 + 3 % Ti (mode No. 1), **Table 1**.

The spraying of powders Amperit 740.0 + 3 % Al (mode No. 3) and Amperit 740.0 + 5 % Al (mode No. 4) promotes the formation of coatings also of similar phase composition (γ-Al_2O_3, α-Al_2O_3, Al) at approximately the same content of forming phase components and levels of integrated microhardness ($HV_{0.3}$), **Table 1**.

As a result, it was revealed that the modification of ceramics Al_2O_3 (Amperit 740.0) using metallic powders with (3 … 5 %) Ti as compared to coatings with (3 … 5 %) Al leads to changes in the structural-phase composition and microhardness ($HV_{0.3}$) of produced coatings. Thus, the

addition of Ti contributes to formation of intermetallic phase AlTi$_3$, which possibly causes an increase in HV$_{0.3}$ (by 1.2 ... 1.3 times) of such coatings.

Results of *electron microscopic examinations on illumination* provided the opportunity to study features of fine structure of coatings and its parameters: changes in density and character of dislocation density (ρ) in different structural components (in the inner volumes and along the structural boundaries); character of the forming substructure, its parameters; size of subgrain (d_S); diameter of particles (d_P) of phase precipitations; effective distances between the forming phases (λ_P) etc. In this regard, for the coatings with the most favorable structural and phase changes (high microhardness, minimum porosity, etc.), namely – Amperit 740.0 + 5 % Ti (mode No. 2, **Figure 2**) and for comparison – Amperit 740.0 + 5 % Al (mode No. 4, **Figure 3**) the following regularities were revealed.

a   b   c
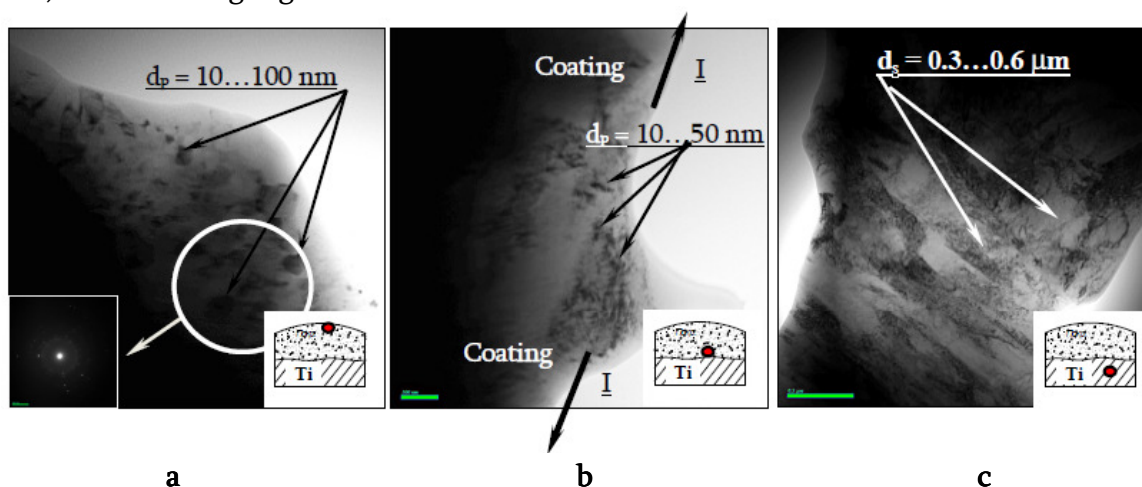
Figure 2. Fine structure: coating No. 2 (Amperit 740.0 + 5 % Ti) sprayed on titanium base at the depth of δ = 150 ... 200 μm from the interface (I) – a, and in the I zone the coating – substrate – b, and the substrate material – c.

a   b   c
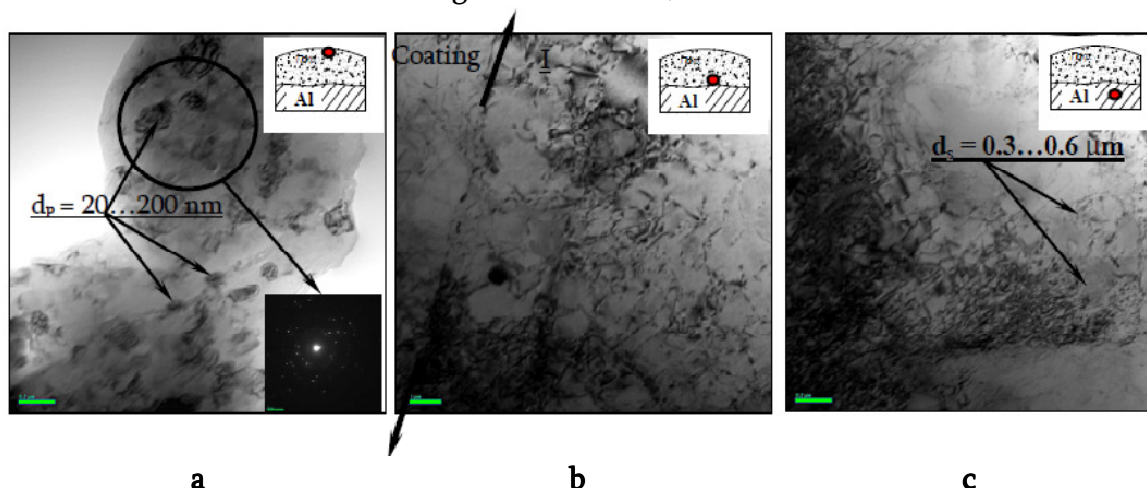
Figure 3. Fine structure: coating No. 4 (Amperit 740.0 + 5 % Al) sprayed on aluminum base at the depth of δ = 200 μm from boundary (I) – a, and in the I zone coating – substrate – b, and the material of substrate – c.

In case of using the powder Amperit 740.0 + 5 % Ti (mode No. 2, **Figure 3a**) the size of particles of phase precipitations of nanosized type (d_P = 10 ... 100 nm) decreases twice in the surface layers of coatings as compared to coatings Amperit 740.0 + 5 % Al (mode No. 4,

Figure 2a). In addition, the distance almost 2 … 2.3 times decreases (λ_P) between the forming dispersed phases (up to $\lambda_P = 10$ … 30 nm), which characterizes an increase in the volume fraction in the matrix of the forming phases. Also, the refining (by 1.4 times) of substructure is observed at increase of dislocation density at the outer surface of coatings: from $(2 … 3) \cdot 10^9$ (mode No. 4) to $(3 … 5) \cdot 10^9$ cm^2 (mode No. 2). At the same time in the coatings near to boundary the dislocation density is changed from $(5 … 6) \cdot 10^9$ cm^2 (**Figures 2b** and **2c**) to $(6 … 7) \cdot 10^{10}$ cm^2 (**Figures 3b** and **3c**).

4. Analytical evaluations of operational properties of coatings

The executed complex of experimental investigations at all the structural levels allowed carrying out analytical evaluations of the specific (differentiated) contribution of different structural and phase factors and parameters, formed in the investigated coatings, in change of strength characteristics σ_T and determining the structural factors cardinal influencing on the character and distribution of local inner stresses ($\tau_{L/IS}$), which are the potential sources of incipience and propagation of cracks in the investigated structural microregions [8 – 11].
Analytical evaluations of strength were carried out according to Archard equation, which includes the well-known dependencies of Hall–Petch, Orowan, etc. [12 – 21]:

$$\Sigma\Delta\sigma_T = \Delta\sigma_0 + \Delta\sigma_{S.S} + \Delta\sigma_G + \Delta\sigma_S + \Delta\sigma_d + \Delta\sigma_{d.h.} \ ,$$

here $\Delta\sigma_0$ is the resistance of metal lattice to the movement of free dislocations (friction stress of lattice or Peierls–Nabarro stress); $\Delta\sigma_{S.S}$ is the hardening of solid solution by alloying elements and impurities (solid solution hardening); $\Delta\sigma_G$, $\Delta\sigma_S$ is the hardening due to changes in grain and sub-grain size (dependences of Hal–Petch, grain boundary and substructure hardening); $\Delta\sigma_d$ is the dislocation hardening, caused by interaction between dislocations; $\Delta\sigma_{d.h.}$ is the hardening, caused by dispersed particles according to Orowan (dispersion hardening).
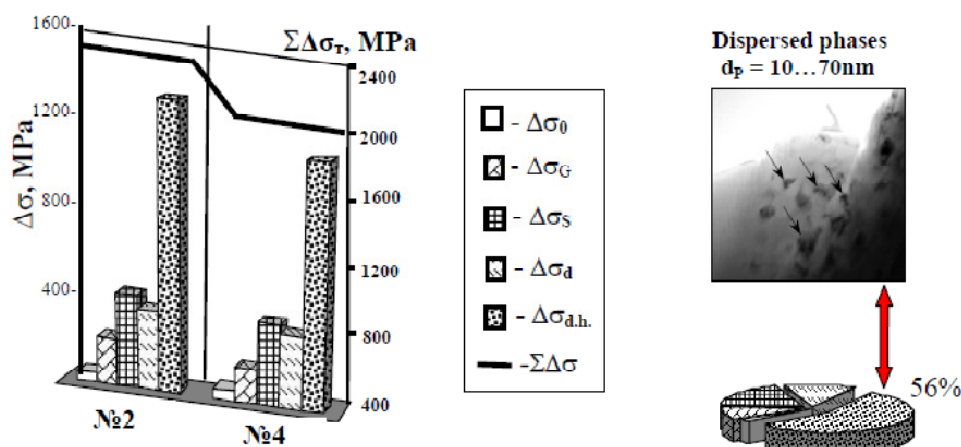
Figure 4. Histograms show the differentiated contribution of grain ($\Delta\sigma_G$), substructure ($\Delta\sigma_S$), dispersion ($\Delta\sigma_{d.h.}$) and dislocation ($\Delta\sigma_d$) hardening to changes in integrated values $\Sigma\Delta\sigma_T$ in the material of coatings sprayed using different modes: Al$_2$O$_3$ + 5% Ti (mode No. 2 – Ti substrate) and Al$_2$O$_3$ + 5 % Al (mode No. 4 – Al substrate) and contribution of phase formations disperse particles to overall level $\Sigma\Delta\sigma_T$.

As a result, it was shown, that in case of using powders Amperit 740.0 + 5 % Ti (mode No. 2) and Amperit 740.0 + 5 % Al (mode No. 4) the integrated values of hardening ($\Sigma\Delta\sigma_T$) for coatings amount to $\Sigma\Delta\sigma_T = 2370$ MPa and $\Sigma\Delta\sigma_T = 2050$ MPa (**Figure 4**). In both cases, the maximum contribution (up to 56 %) to the total value of hardening is introduced by hardening of coatings matrix due to the dispersed particles of phase precipitations of nanosized type (dispersion hardening according to Orowan): $\Delta\sigma_{d.h.} = 1334$ MPa (mode No. 2) and $\Delta\sigma_{d.h.} = 1070$ MPa (mode No. 4). Here the contribution of grain ($\Delta\sigma_G$), subgrain ($\Delta\sigma_S$) and dislocation ($\Delta\sigma_d$) hardening for the investigated coatings amounts to: 8 … 10 % ($\Delta\sigma_G = 90$ … 200 MPa); 12 … 20 % ($\Delta\sigma_S = 100$ … 500 MPa); and 10 … 15 % ($\Delta\sigma_d = 180$ … 200 MPa), respectively.
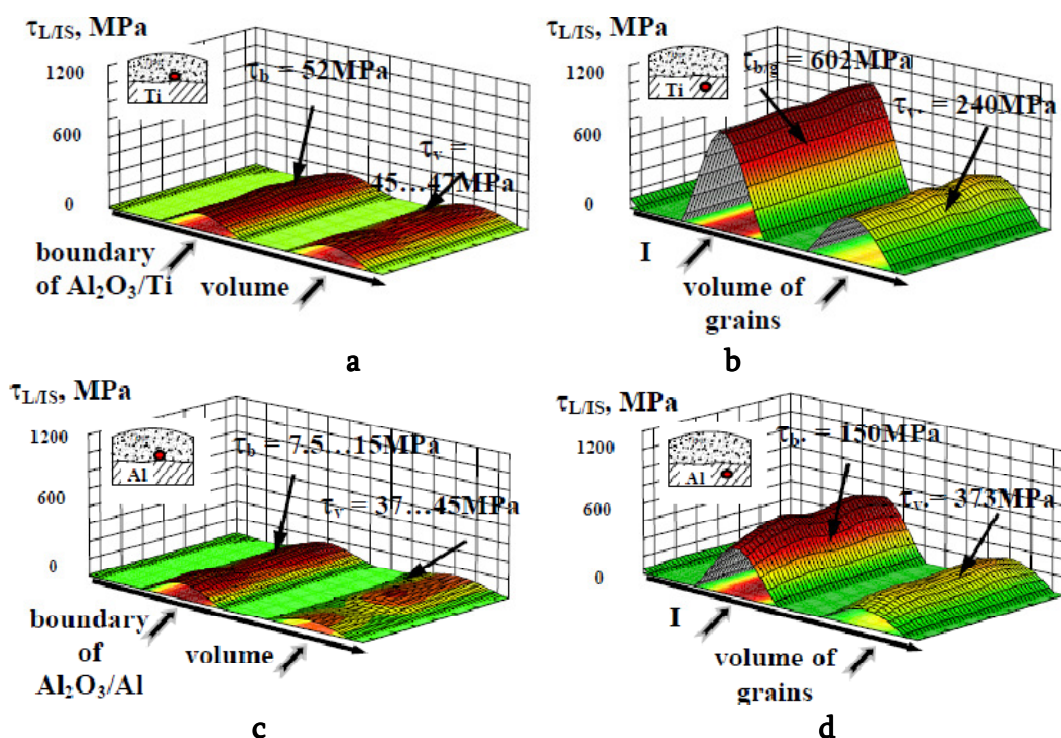
Figure 5. Distribution of local inner stresses ($\tau_{L/IS}$) in the material of coatings (a, c) and substrate (c, d): a, b – coating No. 2 (Amperit 740.0+5%Ti), sprayed on titanium base; and c, d – coating No. 4 (Amperit740.0 + 5 % Al)sprayed on aluminum base.

Calculation-analytical evaluations of the level of local inner stresses ($\tau_{L/IS}$) allowed evaluating the crack resistance of investigated coatings considering the character of dislocation structure, which is quite clearly revealed during examination of fine structure on illumination using the methods of ion thinning of fine foils.

From the analysis of different approaches to determination of mechanisms of incipience of cracks and fracture of materials the evaluation of $\tau_{L/IS}$ was chosen basing namely on the dislocation theory of crystalline solid bodies, connecting the processes of formation of local inner stresses with initiation and rearrangement of dislocation structure [22 – 24]. The field of inner stresses, formed by the dislocation structure (dislocation density) and peculiarities of local inner stresses $\tau_{L/IS}$ – the sources of incipience and propagation of cracks (their level, length, interaction with structural features of coatings), were determined by the dependence of [22]:

$$\tau_{L/IS} = G \cdot b \cdot h \cdot \rho \; / \; [\pi \cdot (1 - \nu)],$$

here G is the shear modulus; b is the Burgers vector; h is the foil thickness, equal to 2×10^{-5} cm; v is the Poisson's ratio; ρ is the dislocation density.

As a result of investigations, it was shown that in all the investigated modes of cumulative-detonation spraying of coatings a low level (without sharp gradients) of local inner stresses is formed (**Figure 5**).

It was revealed that the maximum $\tau_{L/IS}$ are observed in the coating - substrate interface in case of using powders Amperit 740.0 + 5 % Ti (mode No.2, **Figure 5b**) Amperit 740.0 + 5 % Ti (mode No. 2, **Figure 5b**). Here their level does not exceed 600 MPa (or $\tau_{L/IS} = 0.14\cdot\tau_{THEOR}$ from the theoretical level of material shear strength), which provides producing the high-quality coatings with a low tendency to crack formation and, consequently, with optimal operational characteristics.

5. Conclusions

As a result of comprehensive investigations of coatings, sprayed using multi-chamber detonation spraying (MCS) at different structural levels (grain, subgrain, dislocation), it was revealed that the most significant contribution to the properties of strength and crack resistance of investigated coatings is made by: dispersion of grain and sub-grain structures; uniform distribution of the forming hardening phases of dispersed sizes in the absence of extended and dense dislocation clusters - concentrators of local inner stresses (potential zones of incipience and propagation of cracks).

References

1. A. Ya. Kulik, Yu. S. Borisov, A. S. Mnushin, M. D. Nikitin. Gas Thermal Spraying of Composite Powders. 1985, Leningrad, Mashinostroenie.
2. Yu. S. Borisov, A. L. Borisova. Plasma Powder Coatings. 1986, Kyiv, Tekhnika.
3. S. S. Bartenev, Yu. P. Fedko, A. I. Grigorov. Detonation Coatings in Mechanical Engineering. 1982, Leningrad, Mashinostroenie.
4. L. Pawlowski. The Science and Engineering of Thermal Spraycoatings, 2nd Ed. 2008, John Wiley & Sons.
5. Yu. Tyurin, A. Pogrebnyak, O. Kolisnichenko, I. Duda. Comparative analysis of cumulative-detonation and HVOF equipment for thermal spray coatings. Hardening Technol., 2009, 5, 27.
6. Yu. Tyurin, O. Kolisnichenko, M. Poleshuk. Cumulatively-detonation device for thermal spray coatings. Microstructural characteristics of high velocity oxygen. Hardening Technol. & Coating, 2009, 44, 7.
7. M. Karagoez, S. Islak, S. Buytoz, B. Kurt. Microstructural characteristics of high velocity oxygen fuel (HVOF) sprayed NiCrBSi–SiC composite coating on a low alloy steel. 6th Int. Symp. Adv. Technol., 2011, 13.
8. L. I. Markashova, Yu. N. Tyurin, O. V. Kolisnichenko, M. L. Valevich, D. G. Bogachev. Structural-phase state of Nr–Cr protective coatings deposited by method of cumulative-detonation spraying. In: Proc. 6th Int. Conf. "Laser Technol. Welding & Mater.Proc.", 2013, 60.

9. L. I. Markashova, Yu. N. Tyurin, O. V. Kolisnichenko, M. L. Valevich, D. G. Bogachev, I. M. Duda, E. P. Titkov. Structure-phase condition of wear-resistant composite coatings of Cr_3C_2–NiCrsystem, deposited using multi-chamber detonation installation. In: Proc. 7th Int. Conf. "Math.Modelling & IT Welding & Rel. Proc.", 2014, 37.

10. L. I. Markashova, V. D. Poznyakov, A. A. Gaivoronskii, E. N. Berdnikova, T. A. Alekseenko. Estimation of the strength and crack resistance of the metal of railway wheels after long-term operation. Mater. Sci., 2012, 47, 799.

11. L. Markashova, V. Poznyakov, E. Berdnikova, T. Alekseenko. Effect of structural factors on mechanical properties and crack resistance of welded joints of metals, alloys and composite materials. The Paton Welding J., 2014, 6, 22.

12. H. Suzuki. On the yield point of polycrystalline metals and alloys. In: Structure and Mechanical Properties of Metals. 1967, Moscow, Metallurgiya, 255.

13. M. F. Ashby. On the Orowan stress. In: Physics of Strength and Plasticity. 1972, Moscow, Metallurgiya, 88.

14. M. I. Gol'dshtein, V. S. Litvinov, B. M. Bronfin. Metallophysics of High-Strength Alloys. 1986, Moscow, Metallurgiya.

15. H. Conrad. Model of strain hardening for explaining the influence of grain size on the stress of metal flow. In: Ultrafine Grain in Metals (Ed. L. K. Gordienko). 1973, Moscow, Metallurgiya, 206.

16. R. W. Armstrong. Strength properties of metals with ultrafine grain. In: Ultrafine Grain in Metals (Ed. L. K. Gordienko). 1973, Moscow, Metallurgiya, 11.

17. N. J. Petch. The cleavage strength of polycrystalline. J. Iron Steel Inst., 1953, 173, 25.

18. E. Orowan. Dislocation in Metals.1954, New York, AIME.

19. M. F. Ashby. Mechanisms of deformation and fracture. Adv. Appl. Mech., 1983, 23, 118.

20. A. Kelly, R. B. Nicholson. Precipitation Hardening. 1963, New York, Pergamon.

21. R. Ebelling, M. F. Ashby. Yielding and flow of two phase copper alloys. Phil. Mag., 1966, 13, 805.

22. V. E. Panin, V. A. Likhachov, Yu. V. Griyatva. Structural Levels of Deformation of Solids. 1985, Novosibirsk, Nauka.

23. H. Conrad. Effect of grain size on the lower yield and flow stress of iron and steel. Acta Metall., 1963, 11, 75.

24. A. N. Stroh. The formation of cracks as a recoil of plastic flow. Proc. Roy. Soc. A, 1954, 223, 404.

III–V SEMICONDUCTOR NANOSTRUCTURE FOR SOLAR CELLS

O. Kvitsiani, T. Laperashvili

V. Chavchanidze Institute of Cybernetics
Georgian Technical University
Tbilisi, Georgia
orestkv@yahoo.com
lafera2002@yahoo.com

Abstract

Simple method of preparation of nanocrystals on the III–V semiconductor surface is described. This method includes electrochemical deposition of metals of group III on electrochemically etched semiconductor surface. The chlorides of metals are used for indium and gallium deposition. After layer metallization wafers are annealed in hydrogen at the various temperatures in order to form nanoclusters on the surface. Influence of annealing conditions on the characteristics of structures is investigated and possible mechanism of interactions between metal and semiconductor during formation of nanoclusters are discussed. Application of obtained structures for the solar cells with multiple junctions is proposed.

1. Introduction

Environmentally friendly and renewable energy is one of the most important topics in the science and technology. The great challenge of modern science is development of technologies that will make renewable energy sources available for the vast masses of population, and this is why any investigation being able to solve this task is of great scientific interest and has real practical importance.
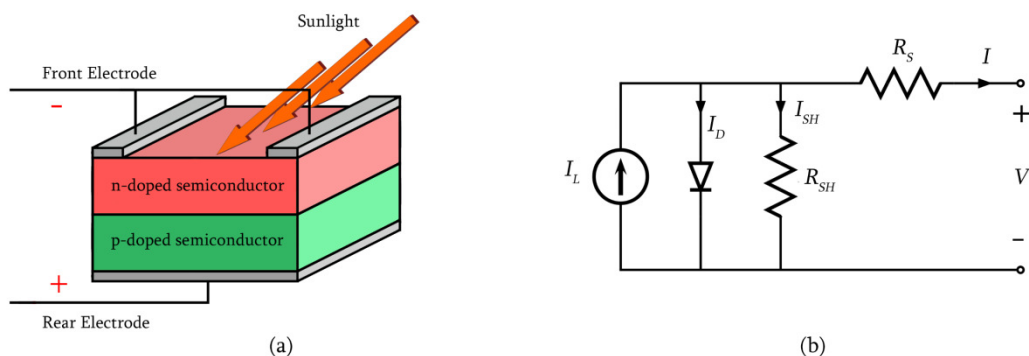
Figure 1. Single junction photovoltaic solar cell (a) and its equivalent electrical scheme (b).

The most important and attractive source of renewable energy is solar radiation, effective utilization of which may solve energy consumption problems without any impact to the environment. Photovoltaic solar cells (PV SCs) (**Figure 1**) are devices directly converting

energy of sunlight to electricity and, hence, are most suitable means for harvesting free and inexhaustible energy in the future.

Sunlight absorption characteristics of solar cell depend on the structure of semiconductor band. Solar irradiation spectrum consists of photons of energy from 0.5 to 3.5 eV (2500 – 250 nm wavelengths). Consequently, every semiconductor with the bandgap within 0.5 – 3.5 eV band absorbs some portion of solar radiation and can be used for PV SC applications. Reasonable part of solar spectrum consists of photons with the energy higher than bandgap of semiconductors that are usually used for fabrication of single-junction and multi-junction commercial solar cells (Si, GaAs, InP, CdTe, Ge, InGaP and InGaN). Effective absorption of high-energy photons from green to ultraviolet band is of significant importance for improvement of conversion efficiency of solar cells.

The overview of the research works concerning enhancement of solar cell efficiency and reduction of photovoltaic cost is conducted regularly. **Figure 2** shows chronological record of energy-conversion efficiencies of solar cells to date [1].
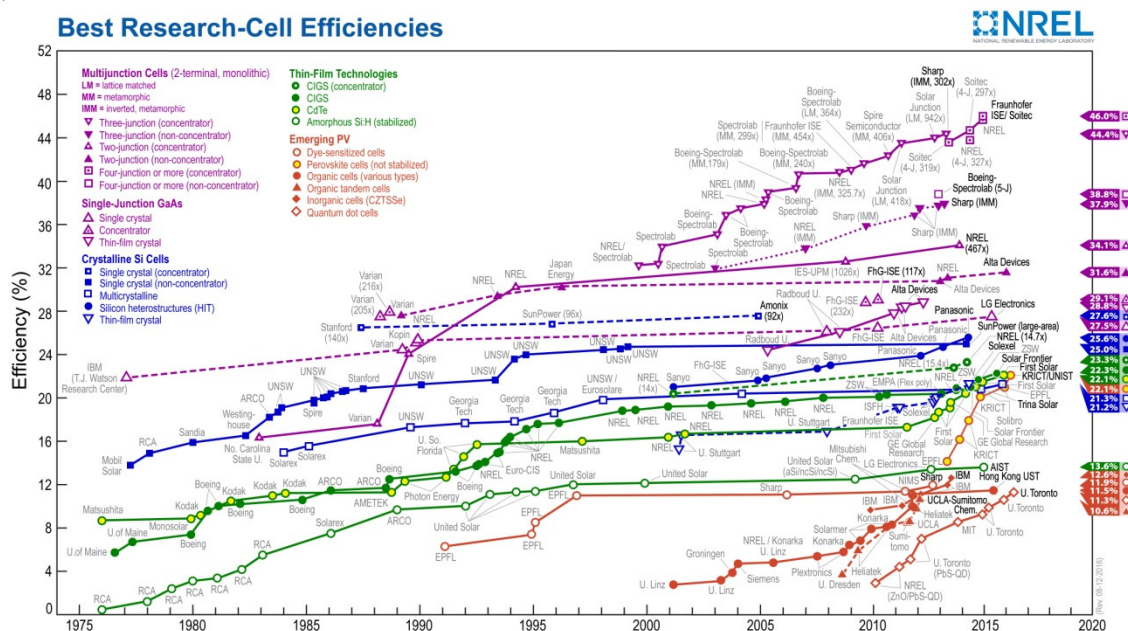
Figure 2. Timeline of solar cell energy conversion efficiencies.

Increasing photovoltaic efficiency is critically important as for the space, as for the terrestrial concentrator PV SC. Incorporation of nanostructured materials into the photovoltaic devices enables improvement of efficiency in excess of the Shockley-Queisser limit. The most promising candidates for this are InP nanostructured materials [2].

For fabrication of multi junction systems, generally III–V compound semiconductors or Ge based materials are used, which are costly. The growth of thin layers of III–V semiconductors on a silicon substrate for multijunction solar cell applications has the benefits of reduced materials cost and well-developed silicon integrated circuit and solar cell technology. The best candidate for development of such structures is gallium phosphide (GaP) because of its lattice parameter compatibility with Si lattice (lattice constants of GaP and Si are 5.4505 and 5.43072 Å, respectively). Matching of lattice parameters is essential for epitaxial growth of high quality GaP layers on the surface of Si substrate. On the other hand, gallium phosphide (GaP) is a good candidate for a solar cell due to its large bandgap (2.26 eV) and well-developed technology.

Nano-sized semiconductor particles, called quantum dots, definitely can realize SC with an operating wavelength range, which covers absorption range of all other existing SC. In addition, they have capability to convert high-energy part of the solar radiation. **Figure 2** shows extremely high performance of SC, which would be unachievable without QDs.

Electron confinement phenomena and calculation of energy levels quantum dots is well known from textbooks [3]. Nanostructures, such as QDs, in the photovoltaic devices allow extension of solar cell absorption spectrum and "tuning" of the bandgap to match spectral conditions [4].

The fundamental requirements imposed on the materials and structures of III-V QDs for solar cell applications are absorption wavelengths covering 2500 – 250 nm band, and compatibility with the well-established processing technique on Si substrate. Due to the properties of QDs, remarkable improvement in performance is purposed.

Various methods of fabrication of QDs were developed. For a long time, the only known method of epitaxial growth of zero-dimensional system was the strain-induced method, based on lattice mismatch. In this work, method of preparation of nanocrystals on the III-V semiconductor surface is presented.

2. Experimental

The original technology of electrochemical deposition of metals on semiconductor surface is elaborated for near-ideal metal / semiconductor (MS) contact fabrication. Distinctive feature of this method is that whole preparation process, namely, surface etching and metal deposition, is carried out in a unified technological process. Semiconductor's surface was etched electrochemically just before metal deposition.

Particularly, electrochemical deposition is performed in an aqueous solution of metallic salts, which at the same time contain electro-chemically etching material. The principal picture of equipment for electrochemical deposition is given in **Figure 3**. Electrolyte is poured into quartz glass; semiconductor wafer is used as the one electrode and platinum as another; the distance between the electrodes was about 1 cm.
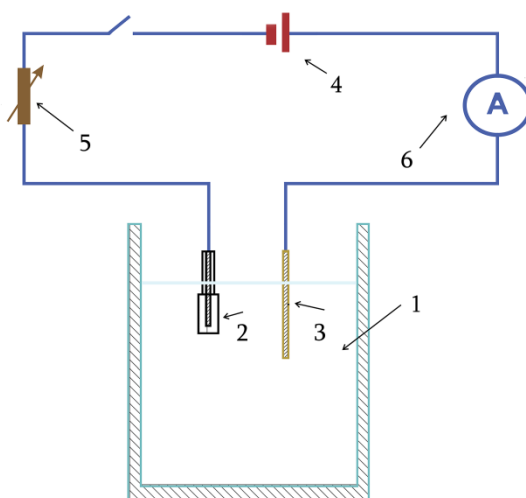
Figure 3. The principal picture of equipment for electrochemical deposition (1 – electrolyte, 2 – semiconductor cathode, 3 – platinum anode, 4 – power source, 5 – resistivity, and 6 – ampermeter).

At our experiments Czochralski grown undoped n-type GaP wafers were used for the fabrication of MS contacts. The thicknesses and carrier concentrations were about 200 – 250 μm and $2 \cdot 10^{16} - 4 \cdot 10^{17}$ cm^{-3} respectively. At first, metallic Ohmic contact was attached to the one side of semiconductor's wafer. Metallic Indium contacts were fabricated by alloying at 600°C temperature during 5 min in cleaned inert gas (nitrogen or hydrogen) atmosphere using specially constructed equipment, schematic picture of which is given in **Figure** 4. Here 1 – 6 represent quartz tubes, coated with heater; tubes 1 and 2 contain palladium alumogel, which ensures mixing of oxygen with water vapor, which then condensates in 7 and 8 glass containers placed into liquid nitrogen (water can be poured out after the end technological process); tubes 3 – 4 contain clean dry alumogel and tubes 5 – 6 contain silicagel.
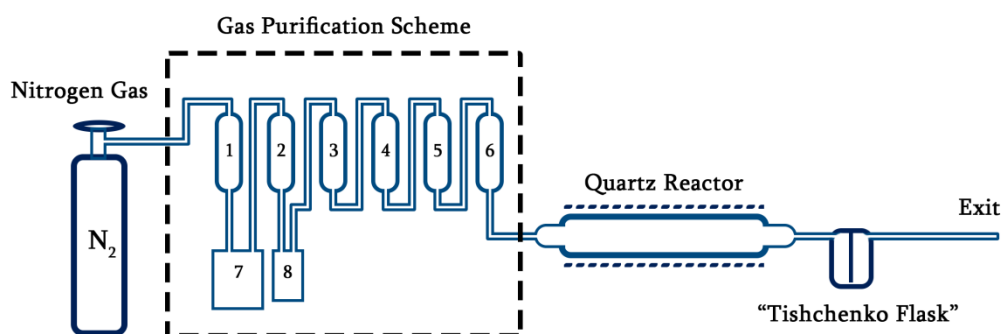
Figure 4. Schematic picture of equipment
for preparation of Ohmic contacts.

Semiconductor wafers with little metallic points placed into graphite cassette, which is located in quartz reactor, which itself is placed into the electric heater, for alloying of contacts. Then the sample with Ohmic contact and power feed wire is covered with the chemically stable polystyrene coating, except the area of metal deposition. The wafers then were etched chemically in HCl +3HNO$_3$ solution, rinsed in distilled water and were immediately transferred into electrolyte for deposition of metals.

Regimes of electrode position of different metals were described in [5]. After electrochemical deposition of metallic thin film, GaP wafers were cut to pieces of 2 – 4 mm^2 area, which were then annealed in hydrogen atmosphere, during various time and at various temperatures. Photo–spectral characteristics of annealed structures were investigated.

The spectral characteristics of samples were measured by equipment consisting of a monochromator type DMR–4, suitable light sources, filters and measurement devices.

3. Results and discussion

Figure 5 represents measured photo-spectral characteristic of In / Gap contact annealed at 290 °C in hydrogen environment during 3 min. Spectral studies of In / GaP structures showed, that 0.2 V reverse biased photoelectric characteristic consists of two separated from each other regions of photosensitivity 1.0 – 2.2 and 2.6 – 3.0 eV. For comparison in **Figure 6** is shown the absorption spectra of GaP measured by AvaSpec–2048 Fiber Optic Spectrometer.

As it can be seen from **Figures 5** and **6**, after annealing of In/GaP exhibits the region of the strong photosensitivity, that is attributed to the formation of a new material (InP or InGaP nanoclusters) on the surface of GaP, as result of interaction between metal (In) and semiconductor (GaP) during annealing of In / GaP contacts.
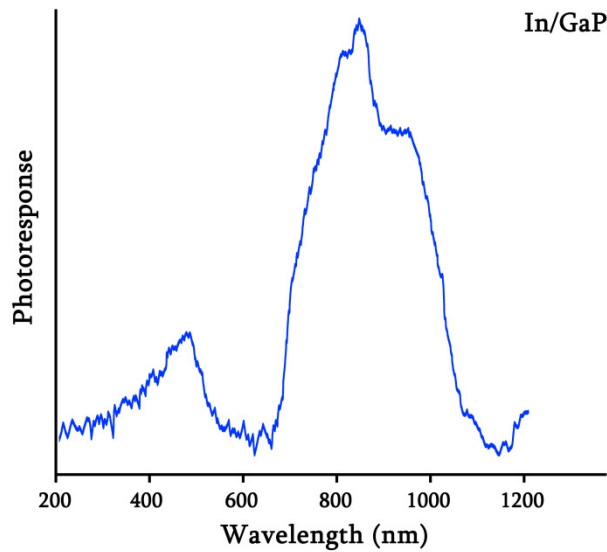
Figure 5. Photo response spectra of InGaP after annealing
at 290 °C during 3 min with the 0.2 V reverse bias.
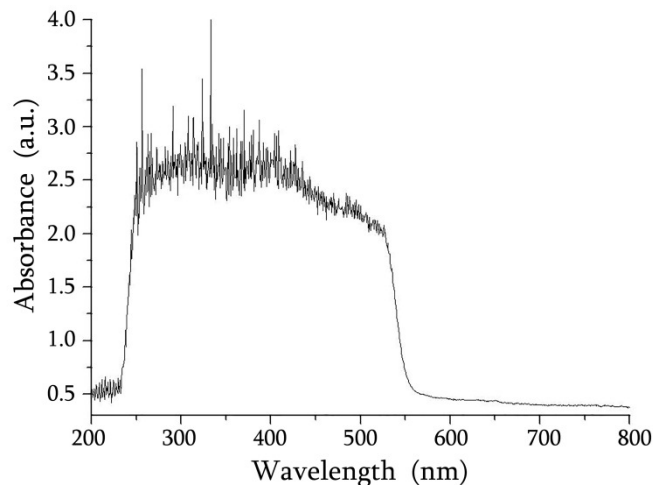

Figure 6. Absorption spectra of GaP.

Although there is no direct approval of this assumption, possible mechanism of formation of InP nanoclusters on the GaP surface is discussed taking into account our experimental results and publication data [6], according to which PL from InP / GaP QDs have peak between 1.9 and 2.0 eV. These photoluminescence data coincide with our photo-spectral measurement results and their comparison confirms our assumption - formation of nanoclusters.

High-energy gap solar cell plays very important role in multi-junction systems. Gallium phosphide is characterized by wide band gap and high carriers mobility; Besides, GaP is well-studied semiconductor, and its lattice matched with Si and GaP-Si technique is well-developed. These properties altogether make gallium phosphide attractive and promising material for Si based MJSC's.

Proposed simple technology of electrochemical deposition of thin metallic films of Indium and low temperature heath treatment may be definitely used for fabrication of islands with III–V semiconductors heterojunctions. Nanostructured optical materials have many advantages compared to bulk or quantum film materials typically used in optoelectronics.

Despite simultaneous microscopy study of the interface morphology of surface layers, it is very difficult to understand influence of annealing temperature on the characteristics of MS structure. However, comparing our results with the literature data [7] a hypothesis can be made that little islands or nanoclusters are formed in the MS interface.

We suppose that fabrication of nanostructured AlGaP layer on GaP epitaxial surface by using technological method mentioned above will serve to expand high-energy absorption band of the solar cell by means of increment (enlargement) of band gap to the high-energy band of solar spectra. This also will ensure increment of open circuit voltage of the cell and in this way improve solar cell conversion efficiency; utilization of concentrator will ensure further increment of efficiency.

5. Conclusions

Study of influence of annealing temperature on In / GaP structure reveals new region of strong photosensitivity that is attributed to the formation of the new material – InP or InGaP nanoclusters on the surface of GaP.

This result gives the possibility of expansion of SC absorption spectra and boost of its efficiency.

References

1. http://www.nrel.gov/pv/
2. M. A. Green, K. Emery, Y. Hishikawa, W. Warta, E. D. Dunlop. Solar cell efficiency tables (Version 48). Prog. Photovolt. Res. Appl., 2016, 24, 905-913.
3. Y. Masumoto, T. Takagahara. Semiconductor Quantum Dots.2002, Berlin – Heidelberg, Springer–Verlag.
4. S. Hubbard, R. Raffaelle. Boosting solar-cell efficiency with quantum-dot-based nanotechnology. SPIE, 2010, Newsroom. DOI: 10.1117/2.1201002.002553.
5. O. Kvitsiani, T. Laperashvili. Mechanisms of formation of Schottky barrier on the III–V semiconductors and their characteristics. J. Sci. &Technol., 2011, 7-9, 8-16.
6. T. Laperashvili, I. Imerlishvili, M. Khachidze, D. Laperashvili. Photoelectric characteristics of contacts In-semiconductor A3B5. Proc. SPIE, Nano & Micro Technol., 2003, 502-506.
7. F. Hatami. Indium Phosphide Quantum Dots in GaP and in $In_{0.48}Ga_{0.52}P$ (Dissertation). 2002, Berlin, Humboldt–Universitatzu Berlin.

FEASIBILITY STUDY ON THE USE OF Gen5 PECVD REACTORS FOR MANUFACTURING OF HIGH-EFFICIENCY SILICON HETEROJUNCTION SOLAR CELLS

S. Abolmasov[1], A. Abramov[1], D. Andronikov[1], K. Emtsev[1],
G. Ivanov[1], I. Nyapshaev[1], D. Orekhov[1], A. Semenov[1], I. Shakhray[1],
G. Shelopin[1], E. Terukov[1], B. Strahm[2], G. Wahli[2], P. Papet[2],
T. Söderström[3], Y. Yao[3], T. Hengst[4], G. Bubnov[5], G. Kekelidze[5]

[1] R&D Center of Thin Film Technologies in Energetics
Ioffe Institute
Petersburg, Russia
[2] Meyer Burger Research AG
Hauterive, Switzerland
[3] Meyer Burger AG
Gwatt, Switzerland
[4] Meyer Burger Global AG
Gwatt, Switzerland
[5] Moscow Technological Institute
Moscow, Russia
e.terukov@hevelsolar.com

Abstract

In this study we evaluate the potential of using Gen5 (1.4 m²) KAI PECVD reactors originally designed for production of thin film silicon modules, for manufacturing of high-efficiency silicon heterojunction (Si-HJ) solar cells. It is shown that Gen5 KAI PECVD reactors can provide an excellent uniformity of optical and electrical properties of hydrogenated amorphous silicon layers across entire surface of a 110×130 cm² wafer carrier. Surface passivation with low surface recombination velocity (< 4 cm / s) is achieved on n-type FZ c-Si wafers. Si-HJ solar cells, with an efficiency as high as 20.4 %, are produced using commercial 6 inch n-type CZ c-Si wafers and Gen5 KAI PECVD reactors. The potential to reach the efficiency above 21 % is also demonstrated.

1. Introduction

Recent reduction of polysilicon price has made amorphous silicon thin film photovoltaics noncompetitive and resulted in shutdown of 'micromorph' module manufacturing by several companies in last few years. Nevertheless, excellent crystalline silicon (c-Si) surface passivation properties of hydrogenated amorphous silicon (a-Si:H) grown by plasma enhanced chemical vapor deposition (PECVD) have been demonstrated [1]. In light of these events many PV players started to look forward to use a-Si:H films for the development of

high-efficiency, crystalline silicon solar cells [2]. A typical example is silicon heterojunction (Si-HJ) solar cell, invented by Sanyo Electric Co. [3], consisting of a monocrystalline silicon (c-Si) wafer with both sides coated with ultra-thin (5 – 10 nm) a-Si:H layers. Simple structure of Si-HJ solar cells in combination with their high efficiency and low temperature processing make them attractive for the solar PV industry. The record R&D Si-HJ cell developed last year by Panasonic [4] using a 98-μm-thick c-Si wafer has an efficiency of 24.7 %.

As recently demonstrated by EPFL team [5], Si-HJ solar cells with efficiencies above 21 % can be produced by using different types of PECVD reactors, including a medium-area (50 × 60 cm²) industrial KAI–M reactor. In this study Gen5 (110 × 130 cm²) KAI PECVD reactors, designed by TEL Solar (the former Oerlikon Solar) for mass production of micromorph modules, are evaluated for manufacturing of high-efficiency Si-HJ solar cells. In order to accelerate this process, the R&D Center of Thin Film Technologies in Energetics and its parent company – Hevel Solar set up collaboration with Meyer Burger – a leader in the Si-HJ solar cell technology. Note that Hevel Solar plans to adapt its 100 MW micromorph module production line into a line delivering more competitive product – high-efficiency Si-HJ solar cells / modules.

2. Experimental details

The a-Si:H films were deposited at 200 °C in two Gen5 KAI PECVD reactors of R&D pilot line, shown in **Figure 1**, designed by TEL Solar for the production and optimization of top a-Si:H and bottom μc-Si:H cells of micromorph modules using an excitation frequency of 40.68 MHz (VHF). Spectroscopic ellipsometry was used to characterize a-Si:H films on both glass and c-Si wafers. For passivation studies, intrinsic a-Si:H of about 15 nm was deposited on both sides of 280-μm-thick, polished, float zone (FZ) or 180-μm-thick, textured, Czochralski (CZ) c-Si wafers. Both FZ and CZ wafers were n-type <100> with a resistivity of 1 – 5 Ω cm. Before a-Si:H deposition, the wafers were immersed into a 5 % HF solution in order to remove the native oxide and produce a hydrogen-terminated surface. The effective minority carrier lifetime (τ) and implied open circuit voltage (V_{OC}) were measured by using a Sinton Consulting WCT–120 tester in both quasi-steady-state and transient mode [6, 7]. The measurements were taken on c-Si wafers with as deposited a-Si:H films.

Figure 1. Pilot line at the R&D Center of Thin Film Technologies in Energetics (Ioffe Institute, St. Petersburg), showing two Gen5KAI PECVD reactors used in this study.

The structure of Si-HJ solar cells was similar to that first developed by Sanyo Electric Co. [3], i.e. Ag front grid / $In_2O_2:SnO_2$ (ITO) 80 nm / p^+ a-Si:H 10 nm / i a-Si:H 5 nm / textured CZ n-type c-Si 180 μm / i a-Si:H 5 nm / n^+ a-Si:H 20 nm / ITO 40 nm / Ag back metallization. The full device process sequence is given in **Table 1**. First, 6 inch CZ c-Si wafers were textured at SingulusStangl Solar GmbH and then shipped to the R&D Center in St. Petersburg for deposition of a-Si:H layers in Gen5 KAI PECVD reactors. However, note that some number of textured wafers were also shipped to Meyer Burger for a comparison (see Section 3.3).Intrinsic and doped a-Si:H layers were deposited using mixtures of SiH_4, H_2, $B(CH_3)_3$ and PH_3. Then the processed wafers were shipped to Meyer Burger, where both ITO and rear Ag layers were deposited by dc magnetron sputtering followed by screen printing of the front grid using a low-temperature Ag-based paste with subsequent curing.

Table 1. Process sequence for Si-HJ solar cells.

Process step	Equipment
1.Wafertexturing	SingulusStangl Solar GmbH
Shipping 1	**Germany → Russia**
2. Deposition ofa-Si:H layers	Gen5 KAI PECVD reactors of R&D pilot line
Shipping 2	**Germany → Switzerland**
3. ITO/Ag	Meyer Burger
4. Screen printing	Meyer Burger
5. Characterization	Meyer Burger

Since the SmartWire interconnection technology offers Ag metallization cost reduction and less contact grid shading, busbar less screen printing has been used. Hence, the Grid^TOUCH system [8] was employed for measuring the current–voltage characteristics of 6 inch Si-HJ solar cells. Photoluminescence imaging was also used to monitor the quality of surface passivation.

3. Results and discussion

3.1. Surface passivation

High-quality surface passivation is of extreme importance for any high-efficiency c-Si solar cells. It has a strong impact on V_{OC} of c-Si solar cells. a-Si:H layers passivate c-Si surfaces mainly by hydrogenation of silicon dangling bonds, leading to a reduction of the interface defect density. A necessary condition for good passivation is that the a-Si:H / c-Si interface should be atomically sharp, meaning that silicon epitaxial growth is avoided, i.e., no crystalline material is deposited [9]. This can be achieved by a proper tuning of PECVD parameters, see, e.g., [10].

Because of the bulk lifetime of CZ c-Si wafers greatly depends on the supplier, and in most cases is usually unknown, surface passivation studies were mainly done using FZ c-Si wafers supplied by Topsil. **Figure 2** shows a typical lifetime curve for a sample with 15-nm-thick ia-Si:H layers deposited on both sides of FZ c-Si wafer. At excess carrier density of 10^{15} cm^{-3}, a carrier lifetime of 4.6 ms is obtained. Under 1-sun illumination, this corresponds to

an implied V_{OC} of 725 mV, as shown in **Figure 2**. This value differs only by 5 mV from that (730 mV) obtained in the so-called *S-Cube* reactor [11] developed by Roth & Rau particularly for mass production of high efficiency Si-HJ solar cells. According to the Topsil specification, the bulk lifetime of FZ c-Si wafers used in this study was above 2 ms, resulting in a value of surface recombination velocity below 4 cm / s.
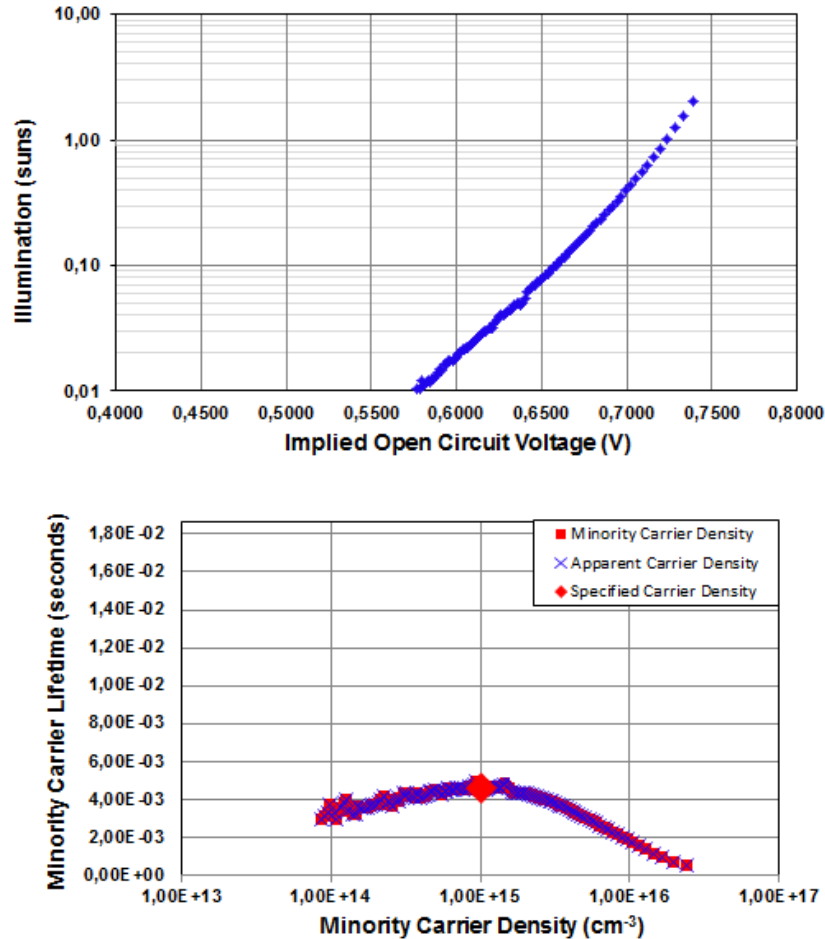

Figure 2. Implied V_{OC} (top) and minority carrier
lifetime (bottom) of passivated n-type FZ c-Si wafers.

Recently, the same value of surface recombination velocity was also obtained for commercial 6 inch CZ c-Si wafers passivated with *i* / *p* and *i* / *n* a-Si:H layers.

3.2. Uniformity of a-Si:H layers

Since Si-HJ solar cells incorporate extremely thin (5 – 10 nm) a-Si:H layers, for successful mass production of such cells, large-area PECVD reactors have to fulfill another important criterion – excellent deposition uniformity [12].

Figure 3 shows the results of spectroscopic ellipsometry for our optimized intrinsic a-Si:H layer deposited on 11 c-Si wafers using Gen5 KAI PECVD reactor. It can be seen that thickness uniformity below 5 % can be achieved over a 110×130 cm^2 area. It should also be mentioned that deposition of the same a-Si:H layer (under otherwise identical conditions) on a 110×130 cm^2 glass substrate results in a thickness uniformity of 7.1 %. This is most likely due to difference in heat transfer in metallic wafer carrier and glass.
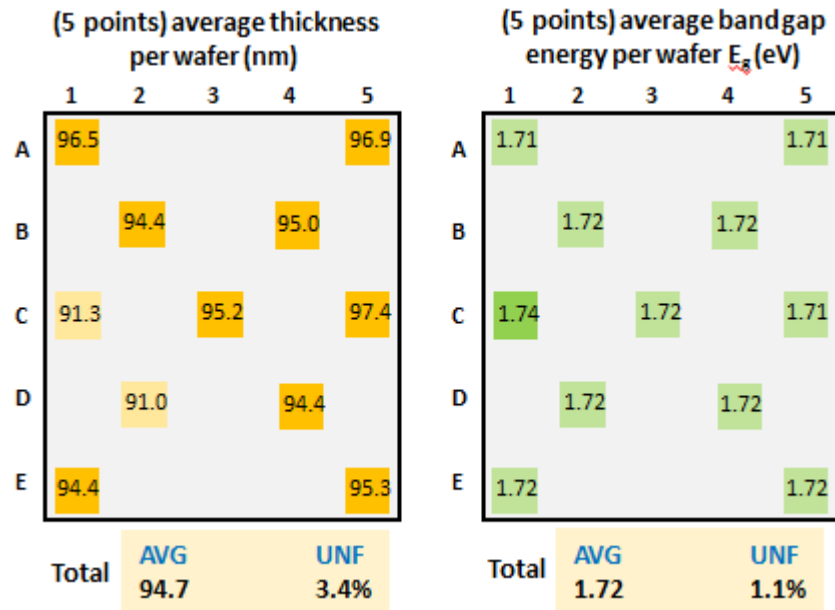
Figure 3. Uniformity of 95 nm thick intrinsic a-Si:H layer over a 110×130 cm² wafer carrier. (left) thickness uniformity, (right) band gap energy distribution.

3.3. 6 inch Si-HJ cells

With the sequence described in **Table 1**, complete Si-HJ solar cells have been fabricated using commercial 6 inch (pseudo square) CZ c-Si wafers. The best cells had an efficiency of 20.4 % with a V_{OC} of 721 mV, a J_{SC} of 36.8 mA / cm² and a fill factor of 77 %, as summarized in **Fig.ure 4**. Note that these results are preliminary and there is still room for improvement, as will be shown below.
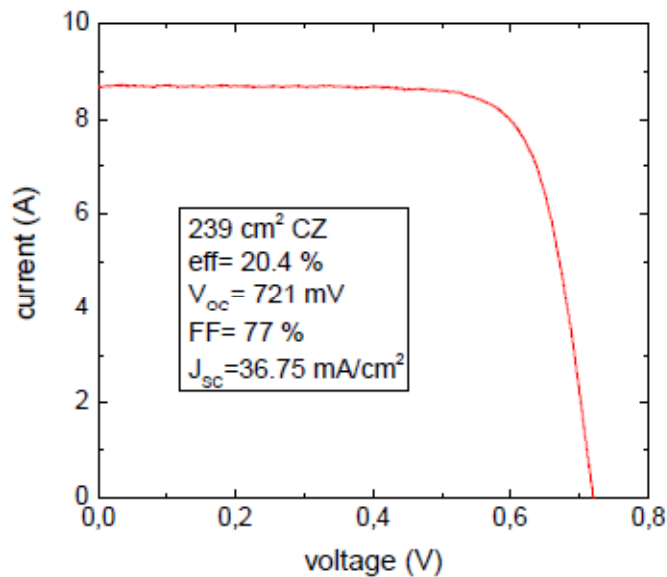
Figure 4. Current–voltage characteristics of Si-HJ solar cell produced using commercial 6 inch CZ c-Si wafer and Gen5 KAI PECVD reactors. The cell has busbar less front side metallization.

In order to determine the impact of two days wafer transportation in hand luggage, particularly shipping 2 (see **Table 1**), on the performance of Si-HJ solar cells some number of textured wafers were split into two groups: 1) reference group in which the wafers were processed at Meyer Burger and 2) travel group, in which the wafers were processed first at the R&D Center and then at Meyer Burger as described in **Table 1**.

(a) Reference group   (b) Travel group
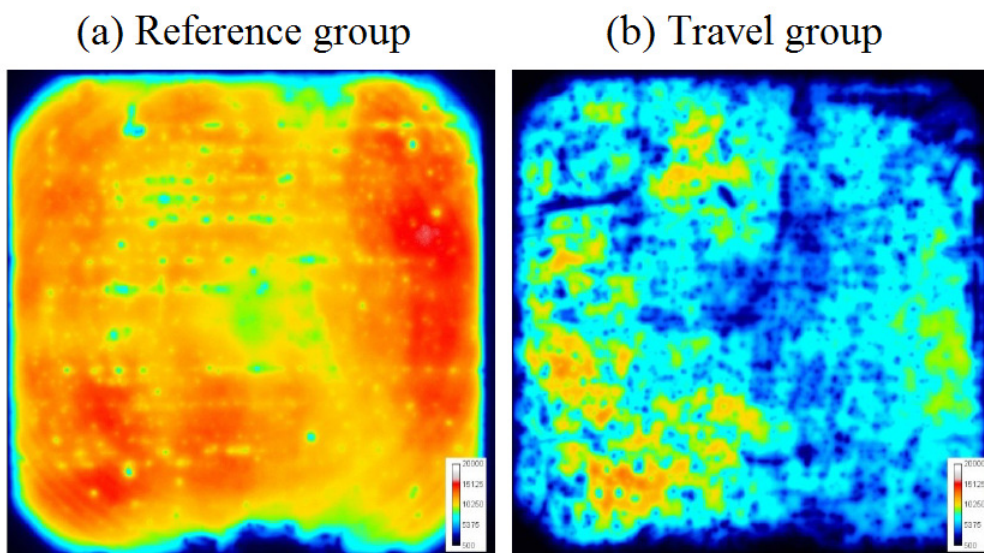
Figure 5. Photoluminescence images of 6 inch CZ c-Si wafers with the same *deposited intrinsic / doped a-Si:H layers (i / p –* front *surface, i / n –* rear surface): (a) reference group and (b) travel group.

Figure 5 shows typical photoluminescence images of passivated wafers from the reference and travel groups, indicating a strong impact of transportation on the quality of surface passivation. The lifetime measurements indicate τ ~ 1.5 / 0.9 ms at excess carrier density of 10^{15} cm^{-3} corresponding to implied V_{OC} ~ 721 / 708 mV for the reference / travel group, respectively. This fact along with some oxidation of a-Si:H layers during the transportation resulted in the measured efficiency loss of 0.6 – 0.9 % abs. Consequently, if the transportation of wafers after deposition of a-Si:H layers is eliminated then the efficiency of such (239 cm^2) Si-HJ solar cells will reach a value ≥ 21 %.

3.4. R&D Si-HJ cells

In order to explore further the potential of Gen5 KAI PECVD reactors for manufacturing of high-efficiency Si-HJ solar cells, attempts to fabricate Si-HJ cells at the R&D Center in St. Petersburg were undertaken. **Figure 6** illustrates the progress in the development of R&D Si-HJ cells, described in detail elsewhere [13].

Note that after about one year research a conversion efficiency of 21.6% (V_{OC} = 725 mV, J_{SC} = 39 mA / cm^2, FF = 76.4 %) has been achieved for 10×10 cm^2 Si-HJ solar cells with 4-busbar front grid. Nevertheless, we believe that further optimization of all production steps (wafer texturing, surface passivation, ITO deposition and screen printing of the front contact grid) will boost the cell efficiency even higher.
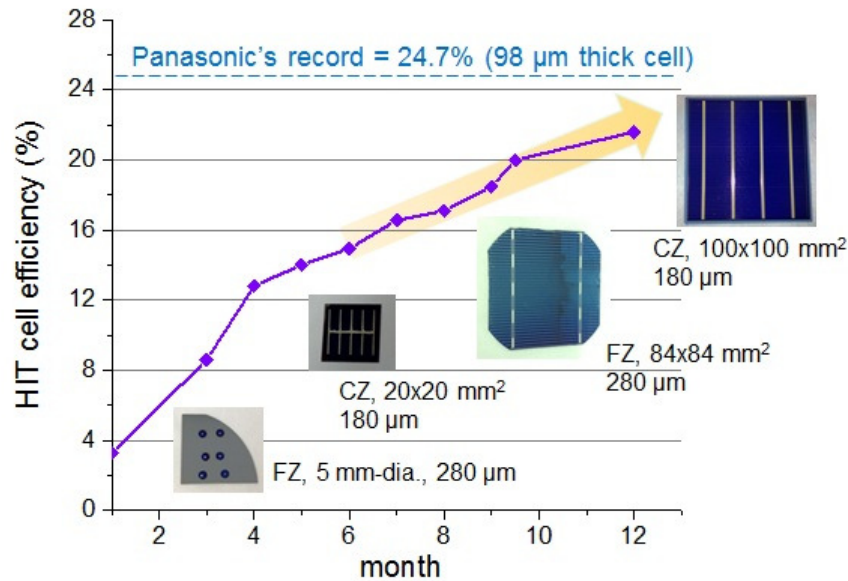
Figure 6. Progress in the development of Si-HJsolar cells
at the R&D Center of Thin Film Technologies in Energetics.

4. Conclusions

It is shown that Gen5 KAI PECVD reactors originally designed for mass production of micromorph modules can be successfully used for manufacturing of Si-HJ solar cells with conversion efficiency above 21 % using commercial n-type CZ c-Si wafers.

Ascknowledgements

References

1. U. K. Das, M. Z. Burrows, M. Lu, S. Bowden, R. W. Birkmire. Appl. Phys.Lett., 2008, 92, 063504.
2. S. D. Wolf, A. Descoeudres, Z. C. Holman, C. Ballif. Green, 2012, 2, 7.
3. M. Tanaka, M. Taguchi, Ts. Takahama, T. Sawada, Sh. Kuroda, T. Matsuyama, Sh. Tsuda, A. Takeoka, Sh. Nakano, H. Hanafusa, Y. Kuwano. Prog. Photovoltaics, 1993, 1, 85.
4. M. Taguchi, A. Yano, S. Tohoda, K. Matsuyama, Y. Nakamura, T. Nishiwaki, K. Fujita, E. Maruyama. IEEE J. Photovoltaics, 2014, 4, 96.
5. A. Descoeudres, Z. Holman, L Barraud, S. Morel, S. De Wolf, C. Ballif. IEEE J. Photovoltaics, 2013, 3, 83.
6. R. A. Sinton, A. Guevas. Appl. Phys.Lett.,1996, 69, 2510.
7. H. Nagel, C. Berge, A. G. Aberle. J. Appl. Phys., 1999, 86, 6218.

8.   N. Bassi, C. Clerc, Y. Pelet, J. Hiller, V. Fakhfouri, C. Droz, M. Despeisse, J. Levrat, A. Faes, D. Bätzner, P. Papet. In: Proc. 29th Eur. Photovoltaic Solar Energy Conf., 1. 2014, Amsterdam, 1180.

9.   H. Fujiwara, M. Kondo. Appl. Phys.Lett., 2007, 90, 013503.

10. A. Descoeudres, L. Barraud, R. Bartlome, G. Choong, S. De Wolf, F. Zicarelli, C. Ballif. Appl. Physi. Lett., 2010, 97, 183505.

11. S. De Wolf, Y. Andrault, L. Barraud, R. Bartlome, D. Bätzner, P. Bôle, G. Choong, B. Demaurex, A. Descoeudres, C. Guérin, N. Holm, M. Kobas, D. Lachenal, B. Mendes, B. Strahm, M. Tesfai, G. Wahli, F. Wuensch, F. Zicarelli, A. Buechel, C. Ballif. In: Proc. 10th Solid-State & IC Technol. IEEE Conf., 1. 2010, Shanghai, 1986.

12. B. Strahm, Y. Andrault, D. Bätzner, D. Lachenal, C. Guérin, M. Kobas, J. Mai, B. Mendes, T. Schulze, G. Wahli, A. Buechel. Proc. Mater. Res. Soc. Symp., 2010, 1245, A01.

13. S. N. Abolmasov, A. S. Abramov, D. A. Andronikov, K. V. Emtsev, A. V. Semenov, E. I. Terukov, I. A. Nyapshaev, D. L. Orekhov, A. V. Kukin. Use of industrial KAI-1200 PECVD reactors for manufacturing of high-efficiency silicon heterojunction solar cells. J – *submitted to* Tech. Phys.

SYNTHESIS AND CHARACTERIZATION CHITOSAN / POLYCAPROLACTONE COMPOSITE FILMS

K. Nagaraj

SathyabamaUniversity
Sathyabama, India
Kaviyarasun@yahoo.co.in

Abstract

Chitosan is a well sought after polysaccharide in biomedical applications and has been blended with various macromolecules to mitigate undesirable properties. Polycaprolactone (PCL) is biodegradable polyester with a low melting point (around 60°C) and the glass transition temperature of about −60°C. The work deals with the preparation and characterization of the chitosan and poly-ε-caprolactone solution casted blended films in various properties (chitosan–PCL ratios are 90 : 10, 75 : 25, and 60 : 40). The casted films were characterized based on the structural functions, optical and electrical studies by using X-ray diffraction, Fourier-transform-infrared, ultraviolet-visible-spectrometer and LCR meter.

1. Introduction

Chitosan (**Figure 1**) is prepared from chitin with the help of three steps namely deproteinization, demineralization and decolorozation [1, 2]. Polycaprolactone (PCL) is a versatile synthetic polymer with low melting point of 60 °C [3, 4]. It is also a biocompatible and biodegradable polymer like chitosan. It has a neutral charge distribution and it has been blended with various amorphous crystalline and polymers including chitosan.
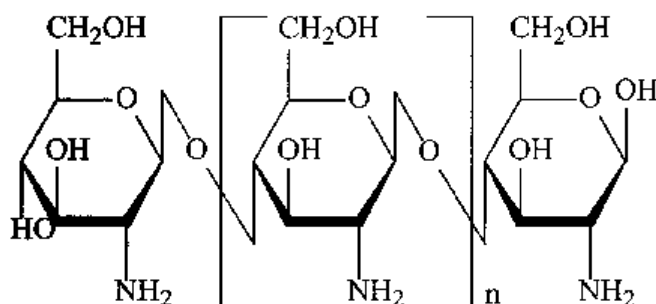
Figure 1. Structure of chitosan.

Chitosan is a linear polysaccharide composed of randomly distributed β-(1-4)-linked D-glucosamine (deacetylated unit) and N-acetyl-D-glucosamine (acetylated unit). It has a number of commercial and possible biomedical uses.

PCL is biodegradable polyester with a low melting point of around 60 °C and a glass transition temperature of about –60°C. PCL is prepared by ring opening polymerization of ε-caprolactone using a catalyst such as stannous octanoate (**Figure 2**). The most common use of polycaprolactone is in the manufacture of specialtypolyurethanes. Polycaprolactones impart good water, oil, solvent and chlorine resistance to the polyurethane produced.
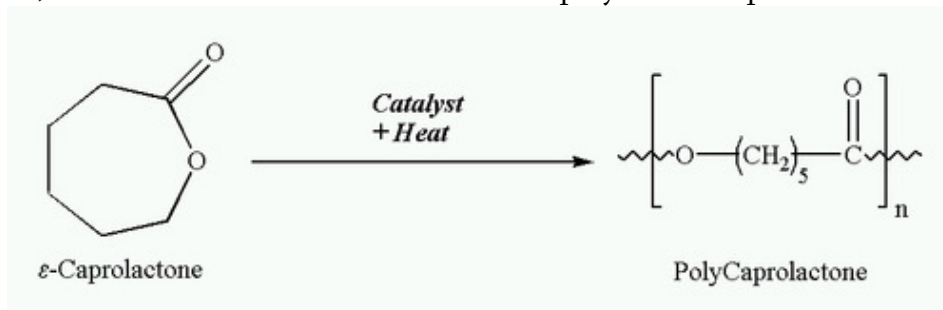
Figure 2. Preparing of polycaprolactone.

This polymer is often used as an additive for resins to improve their processing characteristics and their end use properties (e.g., impact resistance). Being compatible with a range of other materials, PCL can be mixed with starch to lower its cost and increase biodegradability or it can be added as a polymeric plasticizer to PVC. Polycaprolactone is also used for splinting, modeling, and as a feedstock for prototyping systems such as a RepRap, where it is used for Fused Filament Fabrication (similar to the Stratasys' Fused Deposition Modeling or FDM technique).

2. Experimental

Here we observe blending two polymers in an effective way to develop new materials with combinations of properties not processed by individual polymers. Consider also the wide range of physical, chemical properties and processabilities and biological interactions of natural polymers. Since the properties of PCL and chitosan are complementary it is possible that blending two polymers will give composite owning properties of idea; while the scaffold such as biocompatibility promotes the ability of tissue development. The blending of chitosan withPCL has been investigated not only for medical applications but it also is an effective to reduce environmental pollution from plastic waste.

Selection of common solvent. Chitosan is insoluble in water organic solvents. Some organic acids such as acetic acid,formic, lactic and oxalic acids are frequently used for dissolution.PCL dissolves in organic solvents such as chloroform,acetic acid and not in water.Chitosan dissolves in acetic acid but not in many organic solvents.Chitosan and PCL were blended homogeneously in a unique solvent mixture of acetic acid

Preparation of stack acidic acid solution. 10 ml of glacial acetic acid dissolves in 100 ml of distilled water is known as stack acidic acid solution.

Preparation of 0.1 NaOH solution. 0.4 g of NaOH dissolves in 200 ml of distilled water is known as 0.1 NaOH solution.

Preparation of chitosan solution. Stack acetic acid solution is added with 2 wt. % chitosan powder to produce chitosan solution for the blend.

Preparation of PCL solution. The PCL solution prepared by 1.8 % PCL added with glacial acetic acid.

Preparation of film.The polymer solutions are mixed in definite ratios like 60 : 40, 75 : 25, and 90 : 10 in a 20 ml to form blend solution. That blend solutions are kept in a Petri dish and placed in a magnetic stirrer for 4 h with the heat of 55 °C. Then 0.1 M NaOH solution dripped out on the polymer film to remove the amine groups in the chitosan and avoid depolymerization.Finally, the Petri dish were kept in the desiccators to obtain the polymer films and kept till further study.

3. Results

FTIR studies.

3000 – 3600 cm^{-1}	has broad OH stretching.
3200 – 3700 cm^{-1}	is the more intensity due to NH group of chitosan.
1722 (1725) cm^{-1}	has carbonyl groups stretching vibration in PCL.
1650 cm^{-1}	has stretching of amide.
1590 cm^{-1}	has amine deformation in the chitosan 732 due to PCL.
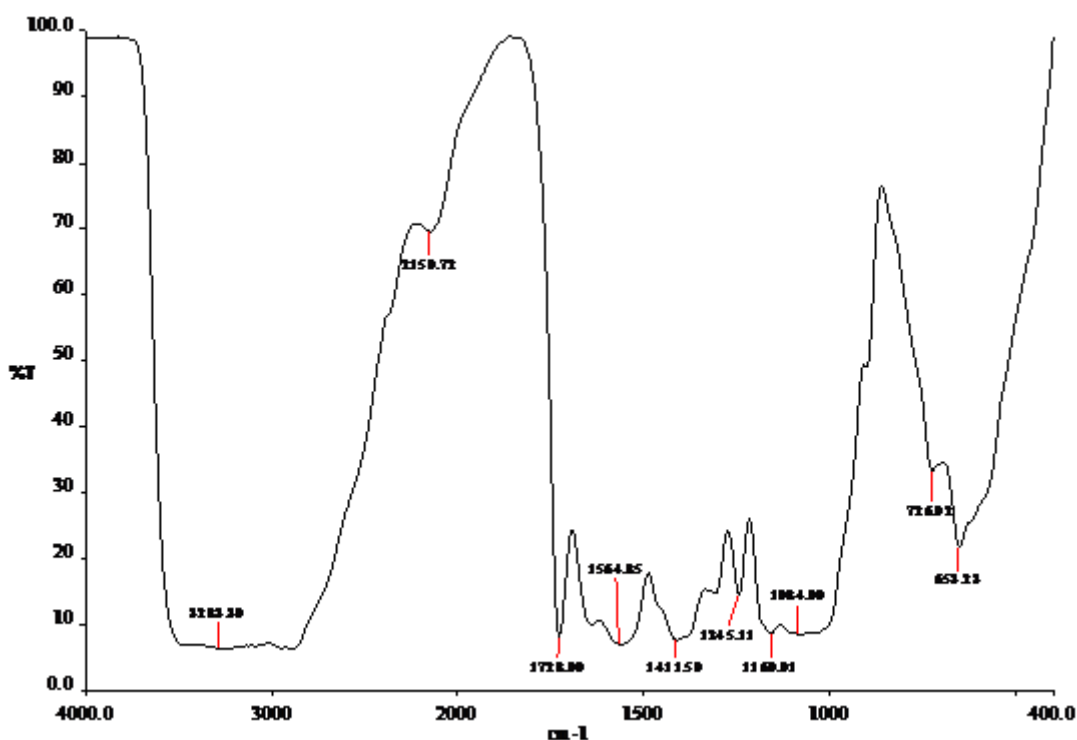
Figure 3. spectrum of blend film.

FTIR spectrum of blend film (**Figure 3**) indicated a shift in peak absorption from 1744 to 1728 (75 : 25) and 1724 cm^{-1} (60 : 40) due to carbonyl group,respectively. The peak absorption due to 732 of PCL representing –C=O rocking has shifted lower wavelength 726 cm^{-1} (75 : 25) and 733 cm^{-1} (60 : 40)in the blended films. This shift in absorption peak indicates the miscibility interaction of two polymers. These peaks are also present in the FTIR spectra of chitosan / PCL blends, although with varying intensities depending on their composition. The higher absorption intensity of 3200 – 3700 cm^{-1} in curve chitosan / PCL (60 : 40) indicates that there is more in chitosan / PCL. The border absorption peak of 3000 – 3700 cm^{-1} in curve chitosan / PCL (60 : 40) indicates that the bonds are weaker than the chitosan / PCL (75 : 25).

UV visible spectroscopy. UV-visible-spectra of the casted films were taken using UV-visible-spectrometer (range 190 – 1100 nm). From the UV visible spectra,it is observed that the film samples are highly absorptive material.The transmission spectra (**Figure 4**) showed that the (60 : 40) film has higher transmission than (75 : 25) film. It is due to stronger bond formed between chitosan and PCL polymers in (60 :40) film.
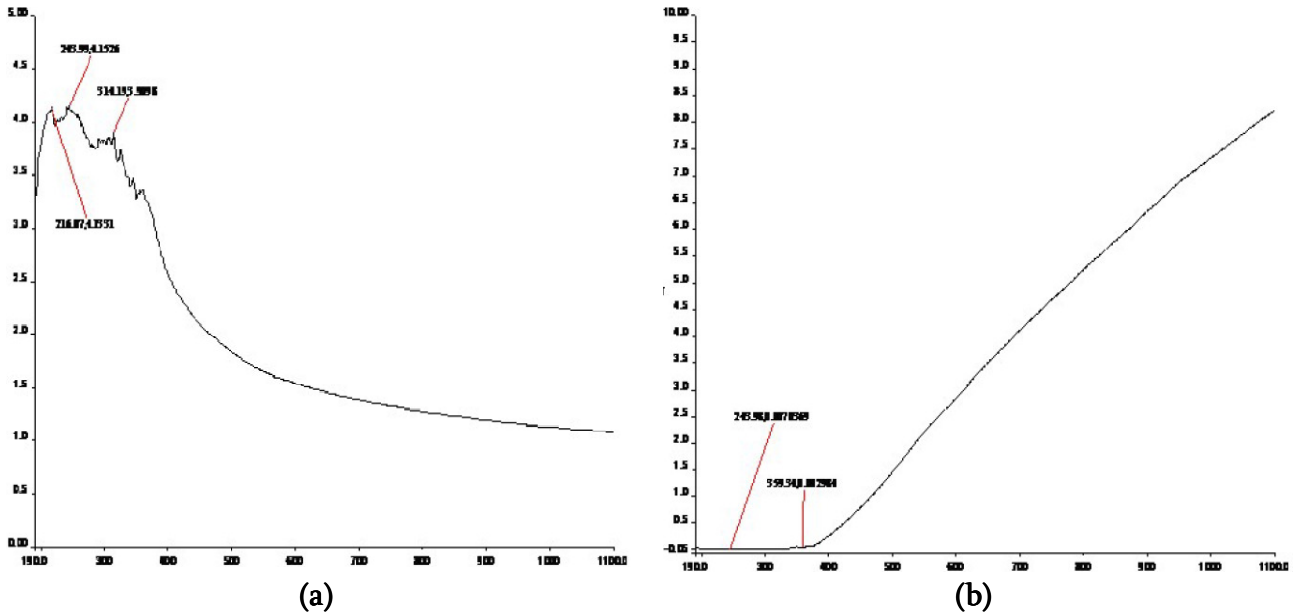

(a)   (b)

Figure 4. Transmission spectra of casted films with chitosan –polycaprolactone ratios of (a) (60 : 40) and (b) (75 : 25).

AC conductive measurements.

Results of AC conductive measurements are presented in **Figures 5** and **6**, and **Table 1**.
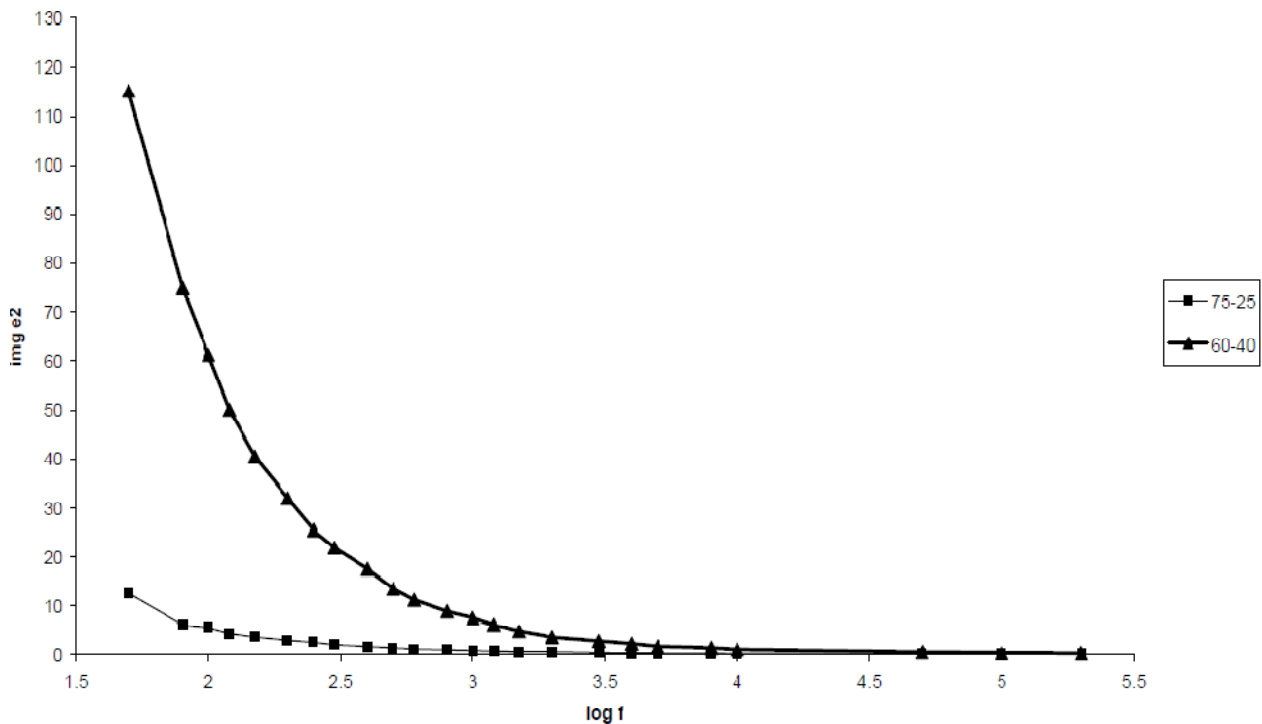
Figure 5. Dielectric constant of casted films with different chitosan–polycaprolactoneratios vs. frequency.

(a) (b)
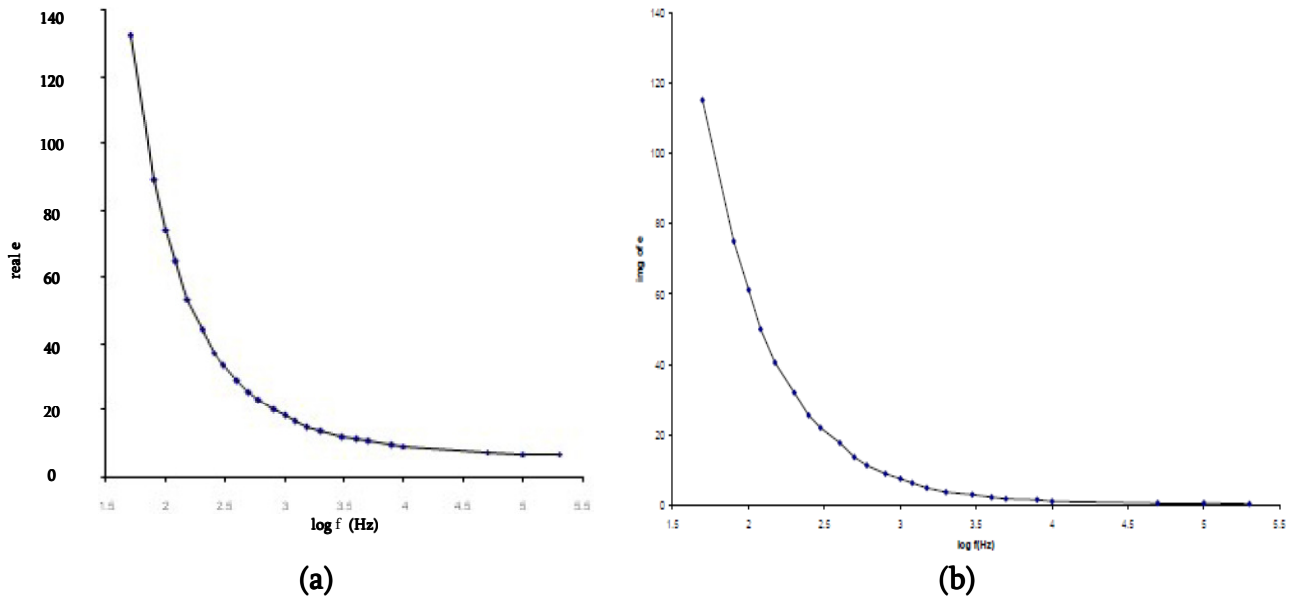
Figure 6. Real (a) and imaginery (b) parts of dielectric constant of casted
films with chitosan–polycaprolactone ratio of 60 : 40 vs. frequency.

Table 1. AC conductive parameters of
casted chitosan–polycaprolactone films.

Frequency, F, Hz	$\log f$	Capacitance C, arb. Units	Dissipation factor, D	Real part of dielectric constant ε'	Imaginary part of dielectric constant ε''
50	1.69897	23.6809	2.45512	5.129235948	12.59288976
80	1.90309	15.1123	1.84821	3.273294191	6.049735058
100	2	14.1632	1.76625	3.067721015	5.418362243
120	2.079181	15.5366	1.27502	3.36519673	4.290693134
150	2.176091	13.3156	1.24772	2.884132537	3.598589849
200	2.30103	12.4429	1.0794	2.695107449	2.90909898
250	2.39794	12.865	0.89316	2.786533471	2.488820235
300	2.477121	11.4306	0.80801	2.475845277	2.000507743
400	2.60206	10.7412	0.70105	2.326522605	1.631008673
500	2.69897	10.3468	0.5901	2.241096348	1.322470955
600	2.778151	9.974	0.5047	2.160348608	1.090327942
800	2.90309	9.5947	0.43377	2.07819298	0.901457769
1000	3	9.50875	0.37743	2.059576381	0.777345913
1200	3.079181	9.16657	0.34213	1.985460872	0.679285728
1500	3.176091	9.00928	0.28156	1.95139217	0.549433979
2000	3.30103	8.80345	0.2934	1.906809801	0.559457996
3000	3.477121	8.48556	0.19783	1.837955457	0.363602728
4000	3.60206	8.25796	0.16705	1.788657749	0.298795277
5000	3.69897	8.24618	0.1504	1.786106224	0.268630376
8000	3.90309	7.96128	0.13043	1.72439745	0.224913159
10000	4	7.82716	0.11797	1.695347324	0.200000124
50000	4.69897	7.24864	0.07523	1.57004104	0.118114187
100000	5	7.14013	0.06205	1.546537989	0.095962682
200000	5.30103	7.35185	0.06225	1.592396121	0.099126659

4. Conclusion

In the present studies, the film samples were prepared successfully by blending chitosan / PCL in acetic acid solutions. The presence of chitosan in composite was proved by FTIRresults. It was clear that adding in to PCL there won't be any change in the crystal structure of PCL. Study of the conductivity of AC shows that the samples have high conductivity at low temperature. The UV visible spectra showed that the chitosan / PCL films were highly absorptive material in nature.

References

1.   C.-M. Lehr, J. A. Bouwstra, E. H. Schacht, H. E. Junginger. In vitro evaluation of mucoadhesive properties of chitosan and some other natural polymers. Int. J. Pharmaceutics, 1992, 78, 1-3, 43-48.
2.   B. Carreño–Gómez, R. Duncan. Evaluation of the biological properties of soluble chitosan and chitosan microspheres. Int. J. Pharmaceutics, 1997, 148, 2, 231-240.
3.   M. A. Woodruff, D. Werner. Hutmacher. The return of a forgotten polymer – Polycaprolactone in the 21st century. Prog. Polymer Sci., 2010, 35, 10, 1217-1256.
4.   M. F. Koenig, S. J. Huang. Biodegradable blends and composites of polycaprolactone and starch derivatives. Polymer, 1995, 36, 9, 1877-1882.

RAPID / SIMPLE SYNTHESIS OF MAGNETITE / DIOPSIDE AS A NOVEL MAGNETIC-BIOACTIVE NANO COMPOSITES USING BONE CANCER THERAPY HYPERTHERMIA TREATMENTS

E. Karamian, A. A. Najafizadeh, M. Zahraei, F. Ranjbar

Advanced Materials Research Center
Faculty of Materials Engineering
Najafabad Branch
Islamic Azad University
Najafabad, Iran
ebkaramian91@gmail.com
ekaramian@pmt.iaun.ac.ir

Abstract

This paper presents a simple method for the rapid synthesis of diopside /magnetite nano composite powder. Superparamagnetic magnetite nanoparticles are firstly synthesized by co-precipitation using ferrous chloride and ferric chloride. Immediately following the synthesis, Diopside, $CaMgSi_2O_6$, particles were prepared by sol–gel method. Then, diopside /magnetite composites synthesized by wet milling diopside synthesized in a dispersed suspension of magnetite nanoparticles, 20 – 70 nm, during which the magnetite nanoparticles are incorporated into the diopside matrix. We observed that the resultant diopside /magnetite possessed a homogeneous dispersion of magnetite nanoparticles, characterized by an absence of large aggregates. When these materials were subjected to an alternating magnetic field, the generated heat increased with increasing of the magnetite concentration. For a magnetite concentration of 20 wt. %, DM20, a temperature increase about 10 °C was achieved in 1 min. These results suggest that our composites exhibit good hyperthermia properties and are promising candidates for investigation of biological tests.

1. Introduction

Diopside ($CaMgSi_2O_6$) is a very common silicate mineral, it belongs to the calcic pyroxenes group [1]. Diopside reveals a variety of physicochemical characteristics and appearance, and is widely used in many fields such as chemical industry and medicine [2]. The structure of diopside is monoclinic and the cell parameters are as follows (**Figure 1**) [3]. It is well known that Fe_3O_4 nanoparticles are biocompatible with the human body. However, there is the concern that the nanoparticles may have long-term toxic effects.

The current therapies available to treat cancer patients mainly rely on surgical operation and chemical therapy.In addition, the serious disadvantage of these cancer therapies methods is that the heat generated during treatments not only kills cancer cells but also normal cells, because it is difficult to heat deep-seated cancerous effectively and locally. So, the therapeutic procedures that can heat carcinomatous area effectively and selectively are urgently needed.

In recent years, hyperthermia, a treatment technique based on deactivation of cancer cells, tumor tissue, by raising the temperature in the range 42 – 46 °C has gained much attention as an alternative therapy to treat cancer. As to ferromagnetic nano particles have the ability to

generate heat in high frequency magnetic field, magnetite is one of the most promising candidates for hyperthermia. If magnetite can be made to accumulate only in the cancer tumor, they can specially heat the cancer cells [4].
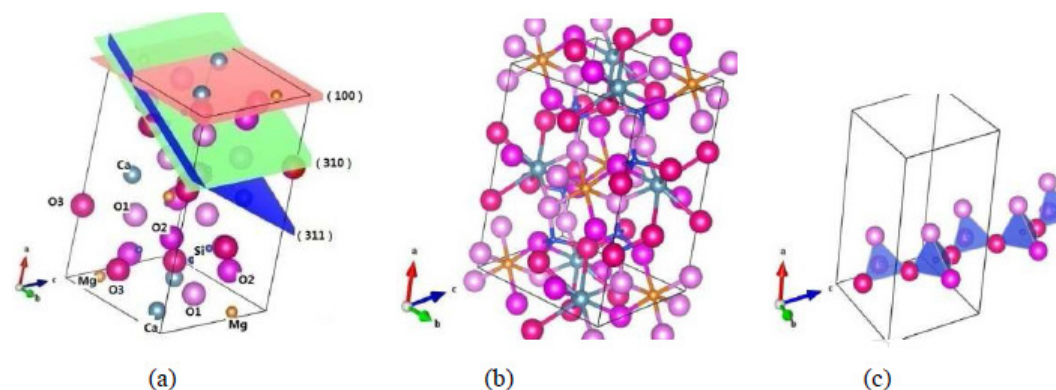

Figure 1. Structure of diopside.

In this paper, we describe a method for quick and easy synthesizing diopside/Fe₃O₄ composite particles. In the method, Fe₃O₄ nanoparticles are firstly prepared by co-precipitation method [5], after which we employ sol–gel method and then a horizontal tumbling ball mill to mechanically synthesize submicron-sized diopside particles. Finally, these materials were composited by high energy ball milling (HEBM) under wet conditions at room temperature. The merits of using horizontal tumbling ball mills are that the device structure is simple, the handling is easy, the energy consumption is relatively low, and scale-up is easily achieved [6]. The wet mechanical process promotes the dispersion of Fe₃O₄ nanoparticles in the diopside matrix. We investigated the factors and conditions that influence the formation of diopside / Fe₃O₄ composites and examined their properties with respect to hyperthermia treatments.

2. Materials and methods

2.1. Preparation of super paramagnetic Fe3O4 nanoparticles

The Fe_3O_4, spinal $FeFe_2O_4$, nanoparticles were synthesized by a co-precipitation method reported previously [2 – 4].

2.2. Preparation of diopside powder

The diopside ceramic was prepared via a modified sol-gel method. Briefly we dissolved a same molar ratio of Ca $(NO_3)_2 \cdot 4H_2O$ and $Mg(NO_3)_2 \cdot 6H_2O$ in an absolute ethanol and stirred vigorously for 30 min in 80 °C to dissolve these precursors in the solvent. $Si(OC_2H_5)_4$ (TEOS) was added to the homogenous solution and slowly stirred to transform to a wet gel. Drying in an oven at 110 °C for 2 h resulted in a dried powder which was grounded in a hand-mortar, then calcined at 1150 °C for further 3 h. Finally it was ball-milled in a zirconia mechanical ball mill for 2 h to supply diopsidenano powder.

2.3. Preparation of hyperthermia-relevant diopside/Fe3O4 nano-composites

At first, 60-mL Fe₃O₄ suspensions with variable concentrations and amount of diopside powder 10, 20 and 30 wt. % of DM10, DM20 and DM30, respectively. Then, the resulting suspension was subjected to a mechanical treatment using a horizontal tumbling ball mill. Wet milling was performed at room temperature for 1 h and rotational speed of the pot was 300 rpm

with ball to powder ratio 10 : 1. After milling, the precipitate from the pot was washed with deionized water and centrifuged. This washing operation was repeated several times. At last, the precipitate was dried overnight at 313 K in vacuum.

2.4. Characterizations

Phase structure analysis was carried out by X-ray diffraction (XRD) (Cu K$_\alpha$ radiation (λ = 0.15418 nm) over the 2θ range of 10 – 90 °). The obtained experimental patterns were compared to the standards compiled by the Joint Committee on Powder Diffraction and Standards (JCDPS) which involved card # 011–0654 for diopside phase.

The average crystallite size of the as-synthesized samples was calculated from the XRD patterns using the modified Scherrer's equation [7].

The morphology of the samples was also observed via field emission scanning electron microscopy. The particle size distributions were determined using a DLS analyzer (Zetasizer Nano ZS, Malvern Instruments, and Worcestershire, UK). The powder has been suspended in the ethanol liquid by ultrasonic irradiation for 30 min before doing DLS analyzer.

In order to evaluate the heat generation ability of magnetic nano composites particles, the powder samples were dispersed in deionized water under ultrasonic irradiation, 1.02 g, was placed in a polystyrene tube (diameter 16 mm) and closely packed by tapping the tube. The loading mass was adjusted such that the packed volume was a constant 0.7 cm^3, regardless of the Fe$_3$O$_4$ concentration. We then inserted the tube into the canter of the coil apparatus in an AC-magnetic field (600 kHz, 2.9 kA / m – 36.5 Oe). Then the increase intemperature was measured using an optical alcohol thermometer.

3. Results and discusion

3.1. Particles size distribution

The results of distribution of the particles size of the synthesized magnetite powder are shown in **Figure 2**. As it is seen there all the particles are in less than 90 nm. It means that the synthesized magnetite powder is nano powder with 40 nm in particles size average.
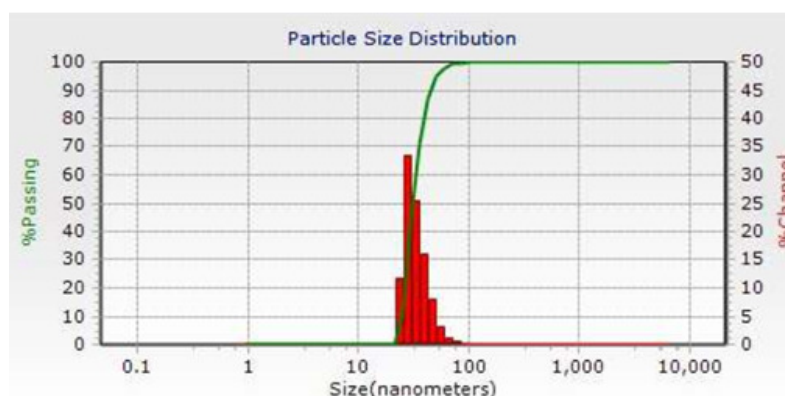
Figure 2. The particles size distribution
of magnetite powder synthesized.

3.2. XRD results (phase analysis)

Phase analysis of synthesized magnetite and diopside powders are shown in **Figures 3**. As you seen at two materials synthesized all peaks belong to crystals planes of Fe$_3$O$_4$ and diopside (CaMgSi$_2$O$_6$) phases. In fact, there is no other phase as the impurities.
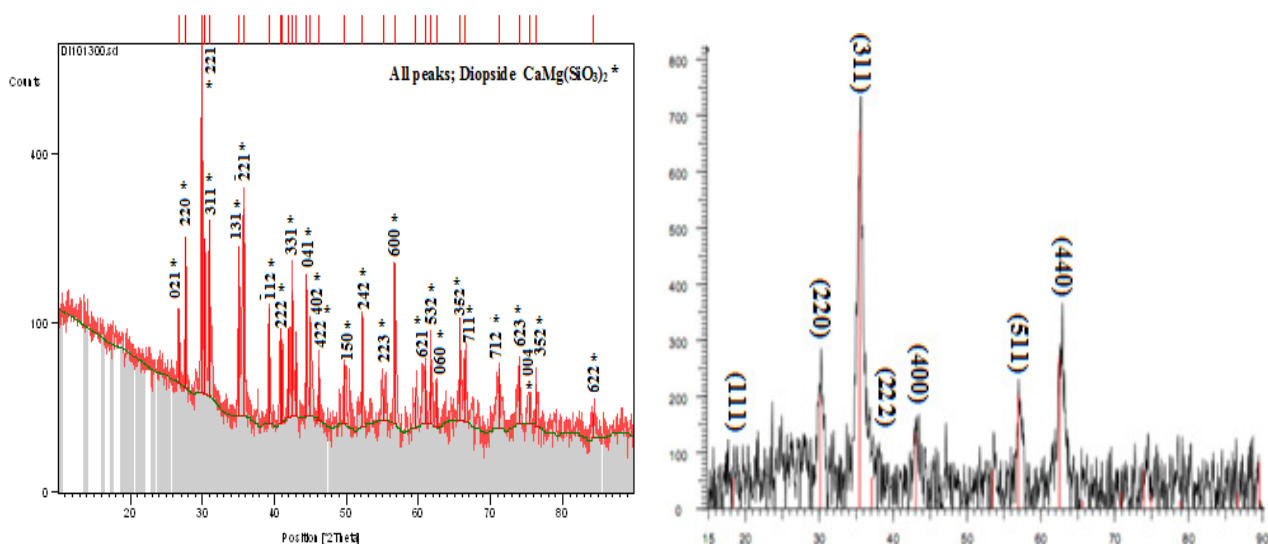
Figure 3. XRD patterns of magnetite (left) and diopside powder synthesized (right).

3.3. Estimation of crystal size

At this sample, **Figure 4**, the linear regression plot is obtained as $y = -6.3433x - 3.3477$. This is equivalent to $\ln \beta = \ln (1 / \cos\theta) + \ln (k\lambda / L)$. From this line, the intercept is -3.3477 and $e^{-3.3477} = k\lambda / L$ and $L = 390$ Å $= 39$ nm. So, the averagesize of the crystals of the synthesized magnetite is 39 nm.
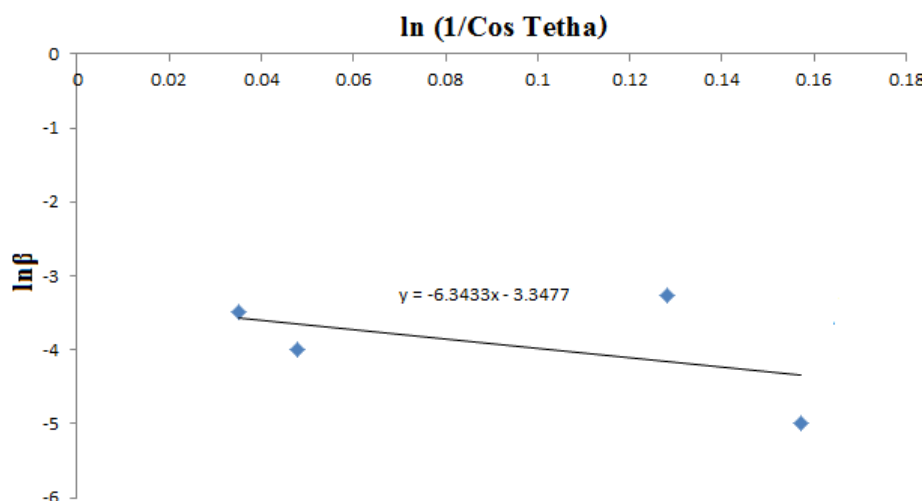

Figure 4. Plot of $\ln \beta$ vs. $\ln (1 / \cos\theta)$
ofthe magnetite powder synthesized .

The calculatedaveragesize of crystals, 39 nm, is close to the average size of particles and was determined by DLS graph, 20 – 70 nm or 35 nm in average (**Figure 2**).

3.4. Induction heating ability (heat generation ability)

The heat generation ability of magnetic nano compositesparticles (1.02 g) was measured by coil apparatus. As one seen, temperature profiles were increased up to 10 °C at the magnetite composite samples containing 20 and 30 wt. % of DM20 and DM30 samples, less than 60 s.

However, these composites showed good hyperthermia-related properties (**Figure 5**), which were similar to or better than those reported elsewhere for these arterials [8 – 10].
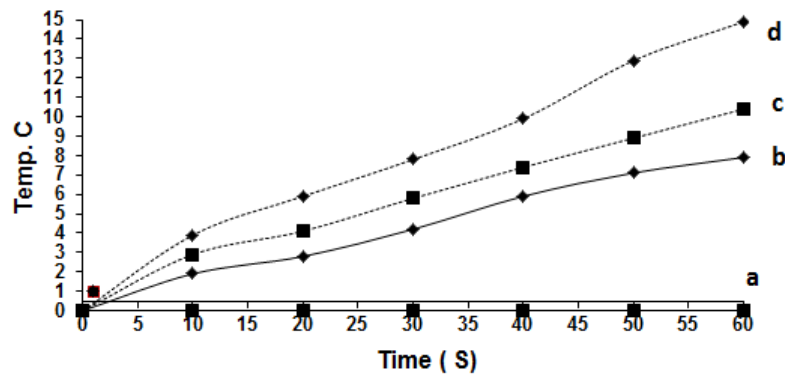
Figure 5. Temperature profiles of (a) diopside free magnetite
(b) diopside/magnetite composite containing 10 (c), 20
and (d) 30 wt. % Fe_3O_4 in an alternating magnetic field .

3.5. SEM micrographs

A representative SEM image of magnetite nanocomposite containing 20 wt. % Fe_3O_4 is shown in **Figure 6**. The figure shows Fe_3O_4 nanoparticles measuring approximately 50 nm embedded in the micron size diopside matrix; the particles are homogeneously dispersed without having formed any large aggregates. As it is shown, large isolated aggregates of Fe_3O_4 nanoparticles were hardly observed on the surface of diopside particles; thus, we confirmed that our synthesis method effectively yields nanostructured diopside / Fe_3O_4 composites. The X-ray map of iron element shows good distribution of Fe in the matrix and confirms formation of diopside / magnetite nano composite. As it is seen, according the iron X-ray map we can measure and conclude that iron oxide particles in the nano composite particles are of 20 – 75 nm size approximately.
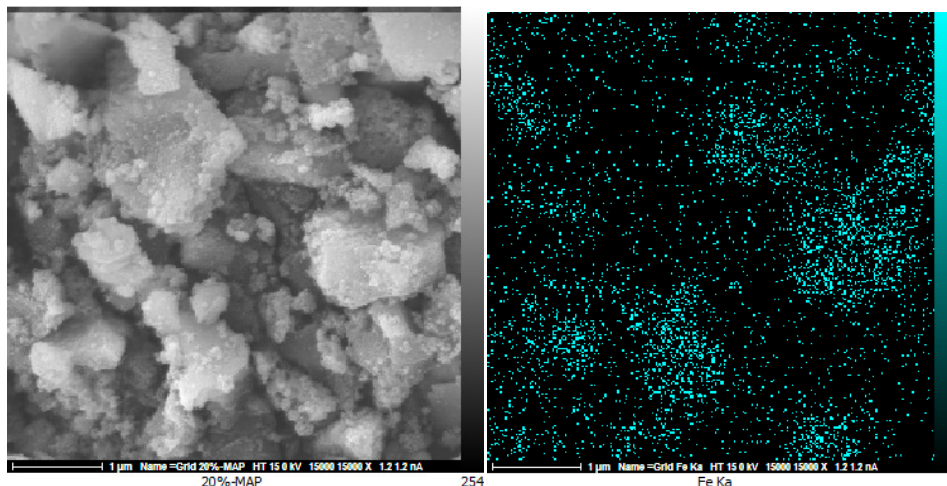
Figure 6. SEM image of diopside / Fe_3O_4 nanocomposite
containing 20 wt. % magnetite nano particles, DM20 composite
sample: (left) and X-ray map of Fe in the SEM micrograph (right).

4. Conclusion and suggestions

According to above discussion, we can represent the following conclusions:
1. A simple-rapid method for the synthesis of diopside/Fe_3O_4 composites was developed. In this method, superparamagnetic Fe_3O_4 nanoparticles, almost 40 nm, and submicron-sized

diopside particles are sequentially prepared in a short period, less than 1 h, and Fe_3O_4 nanoparticles, 20 – 70 nm, are effectively incorporated into the diopside matrix by ball milling.

2. In the diopside/Fe_3O_4 composites thus synthesized, the Fe_3O_4 nanoparticles were observed to be homogeneously dispersed without having formed any large aggregates, even at the absence of anti-agglomeration agents, illustrating the success of the milling process.

3. This property resulted in effective heat generation in the diopside/Fe_3O_4 composites, when the composites were immersed in an alternating magnetic field. In fact, the temperature was increased up to 10 ^0C during less than 1 min at the magnetite composite samples containing 20 and 30 wt. % Fe_3O_4.

4. Therefore, our synthesis method can efficiently provide diopside magnetite composites, containing 20 and 30 wt. % Fe_3O_4, that may be used to investigate the biological-related tests and hyperthermia therapy against malignant bone tumors.

5. Future work will focus on the improvement of the hyperthermia-related properties of the material by optimization of the size of Fe_3O_4 nanoparticles and also on applications of the materials in bone tissue engineering.

Acknowledgements

References

1. A. Dimanov, V. Sautter. Eur. J. Mineral., 2000, 12, 749-760.
2. R. Jindal, R. Jayaganthan, I. V. Singh. Ceram. Int., 2011, 37, 741-748.
3. T. Nonami, S. Tsutsumi. J. Mater. Sci.: Mater. Med., 1999, 10, 8, 475-479.
4. M. Shinkai, H. Honda, T. Kobayashi. J. Chem. Eng. Jpn., 2000, 6, 4, 14-16.
5. T. Iwasaki, N. Mizutani, S. Watano, T. Yanagida, T. Kawai. J. Exp. Nanosci., 2010, 5, 251-262.
6. T. Iwasaki, T. Yabuuchi, H. Nakagawa, S. Watano. Adv. Powd. Technol., 2010, 21, 623–629.
7. A. Monshi, S. S. Attar. Majlesi J. Mater. Eng., 2010, 2, 3, 154-160.
8. S. Murakami, T. Hosono, B. Jeyadevan, M. Kamitakahara, K. Ioku. J. Ceram. Soc. Jpn., 2008, 116, 950-954.
9. E. Andronescu, M. Ficai, G. Voicu, D. Ficai, M. Maganu, A. Ficai. J. Mater. Sci.: Mater. Med., 2010, 21, 2237-2242.
10. A. Inukai, N. Sakamoto, H. Aono, O. Sakurai, K. Shinozaki, H. Suzuki, N. Wakiya. J. Magn. & Magn. Mater., 2011, 323, 965-969.

SYNTHESIS OF GRAPHENE–METAL NANOCOMPOSITE ANODE MATERIALS FOR LITHIUM ION BATTERIES

O. Eksik [1], C. Aksakal [2], R. Yavuz [1], N. Karatepe [2]

[1] Department of Chemical Engineering
Istanbul Technical University
Istanbul, Turkey
[2] Energy Institute
Istanbul Technical University
Istanbul, Turkey

Abstract

Graphene-based nanocomposites have been demonstrated to be promising high-capacity anodes for lithium ion batteries to satisfy the ever growing demands for higher capacity, longer cycle life and better high-rate performance. In this study, graphene–metal based anode materials, which have high mechanical, electrochemical, electrical and thermal properties, were synthesized. To synthesize graphene-based composite anode materials, primarily bulk graphite was oxidized by using modified Hummers method and then graphite oxide was reduced to nano graphene material through thermal exfoliation method. By virtue of this technique, from bulk graphite good quality graphene in high quantities were obtained. Finally, nano metal particles tin (Sn) and molybdenum disulfide (MoS_2) were added into the graphene nano structure to produce graphene-metal hybrid material. Structural characterization of the obtained samples were characterized by surface electron microscope (SEM), X-ray diffraction (XRD) and Raman Spectroscopy. Also electrochemical performance of the prepared composite samples was analyzed in coin cell.

1. Introduction

As portable consumer and wearable electronics continue to be increasingly ubiquitous in the modern society, the demand for better lithium ion batteries powering these devices have risen exponentially [1]. Lithium ion batteries have so far been regarded as an ideal candidate due to the ability to deliver high capacities repeatedly over thousands of cycles of operation at reasonable charge / discharge rates. However, as the aforementioned devices become more integral in the consumer's daily routine, the need for long-lasting batteries has become critical. Further, with an increase in feature-intensive next-generation electronics, the need for higher power density batteries has also drawn significant attention [2]. In general, traditional lithium ion batteries comprising of a graphitic anode and a lithium cobalt oxide or lithium iron phosphate cathode are known for relatively high energy densities but low power densities.

Conventionally, graphite is used as an anode material for commercial lithium ion batteries. However, graphite suffers from an inherently low theoretical charge storage capacity

(372 mA h/ g) and often operate at significantly lower rates that in turn limits the achievable power densities. For the purpose of improving the energy density and power density of batteries, scientists have made great efforts to explore alternative anode materials with higher capacity, such as Fe_2O_3, Fe_3O_4, Co_3O_4, and Mn_2O_3 [3 – 6]. Unfortunately, a large specific volume change commonly occurs in the host matrix of these materials during the cycling process. The resulting partial pulverization of the electrodes leads to a decrease in electrical conductivity and reversible capacity, thereby limiting their commercial viability.

Graphene, a single 2-D carbon sheet with the same structure as the individual layers in graphite, has recently spurred a great interest as lithium ion battery anodes, owing to its high intrinsic surface area and outstanding electrical conductivity [7 – 10]. Yoo et al. first demonstrated the feasibility of incorporating graphene anodes as the host for lithium storage, delivering capacities of 540 mA h / g [11]. The early results with graphene anodes generally suffered from poor coulombic efficiencies and low cycle life [12], attributed to the use of non-conductive polymer binders, high surface area and aggregation of graphene nano-platelets. This hypothesis was proved to be true as subsequent studies revealed that binder-free graphene anodes delivered improved performance characteristics as compared to the traditional slurry-based approach. Another approach commonly employed in improving the coulombic efficiency in graphene-based electrodes have been through the incorporation of a nano metal particles (Sn and MoS_2) to compensate for the irreversible capacity loss during the formation of the solid electrolyte interphase (SEI) in the first few cycles. While graphene anodes have shown tremendous promise as a potential alternative to graphite for high-performance lithium ion batteries, there are certain fundamental constraints to its incorporation.

In this study, graphene–metal based anode materials, which have high mechanical, electrochemical, electrical and thermal properties, were synthesized. To synthesize graphene-based composite anode materials, primarily bulk graphite was oxidized by using modified Hummers method and then graphite oxide was reduced to nano graphene material through thermal exfoliation method. By virtue of this technique, from bulk graphite good quality graphene in high quantities were obtained. Finally, nano metal particles of Tin (Sn) and Molybdenum disulfide (MoS_2) were added into the graphene nano structure to produce graphene-metal hybrid material. Structural characterization of the obtained samples were characterized by surface electron microscope (SEM) and thermogravimetric analysis (TGA) and X-Ray Diffraction (XRD). Also electrochemical performance of the prepared composite samples was analyzed in coin cell.

2. Experimentation

2.2. Synthesis of anode material

2.3. Synthesis of graphite oxide from graphite

Graphite oxide was prepared by modified Hummers method: Graphite powder (1.5 g, 325 mesh) was put into a mixture of 12 ml concentrated H_2SO_4, 2.5 g $K_2S_2O_8$ and 2.5 g P_2O_5. The solution was heated to 80C and kept stirring for 5 h by using oil-bath. In a next step, the mixture was cooled to room temperature and diluted with deionized water (500 ml) overnight. Then, the product was obtained by filtering using 0.2 μm nylon film and dried naturally. The

pre-oxidized graphite was then re-oxidized by Hummers method. Pretreated graphite powder was put into 0°C concentrated H_2SO_4 (120 ml), soon after, 15 g $KMnO_4$ was added gradually under stirring, the temperature of the mixture was kept to be below 20 °C by ice-bath. Successively, the mixture was stirred at 35 °C for 4 h, and then diluted with 250 ml deionized water by keeping the temperature under 50 °C. 700 ml deionized water was then injected into the mixture followed by adding 20 ml 30 % H_2O_2 drop by drop. The mixture was filtered and washed with 1 : 10 HCl aqueous solution (1 L) to remove metal ions followed by 1 L of deionized water to remove the acid. Obtained graphite oxide and graphene were characterized by XRD and Raman spectroscopy.

2.3. Synthesis of grapheene

Thermal exfoliation method was used for the reduction of the GO. In this method graphite oxide powder were exposed to high temperatures (700 °C) in an air environment for short periods of time ranging from 10 to 20 s in order to produce open pore structure graphene. The basic schematic of the fabrication of the entire thermally exfoliated graphene fabrication is shown in **Figure 1**.
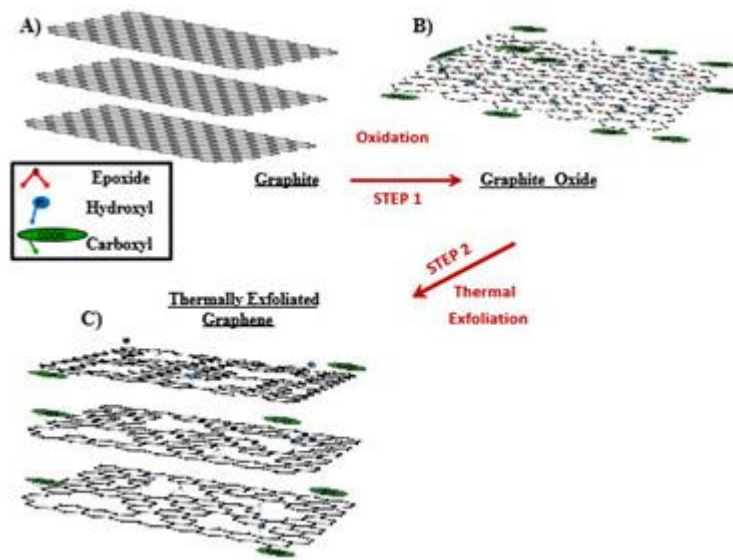
Figure 1. Schematic of the thermally exfoliated graphene fabricationshowing the various steps involved starting from graphite raw material.

2.4. Graphene–metal nanocomposite

Metal-nano particles of tin (Sn) and Molybdenum disulfide (MoS_2) were added into the graphene by mixing physically via using agate mortar for 30 minutes.

2.5. Lithium ion battery cell assembly

Thermally exfoliated graphene and graphene-metal nanocomposites were tested as an anode in LIBs. For this 2032 coin cells were assembled inside a glove box (MBraun Labstar) with oxygen and moisture content < 1 ppm. Lithium foil was used as the counter electrode and

polypropylene membrane was used as the separator. The electrolyte was 1 M LiPF in 1 : 1 mixture of ethylene carbonate (EC) and diethyl carbonate (DEC). MTI battery testing equipment was used to run the charge / discharge cycles.

3. Results

3.1. XRD characterization of graphite oxide

Powder X-ray diffraction studies were done using a PANalytical X'PERT Pro X-ray diffractometer which has a nickel-filtered Cu Kα radiation as the X-ray source. The scanning was done in the 2θ range of 0 to 40° with a step size of 0.2°.

XRD pattern of graphite shows its characteristic peak around 25–26°(**Figure 2a**). This gives an interlayer spacing of approximately 3.7 – 3.8 Å. After oxidizing the graphite by Hummers method, GO shows peak $2\theta = 11$° (**Figure 2b**). This peak corresponds to the interlayer spacing 8.3 Å. The presence of the peak around 11° indicated that oxygenated groups have been inserted in the interlayer of graphite which causes increase in the interlayer spacing .
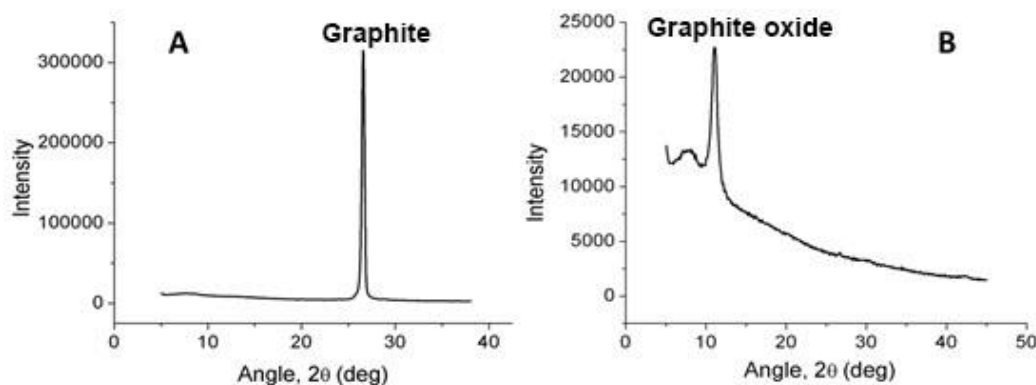
Figure 2. XRD patterns of the graphite (a), graphite oxide (b).

3.2. Raman characterization of graphene

The Raman spectroscopic measurements were carried out. A WITec alpha 300 Confocal Raman system equipped with a Nd:YAG laser was used for 532 nm (2.33 Typical Raman spectra of the graphene showing the Raman G (~ 1584 cm^{-1}) and 2D (~ 2685 cm^{-1}) band peaks that are characteristic of few layer graphene **Figure 3**.
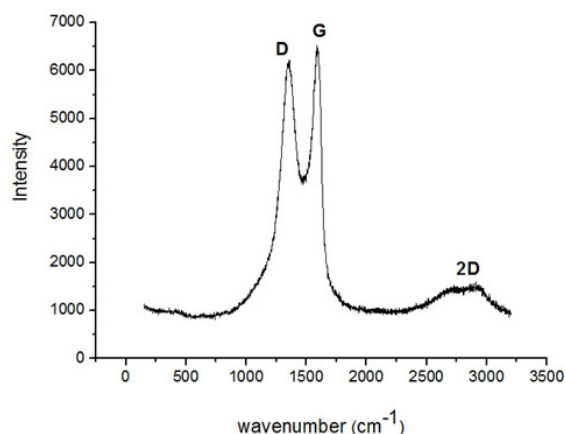
Figure 3. Raman spectra of the graphene.

Strong defect concentration D peak (~ 1350 cm^{-1}) indicates highly defective graphene. Thermal exfoliation of graphite oxide produce graphene, which contains defects and lacks the perfect honeycomb structure. We found that defects band can have significant impact on the shape of the 2D band of graphene. **Figure 3** shows the Raman spectra of graphene. At high defect concentration, the hexagonal network of graphene is disturbed causing the suppression of the smaller two peak form of 2D band.

3.3. Characterization of anode materials

3.3.1. Results of pure graphene as anode material

Figure 4 shows SEM images of graphene slurry layer. Mean thickness of the layer is measured as 106.5 μm. As showed in **Figure 4**, graphene layer has heterogen surface.
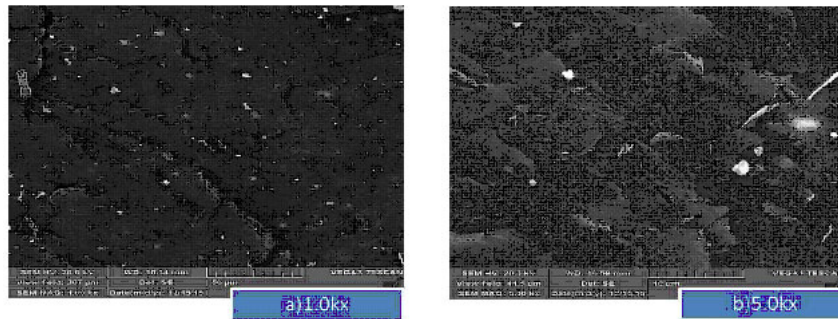
Figure 4. SEM images of graphene layer a) 1.0k_x, b) 5.0k_x.

3.3.2. Results of g raphene–Sn mixture as anode material

Figures 5 and **6** exhibit SEM images of Sn / graphene slurry layers with mixing ratios 30 : 70 and 50 : 50, respectively. SEM images show that tin,graphene and were evenly mixed.
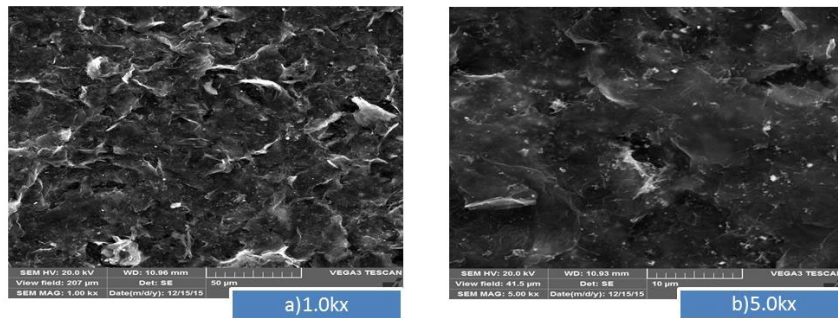
Figure 6. SEM images of Sn–graphene 30 : 70 layer a) 1.0k_x, b) 5.0k_x.
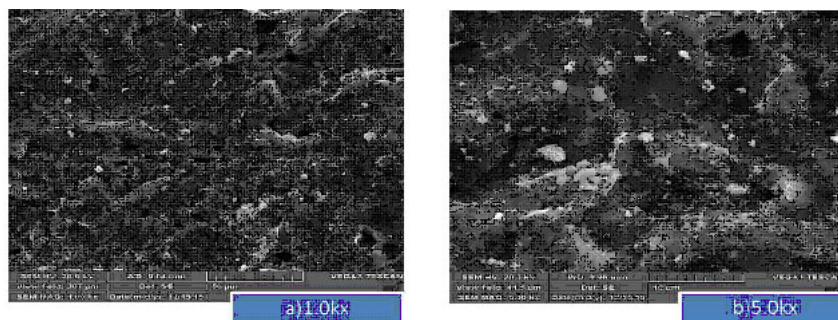
Figure 6. SEM images of Sn–graphene 50 : 50 layer a)1.0k_x, b)5.0k_x.

3.3.3. Results of graphene–MoS₂ mixture as anode material

Figures 7 and **8** exhibit SEM images of MoS_2/graphene slurry layers with mixing ratios of 30 : 70 and 50 : 50 SEM images show that materials were good mixed, but not evenly completely.
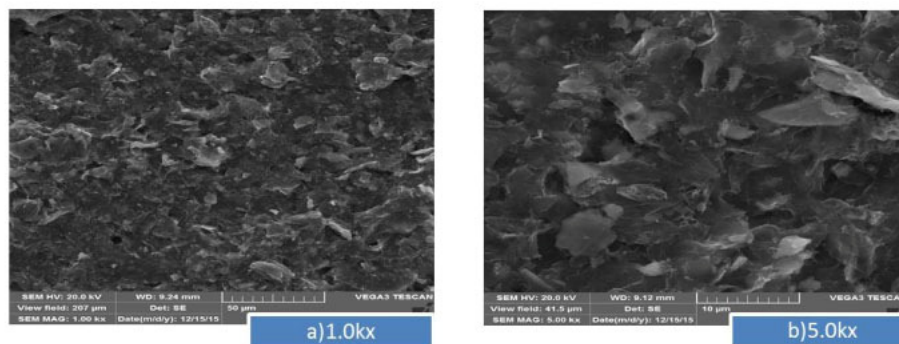

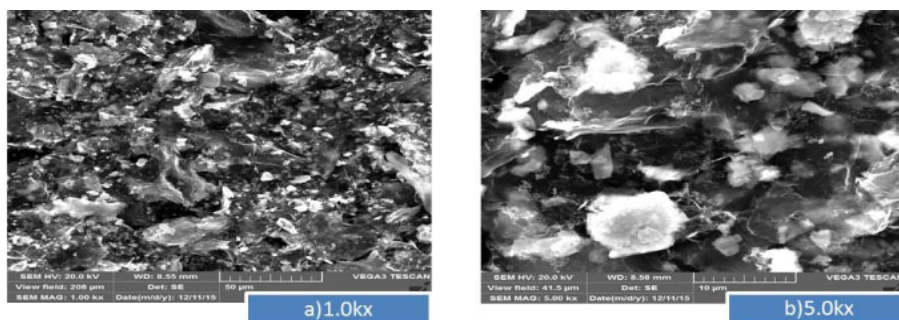**Figure 7.** SEM images of graphene–MoS₂ 30 : 70 layer a) $1.0k_x$, b) $5.0k_x$.

Figure 8. SEM images of graphene–MoS₂ 50 : 50 layer a) $1.0k_x$, b) $5.0k_x$.

3.4. Results of coin battery performances

Thermally exfoliated graphene and graphene-metal nanocomposites eere tested as an anode in LIBs. For this 2032 coin cells were assembled inside a glove box (MBraun Labstar) with oxygen and moisture content < 1 ppm.
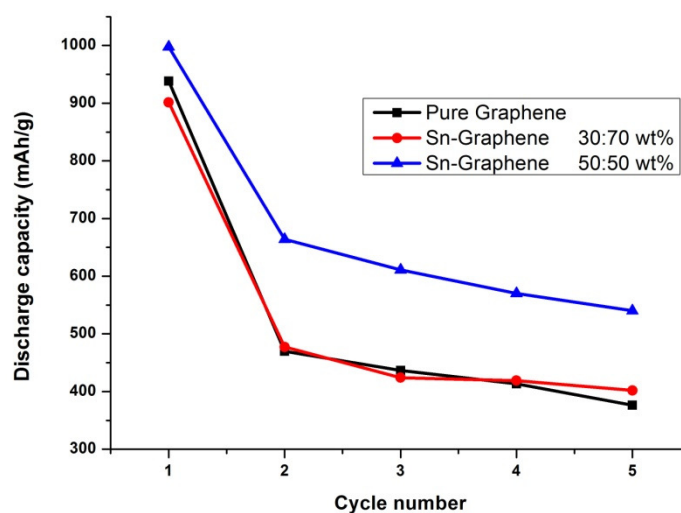
Figure 9. Discharge capacity curves of graphene–Sn samples and pure graphene.

270

Figure 9 shows discharge capacities of 50 and 30 wt. % Sn mixed with graphene samples and pure graphene for the first 5 cycles. Initial discharge capacities of samples are 997 and 901 mA h / g for 50 and 30 wt. % Sn mixed with graphene, respectively. In agreement with literature data, 50 wt. % Sn mixed with graphene's discharge capacity stabilized around ~ 540 mA h / g which is greater than that of the pure graphene.
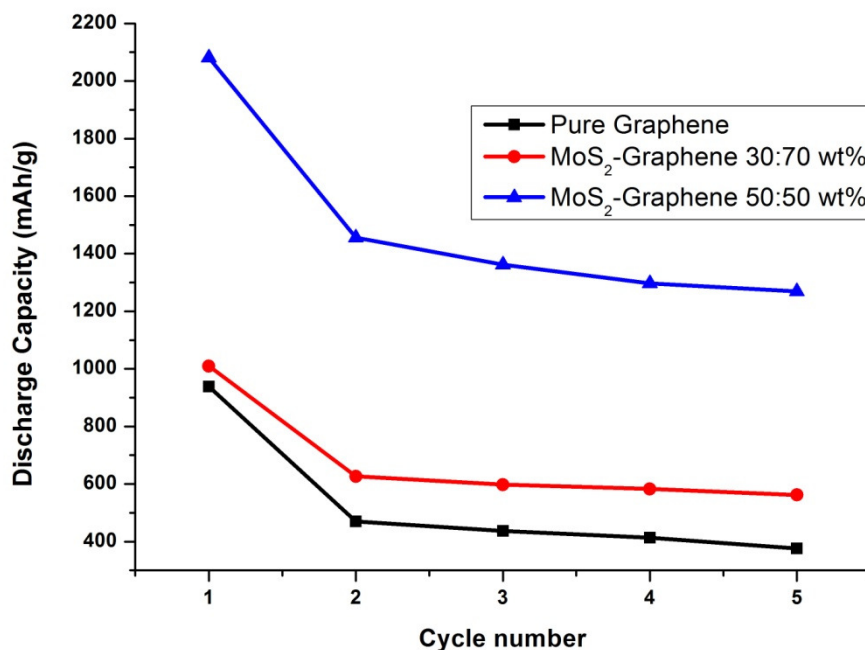

Figure 10. Discharge capacity curves of graphene–MoS₂ samples and pure graphene.
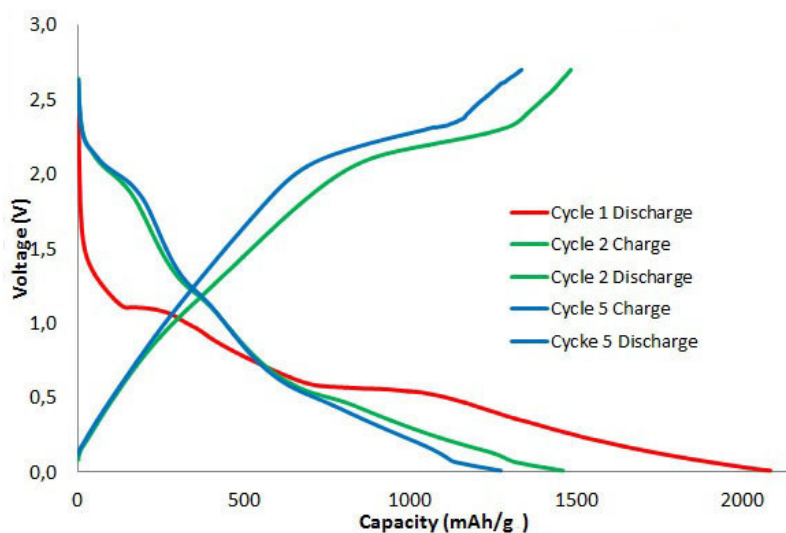

Figure 11. Electrochemical performances of 50 : 50 wt. % MoS₂–graphene. Charge / discharge profile between 2.7 – 0.01 V.

Figure 10 shows discharge capacities of 50 and 30 wt. % MoS₂ mixed with graphene samples and pure graphene for the first 5 cycles. Initial discharge capacities of samples are 2080 and 1009 mA h / g wt. % MoS₂ mixed graphene, respectively. The 50 wt. % MoS₂ mixed with graphene sample seemed to work the best. After first cycle, its discharge capacity stabilized around 1269 mA h / g. **Figure 11** also represents the voltage vs. capacity curves of 50 wt. % MoS₂ mixed with graphene sample at first, second and fifth cycle.

5. Conclusion

In this work, graphene is synthesized by thermal reduction of graphite oxide, properties and battery performances of metal mixed graphene anode for lithium ion batteries have been investigated. Tin, molybdenum disulfide were used as additives. Samples were prepared by mixing mechnacially. No other treatment has been applied to get graphene mixture. Obtained samples are characterized by surface electron microscope (SEM). Graphite oxide and graphene samples were characterized by X-ray diffration (XRD), Raman spectroscopy.

For electrochemical characterization, galvanostatic measurements have been conducted after the fabrication of coin lithium ion batteries. At the galvanostatic measurement of tin mixed graphene, 50 wt. % results has come better than graphene for disharge capacity. On the other hand MoS_2 mixed graphene 50 wt. % cell showed promising electrode performance for lithium ion batteries with large discharge capacity of ~ 2080 mA h / g and stabilized around 1270 mA h / g.

In summary, this study confirms that discharge capacities can be improved by preparing the anode as composites, which consists of metals and graphene, as long as the size of the used particles is in nm-region.

References

1. B. Kang, G. Cedar. Nature, 2009, 458, 190.
2. J. Xu, S. Dou, H. Liu, L. Dai. Nano Energy, 2013, 2, 439.
3. R. Krishnan, T.-M. Lu, N. Koratkar. Nano Lett., 2011, 11, 377.
4. C. Wang, Y. Zhou, M.Y. Ge. J. Am. Chem. Soc., 2010, 132, 46.
5. Z. M. Cui, L.Y. Hang, W. G. Song. Chem. Mater., 2009, 21, 1162.
6. S. B. Yang, G. L. Cui, S. P. Pang. Chem. Sus. Chem., 2010, 3, 236.
7. A. K. Geim, K. S. Novoselov. Nat. Mater., 2007, 6, 183.
8. S. Park, R. S. Ruoff. Nat. Nanotechnol., 2009, 4, 217.
9. F. Y. Su, Y. B. He, B. Li, X. C. Chen. Nano Energy, 2012, 1, 429.
10. W. Wang, I. Ruiz, S. Guo, Z. Favors, H.H. Bay. Nano Energy, 2014, 3, 113.
11. E. J. Yoo, J. Kim, E. Hosono. Nano Lett., 2008, 8, 2277.
12. T. Bharadwaj, A. Antic, B. Pavan. J. Am. Chem. Soc., 2010, 132, 12556.

EFFECT OF PAINT REMOVAL PROCESS ON CRACK DETECTABILITY USING LIQUID PENETRATION INSPECTION METHOD

A. Merati, Ph. Lo, T. Despinic, M. Yanishevsky, M. Genest

National Research Council Canada
NRC Aerospace
Ottawa, Canada
Philip.Lo@nrc-cnrc.gc.ca

Abstract

The removal of paint from aircraft structures is essential in crack detection during routine non-destructive testing (NDT) procedures. Current paint removal methods, including abrasive media blasting and chemical stripping, have the potential to mask surface cracks and decrease the effectiveness of liquid penetrant inspections (LPI). This study utilizes standard NDT practices to compare a new atmospheric plasma technology with conventional paint stripping techniques in their ability to remove paint without negatively affecting the LPI process. Using aerospace aluminium 2024–T3 and 7075–T6 test panels with fatigue induced cracks, the effectiveness of the atmospheric plasma system was compared to chemical paint stripping and media blasting methods undergoing a routine liquid penetrant inspection. The results indicated that atmospheric plasma had no negative ramifications on detecting fatigue cracks in the substrates, and did not alter their heat treatment, conductivity or hardness.

1. Introduction

The conventional methods for removing paint employed throughout the Canadian Forces mainly include environmentally unfriendly chemical stripping and abrasive media blasting [1, 2]. These paint removal methods could also adversely affect the effectiveness of surface inspection during routine maintenance procedures if entrapped media or residues from these paint stripping methods mask surface cracks making routine inspection using liquid penetrant inspection (LPI) [3] less effective and challenging. A new approach to paint stripping, using atmospheric plasma (AP), has the potential to replace conventional de-painting methods. The following subsections briefly introduce the paint removal techniques and non-destructive LPI and eddy current (EC) inspection methods for aerospace structures.

Chemical stripping involves the use of hazardous chemicals, which are typically high in volatile organic compounds (VOC) and hazardous air pollutants (HAP). Long term exposure to these chemicals, which are considered carcinogens and toxins, also pose risk to worker health.

In conventional chemical paint stripping, the chemical paint remover is applied to the surface, left untouched for a specified period of time, and then removed by scraping with soft tools and water. This paint stripping method involves minimal equipment and worker training. A new generation of environmentally safe stripper, EFS–2500, which has low volatility, was used in this study.

In this study we utilized type VII starch-acrylic, which is a gentle abrasive media that consists of grains of corn starch with 5% acrylic content (type VII, MIL–P–85891A), ranged in size from 100 to 900 μm. It is projected using compressed air at low pressures to remove the coating from substrate materials [4].

Abrasive media blasting typically results in a substantial quantity of solid waste consisting of paint and blast residues.Both types waste from chemical and media blasting are subject to control under increasingly stringent environmental and safety regulations and its disposal is costly.

The new atmospheric plasma (AP) paint removal process claims to be environmentally benign with only electricity and compressed air as the feed gas for operation. The process is done in a working chamber that requires an exhaust and a filtration system. The power supply in the AP process produces a high frequency electromagnetic field to generate 'cold' plasma [5]. The plasma generates a high velocity flow of chemically active nitrogen and oxygen radicals. The chemical energy oxidizes the organic component found in paints and coatings, converting much of the removed paint into harmless gases such as water vapour, CO_2, and solid residue.

Liquid penetrant inspection (LPI) is a non-destructive method used for revealing discontinuities that are open to the surface of solid materials (essentially nonporous materials). The liquid used in LPI seeps into various types of minute surface openings by capillary action. After the surface is cleaned, a developer is applied which draws the penetrant back out and forms an indication on the surface. The process is well suited to the detection of all types of surface cracks, laps, porosities, and is extensively used for the inspection of products made of different materials: metals, ceramics, and plastics. The process steps are schematically illustrated in **Figure 1**. LPI is inexpensive and a reasonably rapid inspection process using simple equipment and is applicable on a wide variety of parts with complex geometry. The main limitations of LPI are undetectable subsurface discontinuities that are not open to the surface and materials that are sensitive to surface preparation. Also, entrapped contaminants may mask discontinuities if they are not removed prior to inspection [6].
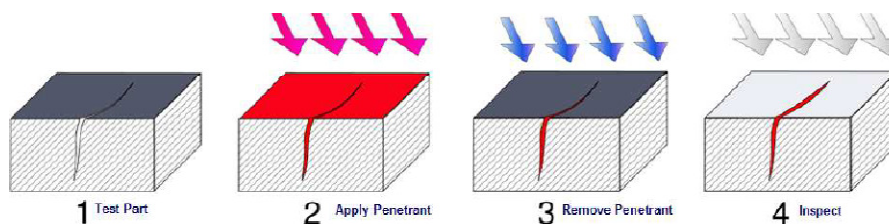

Figure 1. Diagram of the principles and steps of an LPI process.

Eddy current (EC) inspection has developed into one of the most versatile methods that can be used for variety of measurements and inspection of conductive materials. It is based on the principle whereby a coil carrying an alternating current is placed in close proximity to an electrically conductive specimen. Eddy current can be used to measure or identify conditions and properties such as electrical conductivity, heat treatment condition, and physical dimensions such as the thickness of a nonconductive coating and near-surface discontinuities.

The objective in this study was to compare the effectiveness of the AP process with that of chemical and media blasting methods in removing the paint on aluminium panels with cracks, and their effect on crack detectability using non-destructive evaluation (NDE) processes. LPI was employed after the paint removal processes and the cracks were measured before and after for comparative analysis.

2. Materials and procedure

For this study, two heat-treatable conventional aerospace aluminium alloy panels: 2024–T3 thin (0.0625 ″) and 7075–T6 thick (0.250 ″), were prepared with coatings of paint and primer applied to their surface and then exposed to different paint removal methods: AP, starch media blast, and chemical paint stripping. It was assumed that the effective methods of paint removal should not mask surface cracks or compromise the ability to reliably assess the state of damage affecting aircraft structural integrity.

Test panels with 1/8 ″ through holes with 0.015 ″ electron discharge machining (EDM) notches were prepared by Elpa Inc. They were sent to the Quality Engineering Test Establishment (QETE) for surface coating. A schematic of the layout of the holes are shown in **Figure 2a**.
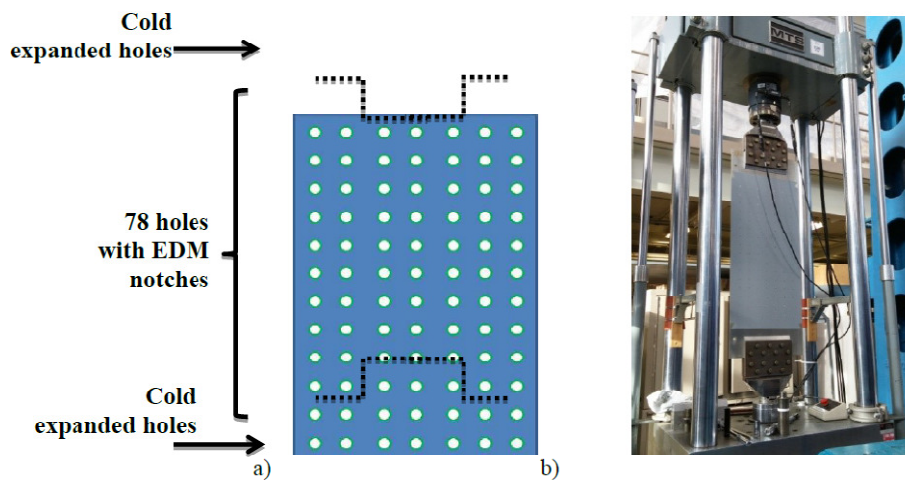

Figure 2. Test panels: a) containing 78 holes 0.125 ″ in diameter with machined 0.015 ″ EDM notches in one side to facilitate crack nucleation and propagation and b) test panel mounted in a MTS uniaxial load frame for fatigue testing.

Both the test panels of 7075–T6 and 2024–T3 aluminium were coated with a yellow MIL–PRF–23377 type 1 class 2 primer, each respectively having white / grey MIL–PRF–85285 Fed–Std–595C topcoats [7].

An MTS uniaxial load frame (ULF) was used to cyclically load the panels and induce fatigue cracking at the notches. As shown in **Figure 2b**, each end of the panel was gripped at the hydraulic actuators / load cell of the load frame and fatigue loaded using a sinusoidal waveform at a gross maximum stress of 14 ksi, load ratio $R = 0.1$, and a frequency of 3 Hz. The testing parameters and the resulting number of cycles to produce cracks of a variety of sizes are listed in **Table 1**.

Table 1. Fatigue parameters used to pre-crack the aluminium panels.

Aluminium panel	Target max / min Loads(lbf)	Target max stress (ksi)	Total average number of cycles	Average machine runtime (h)
2024–T3 (thin 0.0625 ″)*	14000 / 1400	14	164261	16.3
7075–T6 (thin 0.0625 ″)	14000 / 1400	14	80381	8.2
2024–T3 (thick 0.250 ″)	56000 / 5600	14	169276	17
7075–T6 (thick 0.250 ″)*	56000 / 5600	14	54762	6

*Panels used for paint stripping

Fatigue cycling was stopped after each panel showed sufficiently large cracks. In total, four different aluminium panels were prepared by fatigue testing: 2024–T3 and 7075–T6, both with thin (0.0625 ″) and thick (0.250 ″) variations. The panels were then scanned using a TecScaneddy current (EC) Scanner to map out cracks from each hole, as shown in **Figure 3**.
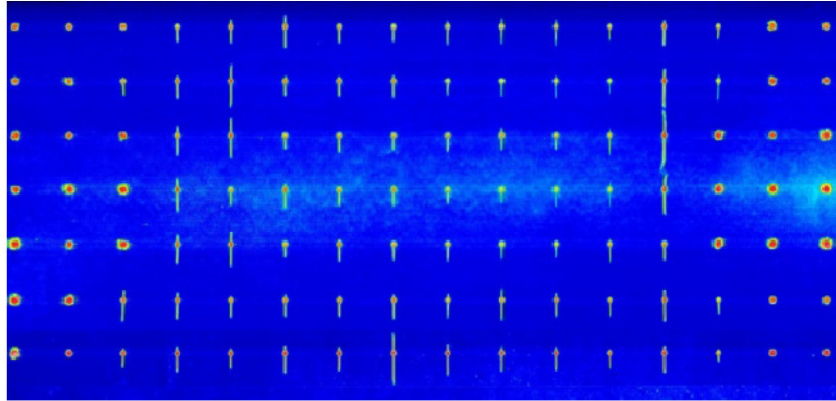

Figure 3. Fatigue tested panels scanned by EC showing
a typical C–Scan of a 7075–T6 aluminium panel outlining
the holes and fatigue cracks of varying sizes.

The fatigue tested panels were then divided into three sections and cut for the comparisons of chemical, starch media blasting, and AP paint removal procedures as shown in **Figure 4**.
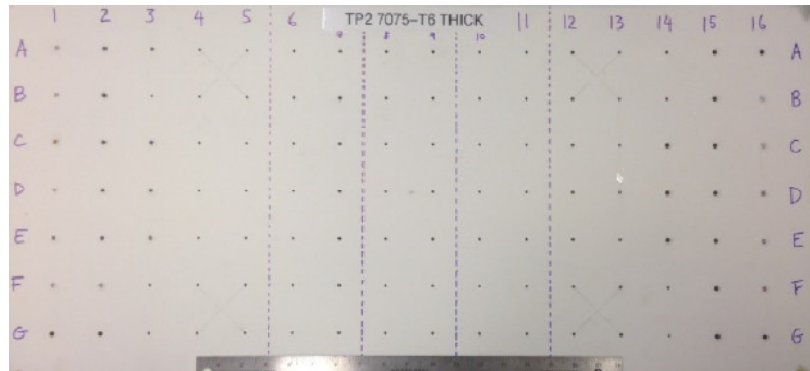

Figure 4. Top view of the 7075–T6 aluminium
testpanel showing coordinate labels and cut lines.

To determine whether the panel sections had been altered due to the excessive heat or the peening effect by media during paint removal, conductivity and hardness tests were performed on all panel sections in accordance to ASTM E1004–09 [8] and ASTM E18–15 [9], before and after the paint removal treatments.

With preparations completed, the test panel sections were exposed to AP, starch-acrylic media (type VII) blasting, and chemical solution paint removal processes for comparative purposes.**Table 2**summarizes process parameters used for each paint stripping method performed.

Once each paint stripping process was completed, each panel section was visually inspected for the extent of paint removal and damages, such as burns or warping. Cracks were then examined in more detail for possible presence of residue entrapped in the cracks. All panel sections were then inspected by LPI to assess and compare the three paint removal techniques, which was the main goal of this report.

Process	Process parameters		Comments
NRC / atmospheric plasma	Plasma pen speed	10 in / s	Constant parameters
	Plasma pen height	0.25 in	Pen to surface distance, constant parameter
	Passes per stripe	1	Number of times the plasma pen passes over a stripe in one direction, constant parameter
	Stripes per swath	15	Number of stripes in one section of set parameters, constant parameter
	Distance between stripes	0.05 in	Constant parameters
Starch-acrylic media(type VII eStripGPX20/50)	Plasma pen movement direction	Parallel to cracks	
	Nozzle pressure	1 bar	For each stripped region
		2 bar	
		2.5 bar	
	Nozzle to surface distance	15 ± 3 cm	Constant parameters
	Nozzle to surface angle	45 ± 10 °	
	Media flow rate	2.5– 3.0 kg/min	
	Blast direction	Perpendicular to cracks	
NRC / Chemical stripping	Solvent	EFS–2500	Panel sections were rinsed and scraped using soft tools following 24 h of exposure to EFS–2500
	Duration	24 h	

3. Results and discussions

As it is listed in **Table 2**, segments of the painted and fatigue tested aluminium panels (**Figure 5**) were exposed to different de-painting processes. The following text describes the condition of the panels and their cracks investigated by visual and optical microscopic methods and a discussion on the findings.
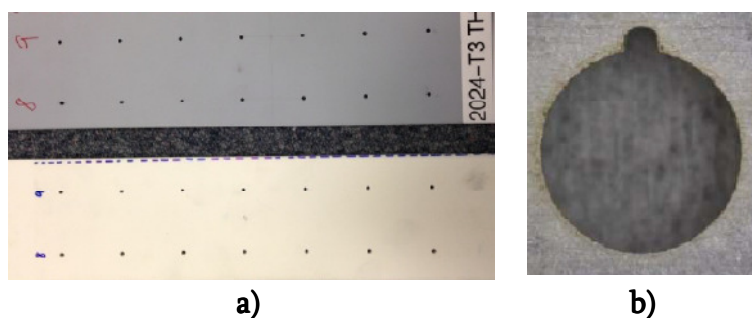

a)   b)

Figure 5. Painted aluminium panels with holes and EDM notches machined prior to fatigue testing: a) top – 2024–T3 aluminium thin panel, bottom – 7075–T6 aluminium thick panel; and b) close up of a hole (1/8 ″ in diameter) and EDM notch.

Each aluminium panel was coated with a yellow epoxy–polyamide (MILGUARD–23377) primer and a white/grey polyurethane (MIL–PRF–85285D) topcoat [10]. An Elcometer instrument, which is an EC thickness measurement device, was used to make thickness maps for both aluminium panels.

Figure 6 shows the cross section for the 2024–T3 aluminium panel in the regions of maximum and minimum total paint thicknesses, which were about 115 and 51 μm, respectively. The corresponding paint thickness measurements using the Elcometer instrument were about 115 and 55 μm for the maximum and minimum thickness areas, respectively
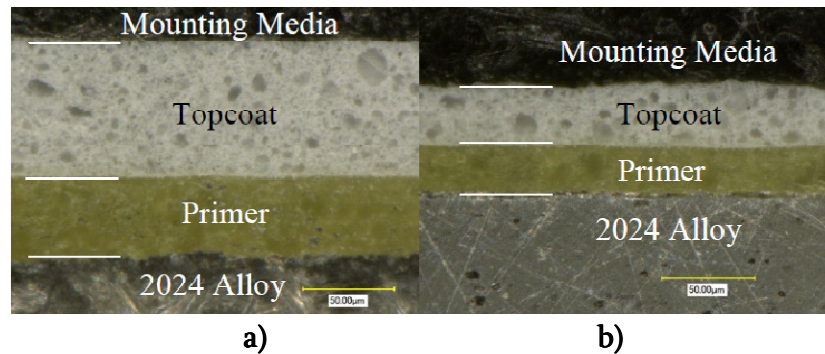

a)   b)

Figure 6. Cross sectional views of the 2024–T3 aluminium panel: a) cross section in the location of the maximum paint thickness (yellow primer approximately 44 μm thick and grey topcoat approximately 73 μm thick)and b) cross section in the location of minimum paint thickness (yellowprimer approximately 30 μm thick and grey topcoat approximately 30 μm thick).

The LPI technique is capable of detecting surface discontinuities. The fluorescent dye is sprayed and allowed to dwell upon the surface to enable it to penetrate into the cracks. Following cleaning and developing, the cracks can be revealed, when exposed to a ultra-violet light, as shown in **Figure 7**.
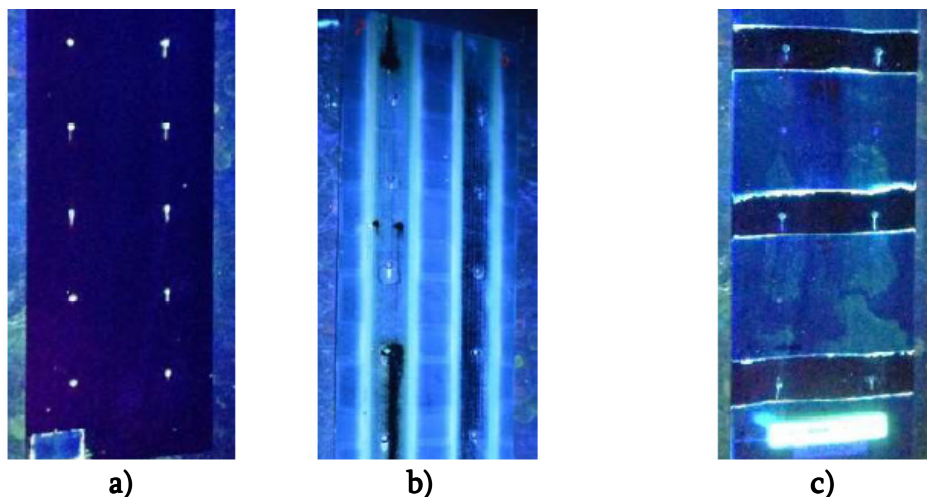

a)   b)   c)

Figure 7. Results of LPI penetrant examination under a ultra-violet light: a) chemical stripped test panel, b) starch mediablasted test panel,and c) AP stripped test panel.

During the LPI process, the tips of the cracks were marked on each panel, as shown in **Figure 8**. Crack measurements were then measured from the marks using an optical microscope to verify that debris had not masked cracks affecting LPI.
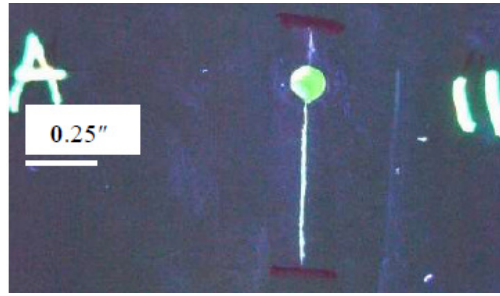
Figure 8. Fluorescent dye observed in
one ofthe cracks under ultra-violet light.

3.1. Chemical paint stripping

The new environmentally safe paint stripper, EFS–2500, was applied to both cutsections from test panels 7075–T6 and 2024–T3 aluminium. The process of the chemical stripping process can be seen in **Figure 9**.
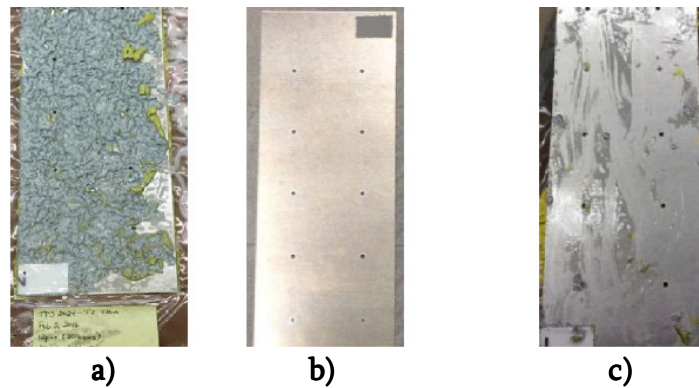

a)   b)   c)

Figure 9. Chemical paint stripping process: a) 20 h after
stripper application, b) 24 h after stripper application
andafter scrapping, and c) after rinsing with water.

Despite the slow stripping process requiring 24 h, the chemical process was successful in the complete removal of the topcoat and primer from the panel sections without harming the substrate, as shown in **Figure 10a**. **Figure 10b** depicts possible residue entrapments on the 7075–T6 panel. Cracks on the 2024–T3 panel sections were generally too narrow to be investigated even under high optical magnification using the Keyence microscope. From LPI, crack length measurements were similar to the original EC measurements, which indicate no negative effect of the chemical process on crack detection.
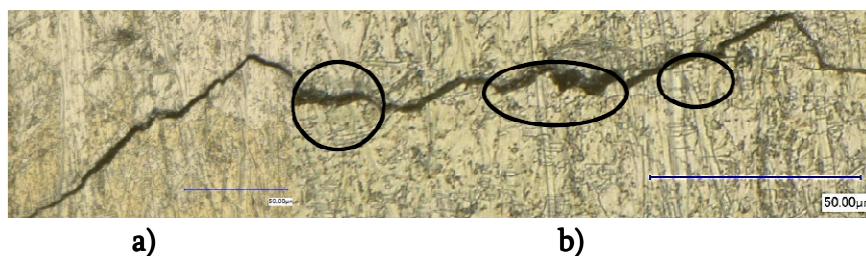

a)   b)

Figure 10. Close-up view of the aluminium panel sections
afterchemical paint removal showing: a) the absence of
residue, and b) an example of a crack with possible debris.

3.2. Starchmedia blast

Type VII starch-acrylic media was used to remove the primer and paint using three different nozzle pressures of 1 bar, 2 bar, and 2.5 bar with a mass flow rate ranging between 2.5 to 3 kg / min. Upon visual inspection of the substrate, the paint appeared to be completely removed from the panel section with no deformation, as shown in **Figure 11**. Further investigation on the cracks showed fine unknown debris trapped inside the cracks, as seen in **Figure 12**.
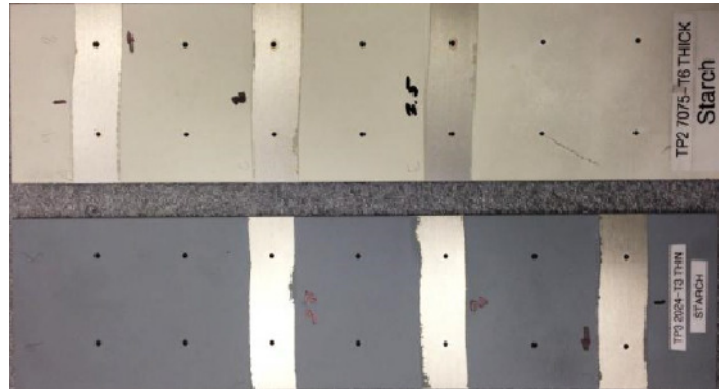

Figure 11. End result of type VII starch-acrylic media blasting.

Figure 12. Close-up view of unknown residues in the cracks(circled) of the test panel 7075–T6 aluminium.

In some cases, the crack was not fully exposed during the de-painting using media blast, which did not allow the optical measurement of some crack lengths. From the measurable crack lengths, the results showed no significant change prior to de-painting or after LPI. Again, despite evidence of some residue entrapment inside the cracks, it appears that this method of paint removal did not have a negative effect on LPI in terms of crack detection.

3.3. Atmospheric plasma

AP paint stripping was performed by NRC using a recently purchased atmospheric plasma solutions (APS) plasmaflux paint removal system shown in **Figure 13**. Prior to stripping the panel sections, optimal parameters were established in order to provide consistency in paint removal. Details of operating procedure for APS plasmaflux system is documented in a previous report [11].

After AP paint stripping, the aluminium panel sections were rinsed with water to remove most of the remaining paint residue left on the surface. **Figure 14** below shows the final condition of the aluminium panel sections after AP paint stripping.

Figure 13. Front view of APS plasma flux paint removal systemwith 3D robot and exhaust cabinet (left). Close up of the plasma plume (right).

Figure 14. Aluminium panels after plasma paint stripping, left-test panel 7075–T6, and right-test panel 2024-T3.

Upon optical analysis presented in **Figure 15**, possible debris appeared to be entrapped in the cracks, but less so when compared to the chemical and starch media blast processes. Each crack length was measured before the paint stripping, after paint stripping, and after the LPI process, which are listed in **Table 3**.

Figure 15. Close up view of a crack on the aluminium panelsection showing possible debris (circled) after plasma paint stripping.

Post-strip panel sections showed no visualdamages caused by the AP process. However, warping was observed on the thinner test panel 2024–T3 during the exposure to the AP plume. After cool-down following paint stripping, a general observation of test panel 2024–T3 showed no signs of permanent warping or damages.

In the case of AP de-painting, it was not necessarily the intent to completely strip the primer off of the panel sections, as long as the crack inspection was not hindered. Thickness measurements were made in the stripped regions after paint stripping and revealed an average thickness of the remaining primer to be 9 μm for the test panel 7075–T6 and approximately zero for test panel 2024–T3. The corresponding original average thicknesses (topcoat + primer) were 92 and 90 μm, respectively.

Further microscopic inspections revealed some localized splatters, which did not cover the entire stripped region, but were observed in isolated areas around the cracks (**Figure 16**). The black and white splatters found on the primer were also observed in previous AP paint removal studies involving aluminium [2].

Table 3. List of crack sizes before and after the AP paint stripping process.

TP2 7075–T6 aluminium – crack length prior to & after paint stripping			
Hole coordinates	Prior to stripping (inch)	After stripping (inch)	
	Eddy current + Image analysis	Microscope (Keyence)	LPI + microscop (Keyence)
E6	0.49	0.50	0.51
C6	0.53	0.53	0.56
C7	0.66	0.74	0.76
B6	0.66	0.73	0.72
B7	0.66	0.62	0.62
A7	0.62	0.73	0.71
D7	0.66	0.61	0.64
F6	0.72	0.77	0.76
E7	0.66	0.62	0.64
F7	0.68	0.83	0.83
G7	0.78	0.80	0.80
D6	0.80	0.89	0.89
TP3 2024–T3 aluminium – crack length prior to & after paint stripping			
Hole coordinates	Prior to stripping (inch)	After stripping (inch)	
	Eddy current + Image analysis	Microscope (Keyence)	LPI + Microscope (Keyence)
A6	0.43	0.44	0.40
A7	0.27	0.28	0.26
B6	0.27	0.28	0.27
B7	0.30	0.31	0.28
E7	0.33	0.34	0.33
C6	0.38	0.37	0.37
C7	0.36	0.37	0.35
D6	0.37	0.35	0.35
D7	0.35	0.35	0.34
E6	0.36	0.35	0.34
F6	0.37	0.37	0.36
F7	0.42	0.41	0.39

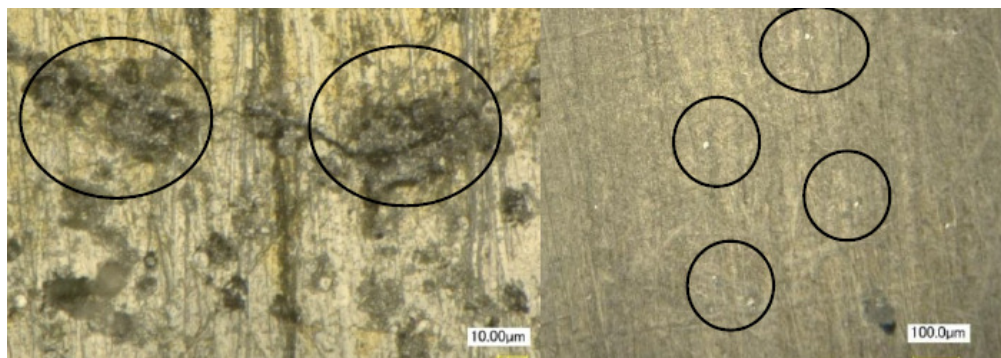a)   b)

Figure 16. Black and white splatters (circled) left on the substrate of the aluminium panels: a) black pits can beseen on 7075–T6; and b) white spots can be seen on 2024–T3.

In terms of the effect on crack detectability, the results showed that the crack measurements at different stages, before and after the AP de-painting process including the LPI inspection did not show different values. Similar to the other two processes, it appears that this method of paint removal did not have a negative effect on LPI in terms of crack detection.

To determine if the paint removal processes had subjected the panels to excessive heat / peening effect, conductivity and hardness measurements were conducted before and after paint stripping treatments, which are documented in **Table 4** below. From the results, it seems that all the measurements for the three paint stripping processes showed negligible differences in conductivity and hardness, which were not large enough to have altered the properties of the material. This illustrates that there was no considerable effect from any of the three processes on heat treatment and consequently the properties of the aluminium panels.

Table 4. Results of conductivity tests for test panel TP2 made of 7075–T6 and test panelTP3 made of 2024–T3 aluminium panels before and after paint removal process.

Process	Paint colour / Aluminiumpanels	Average conductivity (% Cu ~IACS 60 Hz)		Average hardness (Rb)	
		Before de-painting	After de-painting	Before de-painting	After de-painting
Atmospheric plasma	White thick TP2 7075–T6	32.92	32.80	87	87.3
	Grey thin TP3 2024–T3	30.93	30.82	75	76.9
Type VII Starch-acrylic	White thick TP2 7075–T6	32.92	32.92	87	90.7
	Grey thin TP3 2024–T3	30.93	30.91	75	77.4
NRC Chemical	White thick TP2 7075–T6	32.92	32.97	87	90.1
	Grey thin TP3 2024–T3	30.93	30.86	75	77.5

Note: The conductivity and hardness measurements were averaged from five measurements

4. Concluding remarks

The effectiveness of three paint stripping processes: chemical, type VII acrylic starch media, and AP were assessed by two main criteria: the extent of paint removal and the extent of debris entrapped in the cracks, which could affect crack detectability during LPI.

Of the three processes, chemical stripping managed to completely remove the paint and primer with no induced warping or damage to the substrate. Post-strip macroscopic and microscopic examinations for all three processes revealed varying amounts of paint and debris residue in most of the cracks, but in general they did not appear to affect the LPI crack detection process. Also as a general conclusion, the presence of the primer did not appear to affect LPI detectability for the AP process. From the results (**Table 4**), it seems that there was no considerable effect from any of the three processes on heat treatment and consequently, the mechanical properties of the aluminium panels.

In summary, the selection of the appropriate paint removal method for a particular aircraft structure will depend on a number of factors: purpose and the extent of paint removal, accessibility of the structure, local environment and health and safety regulations, costs, and environmental concerns. For instance, if a high level of cleanliness is required, a two-step or combination of methods may be needed to achieve the appropriate end result.

This study has determined that Atmospheric Plasma is a technology that has the potential to replace current hazardous and costly paint removing methods without affecting LPI crack detectability. The results of future studies will help determine its acceptability for industrial use. It is conceivable that, with the environmental and all other advantages of this technology, Atmospheric Plasma technology may become an industrial standard for a wide range of applications in the future.

Acknowledgements

References

1. A. Merati, M. Yanishevsky, T. Despinic, Ph. Lo, V. Pankov. Metallographic Analysis of Paint Stripping Techniques – Atmospheric Plasma.Internal NRC Report – LTR–SMM–2016–0015.2016, Ottawa, NRC.
2. A. Merati, M. Yanishevsky, T. Despinic, Ph. Lo. Effect of Paint Removal Techniques on Crack Detectability – Liquid Penetrant Inspection – LTR–SMM–2016–0062.2016), Ottawa, NRC.
3. ASTM (2012)ASTM E165 / E165M Standard Practice for Liquid Penetrant Examination for General Industry.
4. T. Foster. Examination of the Possible use of Type VII – Technical Memorandum DRDC Atlantic TM2009–293.2010, Defence R&D Canada – Atlantic.
5. P. Yancey. Atmospheric Plasma De-painting.2012, Atmospheric Plasma Solutions, Inc.
6. N. Tracy. Nondestructive Evaluations (DE) Exploratory Development for Air Force Systems – AFRL–RX–WP–TR–2010–4200, 2009.
7. http://www.simcocoatings.com/, 2012, visited 10 May 2016.
8. ASTM E1004–09 Standard Test Method for Determining Electrical Conductivity Using the Electromagnetic (Eddy–Current) Method, 2009.
9. ASTM E18–15 Standard Test Methods for Rockwell Hardness of Metallic Materials, 2015.
10. http://www.resene.co.nz/archspec/cpd_earn_points/pdfs/CPD_primerssealersandunder coats.pdf,2009, visited 10 May 2016.
11. M. Yanishevsky, V. Pankov. NRC Operating Procedure for APS Plasma Flux Paint Removal System – LTR–SMPL–2015–0144.2015. 2015, Ottawa, NRC.

REMARKS TO THE PRESENTATION OF FATHI HABASHI
"PURPLE OF CASSIUS: NANO GOLD OR COLLOIDAL GOLD?"

Learning that Fathi Habashi will give at the Nano 2016 conference a presentation on colloidal gold* I remembered that my father Peter Adolf Thiessen (1899 – 1990) in 1925 wrote a book together with his teacher, Nobel Laureate Richard Zsigmondy: "Das kolloide Gold". The title of his doctor thesis in 1923 at Göttingen University had already the same title. In this book several times they mentioned the "Purple of Cassius". The book was cited by Habashi in his presentation. Habashi also wrote a book: "Gold. History, Metallurgy, Culture" in which he mentioned Purple of Cassius.
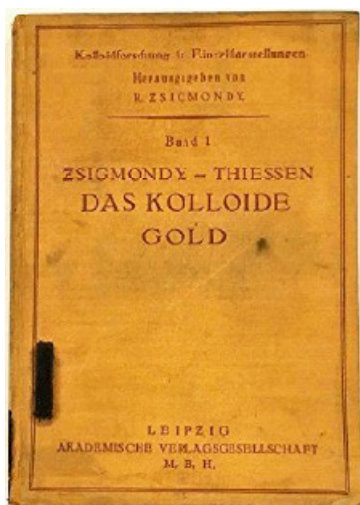
Book on colloidal gold by
Zsigmondy and Thiessen, 1925.
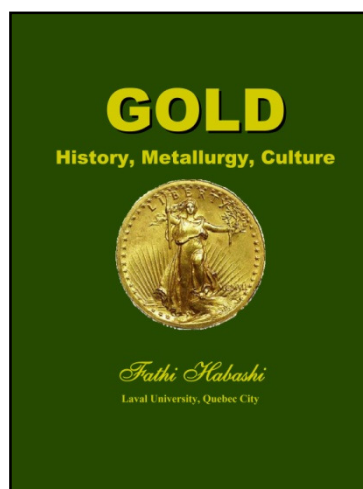
Gold book by
Habashi, 2009.

Peter Adolf Thiessen
(1899 – 1990).

The Thiessen family
in Sukhumi, 1952.

It is quit astonishing that, firstlyI met Fathi Habashi and his wife Nadia not earlier than at the Nano 2014 in Tbilisi, though many times before we were at the same time at the same places in different parts of the world.

Klaus Thiessen, Nadia Habashi
and Fathi Habashi in
Katheti Region (Georgia).

Klaus Thiessen at the Alaverdi
Monastery (Katheti, Georgia).
Photo Nadia Habashi.

Klaus Thiessen, Nadia Habashi
and Fathi Habashi in Tbilisi.

Museum pieces of glass
coloured with purple of Cassius.

We became friends in Georgia – see the pictures at the excursion to the beautiful Kakheti (2014) and Tbilisi (2016).

Klaus Thiessen

November 3, 2016

4th INTERNATIONAL CONFERENCE
"NANOTECHNOLOGIES" (NANO – 2016)

Nanotechnology is known as one of the disruptingthe present-day technologies, which are able to change the life of a society essentially. This is due to the fact that in the presence of a very fine structure, called as nanostructure, many useful properties of common materials are enhanced significantly. Moreover, many of materials reveal fundamentally new properties that are not inherent in the bulk material, the material of same chemical composition, but without the nanostructure.For their part, enhanced and new physical, chemical and technological properties of nanomaterials open the way to wide application in all the fields, such as industry, medicine, ecology, education, etc. This explains the increased interest in nanosciences serving for nanotechnology development.

Prof. Zurab Gasitashvili, Deputy Rector for Science of Georgian Technical University, opens the Nano – 2016 Conference

Plenary and Oral Sessions were held in George Nikoadze Conference Hall

In Georgia, International Conferences on nanotechnology held regularly from 2010 onwards every two years. And interest in these conferences is constantly growing. Suffice it to say that at the 4th International Conference "Nanotechnologies", October 24 – 27, 2016, Tbilisi, Georgia (Nano – 2016) there were submitted 209 papers by authors from many leading universities and research centers of 32 countries (Armenia, Azerbaijan, Belarus, Canada, China, Czech Republic, Denmark, Egypt, Estonia, France, Georgia, Germany, Hungary, India, Iran, Iraq, Israel, Italy, Japan, Kazakhstan, Mexico, Poland, Romania, Russia, Saudi Arabia, Slovak Republic, Spain, Switzerland, Turkey, Tunis, Ukraine, and USA). Such anincreasing interest in Georgia Nanotechsseems to be related not only to the overall relevance of subjects, but to the results achieved by the Georgian scientists in recent years as well, including those from the Georgian Technical University, the organizer of this scientific forum.

The 4th International Conference "Nanotechnologies" (Nano – 2016) devoted the methods of synthesizing of nanomaterials, studying their structure, chemical, physical and technological properties, as well as applications in techniques. The Conference provided an evaluation of the present state-of-art in this field of knowledge, new achievements and prospects of developments in nanotechnologies.

GTU's students lobby of the Conference

Conference organizers: Prof. Alex Gerasimov
(Georgia)and Prof. Levan Chkhartishvili (Georgia)

Nano – 2016 was organized and conducted by the International Scientific Committee: Chairman – Archil Prangishvili (Georgia), Vice-Chairmen – Zurab Gasitashvili (Georgia) and Alex Gerasimov (Georgia), Members – Rosa Abdulkarimova (Kazakhstan), Zhores Alferov (Russia), Hossein Aminian (Canada), Rick Becker (USA), Dieter Bimberg (Germany), Levan Chkhartishvili (Georgia), Russell Dupuis (USA), Toyohisa Fujita (Japan), Fathi Habashi (Canada), Bilgin Kaftanoglu (Turkey), Pawan Khanna (India), Boris Kharisov (Mexico), Laszlo Kotai (Hungary), Haldun Kurama (Turkey), George Kvesitadze (Georgia), Olena Lavrynenko (Ukraine), Sergey Maksimenko (Belarus), Fernand Marquis (USA), Victor Mordkovich (Russia), Valentine Parmon (Russia), Vladimir Sanin (Russia), Lina Sartinska (Ukraine), Sebastian Schlucker (Germany), Karsten Thiessen (Germany), Klaus Thiessen (Germany), Onuralp Yucel (Turkey), Pawel Zukowski (Poland) and Zbigniew Zytkiewicz (Poland), and National Organizing Committee: Chairman – Alex Gerasimov, Secretary – Levan Chkhartishvili, Members – Aliosha Bakuridze, Amiran Bibilashvili, Guram Chikladze, Mikheil Chikhradze, Nikoloz Chikhradze, Raphael Chikovani, George Chiradze, Archil Chirakadze, Guram Dgebuadze, Akaki Gigineishvili, Kakha Gorgadze, George Iluridze, David Jishiashvili, Paata Kervalishvili, Levan Matsaberidze, Vladimer Mikelashvili, Tamaz Minashvili, Shota Sidamonidze, David Tavkhelidze, Michael Vepkhvadze and Otar Zumburidze.

Presentation by Prof. Nodar
Kekelidze (Georgia); Chair:
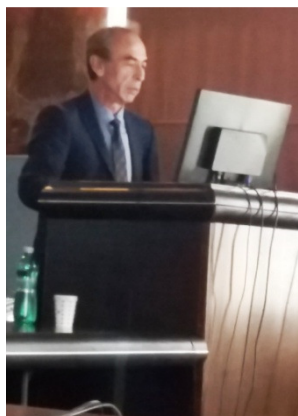Prof. Alex Gerasimov (Georgia)

Presentation
by Prof. Fernand
Marquis (USA)

Presentation
by Dr.Hossein
Aminian (Canada)

Presentation
by Prof. Karsten
Thiessen (Germany)

Presentation
by Prof. Haldun
Kurama (Turkey)

Presentation
by Dr. Lina
Sartinska (Ukraine)

Presentation
by Prof. Victor
Mordkovich (Russia)
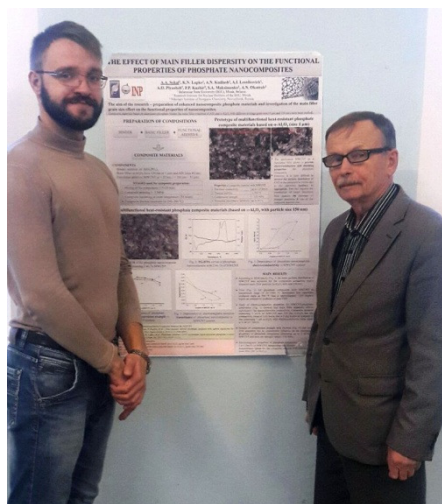
Presentation
by Dr. Elvin
Malikov (Azerbaijan)

Presentation by Prof. Vladimir Sanin (Russia) provoked a lively discussion

In their Invited, Oral and Poster Presentations, participants described the results of experimental investigations of nanosystems, as well as theoretical approaches to their modeling. Conference was a forum of nanoscientists for broad interdisciplinary discussions and, therefore, not only intensified the actual collaboration, but also facilitated the future developments of international cooperation in nanotechnology research.

Aliaksei Sokal (Belarus)
and Prof. Konstantin Lapko
(Belarus) present their Poster

At the Poster Session

Prof. Levan Chkhartishvili (Georgia),
Dr. Nino Ponjavidze (Georgia) and
Prof. Ahmed El-Saghier (Egypt)

Dr. OlenaBerdnikova (Ukraine) in front of the Administrative Campus of the Georgian Technical University; at her Poster together with Prof. Rosa Abdulkarimova (Kazakhtan); and during the banquet

Presentations covered following fields of nanoscience: nanotechnology, nanophysics, nanochemistry, nanobiology and nanomedicine, nano materials science, nanoengineering, nano safety and nano education.
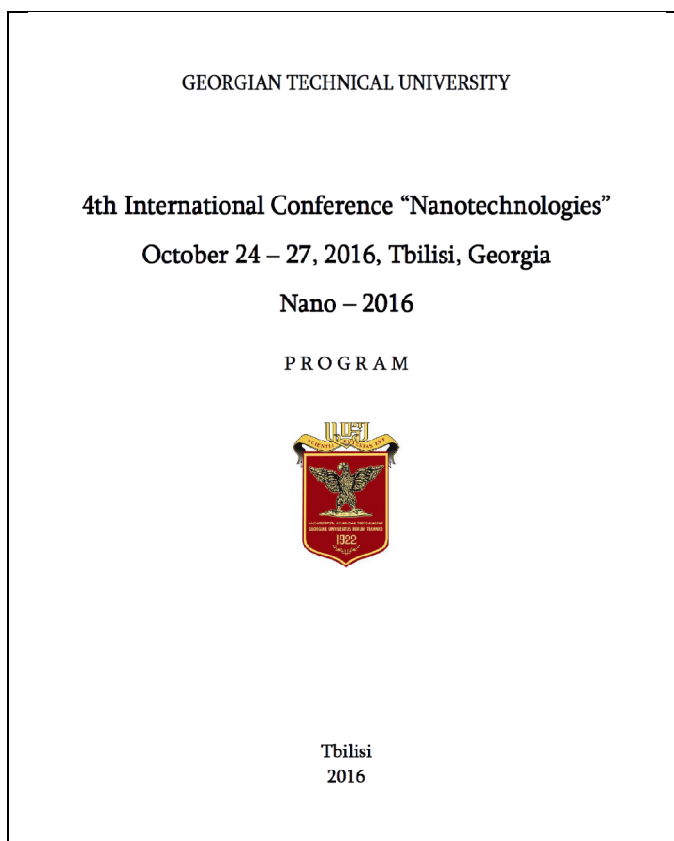
Title page of the Program   Title page of the Abstracts Book

All the submitted papaer-abstracts were published electronically in the Abstracts Book (Compiliers: A. Gerasimov & L. Chkhartishvili; 250 copyies on CDs). Full-texts of the selected conference papers are published in 4 conference journals: Nano Studies, European Chemical Bulletin, Journal of Pharmaceutical & Applied Chemistry, and American Journal of Nano Research & Applications (Special Issue: "Nanotechnologies").

It should be noted that this time, in parallel with the Conference sessions, it was held the Exhibition of measuring and technology equipment used in nanotechnology.

Dr. Rached Jaafar (Switzerland), Eastern European Area Manager of the Swiss company NanoSurf, presented a new atomic force microscope designed for nanoscale-studying of the surface of materials. For universities, it is too important that this company produces not only the research nanotechniques, but also – educational.

Founded in 1997, Nanosurf is a Swiss based high-tech company providing scanning probe microscopes to customers around the globe. The product range starts with very compact AFM and STM instruments, followed by state-of-the-art research atomic force microscope systems, all the way up to fully customized and comprehensive next-level solutions. Its customers in research, industry and teaching value the innovative approach, modularity, and ease of use of products. Nanosurf is the global market leader for AFM-based single-cell and nano manipulation tools, AFM-based diagnostics and automatic nanomechanical analysis, AFM and STM for nanoeducation, compact and mountable AFM systems, and custom-built AFM systems. Nanosurf can be contacted at: info@nanosurf.com or www.nanosurf.com.
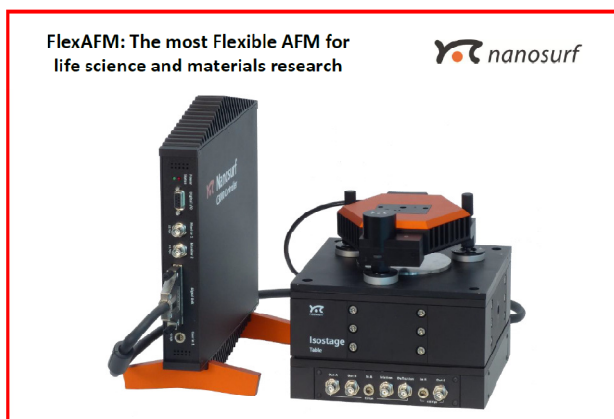

Dr. Rached Jaafar (Switzerland), Eastern European Area Manager of the Swiss company NanoSurf, presenting new atomic force microscope designed for nanoscale-studying of materials surface

Dr. Zaur Berishvili (Georgia) presenting his recent invention "High performance planar magnetron spraying apparatus with rotating magnetic field"protected by the international patent

Dr. Zaur Berishvili (Georgia) presented his recent invention "High performance planar magnetron spraying apparatus with rotating magnetic field" protected by the international patent. It is an improved portable magnetron-facility that allows obtaining extremely thin films of various materials.

The proposed innovation relates to an electronic engineering and can be used to produce thin filmmaterials with improved physical properties using technology of magnetron sputtering in vacuum. It can be used in microelectronics, optics, quantum optics, integrated optics and nanotechnology. Today in research laboratories and manufactures similar manufacturing apparatus for producing thin films do not have such a high target utilization ratio, how has this device (70 – 90 %). Asfor the ability of uniform distribution and control the discharge current density, these issuesare not even considered. Despite some success in this field, to meet the requirements of modern complex technologies it is necessary to examine in more details the processes in a planar magnetron sputtering device with a rotating magnetic field. Presented features and innovations of high-performance planar magnetron sputter coater show that the developed device may be competitive and interest of professionals. Author can be contacted at: zaurberi7@yahoo.com.

FlexAFM: The most Flexible AFM for
life science and materials research

nanosurf

Dr.ph ZAUR BERISHVILI
Planar Magnetron Spraying Apparatus
WIPO PCT/GE 2016000005 C23C 14/35 (2006.01) 26 April 2016
Nanotechnology: Nanofilms Deposition

Dr. George Kekelidze (Russia), Prof. Nodar Kekelidze
(Georgia), Prof. Dieter Bimberg(Germany), Prof. Sergey
Maksimenko (Belarus), Prof. KlausThiessen (Germany),
and Prof. Russell Dupuis (USA) in Old Tbilisi

Conference social program included: welcome partyand gala-banquet for conference participants, and the trip in city Gori and its vicinity. In particular, they visited and learned with a great interest the Joseph Stalin Museum and the ancient cave townUplistsikhe.

The Joseph Stalin Museum is a museum in Gori, dedicated to the life of Joseph Stalin, the leader of the Soviet Union, who was born in Gori.

With the independence movement of Georgia, the museum was closed in 1989, but has since been reopened and retained until recent years its Soviet-era characteristics. In the aftermath of the 2008 Russian–Georgian war, it was announced that the Stalin Museum is a falsification of history – a typical example of Soviet propaganda and it would be reorganized into the Museum of Russian Aggression. However, in 2012 the Municipal Assembly of Gori voted to put an end to plans to change the museum content. Now it is a popular tourist attraction. The museum has three sections, all located in the central square of Gori.

Enshrined within a pavilion there is a small wooden hut, in which Stalin (Jughashvili) was born in 1879 and spent his first four years. The hut is a duplex, and Stalin's father, a local shoemaker, rented the one room on the left hand side of the building and maintained a workshop in the basement.

Joseph Stalin Museum (Exterier)

Joseph Stalin Museum (Interier)

Prof. Rosa Abdulkarimova (Kazakhstan)
and Prof. Levan Chkhartishvili (Georgia)
at wooden hut, in which Stalin was born

Stalin's personal railway carriage

In the main campus of the complex, the exhibits are divided into six halls in roughly chronological order, and contain many items actually or allegedly owned by Stalin, including some of his office furniture, his personal effects and gifts made to him over the years. There is also much illustration by way of documentation, photographs, paintings and newspaper articles. There is Stalin's personal railway carriageto one side of the museum. The green Pullman carriage, which is armour plated, was used by Stalin from 1941 onwards, including his attendances at the Yalta and the Tehran Conferences.

Uplistsikhe– ancient Cave Town (around 11th c. BC)

The cave town was seen in unusually,
for this time of year, cold weather

Dr. Genadji Dolinskiyi (Ukraine),
Dr. Olena Lavrynenko, and
Prof. Levan Chkhartishvili (Georgia)

Uplistsikheis an ancient Cave Townthat witnessed key events of Georgian history.Located in Eastern Georgia, Uplistsikhe (literally "Lord's Fortress") is an abandoned rock-hewn town, which once have played an important role in Georgian state. The town was founded in the late Bronze Age, around 11th c. BC, and continued to be inhabited until 13th century AD. Between the 6th c. BC and the 11th c. AD, Uplistsikhe was one of the most important political and religious centers of pre-Christian and Chtisian (from 4th c.) Kartli – one of the predecessors of the Georgian state.

Gala-banquet

St. George Monument,
Liberty Square, Tbilisi, Georgia

Tbilisi by night, Georgia

All the participants of the 4th International Conference "Nanotechnologies", October 24 – 27, 2016, Tbilisi, Georgia (Nano – 2016) agreed that Conference was a high scintific level forum, which has served as a good platform for a broad exchange of views between experts in all topical areas of nanosciences and helped in establishing and developing fruitful cooperation between the various research centers and scientists.

LevanChkhartishvili

November 11, 2016

რედაქტორისაგან: ჩემი "ნანო – 2016"

ჩემთვის, როგორც ნანომეცნიერებათა მიმართულების მკვლევარისათვის, გასული 2016 წელი საკმაოდ ნაყოფიერი და საინტერესო გამოდგა. ამიტომაც მინდოდა ამ წლის ზოგიერთი შთაბეჭდილება გამეზიარებინა *Namo Studies*-ის მკითხველისათვის.

წელი დაიწყო იმით, რომ დარგის ერთ-ერთ მაღალრეიტინგულ ჟურნალში *Nanoscale Research Letters* გამოქვეყნდა ჩემი სტატია [1], სადაც თეორიულადაა აღწერილი ახალი ნანოეფექტი – ელექტრული ველის წარმოქმნა ფენოვანი სტრუქტურის მქონე კრისტალური ნაჭრთების ნანონაწილაკების ზედაპირის მახლობლად. ეს ფიზიკური მოვლენა უდევს საფუძვლად ნანოსტრუქტურის მქონე ჰექსაგონალური ბორის ნიტრიდის გამოყენებით ნავთობისა და სხვა ორგანული დამაბინძურებლებისაგან წყლის გაწმენდის ახალ მეთოდს. ეფექტის თეორიულმა მექანიზმმა და მისი პრაქტიკული გამოყენების ფართო შესაძლებლობებმა მიიპყრო ჟურნალის *Science* ელექტრონული დამატების *Atlas of Science – Another View on Science* რედაქციის ყურადღება, რომელთაც შემომთავაზეს დამეწერა ჩემი სამეცნიერო სტატიის პოპულარული ვერსია, გასაგები მკითხველთა უფრო ფართო წრისათვის. სურათზე, რომელიც ამ ვერსიიდან [2] არის ამოღებული, თვალსაჩინოდაა ნაჩვენები ჰექსაგონალური ბორის ნიტრიდის თავისუფალ კრისტალურ ზედაპირზე არსებული ნანოზომის "კუნძულის" მახლობლად ელექტრული ველის წარმოქმნის და მის მიერ გარემოდან პოლარიზებული ნაწილაკების ფიზიკურად ადსორბირების პროცესი.
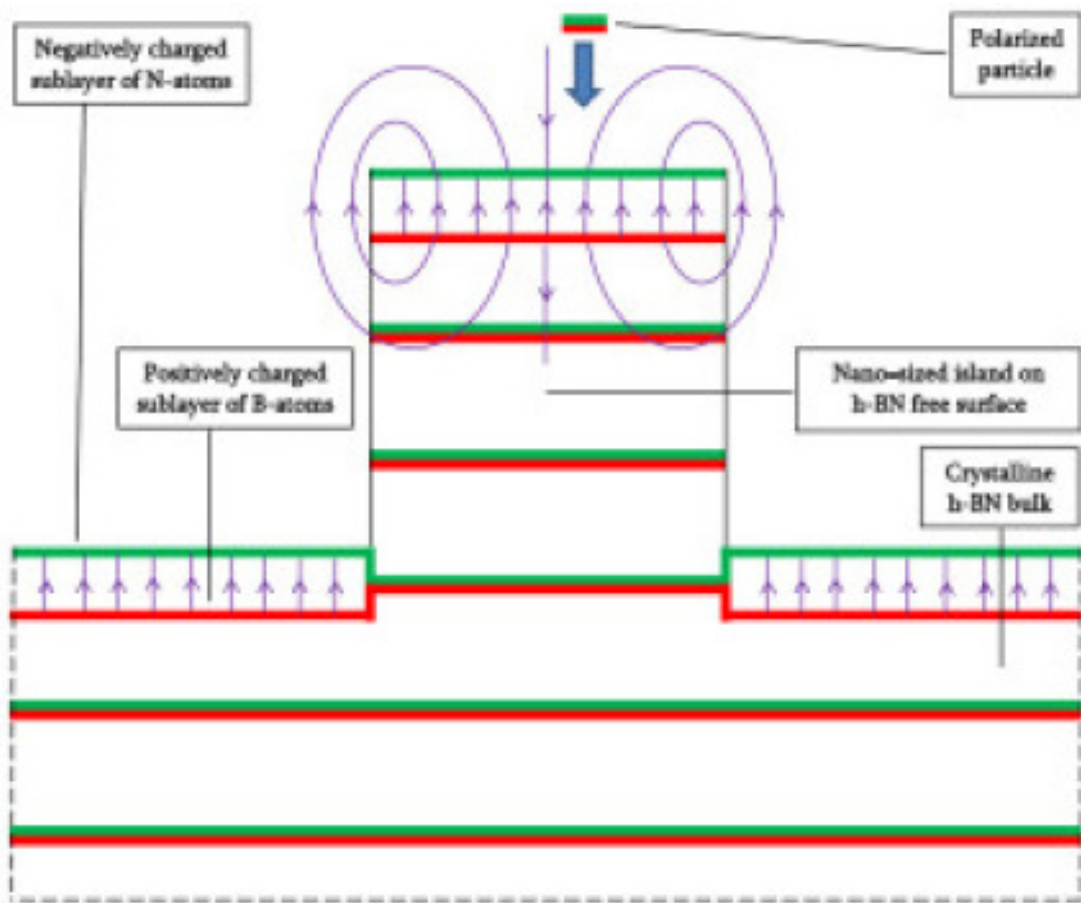
ჰექსაგონალური ბორის ნიტრიდის კრისტალის ნანოსტრუქტურის მქონე ზედაპირის მახლობლად ელექტრული ველის წარმოქმნის მექანიზმი.

აღსანიშნავია, რომ ამავე სტატიამ [1] ნანომედიცინის მიმართულების ათეულამდე აკადემიური ჟურნალის რედაქციის ყურადღებაც მიიპყრო. მათ დაინახეს ამ ნანოეფექტის მედიცინაში გამოყენების პოტენციალი და შემომთავაზეს შემდგომ პუბლიკაციებში შესაბამისი მიმართულებით თემის განვითარება.

2016 წელს გამოვიდა მთელი რიგი სხვა შრომებისა ჩემი (თანა)ავტორობით, რომელიც ეძღვნებოდა ნანოსტრუქტურის მქონე სხვადასხვა მყარი მასალის ფიზიკურ თვისებებს – იხ., მაგალითად, [3 – 15]. მათგან განსაკუთრებით გამოვყოფდი საცნობარო ლიტერატურის აკადემიური გამოცემის უდიდესი ტრადიციის მქონე CRC Press-ის *ნანოტექნოლოგიის მოკლე ენციკლოპედიაში* ჩემ მიერ გამოქვეყნებულ ორ თავს [3, 4], რომლებიც ეძღვნება ბორშემცველ ნანომასალებს, კერძოდ, ელემენტური ბორისა და ბორის ნიტრიდის ნანოსტრუქტურებს.

2016 წელს სხვადასხვა ფორმით მონაწილეობა მივიღე შემდეგ ნანო მასალათმცოდნეობით სამეცნიერო ფორუმებში:

– მეცნიერებათა აკადემიების საერთაშორისო ასოციაციის საბუნებისმეტყველო მეცნიერებათა კომიტეტთან არსებული ახალი მასალების სამეცნიერო საბჭოს 21-ე სესია თემაზე „კომპოზიტური ნანოსტრუქტურული მასალები – მიღება, გამოყენება და რესურსი" (კიევი, უკრაინა);

– კონფერენცია "ლითონებისა და ლითონური სისტემების ფიზიკის უახლესი პრობლემები" (კიევი, უკრაინა).

– მოწინავე და ნანომასალების საერთაშორისო კონფერენცია და გამოფენა – მნმსკგ 2016 (მონრეალო, კანადა);

– მე-9 საერთაშორისო კონფერენცია "მასალები ექსტრემალურ პირობებში" – მეკ 2016 (კიევი, უკრაინა);

– მეტალურგიისა და მასალების მე-18 საერთაშორისო კონგრესი – მმსკ 2016 (სტამბოლი, თურქეთი);

– მე-4 საერთაშორისო კონფერენცია "ნანოტექნოლოგიები" – ნანო 2016 (თბილისი, საქართველო); და

– სრულიად რუსეთის მე-6 კონფერენცია ნანომასალებზე (მოსკოვი, რუსეთი).

ნანო 2016-ში, რომელიც თბილისში, საქართველოში, ჩაატარა საქართველოს ტექნიკურმა უნივერსიტეტმა, ვმონაწილეობდი არამარტო სამეცნიერო მოხსენებებით, არამედ ამ ღონისძიების ერთ-ერთი ძირითადი ორგანიზატორიც გახლდით.

წლის ბოლოს საქართველოს მეცნიერებათა ეროვნულმა აკადემიამ დამაჯილდოვა 2016 წლის საპატიო სიგელით მეცნიერული მიღწევებისათვის *ნანოტექნოლოგიების დარგში*. როგორც აღვნიშნე, ჩემთვის 2016 წელი საერთოდ წარმატებათა მომტანი იყო პროფესიულ საქმიანობაში, მაგრამ ამ ჯილდოს მონიჭებაში სწორედ ნანო– 2016-ის წარმატებით ჩატარებამ შეასრულა არსებითი როლი.

ნანო 2016-თან ერთად უნდა შევჯეხო ჩემ მონაწილეობას მმსკ 2016-შიც. მეტალურგიისა და მასალების მე-18 საერთაშორისო კონგრესში, კერძოდ, ამ გრანდიოზული ფორუმის ფარგლებში გამართულ *ნანომასალების სიმპოზიუმში* ჩემი მონაწილეობა მოკლევადიანი ინდივიდუალური სამოგზაურო სახელმწიფო სამეცნიერო გრანტით ნაწილობრივ დააფინანსა შოთა რუსთაველის ეროვნულმა სამეცნიერო ფონდმა, რისთვისაც ეს ფონდი უდავოდ დაიმსახურებდა ჩემგან დიდ მადლობას, რომ არა ერთი დასასანი გარემოება.

საქმე ისაა, რომ ამ საერთაშორისო სამეცნიერო ღონისძიებაში მონაწილეობის შესახებ საბოლოო ანგარიშის წარმოდგენა დამიგვიანდა და ამ მოტივით მიღებული იქნა

გადაწყვეტილება, რომ ჩემთან, როგორც გრანტის მიმღებთან, სრული ანგარიშსწორება არ მოხდებოდა. ანგარიშის დაგვიანების მიზეზი კი იყო ის, რომ სამოგზაურო გრანტის ანგარიშის მომზადებისა და წარდგენისათვის დადგენილი პერიოდიდაემთხვა მე-4 საერთაშორისო კონფერენციის "ნანოტექნოლოგიები" ჩასატარებლად მზადების დასკვნით ეტაპს და მისმ იმდინარეობას. და ჩემმა ძალზე ინტესიურმა ჩართულობამ ამ პროცესებში არ დამიტოვა არც ერთი თავისუფალი წუთი, რასაც დავუთმობდი რაიმე სხვა საქმეს, მათ შორის, სამოგზაურო გრანტის ანგარიშის მომზადებას.

საქართველოს მეცნიერებათა ეროვნული აკადემიის 2016 წლის საპატიო
სიგელი მეცნიერული მიღწევებისათვის ნანოტექნოლოგიების დარგში.

და რა გამოვიდა? შოთა რუსთაველის ეროვნულმა სამეცნიერო ფონდმა ფაქტობრივად იმავე საქმისათვის – საერთაშორისო სამეცნიერო კონფერენციის ორგანიზებისათვის – დამახჯარიმა, რისთვისაც დამახჯილდოვა საქართველოს მეცნიერებათა ეროვნულმა აკადემიამ. ცხადია, ეს არ შეესაბამება ფონდის მიერ დეკლარირებულ მიზნებს, კერძოდ, საქართველოში საერთაშორისო სამეცნიერო ღონისძიებების ჩატარებისათვის ხელშეწყობას.

ქვემოთ ვაქვეყნებ ამ საკითხთან დაკავშირებით ჩემ მიმართვებს შოთა რუსთაველის ეროვნული სამეცნიერო ფონდის მაშინდელი გენერალური დირექტორისადმი. ვიმედოვნებ, მათი გაცნობით მკითხველი შეიქმნის წარმოდგენას, თუ როგორ დასრულდა ჩემთვის "ნანო – 2016".

*   *   *

2016 წლის 26 დეკემბერი

სსიპ შოთა რუსთაველის ეროვნული სამეცნიერო ფონდის
გენერალურ დირექტორს **მარინე ჩიტაშვილს**
პროფესორ **ლევან ჩხარტიშვილის**
(ა. ყაზბეგისგამზ. 11, ბინა 12, თბილისი, საქართველო,
ტელ.: 5 99 34 07 36, ე-ფოსტა: chkharti2003@yahoo.com)

განცხადება

ქალბატონო მარინე!

მოგმართავთ მოკლევადიან ინდივიდუალურ სამოგზაურო სახელმწიფო სამეცნიერო გრანტთან (# 03 / 75) დაკავშირებით, რომლითაც თქვენდამდი რწმუნებულმა ფონდმა ნაწილობრივ დააფინანსა ჩემი მონაწილეობა მეტალურგიისა და მასალების მე-18 საერთაშორისო კონგრესში (2016 წლის 29 სექტემბერი – 1 ოქტომბერი, სტამბოლი, თურქეთი) – ММК – 2016, კერძოდ, ამ კონგრესის ფარგლებში გამართულ ნანომასალების სიმპოზიუმში.

ეს იყო გრანდიოზული ფორუმი, რომელიც აერთიანებდა 10 სამეცნიერო სიმპოზიუმს, ახალგაზრდა მეცნიერთა საერთაშორისო სკოლას და მეტალურგიული და ქიმიური მრეწველობის ტექნიკის დიდ გამოფენას. დაახლოებით 850 დელეგატმა 300-მდე მოხსენება წარმოადგინა. ჩემი მოხსენების სრული ტექსტი სტატიის სახით გამოქვეყნდა კონგრესის მასალებში: www.metalurji.org.tr. მთლიანობაში ММК – 2016 უაღრესად ნაყოფიერი გამოდგა როგორც წმინდა მეცნიერული, ისე – თანამშრომლობის განვითარების თვალსაზრისითაც.

მაგრამ, სამწუხაროდ, ამ საერთაშორისო სამეცნიერო ღონისძიებაში მონაწილეობის შესახებ საბოლოო ანგარიშის წარმოდგენა დამიგვიანდა და ამ მოტივით მიღებული იქნა გადაწყვეტილება, რომ ჩემთან, როგორც გრანტის მიმღებთან, სრული ანგარიშსწორება არ მოხდება. ანგარიშის დაგვიანების მიზეზი უკვე განვმარტე ფონდისადმი ჩემს განცხადებაში, მაგრამ ამან შედეგი არ გამოიღო. ამიტომ პირადად თქვენც მოგახსენებთ, რომ თავად განსაჯოთ, საპატიო იყო თუ არა ეს მიზეზი.

საქმე ისაა, რომ ამ სამოგზაურო გრანტის ანგარიშის მომზადებისა და წარდგენისათვის დადგენილი პერიოდი დაემთხვა მე-4 საერთაშორისო კონფერენციის "ნანოტექნოლოგიები", 2016 წლის 24 – 27 ოქტომბერი, თბილისი, საქართველო (ნანო – 2016) ჩასატარებლად მზადების დასკვნით ეტაპს და მის მიმდინარეობას საქართველოს ტექნიკურ უნივერსიტეტში.

ნანო – 2016 ჩვენი ქვეყნისათვის უპრეცედენტო მასშტაბის საერთაშორისო სამეცნიერო ღონისძიება იყო: წარმოდგენილ იქნა 209 მოხსენება ავტორების მიერ მსოფლიოს 32 ქვეყნის წამყვანი უნივერსიტეტებიდან და სხვა კვლევითი დაწესებულებებიდან; თბილისში კონფერენციის 100-მდე უცხოელი მონაწილე ჩამოვიდა; კონფერენციის ფარგლებში შვეიცარულმა ფირმა მNanosurf გამართა საკუთარი წარმოების უახლესი ნანოგამზომი აპარატურის გამოფენა; წარმოდგენილი მოხსენებების ნაწილი ფეერ-რეცენზირების შემდეგ ქვეყნდება კონფერენციის პარტნიორ 4 საერთაშორისო სამეცნიერო ჟურნალში და ა.შ.

მე, როგორც კონფერენციის საერთაშორისო სამეცნიერო კომიტეტის წევრი მასპინძელი ქვეყნიდან და ორგანიზატორი დაწესებულებიდან, ეროვნული

საორგანიზაციო კომიტეტის წევრი და მდივანი, მოხსენებათა თეზისების კრებულის და კონფერენციის პროგრამის შემდგენელი, საერთაშორისო მიმოწერაზე და კონფერენციის ფარგლებში გამართულ გამოფენებზე პასუხისმგებელი პირი, კონფერენციის სოციალური პროგრამის ორგანიზატორი, კონფერენციის პარტნიორი საერთაშორისო ჟურნალების რედაქტორი / რედკოლეგიების წევრი და ა.შ., ძალზე ინტენსიურად ვიყავი ჩართული კონფერენციის მომზადებასა და ჩატარებაში. ყოველივე ამან არ დამიტოვა არც ერთი თავისუფალი წუთი, რასაც დავუთმობდი რაიმე სხვა საქმეს, მათ შორის, სამოგზაურო გრანტის ანგარიშის მომზადებას.

ახლახან საქართველოს მეცნიერებათა ეროვნულმა აკადემიამ დამაჯილდოვა 2016 წლის საპატიო სიგელით მეცნიერული მიღწევებისათვის "ნანოტექნოლოგიების" დარგში. ჩემთვის 2016 წელი საერთოდ წარმატებათა მომტანი იყო პროფესიულ საქმიანობაში, მაგრამ ამ ჯილდოს მონიჭებაში სწორედ ნანო – 2016-ის წარმატებით ჩატარებამ შეასრულა არსებითი როლი.

და რა გამოდის? შოთა რუსთაველის ეროვნული სამეცნიერო ფონდი ამავე საქმისათვის – საერთაშორისო სამეცნიერო კონფერენციისო რგანიზებისათვის – მაჯარიმებს. ცხადია, ეს არ შეესაბამება ფონდის მიერ დეკლარირებულ მიზნებს.

ამიტომ დაბეჯითებით გთხოვთ, რომ გადახედოთ მიღებულ გადაწყვეტილებას და სამოგზაურო გრანტთან დაკავშირებით ჩემთან განხორციელდეს სრული ანგარიშსწორება.

პატივისცემით,
ლევან ჩხარტიშვილი

ფიზიკა-მათემატიკის მეცნიერებათა დოქტორი

პროფესორი
საინჟინრო ფიზიკის დეპარტამენტი
საქართველოს ტექნიკური უნივერსიტეტი

უფროსი მეცნიერი თანამშრომელი
ბორშემცველი და კომპოზიტური მასალების ლაბორატორია
ფ. თავაძის მეტალურგიისა და მასალათმცოდნეობის ინსტიტუტი

P.S.   მე-4 საერთაშორისო კონფერენციის "ნანოტექნოლოგიები" ხარჯები მთლიანად თავის თავზე აიღო ორგანიზატორმა – საქართველოს ტექნიკურმა უნივერსიტეტმა. არ შემიძლია ამასთან დაკავშირებით სინანულით არ აღვნიშნო, რომ შოთა რუსთაველის ფონდმა ვერ აუდო ალღო ამ სამეცნიერო ფორუმის მნიშვნელოვნებას და მასშტაბურობას და, ასევე, დარგის პრიორიტეტულობას, და არ დააფინანსა შესაბამისი საკონფერენციო გრანტის პროექტი.

*   *   *

2017 წლის 16 იანვარი

გამარჯობა ქალბატონო მარინე!
2016 წლის 26 დეკემბერს ოფიციალურად მოგმართეთ განცხადებით, რაზეც მივიღე 2017 წლის 12 იანვრით დათარიღებული პასუხი, დამოწმებული თქვენი ფაქსიმილით. სამწუხაროდ, მისი შინაარსი შეუსაბამოა განცხადებაში გამოთქმულ თხოვნასთან. ამიტომ ორივე ამ დოკუმენტს ელექტრონული ფოსტით გიგზავნით.

როგორც ხედავთ, საქმე ეხება ჩემ მიერ სამოგზაურო გრანტის (# 03 / 75) ანგარიშის წარმოდგენის დაგვიანებასთან დაკავშირებით ფონდის მიერ მიღებულ გადაწყვეტილებას, რომ ჩემთან, როგორც გრანტის მიმღებთან, არ მოხდეს სრული ანგარიშსწორება. განცხადებაში მე გთხოვდით, გადაგეხედათ ამ გადაწყვეტილებისათვის, რადგანაც ანგარიშის წარმოდგენის დაგვიანებას ჰქონდა საპატიო მიზეზი – ჩემი უაღრესად ინტენსიური ჩართულობა საქართველოში მასშტაბური საერთაშორისო სამეცნიერო კონფერენციის ორგანიზებასა და ჩატარებაში.

პასუხში მოტანილია სამოგზაურო გრანტების შესახებ არსებული დებულების შესაბამისი მუხლი და ფონდთან ჩემ მიერ გაფორმებული ხელშეკრულების ის პირობები, რასაც თავადვე აღვნიშნავდი განცხადებაში. გაკეთებულია დასკვნა, რომ ფონდი უფლებამოსილი იყო ასე ემოქმედა. <u>პასუხგაუცემელი დარჩა ჩემი კითხვა</u> იყო თუ არა ანგარიშის წარმოდგენის დაგვიანება საპატიო?

ფონდი უფლებამოსილი იყო ასე ემოქმედა, თუ მიზეზს ჩათვლიდა არასაპატიოდ. მაგრამ წინააღმდეგ შემთხვევაში <u>სულაც არ იყო ვალდებული ასე ემოქმედა:</u> თუკი ანგარიშის წარმოდგენის დაგვიანება საპატიო მიზეზით მოხდა, მაშინ ფონდს დებულება არ უკრძალავს ჩემთან სრული ანგარიშსწორების განხორციელებას.

ამრიგად, ქალბატონო მარინე, თქვენგან, როგორც შოთა რუსთაველის ეროვნული სამეცნიერო ფონდის გენერალური დირექტორისაგან, ველოდები ცალსახა განმარტებას, არის თუ არა სამოგზაურო გრანტის ანგარიშის წარმოდგენის დაგვიანებისათვის საპატიო მიზეზი გრანტის მიმღების მიერ საერთაშორისო სამეცნიერო კონფერენციის მომზადება და ჩატარება.

ცხადია, გესმით, რომ ჩემთვის ამჯამად პრინციპულია არა გრანტის ხარჯთაღრიცხვით გათვალისწინებული თანხის 10 %-ის მიღება, არამედ ის, რომ არ აღმოვჩნდე ეროვნული სამეცნიერო ფონდის მიერ ფინანსურად დასჯილი (დაჯარიმებული) საერთაშორისო სამეცნიერო ფორუმის ჩატარებისათვის.

პატივისცემით,
ლევან ჩხარტიშვილი

ფიზიკა-მათემატიკის მეცნიერებათა დოქტორი

პროფესორი
საინჟინრო ფიზიკის დეპარტამენტი
საქართველოს ტექნიკური უნივერსიტეტი

უფროსი მეცნიერი თანამშრომელი
ბორშემცველი და კომპოზიტური მასალების ლაბორატორია
ფ. თავაძის მეტალურგიისა და მასალათმცოდნეობის ინსტიტუტი

*   *   *

<u>2017 წლის 17 იანვარი</u>

გამარჯობა ქალბატონო მარინე!
დიდი მადლობა, რომ გაეცანით ჩემ წერილს და მომეცით განმარტება იქ დასმულ შეკითხვასთან დაკავშირებით.
თუმცა მიჭირს დავეთანხმო დებულების იმგვარ ინტერპრეტაციას, რომ გრანტის მიმღების მიერ ფონდში ანგარიშის წარმოდგენის დაგვიანების საპატიო მიზეზი

მხოლოდ და მხოლოდ ფორს-მაჟორთან ანუ სტიქიურ უბედურებასთან ან საომარ მოქმედებასთან შეიძლება იყოს დაკავშირებული.

ვთქვათ, ჩემი შემოთხვევა – ფონდის დეკლარირებულ მიზნებთან შესაბამისი, მაგრამ მაინც სხვა, საქმით გადაუდებელი დაკავებულობა – არ მიგაჩნიათ საპატიო საპატიო მიზეზად, მაგრამ რა ვუყოთ, მაგალითად, გრანტის მიმღების ავადმყოფობას? არც ეს იქნება საპატიო? ანდა გრანტის მიმღების ყოფნა ქვეყნის გარეთ?

წელს კვლავ ვაპირებ მოგმართოთ სამოგზაურო გრანტისათვის გერმანიაში გასამართ სიმპოზიუმში მონაწილეობასთან დაკავშირებით. ამ სიმპოზიუმის დასრულებიდან 2 დღის შემდეგ უკრაინაში იწყება 6-დღიანი კონფერენცია, რომელშიც ასევე ვმონაწილეობ. ასე რომ, თუ ჩემი აპლიკაცია წარმატებული გამოდგა და სამოგზაურო გრანტი მოვიპოვე, წინასწარ მეცოდინება, რომ ანგარიშის წარმოდგენას 10 სამუშაო დღეში ვერ მოვასწრებ და ისევ „დავჯარიმდები".

გმადლობთ ინფორმაციისათვის, რომ 2017 წლის კონკურსები ახალი ფორმით და წესით ჩატარდება. იმედი მაქვს, რომ საკონფერენციო გრანტების კონკურსის ახალი პირობებით ღონისძიების შეფასებისას სათანადოდ იქნება გათვალისწინებული მისი რეგულარულობა, მასშტაბი, ცნობადობა და თემატიკის პრიორიტეტულობა.

პატივისცემით,
ლევან ჩხარტიშვილი

დამოწმებანი

1. L. Chkhartishvili. Nanoparticles near-surface electric field. Nanoscale Res.Lett., 2016, 11, 1, 48 (1-4).
2. L. Chkhartishvili. Nanostructure makes crystalline compound physically reactive. Atlas Sci., 2016, April 14, 1-2.
3. L. Chkhartishvili. Boron nanostructures: All-boron nanostructures. In: CRC Concise Encyclopedia of Nanotechnology (Eds. B. I. Kharisov, O. V. Kharissova, U. Ortiz–Mendez), 2016, Boca Raton,CRC Press, Ch.7 – 53-69.
4. L. Chkhartishvili. Boron nanostructures: Boron nitride nanostructures. In: CRC Concise Encyclopedia of Nanotechnology (Eds. B. I. Kharisov, O. V. Kharissova, U. Ortiz–Mendez), 2016, Boca Raton,CRC Press, Ch.8 – 70-99.
5. T. Pagava, L. Chkhartishvili, M. Beridze. Formation and annealing of nano-sized atomic clusters in n-Si crystals irradiated with high-energy protons. NATO Sci. Peace & Sec. Ser. B: Phys.& Biophys. – In: Nuclear Radiation Nanosensors and Nanosensory Systems (Eds. P. J. Kervalishvili, P. H. Yannakopoulos), 2016, Dordrecht, Springer Science + Business Media Dordrecht, Ch.4 – 33-51.
6. L. Chkhartishvili, O. Tsagareishvili, G. Tavadze. Neutron detectors based on ^{10}B-containing nanomaterials. NATO Sci. Peace & Sec. Ser. B: Phys.& Biophys. – In: Nuclear Radiation Nanosensors and Nanosensory Systems (Eds. P. J. Kervalishvili, P. H. Yannakopoulos), 2016, Dordrecht, Springer Science + Business Media Dordrecht, Ch.12 – 187-196.
7. A. Oaklay, D. Macharadze, M. Ratishvili, B. Margiev, L. Chkhartishvili. Modification of chromium steel by nano-oxide composite. Proc. Georg. Natl. Acad. Sci. (Chem. Ser.), 2016, 42, 4, 516-519.

8. L. Chkhartishvili. Small elemental clusters in pair interaction approximation.In: Proc. ICANM 2016: Int. Conf. & Exh. Adv. & Nano Mater., 2016, Montreal, IAEMM, 128-132.

9. L. Sartinska, L. Chkhartishvili. Effect of concentrated light on boron nitride nanostructures formation. In: Springer Proc. Phys. Ser. 183 – Nanophysics, Nanophotonics, Surface Studies, and Applications (Eds. O. Fesenko, L. Yatsenko), 2016, Springer Int. Publ., Ch.10 – 117-130.

10. Л. С. Чхартишвили. Расчет емкости наноразмерных конденсаторов. В сб.: Матер. 6-й Всеросс. конф. понаноматер. (НАНО 2016), 2016, Москва, ИМЕТ РАН, 436-437.

11. L. Chkhartishvili, A. Gachechiladze, O. Tsagaeishvili, D. Gabunia. Capacitances built in nanocomposites. In: Proc. 18th Int. Metall. & Mater. Cong., 2016, Istanbul, UCTEA, 306-308.

12. Г. Ф. Тавадзе, Л. С. Чхартишвили. Разработка нанотехнологий получения композиционных материалов в Институте металлургии и материаловедения им. Фердинанда Тавадзе – Достижения и перспективы. Nano Studies, 2016, 13, 59-78.

13. A. Gachechiladze, A. Oakley, B. Margiev, O. Tsagareishvili, L. Chkhartishvili, M. Ratishvili. Some properties of nano objects and on modification of steel melts by nanocomposites. Nano Studies, 2016, 13, 83-92.

14. L. Chkhartishvili, G. Tabatadze, D. Nackebia, T. Bzhalava, I. Kalandadze. Hexagonal boron nitride as a solid lubricant additive (An overview). Nano Studies, 2016, 14, 91-98.

15. L. Chkhartishvili. Quasi-planar elemental clusters in pair interactions approximation. Open Phys., 2016, 14, 1, 617-620.

ლევან ჩხარტიშვილი

2017 წლის 26 აპრილი